Particle Scale Analysis of Soil Stiffness and Elastic Wave Propagation

A thesis submitted in partial fulfilment of the requirements of

the Doctor of Philosophy (PhD) degree

and the Diploma of Imperial College (DIC)

By

Masahide Otsubo

Department of Civil and Environmental Engineering

Imperial College London

London SW7 2AZ

November 2016

Abstract

Soils are granular materials consisting of many particles, and the overall response of a soil can be considered to be a complex accumulation of the inter-particle responses. Small-strain soil stiffness is important to predict the ground deformation in situ and in practice and is often deduced from elastic wave velocity in laboratory experiments. The dynamic properties of soils are also important for dynamic analyses including site response analysis.

Stress waves propagate through soil via the grain contact network, thus the actual particle-scale mechanics differ from those assumed in continuum mechanics which is often used to simulate and analyse stress wave propagation. Thus the particle properties including surface characteristics should have a direct impact on the overall response of soil to stress wave disturbances. Surface roughness effects on the inter-particle response have previously been considered in the experimental work of Cavarretta (2009) and in the dynamic analyses using the discrete element method (DEM) described by O'Donovan (2013).

This research aims to develop understanding of the extent of the sensitivity of soil stiffness to the contact rheology by adopting theoretical, numerical (DEM) and experimental approaches. The theoretical approach follows Yimsiri & Soga (2000) who combined micromechanical effective medium theory and a rough surface contact model; their approach is revisited here considering more recent UK-based tribology studies. The contact laws considered in the DEM analyses presented here include particle surface roughness, partial slip at tangential contacts, and spin resistance based on these developments by the work of O'Donovan (2013). The experimental approach used two types of dynamic tests: bender element tests in a cubical cell apparatus, and shear plate tests in a triaxial apparatus. For both test types, smooth and rough surface spherical ballotini are used to study the surface roughness effects on the sample shear modulus. Shear plates are not commonly used in soil mechanics dynamic testing and so the study also included an assessment of this technology.

The data generated show that the small-strain stiffness of granular materials is measurably reduced sensitively with the surface roughness especially at a low stress level. This explains partially a higher exponent n value in the relationship between the shear modulus and the confining stress ($n > 0.5$). As the stress level increases the shear modulus of the assembly of rough particles approach the smooth equivalent.

Declaration

The work presented in this thesis was carried out in the Department of Civil and Environmental Engineering at Imperial College London.

This thesis is the result of my own work and any quotation from, or description of the work of others is acknowledged herein by reference to the sources, whether published or unpublished. This thesis is not the same as any that I have submitted for any degree, diploma or other qualification at any other university. No part of this thesis has been or is being concurrently submitted for any such degree, diploma or other qualification.

Masahide Otsubo

London, November 2016

Acknowledgements

Firstly, I would like to express my sincere gratitude to my supervisor Dr. Catherine O'Sullivan for her continuous and comprehensive support throughout my PhD. I have been inspired by her motivation and attitude toward research all the time. I would like to express my special appreciation to my co-supervisor Dr. Way Way Sim for her kind support during my PhD study. I have been encouraged by her constructive support especially at the beginning of my PhD. I am proud of having been supervised by them throughout my PhD.

I am also profoundly grateful to Dr. Hanley John Kevin (now at the University of Edinburgh). His enormous support on the numerical part of my research was invaluable.

I would like to thank all the technical staff in Geotechnics section for their technical assistance in laboratory. I especially appreciate Mr. Steven Ackerley and Mr. Parker Duncan for their kind help and passion to develop advanced laboratory techniques.

My deep gratitude is also expressed to Dr. Erdin Ibraim at the University of Bristol for experimental collaboration at the beginning of my PhD program. My sincere thanks go to the examiners of this thesis Prof. David Muir Wood and Dr. Stavroula Kontoe.

This project was founded by Japanese Student Services Organization and the Dixon scholarship by Imperial College London. This thesis would not have been possible without their financial support.

I am also thankful for all the excellent PhD colleagues and academic staff in Geotechnics section. Amongst them, I would like to name Daniel Martinez Calonge, Emil Ushev and Tingfa Liu for their help and useful discussion in laboratory, Dr. Howard Taylor, Christopher Knight, Hoang Nguyen, Dr. Tom Shire, Dr. Matteo Ciantia and Dr. Xin Huang (now at Tongji University) for constructive discussion from a micromechanical perspective, Mr. Kenichi Kawano and Dr. Hidenori Takahashi as my wonderful colleagues from Japan, and Sarah Tallett-Williams, Vasiliki Tsaparli and Klementyna Gawecka for their kindness throughout my PhD life.

Last but not least, I would like to thank my parents for their unconditional support and my wife, Tomomi, for making my life in London fruitful. Without their help, I would not have been able to be as deeply involved in my PhD study.

Table of contents

List of figures

List of tables

List of symbols

A	amplitude of input sinusoidal pulse
a	circular contact area radius
a^{Rough}	circular contact area radius (rough contacts)
a^{Smooth}	circular contact area radius (smooth contacts)
B	constant
b	power function exponent
C	stiffness between neighbouring layers
C_N	coordination number per particle
$\overline{C_N}$	mean coordination number of sample
$\overline{C_N^*}$	mechanical mean coordination number of sample
c	constant
D	particle diameter
E_0	small-strain Young's modulus of sample
E_p	particle Young's modulus
E_p^*	equivalent Young's modulus of contacting particles
e	sample void ratio
e^*	mechanical sample void ratio
F	force
$F(e)$	void ratio correction function for sample small-strain modulus
f	frequency
f_i	eigenfrequency
$f_{i,max}$	maximum eigenfrequency
f_{in}	nominal frequency of input sinusoidal pulse
$f_{low\text{-}pass}$	low-pass frequency
f_r	resonant frequency
$f(e)$	void ratio correction function for wave velocity

G_0	small-strain shear modulus of sample
G_p	particle shear modulus
G_p^*	equivalent shear modulus of contacting particles
g	gravitational acceleration
H	surface hardness
I	moment of inertia of particle
i	particle i
$\boldsymbol{K}$	global stiffness matrix
K_N	secant normal contact stiffness
k_N	normal contact stiffness
k_R	rolling contact stiffness
k_r	twisting (or spin) contact stiffness
k_T	tangential contact stiffness
L	sample length
l	layer spacing
$\boldsymbol{M}$	global mass matrix
M	moment
M_0	small-strain constraint modulus of sample
M_R	inter-particle rolling moment
M_R^{max}	slip limit of inter-particle rolling moment
M_r	inter-particle twisting (or spin) moment
M_r^{max}	slip limit of inter-particle twisting (or spin) moment
m	mass of particle
N	normal inter-particle contact force
N_{T1}	threshold normal inter-particle contact force
N_{T2}	threshold normal inter-particle contact force
n	power function exponent
R	particle radius

R^*	equivalent radius of contacting particles
R_k	contact stiffness ratio (= k_T/k_N)
S_a	average surface roughness
S_q	root mean square (RMS) surface roughness
S_q^*	combined RMS surface roughness of contacting particles
s	tangential contact displacement
T	tangential contact force
T^*	maximum tangential contact force in history
T^{**}	minimum tangential contact force in history
T^{max}	slip limit of tangential contact force
t	time
V_{group}	group velocity
V_{phase}	phase velocity
V_P	compression (*P*-) wave velocity
V_S	shear (*S*-) wave velocity
$V_{S,dL/dt}$	*S*-wave velocity estimated using particle displacement
$V_{S,dispersion}$	*S*-wave velocity estimated using dispersion relation
$V_{S,P\text{-}P}$	*S*-wave velocity estimated using peak-to-peak method
$V_{S,SP}$	*S*-wave velocity estimated using stacked phase method
Z_i	surface elevation relative to reference surface
z	distance from transmitter wall
$\ddot{x}$	acceleration of particle
α	non-dimensional roughness parameter
δ	overlap of contacting particles
δ^{Rough}	overlap of contacting particles (rough contacts)
δ^{Smooth}	overlap of contacting particles (smooth contacts)
δ_1	constant (in displacement)
δ_2	constant (in displacement)

δ_{skin}	skin thickness
δ_{T1}	threshold overlap of contacting particles at $N = N_{T1}$
δ_{T2}	threshold overlap of contacting particles at $N = N_{T2}$
θ	degree of partial slip at tangential contact
θ_r	degree of partial slip at twisting contact
κ	wavenumber (= $2\pi/\lambda$)
λ	wavelength
$\lambda_{low\text{-}pass}$	low-pass wavelength
μ	coefficient of inter-particle friction
μ_{prep}	coefficient of inter-particle friction during isotropic compression
μ_{wave}	coefficient of inter-particle friction during wave propagation
ν_p	particle Poisson's ratio
ν_S	sample Poisson's ratio
ρ_d	dry sample bulk density
ρ_p	particle density
σ'	effective isotropic confining stress
σ'_V	effective vertical stress
ε	axial strain of sample
$\dot{\varepsilon}$	axial strain rate of sample
φ	rotation angle of particle
φ_R	rolling angle of particle
φ_r	twisting (or spin) angle of particle
$\ddot{\varphi}$	angular acceleration of particle
$\boldsymbol{\phi}$	eigenvectors
ω	angular frequency (= $2\pi f$)
χ	correlation index of eigenmode

CHAPTER 1
Introduction

1.1 Background

Accurate knowledge of soil stiffness is important to predict ground deformation during construction, as it directly relates the applied stress to the strain and hence the displacement of the ground (Atkinson, 2000; Clayton, 2011). Soil stiffness is also important to predict site response to earthquake loading and is an input parameter in a finite element modelling (Potts, 2003). Soil stiffness is non-linear; it decreases with increasing strain level. The small-strain stiffness is an upper limit of the stiffness, and it can be estimated using geophysics tests including sound or stress wave propagation tests in situ or in laboratory.

It is also well known that the small-strain shear modulus (G_0) is influenced by the effective confining stress (σ') and the void ratio (e), and is often expressed as $G_0 = AF(e)\sigma'^{n}$ where A and n are constants and $F(e)$ is a void ratio correction function. The density- and stress-dependencies of the small-strain stiffness result from the nature of granular materials. A variety of expressions for $F(e)$ have been proposed by many researchers (Mitchell & Soga, 2005). However, the exponential constant n that describes the stress-dependency of the soils is often approximated to be 0.5. From a micromechanical perspective, the n value directly relates to the response at the contacts (Yimsiri & Soga, 2000). Hertzian contact mechanics (Johnson, 1985) assumes perfectly smooth surfaces and predicts n to be 1/3. The discrepancy between this theoretical prediction and experimental observations can be attributed partially to the non-Hertzian nature of contact behaviour (Goddard, 1990; McDowell & Bolton, 2001).

In the earlier experimental studies by Santamarina & Cascante (1998) and Sharifipour & Dano (2006), surface roughness was shown to measurably reduce G_0; however, they did not quantify (measure) roughness. These experimental results agree with Greenwood & Tripp (1967) who studied the behaviour of a rough contact and found the surface roughness reduces the inter-particle stiffness. Cavarretta (2009) conducted particle compression tests and related the surface roughness to the particle-scale force-deformation relationship, and the constitutive model he proposed was implemented in the DEM simulations conducted by O'Donovan (2013).

In geotechnical engineering dynamic tests are often conducted to study the small-strain stiffness of soils using a resonant column device (Hardin & Richart, 1963) or bender elements (Shirley &

Hampton, 1978). The resonant column device adopts a frequency domain approach to estimate the wave velocity. Both time domain (TD) and frequency domain (FD) approaches can be used for the interpretation of bender element signals. However, it is a challenge to achieve good agreement between the two approaches in bender element testing (Yamashita et al., 2009).

1.2 Scope of research

The overall aim of the thesis is to develop understanding of the nature of the small-strain stiffness and the dynamic behaviour of soil at small strains. Specifically, the influence of surface characteristics on the small-strain shear modulus (G_0) is explored using theoretical, numerical and experimental approaches. To isolate the effect of the surface characteristics from the other particle shape parameters spherical glass beads (ballotini) are used as analogues of soils.

The recent development of optical interferometry has enabled accurate measurement of the surface topography of a soil grain (Altuhafi & Coop, 2011; Yang et al., 2016). The effect of the curvature of a soil grain should be removed to quantify the surface roughness. Once the surface roughness is measured it can be related to the contact stiffness as studied in tribology research (e.g. Greenwood & Tripp, 1967; Gonzalez-Valadez et al., 2010); the contact stiffness can be used in theoretical micromechanical based models (Chang & Liao, 1994) or numerical analysis such as discrete element method (DEM) (Cundall & Strack, 1979).

Effective medium theory relates the sample small-strain stiffness to the contact stiffness, e and mean coordination number ($\overline{C_N}$), i.e. the number of per particle contacts (Chang & Liao, 1994). However, it is difficult to measure $\overline{C_N}$ in practice. Thus the small-strain stiffness of soils is related to e assuming that there is a unique $\overline{C_N}$ - e relationship. This study investigates the packing characteristics of granular materials using ink tests (Bernal & Mason, 1960) and μCT tests. The stress-dependency of the $\overline{C_N}$ - e relationship is further explored comparing with supplemental DEM analyses.

DEM is a powerful tool to study the local and overall responses of granular materials, and the number of published papers relating to DEM has increased significantly over the past 20-25 years (O'Sullivan, 2014). This study uses a modified version of the LAMMPS code (Pinson et al., 1998). When a DEM simulation is performed a contact law, i.e. force-displacement relationship, must be prescribed. Departing from the simplified Hertzian contact theory often used in DEM simulations this study considers a rough surface model, a tangential contact model that considers partial slip and a spin resistance model.

Investigations of the nature of the stress wave propagation through granular media provide essential material properties and are often conducted for engineering applications. The influences of e, $\overline{C_N}$, σ' and contact model on the small-strain stiffness and the system response are discussed using DEM. The DEM simulation method used here follows Mouraille & Luding (2008) and O'Donovan (2013); and the simulations were designed so that the boundary responses can be compared with equivalent measurements in laboratory experiments.

Laboratory dynamic tests were carried out in this study using bender elements in a cubical cell apparatus at the University of Bristol (Sadek, 2006) and using shear plates (Brignoli et al., 1996) in a triaxial apparatus at Imperial College London. Smooth and rough surface ballotini were tested and the G_0 data deduced are discussed. Considering the shear plate test condition, equivalent DEM simulations were conducted to gain additional insight into the system response. Investigating both the TD and FD approaches gives a comprehensive picture of the system response, and the wave velocities based on the two approaches are compared. The DEM analyses give particle scale response and more enhanced methods to determine the wave velocities are compared. Moreover, the low-pass frequency ($f_{low\text{-}pass}$) and wavelength ($\lambda_{low\text{-}pass}$) values are studied using the experiments and DEM.

1.3 Research objectives

This study focuses the following key objectives:

Particle surface roughness

In theoretical micromechanical analyses or DEM analyses a Hertzian contact theory is often assumed with a stick-slip model for the tangential contact interaction, i.e. the simplified Hertz-Mindlin (HM) contact model. The HM contact model is well-documented (Johnson, 1985); however, the simplifying assumptions in the model may cause non-physical (unreasonable) responses of an assembly. The sensitivity of the inter-particle stiffness to the surface roughness has been reported analytically (Greenwood, 1967) and experimentally (Cavarretta, 2009). According to micromechanical effective medium theory (EMT) the small-strain moduli of an assembly vary proportionally with the inter-particle normal contact stiffness (Chang & Liao, 1994). To assess the extent of the influence of surface roughness on the overall small-strain stiffness, this study conducts dynamic geophysics tests using rough particle assemblies by experimental and numerical (DEM) approaches.

Dynamic response in laboratory geophysics tests

Dynamic geophysics tests of stress or sound wave propagation provide essential elastic properties of geotechnical materials. Resonant column tests (Hardin & Richart, 1963) or bender

element tests (Shirley & Hampton, 1978) are widely used to measure the sample shear modulus at small strain levels in laboratory. They are useful; however, those methods consider the data available at only the top and bottom boundaries of the sample. Development of DEM analysis enables simulation of stress wave propagation in a similar manner to the laboratory tests (Mouraille et al., 2006), and the DEM analysis provides additional insight into the particle scale data. To relate the inter-particle responses to the overall responses of an assembly, a series of DEM simulations is carried out in this study. Specifically, dynamic properties including the wave velocity, the sample Poisson's ratio and the low-pass frequency (or wavelength) are investigated by controlling void ratio, stress level and contact models systematically.

Use of shear plates

Use of shear plates in dynamic tests have been proposed as an alternative to the conventional method of using bender elements (Brignoli et al., 1996; Ismail & Rammah, 2005; Suwal & Kuwano, 2013). As shear plates are embedded in the bottom pedestal and top cap, the complex interaction at the interfaces between bender elements and soil is avoided. This also allows the dynamic tests to be more easily modelled using DEM. This study considers shear plates installed in a triaxial apparatus. As summarised in Yamashita et al. (2009) there is poor agreement of the wave velocities obtained in bender element tests when data from time domain interpretation and frequency domain interpretation are compared. This study revisits the source of the discrepancy using both DEM and experimental data.

1.4 Outline of thesis

This thesis contains seven chapters in total. Chapter 1 introduces the research background, the scope of research and the research objectives, and provides an outline of the thesis.

Chapter 2 provides the reader with basis to understand the contents of the thesis. To develop understanding of the nature of the soil stiffness, the literature relating to inter-particle contact behaviour, packing and wave propagation is synthesised. The theoretical basis of the contact models used in the DEM simulations are introduced. The relationship between the mean coordination number and the void ratio is explored. Dynamic small-strain wave propagation tests are reviewed considering both laboratory experiments and DEM simulations. The micromechanics of small-strain stiffness is introduced from an analytical perspective.

Chapter 3 documents surface roughness measurements that were carried out using an optical interferometer. The challenges associated with measuring surface roughness are discussed, and the results of surface roughness measurements are summarized. Experiments and DEM simulations carried out to study the packing characteristics of the materials considered in later

chapters are reported. Data from experiments that were used to study the $\overline{C_N}$-e correlation (ink tests and μCT tests) are compared with the DEM analysis.

Chapter 4 describes the implementation of new contact models in a modified version of the LAMMPS DEM code. A new rough surface contact model, a tangential contact model that considers partial slip effects, and a torsional contact model are explained. The verification of the models' implementation is described considering single contact responses as well as the overall response of face-centred cubic samples. A new servo-control algorithm developed in this study is introduced.

Chapter 5 considers simulations of plane wave propagation through an assembly of uniformly sized (monodisperse) spheres. The DEM simulation approach, and the methods to determine the wave velocities in both the time domain (TD) and the frequency domain (FD) are introduced. The influence of packing on the wave velocity is discussed. The sensitivity of the system response to the contact models as introduced in Chapter 4 is discussed. The wave velocity obtained using the TD and the FD approaches are compared using both sample boundary response and the particle scale response. An eigenmode analysis approach is developed to determine the fundamental resonance mode and relate it to the wave velocity. The relationship between sample properties and $f_{low\text{-}pass}$ (or $\lambda_{low\text{-}pass}$) are discussed.

Chapter 6 studies the effects of particle surface roughness on the sample small-strain shear modulus (G_0) using two experimental approaches: bender element tests in a cubical cell apparatus, and shear plate tests in a triaxial apparatus. The shear plate tests are simulated using DEM considering the material properties and particle size distribution used in the experiments. The influence of excitation and received area for dynamic tests is assessed and the actual sample response near transmitter using a novel design of shear plates is examined.

Chapter 7 summarises the overall conclusions drawn at each chapter and suggests future research that might extend this study.

CHAPTER 2
Literature review

2.1 Introduction

This chapter provides the reader with a basis to understand the contents of the thesis. To develop understanding of the nature of soil stiffness, literature describing particle-scale interaction, packing and wave propagation is investigated. The fundamentals of the discrete element method (DEM) are briefly explained in Section 2.2. The theoretical basis of the contact models used in DEM simulations are introduced in Section 2.3. Contact theory that considers surface roughness effects developed in tribology research is reviewed in Section 2.4. The packing of granular materials specifically considering the relationship between mean coordination number and void ratio is explored in Section 2.5. Dynamic wave propagation is discussed considering both laboratory experiments and DEM simulations in Section 2.6. The micromechanics of small-strain stiffness is introduced from an analytical perspective in Section 2.7.

2.2 Discrete element method

The discrete element method (DEM) is a powerful tool to simulate the responses of assemblies of particles and it has been widely used in many research fields, e.g. powder engineering, geotechnical engineering, geophysics and solid state physics. The DEM algorithm was proposed by Cundall & Strack (1979). The present research uses a modified version of the molecular dynamic LAMMPS code (Plimpton, 1995) for DEM simulations, as it is developed for parallel computing and can be used with distributed memory high performance computers. As the formulation of a DEM code has been well documented in the PFC3D user manual (Itasca, 2007), this section provides only a brief introduction to it.

2.2.1 General introduction to DEM

There are two main steps in the DEM algorithm: updating particle positions and the calculation of contact forces between contacting particles. Newton's second law describes the motion of an individual particle as:

$$F = m(\ddot{x} - g) \tag{2.2.1}$$

$$M = I\ddot{\varphi} \tag{2.2.2}$$

where F = force acting on the particle; m = mass of the particle; $\ddot{x}$ = acceleration of the particle; g = gravitational acceleration; M = moment on the particle; I = moment of inertia of the particle; $\ddot{\varphi}$ = angular acceleration of the particle motion.

Knowing m and I, the accelerations of translation and rotation are calculated using the current F and M, respectively. To update the particle positions and rotations, a centred finite-difference time integration approach is used. Specifically, Verlet explicit integration which is a second order approximation that is commonly used in DEM codes (e.g. Itasca, 2007; Hanley & O'Sullivan, 2016) is used in the current study.

Once the particle positions have been updated, pairs of contacting particles can be found. In particulate DEM, rigid particles that do not deform are used and they can overlap and detach (lose contact). For each contact, the normal contact force (N) is calculated using the overlap (δ) and the secant spring stiffness in the contact normal direction (i.e. secant normal contact stiffness, K_N):

$$N = K_N \delta \tag{2.2.3}$$

The tangential contact force (T) is usually calculated in an incremental manner. Knowing the incremental tangential contact displacement (Δs) and the incremental tangential contact stiffness (k_T), the incremental tangential contact force (ΔT) is obtained as below:

$$\Delta T = k_T \Delta s \tag{2.2.4}$$

If T exceeds the slip limit T^{max} (= μN) the tangential contact force is rescaled to T^{max}.

The particle rotations take place when tangential contact forces are applied, and the moment is calculated using $T \times$ lever arm. There are three axes of rotational motion: two of the rotational degrees of freedom are about axes in the contact plane (referred to here as rolling) and the other rotational degree of freedom is about the contact normal (referred to here as spin or twisting). When rolling resistance is a concern, the incremental rolling moment can be calculated using the incremental rolling angle ($\Delta\varphi_R$) and the incremental rolling stiffness k_R as below:

$$\Delta M_R = k_R \Delta \varphi_R \tag{2.2.5}$$

For the twisting (or spin) moment, the incremental twisting moment can be calculated using the incremental spin angle ($\Delta\varphi_r$) and the incremental twisting stiffness k_r:

$$\Delta M_r = k_r \Delta \varphi_r \tag{2.2.6}$$

The effects of particle shapes on rolling resistance and spin resistance were considered in Ai et al. (2011) and Huang et al. (2016), whereas Mindlin (1949), Lubkin (1951) and Deresiewicz

(1954) considered spin resistance for spheres. Similar to the tangential contact force, if a slip limit is involved, the rolling and twisting moment forces should be rescaled to M_R^{max} and M_r^{max}, respectively. The resultant forces and moments are used to update the particle positions and rotations for the next time step in Eqs. 2.2.1 and 2.2.2.

2.3 Contact model for smooth surfaces

The contact model affects the overall response of granular simulations using DEM. This section introduces the simplified Hertzian contact model which is widely used in both micromechanical analysis and DEM. In addition to the normal contact force, Hertzian-type contact stiffnesses for the tangential and twisting directions are described.

2.3.1 Normal contact

The Hertzian contact model (Hertz, 1882) is a widely used contact model and it is well documented (Johnson, 1985). This model is often considered to be applicable to soils and has been used as a starting point to explain the relationship between soil shear modulus and confining pressure (McDowell & Bolton, 2001). The Hertzian contact model is applicable to smooth surfaces. The resultant force-deformation relationship is non-linear, even when the spheres themselves are considered to be linear elastic. The normal contact force (N) is expressed as (Johnson, 1985):

$$N = \frac{4}{3} E_p^* R^{*0.5} \delta^{1.5} \tag{2.3.1}$$

where E_p^* = equivalent Young's modulus of two contacting particles; R^* = equivalent radius of two contacting particles; δ = overlap of two contacting particles. The overlap is calculated from the particle positions, whereas E_p^* and R^* depend on the material properties and radii of contacting spheres 1 and 2 as:

$$E_p^* = \left(\frac{1-\nu_{p1}^2}{E_{p1}} + \frac{1-\nu_{p2}^2}{E_{p2}} \right)^{-1} \tag{2.3.2}$$

$$R^* = \left(\frac{1}{R_1} + \frac{1}{R_2} \right)^{-1} \tag{2.3.3}$$

where ν_p = Poisson's ratio of the contacting particles. The radius of the circular contact area (a) is a function of the overlap and the equivalent radius of the two contacting particles (Fig. 2.1):

$$a = \sqrt{R^* \delta} \tag{2.3.4}$$

Rearranging and substituting Eq. 2.3.1 into Eq. 2.3.4 gives:

$$a = \left(\frac{3R^*}{4E_p^*} \right)^{1/3} N^{1/3} \tag{2.3.5}$$

It is clear that a is proportional to $N^{1/3}$. The incremental contact stiffness in the normal direction (k_N) is obtained by differentiating N with respect to δ in Eq. 2.3.1:

$$k_N = \frac{dN}{d\delta} = 2E_p^* R^{*0.5} \delta^{0.5} = 2E_p^* a \tag{2.3.6}$$

Note that k_N is the tangent (incremental) stiffness. The secant stiffness in the normal direction K_N is expressed as:

$$K_N = \frac{N}{\delta} = \frac{4}{3} E_p^* R^{*0.5} \delta^{0.5} = \frac{4}{3} E_p^* a \tag{2.3.7}$$

There is a direct relationship between the tangent (k_N) and secant stiffnesses (K_N):

$$k_N = 1.5 K_N \tag{2.3.8}$$

The expression above is valid for the (non-linear) Hertzian contact model. For a linear contact model, the two stiffnesses are identical (i.e. $k_N^{linear} = K_N^{linear}$).

2.3.2 Tangential contact

Mindlin (1949) extended the work by Hertz (1882) to consider the tangential component of the contact interaction. Figs. 2.2(a) and (b) show the normal pressure (p) and shear pressure (τ) distributions along the radial distance (r) on a no-slip contact. Mindlin (1949) derived the incremental tangential contact stiffness (k_T) using a parameter that describes the degree of partial slip (θ) given by:

$$k_T = 8G_p^* a\, \theta \tag{2.3.9}$$

where G_p^* = equivalent shear modulus of two contacting particles given by:

$$G_p^* = \left(\frac{2-\nu_{p1}}{G_{p1}} + \frac{2-\nu_{p2}}{G_{p2}} \right)^{-1} \tag{2.3.10}$$

and θ in Eq. 2.3.9 differs for initial loading (θ^{load}), unloading (θ^{unload}) and reloading (θ^{reload}). Mindlin (1949) expressed the θ^{load} for initial loading case as:

$$\theta^{load} = \left(1 - \frac{T}{\mu N} \right)^{1/3} \tag{2.3.11}$$

where T = tangential contact force; μ = coefficient of inter-particle friction. Eq. 2.3.11 is applicable only for the initial loading in tangential direction. The applied tangential force (T) reduces k_T due to partial slip prior to full slip at $T = T^{max}$ (= μN). Referring to Figs. 2.2(c) and

(d), the area of contact experiencing stress that contributes to the resultant tangential force decreases (the outer radius of contact annulus decreases) (Johnson, 1985).

Mindlin & Deresiewicz (1953) extended the study by Mindlin (1949) in order to consider more general cases of loading. Amongst various cases, unloading or re-loading of tangential contact force at a constant N is expressed by substituting the following expressions for θ into Eq. 2.3.9:

$$\theta^{unload} = \left(1 - \frac{T^* - T}{2\mu N}\right)^{1/3} \tag{2.3.12}$$

$$\theta^{reload} = \left(1 - \frac{T - T^{**}}{2\mu N}\right)^{1/3} \tag{2.3.13}$$

where T^* = tangential contact force at the reversal point from loading to unloading; T^{**} = tangential contact force at the reversal point from unloading to re-loading. Note that substituting $T = T^*$ or $T = T^{**}$ in Eqs. 2.3.12 and 2.3.13 gives $\theta = 1$, giving the initial loading stiffness at $T = 0$. This contact model is referred to here as the Hertz-Mindlin-Deresiewicz (HMD) model.

The HMD model depends on the loading history in both the normal and tangential directions, which cannot easily be considered in an analytical model or a numerical model. Thus, so-called simplified Hertz-Mindlin (HM) contact model is often used by substituting $\theta = 1$ into Eq. 2.3.9:

$$k_T^{HM} = 8G_p^* a \tag{2.3.14}$$

The HM model does not consider partial slip and is independent of the loading sequences. When $T = \mu N$, the tangential contact stiffness is reduced to zero as the contact cannot carry additional increment of T, i.e. stick-slip. This simplified HM model is used widely in DEM analyses. For example, this is implemented in the commercial PFC3D code (Itasca, 2007). The HMD model is less widely used; however, Thornton and his colleagues have used it in much of their research. Examples of its use include Thornton & Yin (1991) and Thornton et al. (2011). Comparing Eqs. 2.3.6 and 2.3.14, the ratio of the contact stiffnesses k_T to k_N for the HM model is found as:

$$\frac{k_T^{HM}}{k_N} = \frac{2\left(1 - \nu_p\right)}{2 - \nu_p} \tag{2.3.15}$$

For $\nu_p = 0.2$, which is often considered for soil grains, Eq. 2.3.15 gives $k_T^{HM}/k_N = 0.8889$. For the HMD contact model, the ratio decreases with increasing T.

2.3.3 Twisting couple

Twisting resistance occurs when contacting particles rotate relative to each other about an axis through the contact centre (Fig. 2.3). Twisting contact interaction is rarely implemented in DEM

studies and the influence of the twisting couple on overall response has not been discussed extensively in the literature. Lubkin (1951) extended the work by Mindlin (1949) to describe the twisting couple problem together with the tangential contact model, and derived a twisting contact stiffness (k_r) for frictional smooth spheres to be:

$$k_r = \frac{16}{3} G_p^* a^3 \theta_r \tag{2.3.16}$$

and θ_r differs for initial loading (θ_r^{load}), unloading (θ_r^{unload}) and reloading (θ_r^{reload}) of torsional moment. Mindlin (1949) expressed the θ_r^{load} for initial loading case as:

$$\theta_r^{load} = \left[2\left(1 - \frac{3}{2} \frac{M_r}{\mu N a} \right)^{-0.5} - 1 \right]^{-1} \tag{2.3.17}$$

where M_r = twisting contact moment. As the twisting moment increases k_r decreases due to partial slip in the spinning direction. Deresiewicz (1954) discussed more general cases for twisting loading in a similar manner to the discussion by Mindlin & Deresiewicz (1953) on tangential stiffness. The unloading and reloading of torsional loading gives:

$$\theta_r^{unload} = \left[2\left(1 - \frac{3}{2} \frac{M_r^* - M_r}{2\mu N a} \right)^{-0.5} - 1 \right]^{-1} \tag{2.3.18}$$

$$\theta_r^{reload} = \left[2\left(1 - \frac{3}{2} \frac{M_r - M_r^{**}}{2\mu N a} \right)^{-0.5} - 1 \right]^{-1} \tag{2.3.19}$$

where M_r^* = twisting contact moment at the reversal point from loading to unloading; M_r^{**} = twisting contact moment at the reversal point from unloading to re-loading. Just as was the case for tangential contact direction in Section 2.3.2, partial slip and counter slip for the spinning motion are taken into account in Eqs. 2.3.17 to 2.3.19. The relevant contact model is denoted HMDT in this study. The maximum twisting moment which can be held by the contact is:

$$M_r^{\max} = \frac{3}{16} \pi \mu N a \tag{2.3.20}$$

When full-slip is invoked, $k_r = 0$. The expressions from Eqs. 2.3.17 to 2.3.19 are approximated, using two terms of Taylor series and the accuracy decreases as M_r approaches M_r^{max}. For example, substituting Eq. 2.3.20 into Eq. 2.3.17 (with $M_r = M_r^{max}$) does not give $\theta_r^{load} = 0$ exactly, which gives an error of 6.1% compared with the analytical value as reported by Deresiewicz (1954). To reduce the error to be within 1% or 2%, the M_r/M_r^{max} value should be less than 0.3 or 0.5, respectively.

When partial slip is not considered in the tangential contact direction (i.e. HM model), the full expression of the twisting model considering partial slip is not appropriated. Instead, a simplified twisting contact model can be used (named here as HMT) in which partial slip in the torsional motion is not considered in a similar manner with HM model as (i.e. $\theta_r = 1$):

$$k_r^{HMT} = \frac{16}{3} G_p^* a^3 \tag{2.3.21}$$

In summary, this section described four different contact models: HM, HMD, HMT, and HMDT. Key differences are whether partial slip is considered or not, and whether twisting resistance against spin motion is considered or not. All the contact models are based on Hertzian contact mechanics and the normal contact interaction is identical for all the cases.

2.4 Contact model for rough surfaces

This section explores the influence of surface roughness on the contact-scale response. Firstly, the definition of surface roughness adopted in the present study is given. Secondly, contact models for rough surfaces are investigated drawing on tribology research including theoretical and experimental studies.

2.4.1 Definition of surface roughness

The term of surface roughness is used in various research fields. The definition of roughness depends on the application. Referring to Nayak (1973) and Thomas (1982), the present study considers a dimensional roughness value applied for contact mechanics. The scale of surface roughness is typically less than 1% of the radius of the particle. For a sand grain with a radius of 100 μm, the surface roughness may be less than 1 μm. This parameter differs clearly from other non-dimensional shape parameters such as roundness or angularity in the scale considered (e.g. Altuhafi & Coop, 2011). To quantify surface roughness, an optical interferometer can be used.

In tribology (the discipline associated with fundamental studies of surface interactions), measurements of surface roughness are typically performed on flat surfaces (Thomas 1982). The particular challenge posed in geomechanics is the curved surface geometry which also results in non-conforming contacts (Cavarretta, 2009). Roughness formulae consider the difference between elevation measures at discrete points and an average (reference) surface elevation. The definition of roughness parameters for engineering purposes is well documented (Johnson, 1985; BS EN ISO 4287). The typical measures of the roughness amplitude are the average roughness (S_a), and the root mean square (RMS) of roughness (S_q) given by:

$$S_a = \frac{1}{n} \sum_{i=1}^{n} |Z_i| \tag{2.4.1}$$

$$S_q = \sqrt{\frac{1}{n}\sum_{i=1}^{n}\left(Z_i^{\,2}\right)} \tag{2.4.2}$$

where n = the number of measured data points and Z_i = the elevation relative to the base surface.

As the surfaces of soil particles are not planar, roughness cannot be approximated as the average of all the surface elevation measurements. Rather the effect of surface curvature needs to be considered when calculating the surface roughness. However, there is no established approach to flatten a curved surface for this purpose. Altuhafi & Coop (2011), Cavarretta et al. (2010 & 2012), and Otsubo et al. (2014) used a motif extraction method to remove the curvature effect, while Alshibli & Alsaleh (2004) did not extract the surface curvature from their measurements.

2.4.2 Normal contact stiffness for rough surfaces

The Hertzian-based contact models described above assume contact between smooth surfaces. However, real soil grains have a finite surface asperities; this differs from the assumption made in Hertzian theory. Referring to Fig. 2.4, there are two types of rough contacts: rough-smooth contacts and rough-rough contacts. Greenwood & Tripp (1967) analytically derived an expression for the normal stiffness of rough-smooth contacts assuming the asperity heights along a surface follow a Gaussian distribution. Studies of rough-rough contacts also have been conducted, for example, by Greenwood & Tripp (1970) and Johnson (1985). Greenwood & Tripp (1970) proposed that the theory for rough-smooth contacts can be applied to rough-rough contacts by using the following expression for the combined RMS roughness (S_q^*):

$$S_q^{*2} = S_{q1}^2 + S_{q2}^2 \tag{2.4.3}$$

Greenwood et al. (1984) and Johnson (1985) suggested use of a simple non-dimensional roughness parameter (α) to consider the influence of surface roughness; their experimental results also support this suggestion, and α is given by:

$$\alpha = \frac{S_q^*}{\delta^{Smooth}} = \frac{S_q^* R^*}{a^{Smooth\,2}} \tag{2.4.4}$$

The symbols δ^{Smooth} or a^{Smooth} are as used in Section 2.3.1, and here their application to smooth surfaces is made clear. In Eq. 2.4.4, S_q^* and R^* are material properties, whereas a^{Smooth} is a function of N (Eq. 2.3.5). Thus, α is not a constant value but changes with N. Johnson (1985) highlighted another non-dimensional roughness parameter λ introduced by Greenwood & Tripp (1967):

$$\lambda = \frac{8}{3}\eta_s S_q^* \left(\frac{2R^*}{\kappa_s}\right)^{\frac{1}{2}} \tag{2.4.5}$$

where η_s = the number of asperity peaks per unit area; and κ_s = the curvature of asperity peaks. λ describes the geometrical characteristics of a rough surface, whereas α in Eq. 2.4.4 relates to the amplitude of roughness. Johnson (1985) demonstrated that the influence of surface roughness can be characterised primarily by α and secondly by λ. Yimsiri & Soga (2000) related α to the ratio a^{Rough} / a^{Smooth} and ignored the effect of λ:

$$a^{Rough} = \left(\frac{-2.8}{\alpha + 2} + 2.4 \right) a^{Smooth} \tag{2.4.6}$$

As the normal contact force increases α decreases. At an extremely large normal force (i.e. $N \rightarrow \infty$), α approaches zero, resulting in $a^{Rough} = a^{Smooth}$. While approximate, Eq. 2.4.6 is useful as the complicated behaviour of rough contacts can then be described as:

$$\delta^{Rough} = \frac{\left(a^{Rough}\right)^2}{R^*} = \frac{1}{R^*} \left[\left(\frac{-2.8}{\alpha + 2} + 2.4 \right) a^{Smooth} \right]^2 \tag{2.4.7}$$

Micromechanics studies including DEM require an expression for contact stiffness. The normal contact stiffness for rough surfaces (k_N^{Rough}) can be derived using Eqs. 2.3.1 and 2.4.7 as below:

$$k_N^{Rough} = \frac{dN}{d\delta^{Rough}} \tag{2.4.8}$$

The result of the calculation is documented in Yimsiri & Soga (2000); however, it is too complex to be incorporated in a simple theoretical model.

2.4.3 Tangential contact stiffness for rough surfaces

From a geomechanical perspective, measurement of the tangential contact stiffness was attempted by Cavarretta et al. (2010) and Senetakis et al. (2013 a&b). In these studies, two particles with curved surfaces were sheared against each other. The experiments are non-trivial and very challenging to interpret as the tangential contact stiffness at very small displacements is needed, which is difficult to measure with actual soil particles. It should be also noted that the tested particles were attached to the loading platens using glue, so the rotation of the particle motion was restricted, and system compliance may affect the very small displacement measurement.

Potential alternatives to particle-particle shearing tests include ultrasound and digital image correlation (DIC) techniques that have been developed recently by UK-based tribology research groups. The ultrasound approach is described in Gonzalez-Valadez et al. (2010), whereas the DIC method is outlined by Kartal et al. (2011a & b). Mulvihill et al. (2013) compared the two approaches, and concluded that the ultrasound technique tends to give a larger contact stiffness

in comparison with the DIC method. The DIC method requires a small amount of tangential displacement to visualise the deformation of the contacting surfaces.

Medina et al. (2013) developed a micromechanical analytical model from a tribology perspective in which the effect of surface asperities on contact stiffnesses is considered separately to the interaction of smooth spherical bodies following Hertzian contacts. The tangential contact stiffness of surface asperities ($k_T^{Asperity}$) for a virgin (initial) loading can be expressed as:

$$k_T^{Asperity} = \frac{2(1-\nu_p)}{2-\nu_p}\frac{N}{S_q^*}\left(1-\frac{T}{\mu N}\right)^{1/3} \tag{2.4.9}$$

Note that the tangential contact stiffness in Eq. 2.4.9 is independent of the particle shear modulus. Eq. 2.4.9 was theoretically derived by Medina et al. (2013) following the ideas of Greenwood & Tripp (1967), the difference between the two approaches being that Greenwood and Tripp assumed a Gaussian distribution of asperity heights, whereas Medina et al. assumed an exponential distribution. Medina et al. (2012) carried out numerical simulations using their micromechanical model and the result agreed with Eq. 2.4.9 at low normal forces. They concluded that the discrepancy between their numerical model and Eq. 2.4.9 at moderate and high normal forces could be explained by the change of the asperity spacing between rough surfaces. They introduced the idea of a hybrid stiffness which acts as two springs connected in series (Fig. 2.5), and is given by:

$$k_T^{Rough} = \left(\frac{1}{k_T^{Asperity}} + \frac{1}{k_T^{Smooth}}\right)^{-1} \tag{2.4.10}$$

Using Eq. 2.4.10, there is a smooth transition from $k_T^{Asperity}$ to k_T^{Smooth} with increasing N.

O'Connor & Johnson (1963) measured the tangential contact stiffness between a smooth sphere and a rough plate, and concluded that there is no considerable difference between smooth-rough contacts and smooth-smooth contacts. Yimsiri & Soga (2000) referred to this experimental evidence when they assumed $k_T^{Rough} = k_T^{Smooth}$ in their analysis which is discussed in greater detail in Section 2.4.4.

2.4.4 Contact stiffness ratio and partial slip for rough contacts

The influence of surface roughness on the contact stiffness ratio k_T/k_N (= R_k) is briefly reviewed in this section. Referring to the HM model as discussed in Section 2.3, the stiffness ratio is a function only of the particle Poisson's ratio when $T < \mu N$:

$$R_k^{HM} = \frac{2(1-\nu_p)}{2-\nu_p} \tag{2.4.11}$$

Consideration of partial slip in the HMD model reduces the R_k values so that R_k decreases to zero at $T = \mu N$ for initial tangential loading:

$$R_k^{HMD,load} = \frac{2(1-\nu_p)}{2-\nu_p}\left(1-\frac{T}{\mu N}\right)^{1/3} \tag{2.4.12}$$

Based on both analytical and numerical studies, Campañá et al. (2011) stated that R_k for rough surfaces is similar to that for smooth contacts, i.e. the reduction in k_T is approximately proportional to the reduction in k_N due to surface roughness effects. Medina et al. (2013) also considered the contact stiffness ratio R_k to be the same as for smooth contacts.

On the other hand, referring to Fig. 2.6, Baltazar et al. (2002), Krolikowski & Szczepek (1993), Yoshioka & Scholz (1989a & b) and Sherif & Kossa (1991) predicted lower R_k values for rough contacts as summarised in Gonzalez-Valadez et al. (2010). The experimental results by Gonzalez-Valadez et al. (2010) using the ultrasound technique also showed a lower R_k value for a rough contact, and the ratio increased as the normal pressure increased (Fig. 2.6(a)). Biwa et al. (2009) also experimentally showed using the ultrasound method that R_k tends to increase with increasing N; in their case, R_k increased from 0.1 to 0.4. These findings contrast to the pioneering research by O'Connor & Johnson (1963). The difference between the ultrasound method and particle shearing tests in O'Connor & Johnson seems to be the magnitude of contact displacements, and the ultrasound method gives the tangential contact stiffness at lower displacements.

It is important to consider combined partial slip effects for rough surfaces. Paggi et al. (2014) numerically investigated the influence of partial slip on rough contacts. They found that tangential loading gives a more significant reduction in tangential contact stiffness for rough surfaces (Eq. 2.4.13) than for smooth surfaces (HMD model, Eq. 2.4.14) as follows:

$$\frac{k_T^{Rough}}{k_{T0}^{Rough}} = 1-\frac{T}{\mu N} \tag{2.4.13}$$

$$\frac{k_T^{HMD}}{k_{T0}^{HMD}} = \left(1-\frac{T}{\mu N}\right)^{1/3} \tag{2.4.14}$$

where k_{T0} stands for the initial tangential contact stiffness at $T = 0$.

In summary, there is ample evidence in the literature to state with confidence that the normal contact stiffness is reduced due to surface roughness. The tangential contact stiffness is also

probably reduced due to surface roughness but there is a lack of consensus on the value of the reduction ratio. The stiffness ratio for rough contacts may be smaller than that for smooth contacts; however, the difference decreases with increasing normal force. The theory of partial slip may also be applicable to rough contacts and the reduction in tangential contact stiffness could be more significant than that for smooth contacts.

2.5 Coordination number and void ratio

The response of granular materials depends on the packing state. It is important to understand the characteristics of packing state to predict the overall response of granular materials as predictions of soil behaviour often consider void ratio (e) but not the mean coordination number ($\overline{C_N}$). Establishing a relationship between $\overline{C_N}$ and e enables the soil stiffness at small strains to be estimated from a micromechanical analysis (Chang et al., 1991) using available data from laboratory tests. The mechanical response of soil also depends on stress level; however, stress-dependency of the packing has been rarely discussed in the literature. This section investigates prior research which has assessed the packing state of granular materials relating $\overline{C_N}$ and e of the sample ($\overline{C_N}$ – e relationship). As summarised by Antwerpen et al. (2010), just considering monodisperse spheres a number of different $\overline{C_N}$ - e relationships exist. This section focuses on prior studies considering packings of non-cohesive spheres that have a narrow distribution of particle size, and relatively low values of void ratio.

2.5.1 Packing theory and numerical simulations

Regular lattice packings or crystal structures are the starting point to understand the correlation between $\overline{C_N}$ and e. Referring to Graton & Fraser (1935), Table 2.1 summarises $\overline{C_N}$, e, p (porosity), and f (volume fraction) for regular arrays; p and f are expressed in terms of e as follows:

$$p = \frac{e}{1+e} \tag{2.5.1}$$

$$f = \frac{1}{1+e} \tag{2.5.2}$$

Smith et al. (1929) attempted to obtain the $\overline{C_N}$ - e relationship for random packings using experimental data which were compared with the values for regular arrays including face-centred cubic (FCC), hexagonal close-packed (HCP) and simple cubic (SC) arrays, and proposed the following expression:

$$\overline{C_N} = 15.76 - 10.73\,e \tag{2.5.3}$$

The expression by Smith et al. (1929) does not agree well with the $\overline{C_N}$ - e data point for the body-centred cubic (BCC) array. There is a difference between regular packings and random packings. It is difficult to achieve the low e value of FCC or HCP arrays (e = 0.351), or even for the BCC array (e = 0.470) using monodisperse random assemblies. Interestingly, it is also difficult to achieve the high e value of the SC array (e = 0.910) using random assemblies of monodisperse spheres. Scott & Kilgour (1969) showed based on their experiments that the e value of random dense packings of spheres (i.e. non-crystalline dense assemblies of spheres) is approximately 0.571.

The packing is sensitive to the sample preparation method. Magnanimo et al. (2008) prepared random samples with slightly different preparation methods using DEM and they had almost identical e but different $\overline{C_N}$ under isotropic pressures; this highlights the sensitivity of sample preparation method to the $\overline{C_N}$ – e relationship. Random dense packings are normally prepared by shaking or tapping; however, Scott et al. (1964) noted that application of repeating shearing can reduce e to be as low as 0.52, indicating the presence of regions of regular packing. Similar experimental observations were reported by Pouliquen et al. (1997) and Camenen et al. (2013). The crystallization of random packings was discussed in Cui & O'Sullivan (2006) and Radin (2008).

The following summarises correlations between $\overline{C_N}$ and e reported in prior literature. Nakagaki & Sunada (1963;1968) used a probability function in their semi-numerical simulations to obtain a $\overline{C_N} - e$ relationship. In their simulations, particles were dropped into a cubic box, and the positon of each particle was found either when attached to three other particles or when attached to another particle and with a chance based on a probability function. The particles continued to move in the direction of the contact planes until the stability condition was satisfied. They proposed the following expression:

$$\overline{C_N} = 1.61\left(\frac{1+e}{e}\right)^{1.48} \tag{2.5.4}$$

Gotoh (1978) mathematically developed a correlation between $\overline{C_N}$ and e considering the relationship between the mean distance between neighbouring particles and e:

$$\overline{C_N} = 20.7\left(\frac{1}{1+e}\right) - 4.35 \qquad (0.429 < e \le 1.13) \tag{2.5.5}$$

Ouchiyama & Tanaka (1980) theoretically derived an expression for the $\overline{C_N} - e$ relationship and good match was reported with experiments by Smith et al. (1929); Arakawa & Nishino (1973).

$$\overline{C_N} = \frac{32}{13}\left[7 - 8\left(\frac{e}{1+e}\right)\right] \tag{2.5.6}$$

Suzuki et al. (1981) developed a theory for the $\overline{C_N} - e$ correlation for mono-sized random packings in which a Gaussian error function was used. Their model captured results of a simulation method that was originally proposed by Tory et al. (1973) and was modified including a zenithal angle, at which stick or slide of contact is determined, to achieve realistic values of *e*.

$$\overline{C_N} = 2.828\frac{(1+e)^{1/3}}{\left(\frac{b}{D}\right)^2\left\{1+\left(\frac{b}{D}\right)^2\right\}} \tag{2.5.7}$$

where *b* = dimensional constant; *D* = diameter of sphere. The *b*/*D* value depends on *e* as:

$$(1+e)^{1/3} = \frac{1+\left(\frac{b}{D}\right)^2}{1+\left(\frac{b}{D}\right)\exp\left\{\left(\frac{D}{b}\right)^2\right\}Erfc\left\{\frac{D}{b}\right\}} \tag{2.5.8}$$

where *Erfc* stands for the Gaussian error function. These theoretical values also agree with experimental reports by Bernal & Mason (1960) and Gotoh (1978).

Zhang et al. (2001) used discrete element method (DEM) simulations of pluviation to prepare various packings by changing simulation parameters such as drop height, deposition intensity, damping coefficient and inter-particle friction. Zhang et al. (2001) fitted their results to:

$$\overline{C_N} = \left[0.183 - 659.2\left(\frac{1}{1+e}\right)^{20.96}\right]^{-1} \qquad (0.587 < e \le 0.818) \tag{2.5.9}$$

The discussions above excluded considerations of stress-dependency of the $\overline{C_N} - e$ relationship. When stress effects are considered, the fabric of packing and the inter-particle interactions including overlap and reaction forces should be described, which hinders the application of existing theories to the problem. Instead, DEM studies can aid to explore the origin of the stress-dependency of packing even in a complex condition. Makse et al. (2000) discussed evolution of the $\overline{C_N} - e$ relationship with increasing isotropic confining stress in which random loose and dense samples did not follow the same path (Fig. 2.7), indicating the additional influence of stresses on the $\overline{C_N} - e$ relationship. Barreto & O'Sullivan (2012) investigated the evolution of $\overline{C_N} - e$ relationship from an isotropic state to a critical state during triaxial loading. The evolution of $\overline{C_N}$ value was more sensitive to the deviatoric stresses than the evolution of *e* value at lower strain levels, which agrees with Thornton (2000). However, a

linear relationship between $\overline{C_N}$ and e was observed (Fig. 2.8) at critical states for various values of inter-particle friction. Note that the mean stress was not kept constant in this comparison. Zhang & Thornton (2005) compared the $\overline{C_N} - e$ relationships during constant volume shearing and constant mean stress shearing. For the systems at a critical state, the loading conditions did not affect the linear relationship between $\overline{C_N}$ and e.

2.5.2 Experimental assessment of coordination number

Prior experimental attempts to develop the $\overline{C_N}$ - e correlation include Smith et al. (1929) who visualized the contact points between lead shot spheres with a diameter of 7.56 mm at different packing densities using 20% solution of acetic acid and found that densely packed samples have a higher $\overline{C_N}$. In addition to theoretical values for regular packings, their experimental data were fitted to Eq. 2.5.3.

Bernal & Mason (1960) used Japanese black ink (Bokuju) to identify contact points on ball bearings (D = 6.35 mm), they submerged the particles in the ink, then allowed the ink to drain; as discussed below this process leaves circular marks on the particles at the contact points. Ink menisci formed between particles that were close to each other but not actually contacting, these can be considered as "virtual" contacts (termed "near" by Bernal & Mason), Bernal & Mason identified these as cases where the menisci radii were less than 5% of the particle radius. Engaged contacts are those contacts that actually transmit force (termed "close" by Bernal & Mason) and Bernal & Mason hypothesized that in this case the radii of the menisci exceeded 5% of the particle radius (Fig. 2.9).

Arakawa & Nishino (1973) also conducted the ink test using polystyrene balls with diameters between 1 mm and 6 mm (Fig. 2.10) and reported that their experimental results were in good agreement with theoretical predictions by Ridgway & Tarbuck (1967) and Smith et al. (1929) particularly at loose packings.

Field (1973) used molten wax to print contact points using well-rounded river gravels (9.53 mm $\leq D \leq$ 114 mm). Both the number of contacts and the contact angles were measured. Based on four test cases with mixtures of various sizes, they reported a unique trend as:

$$\overline{C_N} = \frac{12}{1+e} \tag{2.5.10}$$

From a soil mechanical perspective, Oda (1977) used the ink method of Bernal & Mason (1960) to study contact points on glass ballotini (D = 5.2 mm to 24.7mm) and concluded that the coordination number frequencies in a random assembly of monodisperse spheres can be represented by a Gaussian distribution. They also reported that the standard deviation of coordination number per particle (C_N) increases with increasing e, which can be used an index

of the heterogeneity of fabric. Their experimental results found that the trend of the $\overline{C_N}$ - e relationship is similar for polydisperse spheres and monodisperse spheres, but that the polydisperse spheres give higher $\overline{C_N}$ values with lower e. This finding was inconsistent with Pinson et al. (1998) who considered mixtures of binary sizes of steel spheres and found that $\overline{C_N}$ is independent of the particle size distribution.

German (2014) summarised $\overline{C_N}$ - e correlations considering various packing types: ordered packing, disperse packing, random packing, partially densified structure and full densified packing. Based on 113 reports, they proposed the following relationships:

$$\overline{C_N} = 2 + 11\left(\frac{1}{1+e}\right)^2 \tag{2.5.11}$$

$$\overline{C_N} = -2.8 + 15.1\left(\frac{1}{1+e}\right) \tag{2.5.12}$$

where Eqs. 2.5.11 and 2.5.12 were obtained by fitting the data to a quadratic curve and a linear curve, respectively.

Analysis of 3D images of soil from micro-computed tomography (μCT) can also be used to relate the coordination number and the void ratio. Fonseca et al. (2013) prepared intact and reconstitute Reigate sand samples and sheared them up to a critical state. The tested samples were taken out after impregnated with an epoxy resin. They found a correlation between $\overline{C_N}$ and e to be:

$$e = 1.69\exp^{-0.14\overline{C_N}} \tag{2.5.13}$$

Fonseca et al. (2014) used well-graded (WG) and gap-graded (G1 and G2) sand specimens and observed higher and lower $\overline{C_N}$ values, respectively, for given e values using μCT (Fig. 2.11). Referring to Shire & O'Sullivan (2013) who investigated the $\overline{C_N}$ - e correlation for gap-graded DEM samples comprised of perfect spheres and found lower $\overline{C_N}$ values than the data points in Fonseca et al. using μCT. The data presented in Figure 2.11 were gained using both DEM and μCT and illustrate the fact that there is not a unique relationship between $\overline{C_N}$ and e. Fonseca et al. (2014) concluded that the $\overline{C_N}$ - e correlation depends highly on the shape of the particle size distribution curve, and non-spherical particles tend to show larger C_N values (Fig. 2.11). Eq. 2.5.13 gives a lower $\overline{C_N}$ value for a given e compared with an estimation based on μCT analysis by Hasan & Alshibli (2010) for Otawa sand:

$$e = 2.23\exp^{-0.13\overline{C_N}} \tag{2.5.14}$$

Al-Raoush (2007) developed a methodology of analyzing 3D images such as μCT data and qualitatively discussed fundamental differences between samples of sand and mono-sized spheres. They reported that sand grains with irregular shapes tend to have a larger $\overline{C_N}$ value with a wider range of distribution of C_N than spherical particles. It should be noted that the interpretation of μCT data is non-trivial as the quality of the data is influenced by the scan resolution and the ability to accurately threshold the void and particle phases in the material. μCT scan data cannot provide information on the contact surfaces with the nm level of resolution needed to provide meaningful insight.

2.5.3 Summary of packing correlations

There is a long history of the study of packing of granular materials. Both experimental and analytical studies were reported extensively in the late 1900s, whereas literature reporting numerical simulations increased recently. Understanding the $\overline{C_N}$ - e correlation is important in soil mechanics as the overall responses of soil are often related to e; however, inter-particle responses should also be linked to $\overline{C_N}$, which is difficult to measure in the laboratory or the field, as often discussed in the effective medium theory. The $\overline{C_N}$ – e relationships proposed in the literature are summarised in Table 2.2 and illustrated in Fig. 2.12. Referring to Fig. 2.12(a), the $\overline{C_N}$ values decrease with increasing e for all the expressions; however, the variation in $\overline{C_N}$ for a given e is considerable. For example, the highest and lowest $\overline{C_N}$ values at e = 0.6 are 9.85 and 5.98, respectively. The discrepancy in $\overline{C_N}$ values (9.85-5.98 = 3.87) can be about the half of the mean value of $\overline{C_N}$ = 7.53. Figures 2.12(b) and (c) summarise the correlations proposed based on both analytical and experimental approaches, respectively; however, there is no clear trend observed for any group. Thus the $\overline{C_N}$ – e relationship is specific to the material in question and is quantified for the material tested in this study in Chapter 3.

2.6 Wave propagation through granular materials

Dynamic wave propagation tests such as bender element tests or acoustic emission tests have been conducted widely in soil mechanics and geophysics research. The dynamic properties of granular materials are important to estimate the elastic response of soils or rocks including wave velocity, damping and frequency filtering effects. This section reviews the development of laboratory geophysics tests in soil mechanics research.

2.6.1 Laboratory geophysics tests

Resonant column testing was developed earlier than other methods to evaluate the shear modulus of soil samples at small strain levels (e.g. Hardin & Richart, 1963; Hardin, 1965). The

fundamental resonant mode of a vibrating sample and its corresponding frequency can be found using the device. This method is based on frequency domain interpretation of the signal where the dispersion relation is not considered, i.e. a linear relationship between frequency and wave number is assumed, and the first mode of the vibration is considered (long wave assumption). To measure the shear modulus accurately, careful attention should be placed on the influence of the boundary conditions of the sample and the stiffness of the testing apparatus; otherwise the assumptions of this method may be violated (e.g. Drnevich, 1978; Clayton et al., 2009). It is usual to calibrate the device carefully prior to conducting experiments with real samples. The resonant column technique is still used today and compared with some other techniques based on dynamic wave propagation (e.g. Camacho-tauta et al., 2013).

The development of bender elements was described by Shirley (1978) and Shirley & Hampton (1978) (Fig. 2.13). The purpose of bender element tests is to measure the shear wave velocity traveling through the soil sample. Bender elements are inexpensive and can be installed into a conventional apparatus such as triaxial apparatus or oedometer apparatus. As a result many research institutes use bender elements (Yamashita et al., 2009). Unlike the resonant column apparatus, the interpretation of the test results can be considered straightforward as a complex frequency domain analysis is not always required. Measuring the wave travel time from the source (transmitter) to the receiver enables estimation of wave velocity knowing the distance between two bender elements. As described in Lings & Greening (2001), bender elements can be adapted to form extender elements to measure the compression wave velocity.

To interpret the signals from a dynamic test, either time domain (TD) analysis or frequency domain (FD) analysis can be selected. The time domain methods use signals recorded in time directly. As the distance between two bender elements can be estimated knowing their initial positions and the deformation of the sample during compression, only the travel time is required to determine the wave velocities. However, the challenge of determining the correct arrival time is well known and it has been discussed in the literature (e.g. Yamashita et al., 2009; Clayton, 2011). Referring to Fig. 2.14, the start-to-start (S-S) method finds the first non-zero data point of the received signal, whereas the peak-to-peak (P-P) method finds the first peak of the received signal. The cross-correlation (CC) method is a semi-frequency domain method in which the similarity between input wave $x(t)$ and received wave $y(t)$ is quantified by shifting the input wave by time τ:

$$CC_{xy}(\tau) = \lim_{T\to\infty} \frac{1}{T} \int_0^T x(t) \cdot y(t+\tau) dt \qquad (2.6.1)$$

where CC_{xy} = cross-correlation function, T = recording time. The time delay (τ) with a peak of CC_{xy} is considered to be travel time.

The input wave can be any shape including a step pulse, a triangle pulse or a sinusoidal pulse as summarised in da Fonseca et al. (2009). The input frequency affects the quality of the received signal. In particular, using a low frequency causes a near-field effect as discussed by Arroyo et al. (2003), where the compression (*P*-) wave signals which appear earlier than the shear (*S*-) wave signals interfere with the received *S*-wave signals. This effect can be reduced by using a period of input wave T_{in} to be less than half of the travel time. To avoid any uncertainty regarding frequency, the use of several frequencies is recommended (da Fonseca et al., 2009).

Frequency domain analysis of bender element signals is also useful as it provides us with an alternative means to discuss the wave velocity. Greening & Nash (2004) and Alvarado & Coop (2012) applied frequency domain approaches to calculate the wave velocity; however, good agreement between the time domain analysis and the frequency domain analysis was not reported. A similar observation can be found in the results of a parallel test conducted at many institutes using Toyoura sand (Yamashita et al., 2009). A possible reason for the discrepancy is that signals obtained from bender elements include waves reflected at the side boundaries for both *P*- and *S*-wave components. Also, as noted in Lee & Santamarina (2005), the received signals must be affected by the stiffness and mass of the testing apparatus and the bender elements themselves; however, boundary effects to the received signals are not often considered in bender element testing. In contrast, the resonant column testing apparatus is usually well calibrated to remove the effects of mass and stiffness of the apparatus. Camacho-Tauta et al. (2015) reported a good match in the wave velocities for bender element tests using the time domain method and resonant column tests.

As an alternative to the bender elements, shear plates (plate-shaped piezo electric transducer) have been used recently in soil mechanics research (e.g. Brignoli et al., 1996; Ismail & Rammah, 2005; Suwal & Kuwano, 2013). Shear plates were originally developed half a century ago. For example, Lawrence (1965) placed twelve sets of shear plates (each dimension being 2.54 mm × 15.24 mm) in a shape of wheel to generate a torsional wave, so as to compare with the resonant column test results (Fig. 2.15). Ismail & Rammah (2005) and Suwal & Kuwano (2013) used compression- and shear plates to generate *P*- and *S*-waves simultaneously (Fig. 2.16). Ismail & Rammah (2005) compared signal qualities using bender elements and shear plates for similar samples and observed better signals using the shear plates except for a soft clay sample. Suwal & Kuwano (2013) reported the reliability of using the shear plates by comparing the sample shear modulus deduced from wave velocities obtained using shear plates and accelerometers, and measured directly by static triaxial loading. These papers clearly emphasized that using shear plates has an advantage over conventional bender element tests; the soil samples are not disturbed during the testing procedure. This advantage is important

particularly for intact soils or stiff soils as sample disturbance in the vicinity of conventional bender element is inevitable when they are inserted into the soil sample.

From the perspective of fundamental physics, similar dynamic tests are carried out to study the nature of stress or sound wave propagation (e.g. Duffy & Mindlin, 1957; Jia et al., 1999; Yang et al., 2011; Hasan et al., 2014). Duffy & Mindlin (1957) studied stress wave propagation through a face-centred cubic (FCC) sample, and showed a reasonable match with their theoretical analyses. Jia et al. (1999) generated *P*-wave using disk-type transducers in an oedometer device, and observed a coherent ballistic pulse (denoted as E) and its echo reflected from the bottom and top boundaries (denoted as S) (Fig. 2.17). Frequency domain analysis of the signal showed that the coherent ballistic wave exhibits a clear peak at a low frequency, while its echo contains more wide range of frequencies. Yang et al. (2011) used a granular chain of twenty spheres where a piezo-ceramic plate is installed into each sphere so that propagation of stress waves is detected directly (Fig. 2.18). They showed good agreement with their experimental results and their wave propagation theory developed for an equivalent 1D chain of particles. Hasan et al. (2014) also used a chain of steal spheres to discuss force and displacement responses of boundary particles during a sinusoidal excitation.

2.6.2 Tests on assemblies of rough spheres

Experimental research that has examined the effects of surface roughness on the dynamic responses and the elastic moduli at very small strains has rarely been reported. This is because accurate measurements of surface roughness of soils had been difficult until recently. Now the development of optical interferometry techniques enables quantitative measurement of surface roughness. There are several relevant prior studies available as follows.

Santamarina & Cascante (1998) used a resonant column apparatus with triaxial loading capacity to compare the sample shear modulus of rough (rusted) and smooth (non-rusted) steel spheres. The magnitude of roughness was not quantified in their work. Fig. 2.19 shows the results of resonant column tests with mild-rust and rusted steel spheres. The coefficient of exponent (b) for the best fit curves to the experimental data is shown for both loading and unloading in isotropic compression. The b value is larger for rusted steel spheres than mild-rust steel spheres during both loading and unloading, the trend is clearer in unloading. The magnitude of the *S*-wave velocity which is directly related to the sample shear modus at small strains is larger in smoother spheres than in rusted spheres. It is interesting to note that the *S*-wave velocity is slightly larger during loading than unloading, which is different from the common observation for real sands.

Sharifipour & Dano (2006) performed bender element tests to compare the wave velocities for assemblies of smooth glass beads and rough glass beads. Fig. 2.20 presents their experimental data for *S*-wave velocity measurement; the rough glass beads show lower velocities than the smooth glass beads. It is also obvious that a larger initial void ratio gives a lower *S*-wave velocity for both the smooth and rough samples. The exponential coefficients (b) for the best-fit curves are shown in Fig. 2.20, and the b values for *S*-wave velocities are larger in the rough assemblies ($b = 0.27 – 0.3$) compared with the smooth assemblies ($b = 0.2 – 0.22$). These results agree with Santamarina & Cascante (1998). While useful, these studies are semi-qualitative as the surface roughness of particles was not quantified.

Experiments by Duffy & Mindlin (1957) are sometimes considered to include the influence of surface roughness as the particle diameters were slightly different with each other, which affected the *P*-wave velocity through a face-centred cubic (FCC) sample. Referring to Fig. 2.21, an assembly of high tolerance spheres ($D = 3.18$ mm ± 0.254 μm) shows higher *P*-wave velocity than low tolerance spheres ($D = 3.18$ mm ± 1.27 μm). The *P*-wave velocity of low tolerance spheres increases greater with increasing confining pressure (i.e. larger b value). The difference in *P*-wave velocities becomes smaller as confining stress increases.

There is a consistent observation of lower wave velocities for rough samples compared with smooth samples although the number of experiments are still limited. This finding should be investigated deeper to develop understanding of the effect of surface roughness on wave velocity and sample stiffness. However, controlling the surface roughness systematically in laboratory tests remains challenging. It is important to remove other factors affecting the wave velocity such as void ratio, material properties or fabric anisotropy during laboratory tests. Obviously, use of real sand to study the surface roughness effects is a challenge.

This study focuses on the small-strain stiffness of granular materials; however the surface roughness may increase the peak and residual strength of the sample at larger strain levels (Santamarina & Cascante, 1998; Lee et al., 2013). This result can be understood by the fact that the inter-particle friction increases with increasing surface roughness observed in inter-particle shearing tests by Cavarretta (2009). Section 3.2.2 includes discussion of the effect of surface roughness on the inter-particle friction.

2.6.3 DEM simulations

Just as in the case of laboratory tests, wave propagation in granular materials can be studied using the discrete element method (DEM). As described in Section 2.2, the DEM formulation is based on dynamic interactions between particles, which is suitable to capture the dynamic response of granular materials. Stress wave propagation was studied by Thomas et al. (2009),

Mouraille et al. (2006), Xu et al. (2015) and O'Donovan et al. (2016) amongst others to understand the *S*-wave velocity in model soils comprising spherical particles.

Thomas et al. (2009) investigated the influence of simulation parameters in DEM such as sample width, void ratio, viscous damping and wavelength of input waves on *P*-wave velocity and dispersion relation of waves in order to improve interpretation of resonant column tests. The dispersion relation of waves describes the relationship between frequency and wave number of the propagating waves, which gives group and phase velocities as is discussed in Section 2.6.4. The top boundary disks in a 2D regular array were excited using a continuous sinusoidal *P*-wave analogous to resonant column tests in the laboratory and the propagated wave was received at a specific particle located inside the sample. The time at which the non-zero particle velocity was noted was considered to be the *P*-wave arrival time. They found anomalous dispersion (i.e. velocity increases with increasing excitation frequency), which was less profound for slender samples. Note that the dispersion relation described by Thomas et al. (2009) is based on boundary particle responses; however, Mouraille et al. (2006) and O'Donovan (2013) examined the dispersion relation using data for internal spheres.

Xu et al. (2015) used a disk-shaped region of spheres in a random configuration of polydisperse spheres as transmitter and receiver disks (Fig. 2.22). The mean velocity of particles with time within the disk-shaped regions were processed for the cross-correlation analysis to determine the *S*-wave arrival time. As the sample length (< 8 mm) was by far smaller than a typical laboratory specimen (70 – 100 mm), a high frequency input wave (125 or 200 kHz) was used to reduce the nominal wave length compared with the sample length. An empirical correlation between the *S*-wave velocity and the liquefaction resistance of soil was discussed based on their DEM simulations. Although the test condition was not realistic, an application of wave propagation simulations to soil mechanics tests was demonstrated.

O'Donovan et al. (2015) simulated bender element tests to estimate the elastic modulus for a FCC sample. The methods of estimating the wave velocity were discussed to improve interpretation of equivalent laboratory tests. O'Donovan et al. (2015) considered the HM and HMD contact models, and a rough surface contact model as proposed by Cavarretta et al. (2010) (CM contact model) in their DEM simulations. Referring to Fig. 2.23, the sample shear modulus is smaller for HMD than HM due to a reduction in tangential contact stiffness caused by partial slip prior to full slip. The CM model shows an even lower modulus but a higher slope at lower pressures, and the slope becomes a similar value to the HM model at higher pressures. O'Donovan et al. (2016) used a cubic sample composed of smooth spheres with slight polydispersity (2.4 mm < D < 2.7 mm) to compare with an equivalent laboratory bender element test in a cubical cell apparatus. A quantified surface roughness value for smooth ballotini was

considered in their DEM simulations using the CM model, and a good match of received signals was observed.

A more fundamental approach was used in sound wave studies outside of soil mechanics. Hazzard et al. (1998) simulated acoustic emissions (AE) due to breakage of bond at contacts to study the development of cracking and failure in rocks, and they reported that denser samples show AE events more frequently than looser samples. Mouraille et al. (2006) used a FCC sample with fixed particles boundaries in the direction of wave propagation and periodic boundaries in the other directions. An initial velocity was applied to the fixed boundary particles to generate *P*- or *S*-wave. They used two-dimensional (spatial and temporal) dispersion-relation to obtain wave velocity where particle displacements of the regular array sample were processed to find the relationship between frequency and wave number of propagating waves. Referring to Fig. 2.24 for dispersion relations of *P*- and *S*-waves, where grey-scale corresponds to the amplitude of Fourier coefficients, clear curves of dispersion relation are observed for both *P*- and *S*-waves, and they agree with a theory (Eq. 2.6.3) described in the following section. McNamara (2015) reported that the wave velocity decreased with increasing number of sliding contacts using 2D simulations.

2.6.4 Dispersion relation theory and low-pass filter

Referring to Fig. 2.25 for a case of *P*-wave propagation, the sinusoidal motion of a chain of masses along the *x* direction with time *t* can be expressed as below:

$$u(x,t) = u_0 e^{i(\kappa x - \omega t)} \tag{2.6.2}$$

where u = particle displacement in the x direction; u_0 = amplitude of displacement; ω = angular frequency (= $2\pi f$); f = frequency; κ = wave number (= $2\pi/\lambda$); and λ = wave length.

The dispersion relation describes the relationship between ω and κ of propagating waves. Granular materials have a dispersion relation, i.e. a non-linear ω–κ relationship, which is different from continuous media where there is a linear ω–κ relationship. For a regular packing with uniformly sized spheres, the dispersion relation can be derived as below (Brillouin, 1946; Kittel, 2004; Mouraille, 2009):

$$\omega = \sqrt{\frac{4C}{m}}\left|\sin\left(\frac{\kappa l}{2}\right)\right| \tag{2.6.3}$$

where C = stiffness between neighbouring layers and l = distance between the neighbouring layers. It is clear that the $\omega - \kappa$ relationship in Eq. 2.6.3 is non-linear, and the slope decreases with increasing κ from 0 to π/l, i.e. there is normal dispersion. The presence of the normal dispersion relation in a FCC packing sample was observed by Mouraille & Luding (2008) using

DEM (Fig. 2.24), while in their DEM simulations Thomas et al. (2009) observed an anomalous dispersion, i.e. the slope in the $\omega - \kappa$ relationship increases with increasing κ. The $\omega - \kappa$ relationship enables estimation of the group velocity (V_{group}) and the phase velocity (V_{phase}) given by:

$$V_{group} = \frac{d\omega}{d\kappa} \tag{2.6.4}$$

$$V_{phase} = \frac{\omega}{\kappa} \tag{2.6.5}$$

The group velocity is considered to give information about the energy of the propagating waves. The dispersion relation in granular materials indicates that a wave packet propagates with a particular combination of ω and κ where V_{group} and V_{phase} are obtained in Eqs. 2.6.4 and 2.6.5, respectively. To relate this to the sample stiffness, the largest velocity is of interest. When the long-wave limit is considered, i.e. $\kappa \rightarrow 0$ ($\lambda \rightarrow \infty$), the resultant long-wave velocity V_{long} (= max. V_{group} = max. V_{phase}) is given by:

$$V_{long} = l\sqrt{\frac{C}{m}} \tag{2.6.6}$$

where V_{long} is independent of ω or κ (i.e. non-dispersive). Within this limit, the granular material can be regarded as an equivalent homogenous continuum.

Granular materials act as a low-pass frequency (or wavelength) filter to seismic (stress) or acoustic waves. Santamarina & Aloufi (1999) related the low-pass wavelength to particle size, whereas Mouraille & Luding (2008) related it to the layer spacing. O'Donovan et al. (2016) reported that the low-pass frequency varies with confining pressure in randomly packed monodisperse materials. A better understanding of the material characteristics that determine low-pass limit is desired. In a theoretical viewpoint, the low-pass frequency can be estimated substituting $\lambda/l = 2$ (i.e. $\kappa l = \pi$) into Eq. 2.6.3. In the laboratory, Cha et al. (2009) investigated the dispersion relation of *S*-waves using stacked disks of gypsum (thickness of each disk = S) and observed a clear dispersion relation of *S*-waves. They found a long-wave limit of the *S*-wave velocity when (λ/S > 10), whereas the *S*-wave velocity decreased significantly when λ/S $\rightarrow$ 2 (Fig. 2.26). This agrees with the theoretical estimation of the low-pass wavelength for regular packing when the disk thickness is considered as the layer distance (S = l).

In the laboratory, it is difficult to measure the displacement of individual particles inside a sample. Thus, frequency domain analysis can only be achieved using voltage signals measured at the boundaries of the sample using a resonant column device or bender elements. This limitation can be overcome using DEM simulations for idealised cases as additional information of individual spheres during the wave propagation can be analysed.

2.7 Small strain stiffness of sample

The sample moduli at small-strains are important in soil mechanics as it is directly related to ground deformation under loading (Atkinson, 2000; Clayton, 2011). Soil stiffness is also important to predict site response to earthquake loading and is an input parameter in finite element modelling (Potts, 2003). As discussed above, laboratory geophysics tests are often used to deduce the sample small strain stiffness given by:

$$G_0 = \rho_d \, V_S^2 \tag{2.7.1}$$

$$M_0 = \rho_d \, V_P^2 \tag{2.7.2}$$

$$\nu_S = \frac{M_0 - 2G_0}{2(M_0 - G_0)} \tag{2.7.3}$$

$$E_0 = 2G_0(1+\nu_S) = \frac{G_0(3M_0 - 4G_0)}{M_0 - G_0} \tag{2.7.4}$$

where G_0 = sample small-strain shear modulus; M_0 = sample small-strain constrained modulus; ρ_d = dry sample bulk density; ν_S = sample Poisson's ratio; E_0 = sample small-strain Young's modulus.

Experimental results can be compared with a micromechanical analytical model, which is termed effective medium theory (EMT). EMT assumes a homogeneous isotropic assembly and identical contact interaction at all the contacts. The following sections discuss the basis of EMT and outline how surface roughness can be incorporated in the theory. Another analytical technique that solves the eigenvalue problem to estimate the overall stiffness of DEM samples is briefly investigated.

2.7.1 Effective medium theory

The elastic moduli of an assembly can be analysed assuming the system is homogeneous, isotropic, and comprised of equal spheres. This type of approach is often called effective medium theory (EMT). Examples of its prior use include Duffy & Mindlin (1957) who derived the constrained moduli in two directions for a FCC packing to compare with their equivalent experiments. Santamarina & Cascante (1996) summarised expressions of sample shear modulus for regular packings. For a FCC sample,

$$G_0^{EMT-FCC} = \frac{(4-3\nu_p)}{2(2-\nu_p)}\left[\frac{3G_p^2\sigma'}{2(1-\nu_p)^2}\right]^{1/3} \tag{2.7.5}$$

where σ' = isotropic confining stress; the HM model was employed to derive Eq. 2.7.5. Note that the FCC sample has an anisotropic fabric (transverse isotropy) as indicated by Duffy & Mindlin (1957), and the G_0 values depend on the direction of wave propagation and oscillation (O'Donovan et al. 2015b).

For random packings, more general expressions were derived for porous rocks or an assembly of mono-sized spheres (Digby, 1981; Walton, 1987; Rothenburg & Bathurst, 1989; Chang & Liao, 1994). EMT theory relates the contact stiffnesses k_N and k_T to the overall stiffness of an assembly using the assumption of homogeneity. The principal of virtual work was considered by Chang & Liao (1994) to derive a EMT theory. They considered a kinematic hypothesis which assumes a uniform strain in the assembly, and a static hypothesis which assumes a uniform stress in the assembly, in their calculations. The kinematic and static hypotheses give upper and lower bounds to estimate the elastic moduli. The following expressions for G_0, E_0 and v_s are derived from a kinematic hypothesis:

$$E_0^{EMT-K} = \frac{\overline{C_N}}{2\pi R(1+e)} k_N \frac{2+3R_k}{4+R_k} \tag{2.7.6}$$

$$G_0^{EMT-K} = \frac{\overline{C_N}}{4\pi R(1+e)} k_N \frac{2+3R_k}{5} \tag{2.7.7}$$

$$v_s^{EMT-K} = \frac{1-R_k}{4+R_k} \tag{2.7.8}$$

and the following expressions are based on a static assumption:

$$E_0^{EMT-S} = \frac{\overline{C_N}}{2\pi R(1+e)} k_N \frac{5R_k}{2+3R_k} \tag{2.7.9}$$

$$G_0^{EMT-S} = \frac{\overline{C_N}}{4\pi R(1+e)} k_N \frac{5R_k}{3+2R_k} \tag{2.7.10}$$

$$v_s^{EMT-S} = \frac{1-R_k}{2+3R_k} \tag{2.7.11}$$

where $\overline{C_N}$= mean particle coordination number; $R_k = k_T/k_N$. In the expressions above the following relationship was used (Chang et al., 1991):

$$\frac{CN}{V} = \frac{3\overline{C_N}}{8R^3\pi(1+e)} \tag{2.7.12}$$

where CN = the total number of particle contacts in the sample of volume V.

Referring to Fig. 2.27(a), the shear modulus (G_0) normalised by the modulus at $R_k = 1$ based on Eqs. 2.7.7 and 2.7.10 increases with R_k. It is clear that whichever hypothesis is adopted, R_k has a measurable influence on the overall stiffness. This highlights the sensitivity of the analytically estimated shear modulus to the contact model. Fig. 2.27(b) shows how the sample Poisson's ratio varies with R_k based on Eqs. 2.7.8 and 2.7.11. The difference between the two assumptions is noticeable at lower R_k values, whereas the Poisson's ratio becomes negative when $R_k > 1$; this does not seem physically plausible as soil samples normally exhibit $v_S > 0$.

It is important to use an appropriate contact model in the expressions for EMT as the normal contact stiffness k_N proportionally affects the elastic moduli. For the HM contact model, the normal force determines the normal contact stiffness (see Eqs. 2.3.5 and 2.3.6). The mean normal contact force (N_{mean}) can be estimated using packing parameters and external stress as below (Chang et al., 1991):

$$N_{mean} = \frac{4\pi R^2 (1+e)}{\overline{C_N}} \sigma' \tag{2.7.13}$$

If a no-slip (stick) condition is considered, the tangential contact stiffness can be obtained directly from Eq. 2.3.14 or Eq. 2.3.15 for the HM model. Thus, EMT expressions for the HM contact model using the kinematic assumption (Chang et al., 1991) are:

$$E_{0,HM}^{EMT-K} = \frac{2(5-4\nu_p)}{5-3\nu_p}\left[\frac{\sqrt{3}}{\sqrt{2}\pi(1-\nu_s)}\right]^{2/3}\left[\frac{\overline{C_N}}{(1+e)}\right]^{2/3} G_p^{2/3}\sigma'^{1/3} \tag{2.7.14}$$

$$G_{0,HM}^{EMT-K} = \frac{(5-4\nu_p)}{5(2-\nu_p)}\left[\frac{\sqrt{3}}{\sqrt{2}\pi(1-\nu_p)}\right]^{2/3}\left[\frac{\overline{C_N}}{(1+e)}\right]^{2/3} G_p^{2/3}\sigma'^{1/3} \tag{2.7.15}$$

$$\nu_{s,HM}^{EMT-K} = \frac{\nu_p}{10-8\nu_p} \tag{2.7.16}$$

Substituting $v_p = 0.2$, for example, into Eq. 2.7.16 gives $v_S = 0.0238$.

For the case of partial slip, however, the expression should be modified considering the applied tangential contact force. However, tangential contact forces depend on loading history, and cannot be estimated directly from micromechanical parameters; this makes difficult to use the HMD model in EMT analyses. For example, Duffy & Mindlin (1957), Chang et al. (1991), and Yimsiri & Soga (2000) introduced partial slip in their analytical models; however, an assumption of a negligible tangential contact force ($T = 0$) in a homogeneous isotopic sample under an isotropic stress reduced the HMD model to the HM model in their analyses. The assumption may be correct for regular packings but not for random packings. Duffaut et al. (2010) examined partial slip effects on the sample shear modulus (G_0) of smooth spheres using

EMT with a kinematic assumption (Walton 1987). Referring to Fig. 2.28, both G_0 and wave velocities decrease as partial slip develops. It should be noted that Duffaut et al. (2010) assumed a homogeneous distribution of the tangential contact forces and the reduction in tangential contact stiffness due to partial slip was estimated equally for all the contacts. However, it may not be correct for a random packing where the orientation of the tangential contact forces depend on loading history and counter slip due to unloading of the tangential contact forces should also be considered. Such validation is not trivial using a theoretical model.

In laboratory tests, the sample void ratio can be obtained easily but the mean coordination number is not known; G_0 is often related to e in experimental studies. Magnanimo et al. (2008) observed a clear correlation between G_0 and $\overline{C_N}$ for randomly packed samples rather than the $G_0 - e$ relationship using DEM. Referring to Eqs. 2.7.7 and 2.7.10 for the EMT expressions it is clear that the overall stiffness is sensitive to the mean coordination number as:

$$G_0^{EMT} \propto \left[\frac{\overline{C_N}}{(1+e)} \right]^{2/3} \tag{2.7.17}$$

For example, Chang et al. (1991) used the following expression:

$$e = 1.66 - 0.125\overline{C_N} \tag{2.7.18}$$

whereas Duffaut et al. (2010) selected the following expression:

$$\overline{C_N} = 24 \exp\left\{ -2.547 \left(\frac{e}{1+e} \right) \right\} - 0.373 \tag{2.7.19}$$

As discussed in Section 2.5, there is no global agreement of the correlation between $\overline{C_N}$ and e. For example, an error between 20% and 30% in $\overline{C_N}$ can occur depending on the model adopted, which results in an error up to 20% of estimated elastic moduli. The stress-dependency of the $\overline{C_N} - e$ relationship should also be taken into account to develop a robust model.

2.7.2 Analytical model considering surface roughness

As discussed in Section 2.4, recent tribology research has contributed to develop a rough contact model. Yimsiri & Soga (2000) incorporated the α parameter given in Eq. 2.4.4 into a micromechanical constitutive model (EMT theory) with a static hypothesis derived by Chang & Liao (1994) (Eqs. 2.7.9 and 2.7.10) and demonstrated that the influence of surface roughness on the normal contact stiffness has a measurable effect on the elastic moduli of an assembly of rough spheres. They showed that the surface roughness reduces the elastic moduli at low confining pressures; however the effect becomes less noticeable as the mean confining pressure increases (Fig. 2.29), giving a larger exponent value than that for the equivalent smooth

assembly. This analytical model can capture the experimental observations reviewed in Section 2.6.2 where surface roughness reduces the wave velocity.

When EMT is applied using a rough contact model, contacts are assumed to be identical, thus the surface roughness equally effects all the contact responses. This assumption should be carefully examined using alternative approach such as DEM simulation.

2.7.3 Eigenmode analysis of vibration

If the mass and stiffness matrices of a structure system can be created, for example in finite element or structural matrix analyses, the fundamental natural vibration modes can be found via eigenvalue decomposition, where the eigenvector gives the fundamental shape of vibration associated with an angular frequency (ω) equal to the square root of the corresponding eigenvalue (e.g. Chopra, 2011). As discussed in O'Sullivan & Bray (2004) the particles in a DEM simulation are analogous to the nodes in a finite element model, while the contacts are roughly equivalent to the elements. This conceptual model of a granular material is used in implicit discrete element method formulations such as the particulate form of discontinuous deformation analysis (DDA) as outlined in Ke & Bray (1995). For 3D particle scale analyses of granular assemblies, each particle has 3 translational degrees of freedom and 3 rotational degrees of freedom and so the diagonal mass matrix ($\boldsymbol{M}$) includes the mass (m) and rotational inertia values for each particle.

The global stiffness matrix ($\boldsymbol{K}$) can be created using the stiffness matrix assembly techniques described in Zienkiewicz & Taylor (2000) once the local contact stiffness matrix describing pairwise interaction of two particles is obtained. The local contact stiffness matrix is a 12×12 element matrix; expressions for this matrix are given in Itasca (2007) and the entries depend on the particle coordinates and contact stiffnesses. For a sample composed of n particles, there are 6×n degrees of freedom. The eigenvalue decomposition is achieved by solving:

$$[\boldsymbol{K} - \boldsymbol{\omega}^2\boldsymbol{M}]\boldsymbol{\phi} = 0 \qquad (2.7.20)$$

where $\boldsymbol{\omega^2}$ = eigenvalues and $\boldsymbol{\phi}$ = eigenvectors; each eigenvalue ω_i^2 is associated with a particular eigenvector ϕ_i, and there are 6×n eigenvalues. The frequency of the i th mode is $f_i = \omega_i/(2\pi)$.

Previous researchers have used this approach to analyse the dynamic response of granular materials. Based on their 1D chain model, Lawney & Luding (2014) showed that the low-frequency eigenmodes are not affected by small random variations in particle mass. Somfai et al. (2005) considered a 2D configuration of disks, and linked peaks in the received signal frequency spectrum and to eigenmodes (Figs. 2.30(a) and (b)). They also noted that the eigenmodes corresponding to the low non-zero eigenfrequencies (n = 141 and 142 in Fig. 2.30)

has a trend similar to the particle displacements during wave propagation, whereas higher modes associated with more random or local eigenmodes. Marketos & O'Sullivan (2013) performed an eigenmode analysis for 2D regular arrays and linked to a DEM simulation for the same packing. Application of eigenmode analysis to a 3D packing is challenging, not just due to the increased number of degrees of freedom, but also because the eigenvector (mode) shapes are more complex.

2.8 Summary

This chapter reviewed prior research on how the small-strain stiffness of soil sample can be estimated in experiments, numerical simulations and analytical approaches. The theoretical basis of the contact models and applications for effective medium theory (EMT) and discrete element method (DEM) were described. The important factors affecting the elastic properties of the granular materials such as contact models and the correlation between mean coordination number ($\overline{C_N}$) and void ratio (e) were highlighted. Dynamic laboratory tests including resonant column test and bender element test to measure the sample moduli at small-strains and wave velocities were also reviewed.

This study considers effects of surface roughness, partial slip, and twisting resistance on contact models based on literature. As described above, the sample stiffness at small-strains and elastic wave velocities are influenced by contact models when a theoretical or a numerical approach is considered. Prior experimental studies of the influence of surface roughness showed that increasing surface roughness reduces the sample stiffness. Accurate measurements of surface roughness is important to link a theoretical study and an experimental study.

It is well known that the soil stiffness is affected by e based on experimental literature. Theoretical studies also indicate that $\overline{C_N}$ affects the soil stiffness. The $\overline{C_N}$-e relationship has been studied for a long period. Amongst the literature reviewed here, a considerable discrepancy on the estimation of $\overline{C_N}$ for a given e was noted. In addition, literature that discusses the influence of confining stress or stress state on the correlation are rare. As the soil mechanics research often relates e to the mechanical behaviour of soil sample, it is important to develop understanding of the nature of the $\overline{C_N}$-e relationship for various stress conditions including isotropic, K_0 and the critical state.

Theoretical studies using EMT are useful to relate the soil stiffness to contact models and the $\overline{C_N}$-e relationship. However, a number of simplifying assumptions in EMT are not realistic. Numerical studies using DEM may be more useful for understanding physical systems than this type of theoretical approach.

2.9 Tables

Table 2.1. Mean particle coordination number ($\overline{C_N}$), void ratio (e), porosity (p) and volume fraction (f) for regular arrays.

Packing	$\overline{C_N}$	e	p	f
simple cubic	6	0.910	0.476	0.524
cubic tetrahedral	8	0.654	0.395	0.605
tetragonal-sphenoidal	10	0.432	0.302	0.698
pyramidal	12	0.351	0.260	0.741
tetrahedral	12	0.351	0.260	0.741

Table 2.2. Summary of $\overline{C_N} - e$ relationship in the literature (*data obtained from sands).

Reference	$\overline{C_N} - e$ relationship	Eq.
Smith et al. (1929)	$\overline{C_N} = 15.76 - 10.73e$	2.5.3
Nakagaki & Sunada (1963;1968)	$\overline{C_N} = 1.61\left(\frac{1+e}{e}\right)^{1.48}$	2.5.4
Gotoh (1978)	$\overline{C_N} = 20.7/(1+e) - 4.35 \quad (0.429 < e \le 1.13)$	2.5.5
Ouchiyama & Tanaka (1980)	$\overline{C_N} = \frac{32}{13}\left[7 - 8\left(\frac{e}{1+e}\right)\right]$	2.5.6
Suzuki et al. (1981)	$\overline{C_N} = 2.828\frac{(1+e)^{1/3}}{\left(\frac{b}{D}\right)^2\left[1+\left(\frac{b}{D}\right)^2\right]}$ $(1+e)^{1/3} = \frac{1+(b/D)^2}{1+\left(\frac{b}{D}\right)\exp\left\{\left(\frac{D}{b}\right)^2\right\}Erfc\left\{\frac{D}{b}\right\}}$	2.5.7
Zhang et al. (2001)	$\overline{C_N} = \left[0.183 - 659.2/(1+e)^{20.96}\right]^{-1} \quad (0.587 < e \le 0.818)$	2.5.9
Field (1973)	$\overline{C_N} = 12/(1+e)$	2.5.10
German (2014)	$\overline{C_N} = 2 + 11/(1+e)^2$	2.5.11
German (2014)	$\overline{C_N} = -2.8 + 15.1/(1+e)$	2.5.12
Fonseca et al. (2013)*	$e = 1.69\exp^{-0.14\overline{C_N}}$	2.5.13
Hasan & Alshibli (2010)*	$e = 2.23\exp^{-0.13\overline{C_N}}$	2.5.14

2.10 Figures

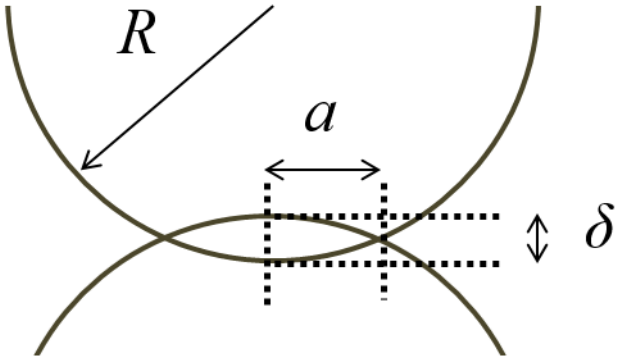

Figure 2.1. Smooth particles in contact.

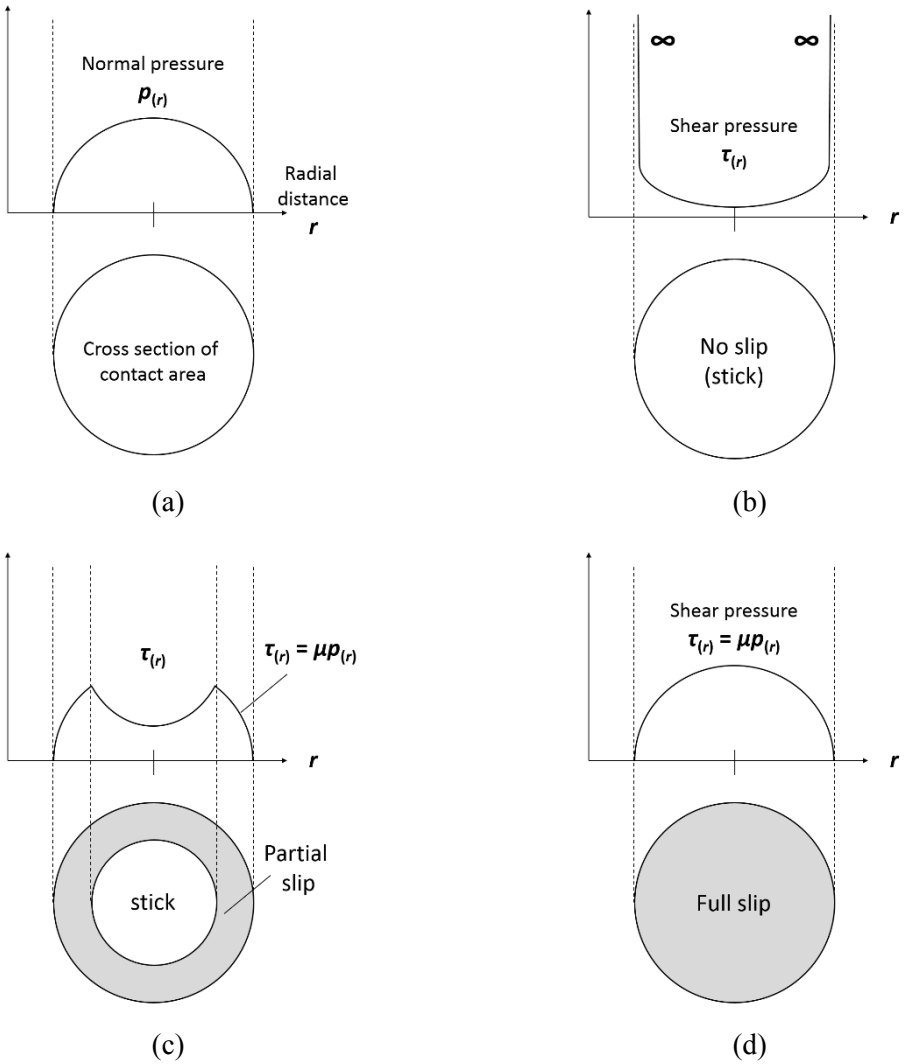

Figure 2.2. Schematic illustrations of stick and slip regions and pressure distribution along the radial distance (r) on a contact. (a) Normal pressure (p) distribution (b) Shear pressure (τ) distribution with no-slip (c) Shear pressure distribution with partial slip (d) Shear pressure distribution with full slip

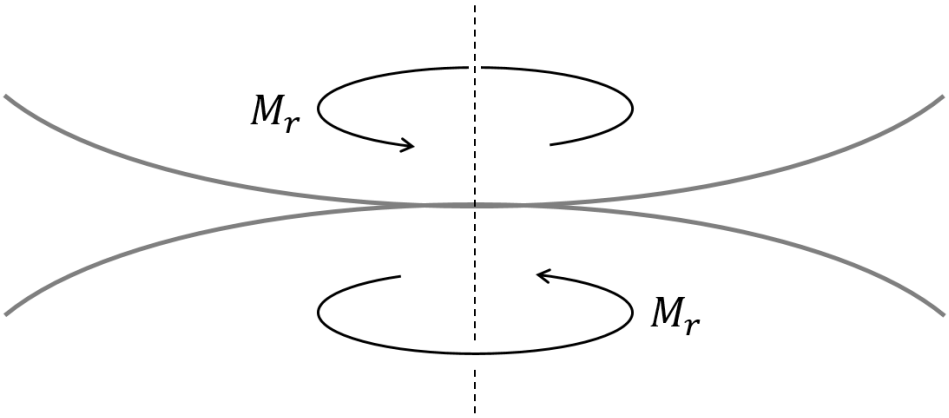

Figure 2.3. Twisting moment applied at contact.

(a) (b)

Figure 2.4. Schematic illustrations of contact between (a) smooth surface and rough surface, and (b) rough surface and rough surface.

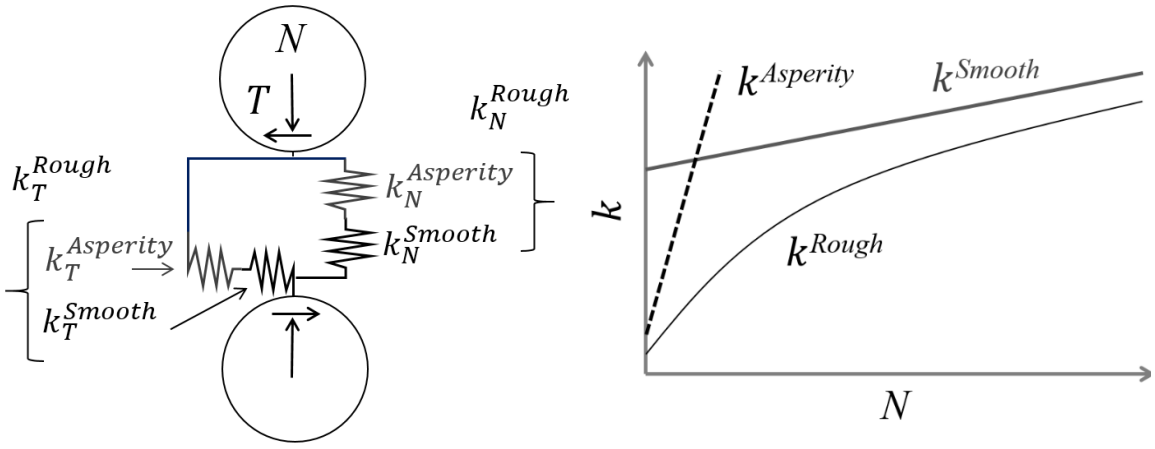

(a) (b)

Figure 2.5. Hybrid stiffness of asperity and smooth contacts as described in Medina et al. (2012): (a) Schematic illustration of springs connected in series, and (b) Relationship between contact stiffness and contact force.

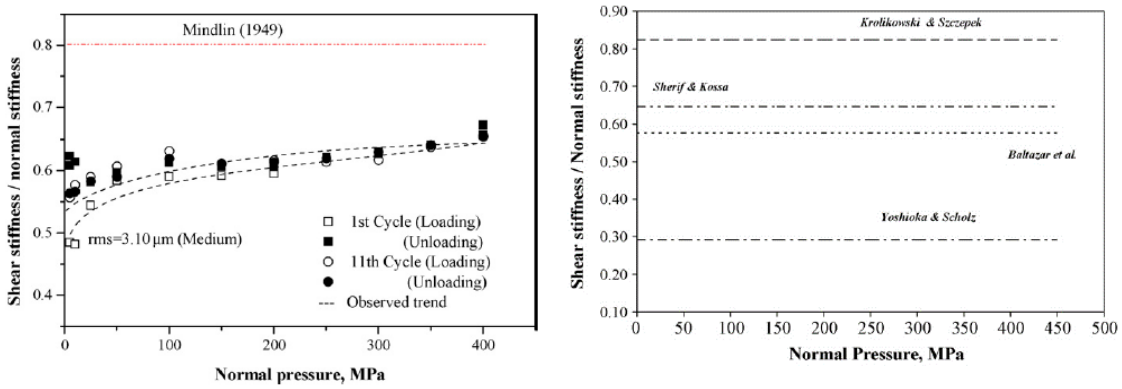

(a) (b)

Figure 2.6. Evolution of contact stiffness ratio (k_T/k_N) with normal pressure for rough contacts: (a) Experimental results by Gonzalez-Valadez et al. (2010), and (b) Other results (Gonzalez-Valadez et al., 2010).

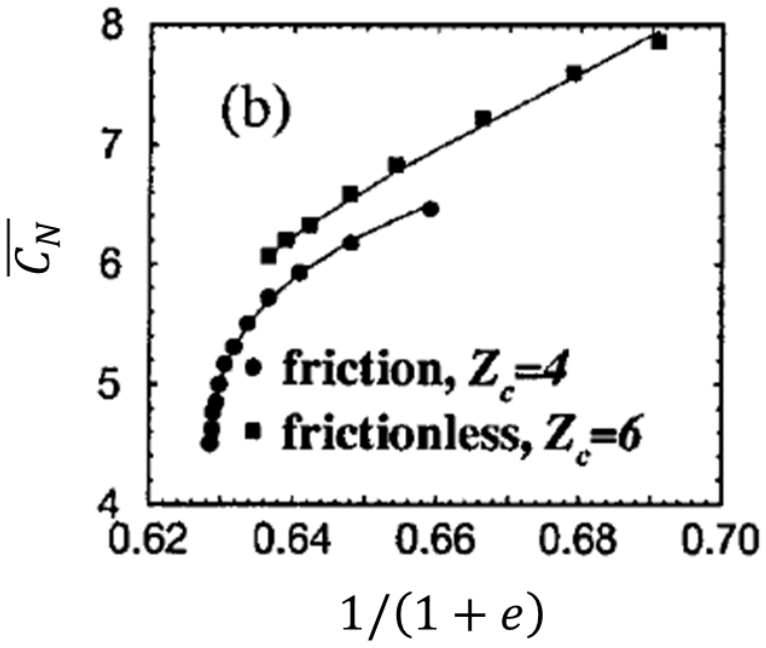

Figure 2.7. Evolution of $\overline{C_N}$ - e relationship for random dense sample (frictionless) and random loose sample during isotropic compression (edited from Makse et al. (2000)).

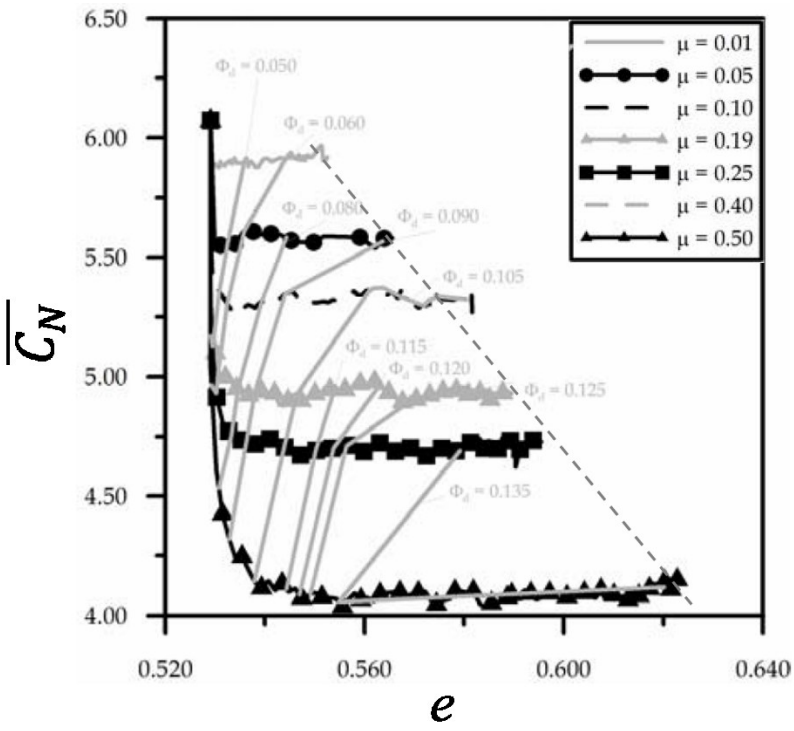

Figure 2.8. Evolution of $\overline{C_N}$ - e relationship during triaxial loading (edited from Barreto & O'Sullivan (2012)).

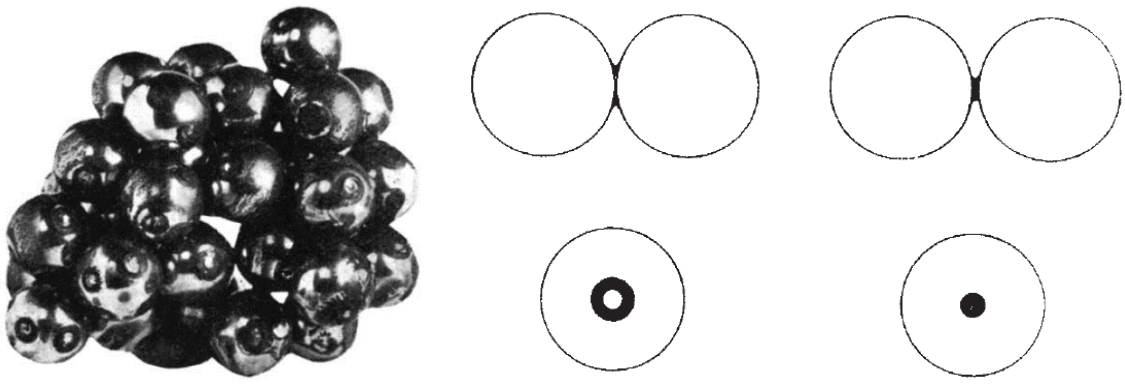

(a) (b)

Figure 2.9. Ink tests by Bernal & Mason (1960). (a) Stuck steel spheres with ink at contacts (b) Schematics of close contact (left) and near contact (right)

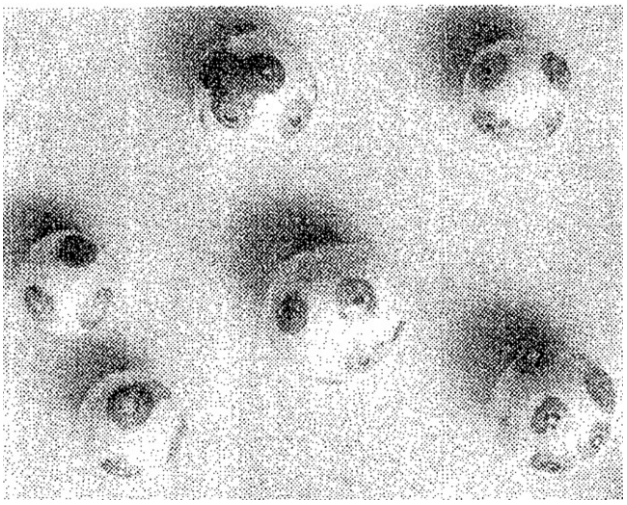

Figure 2.10. Representative results of ink tests by Arakawa & Nishino (1973) using polystyrene balls.

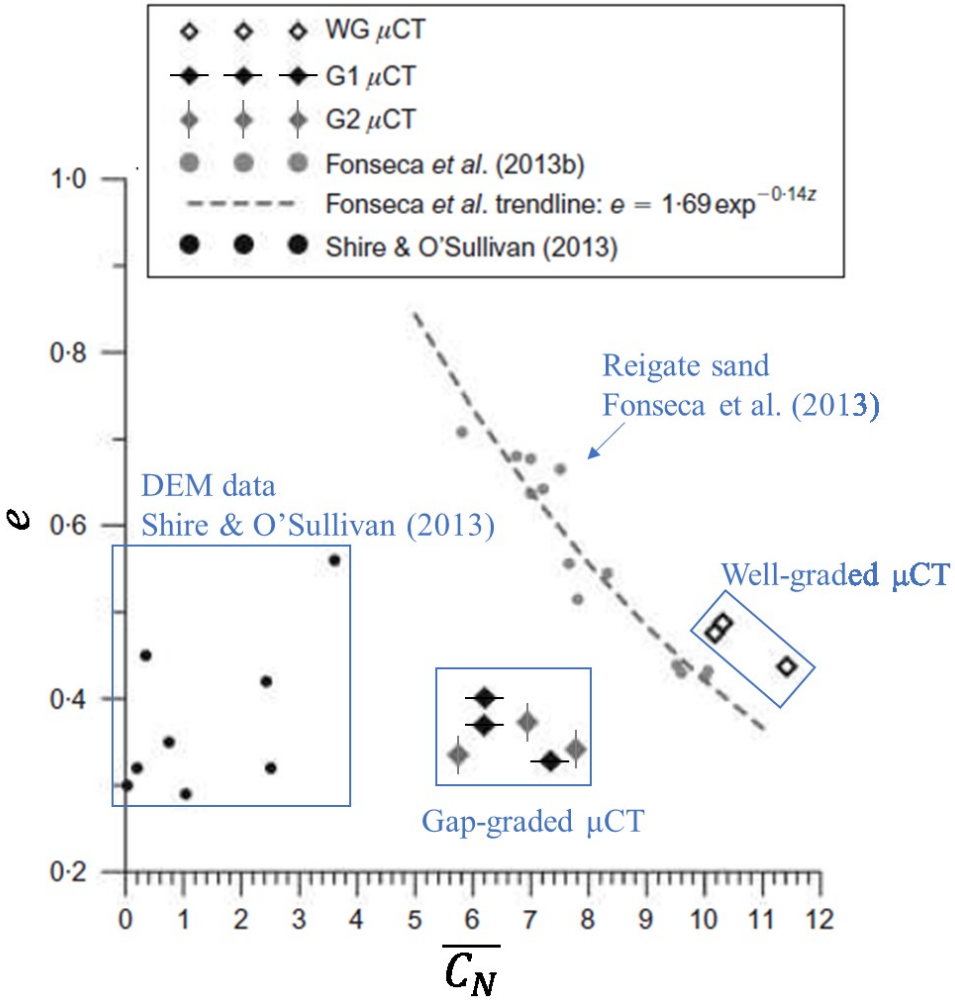

Figure 2.11. Relationship between $\overline{C_N}$ and e based on μCT and DEM results (edited from Fonseca et al, 2014). WG stands for well-graded sand specimens, and G1 and G2 are gap-graded sand specimens that were scanned using μCT.

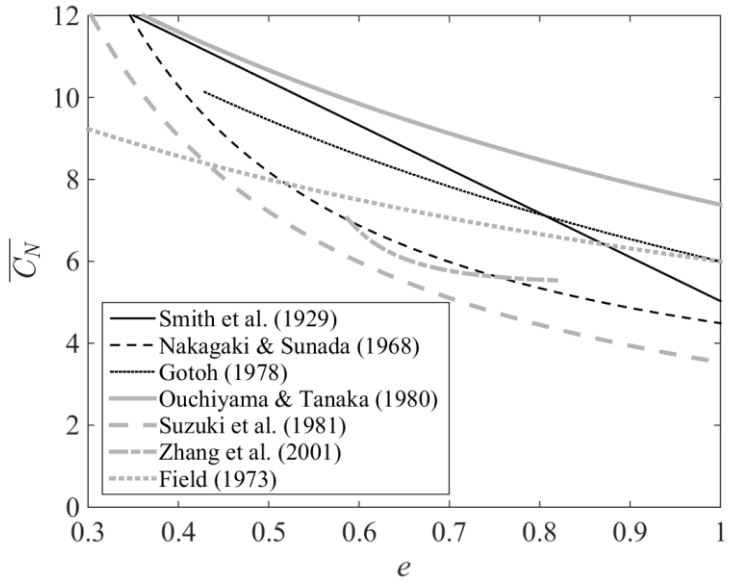

(a)

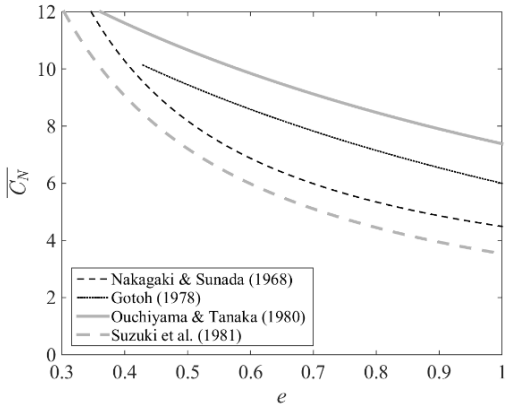

(b)

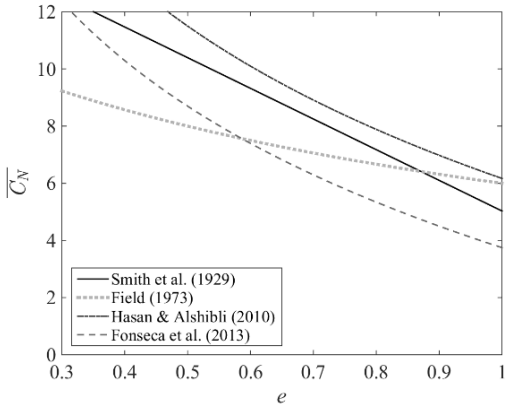

(c)

Figure 2.12. Summary of $\overline{C_N}$ - e relationships given in the literature. (a) All expressions from Eqs. 2.5.3 to 2.5.10 (b) Correlations that were analytically derived (c) Experimentally-based correlations

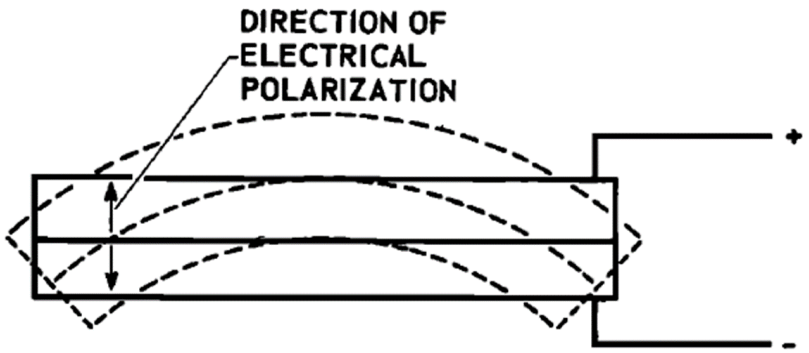

Figure 2.13. Schematic illustration of movement of a ceramic bender element (Shirley, 1978).

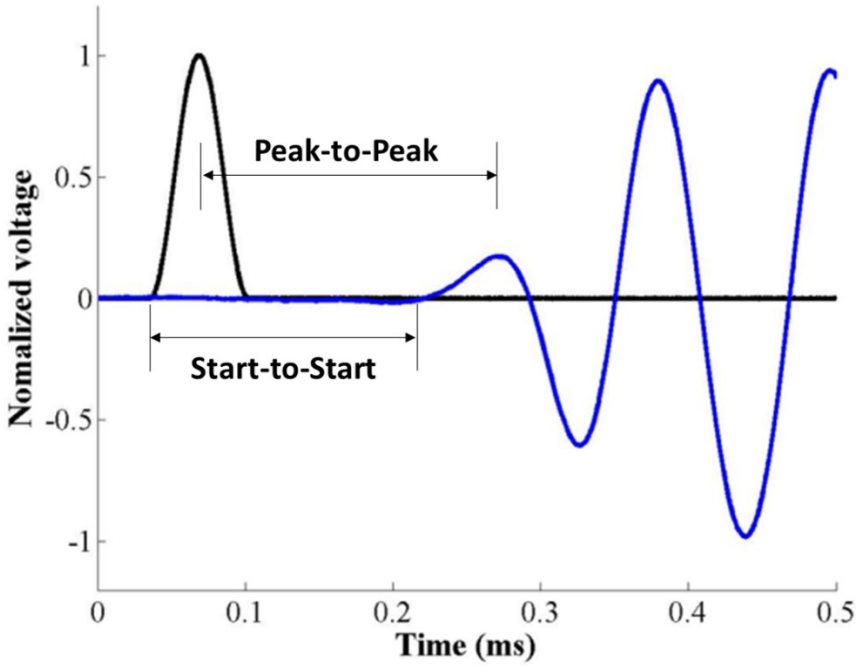

Figure 2.14. Schematic illustration of start-to-start and peak-to-peak methods to determine travel time of waves.

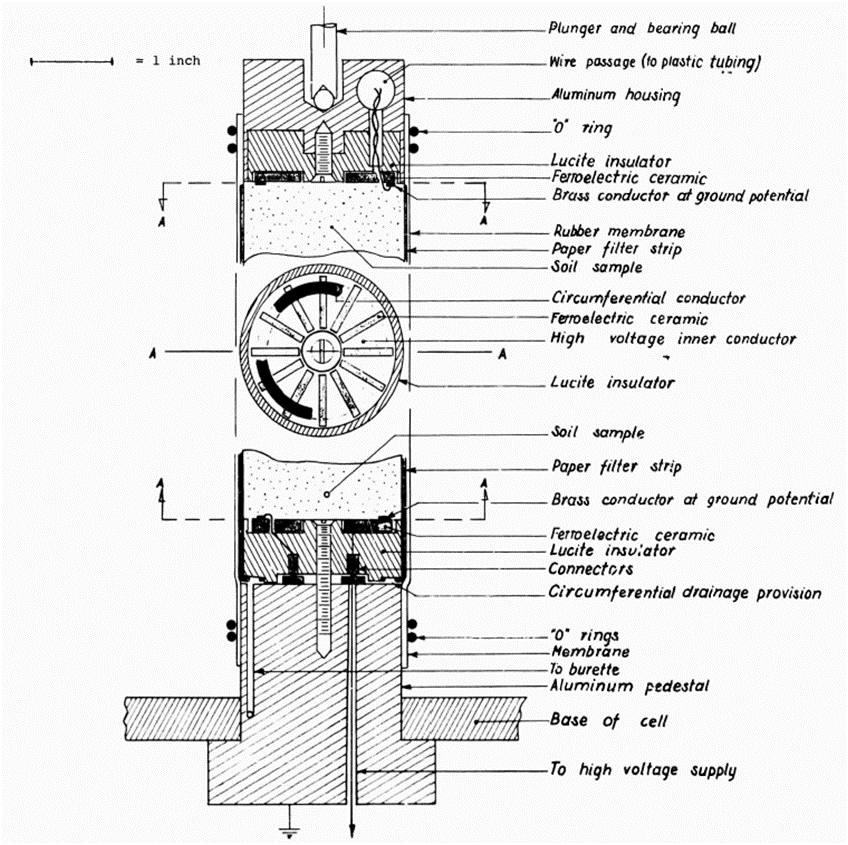

Figure 2.15. Modified triaxial apparatus with capacity of dynamic tests using shear plates (Lawrence, 1965).

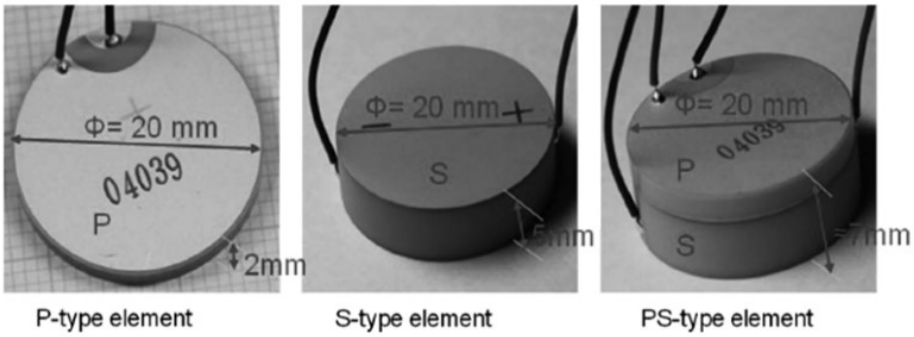

Fig. 3. Pictures of piezo-ceramic elements used in this study.

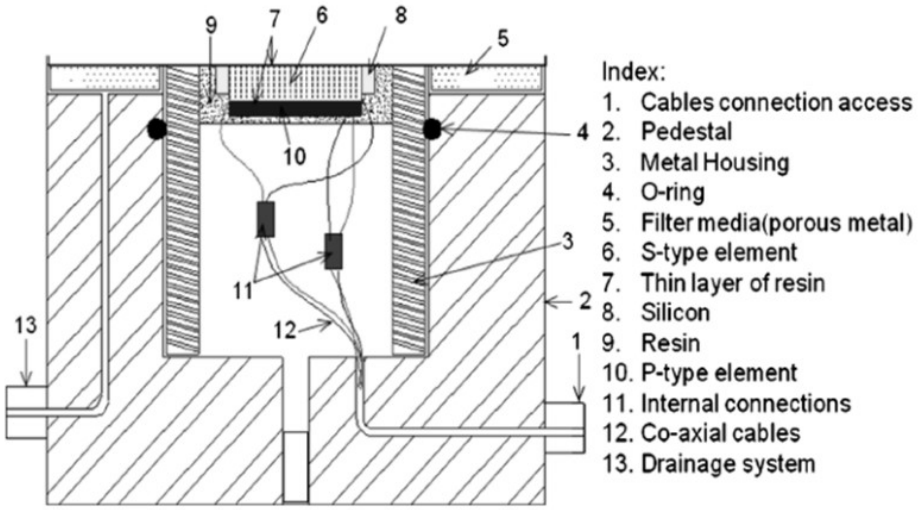

Figure 2.16. Recent development of disk transducers (shear- & compression plates) embedded inside pedestal for triaxial apparatus (Suwal & Kuwano, 2013).

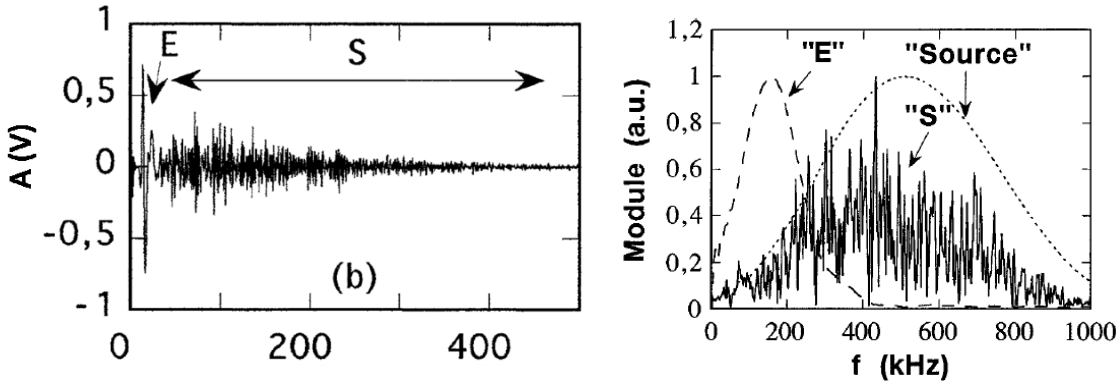

(a) (b)

Figure 2.17. Received signal of *P*-wave using disk-type sensors on glass ballotini (Jia et al., 1999). (a) Variation in amplitude of voltage with time where coherent ballistic wave (denoted as E) arrived earlier than following echo reflected from bottom and top boundaries (denoted S) (b) Variation in amplitude of received signal with frequency

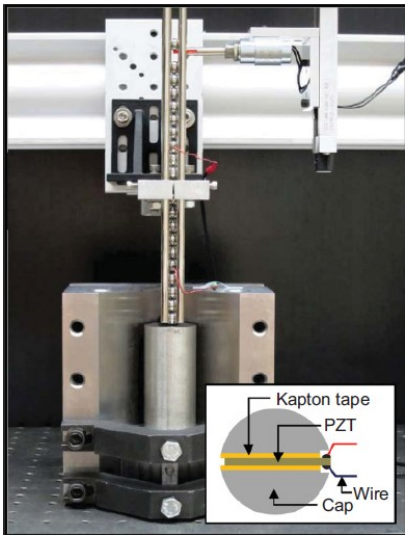

Figure 2.18. A granular chain of spheres with piezo-electric transducers (Yang et al., 2011).

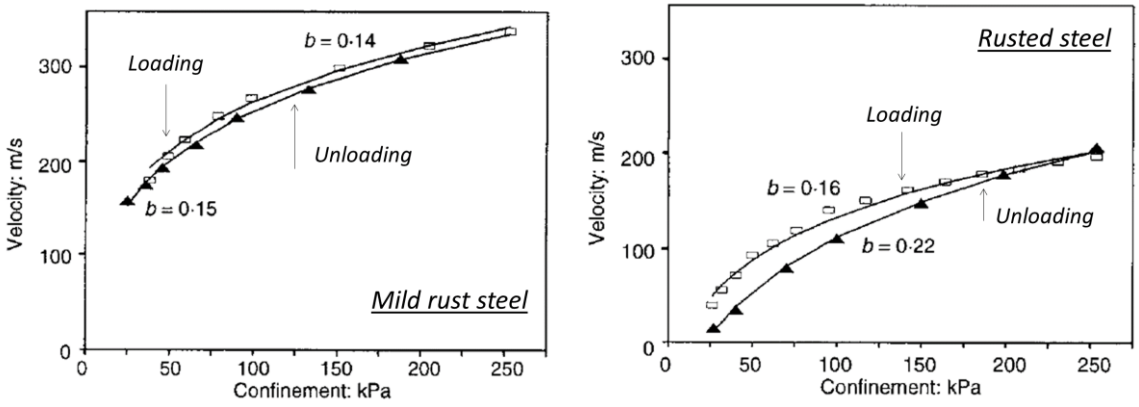

(a) (b)

Figure 2.19. Shear wave velocities in assembly of (a) mild-rust steel spheres, and (b) rusted steel spheres based on resonant column tests (edited from Santamarina & Cascante (1998)).

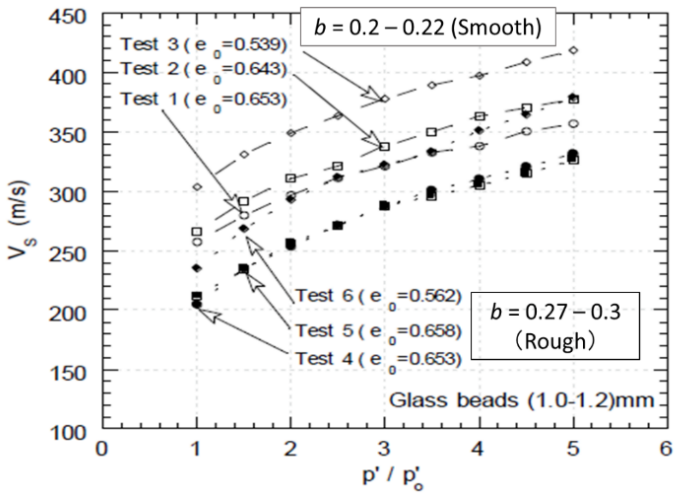

Figure 2.20. Shear wave velocities in smooth ballotini and rough ballotini using bender elements (edited from Sharifipour & Dano (2006)).

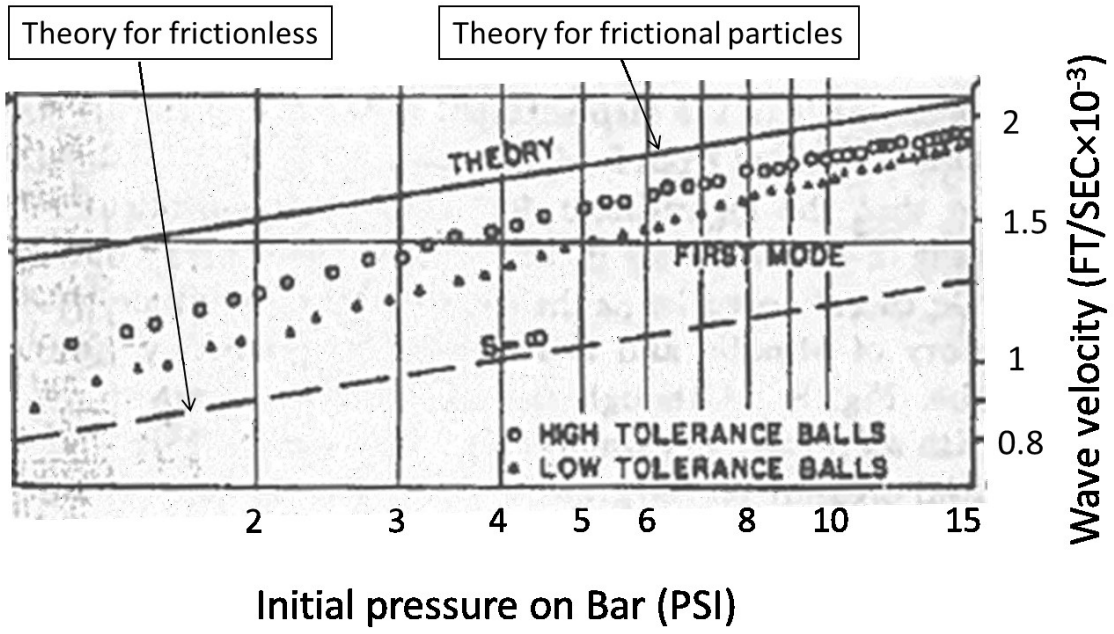

Figure 2.21. Variation in compression wave velocity with confining pressure. Experimental results using high and low tolerance balls are compared with analytical approaches for frictional and frictionless spheres (edited from Duffy & Mindlin (1957)).

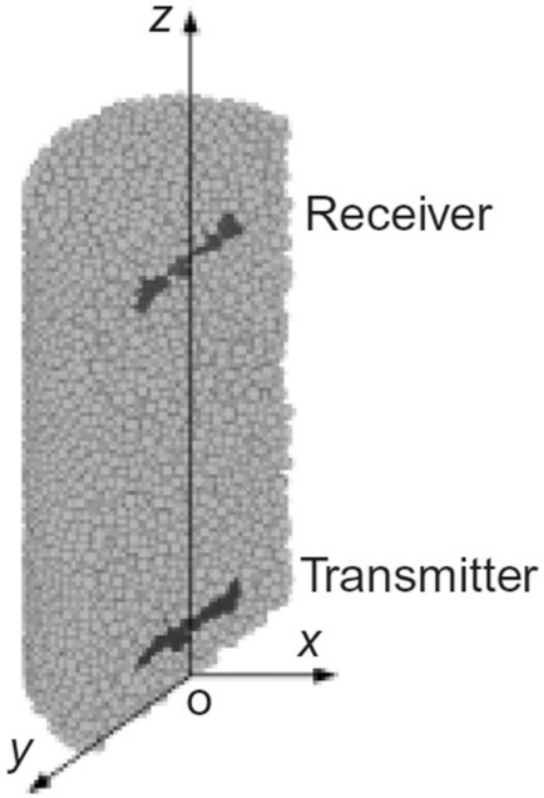

Figure 2.22. Disk-region transducer and receiver in DEM model (Xu et al., 2015).

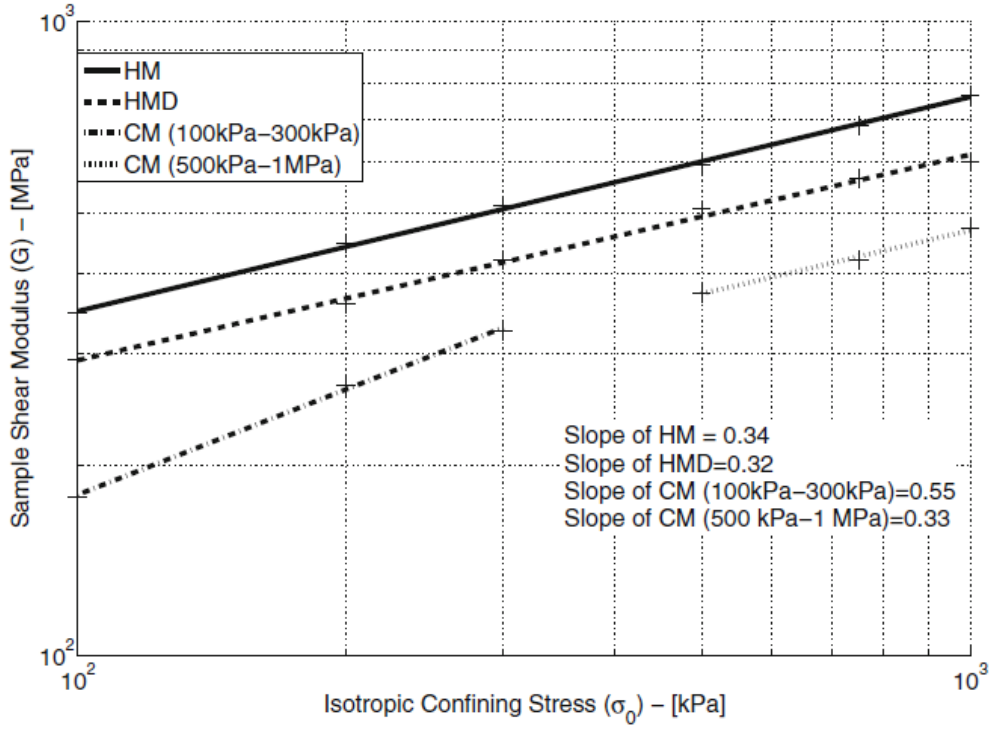

Figure 2.23. Variation in sample shear modulus with isotropic confining stress using Hertz-Mindlin (HM), Hertz-Mindlin-Deresiewicz (HMD), and Cavarretta-Mindlin (CM) contact models (O'Donovan et al., 2015).

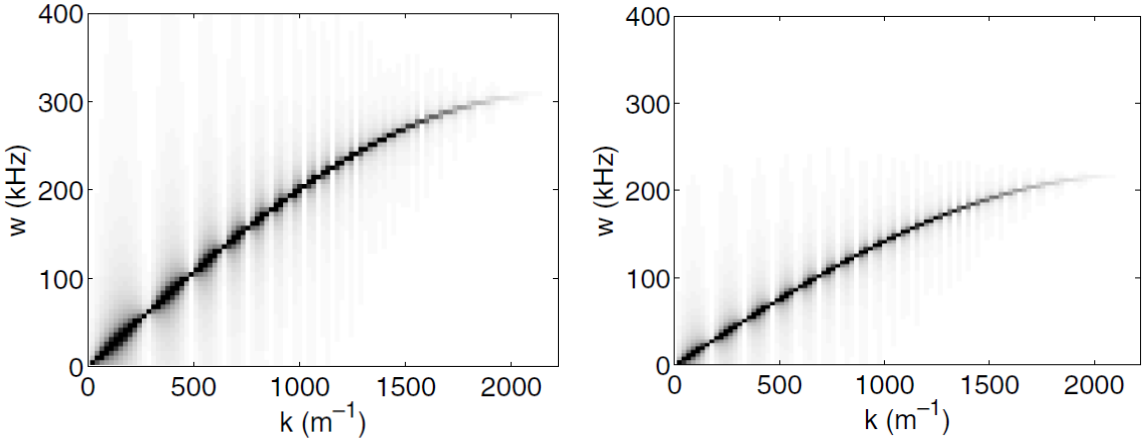

(a) (b)

Figure 2.24. Dispersion relation of (a) *P*-wave and (b) *S*-wave in a face-cantered cubic sample (grey-scale corresponds to the amplitude, absolute value, of Fourier coefficients) (Mouraille et al., 2006).

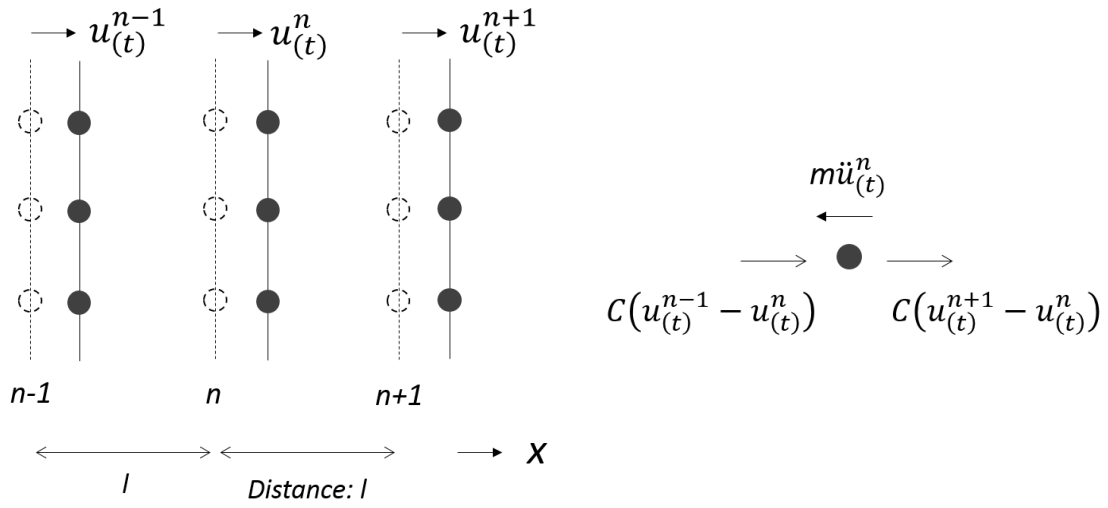

(a) (b)

Figure 2.25. Schematic illustration of interactions of chains (layers) of masses. (a) Motion of a chain of masses, (b) Force interactions between neighbouring chains (layers).

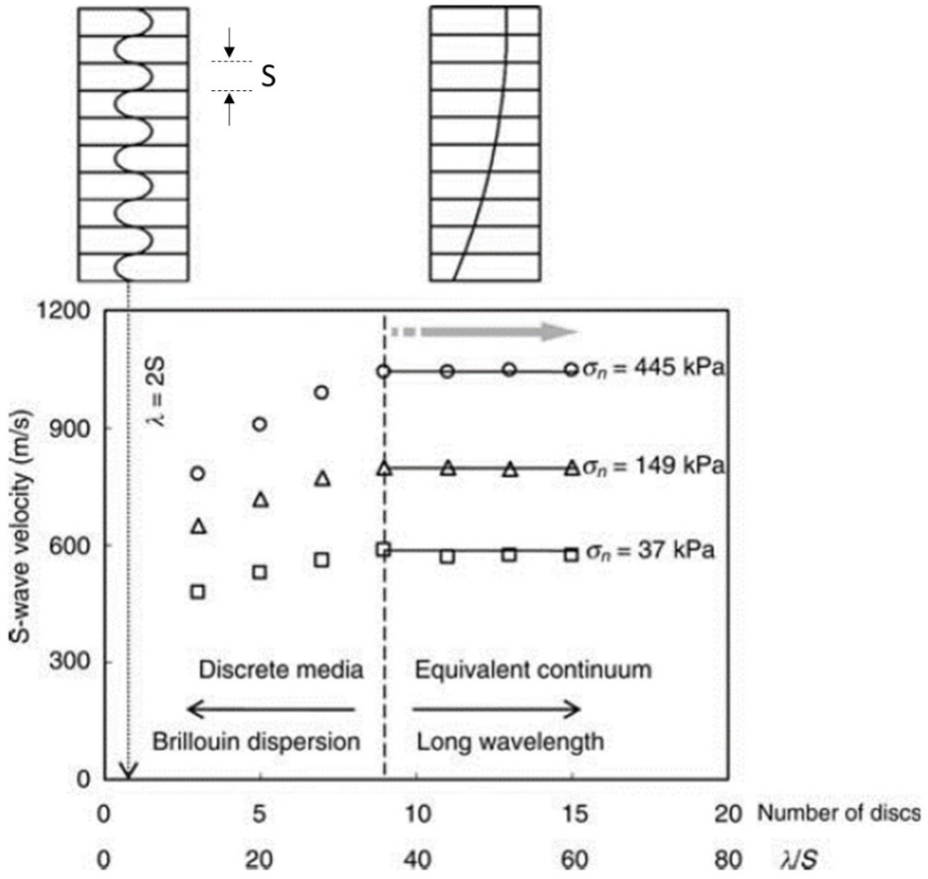

Figure 2.26. *S*-wave velocity affected by ratio of nominal wavelength (λ) to joined spacing of rock column (S) (edited from Cha et al., 2009).

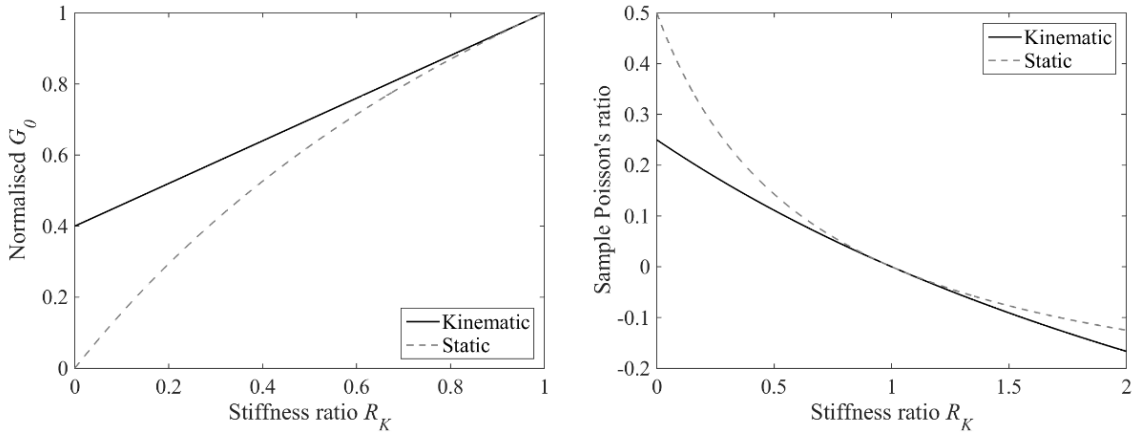

(a) (b)

Figure 2.27. Estimation of sample elastic properties using EMT. (a) Relationship between normalized shear modulus and contact stiffness ratio (b) Relationship between sample Poisson's ratio and contact stiffness ratio (using expressions given in Chang & Liao (1994))

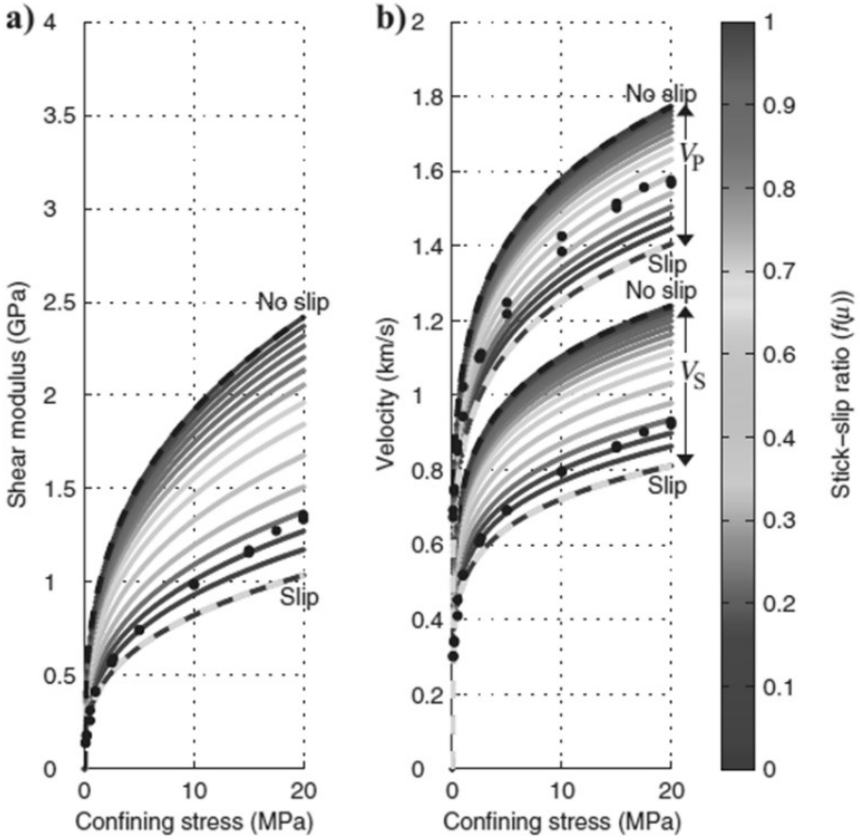

Figure 2.28. Influence of partial slip on (a) shear modulus and (b) wave velocities estimated using EMT with a kinematic assumption (Duffaut et al., 2010).

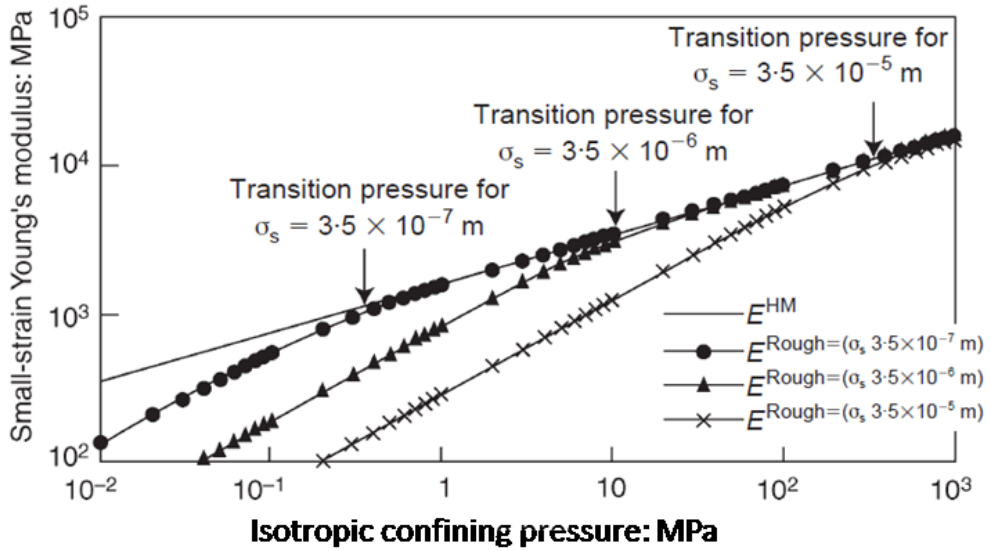

(a)

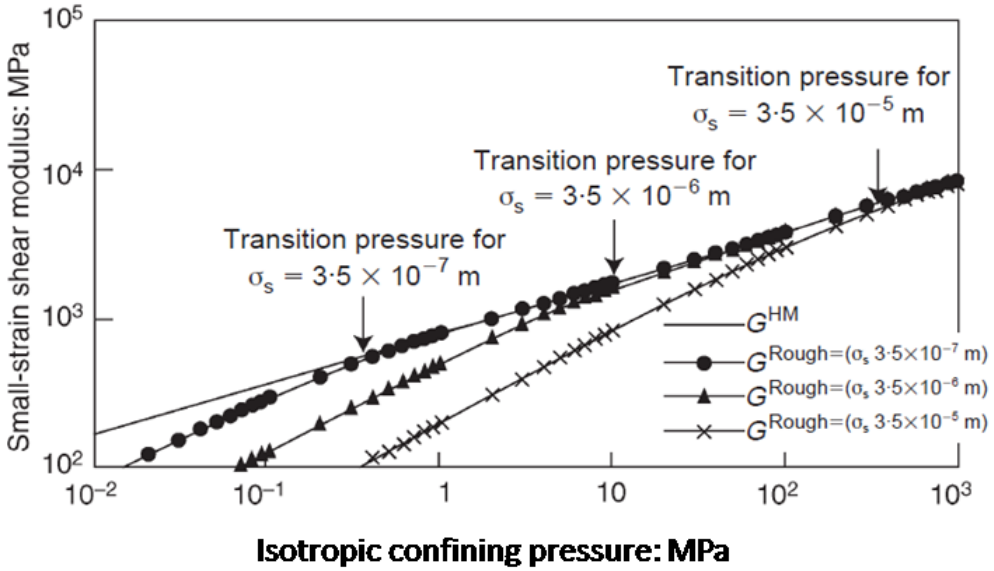

(b)

Figure 2.29. Variation in small-strain moduli with isotropic confining pressure for various surface roughness values (σ_s): (a) Sample Young's modulus, and (b) Sample shear modulus (edited from Yimsiri & Soga (2000)).

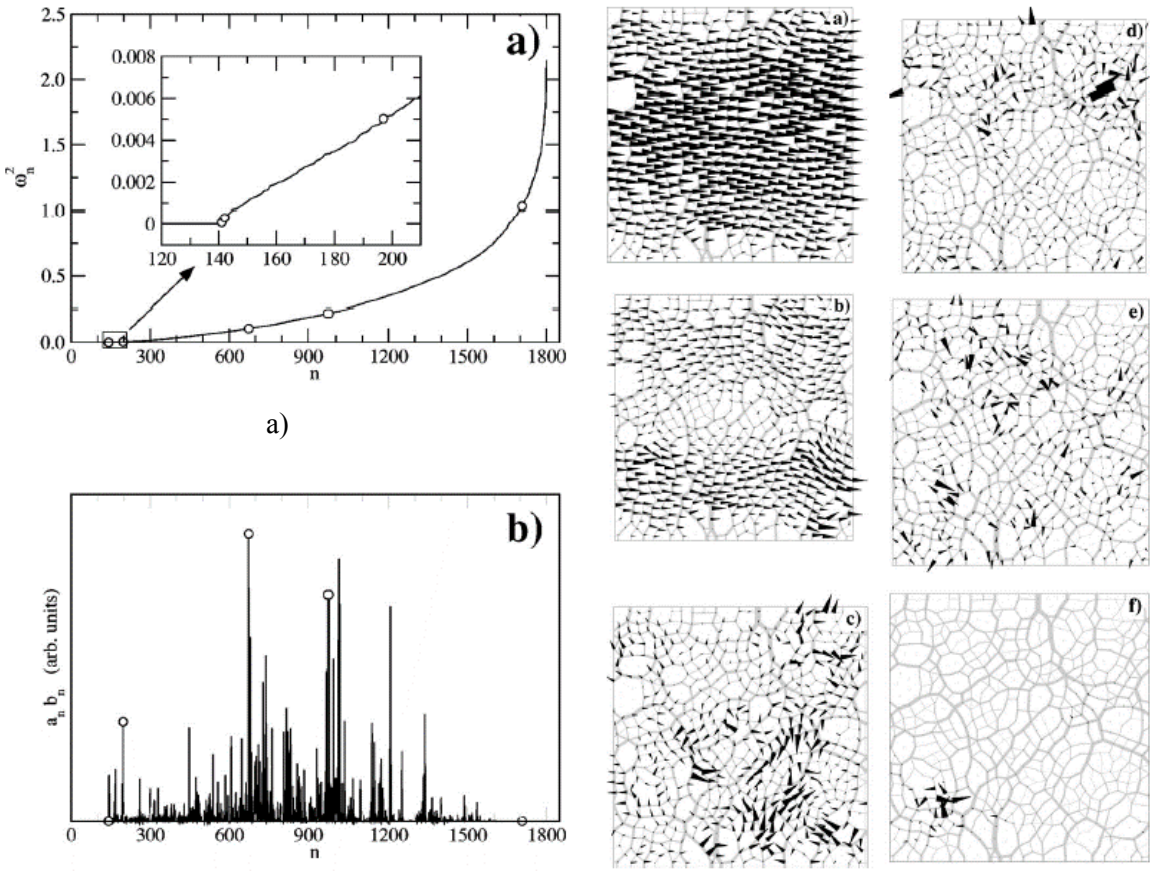

Figure 2.30. Eigenfrequencies and eigenmodes of the linear system for a 2D random packing. (a) Relationship between number of eigenmode (n) and eigenvalue (ω_n^2) (b) Excited eigenmode during wave propagation simulation in DEM (c) Eigenmodes of selected points marked on Figs. 2.30(a&b) (Somfai et al., 2005)

CHAPTER 3
Surface roughness and packing characteristics

3.1 Introduction

According to micromechanical effective medium theory as described in Section 2.7.1 the small strain stiffness of particle assemblies can be deduced knowing both the contact stiffness and packing state (void ratio and coordination number). To estimate the contact stiffness, Hertzian theory can be used if the material properties are known and the surfaces are perfectly smooth. However, as discussed in Section 2.4, the contact stiffness is also influenced by the surface roughness and real soil particles have finite values of surface roughness. Thus, measuring surface roughness gives additional insight into interpretation of laboratory tests.

It is well known that the small-strain shear modulus (G_0) is influenced by the void ratio (e), and the following expression is often used to consider the effect of e on G_0 (e.g. McDowell & Bolton, 2001):

$$G_0 = AF(e)\left(\sigma' / \sigma'_r\right)^n \tag{3.1.1}$$

where A = dimensional material constant, $F(e)$ = void ratio correction function, σ' and σ'_r = current and reference stresses, respectively, and n = material constant. A variety of void ratio correction functions have been proposed (Mitchell & Soga, 2005); probably the most widely used expression for sands with sub-angular particle shapes is that given by Hardin & Richart (1963) and Iwasaki & Tatsuoka (1977):

$$F(e) = \frac{(2.17 - e)^2}{1 + e} \tag{3.1.2}$$

From a micromechanical perspective, it is also important to consider the mean particle coordination number ($\overline{C_N}$); however, measuring $\overline{C_N}$ is difficult in laboratory experiments. Empirical correlations between $\overline{C_N}$ and e were reviewed in Section 2.5.

This chapter documents measurements of surface roughness and experiments and simulations carried out to investigate packing characteristics of the materials used in the stiffness and wave propagation studies considered in later chapters. Section 3.2 discusses challenges of measuring surface roughnesses, and summaries the results of surface roughness measurements. Sections

3.3 and 3.4 summarise experimental approaches to study the $\overline{C_N}$-e correlation using ink tests and μCT tests, respectively. Section 3.5 explores the $\overline{C_N}$-e correlation using the discrete element method (DEM), and Section 3.6 summaries the findings from this chapter.

3.2 Measurement of surface roughness

3.2.1 Measuring roughness along curved surfaces

Measurements of surface roughness are often made in fundamental tribology research when contact mechanics is studied from a more general perspective (e.g. Nayak 1973; Thomas 1982). These measurements are typically made on flat surfaces. The particular challenge posed in geomechanics is the curved surface geometry of the soil particles which results in non-conforming contacts. Roughness formulae (Eqs. 2.4.1 and 2.4.2) consider the difference between elevation measures at discrete points and a reference surface elevation (Fig. 3.1). For soil particles, however, the reference surface is not planar, and cannot be approximated as the average of all the surface elevation measurements. The effect of surface curvature needs to be considered when calculating the surface roughness. However, there is no established methodology to flatten a curved surface for this purpose. Altuhafi & Coop (2011) and Cavarretta et al. (2010; 2012) used a motif extraction method built in Fogale 3D Viewer (Fogale, 2005) to remove the effect of curvature, whereas Alshibli & Alsaleh (2004) apparently made no account for surface curvature.

As a part of the current study, Otsubo et al. (2014) compared two methods to remove the surface curvature: the motif extraction method and the sphere extraction method using ballotini. Both methods extract a baseline surface from the measured surface and the roughness values are calculated by considering the elevation relative to the baseline surface. The basis of the procedure to find a motif surface is described in BS EN ISO 12085 (1997) and the sensitivity of the selection of the motif is discussed in Cavarretta (2009). Otsubo et al. (2014) used a shape motif size of 24 μm that is 25% of the maximum measurement window length (96 μm). On the other hand, the sphere extraction method assumes the ballotini to be a perfect sphere and the roughness is the difference between the best fitting spherical surface and the measured surface. Referring to Otsubo et al. (2014), a comparison of the motif extraction and sphere extraction methods is illustrated in Fig. 3.2, and Otsubo et al. (2014) reported that the roughness extracted using the motif method are between 44 % and 60 % of that extracted using the sphere method. The descripancy is considerable when the contact stiffness is decuded using the roughness data (Greenwood & Tripp, 1967). Yang et al. (2016) proposed use of a fractal dimension to characterise the surface roughness instead of using the motif method. A standarised procedure to remove the effect of curved surfaces is needed in soil mechanics research.

Otsubo et al. (2014) also reported that surface roughness increases with increasing the measurement area, which agrees with Cavarretta (2009). The reason for this is that optical interferometry measures the surface height vertically and the approximaton of the surface as a plane becomes less valid with increasing size of the measured area. In contrast, using a smaller area reduces the number of data points and the standard deviation increases significantly as local topography governs the measured roughness values; thus Otsubo at al. suggested use of 5% to 10% of the particle diameter for roughness measurements. To extend the observation to general soils a more extensive study is needed.

3.2.2 Surface roughness measurements using optical interferometry

A Fogale Microsurf 3D optical interferometer (Fogale, 2005) available at Imperial College London was used to generate high resolution surface elevation data for quantification of surface roughness (Fig. 3.3). Referring to Fig. 3.4 and Cavarretta (2009) white light transmitted from the source is split into two half beams. The beam reflected off the surface being measured is compared with the beam reflected from a reference mirror. A charge-coupled device (CCD) camera can consider the wave interference corresponding to the difference of length between the paths of the two beams to generate a 3D surface map. Depending on the reflectivity of the surface the resolution of the apparatus is in the order of 10 nm. In this study, a motif analysis program available in Fogale 3D Viewer (Fogale, 2005) was used to remove the surface curvature with a shape motif size of 25% of the window length of measurement ($L_{measure}$).

Referring to Fig. 3.5 and Table 3.1, three types of smooth borosilicate ballotini were considered in this study (namely, WLS, WSS and GSS). The WLS (white-large-smooth) and WSS (white-small-smooth) ballotini have mean particle diameters (D_{mean}) of 2.55 mm (2.4 – 2.7 mm) and 1.0 mm (0.8 – 1.2 mm), respectively. The GSS (green-small-smooth) ballotini have a mean particle diameter of 1.09 mm (1 – 1.18 mm), and they were sieved from a sample with a wider particle size distribution (GSSw ballotini with D = 1 – 1.4 mm). The material properties of the ballotini considered are summarised in Table 3.1. As the GSS and GSSw ballotini included non-spherical particles such as clumped particles or strongly ellipsoidal particles, these were carefully removed from this study. The smooth ballotini were processed to increase the surface roughness by milling 20g of ballotini and 10g of Toyoura sand (smaller grains less than 212 μm) in a glass jar for 5 hours (Fig. 3.6) as described in Cavarretta et al. (2012). To produce the samples of ballotini denoted GSRw-5h and GSRw-25h, 30g of the GSSw ballotini was milled with 15g of Toyoura sand for 5 hours and 25 hours, respectively. Representative microscopic images and surface topographies of the rough ballotini produced (namely, WSR, WLR, GSR, GSRw-5h and GSRw-25h) are illustrated in Fig. 3.7.

Equations 2.4.1 and 2.4.2 were used to quantify the average roughness (S_a) and root mean square (RMS) surface roughness (S_q). The surface roughness values were averaged over 40 measurements on each material: roughness values were measured at four different locations on each particle, and 10 particles of each type were examined. The measurement window length ($L_{measure}$) depended on particle diameters and were 96μm for larger particles (WLS and WLR), and 70μm for smaller particles (the other materials). The measured roughness values presented in Table 3.2 were obtained without applying any filter and both flattened and non-flattened data are presented. It is obvious that the rough ballotini show larger S_a and S_q values compared with their equivalent smooth ballotini for all the material types considered. For example, the mean S_q value ($\overline{S_q}$) for the WLS ballotini increased from 36 nm to 661 nm, and $\overline{S_q}$ value for the GSS ballotini increased from 71 nm to 303 nm. There was not a significant change in surface roughness when WSS ($\overline{S_q}$ = 193 nm) and WSR ($\overline{S_q}$ = 222 nm) are compared. The roughness value of the GSSw ballotini ($\overline{S_q}$ = 58 nm) increased to 267 nm and 612 nm with milling time of 5 hours and 25 hours, respectively. Note that the surface roughness values measured before or after washing with distilled water were similar.

The produced rough ballotini (WLR, GSR, GSRw-5h and GSRw-25h) had measurable differences in comparison with their smooth equivalents. Shape parameters including sphericity, aspect ratio and convexity measured for the GSS and GSR ballotini using a Qicpic image analysis sensor available at Imperial College London are listed with examples of 2D images in Table 3.3 and Fig. 3.8. The shape parameters are almost identical for the smooth and rough particles.

The minimum void ratio (e_{min}) and maximum void ratio (e_{max}) for each ballotini type were measured following the JGS standard (JGS 0161, 2009). To obtain e_{min} the side of a container 40 mm in height and 60 mm in diameter was tapped 100 times for each of 10 layers (totalling 1000 blows). To obtain e_{max} ballotini were poured into a container using a funnel that was moved slowly upward from the bottom of the container until the ballotini overflowed from the top of the container. Note that the particle size of the tested ballotini exceeds the maximum recommended particle size for which this test can be applied (up to 2 mm in diameter; JGS 0161, 2009). The influence of size of ballotini was discussed in Okuyama et al. (1999) where larger ballotini tend to show higher void ratios due to presence of side wall. To overcome the limitation, the present study used a larger container (64.31 mm in height and 79.94 mm in diameter) using the same preparation method for GSSw, GSRw-5h and GSRw-25h ballotini. The e_{max} and e_{min} values for the ballotini considered are summarized in Table 3.4. Using a larger container reduced both e_{max} and e_{min} values, which agrees with Okuyama et al. (1999). Both e_{max} and e_{min} increased with increasing the surface roughness, and the range of attainable void ratio

(e_{max} - e_{min}) also increases with surface roughness. Many DEM studies have shown that the packing void ratio increases with increasing inter-particle friction; the results presented here imply that the inter-particle friction is increased with increasing surface roughness.

This section reported the surface roughness data for the smooth and rough surfaces ballotini. The ballotini considered in this section are used for laboratory geophysics tests in Chapter 6 and the surface roughness data measured are used as input parameters for equivalent DEM analyses to study the small-strain shear modulus of an assembly composed of these ballotini.

3.3 Ink tests to identify contact points

As already discussed in Section 2.5.2, since 1929 researchers have been using ink to identify inter-particle contact points. Prior research has always investigated the correlation between the mean coordination number ($\overline{C_N}$) and void ratio (e) without consideration of applied load. Soils are always pressurised in ground and it is the combination of stress level and e that determines soil behaviour. The ink tests conducted in this study used an odometer apparatus and smooth and rough ballotini with a mean diameter of 1.09 mm (GSS and GSR in Table 3.1). Using smaller ballotini enabled ink tests in a conventional oedometer apparatus. The test results have been presented in part in Otsubo et al. (2015) where three test cases using smooth ballotini were summarised. This section briefly summarises the results in Otsubo et al. (2015) and includes the results of a MSc project conducted by Wan-Manshol (2015) co-supervised as part of the current research.

Referring to Table 3.5, six test cases are considered in this study. The void ratio at preparation (e_{prep}), stress level at the ink impregnation point, and particle surface roughness were all controlled in the parametric study. Dry dense samples were prepared by pouring the ballotini in 10 separate layers with each layer being densified by tapping the side walls of the mold with a rubber hammer, while dry loose samples were prepared by pouring the ballotini as slowly as possible using a funnel. The e_{prep} values were obtained at the lowest vertical stresses applied in the oedometer apparatus indicated as $\sigma'_{V,prep}$ in Table 3.5. Additional vertical loading was applied to the sample as indicated in Table 3.5 and creep was allowed to take place before impregnating the sample with ink. The relationship between e and vertical stress (σ'_V) observed for the tested ballotini using the oedometer apparatus is plotted in Fig. 3.9. The point of ink impregnation and drainage for each test are indicated with an arrow. The σ'_V and e values at the points of ink impregnation are listed in Table 3.5.

Following the approach in Oda (1977) a Japanese ink (Bokuju) was used as the tracer ink. The ink solution was empirically diluted with distilled water to reduce viscosity and enable flow

through the sample voids. The sample was slowly impregnated with ink through the base porous stone while maintaining σ'_V constant. To ensure a high degree of saturation, the ink was left in the sample for at least 5 hours prior to being drained out. A photograph of the oedometer apparatus with the sample saturated in the ink solution is shown in Fig. 3.10. The ink was drained from the base of the apparatus while maintaining the applied vertical load during impregnation (i.e. σ'_V did not change). Once drained, the sample was unloaded in a single increment, leaving the mass of the top cap as the only applied load acting on the sample. As the sample remained confined by the top-cap, it was assumed that the fabric did not differ significantly from the fabric under the previously applied load. The sample was then dried in an oven at 105 °C for 24 hours together with the mold and the top porous stones so that the sample packing was not disturbed. After the sample was dried, random ballotini were selected for imaging from the central section of the sample in order to avoid wall effects. Pinson et al. (1998) recommended measuring 100 particles for samples of mono-sized spheres, and 150 particles were considered to get reliable data on the coordination number frequencies in this study.

Representative images of contact points printed on tested ballotini are shown in Fig. 3.11. When two particles were in contact, an annulus of ink was observed around the point of contact due to surface tension effects. The contact was taken to be at the centre of this circular region and the centres are indicated by arrows on Fig. 3.11. When two or more contacts were located close to each other, surface of the ink annuli at neighbouring contacts connected forming a liquid bridge (Fig. 3.11). This was confirmed by Wan-Manshol (2015) who experimentally showed the positions of particles and bridges connecting two neighbouring contacts using three particles (Fig. 3.12). These bridges between neighbouring contact points have not been previously reported in the literature and they may be related with the small void space between the tested spheres as the size of ballotini ($1 \leq D \leq 1.18$ mm) were smaller than those used in prior research. Contacts were defined to be "virtual" if a junction of bridges was formed without showing a clear shape of annulus of contact at the junction. Virtual contacts are indicated by broken circles on Fig. 3.11(a). The virtual contacts found in test case 1, e.g. contacts denoted "1" and "2" in Fig. 3.11(a), relate to a test carried out at σ'_V = 11 kPa. Virtual contacts were rarely observed for the tests where $\sigma'_V \simeq 2$ MPa. A clear criterion was needed to differentiate virtual and engaged contacts. A threshold of 5% was selected, i.e. a contact circle was counted as being "engaged contact" if the radius of contact print exceed 5% of particle radius following Bernal & Mason (1960). The contact denoted "3" in Fig. 3.11(b) was considered to be engaged.

The particle coordination number, i.e. the number of contacts per particle (C_N), was counted for 150 particles collected from the middle part of each sample to reduce effects of the side wall.

The resultant data are given in Table 3.6 where the number of particles associated with each integer coordination number are listed. Corresponding frequency distribution plots are given in Fig. 3.13. The influence of void ratio at lower stress levels ($\sigma'_V \simeq$ 10kPa) and higher stress levels ($\sigma'_V \simeq$ 2 MPa) are compared in Figs. 3.13(a) and (b), respectively. For both cases, denser samples show a higher mean coordination number ($\overline{C_N}$) than that for looser samples. It is clear that occurrences of C_N = 8 or 9 increase, while occurrences of C_N = 5 or 6 decrease with increasing density. The effect of vertical loading on particle coordination number starting from similar initial void ratios is illustrated in Figs. 3.13(c) and (d) for dense and loose samples, respectively. The distribution of C_N values is affected by vertical loading where $\overline{C_N}$ increased with increasing loading. Note that this result also includes the effect of the change in void ratio on C_N values due to the vertical loading although the initial void ratios are similar (Table 3.5). The influence of surface roughness is considered in Fig. 3.13(e) in which smooth ballotini showed higher $\overline{C_N}$ values with slightly lower void ratio at $\sigma'_V \simeq$ 2 MPa. Additional tests using a rough ballotini sample were attempted; however, the contact prints on the rough surface were not always clear. This issue is considered in more detail in Wan-Manshol (2015). Representative data are presented in Fig. 3.14, printed ink was clear at one face of the particle, while other faces showed unclear prints. A possible improvement for this problem is to apply a pressure to the impregnating fluid or circulate the fluid until it flows into all voids.

Although quantifying the effect of roughness on coordination number was not successful, an attempt was made to examine the change in surface roughness associated with loading. Using ballotini that show clear contact points after unloading from $\sigma'_V \simeq$ 700 kPa or 2 MPa, the surface roughness was measured at the centre of a contact print as illustrated in Fig. 3.15(a). The measurement area was 70μm×70μm and the centre of the measurement was carefully adjusted to be the centre of the contact print. The actual contact radius is much smaller than the contact print, and the contact pressure is largest at the centre of the contact point. An equivalent sample DEM with inter-particle friction of μ = 0.1 indicated that the mean diameter of contact circle would be approximately 40 μm at σ'_V = 2 MPa. The roughness values were averaged over 20 results on different contact points. The average surface roughness (S_a) and the RMS roughness (S_q) decreased by approximately 21% and 20%, respectively, compared to the value before the tests (Fig. 3.15(b)). Wan-Manshol (2015) conducted particle compression tests using only three particles in a modified oedometer apparatus, where the rotation and movement of particles were not allowed during the test so that the contact points were always controlled to be vertical. Although a higher vertical stress was applied to the particles, the change in surface roughness was less obvious than in the current study. This discrepancy could be understood by referring to O'Connor & Johnson (1963) who reported that the change in surface roughness is significant when a particle is sheared, whereas the normal compression did not change the surface

roughness significantly (Fig. 3.16). The K_0 compression considered in this study may induce tangential contact forces in the sample. For example, an equivalent DEM sample with inter-particle friction of $\mu = 0.1$ showed that the ratio of tangential contact force / normal contact force can be approximately 8% during an equivalent K_0 compression.

3.4 Analysis of granular structure using μCT

The network of contacting particles can also be analysed using micro-computed-topography (μCT). The two materials considered in the ink test (GSS and GSR) were also considered in μCT tests (Table 3.7). The testing procedure adopted was same as that in Taylor (2016). Dry samples (D = 38 mm) of smooth and rough ballotini were densified by tapping the side wall by 120 times with a nylon hammer after pouring the ballotini slowly into the mold using a funnel. The same procedure was applied to both samples. The dry samples were compressed isotropically to σ' = 30 kPa in a triaxial apparatus (Fig. 3.17(a)). Each sample was impregnated with a two part epoxy resin (EPO-TEK 301) slowly from the bottom of the sample where the rate of flow was controlled by hydraulic head difference. After the resin hardened (approximately 2 hours), the solidified sample was removed from the triaxial cell. A core (D = 9 mm) was drilled out from the middle part of each sample (Fig. 3.17(b)). In this study, X-ray μCT device available at Queen Mary University of London was used (Fig. 3.18). The details of the test procedure are given in Taylor (2016). In principle, the material density of ballotini, epoxy resin, and air can be distinguished by the extent to which each phase attenuates X-ray energy. The micro-CT images were reconstructed using the software CT Pro 3D (NikonMetrology, 2013), and the software AVIZO 9.0 (FEI Visualization Sciences Group, 2015) used to analyse 3D images including filtering the data to reduce the impact of noise, thresholding the images into solids and voids, and separating particles using a watershed method as described in Taylor (2016).

Three dimensional images of the samples generated using the μCT data are shown in Figs. 3.19(a) and (b). In these images the grey scale indicates the amount of X-ray attenuation at a particular point. The μCT images contained 1000×1000×1000 voxels. The voxel sizes were 9.54 μm and 10.7 μm for the smooth and rough ballotini samples, respectively. After applying a median filter (3×3) to reduce the noise, a threshold grey level was selected to differentiate the solid particles and the epoxy-filled voids. Rectangular volumes from the centre of each scan were selected and binary images of these sub-volumes are illustrated in Figs. 3.19(c) and (d). The void ratios were calculated by taking the mean value of the void ratios of the 920 2D better phase images, giving e = 0.585 and 0.629 for the smooth and rough ballotini samples, respectively. As discussed in Section 3.3, the void ratios are obviously affected by the surface roughness although the same preparation method was used. The particle coordination number

(C_N) of the non-edge particles (i.e. particles whose entire volume is located inside the boundary) were counted for 142 particles and 180 particles for smooth and rough samples, respectively. Note that the contacts between the edge particles and non-edge particles were also included in counting the particle coordination number. The frequency distribution of C_N for the smooth and rough samples are illustrated in Fig. 3.20 in which the mean coordination number ($\overline{C_N}$) was 7.05 and 6.18, respectively. The highest value of C_N was 10 and 9 for the smooth and rough ballotini samples, respectively. An example of a particle with C_N = 10 and contacting particles were picked up from the smooth ballotini sample and shown in Fig. 3.21(a). In contrast, an example of smaller coordination number of 4 picked up from the rough ballotini sample is illustrated in Fig. 3.21(b). It should be noted that the surface roughness was not visualised in μCT images as the order of the roughness is less than 1μm, which is small compared to the voxel size of the images of about 10μm.

The $\overline{C_N}$-e relationship obtained from both ink tests and μCT tests are illustrated in Fig. 3.22. Using the test results, best-fit linear curves were sought for all the data points (Eq. 3.4.1) and for the smooth ballotini only (Eq. 3.4.2):

$$\overline{C_N} = 14.14 - 11.98\, e \qquad \text{(all data)} \qquad (3.4.1)$$

$$\overline{C_N} = 12.41 - 8.930\, e \qquad \text{(smooth)} \qquad (3.4.2)$$

where coefficients of determination (R^2) are 0.57 and 0.66, for Eqs. 3.4.1 and 3.4.2, respectively. The influence of confining stress on the $\overline{C_N}$-e relationship is illustrated in Fig. 3.22(a) where higher stress levels showed slightly higher $\overline{C_N}$ values compared with the overall fitting curve; however the difference was not very obvious. The effect of particle surface roughness on the $\overline{C_N}$-e relationship is also illustrated in Fig. 3.22(a) in which two data points for rough ballotini locate below the best-fit curve for smooth ballotini results, i.e. $\overline{C_N}$ is lower for rough ballotini at a given void ratio. While it is useful, more data points for rough ballotini are desired to give a reliable conclusion considering the variation of the test results.

All the laboratory data points were compared with various experimental $\overline{C_N}$-e relationships for uniform spheres reported in the literature (Smith et al., 1929; Bernal & Mason, 1960; Oda, 1977; Pinson et al., 1998) as introduced in Section 2.5.2. Referring to Fig. 3.22(b) the $\overline{C_N}$-e relationship for the current study gives a lower coordination number than those reported in the literature except for Bernal & Mason (1960) who excluded the virtual contacts when calculating the mean coordination number. The virtual contacts are counted when a contact print is observed but its diameter is less than 5% of the particle diameter. Note that the current study also considered the same criteria as discussed in Section 3.3 and the data points for current study include the engaged contact only. It is seen that the estimation by Smith et al. (1929)

differs from the other recent experimental data points, while the best-fit curve from the current study (Eq. 3.4.1) gives lower coordination number; however, the slope of the curve agrees with Smith et al. (1929) for the range of void ratio considered in the current study (i.e. $0.58 < e < 0.65$).

3.5 Investigation of sample packing with DEM

It is not easy to investigate the packing of a particle assembly using an experimental approach. Alternatively, an equivalent study can be conducted using the discrete element method (DEM) where analogue particles that have the same material properties and particle size distribution can be considered. Although some simplifying assumptions are used in DEM analysis, it is still useful to investigate the sample packing so that additional insights can be gained to support experimental findings.

In the DEM analyses, idealised perfect spheres that have the material properties and particle size distribution of glass beads ballotini (GSS) were considered (see Table 3.1) where the inter-particle friction μ varied between 0 and 0.5 to generate a wide range of void ratios. Referring to Section 2.3, the simplified Hertz-Mindlin contact model (HM model) was used. Unlike experimental approaches, initial clouds of non-contacting particles were created randomly in a cubic space where the void ratio was set to be 2 as illustrated in Fig, 3.23(a) where the particles are coloured by the diameter ($1\text{mm} < D < 1.18$ mm). The boundary conditions were periodic in all directions and the particles were compressed to achieve an isotropic confining stress (σ') = 1 kPa (defined here as the initial packing). Stress control was achieved using the servo-control algorithm implemented in a modified version of LAMMPS. This algorithm is discussed further in Section 4.4.1. The maximum strain rate was 0.01 s^{-1}. Damping was applied to remove the kinetic energy of vibrating particles after σ' = 1 kPa was achieved. The resultant void ratio depends on the inter-particle friction; an example of the initial packing with μ = 0.1 is illustrated in Fig, 3.23(b) where the particles are coloured by the per particle coordination number (C_N). The initial packings were compressed further isotropically up to 10 MPa or vertically simulating K_0 condition, where the horizontal boundaries were fixed and the vertical stress (σ'_V) was increased up to 10 MPa.

The resultant mean coordination numbers ($\overline{C_N}$) and void ratios (e) at σ' = 1 kPa are listed in Table 3.8 for various inter-particle frictions (μ). As expected, higher μ values resulted in looser packing with lower coordination number under the same preparation method. The frequency distributions of C_N at e = 0.553, 0.654, and 0.705 are compared in Fig. 3.24(a). It is clear that lower e values increase the proportion of higher C_N, which agrees with laboratory tests. However, the number of particles with C_N = 0, 1, 2, or 3 increased with increasing void ratio,

which is different from the laboratory tests. In this DEM study, a gravitational force was not included; thus non-contacting particles (i.e. $C_N = 0$) and non-constrained particles (i.e. $C_N = 1$ or 2) were observed.

From a physical perspective, Edwards (1998) argued that particles with $C_N < 4$ are free to move. On the other hand, Thornton (2000) considered a mechanical mean coordination number in which particles with $C_N = 0$ or 1 are excluded when calculating the mean coordination number as those particles do not contribute to force chains in the packing. To determine a threshold C_N value, a redundancy analysis was carried out using a loose packing ($\overline{C_N}$ = 4.13 and e = 0.705 with μ = 0.5) in this study. Particles with $C_N < 1$, 2, or 3 were deleted from the DEM sample with maintaining σ' = 1 kPa to examine the stability of the packing without the deleted particles. The sample was stable even after removing particles with $C_N < 1$ or $C_N < 2$, whereas the sample could not maintain its packing stably when particles with $C_N < 3$ were deleted (i.e. $\overline{C_N}$ decreased significantly). Therefore, particles with $C_N < 2$ are regarded as rattler particles in this study, which agrees with the definition in Thornton (2000). The mechanical mean coordination number ($\overline{C_N^*}$) is defined as:

$$\overline{C_N^*} = \overline{C_N^{C_N \geq 2}} = \frac{\sum_{i=2} n^i i}{\sum_{i=2} n^i} \tag{3.5.1}$$

where n^i = number of particles with $C_N = i$.

The rattler particles can be considered as voids as the sample is stable even if the rattler particles are removed from the system. Thus, mechanical void ratio (e^*) can be defined as:

$$e^* = e^{C_N \geq 2} = \frac{V_{total} - \sum_{i=2} V_S^i}{\sum_{i=2} V_S^i} \tag{3.5.2}$$

where V_{total} = total volume of sample, V_S^i = summation of volume of solids (particles) with $C_N = i$. The calculated mechanical mean coordination number and void ratio are listed in Table 3.8 together with the proportion of rattler particles in each sample. The loose sample with μ = 0.5 includes a considerable number of rattler particles (14.9%) whereas rattler particles are only 1.9% for dense packing with μ = 0. An example of frequency distribution of C_N is illustrated in Fig. 3.24(b). The influence of removal of rattler particles on the $\overline{C_N}$–e relationship is seen in Fig. 3.24(c) where curves for $C_N \geqq 1$ and $C_N \geqq 2$ are almost identical as the particles with $C_N = 1$ rarely exist (Fig. 3.24(a)).

Both isotropic and K_0 stresses were applied to the initial packing using μ = 0, 0.02, 0.05, 0.1, 0.2 and 0.35. The evolution of the $\overline{C_N}$ – e relationships influenced by increasing compressive load

is illustrated in Fig. 3.25 where the rattler particles are included. It is seen that the applied stress increased the coordination number for both isotropic and K_0 compression. The $\overline{C_N} - e$ relationships for the same samples excluding rattler particles, i.e. the $\overline{C_N^*} - e^*$ relationship, using Eqs. 3.5.1 and 3.5.2 are illustrated in Fig. 3.26 where the stress-dependency on the $\overline{C_N^*} - e^*$ relationship is not obvious. Referring to Fig. 3.26(c), the influence of loading type on the $\overline{C_N^*} - e^*$ relationship is also not noted. Thus, the relationship between mechanical mean coordination number and void ratio is not sensitive to either stress levels or loading types, i.e. the data presented here suggest that $\overline{C_N^*} - e^*$ relationship is unique for a given material and particle size distribution.

The DEM results are compared with laboratory data obtained in this study and plotted in Fig. 3.27 where theoretical expressions by Nakagaki & Sunada (1968) and Suzuki et al. (1981) are also given. Amongst the other theoretical expressions in the literature (Section 2.5), those two expressions give the best agreement with the DEM results in this study. The lower bound of the DEM data points is captured well by Suzuki et al. (1981) where good agreement is seen at void ratios lower than 0.65. On the other hand, the laboratory data points show higher coordination numbers than the DEM data points by approximately 1 in the $\overline{C_N} - e$ relationship, which agrees better with Nakagaki & Sunada (1968).

For the ink tests, the coordination number should be affected by the criteria used to distinguish the engaged contacts or the virtual contacts as described above; however, it is not easy to assess the sensitivity of the coordination number to these criteria using microscopic images. Alternatively, DEM analysis enables investigation of the sensitivity of the virtual contact by considering the distance from non-contacting neighbouring particles. Referring to Fig. 3.28(a) the skin thickness (δ_{skin}) is defined as the distance from the particle surface to the virtual surface where virtual contact points can be found using the virtual radius ($R + \delta_{skin}$). The evolution of the mean coordination number against an index of δ_{skin}/R is illustrated in Fig. 3.29(a) for DEM samples at σ' = 11 kPa. The $\overline{C_N}$ values increase with increasing δ_{skin}/R values in which the increment in the coordination number is larger at a smaller skin thickness particularly at $\delta_{skin}/R <$ 1%. The frequency distribution of C_N values are illustrated in Fig. 3.29(b) for e = 0.553. Note that the coordination number and void ratio shown in Fig. 3.29 include rattler particles, i.e. the mechanical mean coordination number is not considered.

A comparison between the laboratory tests and DEM analyses was conducted where sensitivity of the $\overline{C_N} - e$ relationship to δ_{skin} was established. Data for the stress levels considered in the laboratory tests were considered. The results are summarised in Fig. 3.30. Considering the ink test results (Figs. 3.30(a-c)) it can be seen that laboratory data points lie in a range between

δ_{skin}/R = 1% and 3% in which the mean difference is roughly 2%. It is worth noting that even a small value of δ_{skin}/R affects the overall relationship between $\overline{C_N}$ and e, and the laboratory test results might be affected by creation of menisci between non-contacting particles (Fig. 3.28(b)). This sensitive nature of coordination number was reported in Bernal & Mason (1960) who showed a possible change in counting coordination number in experiments depending on the criteria for counting the contact points (Fig. 3.22(b)). For example, the lower estimate in Bernal & Mason (1960) give a close match with the DEM analysis here. In this study, for ink tests, contact circles were regarded as engaged when the radius of printed circles exceeds 5% of the particle radius, whereas small circles less than 5% of the particle radius were considered as virtual following Bernal & Mason (1960) (Fig. 3.11). However, following the criteria becomes difficult as the particle size decreases.

Referring to Fig. 3.30(d), the μCT test results give a close match with DEM results with lower δ_{skin}/R values about 1%, giving $\delta_{skin} \approx$ 5.5μm. On the other hand, the accuracy of the μCT test results depends on the resolution of image where the resolution of the created μCT images in this study was approximately 10μm. Note that surface roughness (< 1μm) was too small to observe in the created images (see Figs. 3.19 and 3.20). Thus, the discrepancy between laboratory data and DEM data can be understood by considering the accuracy of the laboratory tests. It should also be emphasized that this DEM analysis includes a number of simplifying assumptions, e.g. all particles are perfect spheres, and this differs from in reality. Also, the preparation method considered in DEM was different from pluviation method used in the laboratory tests. As reported in Bernhardt et al. (2015), void ratio and fabric of sample depend on sample preparation method in DEM, and this effect on the $\overline{C_N} - e$ relationship should be examined.

3.6 Summary

This chapter discussed particle-scale experiments with supplemental DEM analyses. First, the surface roughness of the ballotini considered in later chapters was measured using optical interferometry. A challenge of measuring roughness along curved surfaces was highlighted. A standardised procedure to measure surface roughness for soil mechanics research is required. The influence of surface roughness on the maximum and minimum void ratios was discussed experimentally to relate the surface roughness to packing characteristics. The most plausible explanation for the effect of roughness on packing is a link between roughness and friction.

This chapter also investigated the relationship between mean coordination number ($\overline{C_N}$) and void ratio (e), i.e. the $\overline{C_N} - e$ relationship, of assemblies of slightly polydisperse spherical particles using laboratory tests and DEM simulations. Both $\overline{C_N}$ and e are important when the

sample stiffness is deduced using a micromechanical theory (Section 2.7.1). The coordination number is difficult to measure in normal laboratory tests in soil mechanics research; thus, a correlation between $\overline{C_N}$ and e helps relate laboratory experimental data to the micromechanical theory. Considering the mechanical mean coordination number and void ratio, the DEM data were in good agreement with a theoretical study by Suzuki et al. (1981), while laboratory test data were captured by Nakagaki & Sunada (1968). The laboratory test results gave higher $\overline{C_N}$ than that obtained from the DEM analyses; however, the discrepancy can be within tolerance by considering the accuracy of laboratory tests. It was found that, through the DEM analyses, the $\overline{C_N} - e$ relationship is essentially independent of stress level or loading types considered here (isotropic and K_0 compression), i.e. all the factors are empirically included in the $\overline{C_N} - e$ relationship. The $\overline{C_N} - e$ relationship for slightly polydisperse spheres can be estimated by Suzuki et al. (1981) and Nakagaki & Sunada (1968) giving a lower and an upper bounds to the data, respectively.

Due to experimental difficulties, the influence of surface roughness on the $\overline{C_N} - e$ relationship was not clearly established. Additional studies are needed to understand this.

3.7 Tables

Table 3.1. Material properties of tested ballotini.

ID	ρ_p kg/m^3	E_p GPa	G_p GPa	ν_p	D_{min} mm	D_{mean} mm	D_{max} mm
WLS	2230	60	25	0.2	2.4	2.55	2.7
WLR							
WSS					0.8	1.0	1.2
WSR							
GSS	2600	70	29.2	0.2	1.0	1.09	1.18
GSR							
GSSw							
GSRw-5h					1.0	1.2	1.4
GSRw-25h							

Table 3.2. Summary of surface roughness measurements.

ID	$L_{measure}$ [μm]	S_a [nm] (S_a without flattening)				S_q [nm] (S_q without flattening)			
		mean	max	min	std	mean	max	min	std
WLS	96	13	22	9	3	36	63	18	12
		(275)	(320)	(215)	(29)	(335)	(402)	(263)	(35)
WLR		420	631	317	75	661	975	538	111
		(1270)	(1767)	(860)	(218)	(1568)	(2252)	(1087)	(264)
WSS	70	125	169	100	17	193	263	151	25
		(476)	(582)	(422)	(40)	(595)	(734)	(524)	(51)
WSR		154	195	121	17	222	298	173	24
		(494)	(644)	(411)	(49)	(618)	(789)	(522)	(57)
GSS	70	34	68	19	11	71	166	40	27
		(433)	(581)	(376)	(39)	(534)	(822)	(457)	(65)
GSR		216	272	174	22	303	399	245	32
		(601)	(744)	(484)	(66)	(771)	(1027)	(620)	(93)
GSSw	70	26	102	15	14	58	285	30	43
		(342)	(709)	(241)	(76)	(434)	(1146)	(304)	(134)
GSRw-5h		192	237	152	21	267	332	210	29
		(419)	(552)	(286)	(65)	(544)	(737)	(357)	(89)
GSRw-25h		428	668	310	78	612	964	446	115
		(764)	(1191)	(513)	(160)	(979)	(1518)	(663)	(200)

*motif size for flattening curved surface = $0.25L_{measure}$

Table 3.3. Shape parameters of tested materials (average value of 100 particles).

Material	Sphericity	Aspect ratio	Convexity
WLS*	0.95	0.98	0.98
WSS*	0.94	0.98	0.99
GSS	0.95	0.98	0.98
GSR	0.95	0.98	0.98

*data obtained from Cavarretta et al. (2012).

Table 3.4. Maximum and minimum void ratios for material considered.

Material	WLS	WLR	WSS	WSR	GSS	GSR	GSSw*	GSRw -5h*	GSRw -25h*
e_{min}	0.565	0.593	0.611	0.627	0.601	0.625	0.524	0.574	0.577
e_{max}	0.707	0.755	0.700	0.720	0.677	0.718	0.626	0.691	0.704
e_{max} - e_{min}	0.142	0.162	0.090	0.093	0.077	0.093	0.101	0.117	0.127

*Test cases with a larger container.

Table 3.5. Specifications of ink test cases.

Test ID	Test label	e_{prep}	$\sigma'_{V,\,prep}$ (kPa)	e	$\overline{C_N}$	σ'_V (kPa)	Surface
1	dense-10k-S	0.593	11	0.593	6.87	11	Smooth
2	dense-700k-S	0.594	44	0.585	7.29	703	Smooth
3	dense-2M-S	0.596	58	0.582	7.39	2010	Smooth
4	loose-10k-S	0. 646	11	0.646	6.61	11	Smooth
5	loose-2M-S	0.652	11	0.617	7.03	1963	Smooth
6	dense-2M-R	0.612	11	0.590	6.91	1998	Rough

Table 3.6. Summary of per particle coordination number (C_N) for ink tests.

Test ID	Test label	C_N									Total
		3	4	5	6	7	8	9	10	11	
1	dense-10k-S	0	3	13	38	51	36	9	0	0	150
2	dense-700k-S	0	1	5	27	54	44	17	2	0	150
3	dense-2M-S	0	1	6	23	51	44	23	2	0	150
4*	loose-10k-S	0	1	9	44	57	29	8	2	0	150
5*	loose-2M-S	0	1	20	52	46	25	6	0	0	150
6*	dense-2M-R	0	0	6	41	56	38	8	1	0	150

*data presented in Wan-Manshol (2015).

Table 3.7. Test cases for μCT scanning.

Test ID	Test label	e	$\overline{C_N}$	σ'_{iso} (kPa)	Surface
1	dense-30k-S	0.585	7.05	30	Smooth
2	loose-30k-R	0.629	6.18	30	Rough

Table 3.8. Mechanical mean coordination numbers and corresponding void ratios obtained from DEM simulations.

μ	$\overline{C_N}$ $C_N \geqq 0$	$\overline{C_N^*}$ $C_N \geqq 2$	e $C_N \geqq 0$	e^* $C_N \geqq 2$	Proportion of $C_N < 2$ (%)
0	5.96	6.01	0.553	0.583	1.9
0.001	5.93	5.99	0.564	0.592	1.8
0.02	5.68	5.76	0.591	0.636	2.7
0.05	5.45	5.53	0.623	0.678	3.4
0.1	5.17	5.27	0.654	0.730	4.4
0.2	4.69	4.81	0.687	0.823	7.5
0.35	4.27	4.43	0.697	0.947	12.9
0.5	4.13	4.28	0.705	1.003	14.9

3.8 Figures

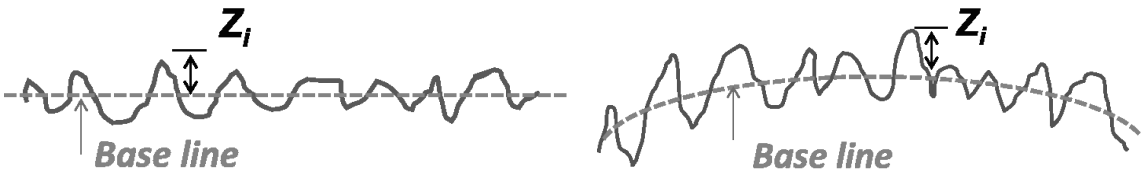

(a) (b)

Figure 3.1. Measurement of surface roughness on (a) planar surface and (b) curved surface.

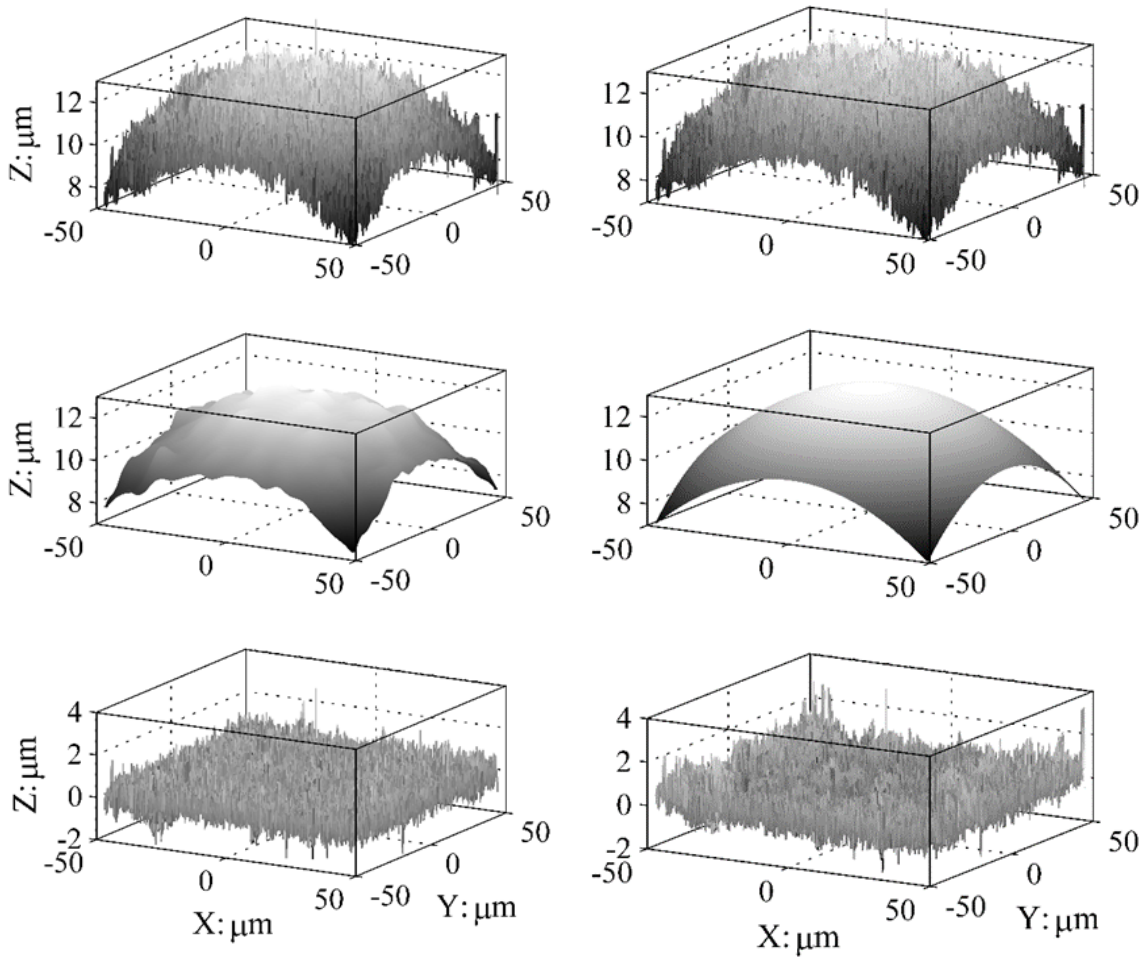

(a) (b)

Figure 3.2. Comparison of methods of flattering curved surfaces: (a) Motif extraction method, and (b) Sphere extraction method as presented in Otsubo et al. (2014). The top images are the surface topography as measured, the middle images are the reference surfaces, and the bottom images are flattened surfaces and used for calculating surface roughness.

Figure 3.3. Optical interferometer used in this study (Fogale Microsurf 3D).

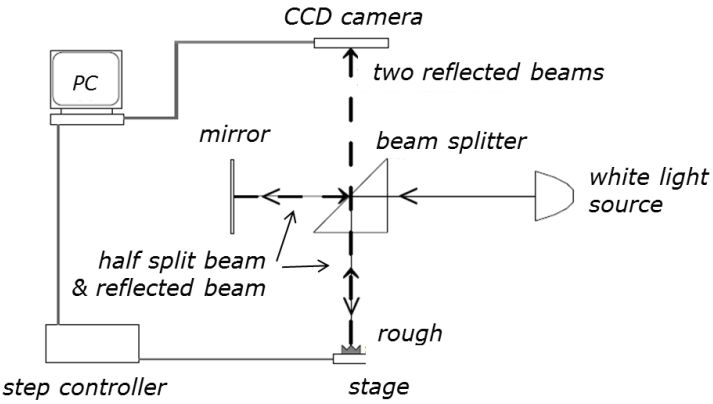

Figure 3.4. Schematic of optical interferometry to measure surface elevation (edited from Cavarretta (2009)).

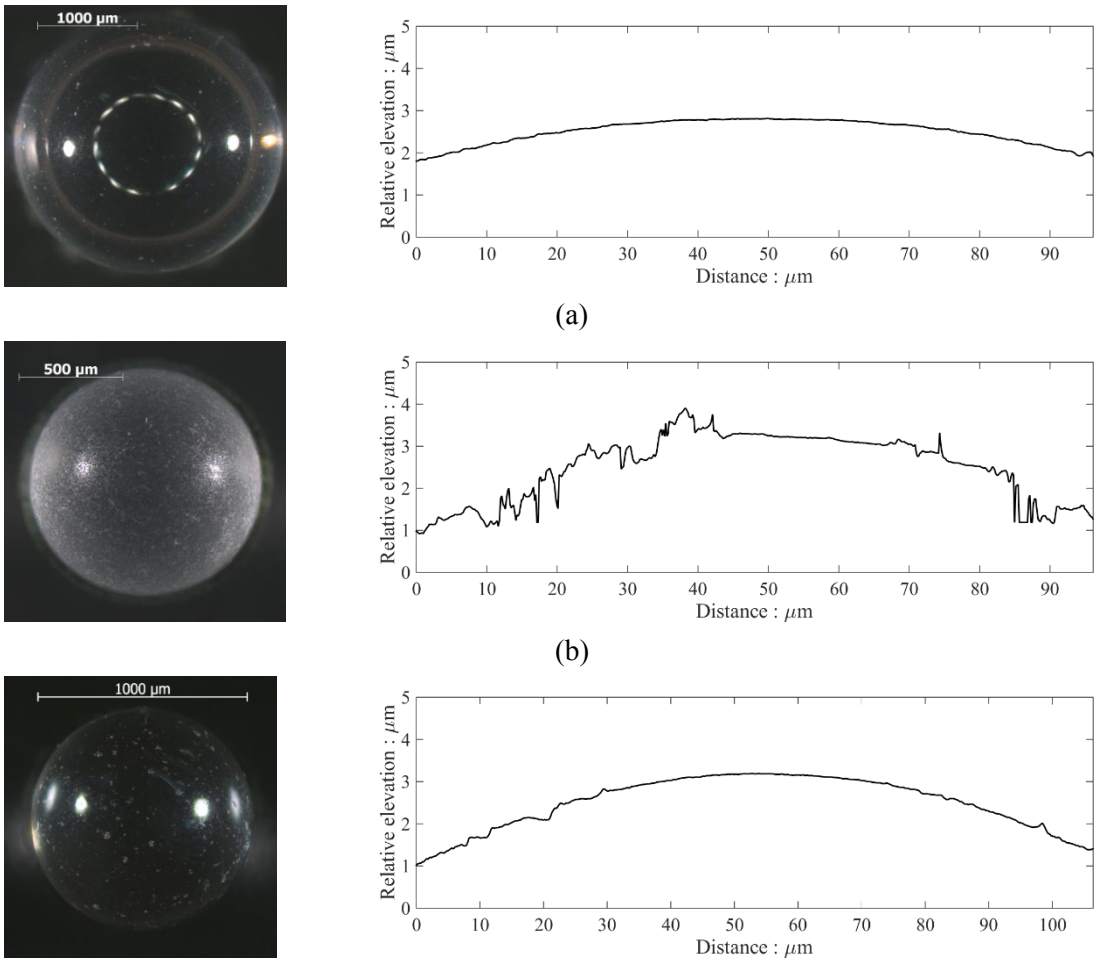

Figure 3.5. Representative microscope images and surface topographies of ballotini. (a) WLS, white-large-smooth (b) WSS, white-small-smooth (c) GSS, green-small-smooth

Figure 3.6. Ballotini and Toyoura sand inside jars (left) and milling machine (right).

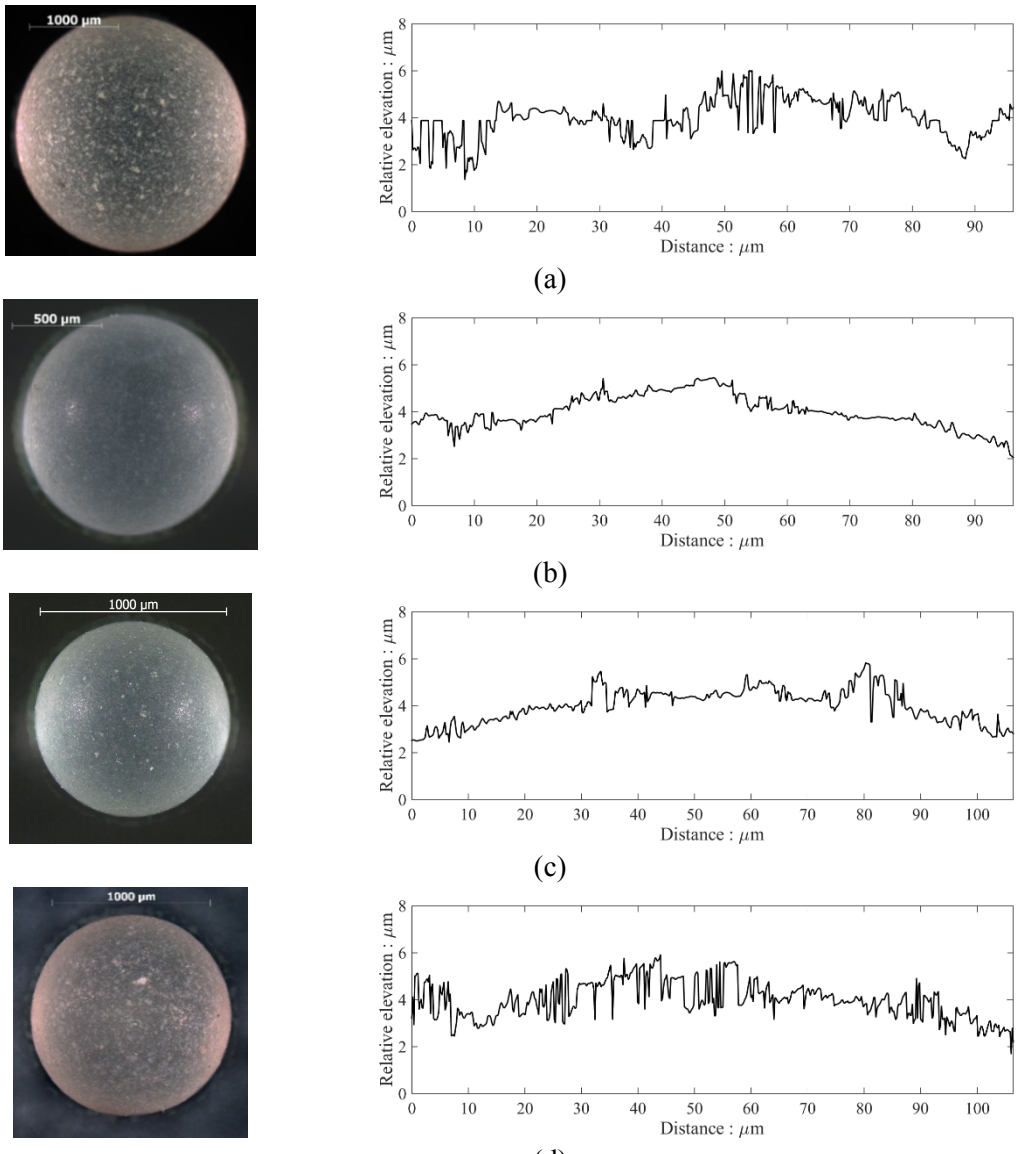

Figure 3.7. Representative microscope images and surface topographies of ballotini. (a) WLR (b) WSR (c) GSRw-5 and (d) GSRw-25h

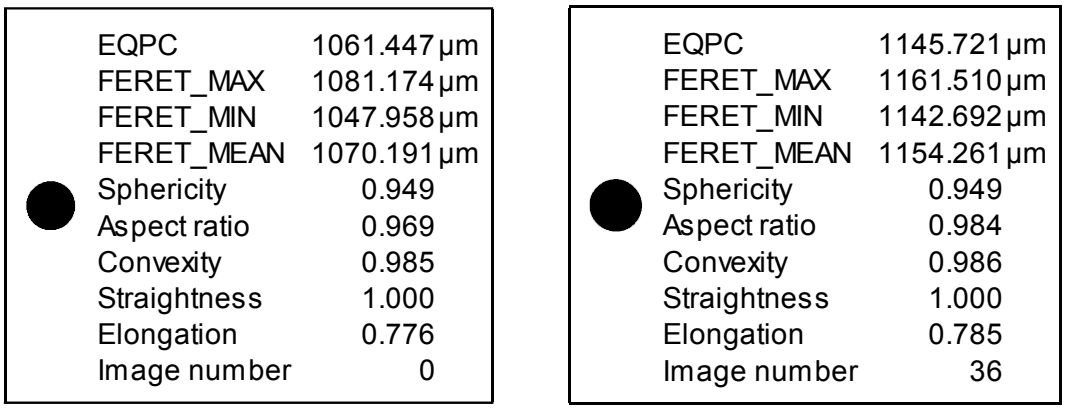

(a)

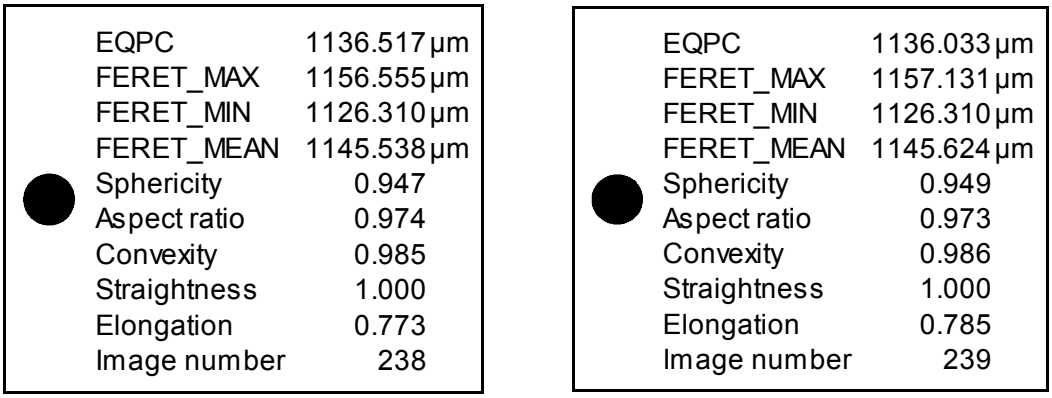

(b)

Figure 3.8. Representative 2D images of particle shape obtained using Qicpic image analysis sensor. (a) Smooth ballotini (GSS) (b) Rough ballotini (GSR)

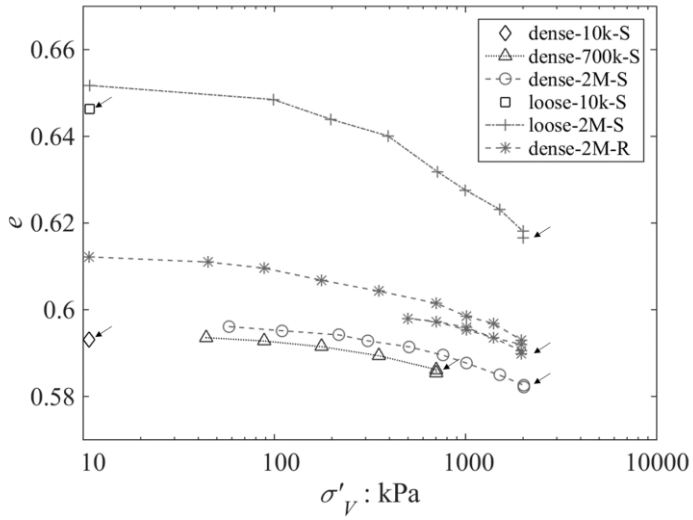

Figure 3.9. Evolution of void ratio associated with K_0 vertical compression.

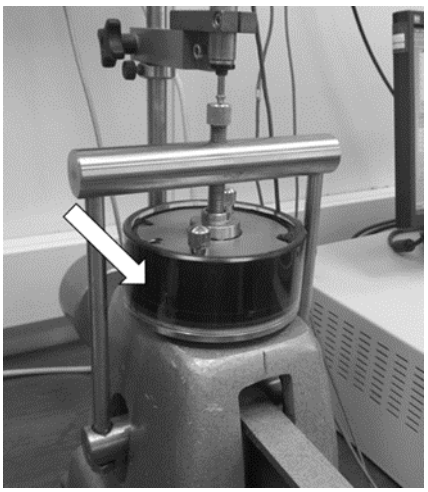

Figure 3.10. Oedometer apparatus used for ink tests.

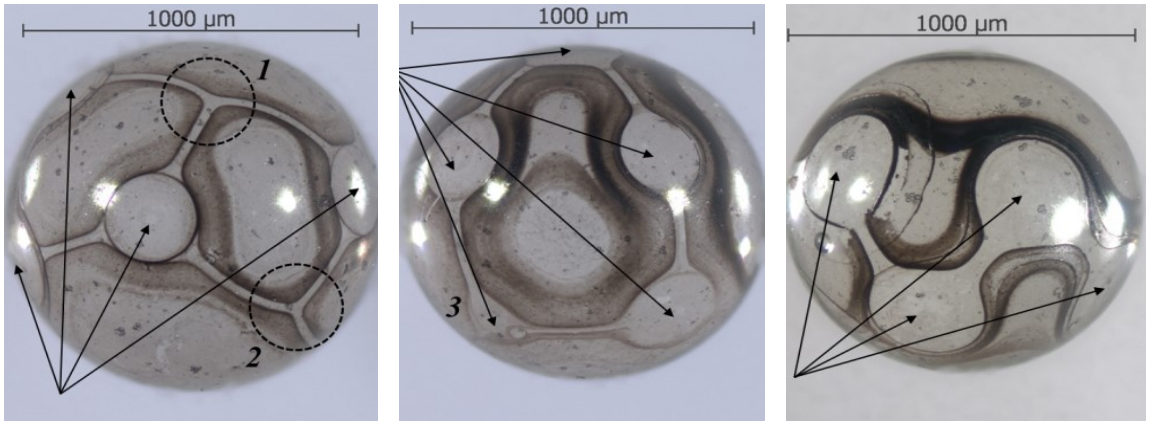

(a) (b) (c)

Figure 3.11. Contact points on ballotini: (a, b) Virtual and engaged contacts from test ID 1 (11 kPa) and (c) Engaged contacts from test ID 2 (703 kPa) (Black arrows indicate the inferred center of engaged contacts).

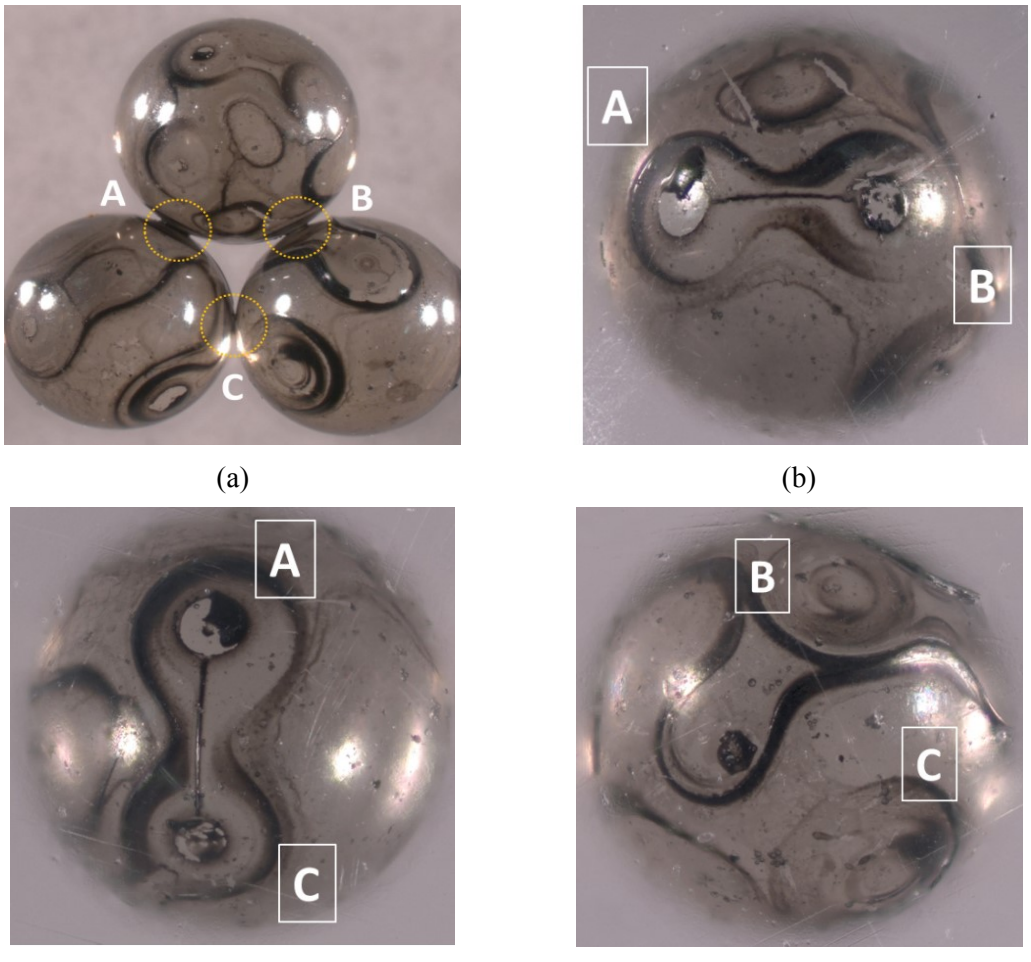

(a) (b)

(c) (d)

Figure 3.12. Contact prints connected with liquid bridges. (a) Three particles in contacts (b) A liquid bridge connecting contact point A and point B (c) A liquid bridge connecting contact point A and point C (d) No ink bridge created between contact point B and point C (edited from Wan-Manshol, 2015)

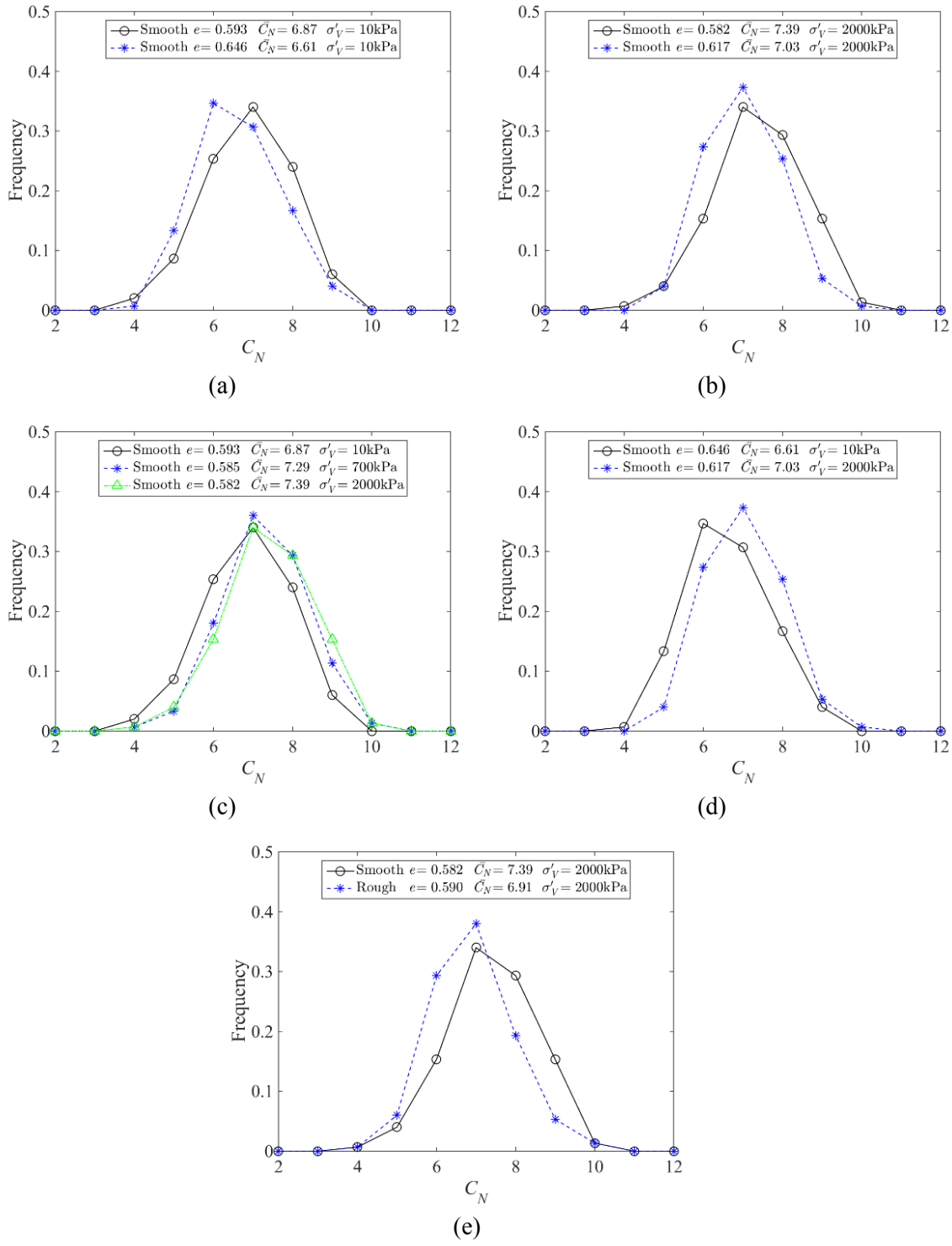

Figure 3.13. Frequency distribution of coordination number per particle (C_N) counted for 150 particles from each sample. (a) Influence of void ratio at low vertical stresses (b) Influence of void ratio at high vertical stresses (c) Influence of vertical stresses starting from similar low void ratios (d) Influence of vertical stresses starting from similar large void ratios (e) Influence of particle surface roughness at high vertical stresses for dense packing

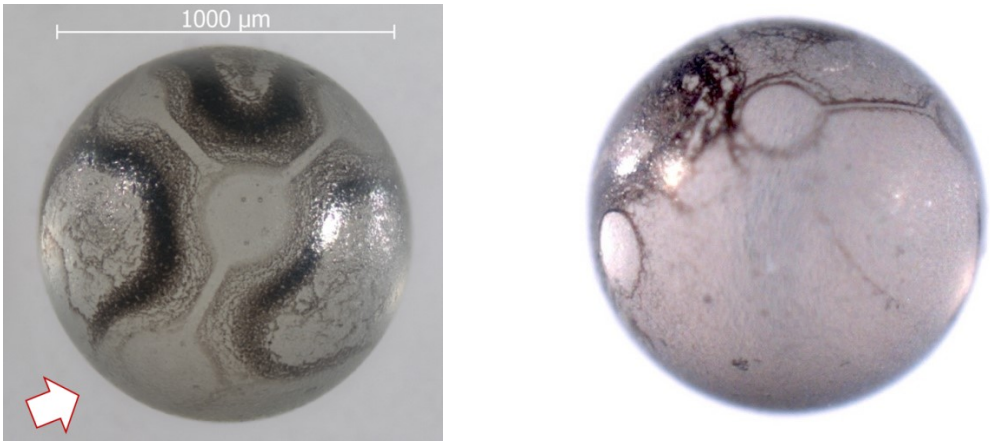

(a) (b)

Figure 3.14. Difficulty in printing contact points accurately using rough surface ballotini (Fig. 3.14(b) was presented in Wan-Manshol, 2015).

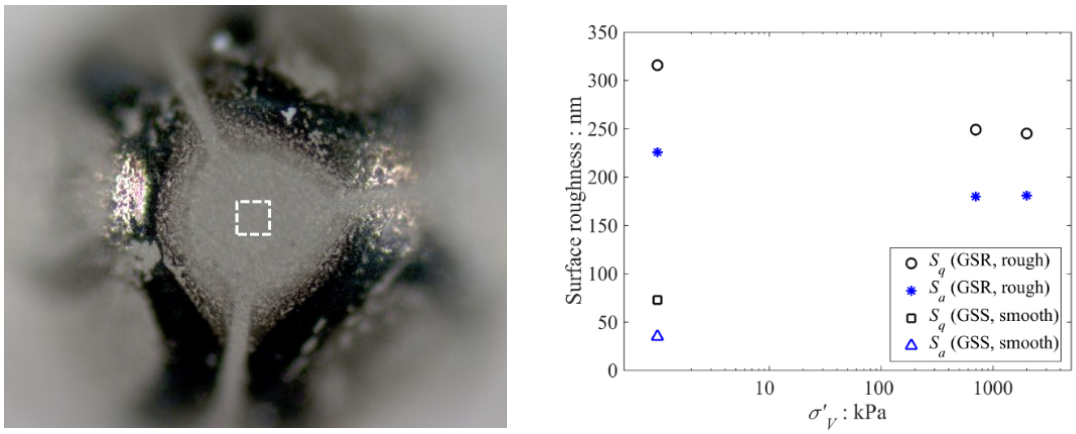

(a) (b)

Figure 3.15. Reduced surface roughness with increased vertical pressures in oedometer apparatus. (a) Surface area measured to quantify the surface roughness (b) Surface roughness measured after application of vertical stresses $\approx$ 700 kPa and 2 MPa.

(a) (b) (c)

Figure 3.16. Surface roughness (a) before test (b) after normal compression, and (c) after shearing at a constant normal force (O'Connor & Johnson (1963)).

(a) (b)

Figure 3.17. Preparation for μCT scanning. (a) Sample compressed at an isotropic pressure of 30 kPa (b) Solidified sample with an epoxy resin and its drilled core for μCT scanning

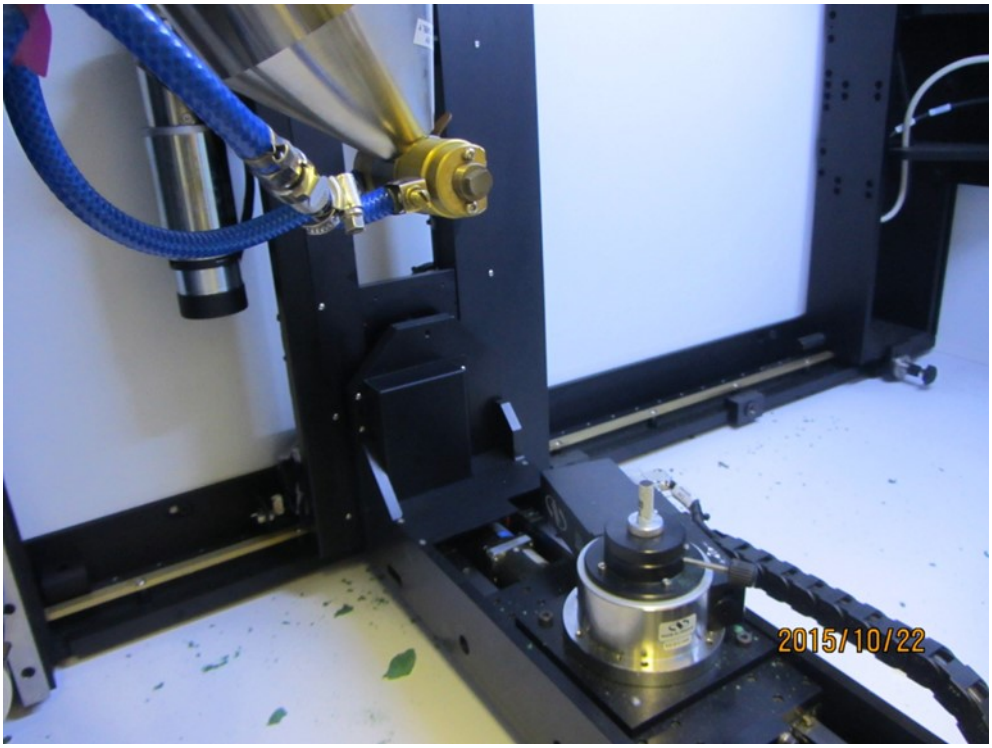

Figure 3.18. X-ray μCT scan device available at Queen Mary University of London.

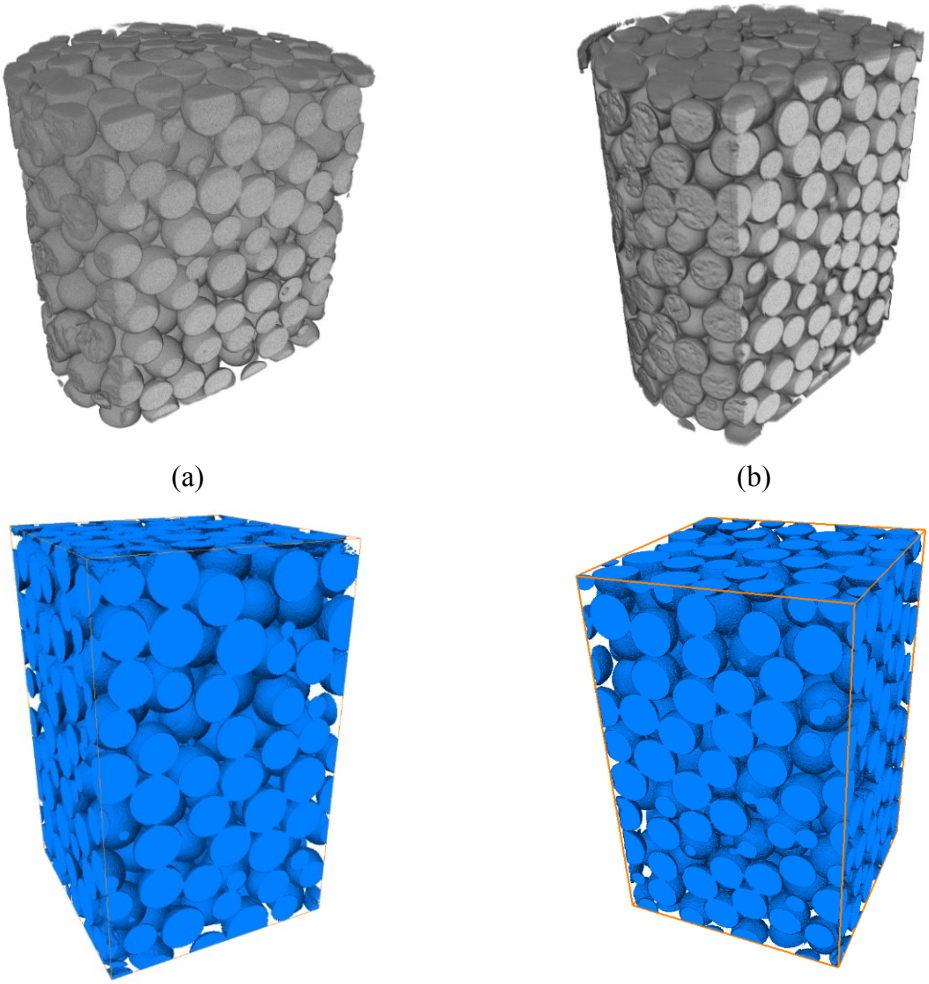

(a) (b)

(c) (d)

Figure 3.19. X-ray micro-CT images. (a&b) Full-size images without application of filters for smooth and rough ballotini samples, respectively (c&d) Binary images of centered sub-volumes for smooth and rough ballotini samples, respectively

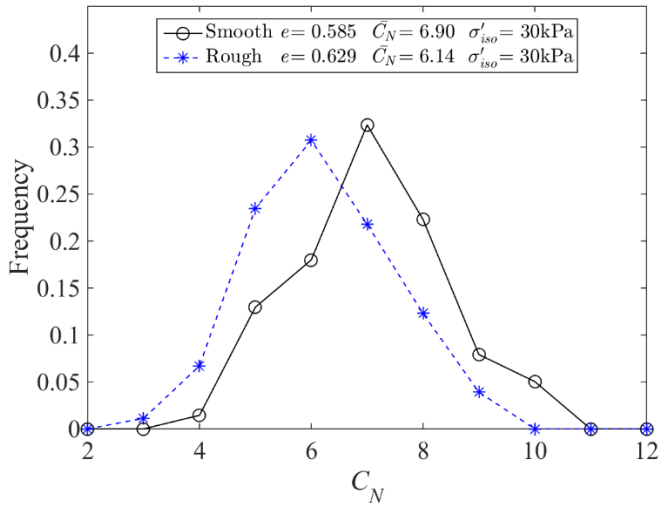

Figure 3.20. Frequency distribution of coordination number per particle (C_N) obtained from μCT images using 142 particles and 180 particles for smooth and rough ballotini samples, respectively.

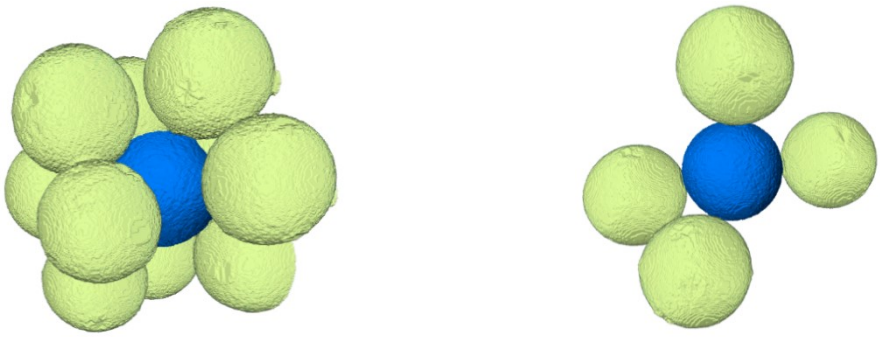

(a) (b)

Figure 3.21. Examples of μCT images for a particle with C_N = 10 and a particle with C_N = 4 obtained from smooth and rough ballotini samples, respectively.

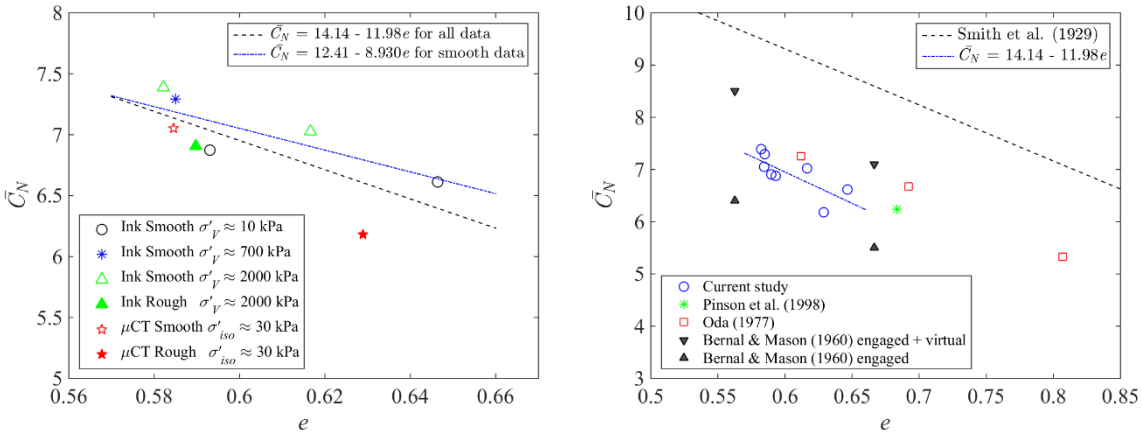

(a) (b)

Figure 3.22. Summary of $\overline{C_N} - e$ relationship obtained from laboratory tests. (a) Lab data with linear fitting curves (b) Comparison between lab data and literature

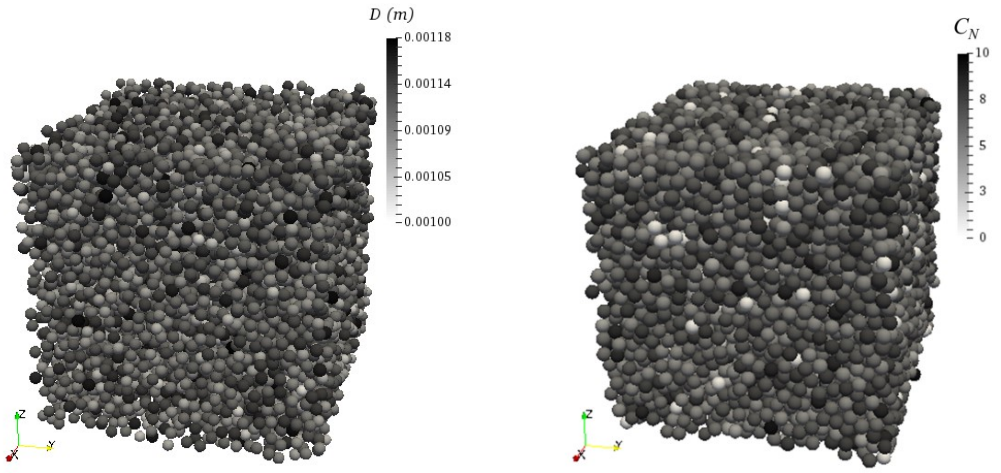

(a) (b)

Figure 3.23. Sample preparation in DEM simulations using 10,000 particles with glass beads properties. (a) Initial clouds of non-contacting particles with void ratio = 2 (b) Isotropically compressed sample at σ' = 1 kPa with μ = 0.1

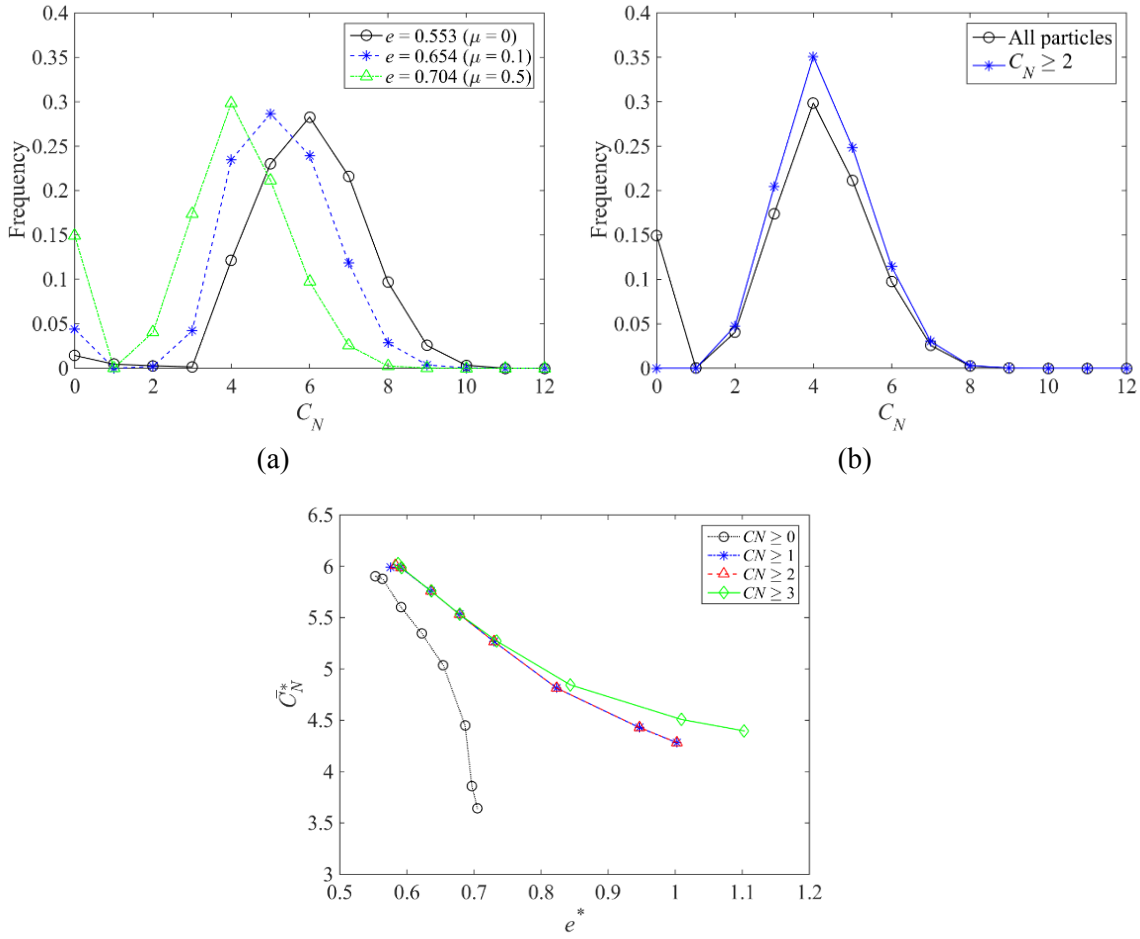

Figure 3.24. Coordination number and void ratio data of initial packing at σ' = 1 kPa. (a) Frequency distribution of coordination number per particle (C_N) (b) Influence of excluding particles with $C_N \leq 1$ on frequency distribution of C_N values with μ= 0.5 (c) Influence of excluding particles with $C_N \leq 1$ on $\overline{C_N}$ - e relationship

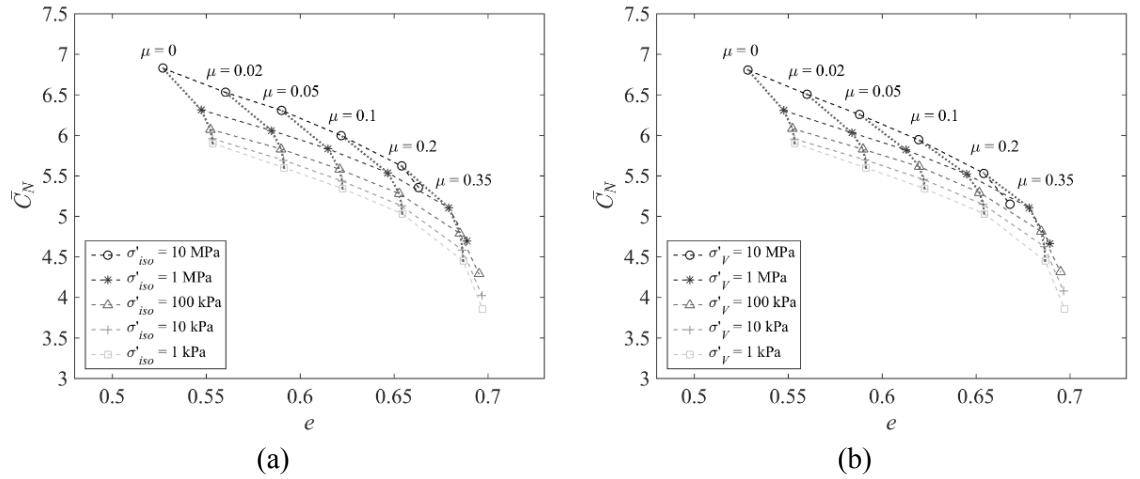

Figure 3.25. Relationship between mean coordination number ($\overline{C_N}$) and void ratio (e) at various confining stresses. (a) Isotropic compression at σ' = 0.001, 0.01, 0.1, 1, and 10 MPa (b) K_0 compression at σ'_V = 0.001, 0.01, 0.1, 1, and 10 MPa

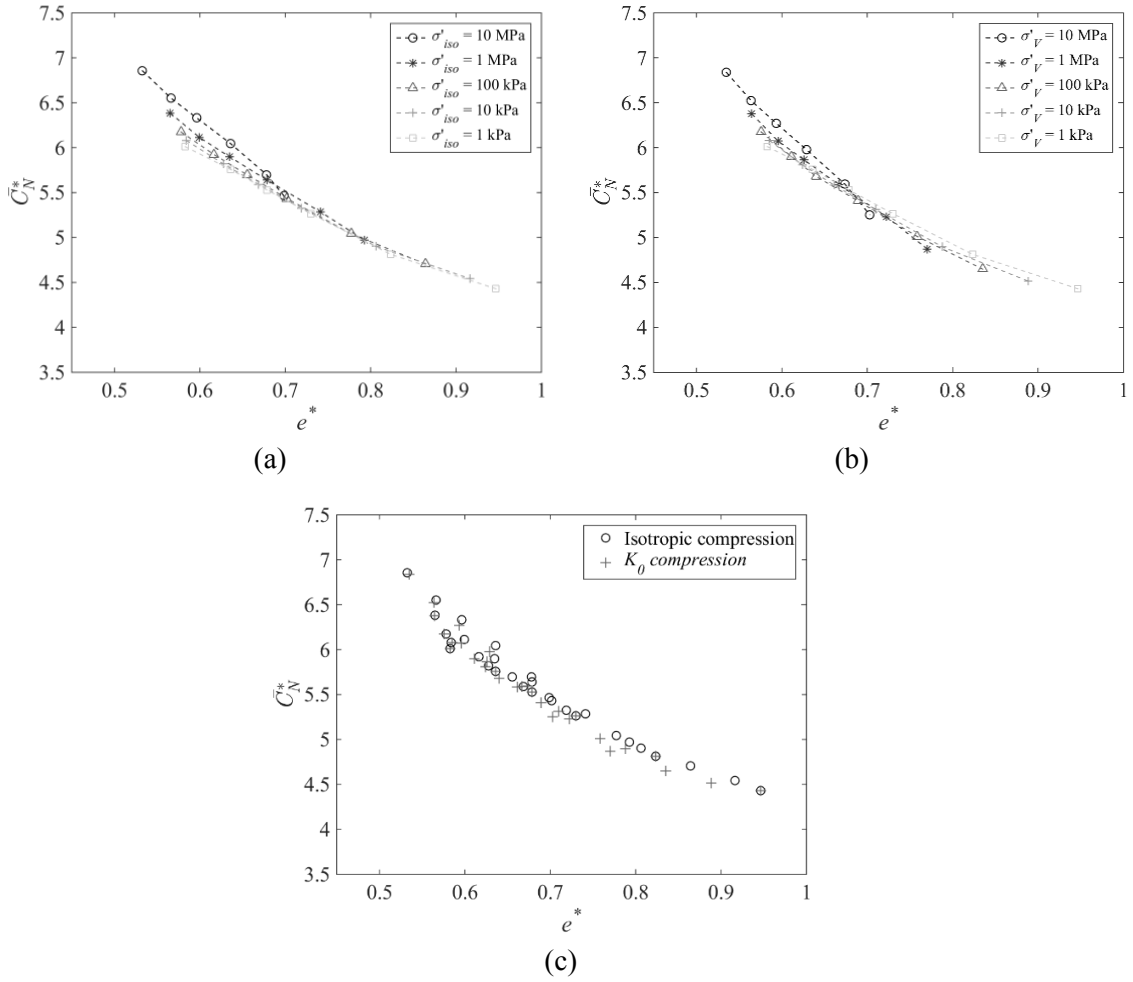

Figure 3.26. Relationship between mechanical mean coordination number ($\overline{C_N^*}$) and mechanical void ratio (e^*) at various confining stresses. (a) Isotropic compression at σ' = 0.001, 0.01, 0.1, 1 and 10 MPa (b) K_0 compression at σ'_V = 0.001, 0.01, 0.1, 1, and 10 MPa (c) Comparison between isotropic compression and K_0 compression

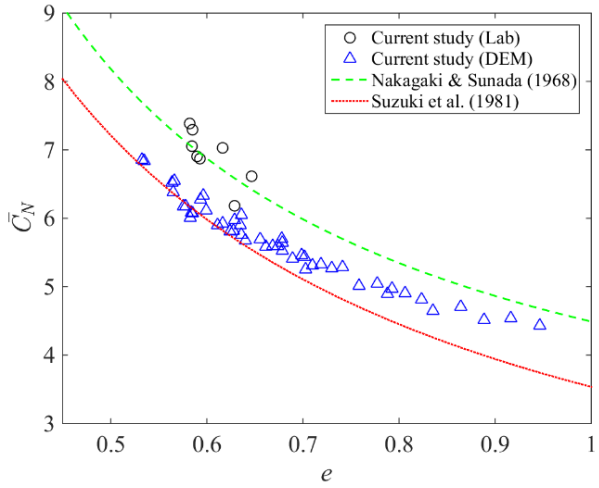

Figure 3.27. Relationship between mean coordination number and void ratio for laboratory, DEM, and theories. DEM data points show mechanical mean coordination number ($\overline{C_N^*}$, Eq. 3.5.1) and void ratio (e^*, Eq. 3.5.2).

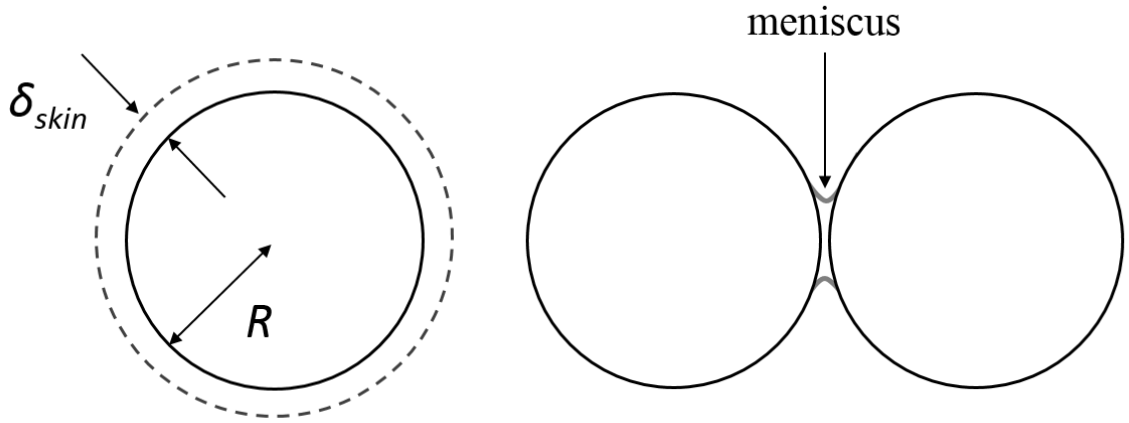

(a) (b)

Figure 3.28. Schematic illustration of (a) skin thickness (δ_{skin}) and (b) meniscus acting between non-contacting particles.

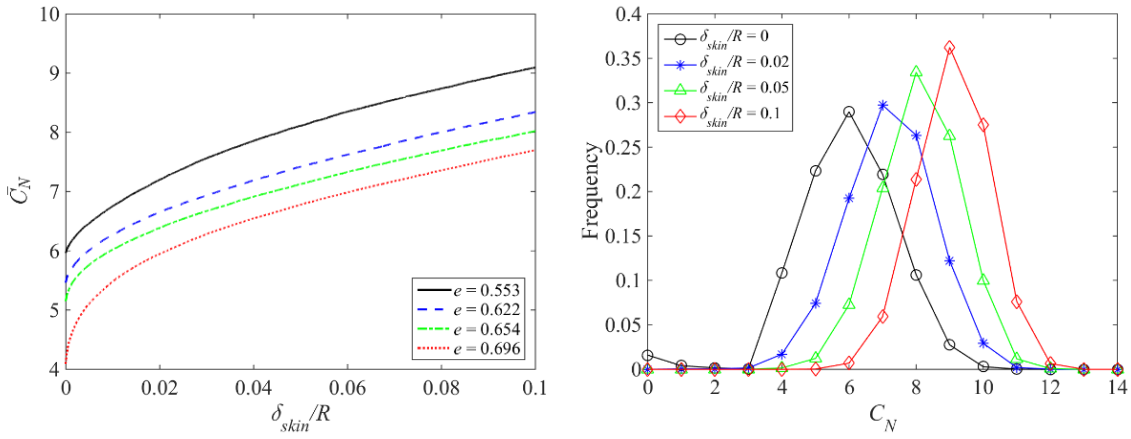

(a) (b)

Figure 3.29. Influence of skin thickness (δ_{skin}) on (a) mean coordination number ($\overline{C_N}$) at a confining stress of σ' = 11 kPa, and (b) coordination number per particle (C_N) at e = 0.553 and σ' = 11 kPa. (Note that mechanical mean coordination number and void ratio are not considered here).

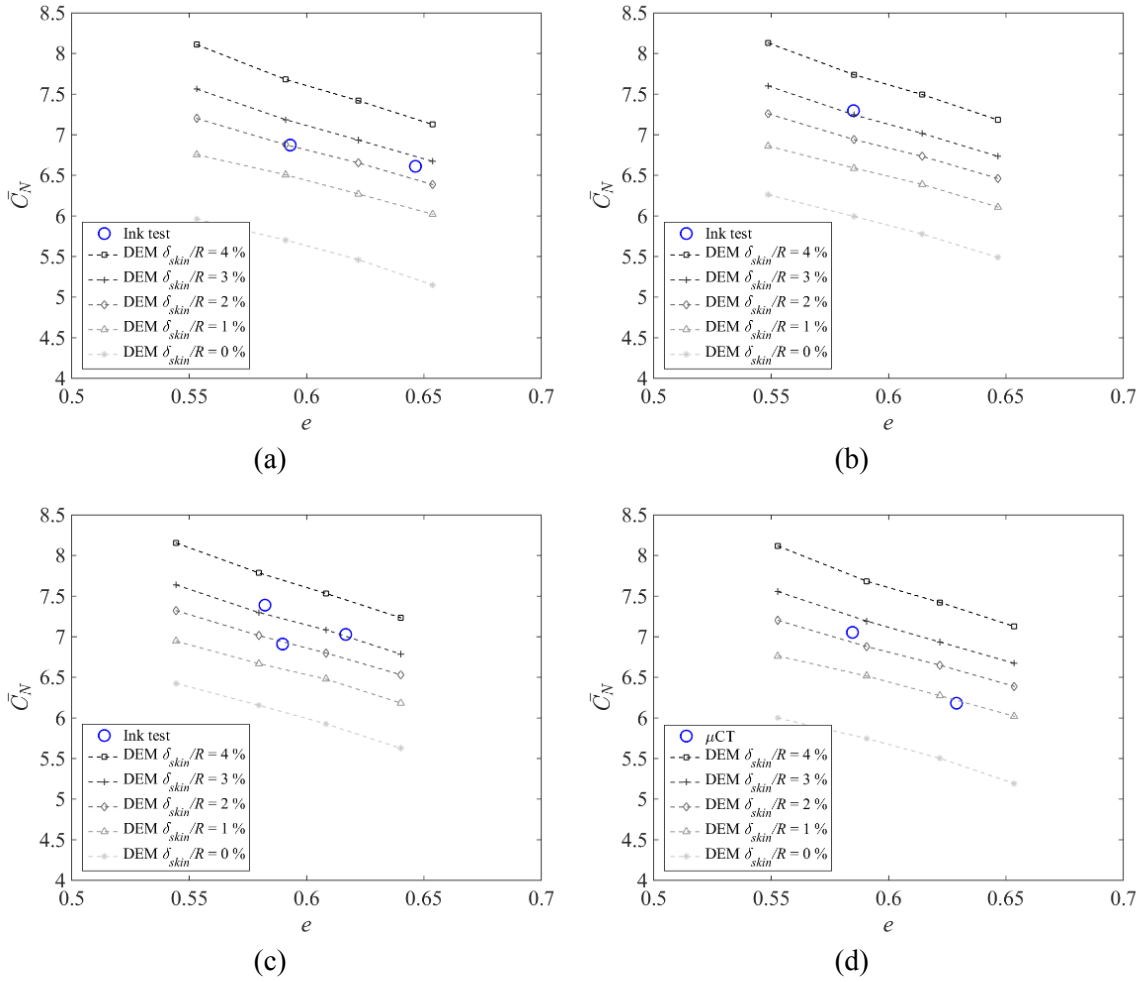

Figure 3.30. Relationship between mean coordination number and void ratio for lab tests and equivalent DEM simulations at: (a) σ'_V = 11 kPa (ink tests), (b) σ'_V = 700 kPa (ink test), (c) σ'_V = 2 MPa (ink tests), and (d) σ' = 30 kPa (μCT tests). DEM data points show mechanical mean coordination number ($\overline{C_N^*}$, Eq. 3.5.1) with varying δ_{skin} and the mechanical void ratio (e^*, Eq. 3.5.2) with δ_{skin} = 0.

CHAPTER 4
Implementation of contact models in DEM

4.1 Introduction

This chapter describes the implementation of new contact models in a modified version of the LAMMPS code. Section 4.2 discusses the contact models in detail; a rough surface (normal) contact model introduced in Section 4.2.1, a tangential contact model that considers partial slip effects is discussed in Section 4.2.2, and Section 4.2.3 considers a torsional contact model. Verification of the models' implementation is described in Section 4.3 and 4.4. Section 4.3 looks at two particles and a single contact, while Section 4.4 looks at an assembly of particles. A new servo-control for wall boundaries developed in this study is introduced in Section 4.4.

Specifically, this study develops a new rough contact model modified based on Cavarretta et al. (2010). This rough contact model differs from that proposed and implemented by O'Donovan (2013). The model proposed here is not based on O'Donovan's model (which for example includes a hardness parameter) rather it was developed by a fundamental examination of the work of Cavarretta et al. and others as discussed below. The partial slip model in tangential contact was theoretically expressed in Mindlin & Deresiewicz (1953), and this study follows the implementation algorism described by Thornton & Yin (1991) and O'Donovan (2013), who implemented the model in other DEM codes. The spin resistance model was theoretically described by Deresiewicz (1954) and no documentation describing the implementation of the spin resistance model described by Deresiewicz (1954) in any DEM code could be found. In the current study these models were implemented in the LAMMPS code.

The normal, tangential and torsional contact models can be combined, and notation used to identify a particular combination of contact models is summarised in Table 4.1. Two types of normal contact models are used; H stands for smooth Hertzian contact model, and R stands for rough surface contact model. Two types of tangential contact models are considered; M stands for Mindlin-type contact model, and MD (Mindlin-Deresiewicz) accounts for partial slip effects. A torsional contact model denoted by T can be added optionally to the tangential contact model with or without considering partial slip effects in torsion-spin interactions. When partial slip in tangential contact is considered, torsional contact model also include partial slip effects.

4.2 Implementation of contact models in LAMMPS

4.2.1 Rough surface model

As introduced in Section 2.4 the theoretical basis of contact models for rough surfaces has been developed by researchers working in the area of tribology. Real sand particles have a finite surface roughness due to the presence of surface asperities. For example, Altuhafi & Coop (2011) reported average surface roughness values (S_a, Eq. 2.4.1) of up to 200 nm for Leighton Buzzard Sand; the glass ballotini used in the current research had RMS surface roughness values between S_q = 36 nm (S_a = 13 nm) and S_q = 661 nm (S_a = 420 nm) (Section 3.2). Yimsiri & Soga (2000) derived a contact law for rough surfaces to be incorporated in a micro-mechanics based analytical expression for the stiffness of an assembly of particles as discussed in Section 2.4.2. However, the expression they used to relate the normal contact force (N) and normal contact stiffness (k_N) to the contact overlap (δ) is too complex for practical implementation in a DEM code as their expression for the k_N - δ relationship is intricate and their expression for the N - δ relationship is not provided. Therefore, a new contact law for rough surfaces is developed here; this model is based on the roughness model proposed by Cavarretta et al. (2010), and is also discussed in Otsubo et al. (2016).

Based on a theoretical study of contact between rough spheres, Greenwood & Tripp (1967; 1970) noted that the $N - \delta$ response of a rough contact becomes equivalent to the smooth Hertzian contact when the normal force, $N > N_{T2}$ where

$$N_{T2} = 100 S_q^* E^* \sqrt{2 R^* S_q^*} \tag{4.2.1}$$

where S_q^* = combined RMS surface roughness (Eq. 2.4.3); E^* = equivalent Young's modulus (Eq. 2.3.2); R^* = equivalent radius (Eq. 2.3.3). Cavarretta et al. (2010 & 2012) confirmed experimentally the applicability of Hertzian contact mechanics when N exceeds N_{T2}, and proposed a rough contact model, this contact model which is described in Cavarretta et al. (2010) is referred to as the "Cavarretta model" here.

Greenwood & Tripp (1967) also noted that the asperity deformation dominates the N - δ interaction when $N < N_{T1}$:

$$N_{T1} = S_q^* E^* \sqrt{2 R^* S_q^*} \tag{4.2.2}$$

Referring to Fig. 4.1, a new N - δ relationship for rough surfaces is proposed here that considers three phases: an asperity-dominated response (Eq. 4.2.3), a transitional response (Eq. 4.2.4), and a Hertzian response (Eq. 4.2.5):

$$N = N_{T1}\left(\frac{\delta}{\delta_{T1}}\right)^{c} \qquad \delta < \delta_{T1} \qquad (4.2.3)$$

$$N = N_{T2}\left(\frac{\delta - \delta_1}{\delta_{T2} - \delta_1}\right)^{b} \qquad \delta_{T1} \le \delta < \delta_{T2} \qquad (4.2.4)$$

$$N = \frac{4}{3} E_p^* R^{*0.5} \left(\delta - \delta_1 - \delta_2\right)^{1.5} \qquad \delta_{T2} \le \delta \qquad (4.2.5)$$

where δ_{T1} and δ_{T2} = contact (threshold) displacements at $N = N_{T1}$ and N_{T2}, respectively; b and c = constants; δ_1 and δ_2 = dimensional constants. The $N - \delta$ relationsihp in Eq. 4.2.5 is the Hertzian curve offset by $\delta_1 + \delta_2$ from Eq. 2.3.1. The dimensional constants δ_1 and δ_2 control the overall N - δ relationship. The Cavarretta model relates δ_2 to the surface hardness (H) as:

$$\delta_2^{Cavarretta} = r\left(\frac{3\pi}{4}\frac{H}{E_p^*}\right)^{2} \qquad (4.2.6)$$

where r is a function of the particle radius, roundness and shape. The surface hardness may be influenced by surface roughness and using Eq. 4.2.6 makes it difficult to isolate the influence of surface roughness alone. Taking $\delta_2 = \delta_2^{Cavarretta}$ (Eq. 4.2.6) and $\delta_1 = 0$ (also $N_{T1} = 0$ & $\delta_{T1} = 0$) reduces the proposed contact model to the Cavarretta model.

The normal contact stiffness for rough surfaces (k_N^{Rough}) is obtained by taking the derivative of N in Eqs. 4.2.3 to 4.2.5 with respect to δ:

$$\frac{dN}{d\delta} = c\,\frac{N_{T1}}{\delta_{T1}}\left(\frac{\delta}{\delta_{T1}}\right)^{c-1} \qquad \delta < \delta_{T1} \qquad (4.2.7)$$

$$\frac{dN}{d\delta} = b\,\frac{N_{T2}}{\delta_{T2} - \delta_1}\left(\frac{\delta - \delta_1}{\delta_{T2} - \delta_1}\right)^{b-1} \qquad \delta_{T1} \le \delta < \delta_{T2} \qquad (4.2.8)$$

$$\frac{dN}{d\delta} = 2E_p^* R^{*0.5}\left(\delta - \delta_1 - \delta_2\right)^{0.5} \qquad \delta_{T2} \le \delta \qquad (4.2.9)$$

Replacing δ in the right hand side of Eqs. 4.2.7 to 4.2.9 with N using Eqs. 4.2.3 to 4.2.5, respectively, gives $k_N^{Rough} - N$ relationships as:

$$\frac{dN}{d\delta} = c\,\frac{N_{T1}}{\delta_{T1}}\left(\frac{N}{N_{T1}}\right)^{(c-1)/c} \qquad N < N_{T1} \qquad (4.2.10)$$

$$\frac{dN}{d\delta} = b\,\frac{N_{T2}}{\left(\delta_{T2} - \delta_1\right)}\left(\frac{N}{N_{T2}}\right)^{(b-1)/b} \qquad N_{T1} \le N < N_{T2} \qquad (4.2.11)$$

$$\frac{dN}{d\delta} = \left(6E^{*2}R^*\right)^{1/3} N^{1/3} \qquad N_{T2} \le N \qquad (4.2.12)$$

As expected, Eq. 4.2.12 is identical to the normal contact stiffness of the Hertzian contact (Eq. 2.3.5 and Eq. 2.3.6).

Referring to Fig. 4.1, in the rough surface model the threshold displacements δ_{T1} and δ_{T2} are expressed in terms of δ_1 and δ_2 as follows:

$$\delta_{T2} = \left(\frac{3}{4} \frac{N_{T2}}{E^* R^{*0.5}} \right)^{2/3} + \delta_1 + \delta_2 \tag{4.2.13}$$

$$\delta_{T1} = \left(\frac{N_{T1}}{N_{T2}} \right)^{1/b} (\delta_{T2} - \delta_1) + \delta_1 \tag{4.2.14}$$

The constants b and c in Eqs. 4.2.3, 4.2.4 and 4.2.14 can be obtained by imposing a constraint that the three curves of the $N - \delta$ relationship connect smoothly, i.e. Eq. 4.2.10 must equal Eq. 4.2.11 at $N = N_{T1}$, and Eq. 4.2.11 must equal Eq. 4.2.12 at $N = N_{T2}$, giving

$$b = 1.5 \left(1 + \frac{\delta_2}{\delta_{T2} - \delta_1 - \delta_2} \right) \tag{4.2.15}$$

$$c = 100 b \delta_{T1} \frac{(\delta_{T1} - \delta_1)^{b-1}}{(\delta_{T2} - \delta_1)^b} \tag{4.2.16}$$

This $N - \delta$ relationship still depends on δ_1 and δ_2 and they should be related to surface roughness.

Yimsiri & Soga (2000) related the ratio of the radius of a rough contact (a^{Rough}) to the radius of a smooth contact (a^{Smooth}) to the roughness index α (Eq. 2.4.4) introduced by Greenwood et al. (1984) (as discussed in Section 2.4.2) as follows:

$$\frac{a^{Rough}}{a^{Smooth}} = \left(\frac{-2.8}{\alpha + 2} + 2.4 \right) \tag{4.2.17}$$

where the smooth contact radius can be calculated using Eq. 2.3.5 for a given normal force and rough contact radius may be calculated in a similar manner as:

$$a^{Rough} = \sqrt{R^* \delta^{Rough}} \tag{4.2.18}$$

where δ^{Rough} is calculated for a given normal force using Eq. 4.2.3, 4.2.4 or 4.2.5.

Considering the radius ratio a^{Rough}/a^{Smooth}, Fig. 4.2 compares the experimental data of Greenwood et al. (1984) with the proposed contact model using δ_1=0.82 S_q^* and δ_2=1.24 S_q^* as obtained from iterative curve fitting to Eq. 4.2.17. The proposed roughness model agrees well with the model proposed by Yimsiri & Soga (2000) (within 5%) and captures the trend of experimental data by Greenwood et al. (1984).

Substituting δ_1=0.82 S_q^* and δ_2=1.24 S_q^* into Eqs. 4.2.13 and 4.2.14 gives:

$$\begin{aligned} \delta_{T1} &\approx 2.11\, S_q^* \\ \delta_{T2} &\approx 24.47\, S_q^* \end{aligned} \tag{4.2.19}$$

Substituting Eq. 4.2.19 into Eqs. 4.2.15 and 4.2.16 gives:

$$\begin{aligned} b &= 1.58 \\ c &= 2.59 \end{aligned} \tag{4.2.20}$$

Using Eqs. 4.2.19 and 4.2.20 the $N - \delta$ relationships shown in Eqs. 4.2.3 to 4.2.5 are reduce to:

$$N = N_{T1}\left(\frac{\delta}{2.11 S_q^*}\right)^{2.59} \qquad \delta < 2.11\, S_q^* \tag{4.2.21}$$

$$N = N_{T2}\left(\frac{\delta - 0.82 S_q^*}{23.65 S_q^*}\right)^{1.58} \qquad 2.11\, S_q^* \le \delta < 24.47\, S_q^* \tag{4.2.22}$$

$$N = \frac{4}{3} E_p^* R^{*0.5} \left(\delta - 2.06 S_q^*\right)^{1.5} \qquad 24.47\, S_q^* \le \delta \tag{4.2.23}$$

Similarly, expressions for the normal contact stiffness (Eqs. 4.2.10 to 4.2.12) become:

$$\frac{dN}{d\delta} = 2.59 \frac{N_{T1}}{2.11 S_q^*}\left(\frac{N}{N_{T1}}\right)^{0.614} \qquad N < N_{T1} \tag{4.2.24}$$

$$\frac{dN}{d\delta} = 1.58 \frac{N_{T2}}{23.65 S_q^*}\left(\frac{N}{N_{T2}}\right)^{0.368} \qquad N_{T1} \le N < N_{T2} \tag{4.2.25}$$

$$\frac{dN}{d\delta} = \left(6 E^{*2} R^*\right)^{1/3} N^{1/3} \qquad N_{T2} \le N \tag{4.2.26}$$

The rough contact model proposed in this study is based on Eqs. 4.2.21 to 4.2.26. Using the material properties for glass ballotini (Table 4.2) and realistic values of S_q^* for the ballotini (≤ 1.0 μm) as discussed in Section 3.2. The $N - \delta$ relationship for this model is given in Fig. 4.3. Referring to Fig. 4.3(a) the initial slope of the $N - \delta$ relationship is reduced with increasing surface roughness, indicating softer responses at the contact. It is clear that k_N decreases with increasing S_q^* values especially at lower N values (Fig. 4.3(b)). The power coefficients of k_N - N relationship obtained from Eqs. 4.2.24 to 4.2.26 give 0.614 ($N < N_{T1}$), 0.368 ($N_{T1} <= N < N_{T2}$), and 1/3 ($N_{T2} <= N$). For a perfectly smooth contact (S_q^* = 0), the power coefficient is 1/3 as expressed by the Hertzian theory. The approximately bi-linear trend in the k_N - N relationship can be seen in Fig. 4.3(b) with the model converging to the Hertzian curve at $N = N_{T2}$. This k_N - N relationship contrasts with Yimsiri & Soga (2000) and their model gives a smooth transition in the k_N - N relationship; however the overall trend is similar.

The rough surface model presented here idealises the real physical system: it does not consider yielding, squashing or vibration of asperities or the change in the inter-particle friction due to the plastic compression of asperities (Hanaor et al., 2013). Thus the unloading and reloading curves are identical to the initial loading curve. In future research, a plastic displacement due to the asperity squashing might be included.

Tangential contact stiffness for rough contact model

Referring to Sections 2.4.3 and 2.4.4, the tangential contact stiffness for rough surfaces has been discussed in the tribology literature (e.g. Gonzalez-Valadez et al., 2010) and the contact stiffness ratio for rough surfaces (k_T^{Rough}/k_T^{Smooth}) is likely to be equal or smaller than that for smooth surfaces. This study assumes that the contact stiffness ratio is equal between smooth surfaces and rough surfaces as below:

$$\frac{k_T^{Rough}}{k_N^{Rough}} = \frac{k_T^{Smooth}}{k_N^{Smooth}} \tag{4.2.27}$$

The rough contact model can be coupled with any tangential contact model using the expression in Eq. 4.2.27 as indicated in Table 4.1.

4.2.2 Partial slip in tangential contact

Section 2.3.2 described the theoretical basis for including partial slip effects in a tangential contact for the case of constant normal force. Based on the theory described by Mindlin & Deresiewicz (1953), a partial slip model for use in a DEM code was described by Thornton & Yin (1991). In this model, for loading, unloading, and reloading, the incremental tangential displacement (Δs) is expressed as:

$$\Delta s = \frac{1}{8G_p^* a}\left(\pm \mu \Delta N + \frac{\Delta T \mp \mu \Delta N}{\theta} \right) \tag{4.2.28}$$

The incremental tangential contact stiffness is obtained by rearranging Eq. 4.2.28 given by:

$$k_T = 8G_p^* \theta a \pm \mu(1-\theta)\frac{\Delta N}{\Delta s} \tag{4.2.29}$$

where the positive signs in Eqs. 4.2.28 and 4.2.29 are used for initial loading and reloading of tangential contact force (T), whereas the negative signs are invoked for unloading. The parameter θ depends on the loading cases of T as:

$$\theta^{load} = \left[1 - \frac{T + \mu \Delta N}{\mu N} \right]^{1/3} \tag{4.2.30}$$

$$\theta^{unload} = \left[1 - \frac{T^* - T + 2\mu\Delta N}{2\mu N}\right]^{1/3} \tag{4.2.31}$$

$$\theta^{reload} = \left[1 - \frac{T - T^{**} + 2\mu\Delta N}{2\mu N}\right]^{1/3} \tag{4.2.32}$$

where T^* and T^{**} = the maximum and minimum tangential contact forces in history.

Using the expressions given by Thornton & Yin (1991), the response predicted by the HMD model is contrasted with the response given by the HM model in Fig. 4.4. For the cases considered in Fig. 4.4, N was taken to be 1 N (constant) and an inter-particle friction of $\mu = 0.2$ was used with two T^{**} values (Figs. 4.4(a) and (c) had $T^{**} > 0$ and Figs. 4.4(b) and (d) had $T^{**} < 0$). The material properties are those listed in Table 4.2. Referring to Figs. 4.4(a) and (b) for the HMD model, the $T - s$ relationship is non-linear due to partial slip, and hysteresis of loading curves is observed. The area enclosed by the unloading and reloading curves is dissipated energy done by partial slip. In contrast, a linear-elastic relationship is seen for the HM model below the slip-limit (i.e. $T < \mu N$).

Strictly speaking, the re-unloading curve should be determined by considering (and recording) the tangential contact force at the reversal from the reloading (T^{***}). Fig. 4.5 illustrates analytical $T - s$ curves including the re-unloading and re-reloading. Referring to Fig. 4.5, in general, the $T - s$ curve of the second loop is close to linear and the hysteresis is smaller than that for the first loop. Following Thornton & Yin (1991) and O'Donovan (2013), here the re-unloading case is considered to be identical to the reloading case (Eq. 4.2.32), i.e. there is no hysteresis during the re-unloading case.

As noted in Mindlin & Deresiewicz (1953), in a given increment the T^* and T^{**} values should be updated from those at the previous increment (T^*_{old} and T^{**}_{old}) depending on the change in normal contact force:

$$\begin{aligned} T^* &= T^*_{old} + \mu\Delta N \\ T^{**} &= T^{**}_{old} - \mu\Delta N \end{aligned} \tag{4.2.33}$$

According to Mindlin & Deresiewicz (1953) there is a required incremental tangential displacement (Δs^{min}) when $\Delta N > 0$ so that the tangential force is updated correctly considering ΔN given by:

$$\Delta s^{\min} = \frac{\mu\Delta N}{8G^*_p a} \tag{4.2.34}$$

For the case of $\Delta s < \Delta s^{min}$ with $\Delta N > 0$, $\theta = 1$ can be used in Eqs. 4.2.30 to 4.2.32 as considered by Thornton & Yin (1991) and O'Donovan (2013) until the following condition is satisfied:

$$8G_p^* a \sum |\Delta s| \geq \mu \sum \Delta N \tag{4.2.35}$$

Referring to Fig. 4.6 where N increases from 1 N to 1.5 N during either loading, unloading or reloading of the tangential force, setting $\theta = 1$ gives a higher slope in the $T - s$ curve, and the updated T values would lie onto the theoretical curve for $N = 1.5$ N when Eq. 4.2.35 is satisfied.

Directionality of tangential contact displacement

The implementation of the HMD model considered here treats the local axes in the contact planes (e.g. X^{local} and Y^{local}) equally when partial slip effect is considered. For example, partial slip induced due to loading in the X^{local} direction reduces the contact stiffness in both the X^{local} and Y^{local} directions equally. This fact does not affect two-dimensional simulations. Referring to Fig. 4.7(a), for three-dimensional simulations, the global tangential displacement ($\vec{s}$) is updated considering the incremental global tangential displacement in X and Y axes ($\overrightarrow{\Delta s_X}$ and $\overrightarrow{\Delta s_Y}$) as:

$$\Delta\vec{s} = \Delta\vec{s}_X + \Delta\vec{s}_Y \tag{4.2.36}$$

$$\vec{s} = \vec{s}_{old} + \Delta\vec{s} \tag{4.2.37}$$

The increment in the local contact displacement (Δs^{local}) and the accumulated local tangential displacement (s^{local}) is obtained comparing $\vec{s}$ and $\overrightarrow{s_{old}}$ given by:

$$\Delta s^{local} = |\vec{s}| - |\vec{s}_{old}| \tag{4.2.38}$$

$$s^{local} = s_{old}^{local} + \Delta s^{local} \tag{4.2.39}$$

Depending on the sign of Δs^{local} and its history, either loading, unloading or reloading is determined. Updating θ using Eqs. 4.2.30 to 4.2.32 gives an updated tangential contact stiffness for the HMD model (k_T^{HMD}) and an incremental tangential contact force ΔT^{local} as:

$$\Delta T^{local} = k_T^{HMD} \Delta s^{local} \tag{4.2.40}$$

The k_T^{HMD} value is determined from local variables; however this is used to update global tangential contact force equally for both the X and Y directions:

$$\begin{aligned} \Delta T_X &= k_T^{HMD} \Delta s_X \\ \Delta T_Y &= k_T^{HMD} \Delta s_Y \end{aligned} \tag{4.2.41}$$

Following this approach it is difficult to identify when the sign of s^{local} becomes negative. Fig. 4.7 shows an example of loading sequence to highlight this limitation. Referring to Fig. 4.7(b) and Eqs. 4.2.38 and 4.2.39, s^{local} increases continuously from the origin to point 3 (i.e. $\Delta s^{local} >$

0), and decreases from point 3 to point 5 (i.e. $\Delta s^{local} < 0$). When s^{local} moves from point 5 to point 6, $\Delta s^{local} = 0$ as $\left|s^{local}\right| = \left|s_{old}^{local}\right|$ in Eq. 4.2.38. From point 6, Δs^{local} increases again as $\Delta s^{local} > 0$, and the resultant T^{local}- s^{local} curve is illustrated in Fig. 4.7(c) where $s^{local} \geqq 0$. However, it is more sensible to reverse the sign of s^{local} when s^{local} moves from point 5 to point 6. To overcome this limitation, the current implementation records the global displacement vectors $\vec{s}^*$ that are recorded when $T = T^*$, and when the inner-product of the current global displacement vector $\vec{s}$ and $\vec{s}^*$ becomes negative, the sign of s^{local} is reversed to negative as:

$$s^{local} = -\left|s^{local}\right| \qquad \text{if } \vec{s} \cdot \vec{s}^* < 0 \tag{4.2.42}$$

where $\vec{s}^*$ is the vector from the origin to point 3 in the example shown in Fig. 4.7(b). Implementing Eq. 4.2.42 gives the T^{local}- s^{local} relationship as illustrated in Fig. 4.7(d) where points 6, 7, and 8 in Fig. 4.7(b) show negative values of s^{local}.

4.2.3 Partial slip in twisting contact model

Implementing a twisting contact model in a DEM code is similar to the implementation of the tangential contact model as discussed in the previous section. As there is only one direction of spin about the contact normal, it is less complex compared with the tangential contact. The influence of varying normal contact force (N) was not discussed in Deresiewicz (1954); however, using the expressions for the tangential load-deformation behaviour, the torsion-spin relationship can be extended to more general cases by considering a change in N as:

$$\Delta\varphi_r = \frac{3}{16G_p^* a^3}\left(\pm\frac{3}{16}\pi\mu\Delta N a + \frac{\Delta M_r \mp \frac{3}{16}\pi\mu\Delta N a}{\theta_r}\right) \tag{4.2.43}$$

where φ_r = angle of spin; M_r = twisting moment. The twisting contact stiffness (k_r) in Eqs. 2.3.16 can be extended to consider ΔN, given by:

$$k_r = \frac{16}{3}G_p^*\theta_r a^3 \pm \frac{3}{16}\pi\mu a(1-\theta_r)\frac{\Delta N}{\Delta\varphi_r} \tag{4.2.44}$$

where the positive signs in Eqs. 4.2.43 and 4.2.44 are used for initial loading or re-loading by a twisting moment, whereas the negative signs are invoked for the unloading case, and θ_r in Eq. 4.2.44 is given by:

$$\left[\theta_r^{load}\right]^{-1} = 2\left(1 - \frac{3}{2}\frac{M_r + \frac{3}{16}\pi\mu a\Delta N}{\mu N a}\right)^{-0.5} - 1 \qquad \text{(loading)} \tag{4.2.45}$$

$$\left[\theta_r^{unload}\right]^{-1} = 2\left(1-\frac{3}{2}\frac{M_r^* - M_r + \frac{3}{8}\pi\mu a\Delta N}{2\mu N a}\right)^{-0.5} - 1 \qquad \text{(unloading)} \qquad (4.2.46)$$

$$\left[\theta_r^{reload}\right]^{-1} = 2\left(1-\frac{3}{2}\frac{M_r - M_r^{**} + \frac{3}{8}\pi\mu a\Delta N}{2\mu N a}\right)^{-0.5} - 1 \qquad \text{(reloading)} \qquad (4.2.47)$$

where M_r^* and M_r^{**} = the maximum and minimum twisting contact moments experienced by the current contact. As in the case of the tangential contact, the M_r^* and M_r^{**} values should be updated from those at the previous increment ($M_{r,old}^*$ and $M_{r,old}^{**}$) when N varies:

$$\begin{aligned} M_r^* &= M_{r,old}^* + \frac{3}{16}\pi\mu a\Delta N \\ M_r^{**} &= M_{r,old}^{**} - \frac{3}{16}\pi\mu a\Delta N \end{aligned} \qquad (4.2.48)$$

The re-unloading case can be taken to be same as the reloading case following the approach considered in the tangential force-deformation relationship.

Referring to Eqs. 4.2.34 and 4.2.35, as considered in Mindlin & Deresiewicz (1953) for the tangential force-deformation relationship, there is a spin angle ($\Delta\varphi_r^{min}$) required to update M_r correctly when ΔN (> 0):

$$\Delta\varphi_r^{\min} = \frac{\frac{3}{16}\pi\mu a\Delta N}{\frac{16}{3}G_p^* a^3} = \frac{9}{256}\frac{\pi\mu\Delta N}{G_p^* a^2} \qquad (4.2.49)$$

For the case of $\Delta\varphi_r < \Delta\varphi_r^{min}$ with $\Delta N > 0$, $\theta_r = 1$ can be used in Eqs. 4.2.45 to 4.2.47 until the following condition is satisfied:

$$\frac{16}{3}G_p^* a^3 \sum\left|\Delta\varphi_r\right| \geq \frac{3}{16}\pi\mu a\sum\Delta N \qquad (4.2.50)$$

An example of M_r - φ_r relationship including partial slip both in tangential and torsional contacts (HMDT model, see Table 4.1) is illustrated in Fig. 4.8 where it is compared with a linear twisting contact model (stick-slip) with $\theta_r = 1$ (HMT model) where $N = 1$ N (constant) and $\mu = 0.2$ are used with two M_r^{**} values (Figs. 4.8(a) and (c) for $M_r^{**} > 0$ and Figs. 4.8(b) and (d) for $M_r^{**} < 0$). The material properties are listed in Table 4.2. Referring to Figs. 4.8(a) and (b) for the partial slip model, the M_r - φ_r relationship is non-linear, and the area enclosed by the unloading

and reloading curves is the energy dissipated due to partial slip in the M_r - φ_r relationship. In contrast, a linear-elastic M_r - φ_r relationship is seen when partial slip effects are neglected as illustrated in Figs. 4.8(c) and (d).

Referring to Table 4.1, coupling between rough surface (normal) contact model and torsional contact model is not considered in this study as the literature to validate the combination is still needed.

4.3 Single contact simulations

A set of single contact simulations were carried out in order to validate the newly implemented contact models as described in Section 4.2. Section 4.3.1 investigates tangential contact interactions under gravity, and Section 4.3.2 discusses oblique impacts between a particle and a wall considering surface roughness effects in the normal force-overlap (N-δ) relationship (RM model, Table 4.1) and partial slip effects in the tangential force-deformation (T-s) relationship (HMD model), and coupled effects of partial slip and surface roughness effects (RMD model). Section 4.3.3 considers oblique impacts between two spherical particles using the simplified Hertz-Mindlin (HM) contact model and the HMD model. The influence of twisting resistance under gravity is described in Section 4.3.4 by considering partial slip effects in the torsion-spin (M_r - φ) relationship (HMDT model). Section 4.3.5 explores the effects of twisting resistance during normal impacts with spin.

4.3.1 Horizontal displacement (shearing) with vertical body force

Referring to Fig. 4.9 the first test case considered the response of a resting sphere on a horizontal boundary subject to gravitational loading and an applied horizontal velocity. The same material properties used are listed in Table 4.3. In the first step of the simulation, gravity was applied. In the absence of damping the sphere would oscillate with a sinusoidal shape, and so the kinetic energy was removed using both local damping and viscous damping. Referring to Fig. 4.9, once the vibration became negligible, a horizontal translational velocity in the X direction (V_{X0}) was applied to the sphere. As in O'Donovan (2013), rotation of the sphere was not permitted during the simulation.

The simulation results are illustrated in Fig. 4.10 where the time history of tangential contact displacement (s) is plotted in Fig. 4.10(a). Fig. 4.10(b) considers the variation in kinetic energy with time. When all the applied translational kinetic energy was reduced to zero (Fig. 4.10(b)) (i.e. converted to the strain energy), the sphere started moving backwards. As the HM model is purely elastic when the friction limit is not exceeded (i.e. $T < \mu N$), the sphere kept vibrating with no variation in amplitude. The kinetic energy gradually decreased due to frictional dissipation

when partial slip was included using the HMD model. Note that energy dissipation did not take place after re-unloading due to the simplifying assumption discussed in Section 4.2.2. Referring to Figs. 4.10(c) and (d), the *T-s* relationship shows a hysteresis for the HMD model but not for the HM model. The enclosed area of the hysteresis is identical to the energy dissipated by partial slip. When gravity is increased to 2g, the slope of *T-s* curve increases and the maximum tangential displacement is reduced under the same initial translational velocity given to the sphere. Referring to Fig. 4.11, the data presented in Fig. 4.10(d) for the HMD model are identical to those in O'Donovan (2013).

The effect of surface roughness of the sphere and wall was considered in the same simulation using the RMD model, and the slope of *T-s* curve was reduced due to the lowered tangential contact stiffness (asperities-dominate response) in the RMD model (Fig. 4.12(a)). The observed hysteresis due to partial slip was similar between the RMD model and the HMD model. The RMS roughness value considered (S_q = 1 nm) is larger than the maximum value of *s* developed during the simulation (< 1 nm), and so there was a considerable reduction in the contact stiffness and the period of sinusoidal oscillation of the sphere (Fig. 4.12(b)) when the RMD, rather than HMD, model was used.

4.3.2 Oblique impact on wall

Referring to Fig. 4.13, the second test case considered the response of a sphere moving toward a horizontal boundary subject to an applied velocity (V_0) with an angle of impact (α). The contact models considered were the HM, HMD, RM and RMD models. An elastic sphere was generated to just touch on an elastic wall without gravity, and an initial translational velocity of V_0 = 5.0 m/s was applied. The direction of V_0 varied between α = 5°, 20° and 40° from the vertical (Z-) axis (Fig. 4.13) to a horizontal (X-) axis. Unlike the previous simulation in Section 4.3.1, gravity was not included and rotation of the sphere about the Y-axis was permitted. The material properties were determined following Thornton et al. (2011) and O'Donovan (2013) (Table 4.4).

The observed *T-s* curves are illustrated in Fig. 4.14, and the relationships between the tangential and normal contact forces (*T-N* relationship) are illustrated in Fig. 4.16 for varying impact angles. Referring to Fig. 4.14, the initial slope of *T-s* curve is not affected by partial slip, i.e. the HM and HMD models, and the RM and RMD models are equivalent. The effect of partial slip is observed during unloading and reloading of tangential force for α = 5° and 20° (Figs. 4.14(a) and (b)), while no effect of partial slip was observed for α = 40° as full slip was mobilised (i.e. $T > \mu N$) during the entire simulation (Fig. 4.14(c)). The data for the HM and HMD models were compared with Thornton et al. (2011) and O'Donovan (2013) for the same impact simulations. Fig. 4.15 compares the *T-s* relationship observed in this study and Thornton et al. (2011), and

they are in good agreement. Referring to Fig. 4.16, the effect of partial slip becomes more obvious in the *T-N* curves during unloading and reloading of the tangential force. These results for the HMD contact model are in good agreement with Thornton et al. (2011) and O'Donovan (2013). A quantitative investigation was made considering various RMS surface roughness values (S_q) using the RMD model and the results are summarised in Figs. 4.14(d) and 4.16(d) for cases with $\alpha = 5°$. Referring to Figs. 4.14(d) and 4.16(d), the initial slope of *T-s* curve becomes lower as the S_q value increases, while the overall response of the *T-N* curves are similar. The S_q values considered in the simulations ($S_q \leq 20$ μm) were similar with the magnitude of *s* developed during the simulations ($s \leq 15$ μm).

Note that the tangential contact displacement (*s*) plotted in Fig. 4.14 is the translational component, whereas the rotational component was measured as the angular velocity. The variation of the angular velocity in Y direction (ω_Y) and the kinetic energy of the sphere with time are shown in Fig. 4.17(a) and Fig. 4.17(b), respectively, using the HMD model. Both ω_Y and the kinetic energy are affected by α.

4.3.3 Oblique impact between identical spheres

Thornton & Yin (1991) and O'Donovan (2013) documented oblique impact simulations between equal spheres and the same scenario is considered in this section. Two identical elastic spheres, whose properties are listed in Table 4.5, are initially just touching with an inclined contact plane as illustrated in Fig. 4.18, where α is varied from 15° to 75°. An initial vertical velocity of $V_{Z0} = \pm 0.05$ m/s was applied to both spheres to simulate an impact of the spheres.

The tangential force-displacement (*T-s*) interactions observed using the HM and HMD contact models are illustrated in Figs. 4.19(a) and (b), respectively. At larger α values the differences between the HM and HMD models became less significant as full slip was mobilised over a longer period during the collision for the HMD case. The initial linear slope in Figs. 4.19(c) and (d) indicates that either full slip or the special case is invoked (Eq. 4.2.35 with $\Delta N > 0$), and this slope equals the value of μ. The influence of partial slip is clear at lower α values (e.g. $\alpha = 15°$) as partial slip dominates during the collision, and the response observed for the HMD model is smoother than that for the HM model due to a smooth transition to full slip. The results shown here are in good agreement with the results in Thornton & Yin (1991) and O'Donovan (2013), e.g. Fig. 4.20 shows the *T-s* relationship and the *T-N* relationship for the HMD model reported in Thornton & Yin (1991).

The conservation of energy during a collision at $\alpha = 30°$, 60° and 75° using HMD model is considered in Fig. 4.21 where the variation in translational and rotational kinetic energy, and the normal and tangential strain energy (including frictional dissipation due to partial slip or full

slip) are compared with time. The strain energy develops significantly at lower impact angles, whereas the kinetic energy remains high with larger impact angles. The normal and tangential elastic strain energy decrease to zero when the spheres detach; however, the residual tangential energy is identical to the amount of dissipated energy due to partial or full slip during the collision. The summation of the four energy components is also plotted in Fig. 4.21; it is clear that the summation is constant over time, indicating the energy is correctly conserved. The results of energy distribution agree with data presented in Thornton & Yin (1991).

4.3.4 Spinning sphere with vertical body force

Referring to Fig. 4.22, this simulation considers the torsion-spin (M_r-φ_r) response of a sphere resting on a horizontal boundary subject to gravitational loading with an applied angular velocity about contact normal. The material properties considered were listed in Table 4.3. The simplified twisting model (without partial slip) coupled with the HM model (HMT model) and partial slip twisting model coupled with the HMD model (HMDT model) were used. Following the simulation method described in Section 4.3.1, the kinetic energy of sphere was removed using both local damping and viscous damping, and then an angular velocity of 0.02 rad/s about the Z axis was applied (Table 4.6).

The sphere spins about the Z-axis at a fixed position throughout a simulation. The direction of spin reversed when the rotational kinetic energy reached zero (Figs. 4.23(a) and (b)). If a twisting contact model is not included such as the HM or HMD contact model, the sphere keeps spinning with a constant angular velocity. The twisting contact model acts as a spring affecting only spinning motion and the observed results are qualitatively similar with the *T*-*s* relationship observed in Section 4.3.1 for the tangential interactions (Fig. 4.10). The partial slip effects in spinning direction also affect the M_r-φ_r relationship in a similar manner to the *T*-*s* relationship for tangential interactions.

It is interesting to note that the twisting contact stiffness k_r (slope in Figs. 4.23(c) and (d)) developed noticeably when an increased acceleration (2g) was applied. Referring to Eq. 4.2.44, the k_r value is proportional to a^3, whereas a is proportional to $N^{1/3}$. Thus, the initial twisting stiffness for HMDT (with $\theta_r = 1$) or the stiffness for HMT has a simple relationship with N:

$$k_r^{HMT} \propto N \tag{4.3.1}$$

The slope for 2g illustrated in Figs. 4.23(c) and (d) is twice larger than that for 1g. This highlights the stress-dependent nature of the twisting contact stiffness.

4.3.5 Normal impact with spin on wall

Impact between a spinning sphere and a wall was simulated as illustrated in Fig. 4.24. The material properties considered are detailed in Table 4.7. The impact angle was set to be collinear with the contact normal (Z-axis) with varying initial angular velocity of ω_{Z0} = 10, 30, 100 and 300 rad/s. To maintain a simple and clear test scenario, the effect of impact angle is not investigated in this section. The HMT and HMDT contact models were used in the simulations; however, a measurable difference between two models was not noticed as the special case (Eq. 4.2.50) was invoked for a longer period during the collision, i.e. $\theta_r = 1$ was used for the HMDT model in Eq. 4.2.44. Thus the following describes the results obtained using the HMDT model.

Referring to Fig. 4.25(a), the twisting moment (M_r) develops with time, and M_r reaches its frictional limit ($M_r^{max} = 3\pi\mu Na/16$) for the simulation with a larger ω_{Z0} value at an earlier time. The angular velocity (ω_{Z0}) is affected by the collision, and normalised angular velocities (ω_Z/ω_{Z0}) are compared in Fig. 4.25(b). The lower ω_{Z0} values show a greater reduction in the velocity ratio as the full slip was mobilised at a later time. The twisting moment-normal force (M_r - N) relationship and the twisting moment-spin angle (M_r - φ_r) relationship are summarised in Figs. 4.25(c) and (d). When full slip occurs, all the plots reveal the same non-linear M_r - N relationship (Fig. 4.25(c)) where the slope increases proportionally to the radius of contact circle (a). Referring to Fig. 4.25(d), the φ_r value increases during the simulations particularly for a larger ω_{Z0} value.

Including the twisting contact model allowed the twisting contact moment to develop during the impact although the angular velocity was not affected considerably. Referring to Fig. 4.25(b), the change of the angular velocity was less than 5%.

Lim & Stronge (1994), who studied analytically the impact between a spinning sphere and a horizontal wall by considering the twisting contact resistance following Deresiewicz (1954), related a non-dimensional angular velocity (ψ) to the influential factors on the final angular velocity (ω_{Zf}) given by:

$$\psi = 0.3691 \frac{R\omega_{Z0}}{\mu C V_{Z0}} \tag{4.3.2}$$

where C is a function of material properties and initial translational velocity (V_{z0}) as

$$C = \left[\frac{15 m V_{Z0}^2 (1-\nu_p)}{32 G_p R^3} \right]^{1/5} \tag{4.3.3}$$

where m = mass of sphere. Lim & Stronge (1994) noted that a material type has a critical value of ψ (i.e. ψ_C), below which $\omega_{Zf} < 0$ (i.e. back spin), whereas $\psi > \psi_C$ gives $\omega_{Zf} > 0$. Referring to

Eq. 4.3.2, a larger ω_{Z0} value gives a larger ψ value, and ω_{Zf} tends to increase, which agrees with the results observed in Fig. 4.25(b).

To increase the effects of twisting contact resistance, a softer sphere with material properties as listed in Table 4.8 was considered for the same test condition. The material properties considered here are similar to Lim & Stronge (1994). The simulation results are illustrated in Fig. 4.26 for ω_{Z0} = 10, 30, 100, and 200 rad/s where qualitatively similar results with Fig. 4.25 are seen. The collision time is approx. 4.58 ms using the soft sphere (Fig. 4.26(a)) compared with 0.126 ms for the hard sphere considered in previous simulations (Fig. 4.25(a)). Referring to Fig. 4.26(b), the longer collision time leads a significant change in ω_Z/ω_{Z0} in which the case for ω_{Z0} = 10 rad/s exhibits back spin (i.e. $\omega_Z < 0$). The ω_{Zf} and ω_{Z0} values are compared in Fig. 4.27(a) where lower ω_{Z0} values give $\omega_{Zf} < 0$. The observed trend agrees qualitatively with the results presented in Lim & Stronge (1994) (Fig. 4.27(b)). Note that the test conditions are not identical as all the input parameters are not provided in Lim & Stronge (1994). Thus the current study used the test condition considered for the stiffer sphere (Fig. 4.25). The critical initial angular velocity obtained was 16.3 rad/s when ω_{Zf} = 0 (Fig. 4.27). Using Eqs. 4.3.2 and 4.3.3 give ψ_C = 0.207 for the material type considered here. Knowing the ψ_C value enables prediction of the final angular velocity of the spinning sphere.

4.4 Triaxial compression of FCC packing

Triaxial compression simulations using a FCC packing sample are often used to validate newly implemented DEM codes. An analytical expression for the peak strength of this type of sample was studied by Thornton (1979) and the DEM simulation results for the triaxial loading case were documented in the PFC 3D user manual (Itasca, 2007). This section describes DEM simulations of triaxial compression for validation of the newly implemented contact models and a servo-control for wall boundary as detailed below.

4.4.1 Implementation of a servo-control for wall boundary

The data presented were generated using a combined boundary condition in which one direction is bounded by wall boundaries, whereas the periodic boundaries are placed in the other directions. To prepare a sample under a specified confining stress, the wall boundary and periodic boundary must be controlled in a similar manner. Following the approach used to achieve a servo-control on stress with a system for periodic boundaries that were implemented in the modified version of LAMMPS code used here by Dr. Kevin Hanley, and controlling stress using rigid wall boundaries was implemented in the current study. The boundary velocity

($V_{boundary}$) is controlled using the current mean effective stress σ' and the target stress (σ'_{target}) normal to the wall boundary given by:

$$\begin{aligned} V_{boundary} &= V_{\max} && \sigma' < 0.5\sigma'_{target} \\ V_{boundary} &= 2V_{\max}\left(1-\sigma'/\sigma'_{target}\right) && \sigma' \geq 0.5\sigma'_{target} \end{aligned} \tag{4.4.1}$$

where the maximum boundary velocity V_{max} is calculated using the user-defined maximum strain rate $\dot{\varepsilon}_{max}$ and the initial sample length (l_0) as:

$$V_{\max} = l_0 \dot{\varepsilon}_{\max} \tag{4.4.2}$$

When a boundary wall moves inward and contacts particles, an external energy is given to the particle system. To consider the work done by the wall boundary, the following calculation was included in the code:

$$\Delta E_{boundary} = \left(\sigma'_{XX}\,\dot{\varepsilon}_{XX} + \sigma'_{YY}\,\dot{\varepsilon}_{YY} + \sigma'_{ZZ}\,\dot{\varepsilon}_{ZZ}\right) \times \Delta t \times vol \tag{4.4.3}$$

where Δt = time increment and vol = sample volume. This command was implemented by Dr. K. Hanley for periodic boundaries; the strain rate of the periodic boundary can be simply replaced by that for the wall boundary in the newly implemented LAMMPS code.

The energy calculation in Eq. 4.4.3 is applicable only to the orthogonal movement of boundaries. When a wall boundary slides while maintaining its vertical position, this energy is not counted in Eq. 4.4.3 as there is no volume change during the sliding motion. As the current study applies shear forces to a sample by sliding a wall boundary, the following energy calculation was also implemented as boundary work in this study:

$$\Delta E_{boundary} = F_{wall} V_{boundary} \Delta t \tag{4.4.4}$$

where F_{wall} = force acting on wall boundary.

To check the servo-control during an isotropic compression of samples bounded by walls in Z-axis and periodic boundaries in X- and Y-axes, a DEM simulation of a FCC sample (4×4×200 spheres, as illustrated in Fig. 4.28) was performed using the HM contact model and the results are plotted in Fig. 4.29(a). The three principal stresses developed equally during the compression in which a maximum strain rate of 0.01 s^{-1} was used for all the direction. Note that the wall velocities were not equal as the sample dimensions are not cubic. The variation of energy distribution with time is illustrated in Fig. 4.29(b), and it is clear that all the boundary energy is converted to normal strain energy. The absolute value of energy balance (i.e. kinetic energy + normal strain energy – boundary energy) is also illustrated, which is small compared with the accumulated normal strain. Note that there is no tangential contact strain energy in this case because of the idealised lattice structure of the FCC sample.

4.4.2 Check on peak strength of FCC packing

To validate the newly implemented contact models and the servo-control of wall boundaries triaxial loading tests for a FCC sample were conducted. For a drained triaxial loading condition, in which the vertical stress (σ'_1) develops until its peak value is obtained whereas the horizontal stresses (σ'_2 and σ'_3) are kept constant with $\sigma'_2 = \sigma'_3$, the maximum stress ratio of σ'_1/σ'_3 can be estimated as (Thornton, 1979; Itasca, 2007):

$$\left[\frac{\sigma'_1}{\sigma'_3}\right]^{\max} = \frac{2(1+\mu)}{1-\mu} \tag{4.4.5}$$

The stress ratio at failure depends on only the inter-particle friction μ. Barreto (2009) documented DEM simulations to consider effects of the intermediate stress where $\sigma'_2 \neq \sigma'_3$.

A set of DEM simulations were carried out using inter-particle frictions μ = 0, 0.02, 0.05, 0.1, 0.2, 0.35 and 0.5 with the HM contact model. The material properties considered are tabulated in Table 4.8. Referring to Fig. 4.28 a FCC sample composed of 3200 spheres (4×4×200) was initially isotropically compressed to 100 kPa and was then sheared by triaxial loading in the σ'_1 direction with a constant shearing rate of 0.001 s^{-1}. Rotation of the spheres was permitted during shearing unless otherwise noted. The variation of stress ratio, void ratio (e) and mean coordination number ($\overline{C_N}$) with time are illustrated in Fig. 4.30 for μ = 0, 0.1, 0.2 and 0.35 and variation in the peak stress ratios with μ are plotted in Fig. 4.30(d). Referring to Fig. 4.30(b), a tri-linear response can be seen: (1) relatively high initial slope was observed (except for the frictionless packing (μ = 0)), (2) followed by a lowered slope which is similar with the initial slope of frictionless packing, and (3) post-peak slope which is flat or which exhibits strain softening. When the peak stress ratio is mobilised, there is a sudden reduction in the mean coordination number to 8 and dilation of packing takes place simultaneously. The mean coordination number for the frictionless packing was increased again to 10.5 after dropping to 8 once; however, this does not affect the stress ratio. Good agreement is seen between DEM simulations and Eq. 4.4.5 for the peak stress ratio (Fig. 4.30(d)).

The influence of rotational degrees of freedom was investigated using μ = 0.5 and the results are shown in Fig. 4.31. It is clear that the stress ratio is kept constant after reaching its peak value when rotation is not allowed during the simulation, whereas the permitted rotation reduces the stress ratio after the peak. This observation agrees with Itasca (2007) who restricted rotation of spheres during their simulations to validate contact models. The $\overline{C_N}$ value drops sharply to 8 and less dilation is observed when the rotation is not permitted.

4.4.3 Influence of surface roughness

The influence of surface roughness on the peak stress ratio was investigated using the RM contact model. A RMS surface roughness S_q of 0.5 μm was selected and the other parameters are given in Table 4.8. Following the procedure in the previous section, drained triaxial loading tests were conducted. Referring to Fig. 4.32, the test results using the RM model are qualitatively similar with those for the HM model discussed in the previous section; however, a low stress ratio is seen for $\mu = 0.5$ compared with the HM model or the theoretical value.

To understand the reason for the lower stress ratio using the RM model with $\mu = 0.5$, another simulation was run in which rotation of sphere was not allowed. Removing the rotation of spheres, the peak stress ratio agrees with the theoretical value as compared in Fig. 4.33.

A set of simulations were conducted using $S_q = 0$ μm (HM model), 0.25, 0.5, and 1.0 μm with $\mu = 0.2$. The rotation of spheres was permitted in the simulations. Referring to Fig. 4.34, it is obvious that the stress-strain relationship is affected noticeably by the surface roughness. The overall responses are similar; the peak strength is not affected by the S_q value although a larger axial strain to reach the peak strength is required with increasing S_q.

4.4.4 Influence of twisting resistance model

The influence of spin resistance on the peak strength of a FCC packing is examined in this section. The data presented in Fig. 4.35 show almost identical stress-strain relation for the HM and HMT contact models; thus, the effect of twisting resistance was negligible. This can be explained by the fact that the angular velocity and spin angle are negligible during the triaxial loading simulation on the FCC packing. Another possible reason for the insignificant effect of twisting model is that the material properties considered in the simulation was less sensitive to the twisting resistance. As discussed in Section 4.3.5, softer materials show more significant effects of twisting contact resistance as the twisting contact stiffness increases proportionally with the cubic of the radius of contact circle, whereas the normal or tangential contact stiffness develops proportionally with the radius of contact.

4.5 Summary

This chapter summarised mathematical expressions of contact models for implementation into a DEM code in Section 4.2, discussed validation tests of single contact response using the implemented contact models in Section 4.3, and investigated the peak strength of a FCC sample for code validation as described in Section 4.4.

A full derivation of rough surface (normal) contact model proposed in this study was provided in Section 4.2.1. The rough contact model captures weak responses of surface asperities at lower normal contact forces as reported in the literature, while the rough surface model gradually approaches a Hertzian contact with increasing normal force. Partial slip effects in tangential and twisting contact interactions were provided in Sections 4.2.2 and 4.2.3, respectively. Both tangential and torsional contact stiffnesses decrease with partial slip, and approach full slip gradually.

A variety of single contact simulations were carried out to validate and explore the influence of implemented contact models in Section 4.3. To validate the HMD contact model, shearing under gravity and oblique impacts were considered to compare with prior research, and good agreement was observed. In addition, the effects of surface roughness were explored where lower contact stiffnesses with rougher surfaces affected the single contact interaction. The torsion-spin relationship including partial slip effects were examined, and it was found that the twisting contact stiffness is sensitive to variation in normal contact force. The spin velocity was affected considerably when a softer material was considered.

A new algorithm for servo-control wall boundaries was introduced in Section 4.4.1. Drained triaxial loading simulations were carried out to check the peak stress ratio of a FCC sample using the implemented contact models and servo-control of wall boundaries in Sections 4.4.2 to 4.4.4. Good agreement with Itasca (2007) and theory indicates that the implemented servo-control works correctly with new contact models. The influence of twisting contact model on the peak stress ratio was negligible.

4.6 Tables

Table 4.1. Contact model contributions permitted with modified code.

Name	Normal contact stiffness	Tangential contact stiffness	Twisting contact stiffness
HM	$k_N^{Smooth} = 2E_p^* a$ (Section 2.3.1)	$k_N^{Smooth} = \frac{2(1-\nu_p)}{2-\nu_p} k_N^{Smooth}$ (Section 2.3.2)	-
HMD		$k_T^{Smooth} = \frac{2(1-\nu_p)}{2-\nu_p} k_N^{Smooth} \theta$ (Section 2.3.2)	
HMT		$k_N^{Smooth} = \frac{2(1-\nu_p)}{2-\nu_p} k_N^{Smooth}$ (Section 2.3.2)	$k_r^{Smooth} = \frac{16}{3} G_p^* a^3$ (Section 2.3.3)
HMDT		$k_T^{Smooth} = \frac{2(1-\nu_p)}{2-\nu_p} k_N^{Smooth} \theta$ (Section 2.3.2)	$k_r^{Smooth} = \frac{16}{3} G_p^* a^3 \theta_r$ (Section 2.3.3)
RM	$k_N^{Rough} = \frac{dN}{d\delta^{Rough}}$ (Section 4.2.1)	$k_N^{Rough} = \frac{2(1-\nu_p)}{2-\nu_p} k_N^{Rough}$ (Section 2.3.2)	-
RMD		$k_T^{Rough} = \frac{2(1-\nu_p)}{2-\nu_p} k_N^{Rough} \theta$ (Section 2.3.2)	

*Expressions above for tangential and twisting contact stiffnesses assume a constant normal force.

Table 4.2. Testing parameters used in Section 4.2 (Figs. 4.3 to 4.8).

Parameter	Value
Particle radius, R	2.54×10^{-3} m
Inter-particle fiction coefficient, μ	0.2
Particle shear modulus, G_p	25.0 GPa
Particle Poisson's ratio, ν_p	0.2

Table 4.3. Testing parameters for shearing sphere with vertical body force (Figs. 4.9 to 4.12).

Parameter	**Value**	**Contact models considered**
Particle radius, R	0.5 mm	HM HMD RM RMD
Particle & wall fiction coefficient, μ	0.2	
Particle & wall shear modulus, G_p	28.68 GPa	
Particle & wall Poisson's ratio, v	0.2	
Particle & wall density, ρ	2570 kg/m^3	
Gravitational acceleration, g	9.81 m/s^2	
Initial translational velocity, V_{X0}	10.0×10^{-6} m/s	
Viscous & Local damping	0.0 (during shearing) 0.7 (before shearing)	
Surface roughness, S_q (if applicable)	1.0 nm	

Table 4.4. Testing parameters for oblique impact simulations on wall (Figs. 4.13 to 4.17).

Parameter	**Value**	**Contact model**
Particle radius, R	25.0×10^{-3} m	HM HMD RM RMD
Particle & wall fiction coefficient, μ	0.1	
Particle & wall shear modulus, G_p	26.923 GPa	
Particle & wall Poisson's ratio, v_p	0.3	
Particle & wall density, ρ_p	2650 kg/m^3	
Initial translational velocity, V_0	5.0 m/s	
Surface roughness, S_q (if applicable)	5.0, 10, 20 μm	

Table 4.5. Testing parameters for oblique impact simulations between identical spheres (Figs. 4.18 to 4.21).

Parameter	**Value**	**Contact model**
Particle radius, R	0.10×10^{-3} m	HM HMD
Particle friction coefficient, μ	0.35	
Particle shear modulus, G_p	26.92 GPa	
Particle Poisson's ratio, v_p	0.3	
Particle density, ρ_p	2650 kg/m^3	
Initial translational velocity, V_{Z0}	50×10^{-3} m/s	

Table 4.6. Testing parameter for spinning sphere with vertical body force (Figs. 4.22 & 4.23).

Parameter	**Value**	**Contact model**
Initial angular velocity, ω_{Z0}	0.02 m/s	HMDT

Table 4.7. Testing parameters for normal impact simulations with spin on wall (Figs. 4.24 to 4.27).

Parameter	**Value**	**Contact model**
Particle radius, R	25.0×10^{-3} m	HMDT
Particle & wall fiction coefficient, μ	0.3	
Particle & wall shear modulus, G_p	1.0×10^{-3} GPa	
Particle & wall Poisson's ratio, ν_p	0.5	
Particle & wall density, ρ_p	1100 kg/m^3	
Initial translational velocity, V_{Z0}	5.0 m/s	
Initial angular velocity, ω_{Z0}	1 - 300 rad/s	

Table 4.8. Testing parameters for triaxial loading tests (Figs. 4.29 to 4.35).

Parameter	**Value**
Particle radius, R	2.54×10^{-3} m
Particle shear modulus, G_p	25.0 GPa
Particle Poisson's ratio, ν_p	0.2
Particle density, ρ_p	2230 kg/m^3
Strain rate of shearing	0.001 s^{-1}
Viscous damping	0.1

4.7 Figures

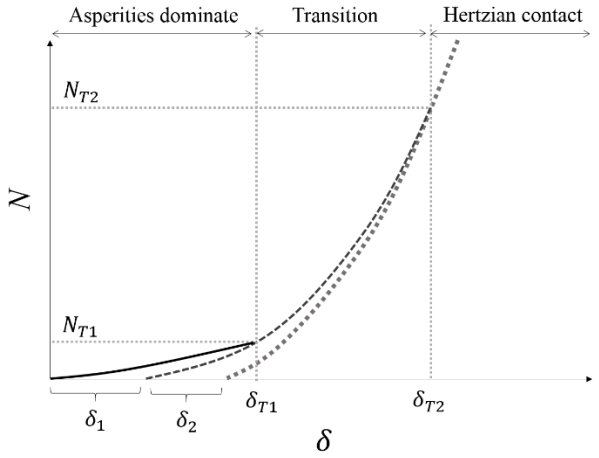

Figure 4.1. Schematic illustration of force-overlap relationship using rough surface contact model.

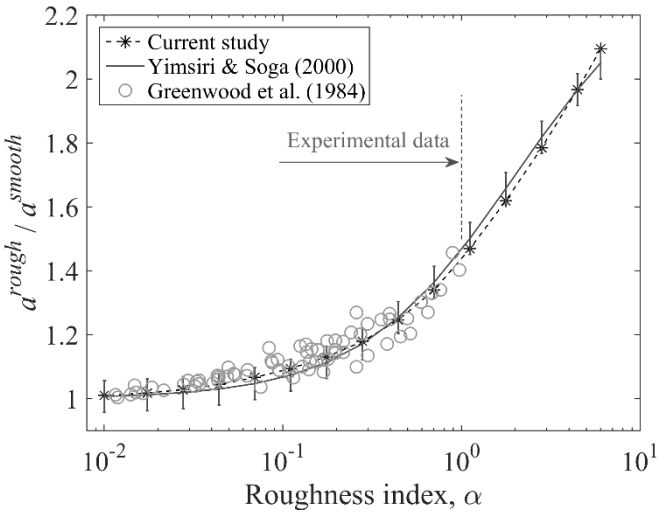

Figure 4.2. Variation in ratio a^{rough}/a^{smooth} with roughness index α: comparison between current study and literature (Greenwood et al., 1984; Yimsiri & Soga, 2000).

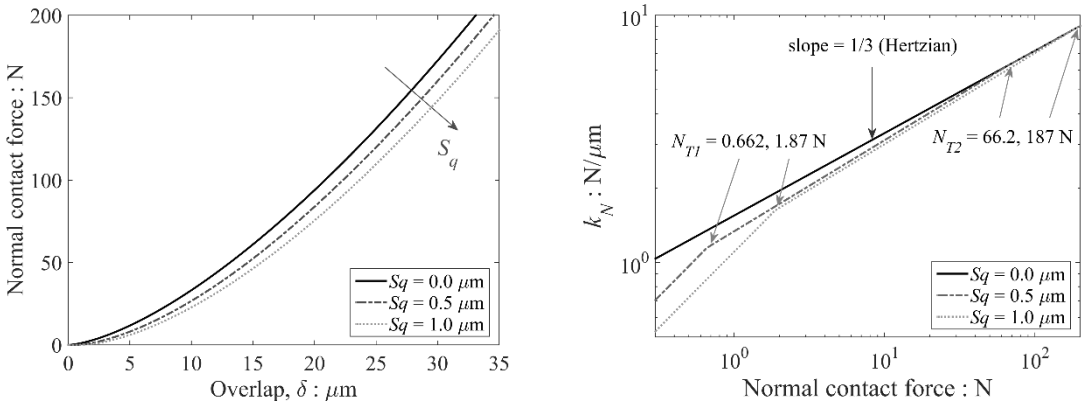

Figure 4.3. Proposed rough surface contact model: (a) Relationship between normal contact force and overlap for various S_q values, and (b) Relationship between normal contact stiffness (k_N) and normal contact force.

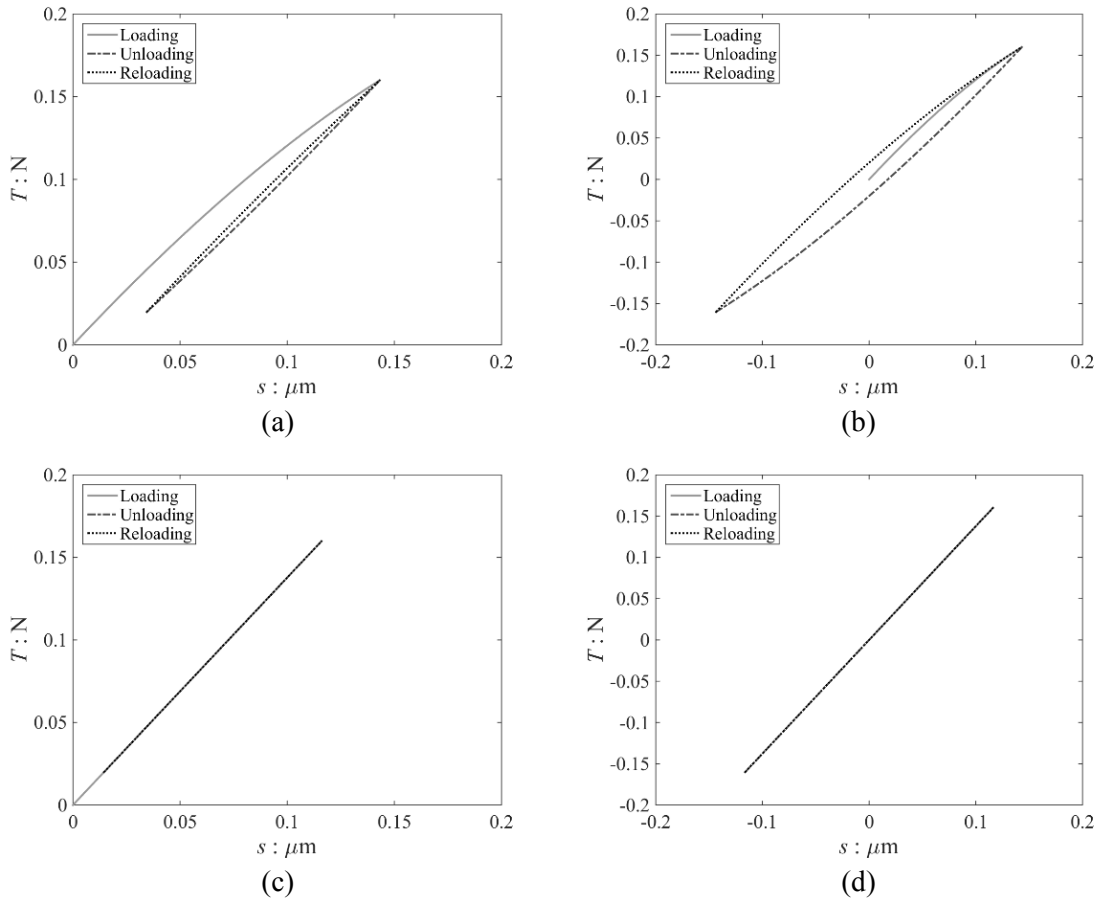

Figure 4.4. Representative tangential contact force (T) and shear displacement (s) relationships with a constant normal force N (= 1 N) with inter-particle friction μ = 0.2 during loading, unloading and reloading of tangential contact force: (a) HMD model with T^{**} = 0.02 N, (b) HMD model with T^{**} = -0.16 N, (c) HM model with T^{**} = 0.02 N, and (d) HM model with T^{**} = -0.16 N. (Material properties considered are listed in Table 4.2).

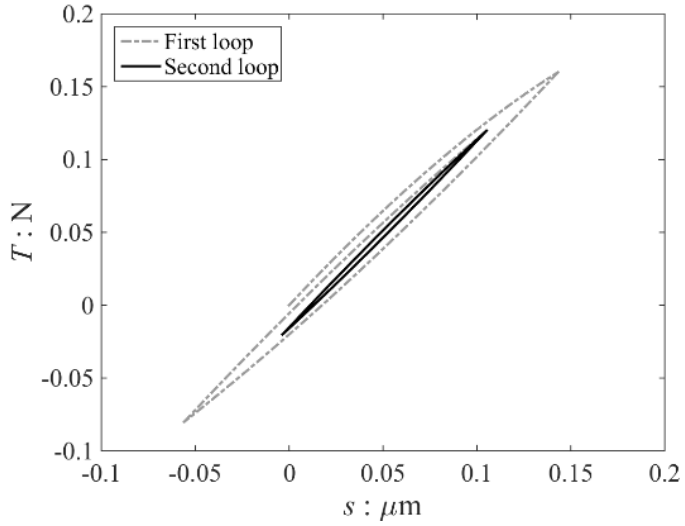

Figure 4.5. Comparison between first loop and second loop of tangential contact force and displacement relationship where T^{*} = 0.16 N, T^{**} = -0.8 N, T^{***} = 0.12 N, and T^{****} = -0.02 N. (Material properties considered are listed in Table 4.2).

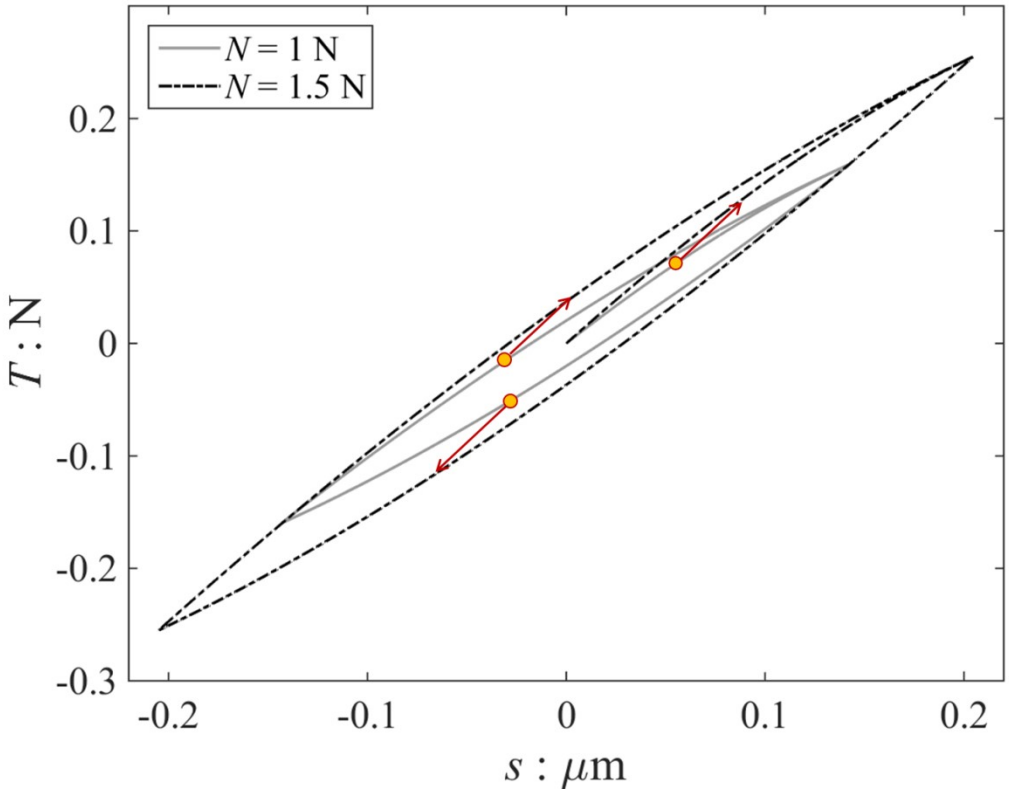

Figure 4.6. Relationship between tangential contact force (T) and tangential contact displacement (s) for varying normal force (N) from 1 N to 1.5 N using HMD contact model. (Material properties considered are listed in Table 4.2).

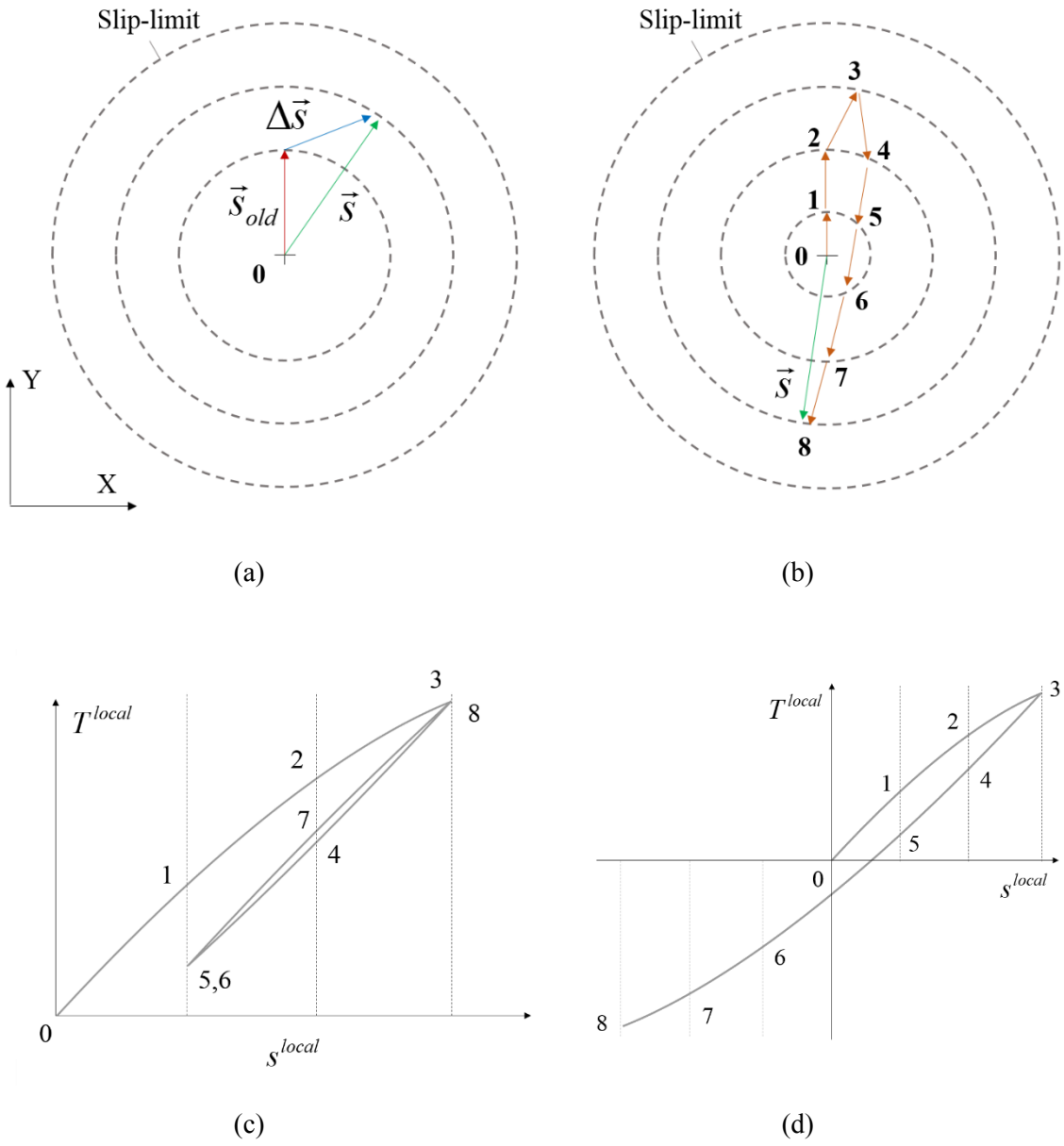

Figure 4.7. Relationship between tangential contact force (T) and tangential contact displacement (s): (a) Schematic of global tangential contact displacement, (b) An example of global displacement sequence, (c) Relationship between T^{local} and s^{local} without consideration of sign reversal in s^{local}, and (d) Relationship between T^{local} and s^{local} by considering sign reversal of s^{local} (Eq. 4.2.42).

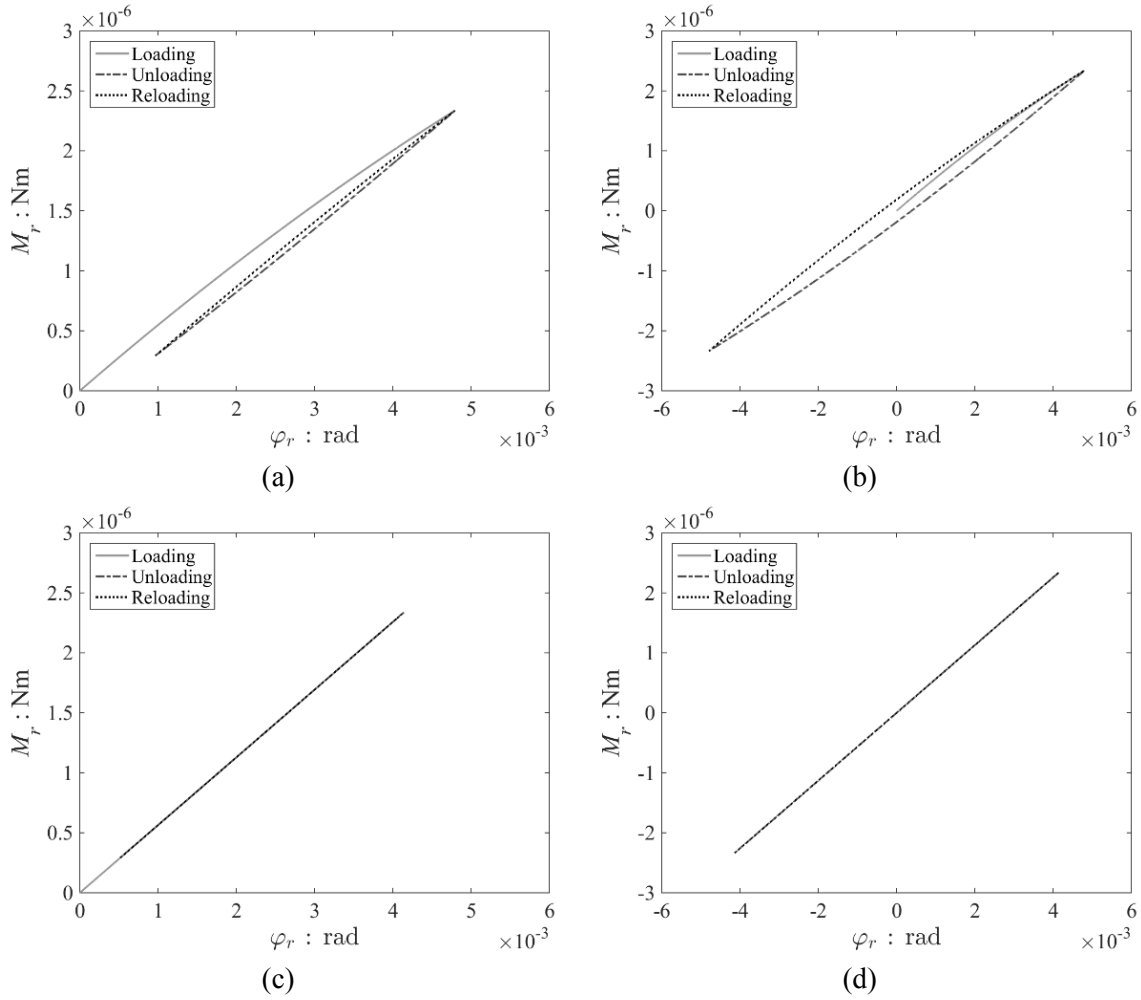

Figure 4.8. Representative relationships of twisting contact moment (M_r) and spin angle (φ_r) at a constant normal force N (= 2N) with inter-particle friction μ = 0.2 during torsional loading, unloading and reloading: (a) HMDT model with M_r^{**} = 2.92×10^{-7} Nm, (b) HMDT model with M_r^{**} = -2.34×10^{-6} Nm, (c) HMT model with M_r^{**} = 2.92×10^{-7} Nm, and (d) HMT model with M_r^{**} = -2.34×10^{-6} Nm. (Material properties considered are listed in Table 4.2).

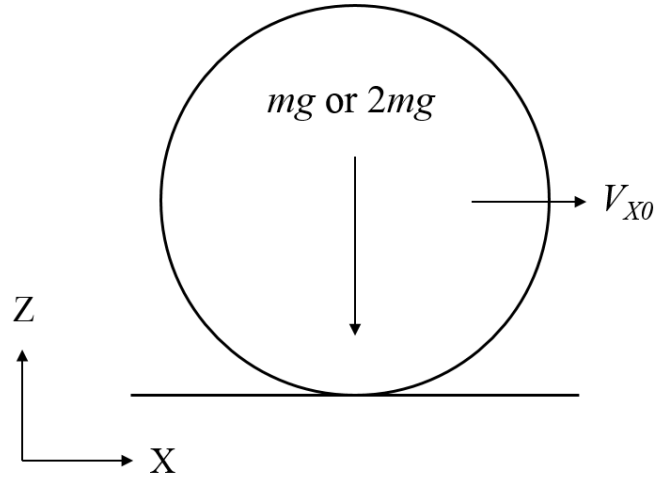

Figure 4.9. Schematics of shearing sphere on wall under gravity (rotation is not permitted).

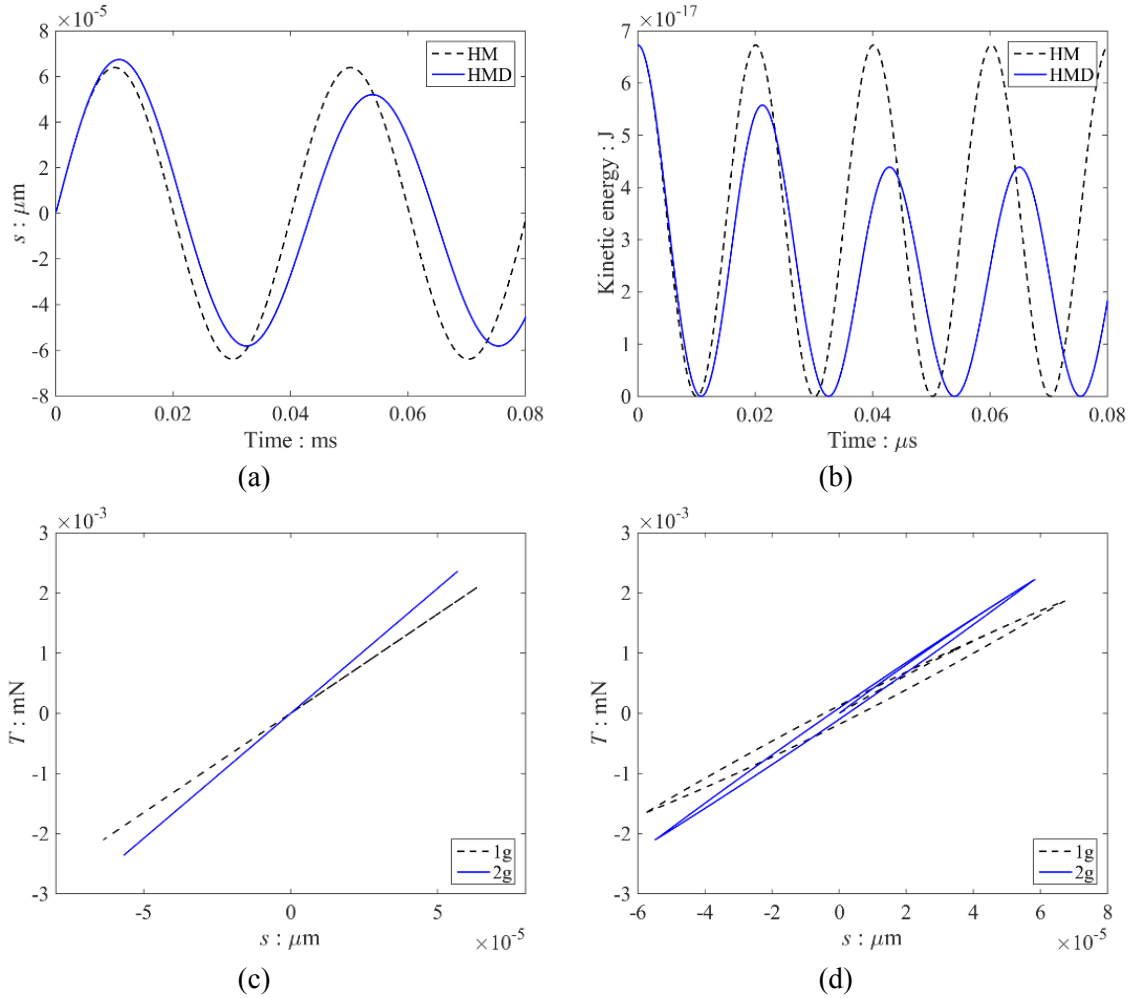

Figure 4.10. Simulation results of shearing sphere on wall under gravity using HM and HMD models: (a) Variation in tangential displacement (s) with time, (b) Variation in kinetic energy with time, (c) Force-displacement (T-s) relationship during loading, unloading and reloading using HM model, and (d) Force-displacement relationship during loading, unloading and reloading using HMD model.

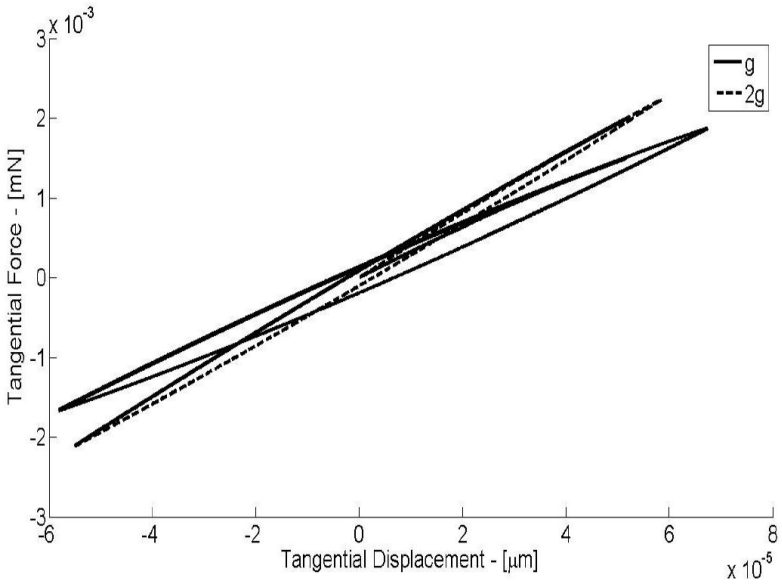

Figure 4.11. Comparison of HMD contact model with literature. Tangential contact force-displacement relationship using HMD model (O'Donovan, 2013).

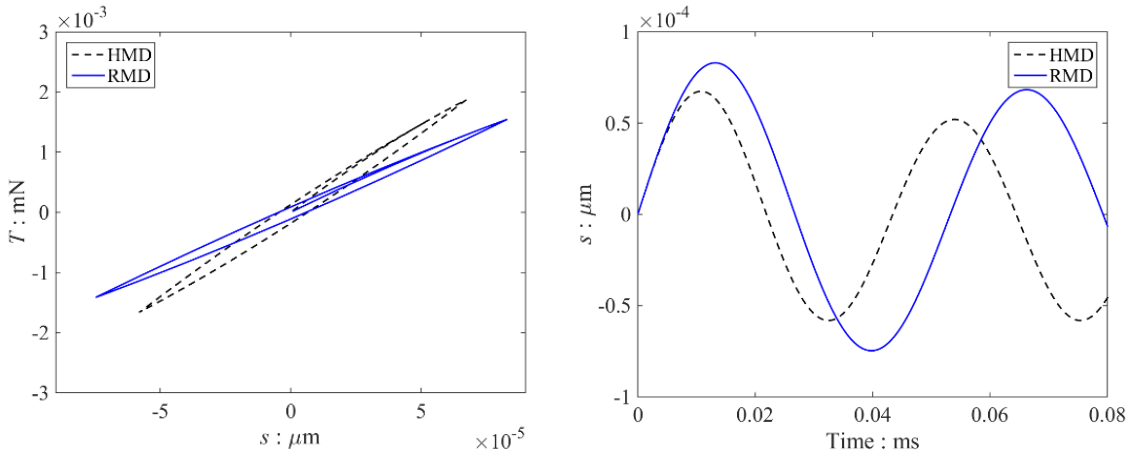

(a) (b)

Figure 4.12. Influence of partial slip on smooth and rough surface contact models: (a) Tangential force-displacement interaction, and (b) Variation in tangential displacement with time.

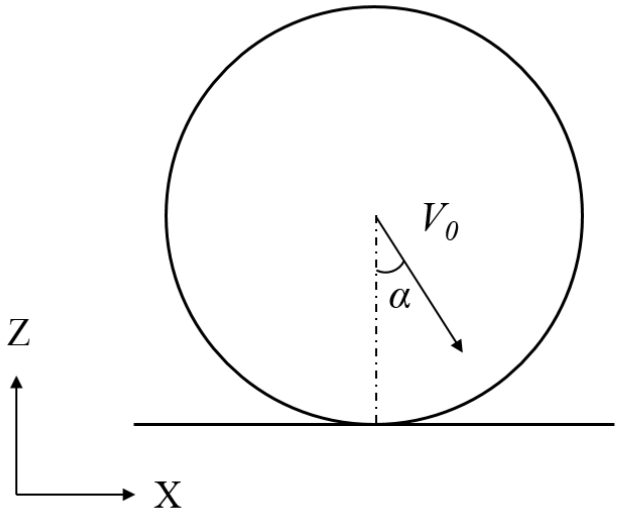

Figure 4.13. Schematics of impact between a sphere and a wall with varying impact angle α.

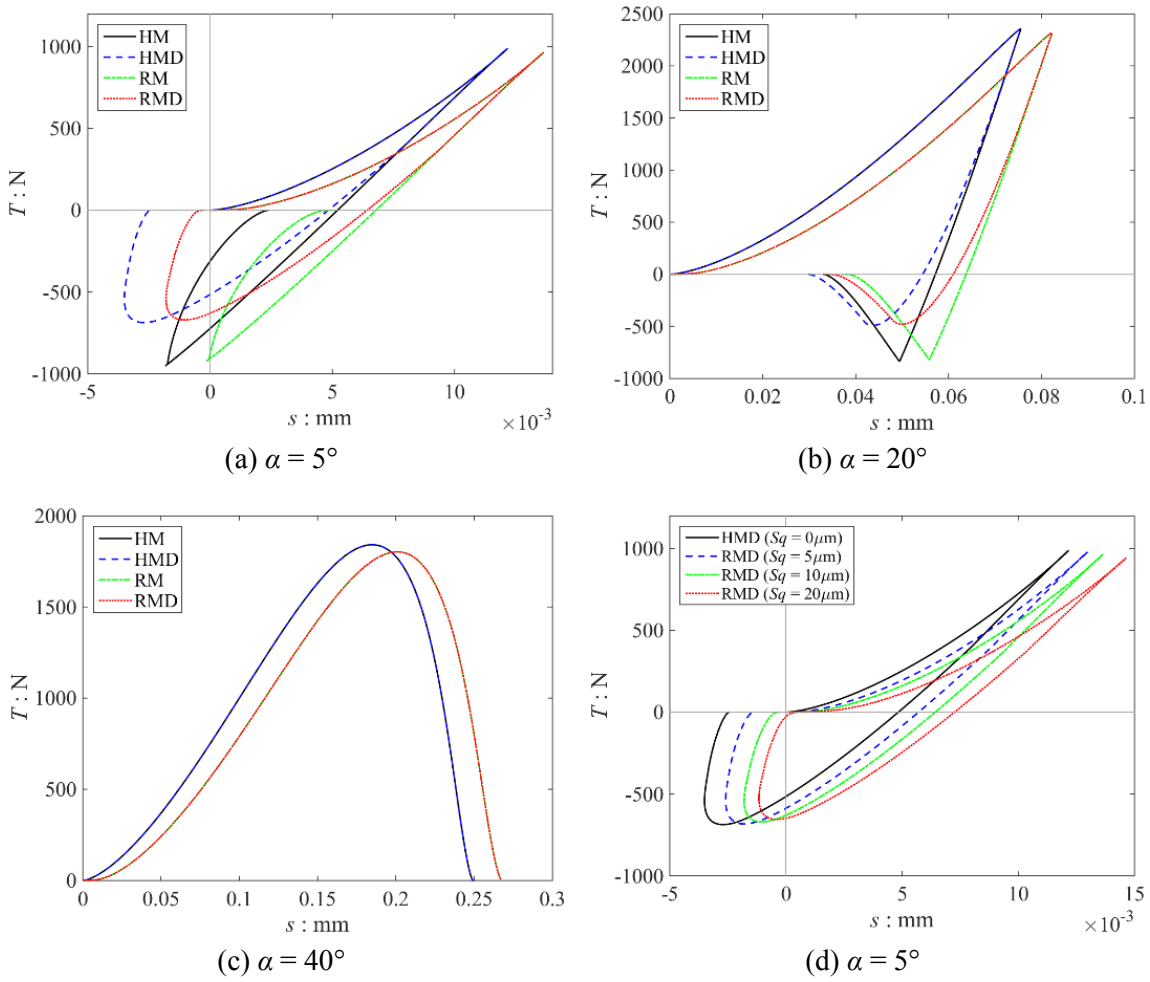

(a) $\alpha = 5°$ (b) $\alpha = 20°$

(c) $\alpha = 40°$ (d) $\alpha = 5°$

Figure 4.14. Tangential force-displacement curves for various impact angles of (a) $\alpha = 5°$, (b) 20°, (c) 40° and (d) $\alpha = 5°$ for various surface roughness values.

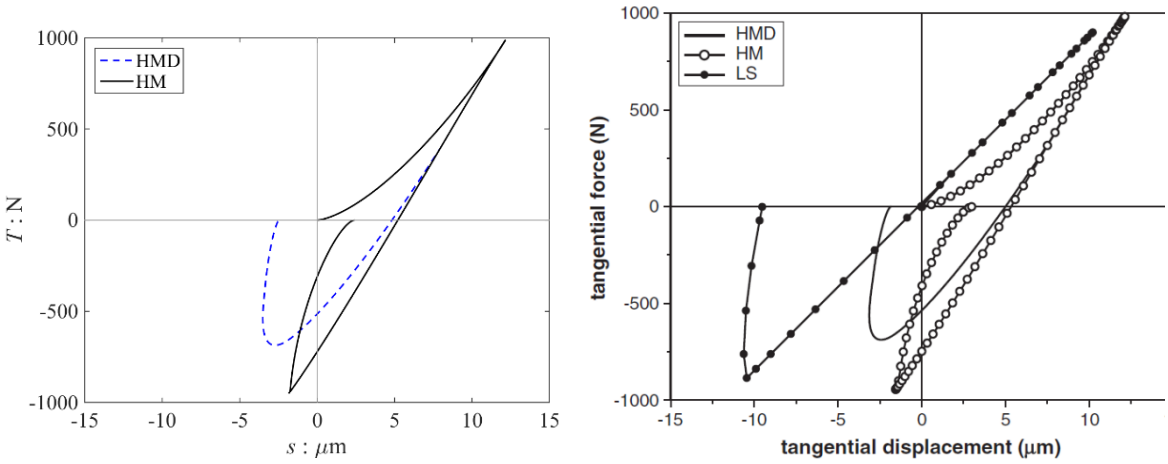

(a) (b)

Figure 4.15. Comparison of HM and HMD contact model with literature. Tangential contact force-displacement relationship for impact angle of $\alpha = 5°$ using HM and HMD models: (a) Current study, and (b) Thornton et al. (2011).

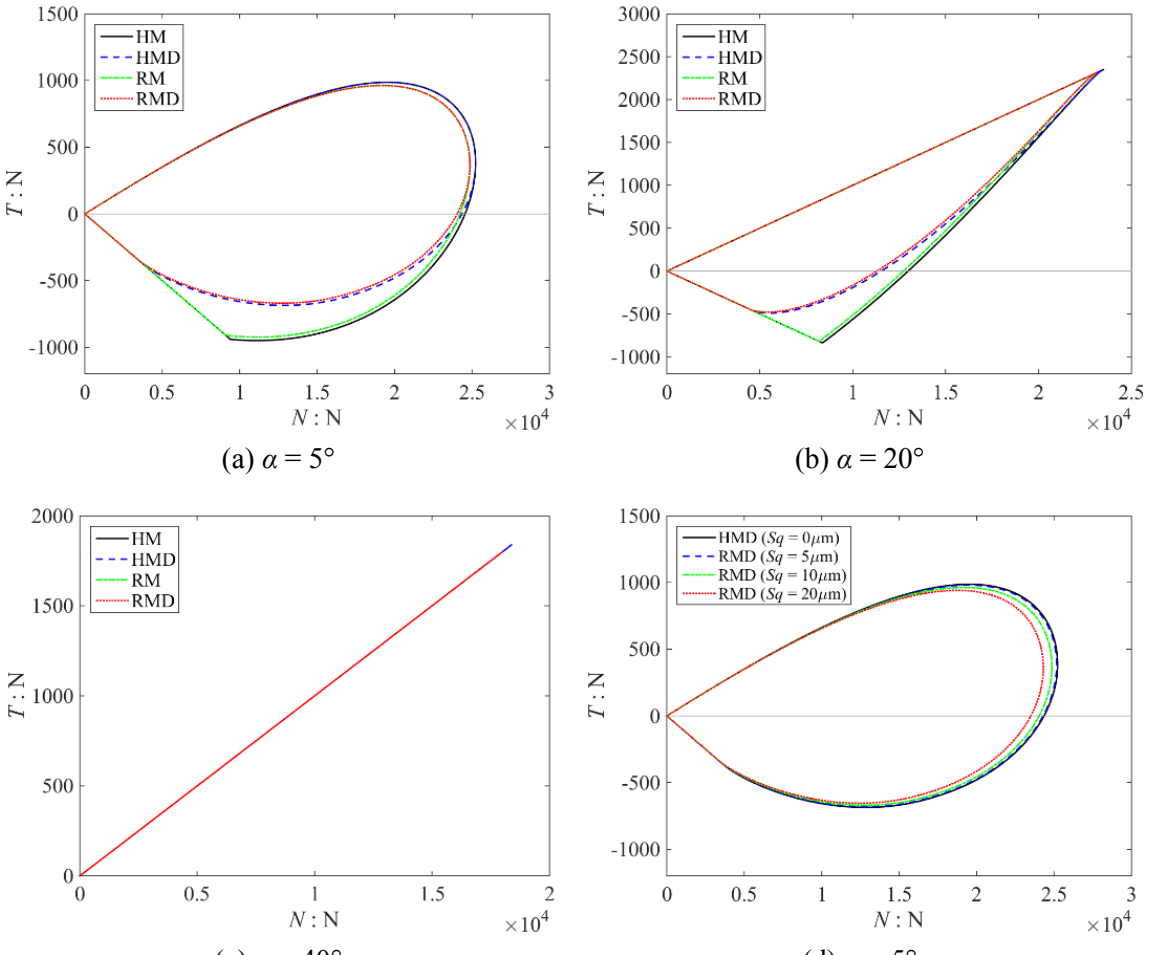

(a) $\alpha = 5°$ (b) $\alpha = 20°$

(c) $\alpha = 40°$ (d) $\alpha = 5°$

Figure 4.16. Relationship between normal force (N) and tangential contact force (T) at impact angles of (a) $\alpha = 5°$, (b) 20°, (c) 40° and (d) $\alpha = 5°$ for various surface roughness values.

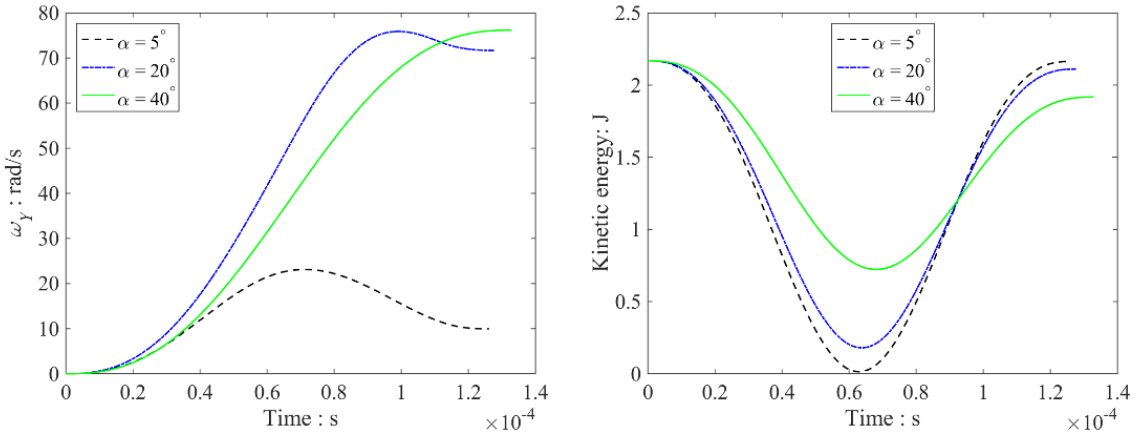

(a) (b)

Figure 4.17. Variation in (a) angular velocity with time, and (b) kinetic energy with time using HMD contact model.

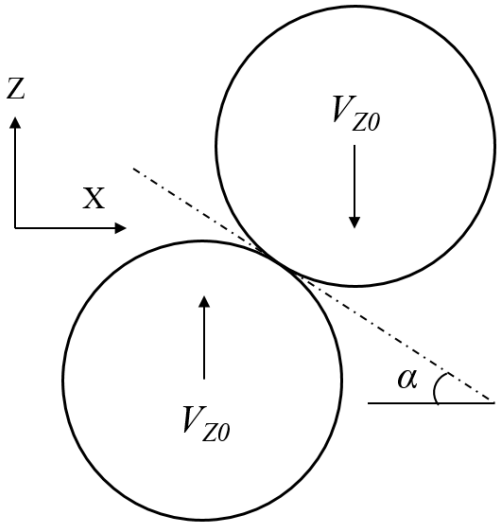

Figure 4.18. Schematics of impact between identical spheres with varying impact angle α.

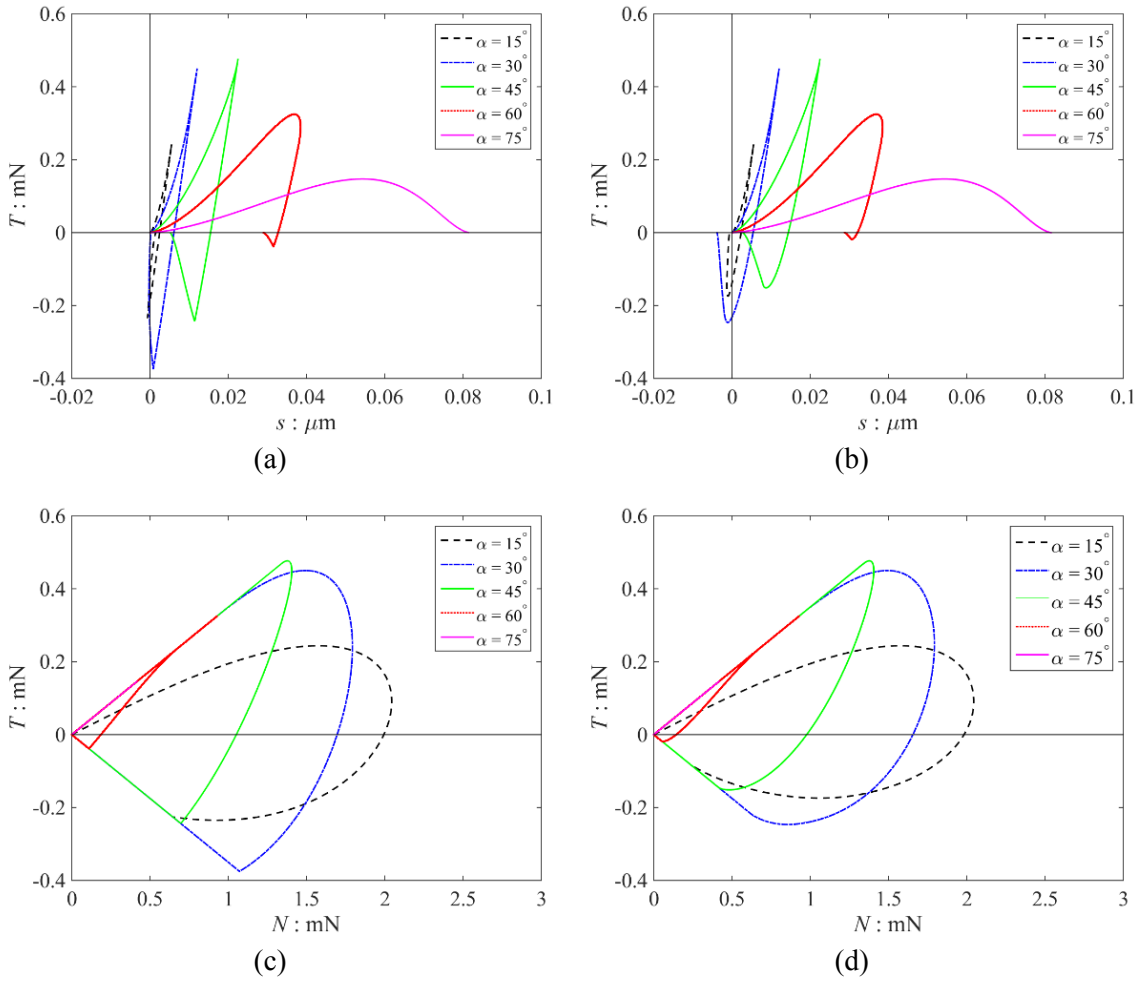

Figure 4.19. Influence of impact angle α on normal and tangential contact forces using (a) HM model and (b) HMD model, and tangential contact force-displacement relationship using (c) HM model and (d) HMD model.

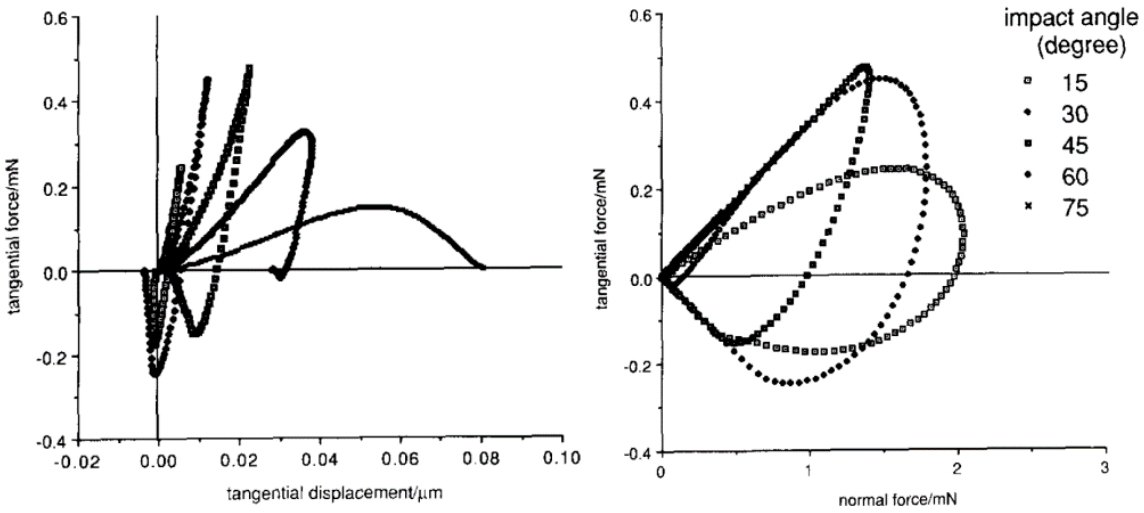

(a) (b)

Figure 4.20. Comparison of HMD contact model with literature. (a) tangential contact force-displacement relationship and (b) tangential-normal contact force relationship using HMD model (Thornton & Yin, 1991).

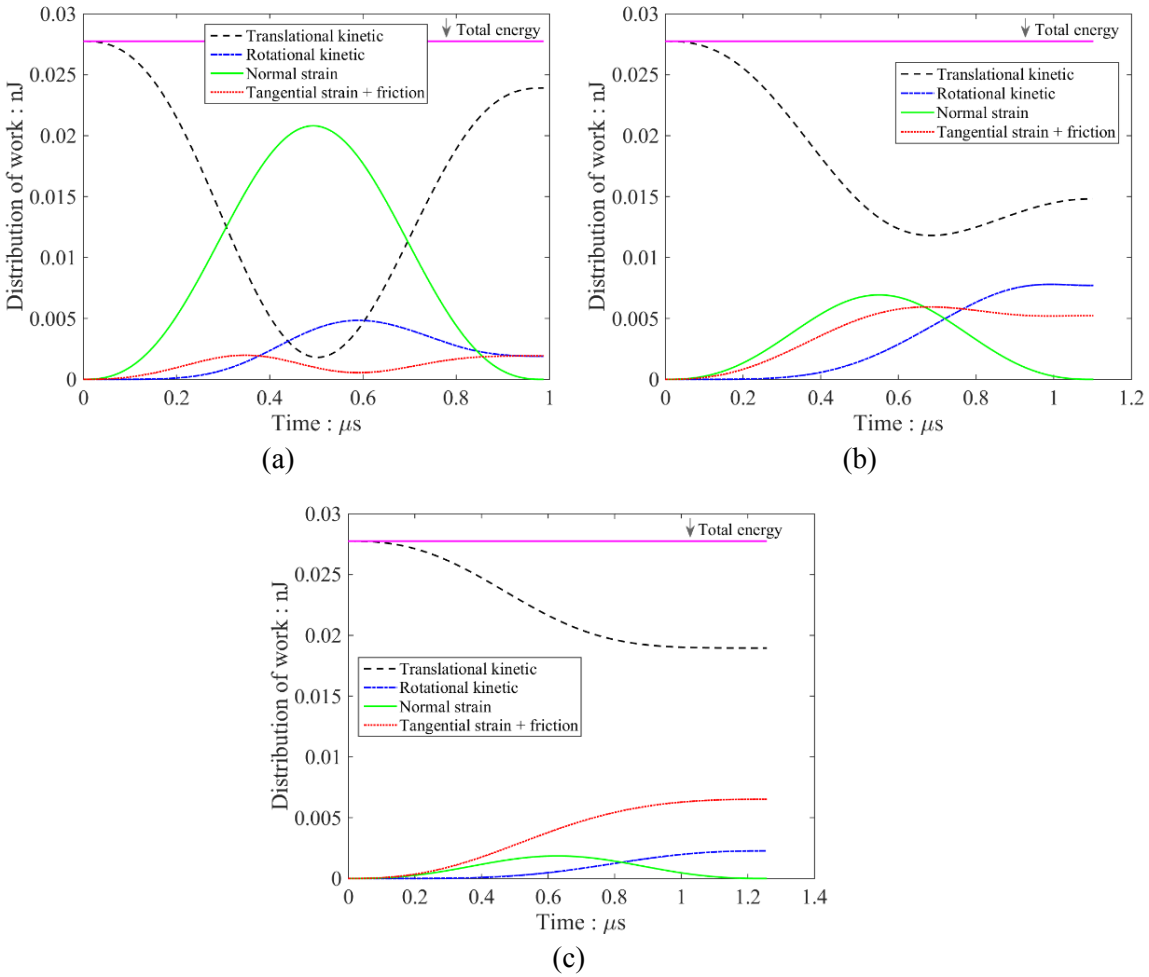

(a) (b)

(c)

Figure 4.21. Variation in energy distribution with time for various impact angles of (a) $\alpha = 30°$, (b) $\alpha = 60°$, (c) $\alpha = 75°$ using HMD contact model (tangential strain energy includes frictional dissipation due to partial- or full-slip).

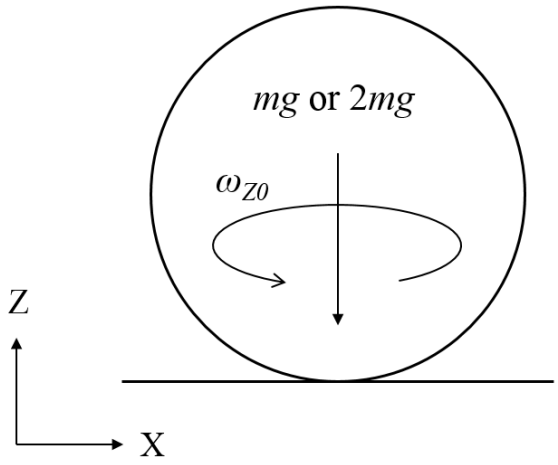

Figure 4.22. Schematics of spinning sphere on wall under gravity.

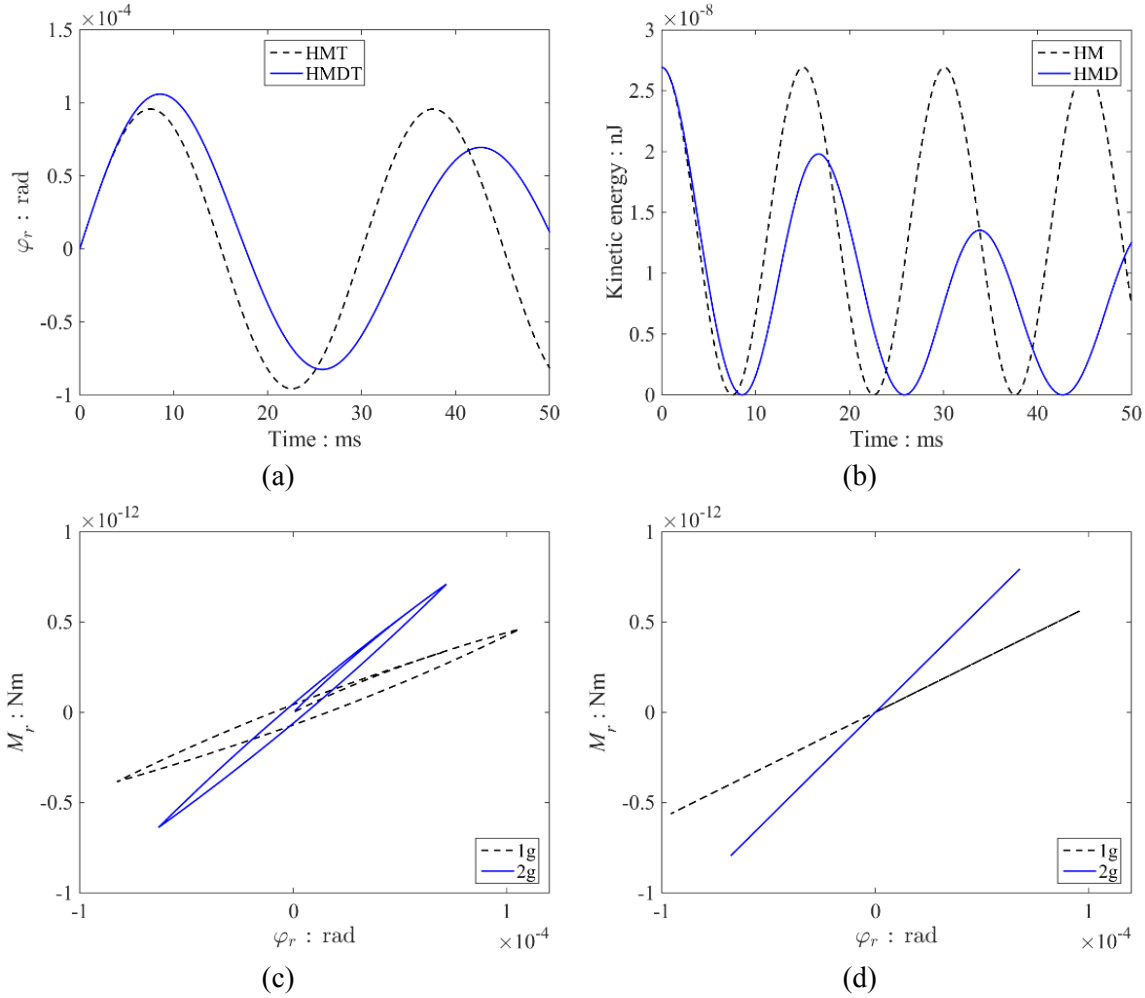

Figure 4.23. Simulation results of spinning sphere on wall under gravity using HMT and HMDT models. (a) Variation in spin angle with time (b) Variation in kinetic energy (rotational kinetic) with time (c) moment-spin relationship during loading, unloading and reloading or torsional moment

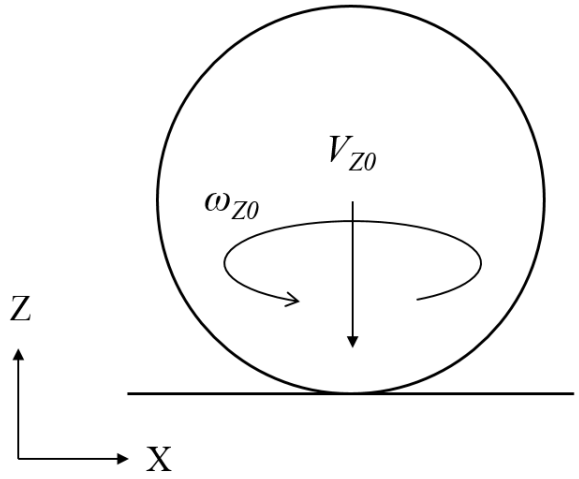

Figure 4.24. Schematics of impact between a spinning sphere and a wall.

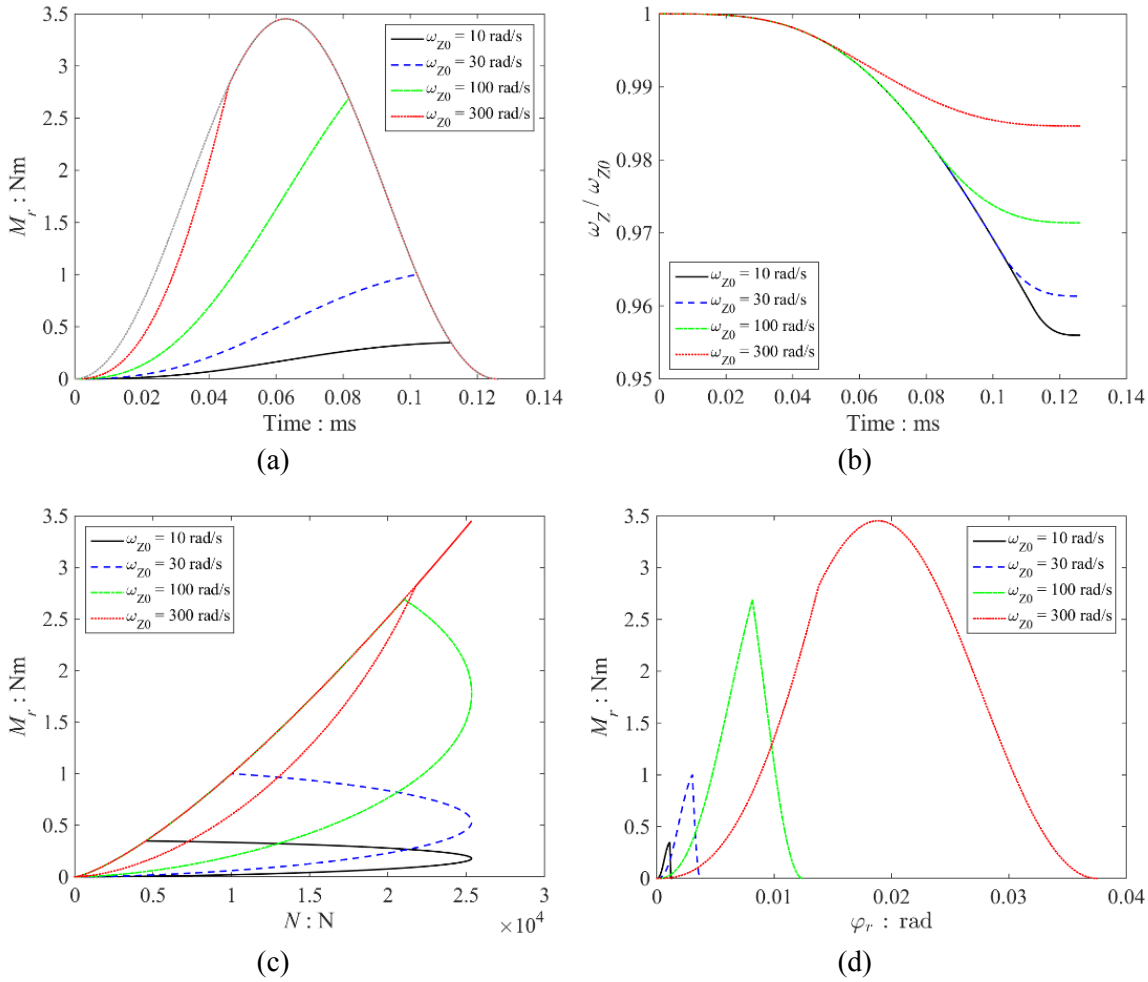

Figure 4.25. Simulation results of impact between a spinning sphere and a wall using HMDT model: (a) Variation in twisting moment (M_r) with time, (b) Variation in angular velocity (ω) with time, (c) Relationship between twisting moment-normal force, and (d) Relationship between twisting moment and spin angle.

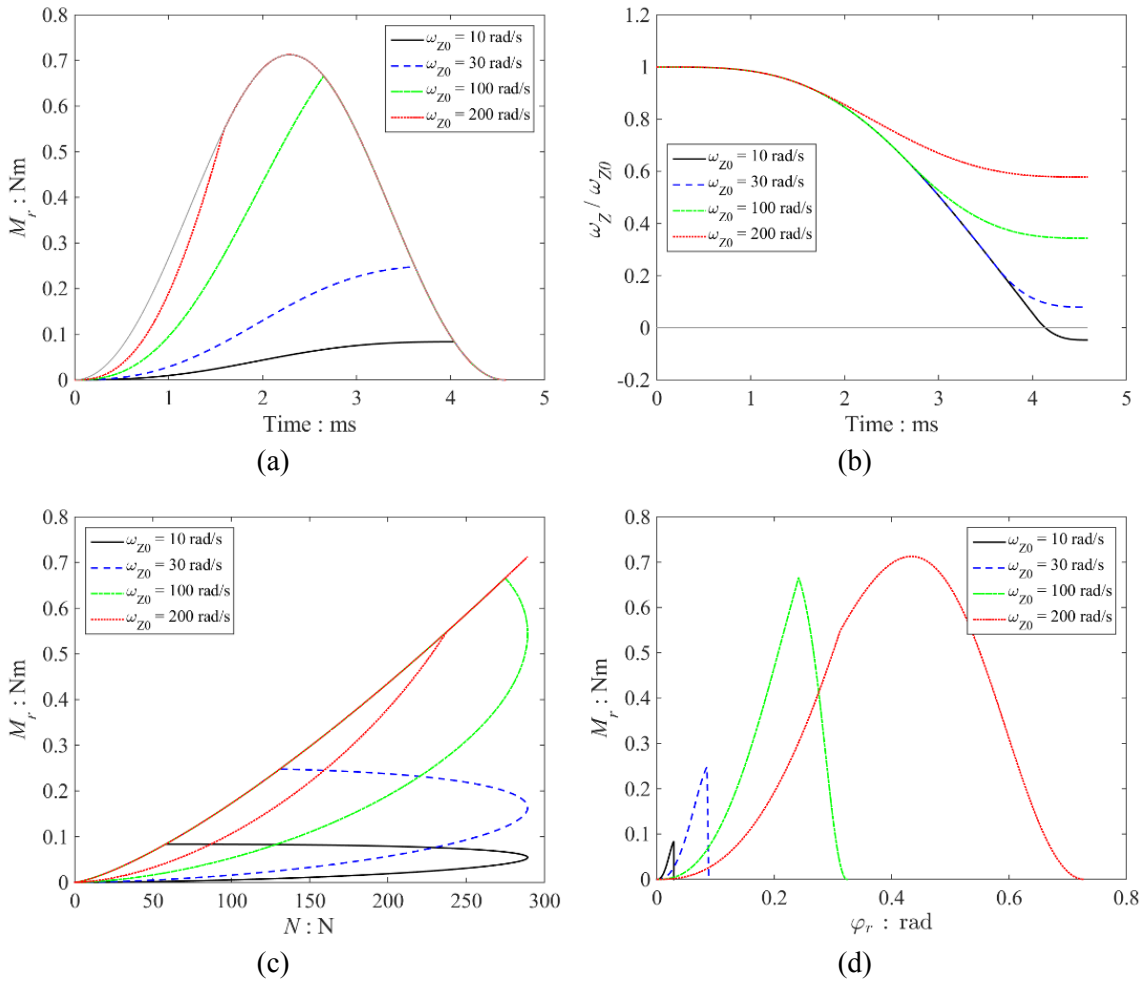

Figure 4.26. Impact between a softer sphere and a softer wall with spin using HMDT model: (a) Variation in twisting moment (M_r) with time, (b) Variation in angular velocity (ω) with time, (c) Relationship between twisting moment-normal force, and (d) Relationship between twisting moment and spin angle.

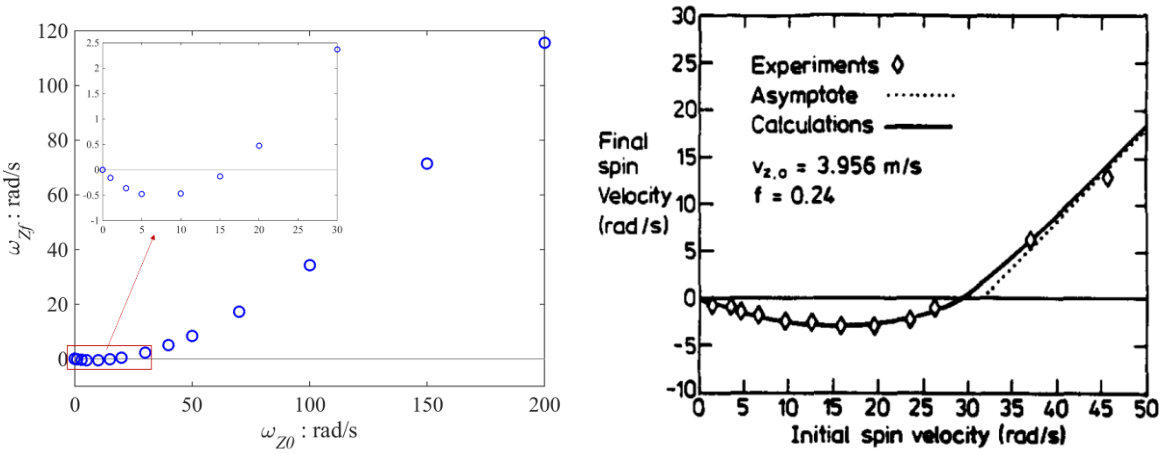

Figure 4.27. Summary of initial and final angular velocities using HMDT model. (a) Simulation results obtained from this study (b) Equivalent data presented in Lim & Stronge (1994)

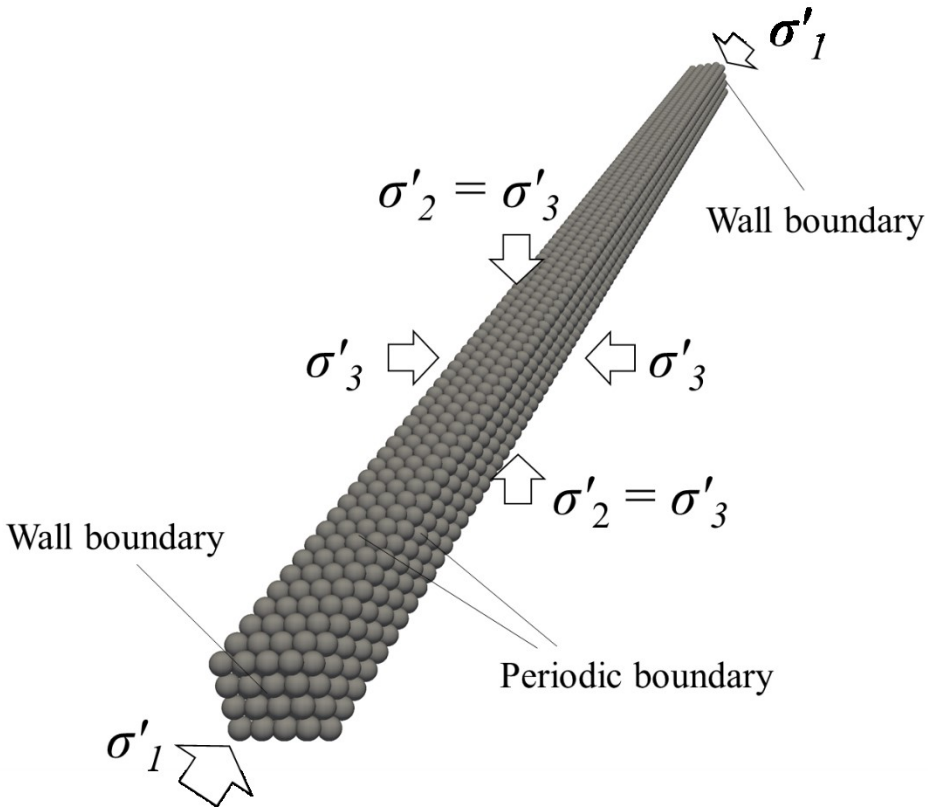

Figure 4.28. FCC sample composed of 3200 particles (4×4×200 layers) used for triaxial loading tests in Section 4.2.2.

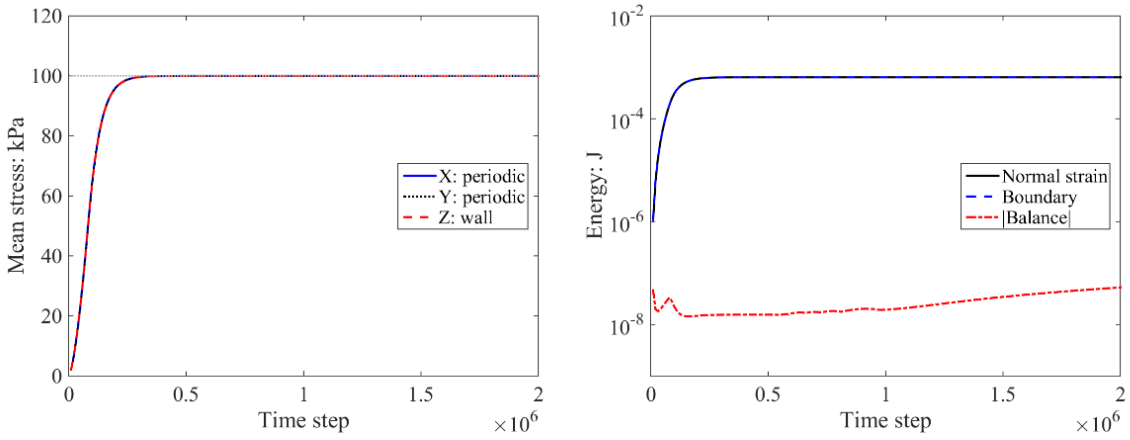

Figure 4.29. Isotropic compression (σ' =100 kPa) on FCC sample bounded by wall boundaries in σ'_1 direction (Z) and periodic boundaries in σ'_2 and σ'_3 directions (X and Y) using HM contact model: (a) Variation in mean effective stress with time step, and (b) Variation in energy contributions with time step.

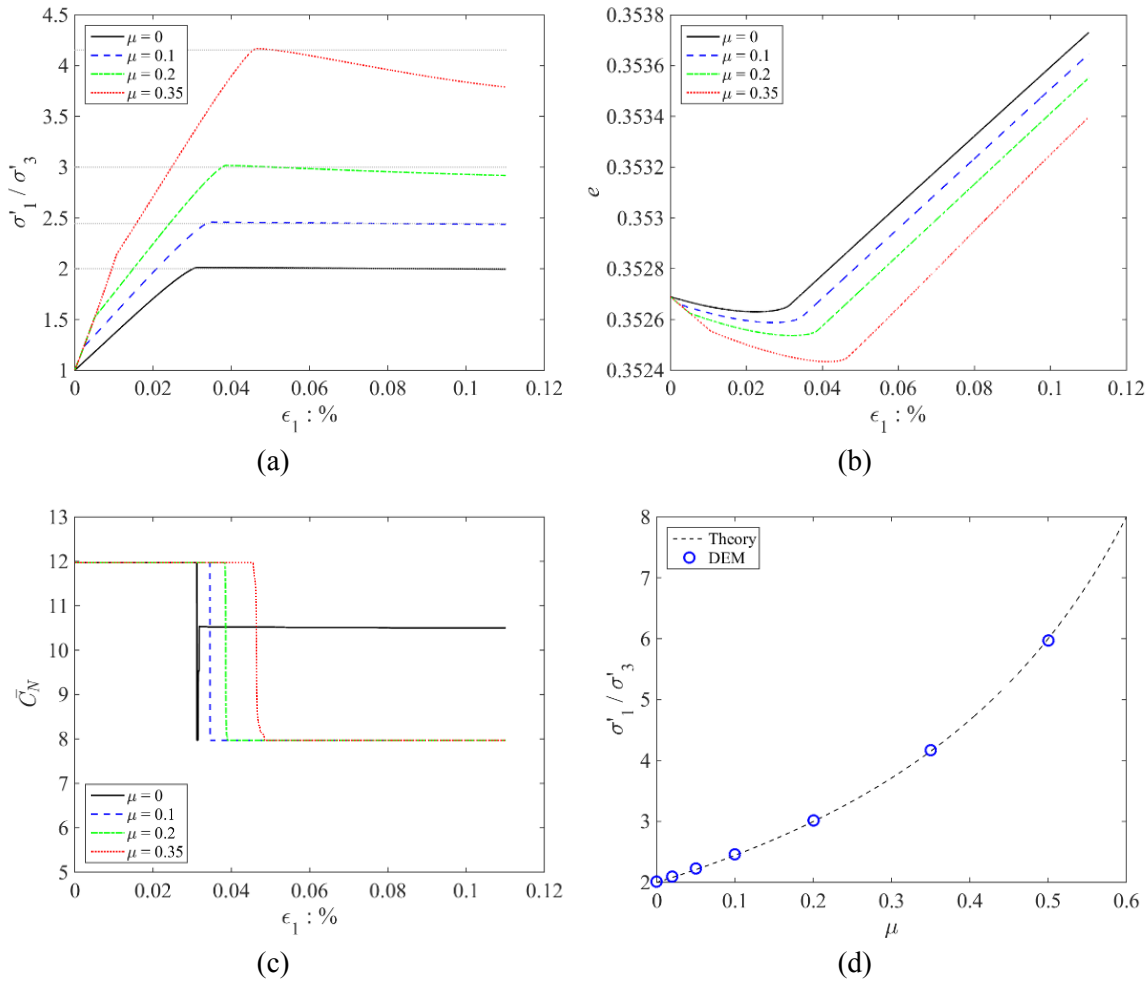

Figure 4.30. Drained triaxial compression on FCC sample bounded by wall boundaries in σ'_1 direction (Z) and periodic boundaries in σ'_2 and σ'_3 directions (X and Y) using HM contact model: (a) stress ratio (σ'_1/σ'_3), (b) void ratio (e), (c) mean coordination number ($\overline{C_N}$), and (d) comparison with micromechanical theory on peak stress ratio for various inter-particle friction values.

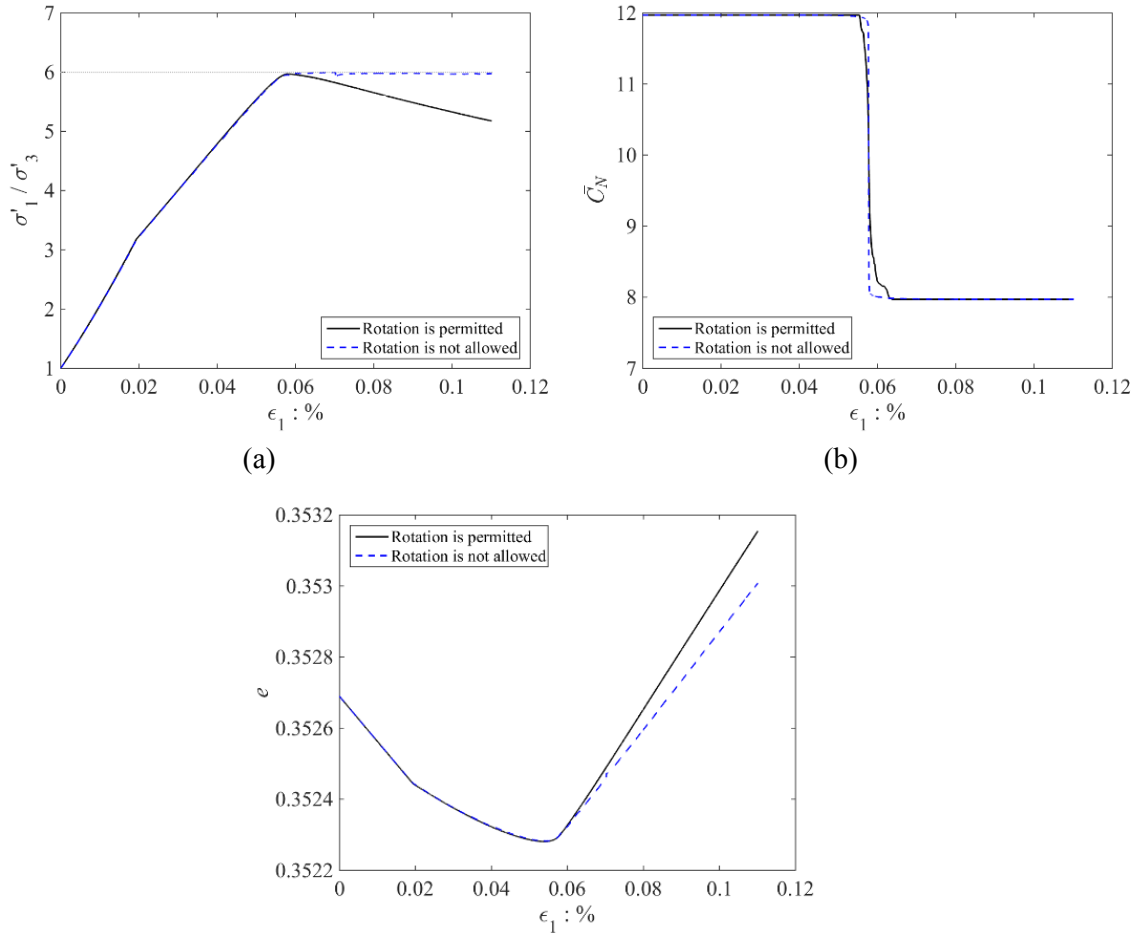

Figure 4.31. Influence of rotational degrees of freedom on development of (a) stress ratio, (b) mean coordination number ($\overline{C_N}$), and (c) void ratio using HM contact model with inter-particle friction $\mu = 0.5$.

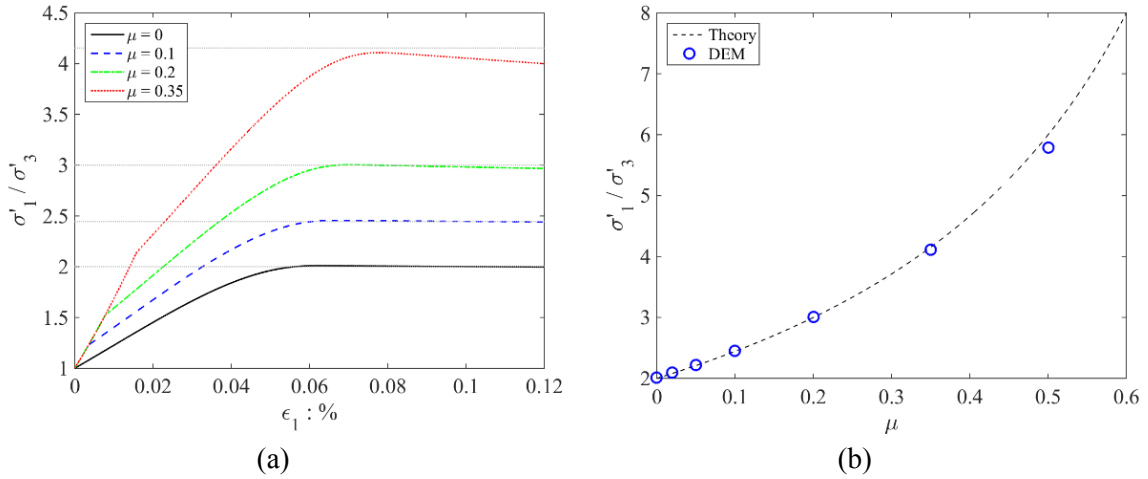

Figure 4.32. Drained triaxial compression on FCC sample using RM contact model with surface roughness $S_q = 0.5$ μm: (a) stress ratio (σ'_1/σ'_3), and (b) comparison with micromechanical theory on peak stress ratio for various inter-particle friction values.

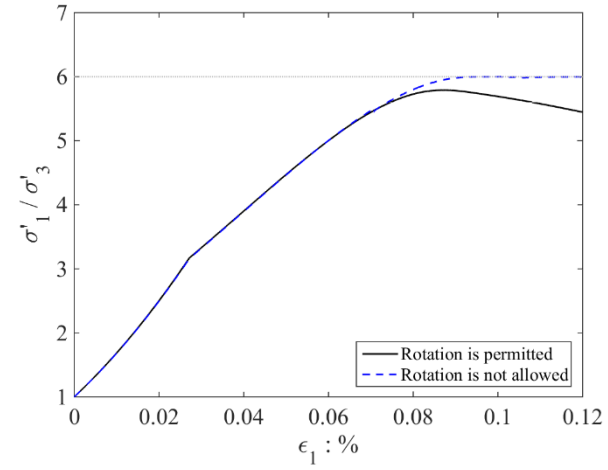

Figure 4.33. Influence of rotational degrees of freedom on stress ratio (σ'_1/σ'_3) using RM contact model with S_q = 0.5 μm and inter-particle friction μ = 0.5.

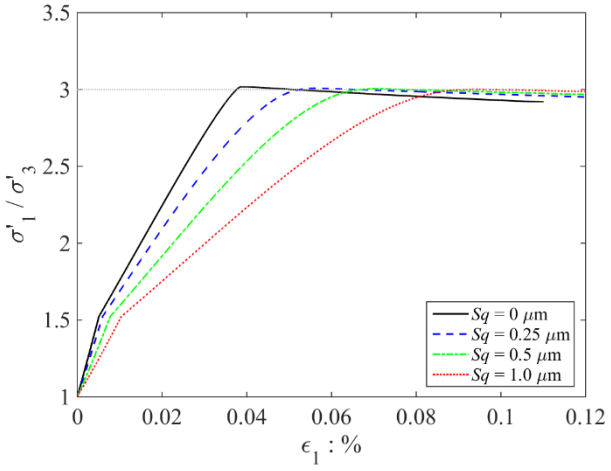

Figure 4.34. Influence of surface roughness on stress ratio (σ'_1/σ'_3) using RM contact model with inter-particle friction μ = 0.2.

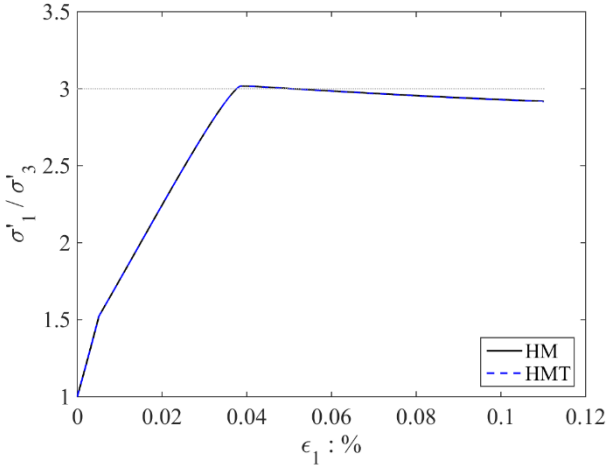

Figure 4.35. Influence of twisting resistance on stress ratio (σ'_1/σ'_3) using HM and HMT contact models with inter-particle friction μ = 0.2.

CHAPTER 5
DEM simulations of wave propagation

5.1 Introduction

Investigations of the nature of stress wave propagation through granular media provide essential material properties and are often conducted for engineering applications. Specifically, the velocity of the propagating wave can be related to the small-strain stiffness and the Poisson's ratio of granular materials and these properties are important in geophysics, geotechnical engineering and fundamental research into granular materials (Jia, 2004; Boore, 2006; Clayton et al., 2009). Granular materials act as a low-pass filter to seismic (stress) or acoustic waves. The low-pass frequency ($f_{low\text{-}pass}$) and the wavelength ($\lambda_{low\text{-}pass}$) are also useful to characterise the properties of granular materials.

Bender element tests (Shirley, 1978; Shirley & Hampton, 1978) are widely used in soil mechanics research (Yamashita et al., 2009). In dynamic geophysics tests including bender element tests, the wave velocity can be estimated using either time domain (TD) techniques or frequency domain (FD) techniques. As described in Section. 2.6.1, there are few reports documenting a good match between the TD and FD methods. Using the discrete element method (DEM) enables a better understanding of the particle-scale response of soil during the wave propagation. The wave velocity estimated from DEM simulations can be validated using an eigenvalue analysis where combinations of the fundamental resonance modes and the corresponding frequencies give a dispersion relation (Lawney & Luding 2014).

The compression (primary, *P*-) wave velocity (V_P) and the shear (secondary, *S*-) wave velocity (V_S) are known to be influenced by void ratio (e) and stress level (σ'). From a micromechanical perspective, wave velocities and sample moduli should also be influenced by the mean coordination number ($\overline{C_N}$) (Section 2.7.1). As discussed in Chapter 4, single contact responses are affected by surface roughness and partial slip, and wave velocities can also be influenced by surface characteristics (Santamarina & Cascante (1998); Duffaut et al. (2010)). Using DEM analyses can inform understanding of how these factors influence V_P and V_S.

This chapter considers simulations of planar wave propagation through an assembly of uniformly sized spheres. Section 5.2 describes the DEM simulation approach, and the methods

used to determine the wave velocities using the TD and FD approaches are introduced. The remainder of the chapter then explores a number of key questions:

- How are the dynamic properties of granular materials affected by sample packing? The discussion in Section 5.3 includes consideration of the influences of e and $\overline{C_N}$ on dynamic properties of assemblies including V_P, V_S and the sample Poisson's ratio (ν_S).
- How sensitive is the overall sample response to the contact rheology? The effects of using the contact models discussed in Chapter 4 that can account for partial slip, spin resistance, and surface roughness effects are investigated in Section 5.4.
- Is it possible to achieve good agreement between the wave velocities obtained using TD and FD approaches? The results obtained using various methods to determine the wave velocities are compared in Section 5.4.
- Can eigenmode analyses add insight into wave velocity data obtained from DEM simulations? Eigenmode analyses of the DEM samples were performed to determine the fundamental resonance mode and relate it to the wave velocity in Section 5.5.
- What factors determine the filtering properties of granular materials? The $\lambda_{low\text{-}pass}$ was related to particle size by Santamarina & Aloufi (1999), and layer spacing of a FCC array by Mouraille & Luding (2008). O'Donovan et al. (2015) related $f_{low\text{-}pass}$ to σ'. The relationship between sample properties and $f_{low\text{-}pass}$ (or $\lambda_{low\text{-}pass}$) are discussed in Section 5.5.

5.2 Wave propagation simulations

The contact models described in Chapter 4 were implemented in a modified version of the LAMMPS molecular dynamics code (Plimpton, 1995). The samples considered in this study were face-centred cubic (FCC) samples and various randomly configured samples (random samples) all composed of uniformly sized spheres. Use of monodisperse spheres enables the effects of fabric and contact model to be isolated from any particle inertia effects. Examples of the sample configuration for the DEM simulations of wave propagation are illustrated in Fig. 5.1. The lateral boundaries (X- and Y-directions) were periodic, while rigid wall boundaries were placed at the bottom and top of the samples (in the Z-direction). For all cases, particles with a diameter (D) of 2.54 mm were used with a particle shear modulus G_p = 25 GPa, particle Poisson's ratio ν_p = 0.2, and particle density ρ_p = 2230 kg/m^3 as shown in Table 5.1. The surface roughness values considered were S_q = 0, 0.5, and 1 μm (where S_q = RMS surface roughness). The material properties are appropriate for the tested materials (WLS and WSR ballotini) listed in Table 3.1, and the surface roughness values encompass the measured mean S_q value of 0.661

μm for the rough ballotini (WSR, Table 3.2). The same material properties and the contact models were used for wall boundaries with $D = \infty$.

The FCC sample consisted of 3,200 particles (4×4×200 layers) and is equivalent to that considered by Mouraille et al. (2006); it was created by considering the lattice geometry of the packing. The random samples consisted of 35,201 particles and the sample lengths (L) were 141D to 144D with aspect ratios ≈10. The sample lengths of the random samples were adjusted to be similar to those of the FCC samples. The random samples were initially created as clouds of non-contacting spheres with an inter-particle friction coefficient (μ_{prep}); here the subscript *prep* stands for the inter-particle friction coefficient used during the isotropic compression. The μ_{prep} values varied between 0 and 0.4 to create a range of packing densities. A servo-controlled compression process as described in Section 4.4.1 was applied to achieve an intermediate state with an isotropic confining stress (σ') of 1 kPa. A maximum strain rate of 0.01 s^{-1} was used for all cases. Viscous damping was applied to remove the kinetic energy of vibrating particles once σ' reached 1 kPa. This viscous damping remained active during the subsequent compression and was then deactivated during the wave propagation simulation. The mean particle coordination numbers ($\overline{C_N}$) and the void ratio (e) data of the samples at σ' = 1 kPa are listed with a subscript of "1kPa" in Table 5.2 where the mechanical mean particle coordination number ($\overline{C_N^*}$) (Eq. 3.5.1) and the corresponding mechanical void ratio (e^*) (Eq. 3.5.2) data are also given. Subsequent additional isotropic compressive stress was applied to prepare samples at σ' = 0.01, 0.1, 1, and 10 MPa. To consider the effects of the contact models, samples at σ' = 0.2, 0.3, and 0.5 MPa were also prepared. The $\overline{C_N}$, $\overline{C_N^*}$, e and e^* data of the prepared samples are listed in Table 5.2. When surface roughness effects were considered, the rough surface contact model (RM model, Table 4.1) was used from the start of the simulation, and the resultant $\overline{C_N}$ and e values are not influenced noticeably by surface roughnesses for a given μ_{prep} value. Note that the influences of surface roughness and inter-particle friction on the system response were assessed independently in this numerical study.

The bottom boundary (at z=0) was used as a transmitter wall, while the top boundary (at z=L) was used as a receiver wall. Referring to Fig. 5.2, planar *P*- and *S*-waves were generated by moving the lower transmitter boundary (at z=0) in the longitudinal (Z) and a transverse (X) directions, respectively. As the entire transmitter wall was moved, planar waves were generated. A sinusoidal pulse with a phase delay of 270 degrees and a double amplitude (2A) of 5 and 20 nm was used in Sections 5.3 and 5.4 and Section 5.5, respectively, so that $2A/L \simeq 1.4\times10^{-8}$ to 5.5×10^{-8}, or $2A/D \simeq 2.0\times10^{-6}$ to 7.9×10^{-6} (Fig. 5.2). The nominal frequency (f_{in}) of the sinusoidal pulse inserted into samples was 20 kHz in Sections 5.3 and 5.4, while f_{in} = 100 and 200 kHz were used in Section 5.5. The wave propagated in the Z-direction and the response was recorded

at the opposite boundary (z=L). This system configuration better resembles physical experiments using compression plates or shear plates (e.g. Suwal & Kuwano, 2013) than a bender element set-up. No damping was applied to the particles during wave propagation. Equivalent samples were needed to consider the effect of partial slip during wave propagation, and so identical samples, prepared using the HM model, were used for both simulations using the HM and HMD contact models. The HMD model was activated before applying the input motion at the transmitter wall. A similar approach was used in the case of spin resistance.

Following the approach considered in Magnanimo et al. (2008), the μ_{prep} value was increased by at least 0.05 (see Tables 5.3 and 5.8 for μ_{wave}) before applying the input motion at the transmitter wall boundary to avoid particle sliding and ensure the elastic response of the samples. The subscript *wave* refers to the inter-particle friction coefficient used for the wave propagation simulations. The sensitivity of the observed response to the increment in friction was explored by considering sample P-22 (Table 5.3). For this sample the preparation friction value was μ_{prep} = 0.15 and the system responses were compared for cases where μ_{wave} = 0.15, 0.16, 0.17 and 0.25 during a *P*-wave propagation. The responses observed at the transmitter and receiver walls are given in Fig. 5.3. When $\mu_{wave} = \mu_{prep} = 0.15$, the response of the received signal exhibited a reduction in normal stress ($\Delta\sigma'_Z$) although a compression wave was generated. Stable and similar signals were observed at both transmitter and receiver walls for the other μ_{wave} values considered. When $\mu_{wave} \geq \mu_{prep}+0.02$ is considered, there is no noticeable difference in the responses given in Fig. 5.3; this supports use of $\mu_{wave} > \mu_{prep}$ approach to ensure the elastic response of samples in this study. Fig. 5.4(a) gives the frequency distribution of the tangential contact force (T) and the slip-limit ($N\times\mu_{prep}$), and Fig. 5.4(b) shows that approximately 60% of the total contacts exhibit $T/(N\times\mu_{prep})$ values close to 1. This explains the unstable system responses during *P*-wave propagation when $\mu_{wave} = \mu_{prep}$ was adopted. As the amplitude of the transmitter wall displacement is small compared to the particle diameter, increasing μ values by only 0.02 can prevent slip at contacts.

As described in Section 2.6.1, there has been discussion on the choice of method to determine wave velocities in bender element tests, and researchers have found that it is difficult to obtain a close match between the TD and FD techniques. O'Donovan (2013) simulated bender element tests using DEM and found a similar discrepancy amongst methods used to determine the wave velocities. Recognising the results may be sensitive to the interpretative approach used, this study considers four methods to determine the wave velocities: (1) peak-to-peak method, (2) stacked phase method, (3) peak displacement method, and (4) dispersion relation method. Using a FCC sample with μ_{wave} = 0.2 at σ' = 100 kPa (with the HM contact model), these methods are explained here by considering *S*-wave propagation with f_{in} = 20 kHz.

Peak-to-peak method, $V_{P\text{-}P}$

The stress responses at both on the transmitter and receiver walls are considered in this approach. The time difference between the first peaks in the incremental shear stress ($\Delta\sigma'_X$) on both walls is considered as the travel time (T_{travel}) (Fig. 5.5(a)). The distance between the two end walls is the sample length (L), and the wave velocity is determined as $V_{S,P\text{-}P} = L/T_{travel}$.

Stacked phase method, V_{SP}

A Fast Fourier Transform was applied to the time domain responses of both the transmitter and receiver walls to obtain the frequency domain responses of the system as illustrated in Fig. 5.5(b). Referring to Fig. 5.6(a), the phase shift between two FFT signals were used to draw the relationship between frequency (f) and stacked phase (Φ_{stack}) (Viggiani & Atkinson, 1995; Alvarado & Coop, 2012; Greening & Nash, 2004). The secant slope (i.e. f/Φ_{stack}) and the tangent slope (i.e. $df/d\Phi_{stack}$) of the f- Φ_{stack} relationship give the phase velocity (V_{phase}) and the group velocity (V_{group}), respectively (Fig. 5.7(b)). The two velocities approach the long-wave limit as the frequency decreases, and this shear wave velocity is denoted here as $V_{S,SP}$. In this study, the "*fft*", "*phase*" and "*unwrap*" functions available in MATLAB (MathWorks, 2015) were used to analyse the data and apply this method.

Peak displacement method, $V_{dL/dt}$

While the peak-to-peak and stacked phase methods can be applied to experimental data, this method can only be applied where detailed data on the particle scale responses are available as is the case with DEM simulation data. The displacement of particles joining transmitter and receiver walls in the oscillation (Z-) direction was considered. For the FCC samples, the displacement of 200 particles was considered, while approximately 150 particles were considered for the random samples. For the random samples, linear interpolation was used to project the displacements onto regularly-spaced points along a straight line through the sample joining the transmitter and receiver walls. Drawing a contour plot of particle displacement with time and distance from the transmitter wall, the best-fit line through the peak displacement (darkest contour) at each time gives $V_{dL/dt}$ (Fig. 5.7(a)). The lightly coloured line evident after about 0.7 ms in Fig. 5.7(a) indicates that the waves are reflected back at the receiver wall, and the reflected response is not considered when this method is applied here. This direct measurement of the particle displacement is used to provide reference data in this study for comparison with the other methods.

Dispersion relation method, $V_{dispersion}$

Considering the same data set used in the peak displacement method above, a two-dimensional Fast Fourier Transform was applied to particle displacement data in the time and space domains

to obtain a dispersion relation for the propagating waves (Section 2.6.4). Following Mouraille & Luding (2008) and O'Donovan (2013), the dispersion relation for *S*-waves is illustrated as Fig. 5.7(b) where the reflected waves at the receiver wall are not included. The phase and group velocities are the secant ($2\pi f/\kappa$) and tangent ($2\pi df/d\kappa$) slopes of the f - $\kappa/(2\pi)$ (i.e. ω-κ) relationship according to Eqs. 2.6.4 and 2.6.5. Just as is the case for the stacked phase method, the shear wave velocity is taken as the long-wave velocity where $V_{group} = V_{phase}$ is denoted $V_{dispersion}$ here. In this study, the "*fft2*" function available in MATLAB (MathWorks, 2015) was used to analyse the data.

For the examples considered here $V_{S,P\text{-}P}$ = 542.2 m/s, $V_{S,SP}$ = 545.4 m/s, $V_{S,dL/dt}$ = 544.5 m/s and $V_{S,dispersion}$ = 547.8 m/s (see Table 5.6). The $V_{S,P\text{-}P}$ and $V_{S,SP}$ values can be compared with laboratory data, while the $V_{S,dL/dt}$ and $V_{S,dispersion}$ data are obtained from internal information only available for DEM samples. The discrepancy in the V_S values amongst the considered methods was at most 1% for the FCC sample. In the parametric studies later in the chapter this observation of agreement between the methods was repeatedly made, reinforcing this conclusion.

5.3 Influence of packing on wave velocity

This section relates the *P*- and *S*-wave velocities (V_P and V_S) to the mean coordination number ($\overline{C_N}$), the void ratio (e), and the confining stress (σ'). As reviewed in Sections 2.6 and 2.7, both the soil stiffness and the wave velocity vary with e and σ'. As discussed in Section 3.5, the $\overline{C_N}$ - e relationship depends on stress level and stress state even in the case of monodisperse spherical particles. In contrast, the relationship between the mechanical mean coordination number ($\overline{C_N^*}$) and the corresponding mechanical void ratio (e^*) (Eqs. 3.5.1 and 3.5.2) is unique for a monodisperse sample; thus both expressions are considered here to analyse the V_P and V_S data.

Wave propagation simulations were carried out following the procedure described in Section 5.2 using the HM contact model. The nominal input frequency (f_{in}) of the inserted sinusoidal pulse was 20 kHz and the pulse had a double amplitude of $2A$ = 20 nm (Fig. 5.2). The wave velocities were determined using the peak-to-peak method (Fig. 5.5(a)). Referring to Table 5.3, a FCC sample and seven random sample types were considered, and wave propagation simulations were performed at σ' = 0.01, 0.1, 1, and 10MPa for each sample, totalling 32 cases. The $\overline{C_N} - e$ and $\overline{C_N^*} - e^*$ correlations for the samples considered are illustrated in Fig. 5.8. The results are qualitatively similar to the data shown in Figs. 3.25(a) and 3.26(a).

For samples at the lowest confining stress of 10 kPa, the system response was not elastic due to slip at contacts (i.e. $T = N \times \mu_{wave}$) during the wave propagation. To restrict consideration to the

elastic response of the sample, the excitation amplitude was reduced from $2A$ = 20 nm to 2 nm for the simulations at σ' = 10 kPa, and Table 5.3 shows the results based on $2A$ = 2 nm. For example, test case P-17 (Table 5.3) at σ' = 10 kPa gave V_S = 214.2 m/s with $2A$ = 2 nm compared with V_S = 213.4 m/s with $2A$ = 20 nm. The reduction in V_S due to slip was less than 1%.

The time domain responses of the incremental normal stress ($\Delta\sigma'_Z$) on the transmitter and receiver walls subjected to the *P*-wave excitation (in Z-axis) are summarised in Fig. 5.9. The subplots consider each type of sample (all with the same μ value) for three stresses of σ' = 0.1, 1, and 10 MPa; the e values are affected by σ'. The amplitude of the received waves decreased with increasing e and reducing σ'; thus the amplitudes of $\Delta\sigma'_Z$ for lower stresses were magnified (scaled) using the scaling factors noted on Fig. 5.9. Referring to Fig. 5.2, the displacement of the transmitter wall was controlled to be a sinusoidal shape with a single period, and the resultant stress responses on the transmitter wall also had a sinusoidal shape with a single period (without a phase delay). The stress responses at the received wall are sinusoidal shapes, and the wave-shapes differ from the inserted waves. At a given stress level, the waves travel faster in denser packings, and the period of the propagating wave reduces with increasing density. In a similar way, the time domain responses of the incremental shear stress ($\Delta\sigma'_X$) on the transmitter and receiver walls subjected to the *S*-wave excitation (in the X-direction) are summarised in Fig. 5.10. As expected, the *S*-waves propagate more slowly than the *P*-waves; however, the amplitude and shape of the received waves are qualitatively similar to the *P*-wave responses.

As the first peaks of the inserted and received waves were clear, the peak-to-peak method was used to obtain both V_P and V_S, and the data are summarised in Table 5.3. The stress-dependency of the wave velocities obtained is illustrated in Fig. 5.11 where both V_P and V_S increase with increasing σ' for all the samples. The wave velocities increase linearly with σ' when a (double) logarithmic scale is used, and the power coefficients of the best-fit lines to the data are given in Table 5.4. The exponential slope increased with e and was between 0.1669 and 0.1910 for the *P*-wave data, while for the *S*-wave data the power coefficient ranged from 0.1662 to 0.2121. At a given stress level, lower e values gave higher wave velocities, and the FCC sample with e_{1kPa} = 0.353 gave the largest values of V_P and V_S.

Knowing V_P and V_S for elastic and isotropic samples, the sample Poisson's ratio (ν_S) can be obtained as (Madhusudhan & Kumar, 2010):

$$\nu_S = \frac{V_P^2 - 2V_S^2}{2V_P^2 - 2V_S^2} = \frac{1 - 2\left(V_S / V_P\right)^2}{2 - 2\left(V_S / V_P\right)^2} \tag{5.3.1}$$

The variation in v_S with σ' is illustrated in Fig. 5.12 in which v_S decreases with increasing σ' for the random samples, while the v_S values for the FCC samples are close to zero. These values are slightly smaller than the values for dry sands reported by Madhusudhan & Kumar (2010) where v_S = 0.17 to 0.26 at stress levels between σ' = 100 and 500 kPa. Looser samples showed larger v_S values at low σ'; however the density dependence is less significant for larger σ' values. Referring to Fig. 5.13, v_S decreases with increasing V_P and V_S for the random samples. According to Eq. 5.3.1, v_S decreases with increasing the velocity ratio V_S/V_P, i.e. V_S increases with σ' more sensitively than V_P and is reflected in the higher power slopes observed in the V_S - σ' relationship when compared with the V_P - σ' relationship (Fig. 5.11).

The influences of $\overline{C_N}$ and $\overline{C_N^*}$ on the wave velocities are illustrated in Fig. 5.14. At a given stress level both V_P and V_S increase with increasing $\overline{C_N}$ and $\overline{C_N^*}$ and it can reasonably be argued that they approach the FCC data points as $\overline{C_N}$ and $\overline{C_N^*}$ increase. For a given coordination number, the wave velocities are larger at higher stresses, and the trends observed for the V-$\overline{C_N}$ and V-$\overline{C_N^*}$ relationships are similar. Fig. 5.15 shows that an increasing coordination number reduces v_S values, again with some extrapolation it can be argued that they tend to approach the FCC sample values at high $\overline{C_N}$ (or $\overline{C_N^*}$). The stress-dependency of v_S is not obvious in Fig. 5.15. The highest v_S value observed was 0.241 for the loosest packing (e = 0.688) at the lowest stress (σ' = 10 kPa).

The effects of e and e^* on V_P, V_S, and v_S are shown in Figs. 5.16 and 5.17. Referring to Figs. 5.16(a) and (c), at a given stress level increasing e reduces both V_P and V_S. The rate of reduction in the velocities with e increases as e increases. In comparison with the sensitivity to e there is a more gradual reduction in both V_P and V_S with e^* (Figs. 5.16(b) and (d)). The variation in v_S with e and e^* is presented in Fig. 5.17, and it is clear that larger e or e^* values give larger v_S values (Fig. 5.17). The v_S - e relationship appears to be non-linear and the stress-dependency relationship is non-trivial although it is clear that wave velocities increase with σ' at a given e. Recalling that there is a unique correlation between $\overline{C_N^*}$ - e^* (Fig. 5.8), the v_S - e^* relationship is directly linked to the v_S - $\overline{C_N^*}$ relationship.

Referring to Figs. 5.11, 5.14 and 5.16, the elastic wave velocities in the DEM samples considered depend on σ', $\overline{C_N}$, and e. Assuming a unique correlation between $\overline{C_N}$ and e or $\overline{C_N^*}$ and e^*, the elastic wave velocities can be expressed as a function of σ' and e (or e^*) as:

$$V = a\, f(e)\, \sigma'^{b} \tag{5.3.2}$$

where a and b are material constants, and $f(e)$ is void ratio correction function for wave velocity. Following an approach considered in Hardin & Richart (1963), the variation in the wave velocities with e can be fitted to the following linear expression:

$$V = C_1 + C_2\, e \tag{5.3.3}$$

where C_1 and C_2 are constants. To consider the void ratio effect on the wave velocity in Eq. 5.3.2, the following expression for $f(e)$ can be obtained:

$$f(e) = B - e \tag{5.3.4}$$

where $B = -C_1/C_2$. The data set for the random samples considered here were fitted to Eq. 5.3.3, and the best-fit B value (according to least square regression) for each stress level is summarised in Table 5.5 where B values obtained by fitting to e^* are also considered. Referring to Fig. 5.18, the variation in the wave velocities with e can be fitted to a liner curve using Eq. 5.3.3, and the associated R^2 (coefficient of determination) values are higher when e^* is considered (Table 5.5). The B values obtained vary slightly with the stress level, and the mean B values for V_P and V_S are 1.230 and 1.186, respectively, over the stress range considered, whereas the mean B values obtained by considering e^* are 1.586, and 1.484 for V_P and V_S, respectively. The B values obtained here are larger for V_P than V_S, and larger when e^* is considered. Note that a larger B value indicates that the wave velocity is less sensitive to the variation in e.

Referring to Fig. 5.19, there are clear relationships between $V/f(e)$ and σ' for both P- and S-waves when the $f(e)$ expressions derived above are used. Considering all 28 random samples included in Fig. 5.19, the best-fit curves were given by:

$$\begin{aligned} V_P &= 1195\,(1.230 - e)\sigma'^{\,0.1736} \\ V_S &= 854.0\,(1.186 - e)\sigma'^{\,0.1818} \end{aligned} \tag{5.3.5}$$

when e^* is considered the above expressions become:

$$\begin{aligned} V_P &= 787.4\,(1.586 - e)\sigma'^{\,0.1651} \\ V_S &= 586.2\,(1.484 - e)\sigma'^{\,0.1719} \end{aligned} \tag{5.3.6}$$

Hardin & Richart (1963) reported $B = 2.174$ and $b = 0.25$ for V_S considering rounded sands and gave:

$$V_S = 78.2\,(2.174 - e)\sigma'^{0.25} \tag{5.3.7}$$

The B and b values obtained in this study are therefore lower than those reported by Hardin & Richart. The DEM simulations for the random samples, the b values in Eqs. 5.3.5 and 5.3.6 are also well below the value of $b = 0.25$ for rounded sands. The lower b values ranging between 0.165 and 0.181 observed in the DEM analyses capture physical laboratory test results using

spherical particles (glass ballotini) as is discussed in Chapter 6. Cho et al. (2006) reported that the exponent b reduces as particle shape indices (e.g. roundness, sphericity and regularity) increase, and that a sample comprised of perfect spheres would give a lower bound b value. The DEM simulations for the FCC samples gave b = 0.1669 and 0.1662 for V_P and V_S, respectively, which is almost identical to the Hertzian theory of b = 0.1667 for both V_P and V_S.

5.4 Influence of contact characteristics on stiffness

As discussed in Section 4.3, the individual contact response is influenced by surface characteristics including surface roughness and partial slip. This section relates the overall sample stiffness to the surface characteristics by comparing responses obtained using the HM, HMD, HMT and RM contact models (Table 4.1). The methods used to determine V_S were introduced in Section 5.2. Two types of random samples were considered in addition to FCC samples; they are named here as the random dense packing (RDP) and the random loose packing (RLP). The FCC samples are identical to those considered in Section 5.3. The RLP samples are also same as the samples labelled as R015 in Section 5.3 (Tables 5.2 and 5.3). For the RDP samples an inter-particle friction μ_{prep} = 0 was used during the initial isotropic compression up to σ' = 1 kPa, and μ_{prep} was increased to 0.15 prior to the subsequent additional isotropic compression so that a non-zero tangential contact force develops during the simulation; thus the prepared samples differ from the R0 samples considered in Section 5.3. The erroneous (non-physical) small-strain (pre-peak) behaviour that is obtained when a μ value of 0 is used throughout sample preparation is discussed in Bernhardt et al. (2016). The isotropic stress levels considered for wave propagation simulations are 0.1, 0.2, 0.3, 0.5, 1, and 10 MPa. The RM contact model was used from the start of the isotropic compression stage, whereas the HMD contact model was activated only for the wave propagation simulations so that the samples were identical to those prepared using the HM contact model. In the modified LAMMPS code, the HMD contact model can be activated or switched on from the HM contact model. Knowing the tangential contact force (T) acting on each contact, the tangential contact displacement (s) is approximated using the following expression for an initial loading of T (Mindlin & Deresiewicz, 1953):

$$s = \frac{3\mu N}{16 G_p^* a}\left[1-\left(1-\frac{T}{\mu N}\right)^{2/3}\right] \tag{5.4.1}$$

Differentiating Eq.5.4.1 with T gives the inverse expression to Eq. 2.3.9.

Referring to Tables 5.6 and 5.7, 72 simulations were carried out; the e and $\overline{C_N}$ data for the simulations given indicate that S_q did not noticeably influence the samples' packing densities for

a given μ_{prep}. The μ_{prep} value was increased to μ_{wave} = 0.2 for all the simulations to prevent contact slip during the wave propagation as described in Section 5.2 (Fig. 5.3).

5.4.1 Partial slip effects

The influence of partial slip at the contacts on the elastic properties was investigated by comparing the responses obtained using the HM and HMD contact models. The variation in particle displacement in the X-direction with time and distance from the transmitter wall are illustrated as contour plots in Fig. 5.20 considering the first 0.65 ms after the start of the excitation and σ' =100 kPa. The peak displacement (the darkest contour) propagated with a virtually constant velocity in all cases. The best-fit slope through the peak displacements gives the $V_{S,dL/dt}$ data, and they are listed on Tables 5.6 and 5.7. These values are a direct measure of the propagating wave front; hence they are taken to be the most accurate estimates of V_S and used as a benchmark for the other interpretative methods considered here. As discussed in Section 5.3, denser packings exhibited larger $V_{S,dL/dt}$, i.e. $V_{S,FCC}>V_{S,RDP}>V_{S,RLP}$. For the FCC packings the responses for the HMD and HM cases are indistinguishable (Figs. 5.20(a) and (b)). For the RDP and RLP samples, the slopes of the darkest lines are similar for the HMD and HM cases, while the amplitude of particle displacement is reduced when partial slip is considered (compare Figs. 5.20(c) and (d), and Figs. 5.20(e) and (f)). Referring to Table 5.7, for the random samples, use of the HMD model noticeably reduces $V_{S,dL/dt}$ by up to 3.3%.

An indication of the propagation of the kinetic energy in the system as a whole is given by plotting the square of the maximum particle velocity ($V_{X,max}^2$) in the oscillation (X-) direction considering a chain of contacting particles along the central axis of the sample versus position; the FCC samples show little variation for either contact model (Fig. 5.21). O'Donovan et al. (2015) simulated bender element tests using a FCC sample and found a reduction in V_S by approximately 20% using the HMD model when compared with the HM model; they used a larger input displacement of a transmitter particle with a double amplitude $2A$ = 250 nm and a lower μ_{wave} (= 0.088), which increased $T/\mu N$ considerably during the wave propagation. For the RDP samples there is considerable attenuation in $V_{X,max}^2$ for both the HM and HMD contact models, and the HMD case exhibits a greater reduction in $V_{X,max}^2$ due to partial slip.

To understand the contact scale responses during *S*-wave propagation, tangential force-displacement (T-Δs) relationships for representative contacts located close to the transmitter wall are illustrated in Fig. 5.22. Referring to Fig. 5.22(a) for the FCC samples, the T-Δs response is almost identical for the HM and HMD cases as the maximum value of $T/\mu N$ is only 0.023; for this example, the tangential contact stiffness (k_T) is reduced by merely 0.7% due to partial slip according to Eqs. 2.3.9 and 2.3.11. For the RDP samples, the T-Δs response was

clearly affected by partial slip; the initial value of $T/\mu N = 0.765$ resulted in a 38% reduction in k_T due to partial slip for the initial loading case. As expected, the HM contact presents a linear response when the T-Δs curve is considered as $T/\mu N < 1$, whereas the HMD contact exhibits a softer response for the initial loading. However, the unloading and reloading stiffnesses (dT/ds) are almost identical to the HM contact.

Following Mouraille & Luding (2008), the variation in the frequency response with distance from the transmitter wall is illustrated in Fig. 5.23. This figure was created by taking the FFT of the time domain data for each distance from the transmitter. The shading then gives the amplitude associated with a given frequency (f) at a particular distance. Visual analysis of the spatial variation of the frequency responses revealed that the high frequency contents did not penetrate far into the random samples, whereas there was no variation in the frequency contents with distance for the FCC sample. When partial slip is considered (Figs. 5.23(b), (d) and (f)), a similar variation of frequency with distance is observed although the amplitude decreases as the energy of the propagating wave attenuates with distance due to partial slip (Fig. 5.21).

Recalling the discussion in Section 5.2, the dispersion relations for the propagating waves are illustrated in Fig. 5.24. As detailed in Section 2.6.4 the dispersion relation describes the relationship between frequency (f) and wavenumber ($\kappa = 2\pi/\lambda$; λ is wave length) of the propagating waves. The group velocity (V_{group}) and phase velocity (V_{phase}) converge at low wavenumbers (or low frequencies) to give $V_{S,dispersion}$; the resultant data for all samples are given in Tables 5.6 and 5.7. The systems here are clearly dispersive as these velocities diverge with increasing κ (non-linear relationship), and so the tangent slope of the best-fit line through the maxima gives V_{group}, while the secant slope gives V_{phase}. The dispersive nature of the FCC sample is not evident in Figs. 5.24(a) and (b) due to the low nominal frequency (f_{in} = 20 kHz) inserted; however using f_{in} = 100 kHz enabled visualisation of dispersion relation as discussed in Section 5.5. The dispersive nature of soils has been confirmed in experimental work by Greening & Nash (2004) and Alvarado & Coop (2012) and the data indicate that both the FCC and random samples exhibit normal dispersion, i.e. V_{group} and V_{phase} decrease with increasing wavenumber or frequency (Section 2.6.4). For the random samples, considering the DEM simulations using the HMD contact model, there was a discontinuity observed in the f - κ plot at very low κ; thus the $V_{S,dispersion}$ values are obtained by considering a steeper curve rather than a very low slope of the f - κ plot. Greening & Nash (2004) also reported problems with interpretation of low-frequency data when estimating the group and phase velocities. The initial low velocity data are indicative of a wave that arrives after the main shear disturbance. The $V_{S,dispersion}$ and $V_{S,dL/dt}$ values are in good agreement (within 1% for the FCC samples and 2% for the random samples) as summarised in Tables 5.6 and 5.7.

Stress response on wall boundaries

For each simulation the incremental shear stresses in the X-direction ($\Delta\sigma'_X$) were recorded at the receiver and transmitter walls. Considering the FCC and random samples at σ' = 100 kPa, the inserted and received stress responses are illustrated in Fig. 5.25 for both the HM and HMD contact models considering both the time and frequency domains. Referring to Figs. 5.25(a), (c) and (e), the amplitude in the received signal is greater than the amplitude of the inserted signal for the FCC samples because the receiver wall is completely fixed (energy tracing was enabled during the DEM simulations to confirm that there was no spurious numerical energy dissipation). For the random samples the high frequency and low amplitude stress oscillations are observed after the inserted stress pulse ends. The reason can be understood by applying frequency domain interpretation as discussed below in this section. Note that the stress oscillations continued over the simulation duration as no local or viscous dumping was considered in the wave propagation simulation. In comparison with typical point source bender element test data or the DEM simulations by O'Donovan et al. (2016) which also used a point source there is no evidence of near-field effects (Arroyo et al., 2003) in Fig. 5.25 most likely because this study considers plane wave propagation. The $V_{S,P\text{-}P}$ values were calculated by applying the peak-to-peak method to these data; referring to Tables 5.6 and 5.7, these data are slightly lower (within 1%) than the $V_{S,dL/dt}$ approach for the FCC samples. A similar magnitude of difference is observed in the RLP samples; however, in this case mostly $V_{S,P\text{-}P} \geq V_{S,dL/dt}$. When the HMD model is used to consider partial slip the V_S values reduce, e.g. from $V_{S,P\text{-}P}$ = 368.4 to 357.9 m/s for the RDP sample at σ' = 100 kPa. The mean value of the ratio of the tangential contact force to the slip limit (i.e. $T/N \times \mu_{wave}$) at each contact was 56 - 58% for the RDP samples, and so a relatively large amount of partial slip occurred.

Additional insight into the system's dynamic response and its sensitivity to the contact model is achieved by applying Fast Fourier Transforms (FFTs) to the time domain data. Figs. 5.25(b), (d) and (f) present the responses for the transmitter wall, considering only the first (main) cycle of stress response, and the receiver wall. For f_{in} = 20 kHz a single period sinusoidal pulse includes a range of frequencies. For the FCC packing, the shapes of the inserted and received signals are almost identical for the HM and HMD models, and there is little attenuation for the HMD case (Fig. 5.25(a)). Granular materials act as a filter of high-frequency signals (e.g. Santamarina & Aloufi, 1999), and as almost the full range of inserted frequencies are observed in the received signal, it indicates that most of the inserted signal frequencies were lower than the system cut-off frequency for the FCC samples. As would be expected from the data presented in Figs. 5.25(d) and (f) there is a measurable reduction in amplitude when the inserted and received signals for random samples are compared, and the reduction is greater when the HMD model is used. The maximum frequency that reached the receiver was about 20 kHz for the RDP samples

and 11 kHz for the RLP samples; so that in these cases the samples clearly acted as the low-pass filters to the signals, and frequency contents higher than the low-pass limit kept interacting with the transmitter wall during the simulations as observed in the time domain responses in Figs. 5.25(c) and (e). It is also clear that the low-pass filter limit is affected by packing density, and this is investigated in Section 5.5. The maximum frequency transmitted was not affected by partial slip although the amplitude decreased over the entire range of frequencies received.

In their frequency domain analysis, Alvarado & Coop (2012) considered the gain factor (the ratio of the amplitudes of the received and inserted signals) plotted against frequency and they related the frequencies of the local maxima in the gain factor to the resonance modes of vibration of the sample. Referring to Fig. 5.26, the gain factor-frequency plot is smooth for the FCC samples, and the gain factor reduces slightly with increasing *f* where partial slip effects are not obvious. For the RDP and RLP samples, the peaks in the gain factor occur at slightly different frequencies for both contact models, indicating that the variation in contact model influences the system's dynamic response at both low and high frequencies. It is also clear that the gain factor decreases due to partial slip where the HMD contact model is used. The relationship between the stacked phase shift (Φ_{stack}) and *f* is given in Fig. 5.27, and the $V_{S,SP}$ values (Tables 5.6 and 5.7) were obtained as described in Section 5.2. For the FCC sample the $V_{S,SP}$ values were within 1% of $V_{S,dL/dt}$; a larger discrepancy was observed, with a difference of up to 5.6%, for a RDP sample with the HMD model (Tables 5.6 and 5.7). The discrepancies amongst the V_S values calculated with the four methods are less than the values reported in O'Donovan et al. (2015); the difference may be because O'Donovan et al. used point source transmitters and receivers.

The variation in V_S with σ' for all the simulations considered is plotted in Fig. 5.28(a) using the $V_{s,P\text{-}P}$ data. Referring to Eq. 2.7.1, the small-strain shear modulus (G_0) was deduced by $G_0 = \rho_d V_S^2$ where ρ_d is the bulk density of dry sample, and the variation in G_0 with σ' is illustrated in Fig. 5.28(b). For the FCC packing the HM and HMD cases give the almost identical V_S - σ' and G_0 - σ' relationships; however the V_S and G_0 values of the RDP and RLP samples are measurably reduced by partial slip. When the HMD model was used, there was a 2-3% reduction in V_S and a 4-6 % reduction in G_0 with a similar reduction being found for both the RDP and RLP samples. Considering all the methods used to determine V_S in this study, the maximum reduction in G_0 obtained by accounting for partial slip was 8.7%. The data do not indicate any measurable sensitivity of the power coefficient *n* in the G_0 - σ' relationship to partial slip effects. From a micromechanical perspective, the *n* value is affected if the degree of partial slip, i.e. $T/(\mu N)$, varies with σ' (Eqs. 2.4.12 and 2.7.7); the samples prepared in this study gave a narrow variation of $T/(N \times \mu_{wave})$ = 55 – 60% for the random samples.

5.4.2 Spin resistance effects

The effects of spin resistance described in Section 4.2.3 on the system response were also considered. Adding spin resistance (HMT model) produced a looser packing compared with the HM contact model for $\mu_{prep} > 0$. To isolate the influence of spin resistance only, FCC and random samples were prepared using the HMT contact model without activating the spin resistance so that no torque was accumulated during the isotropic loading, i.e. the HMT model is equivalent to the HM model. The spin resistance was activated only for the wave propagation simulations. For both the FCC and RDP samples, V_S was not measurably affected by including the spin resistance (Figs. 5.29(a) and (b)). The RLP samples had $\mu_{prep} = 0.15$, and the V_S values were only slightly increased (by 0.03% and 0.08% at $\sigma' = 100$ kPa and 10MPa, respectively) when spin resistance was included (Figs. 5.29(c) and (d)). It was found that the effect of spin resistance increased with increasing confining stress. However, considering the very small difference between the HM and HMT models; it seems that the effect of spin resistance on the dynamic response is not significant for the materials considered. This observation agrees with the single contact response observed in Section 4.4.4 where the effects of spin resistance became significant only for softer materials, e.g. rubber. However, sphere rigidity is assumed in DEM simulations as a rule of thumb this restricts the particle overlap to be below 5% of the diameter.

This study considers a spin resistance developed for a perfect sphere with a finite friction (Mindlin, 1949; Deresiewicz, 1954), while some authors have proposed rotational resistance models to capture the rotational contact reaction that occurs when non-spherical particles contact. Rotational resistance models include Iwashita & Oda (1998), Ai et al. (2011), Jiang et al. (2015), and Huang et al. (2016); all these authors reported considerable effects on sample responses at large strains using their rotational resistance models. Following Ting et al. (1989) other authors, e.g. Calvetti (2008), Arroyo et al. (2011) and Butlanska et al. (2014), supress particle rotation completely in their simulations. To assess the potential influence of including spin and rolling resistances, the rotational degrees of freedom were suppressed during the *P*- and *S*- wave propagations; this case is equivalent to including infinite resistance to spin and rolling. For the FCC sample at $\sigma' = 100$ kPa, Fig. 5.30(a) shows no effect on the *P*-wave propagation as there is no rotation involved during the planar wave propagation for this lattice configuration. The *S*-wave travels with a similar velocity of the *P*-wave when particle rotation is restricted. For the RDP sample, excluding the rotational degrees of freedom of particles gives considerably larger V_P and V_S where $V_P \approx V_S$ compared with the cases allowing the rotation of particles (Fig. 5.30(b)). This indicates that the *P*- and *S*-wave velocities might be reduced as the rotational kinetic energy that is not related to the *P*- and *S*-wave vibration modes increases.

5.4.3 Surface roughness effects

For the range of RMS surface roughness (S_q) values considered (S_q = 0, 0.5, 1 μm), the systems were more sensitive to consideration of surface roughness than partial slip. When examining the effect of surface roughness, a range of confining stresses were considered as the contact model response depends on the magnitude of N relative to N_{T1} (Eq. 4.2.2) and N_{T2} (Eq. 4.2.1) as discussed in Section 4.2. Fig. 5.31 shows the variation in particle displacements with time and distance from the transmitter wall along a straight line for S_q values of 0 (smooth case), 0.5 and 1 μm. At the stress level considered, σ' = 100 kPa, the wave velocity is clearly reduced by surface roughness for both the FCC and random samples. The amplitude of particle displacement (indicated as grey-scale) is also slightly reduced with increasing surface roughness. The $V_{S,dL/dt}$ values obtained are summarised in Tables 5.6 and 5.7. For the lowest stress level considered here (σ' = 100 kPa), the reductions in $V_{S,dL/dt}$ were 20.7% and 31.6% for S_q = 0.5 and 1 μm, respectively for the FCC samples, and 11-12% and 21-23% for S_q = 0.5 and 1 μm, respectively, for both the RDP and RLP samples.

The variation in frequency response of the particle displacement with distance is visualised in Fig. 5.32. For the FCC samples, no variation in frequency with distance is observed, although the amplitudes of particle displacement decreases with increasing S_q. For the random samples, the penetrating frequencies are measurably reduced with increasing surface roughness. For example, for the RDP sample with S_q = 1 μm (Fig. 5.32(f)), the frequencies higher than 20 kHz is not seen at a distance = 0.3 m, while the smooth data (Fig. 5.32(b)) contain non-negligible amplitudes with frequencies exciding 20 kHz.

The sensitivity of the *S*-wave dispersion relations to S_q is presented in Fig. 5.33. The $V_{S,dispersion}$ values (i.e. slopes in the plots at low wavenumber or frequency) decrease clearly with increasing surface roughness. For the RDP sample with S_q = 1 μm (Fig. 5.33(f)), the maximum frequency observed in the dispersion relation is clearly less than 20 kHz, which agrees with the observation in Fig. 5.32(f). Here, the roughness-dependency of the maximum transmitted frequency or wavenumber is confirmed. Santamarina & Aloufi (1999) emphasised a link between the low-pass wavelength and the particle size. Figs. 5.32 and 5.33 confirm the density-dependency of the low-pass limit as the higher frequencies could not penetrate as far in the looser RDP samples when compared with the very dense FCC samples. The $V_{S,dispersion}$ values are summarised in Tables 5.6 and 5.7 where the discrepancies between $V_{S,dL/dt}$ and $V_{S,dispersion}$ were at most 1% for the FCC samples, and within 2% and 3% for the RDP and RLP samples.

The time histories of the incremental shear stress in the oscillation direction ($\Delta\sigma'_X$) on the transmitter and receiver walls for the FCC and RDP samples with S_q = 0 (smooth) and 1 μm

(rough) at σ' = 0.1, 0.3 and 1 MPa are illustrated in Fig. 5.34. It is clear that the shear waves propagate faster through the samples at higher stress levels for all cases. $V_{S,P\text{-}P}$ clearly decreases with surface roughness for both the FCC and the RDP samples and the difference is more marked at lower stresses especially for the FCC samples. The attenuation caused by introducing surface roughness decreases with increasing stress level and the shapes of the received signals also became more similar at the higher stresses. The $V_{S,P\text{-}P}$ values are summarised in Tables 5.6 and 5.7 where the discrepancies between $V_{S,dL/dt}$ and $V_{S,P\text{-}P}$ were within 1% for both the FCC and RDP samples, and within 3% for the RLP samples. The reason for the higher discrepancy for the looser samples with lower stresses is that the nominal frequency of the inserted wave (f_{in} = 20 kHz) did not reach the receiver wall as granular materials act as a low-pass filter.

For the FCC samples, the spectra of the inserted and received signals are similar, and they are not shown here. The frequency contents of the inserted and received signals at σ' = 0.1 and 1 MPa for the RDP samples are compared in Fig. 5.35. The frequency range of the received signals varies with both surface roughness and stress. The frequency corresponding to the maximum amplitude is also affected by surface roughness. The variations in the gain factor and the stacked phase with frequency are plotted in Fig. 5.36. For the RDP sample, the cut-off frequency reduces with increasing surface roughness (e.g. from 20 kHz to 15 kHz at σ' = 0.1 MPa); however, the difference becomes less marked at σ' = 1MPa. The combined effects of the surface roughness and stress level influence the dynamic response at all frequencies below the cut-off frequency as is evident from the variation in the frequencies of the local maxima of the gain factor. The $V_{S,SP}$ values obtained from the f-Φ_{stack} plots are summarised in Tables 5.6 and 5.7. The maximum discrepancy between $V_{S,dL/dt}$ and $V_{S,SP}$ amongst all the cases using the HM and RM contact models was 2.5%.

Considering the $V_{S,P\text{-}P}$ data, the variation of V_S with σ' is illustrated in Fig. 5.37 for the three roughness values (S_q = 0, 0.5 and 1 μm) and the three sample types. Qualitatively similar trends are observed for the three sample types; V_S reduces with increasing S_q, and the reduction is more significant at lower σ'. As σ' increases, the three curves for S_q = 0, 0.5 and 1 μm converge gradually so that the responses for S_q = 0.5 and 1 μm join the curve for the HM contact model (S_q = 0). This correlates with the particle-scale response of the rough particles; the rough contact response becomes equivalent to a Hertzian contact at a large contact force (when $N > N_{T2}$) as discussed in Section 2.4 (see Fig. 4.3(b)). Similar observations are made by considering the variation of G_0 with σ' presented in Fig. 5.38. Fig. 5.38 includes data from a micromechanical analysis (EMT) based on Yimsiri & Soga (2000). Note that the tangential contact stiffness for the rough surface model in the EMT approach was modified to be equivalent to the RM contact model considered in this study (i.e. Eq. 4.2.27 is adopted), and partial slip effects were not

considered. When the relationship between G_0 and σ' is compared with other cases, it is usual to apply a void ratio correction function so that the effect of void ratio (e) is removed. However, referring to Tables 5.6 and 5.7, the difference in e values at each stress level is very small; thus the G_0 values are directly compared in Fig. 5.38. To calculate G_0 values using EMT, the e and $\overline{C_N}$ data were obtained from the DEM samples. For the FCC case, the uniformity of the contact forces for this lattice packing means that all the contacts will transit between the three ranges in the normal contact model (i.e., $N<N_{T1}$, $N_{T1}\leq N<N_{T2}$ and $N>N_{T2}$) simultaneously, and so there is a distinct change in the slope to the $G_0 - \sigma'$ relationship for the DEM data (see Fig. 4.3(b) for single contact response). The higher G_0 values predicted by the analytical model for the random packings are due to the simplifying assumptions of contact homogeneity in EMT, and the effect is more significant in the RLP case. The relative reduction in G_0 is greater in the denser packing than in the looser packing. To understand the density-dependent nature of the response, the cumulative distributions of N at σ' = 100 kPa for the three sample types considered along with the values of N_{T1} (Eq. 4.2.2) for S_q = 0.5 and 1 μm are given in Fig. 5.39. It is clear that for both S_q = 0.5 and 1 μm, $N<N_{T1}$ for all the contacts in the FCC sample; however the proportion of contacts with $N>N_{T1}$ is higher for the looser packing, and so the surface roughness effects on sample stiffness are less marked for the looser packing. The proportion of contacts with $N>N_{T1}$ is higher for the RLP case than the RDP case as $\overline{C_N}$ values are lower for the RLP case.

As illustrated in Fig. 5.11(b), the power coefficient in the V_S - σ' relationship depends on e. To remove the effect of e, a void ratio correction function for G_0 ($F(e)$) was found by extending the void ratio correction function for V_S ($f(e)$ in Eq. 5.3.4) as below:

$$F(e) = \frac{(B-e)^2}{1+e} \tag{5.4.2}$$

According to Table 5.5 for the material considered in this section, B = 1.186 can be used in Eq. 5.4.2. When the mechanical void ratio (e^*) is considered, B = 1.484 can be used, replacing e with e^* in Eq. 5.4.2. The B value considered here agrees with Xu et al. (2013) (B = 1.164) based on similar DEM analyses, whereas B = 1.186 is significantly smaller than B = 2.17 or B = 2.97 reported for experimental data on sands (Hardin & Richart, 1963; Iwasaki & Tatsuoka, 1977). Note that Eq. 5.4.2 cannot be used if e exceeds B. A number of alternative expressions of $F(e)$ have been proposed in the prior literature as summarised in Mitchell & Soga (2005).

For the EMT approach, the following expression is used in the EMT approach to describe the packing correction (see Eq. 2.7.17):

$$F_{EMT} = \left[\frac{\overline{C_N}}{1+e}\right]^{2/3} \tag{5.4.3}$$

The expressions of $F(e)$ for DEM (Eq. 5.4.2 with B = 1.186), and F_{EMT} for EMT (Eq. 5.4.3) were applied to obtain $G_0/F(e)$ and G_0/F_{EMT}, respectively, and the n values at various σ' intervals are presented in Fig. 5.40 for the three sample types (the horizontal axis shows the average values of each stress interval). It is clear that the n values increase with increasing surface roughness. For the FCC case, the DEM data give a distinct shift from $n\approx0.6$ to 0.35 as σ' increases due to the uniform contact forces as discussed above, while EMT data give a more gradual change from $n\approx0.7$ to 0.35. The lower limit of n is the case for the smooth sample type (S_q = 0) where n=1/3 is directly obtained from Hertzian theory. For the random samples, both the DEM and EMT data show a similar smooth reduction in n values with increasing σ', and EMT data give higher n values than the DEM data at the lower stresses. The n values depend on both S_q and σ', and both the random samples exhibit qualitatively similar trends.

5.5 Eigenmode analysis and system dynamics

As reviewed in Section 2.7.3, eigenmode analyses give the natural vibration modes and corresponding frequencies of a sample, and the dynamic response of the sample during wave propagation can be expressed as a superposition of the fundamental vibration modes assuming a linear-elastic system response. Eigenmode analyses enable estimation of the possible range of vibration frequencies of the system subjected to an external disturbance. On the other hand, granular materials act as a low-pass filter to high frequency contents (Section 2.6.4). The DEM simulations presented in Sections 5.3 and 5.4 highlighted that void ratio (e), confining stress (σ'), and contact models also affect the maximum transmitted frequencies ($f_{low\text{-}pass}$) into samples. This finding agrees with O'Donovan (2013). This section aims to quantify how $f_{low\text{-}pass}$ and the low-pass wavelength ($\lambda_{low\text{-}pass}$) are influenced by e and σ', and relates $f_{low\text{-}pass}$ to the eigenfrequencies of the system. This section also investigates the relationship between the resonant frequencies and the frequencies associated with the local maxima in the gain factor - frequency relationship obtained using wave propagation simulations.

The samples considered here are identical to those considered in Section 5.3; the HM contact model was used and data for these samples are listed in Table 5.8. Referring to Figs. 5.1 and 5.41, P-waves were generated by moving the lower transmitter boundary (at z = 0) in the longitudinal (Z-) direction. A double amplitude ($2A$) of 5 nm and a nominal frequency (f_{in}) of 100 kHz were used for most of the simulations. A pulse with f_{in} = 100 kHz can excite a broad range of frequencies including the main frequencies of up to 200 kHz (Fig. 5.41(b)). A higher nominal frequency of f_{in} = 200 kHz was used for two of the FCC samples at σ' = 1 and 10 MPa (test cases P-3 and P-4 in Table 5.8) when the frequency domain analysis was performed (and so frequencies of up to 400 kHz were inserted).

5.5.1 Eigenmode analysis

As detailed in Section 2.7.3, the global stiffness matrix (***K***) and the global mass matrix (***M***) can be created using DEM data. Here the local contact stiffness matrix was created using the data available in the DEM model. The local contact stiffness matrix is a 12×12 element matrix; the expressions for this matrix are given in the PFC user manual (Itasca, 2007) and the entries depend on the particle coordinates and contact stiffnesses. For the analyses presented here, the data required to construct the local stiffness matrix (particle coordinates, contact orientations and contact stiffnesses) were obtained from the DEM sample configurations following isotropic compression. The inter-particle friction was set at μ_{wave} and a no-slip condition was assumed. For a sample composed of n particles, there are $6\times n$ degrees of freedom; for the systems considered here $\boldsymbol{K}$ consisted of 19,200×19,200 elements for the FCC samples, and 211,206×211,206 elements for the random samples. When the rotational degrees of freedom are ignored, the size of $\boldsymbol{K}$ is reduced to one quarter of the full size. The contact stiffness between particles and boundaries were also included in $\boldsymbol{K}$. The eigenvalue decomposition is achieved by solving Eq. 2.7.20. Here, built-in MATLAB functions (MathWorks, 2015) of "eig" and "eigs" were used to obtain the eigenvalues $\boldsymbol{\omega^2}$ and eigenvectors $\boldsymbol{\phi}$ where each ω_i^2 is associated with a particular eigenvector ϕ_i. The eigenfrequency of the i th mode is $f_i = \omega_i/2\pi$.

The natural frequencies (f_i) are plotted against the normalised mode number in Fig. 5.42(a) for the FCC (P-2), RDP (P-6), and RLP (P-30) samples at σ' = 100 kPa (Table 5.8). Note that the RDP and RLP samples refer to the random samples prepared using μ_{prep} = 0 and 0.4, respectively, and this designation differs from that used in Section 5.4. The corresponding density distributions of f_i are given in Fig. 5.42(b). Fig. 5.42(a) includes data for a FCC sample where the rotational degrees of freedom are ignored (referred here as FCC trans. only sample), this is discussed further below. Excluding consideration of the FCC trans. only, the natural frequencies are distributed between 0.7534 and 211.2 kHz for the FCC sample, between 0 and 216.1 kHz for the RDP sample, and between 0 and 214.1 kHz for the RLP sample. It is clear that the three samples exhibit similar maximum f_i values. The relationship between f_i and the normalised mode number is not affected by excluding the rotational degrees of freedom at lower mode numbers although they diverge at higher mode numbers (Fig. 5.42(a)). The very low frequency data ($\approx$ 0 kHz) are associated with the presence of rattler particles as pointed in Somfai et al. (2005), and the low frequencies are most prevalent in the RLP sample (Fig. 5.42(b)). The density distribution of f_i indicates several peaks (local maxima) for the FCC sample which are not evident in the data for the random samples. Note that the density distribution of f_i is affected by the dimensions of the sample considered particularly at low

frequencies, while the highest frequencies are related to the local packing configuration. A similar sensitivity to the sample shape was reported in Marketos & O'Sullivan (2013).

The variation in the maximum eigenfrequency ($f_{i,max}$) with stress level for the three sample types are illustrated in Fig. 5.43, again data for the FCC sample where the rotational degrees of freedom are suppressed are also included. The three samples exhibit similar $f_{i,max}$ values and the difference between them was less than 3% across the wide range of the stress considered (10 kPa to 10 MPa). The $f_{i,max}$ values relate to the element with the highest ratio of stiffness/mass in the system (Belytschko et al., 2000), so that a higher contact stiffness gives a higher eigenfrequency for monodisperse packing. Following O'Sullivan & Bray (2004), the mass of each particle is distributed to its contacts (which represent the elements); so when the contact density is higher, less mass is assigned to each contact. Assuming a uniform contact stiffness, the maximum value of the stiffness/mass is therefore determined by the particle with the greatest number of contacts. While the random samples had the mean coordination numbers ($\overline{C_N}$) that were significantly lower than that for the FCC sample (5.91 and 3.84 in comparison with 12), in each case there were local regions of dense packing so that particles with contact numbers of 11-12 were observed in all the RDP samples and contact numbers of 9-10 were locally found in the RLP samples. It should be also noted that each contact has a larger contact force and consequently stiffness in a looser packing at the same stress level (see Fig. 5.39) (as less contacts transmit the same total force). These combined effects on the ratio of stiffness/mass explain the lack of sensitivity of $f_{i,max}$ to the packing. Using the analysis approach, the effect of various parameters on $f_{i,max}$ including the particle mass, confining stress and polydispersity were investigated in Otsubo et al. (2017).

To find the fundamental eigenmodes associated with the *P*-wave propagation, a correlation index (χ_{zi}) was calculated for each eigenmode i:

$$\chi_{zi} = \frac{1}{n}\sum_{s=1}^{n} u_{zi,s}^{-2} \tag{5.5.1}$$

where $\bar{u}_{Zi,s}$ = Z component of the normalised eigenvector of mode i for particle s. When $\chi_{zi} = 1$ the displacement of all the particles is orientated in the Z-direction (i.e. the eigenvectors have no X or Y components). Processing Eq. 5.5.1 for the full-set of eigenvectors is computationally expensive, and so for the analyses presented here a linear chain of particles connecting the transmitter and receiver wall boundaries was considered. The index χ_{zi} is plotted against f_i for both the FCC and the RDP samples at $\sigma' = 100$ kPa in Fig. 5.44. For the FCC packing (Figs. 5.44(a) and (b)), the eigenmodes giving $\chi_{zi} = 1$ were observed across the entire range of f_i. For the RDP sample, eigenmodes with $\chi_{zi} = 1$ were rarely observed; $\chi_{zi} > 0.9$ were evident for $f_i < 10$ kHz; however, the peak values of χ_{zi} dropped to about 0.33 for $f_i > 15$ kHz, indicating a random

displacement occurring in any direction. For the looser samples (e.g. RLP sample) the peak χ_{zi} values observed decreased below 0.9 at lower f_i values in comparison with the data in Fig. 5.44(c), while at a higher stress the maximum χ_{zi} values attained were higher (> 0.9) and these high χ_{zi} values were observed up to a higher f_i value than those illustrated in Fig. 5.44(c). Mode shapes associated with typical resonant frequencies (f_r) are illustrated in Fig. 5.45 for the FCC and RDP samples. The boundary conditions in the propagation (Z-) direction considered in this analysis are the fixed-wall boundaries used in the DEM simulations. The wave length (λ_r) and the wavenumber (κ_r) for the resonant mode r of a sample with a length L can be expressed as:

$$\lambda_r = \frac{2L}{r} \tag{5.5.2}$$

$$\kappa_r = \frac{2\pi}{\lambda_r} = \frac{\pi}{L} r \tag{5.5.3}$$

The mode shapes (determined from the z-component of eigenvector) associated with the 1st, 2nd, 5th, 10th maxima of χ_{zi} are shown in Figs. 5.45(a-d); the wavelengths associated with these sinusoidal mode shapes agree with Eq. 5.5.2 for the FCC sample. The mode shapes illustrated in Figs. 5.45(e) and (f) also correspond with χ_{zi} = 1; however, referring to Figs. 5.42(b) and 5.44(a), at these eigenfrequencies (e.g. f_{50} = 52.1 kHz or f_{200} = 137.6 kHz) there are a large number of eigenmodes present with very similar f_i values. Therefore the fundamental resonant modes were identified from both the χ_{zi} values and visual observation of the mode shapes. Using Eqs. 5.5.2, the 1st mode of resonance (Fig. 5.45(a)) at f_1 = 1.06 kHz gives a wave length $\lambda = 2L$, while the 200th mode of resonance (Fig. 5.45 (f)) at 137.6 kHz gives $\lambda = L/100$. At the 1st mode of resonance, all the particles move in the same direction ($\Delta z > 0$), while for the 200th mode neighbouring layers move in opposite directions; in all cases the horizontal (x, y) components of the eigenvectors were negligible. As shown in Fig. 5.44(a), the f_i values higher than 137.6 kHz exist for the FCC sample; however, these modes excite the rotational components and the resultant eigenvectors are more complex shapes than purely the compressional modes with displacement restricted in the propagation (Z-) direction. For the RDP sample, the resonant modes were more easily identified by simply considering the maxima of χ_{zi} in Fig. 5.44(c). Referring to Figs. 5.45(g-k) the lowest resonant modes were clearly identifiable just as in the case of the FCC packing, which agrees with the observations in Somfai et al. (2005). As f_i increases and χ_{zi} decreases, the resonant eigenvectors identified do not have a clean sinusoidal shape. This may indicate the presence of the low-pass filter to wavelength. For the RDP sample the rattler particles were not involved in any mode of vibration, and they showed zero displacement as confirmed in Figs. 5.45(g-k). The combinations of f_r and κ_r obtained for the first 10 modes for all the packings considered at σ' = 100 kPa are tabulated in Table 5.9.

A comparison of data from the eigenmode analyses with the DEM wave propagation simulations serves to verify the ability of the DEM model to correctly give data on the system's elastic properties. Using the measurements of stress recorded at the transmitter and receiver walls, and applying the frequency domain analyses (Greening & Nash, 2004) the group velocity (V_{group}) and phase velocity (V_{phase}) were found at $\sigma' = 100$ kPa as given in Figs. 5.46(a) and (b), for the FCC and RDP samples. Note that the inserted signal contains a broad range of frequency components and V_{phase} is the velocity of a particular component, and V_{group} is the velocity with which the overall waveform propagates through the sample. Referring to Fig. 5.46(a), both V_{group} and V_{phase} converge at low frequency to give a long-wave velocity, and the velocities are in good agreement with the V_P values based on direct measurements (i.e. $V_{P,dL/dt}$). While there are some fluctuations in the data for the RDP sample in Fig. 5.46(b), both V_{group} and V_{phase} give a similar velocity at low frequencies, which agrees well with the $V_{P,dL/dt}$ value. The $V_{P,dL/dt}$ values for all test cases are summarised in Table 5.8. Comparing with Table 5.3 for the $V_{P,dL/dt}$ values based on f_{in} = 20 kHz, the discrepancy in $V_{P,dL/dt}$ between f_{in} = 20 kHz and f_{in} = 100 kHz was within 1% for the FCC samples, and up to 2.2% for the random samples where the mean difference for the random samples was less than 1%. The V_{group} and V_{phase} were also directly calculated from the eigenmode analysis data as $V_{group} = d\omega_r/d\kappa_r$ and $V_{phase} = \omega_r/\kappa_r$; these can be derived from the data in Table 5.9. The V_{group} and V_{phase} data based on the eigenmode analysis are plotted in Figs. 5.46(c) and (d), and for the low frequency modes considered, the group and phase velocity data calculated using both methods agree and they agree with $V_{P,dL/dt}$. The direct comparison with the eigenmode analyses presented here further increases confidence in the use of simple interpretation of the received signal to infer elastic properties for these systems.

5.5.2 Frequency response and filtering effects

Using the DEM dataset in combination with the eigenvalue decomposition and the dispersion relation enabled a comprehensive picture of the frequency domain response of the system to be developed. The synthesis of the available data focussed on two aspects of the response: the maximum transmitted frequency and resonance.

Dispersion relation for FCC packing

The dispersion relation describes the ω-κ relationship for the propagating waves. The theoretical derivation for lattice packings was provided in Section 2.6.4. Referring to Eq. 2.6.3, the dispersion relation for a *P*-wave propagating through a FCC array is given by:

$$\omega = 2\sqrt{\frac{C^{FCC}}{m}}\left|\sin\left(\frac{l^{FCC}}{2}\kappa\right)\right| \tag{5.5.4}$$

where l^{FCC} is the layer distance and is approximately $\sqrt{2}R$ for the considered propagation (Z-) direction assuming the contact overlap is negligible compared with R. The layer stiffness for a FCC packing (C^{FCC}) in the Z-direction can be expressed using the normal contact stiffness (k_N^{FCC}) and the tangential contact stiffness (k_T^{FCC}) considering the lattice configuration (see Appendix A):

$$C^{FCC} = 2\left(k_N^{FCC} + k_T^{FCC}\right) \tag{5.5.5}$$

where rotation of particles is not involved in the P-wave vibration mode. Note that the expressions for l^{FCC} and C^{FCC} depend on the direction considered in the FCC packing due to its transverse isotropy. Here the k_N^{FCC} and k_T^{FCC} data were extracted from the DEM results to calculate C^{FCC}; in the absence of DEM data, the k_N^{FCC} and k_T^{FCC} values can be estimated as explained in Chang et al. (1991) and Yimsiri & Soga (2000); a cross-check confirmed that this approach gives equivalent data. Referring to Eq. 2.6.6 an expression for the long-wave velocity, $V_{P,dispersion}$ can be developed to give:

$$V_{P,dispersion} = 2R\sqrt{\frac{k_N^{FCC} + k_T^{FCC}}{m}} \tag{5.5.6}$$

The maximum frequency, i.e. the low-pass frequency limit ($f_{low\text{-}pass}$), in Eq. 5.5.4 is obtained when $\kappa = \pi/l^{FCC}$:

$$f_{low-pass} = \frac{\omega_{low-pass}}{2\pi} = \frac{\sqrt{2}}{\pi}\sqrt{\frac{k_N^{FCC} + k_T^{FCC}}{m}} \tag{5.5.7}$$

The $V_{P,dispersion}$ and $f_{low\text{-}pass}$ values obtained for FCC samples at 0.01, 0.1, 1 and 10 MPa using Eqs. 5.5.6 and 5.5.7 are given in brackets in Table 5.8. In theory, the frequencies higher than $f_{low\text{-}pass}$ cannot penetrate into the FCC packing during P-wave propagation. Comparison between Eqs. 5.5.6 and 5.5.7 gives a linear relationship between $V_{P,dispersion}$ and $f_{low\text{-}pass}$ as:

$$V_{P,dispersion} = \sqrt{2}\,\pi R\, f_{low-pass} \tag{5.5.8}$$

Maximum transmitted frequency

The variation in the frequency content of the particle displacement responses with the distance from the transmitter wall was investigated as described above. Referring to Fig. 5.47, four samples were considered, given as test cases P-2, P-6, P-22 and P-30 in Table 5.8, all at $\sigma' = 100$ kPa. The maximum transmitted frequency ($f_{low\text{-}pass}$) varies with distance in all cases. The regular lattice structure of the FCC packing enables significantly higher frequencies to be transmitted in comparison with the random samples. Comparing with Fig. 5.23(a) for the same FCC sample where a lower input frequency of f_{in} = 20 kHz is used, Fig. 5.47(a) shows that higher frequencies can penetrate into the sample. The trend for $f_{low\text{-}pass}$ to reduce with distance for the

FCC sample resulted from the short recording time period (Mouraille & Luding 2008). The recording time was limited to exclude the interference in the signals due to the reflection at the receiver wall. For the random packing, $f_{low\text{-}pass}$ attained a stable value after a relatively small distance (e.g. 0.05 m), and the range of transmitted frequencies with distance are similar with data in Figs. 5.23(c) and (e), indicating the sample cannot pass frequency contents higher than the low-pass limit. Similar to the FCC sample, the higher frequencies attenuated at a distance > 0.25m due to the short recording time period. The stress-dependency of $f_{low\text{-}pass}$ was examined; Fig. 5.48 confirms the observations based on data in O'Donovan et al. (2016) and shows that $f_{low\text{-}pass}$ increases with stress level for the RDP samples (test cases P-7 and P-8).

To quantify the $f_{low\text{-}pass}$ value for each sample, $f_{low\text{-}pass}$ was taken to be the frequency associated with a displacement amplitude of 2% of the maximum value; these data are summarised in Table 5.8. The threshold of 2% was determined so that the $f_{low\text{-}pass}$ value obtained captures the visual analysis as illustrated in Figs. 5.47 and 5.48. For the FCC sample in Fig. 5.47(a), the DEM analysis gave $f_{low\text{-}pass}$ = 138.1 kHz, and this value agrees closely with $f_{low\text{-}pass}$ = 137.7 kHz calculated using the dispersion theory (Eq. 5.5.7), and f_{200} = 137.6 kHz for the highest eigenfrequency associated with the *P*-wave motion (Fig. 5.45(f)). It is also interesting to examine the link between $f_{low\text{-}pass}$ and the maximum eigenfrequency ($f_{i,max}$). Referring to Fig. 5.43, when the rotational degrees of freedom are included, the $f_{i,max}$ values are significantly larger than $f_{low\text{-}pass}$; e.g. for the RDP sample at 100 kPa $f_{i,max}$ = 216.1 kHz, while $f_{low\text{-}pass}$ is merely 21.9 kHz. However, for the FCC sample, when the rotational degrees of freedom are excluded from the eigenvalue decomposition analysis, $f_{low\text{-}pass} \approx f_{i,max}$ is confirmed; the $f_{low\text{-}pass}$ data obtained from the dispersion theory for the FCC sample are overlain on Fig. 5.43. It is confirmed that the result of the dispersion relation for the *P*-wave propagation though the FCC sample is not affected by excluding the rotational degrees of freedom as *P*-wave vibration modes does not induce any rotation of particles, i.e. purely translation. Thus for the case where only translational movement is allowed, there is good agreement amongst the $f_{low\text{-}pass}$ estimates calculated using dispersion theory, DEM analysis and eigenmode analysis.

Figures 5.49 and 5.50 show the dispersion relation for the samples discussed in Figs. 5.47 and 5.48. The results of eigenmode analyses summarised in Table 5.9 are overlain on the DEM data in Figs. 5.49 and 5.50 as open white circular symbols for the random samples and open black circular symbols for the FCC sample. For the FCC sample the theoretical dispersion relationship (Eq. 5.5.4) is also shown as a dashed line, and the three types of data give an identical dispersion relation (Fig. 5.49(a)). For the random samples, the dispersion relation is linear at lower f or κ, and this is captured by data obtained from the eigenmode analyses. The curvature of the dispersion relation at higher f or κ is not observed, and clear resonant vibration mode is

also not observed from the eigenmode analyses as discussed above (Figs. 5.45(g-l)). However, this should be noted that the DEM generated dispersion relation is effectively validated using the eigenmode analyses.

Figure 5.51 summarises the combined effects of void ratio and stress on $f_{low\text{-}pass}$. For the FCC samples at σ' = 1 and 10 MPa, f_{in} = 200 kHz was used (Fig. 5.41) so that $f_{low\text{-}pass}$ can be observed clearly. The observed trends exhibit a similarity with the V_P data in Figs. 5.11(a) and 5.16(a); $f_{low\text{-}pass}$ is observed to increase with increasing the stress and packing density. This suggests a close relationship between V_P and $f_{low\text{-}pass}$; Fig. 5.52 shows the V_P - $f_{low\text{-}pass}$ relationship in which the FCC sample type follows a linear relationship in a double logarithmic scale. This agrees with the dispersion relation theory where $f_{low\text{-}pass}$ is proportional to V_P (Eq. 5.5.8). For the random samples, the relationship differs slightly; if the data are grouped by e_{1kPa}, the V_P - $f_{low\text{-}pass}$ relationship is again linear, with an exponential slope of between 1.2 and 1.4; this slope increases with increasing e. Note that these data were generated assuming an (arbitrary) amplitude threshold of 2% of the maximum displacement; if the threshold amplitude is reduced the data shift upwards, but the slopes are almost invariant.

The low-pass wavelength ($\lambda_{low\text{-}pass}$) which corresponds with $f_{low\text{-}pass}$ for each sample was obtained using the DEM dispersion relation data (Figs. 5.49 and 5.50) (recall that $\lambda_{low\text{-}pass}=2\pi/\kappa_{low\text{-}pass}$); the resultant data are tabulated in Table 5.8, and Fig. 5.53 illustrates the variation in $\lambda_{low\text{-}pass}$ normalised by particle diameter (D) with e. The lattice geometry of the FCC samples is invariant and so the resultant $\lambda_{low\text{-}pass}$ is insensitive to change in σ', which contrasts from the observations for V_P or $f_{low\text{-}pass}$. In contrast, for the random samples there are variations in the sample topology with stress or μ_{prep}. For the random samples the $\lambda_{low\text{-}pass}$ values increase with increasing e, whereas $\lambda_{low\text{-}pass}$ is not sensitive to σ'. The data here give $\lambda_{low\text{-}pass}$ values of between about 7D to 18D. When the mechanical void ratio (e^*) was considered, a more linear variation between $\lambda_{low\text{-}pass}/D$ and e^* was observed in Fig. 5.53(b). Santamarina & Aloufi (1999) and Santamarina et al. (2001) assumed D to be an internal scale (α) of granular materials where $\lambda_{low\text{-}pass}$ = 2α, while Mouraille & Luding (2008) considered α to be the layer distance for a FCC sample, i.e., α = $\sqrt{2}R$. The DEM and eigenmode analysis data for the FCC packing support the observation by Mouraille & Luding (2008). For the random samples $\lambda_{low\text{-}pass}$ is density dependant (Fig. 5.53). It seems logical that there must be some link between e and layer distance; a lower e indicating a shorter layer distance. However, in a random packing this link cannot be simply determined. It seems more appropriate to qualify the conclusions in Santamarina et al. (2001) and Santamarina & Aloufi (1999) and state that $\lambda_{low\text{-}pass}$ depends on both e and particle size.

Following earlier geomechanics contributions (Greening & Nash, 2004; Alvarado & Coop, 2012), a frequency domain technique was applied that considered the gain factor: the ratio of the frequency spectra of the stress responses at the transmitter and receiver walls. The gain factor data for the FCC samples and random samples at σ' = 0.1, 1 and 10 MPa (test cases P-2-4 and P-6-8) are illustrated in Figs. 5.54(a) and (b) across the entire range of the received frequencies. The maximum value of the gain factors exceeded 1 because of the fixed-end condition at the receiver wall as discussed above. As is clear from the data presented in Figs. 5.47 and 5.48, higher frequencies propagated through the FCC samples in comparison with the random samples. Restricting consideration to the low frequency data < 10 kHz, Figs. 5.54(c) and (d) compare the gain factor with the resonant frequencies data from Table 5.9. The frequency interval at which local maxima in the gain factor are observed, roughly corresponds to the frequency interval at which the natural (resonant) frequencies are observed. However, the peaks in the gain factor did not correspond exactly with the resonant frequencies. This contrasts with the discussions/hypotheses in Alvarado & Coop (2012). Somfai et al. (2005) also did not find a perfect match between the resonant modes and actually excited frequencies using a 2D sample.

5.6 Summary

This chapter addressed a series of DEM simulations of planar wave propagation in both FCC and random samples. In all cases the particles were uniformly sized spheres to isolate inertia effects on the observed response, and the main conclusions are summarised in this section.

This study compared various methods to determine the wave velocity considering both the TD and FD methods applied to analyse the responses of the particles and the boundary walls. The detailed particle scale data provided direct measurement of the wave propagation and calculation of V_S ($V_{S,dL/dt}$). The dispersion relations (derived from particle-scale frequency domain analysis) gave a $V_{S,dispersion}$ within 2.0% of $V_{S,dL/dt}$. The $V_{S,dL/dt}$ values were within 3.0% of those obtained by applying the peak-peak interpretative approach ($V_{S,P\text{-}P}$) that is commonly used in experimental research. The frequency domain techniques based on the inserted and received signals at wall boundaries provided wave velocities ($V_{S,SP}$), and they were within 5.6% of $V_{S,dL/dt}$. These data indicate that provided the signal quality is adequate the simple peak-to-peak approach can be used to interpret bender element test data.

The influence of surface roughness on the small-strain stiffness and dynamic response of granular materials was explored. The V_S values decreased with increasing surface roughness (S_q), with consequent reductions in G_0. The maximum reduction in V_S or G_0 was 31.6% or 53.2%, respectively, when S_q= 0 and S_q = 1 μm were compared. The reduction in G_0 was substantial at a low σ', whereas it gradually disappeared as σ' increased. The power coefficient

(n) in the G_0 - σ' relationship increased with increasing S_q; however as σ' increased, n approached the value for $S_q = 0$ (Hertzian contact model). This finding qualitatively agrees with prior analytical modelling by Yimsiri & Soga (2000); the quantitative differences with the micromechanical model can largely be attributed to a number of simplifying assumptions in the analytical model.

The effect of pre-sliding partial slip on G_0 was also explored. The degree of partial slip depends on the ratio $T/\mu N$ at the contacts. For the FCC lattice packing, partial slip did not influence the response. The random packings were more sensitive to partial slip; accounting for partial slip gave a maximum reduction in V_S or G_0 of 3.3% or 6.4%, respectively. The influence of the spin resistance was also examined. Adding spin resistance to the HM contact model did not show measurable effects for either the FCC sample or the random sample.

The natural (fundamental) frequencies of the samples were obtained using eigenvalue decomposition of the mass and stiffness matrices derived from the DEM data. The resonant frequencies and corresponding wavelengths agreed with the dispersion relation obtained using the DEM data; for the FCC samples there was also agreement with the theoretical dispersion relationship (Eq. 5.5.4). The good agreement in the data serves as a cross-validation of the three approaches considered. The agreement also verifies the use of simple analysis of received signals to infer elastic parameters from laboratory geophysics experiments.

Increasing either stress or density resulted in a larger wave velocity and higher $f_{low\text{-}pass}$. A linear relationship between V_P and $f_{low\text{-}pass}$ was observed. The $\lambda_{low\text{-}pass}$ was not sensitive to the stress level but was affected considerably by the void ratio. For the FCC samples $\lambda_{low\text{-}pass}/D \approx \sqrt{2}$, i.e. $\lambda_{low\text{-}pass}$ is identical to twice the layer spacing. The ratio $\lambda_{low\text{-}pass}/D$ observed for the random samples varied between 7 and 18 depending on e. These data highlight that for non-crystalline materials it is difficult to quantitatively relate $\lambda_{low\text{-}pass}$ to a characteristic of the sample.

The relationship between the $f_{low\text{-}pass}$ and $f_{i,max}$ of samples was also investigated. For the P-wave propagation, $f_{low\text{-}pass} < f_{i,max}$ for all the samples; however, for the FCC samples $f_{low\text{-}pass} \approx f_{i,max}$ when the rotational degrees of freedom were excluded from the eigenvalue decomposition analysis. While the resonant frequencies were found close to the local maxima in the gain factor, the data presented here do not support earlier hypotheses that the peaks in the gain factor represent resonant frequencies, as the local maxima in the gain factor do not correspond with resonant frequencies corresponding to a motion that agreed with the applied disturbance; nor do they give an exact match with any other resonant frequency.

5.7 Tables

Table 5.1. Material properties and simulation parameters considered in Chapter 5.

Parameter	**Value**
Particle radius, R	2.54×10^{-3} m
Particle shear modulus, G_p	25 GPa
Particle Poisson's ratio, ν_p	0.2
Particle density, ρ_p	2230 kg/m^3
Inter-particle fiction coefficient, μ	0.2
Surface roughness, S_q	0, 0.5 and 1 μm
Viscous or Local damping	0.0 during wave propagation

Table 5.2. Summary of packing data at initial packing (σ' = 1 kPa).

Packing	Contact model	S_q μm	μ_{prep}	e_{1kPa}	e^*_{1kPa}	$\overline{C_N}_{1kPa}$	$\overline{C^*_N}_{1kPa}$
FCC	HM	0	0	0.353	0.353	12.0	12.0
R0			0	0.545	0.574	5.91	6.02
R002			0.02	0.581	0.615	5.64	5.75
R005			0.05	0.608	0.649	5.41	5.55
R01			0.1	0.630	0.696	5.05	5.25
R015			0.15	0.648	0.728	4.80	5.03
R025			0.25	0.674	0.830	4.30	4.70
R04			0.4	0.689	0.944	3.84	4.42
FCC	RM	0.5	0	0.352	0.352	12.0	12.0
R0			0	0.547	0.575	5.98	6.08
R015			0.15	0.649	0.735	4.84	5.09
FCC	RM	1	0	0.351	0.351	12.0	12.0
R0			0	0.544	0.570	6.00	6.09
R015			0.15	0.646	0.729	4.86	5.10

Table 5.3. Summary of *P*- and *S*- wave velocities using Hertz-Mindlin contact model (Section 5.3). Packing details including mechanical mean coordination number ($\overline{C_N^*}$) and corresponding void ratio (e^*) are also listed.

Test case	Packing	σ' MPa	μ_{prep} (μ_{wave})	e	e^*	$\overline{C_N}$	$\overline{C_N^*}$	$V_{P,P\text{-}P}$ m/s	$V_{S,P\text{-}P}$ m/s	vs
P-1	FCC	0.01	0 (0.1)	0.353		12.0		524	370	0.001
P-2		0.1		0.353		12.0		767	542	0.002
P-3		1		0.351		12.0		1128	796	0.005
P-4		10		0.341		12.0		1659	1167	0.011
P-5	R0	0.01	0 (0.1)	0.545	0.576	5.96	6.08	368	240	0.129
P-6		0.1		0.535	0.560	6.09	6.18	544	358	0.119
P-7		1		0.539	0.555	6.36	6.43	812	539	0.105
P-8		10		0.516	0.523	6.93	6.96	1235	830	0.089
P-9	R002	0.01	0.02 (0.12)	0.581	0.612	5.70	5.81	358	234	0.124
P-10		0.1		0.580	0.606	5.81	5.90	527	347	0.116
P-11		1		0.574	0.591	6.05	6.11	788	524	0.103
P-12		10		0.549	0.555	6.58	6.60	1207	809	0.091
P-13	R005	0.01	0.05 (0.15)	0.607	0.634	5.51	5.60	347	227	0.123
P-14		0.1		0.606	0.620	5.64	5.69	512	338	0.113
P-15		1		0.600	0.605	5.89	5.91	767	513	0.096
P-16		10		0.574	0.582	6.36	6.39	1178	794	0.084
P-17	R01	0.01	0.1 (0.2)	0.629	0.690	5.13	5.31	329	214	0.133
P-18		0.1		0.628	0.676	5.28	5.43	489	322	0.117
P-19		1		0.621	0.652	5.57	5.67	736	494	0.092
P-20		10		0.595	0.605	6.12	6.15	1139	772	0.074
P-21	R015	0.01	0.15 (0.25)	0.648	0.731	4.86	5.09	314	201	0.150
P-22		0.1		0.646	0.711	5.03	5.23	469	306	0.129
P-23		1		0.640	0.680	5.36	5.49	712	476	0.096
P-24		10		0.613	0.629	5.91	5.96	1106	752	0.070
P-25	R025	0.01	0.25 (0.35)	0.674	0.797	4.49	4.80	292	180	0.192
P-26		0.1		0.672	0.766	4.72	4.97	442	282	0.156
P-27		1		0.665	0.722	5.09	5.25	677	449	0.107
P-28		10		0.638	0.654	5.67	5.72	1063	723	0.070
P-29	R04	0.01	0.4 (0.5)	0.688	0.874	4.15	4.59	275	161	0.241
P-30		0.1		0.687	0.813	4.48	4.79	423	262	0.187
P-31		1		0.680	0.746	4.90	5.08	652	426	0.129
P-32		10		0.652	0.674	5.49	5.55	1032	697	0.082

Table 5.4. Best-fit curves for relationship between wave velocity and stress (σ').

Packing	$V_P = a\,\sigma'^{\,b}$ [m/s]			$V_S = a\,\sigma'^{\,b}$ [m/s]		
	a	b	R^2	a	b	R^2
FCC	1128.7	0.1669	1.000	795.6	0.1662	1.000
R0	819.0	0.1750	1.000	544.4	0.1792	1.000
R002	796.6	0.1759	0.999	529.8	0.1795	0.999
R005	776.1	0.1768	0.999	518.3	0.1810	0.999
R01	745.0	0.1795	0.999	498.5	0.1857	0.999
R015	719.6	0.1823	0.999	480.1	0.1909	1.000
R025	684.4	0.1869	0.999	451.8	0.2011	1.000
R04	659.1	0.1910	1.000	426.8	0.2121	1.000

Table 5.5. Best-fit curves for relationship between wave velocity and void ratio (e).

σ'	$V_P = C_1 + C_2\,e$			B	$V_S = C_1 + C_2\,e$			B
MPa	C_1	C_2	R^2	$(-C_1/C_2)$	C_1	C_2	R^2	$(-C_1/C_2)$
0.01	739.8	-662.1	0.954	1.117	551.8	-549.9	0.905	1.004
0.1	997.4	-821.6	0.952	1.214	709.2	-631.6	0.914	1.123
1	1444.1	-1149.8	0.974	1.256	979.6	-796.0	0.948	1.231
10	2041.5	-1530.2	0.978	1.334	1340.0	-967.7	0.965	1.385
mean				1.230				1.186
σ'	$V_P = C_1 + C_2\,e^*$			B	$V_S = C_1 + C_2\,e^*$			B
MPa	C_1	C_2	R^2	$(-C_1/C_2)$	C_1	C_2	R^2	$(-C_1/C_2)$
0.01	552.2	-322.0	0.992	1.715	401.5	-275.1	0.996	1.459
0.1	820.1	-491.6	0.996	1.668	577.7	-384.8	0.992	1.501
1	1274.1	-829.5	0.997	1.536	865.1	-579.0	0.986	1.494
10	1970.7	-1382.1	0.988	1.426	1296.0	-875.3	0.977	1.481
mean				1.586				1.484

Table 5.6. Shear wave velocities for FCC samples calculated using particle scale and boundary data (values in italics and parentheses give error relative to direct measurement of wave passage ($V_{dL/dt}$)) (Section 5.4).

Contact model	S_q μm	σ' MPa	e	$\overline{C_N}$	$V_{S,dL/dt}$ m/s	$V_{S,P\text{-}P}$ m/s		$V_{S,SP}$ m/s		$V_{S,dispersion}$ m/s	
HM	0	0.1	0.353	12	545	542	*(-0.4%)*	545	*(-0.2%)*	548	*(-0.6%)*
		0.2	0.352	12	612	610	*(-0.4%)*	612	*(0.0%)*	615	*(-0.4%)*
		0.3	0.352	12	656	652	*(-0.5%)*	655	*(-0.1%)*	657	*(-0.2%)*
		0.5	0.352	12	715	710	*(-0.7%)*	713	*(-0.2%)*	715	*(0.0%)*
		1	0.351	12	804	796	*(-1.0%)*	801	*(-0.3%)*	802	*(-0.3%)*
		10	0.341	12	1175	1167	*(-0.7%)*	1171	*(-0.3%)*	1167	*(-0.7%)*
HMD	0	0.1	0.353	12	544	542	*(-0.4%)*	546	*(-0.4%)*	547	*(-0.5%)*
		0.2	0.352	12	612	609	*(-0.4%)*	612	*(0.0%)*	614	*(-0.3%)*
		0.3	0.352	12	656	652	*(-0.5%)*	655	*(-0.1%)*	657	*(-0.2%)*
		0.5	0.352	12	715	710	*(-0.7%)*	712	*(-0.4%)*	715	*(0.0%)*
		1	0.351	12	803	796	*(-1.0%)*	800	*(-0.5%)*	802	*(-0.2%)*
		10	0.341	12	1175	1167	*(-0.7%)*	1169	*(-0.5%)*	1167	*(-0.7%)*
RM	0.5	0.1	0.352	12	432	431	*(0.0%)*	434	*(-0.6%)*	434	*(-0.6%)*
		0.2	0.351	12	535	533	*(-0.4%)*	536	*(-0.3%)*	539	*(-0.7%)*
		0.3	0.351	12	604	602	*(-0.4%)*	605	*(-0.1%)*	607	*(-0.5%)*
		0.5	0.35	12	665	661	*(-0.5%)*	664	*(-0.1%)*	667	*(-0.3%)*
		1	0.349	12	756	750	*(-0.8%)*	755	*(-0.2%)*	757	*(-0.1%)*
		10	0.339	12	1152	1144	*(-0.6%)*	1149	*(-0.3%)*	1144	*(-0.7%)*
	1	0.1	0.351	12	373	373	*(-0.2%)*	374	*(-0.5%)*	377	*(-1.0%)*
		0.2	0.351	12	461	461	*(-0.1%)*	463	*(-0.4%)*	465	*(-0.8%)*
		0.3	0.35	12	523	521	*(-0.3%)*	526	*(-0.5%)*	527	*(-0.7%)*
		0.5	0.349	12	613	611	*(-0.3%)*	614	*(-0.1%)*	616	*(-0.4%)*
		1	0.348	12	743	737	*(-0.8%)*	741	*(-0.2%)*	742	*(0.0%)*
		10	0.337	12	1130	1124	*(-0.6%)*	1127	*(-0.2%)*	1125	*(-0.5%)*

Table 5.7. Shear wave velocities for random samples calculated using particle scale and boundary data (values in italics and parentheses give error relative to direct measurement of wave passage ($V_{dL/dt}$)) (Section 5.4).

Packing	Contact model	S_q μm	σ' MPa	e	$\overline{C_N}$	$V_{S,dL/dt}$ m/s	$V_{S,P\text{-}P}$ m/s		$V_{S,SP}$ m/s		$V_{S,dispersion}$ m/s	
RDP	HM	0	0.1	0.544	6.02	365	368	*(0.9%)*	373	*(2.1%)*	370	*(1.3%)*
			0.2	0.543	6.07	411	415	*(0.8%)*	420	*(2.1%)*	417	*(1.4%)*
			0.3	0.543	6.1	442	445	*(0.7%)*	447	*(1.1%)*	447	*(1.1%)*
			0.5	0.542	6.15	483	486	*(0.6%)*	495	*(2.4%)*	488	*(1.1%)*
			1	0.54	6.24	546	549	*(0.5%)*	560	*(2.5%)*	552	*(1.0%)*
			10	0.519	6.69	831	831	*(0.0%)*	849	*(2.2%)*	837	*(0.8%)*
	HMD	0	0.1	0.544	6.02	355	358	*(0.9%)*	370	*(4.3%)*	359	*(1.2%)*
			0.2	0.543	6.07	400	404	*(1.1%)*	408	*(2.1%)*	406	*(1.5%)*
			0.3	0.543	6.1	428	432	*(1.0%)*	452	*(5.6%)*	435	*(1.6%)*
			0.5	0.542	6.15	470	474	*(0.8%)*	473	*(0.6%)*	477	*(1.4%)*
			1	0.54	6.24	531	533	*(0.5%)*	558	*(5.2%)*	538	*(1.4%)*
			10	0.519	6.69	811	807	*(-0.4%)*	850	*(4.8%)*	822	*(1.4%)*
	RM	0.5	0.1	0.544	6.13	324	327	*(0.9%)*	328	*(1.5%)*	327	*(1.1%)*
			0.2	0.543	6.16	382	384	*(0.8%)*	389	*(1.9%)*	386	*(1.2%)*
			0.3	0.543	6.19	414	417	*(0.6%)*	420	*(1.3%)*	416	*(0.4%)*
			0.5	0.542	6.23	457	460	*(0.5%)*	465	*(1.7%)*	462	*(1.0%)*
			1	0.539	6.3	523	525	*(0.3%)*	535	*(2.2%)*	528	*(0.9%)*
			10	0.518	6.7	827	825	*(-0.2%)*	840	*(1.6%)*	828	*(0.1%)*
		1	0.1	0.541	6.16	282	284	*(0.7%)*	285	*(0.9%)*	286	*(1.5%)*
			0.2	0.54	6.2	349	351	*(0.8%)*	355	*(1.9%)*	354	*(1.5%)*
			0.3	0.539	6.22	393	395	*(0.4%)*	398	*(1.3%)*	398	*(1.2%)*
			0.5	0.538	6.25	445	446	*(0.3%)*	453	*(1.7%)*	450	*(1.2%)*
			1	0.536	6.31	514	514	*(0.0%)*	516	*(0.6%)*	519	*(1.0%)*
			10	0.514	6.72	813	811	*(-0.2%)*	819	*(0.7%)*	819	*(0.7%)*
RLP	HM	0	0.1	0.646	5.03	301	306	*(1.7%)*	303	*(0.8%)*	306	*(1.6%)*
			0.2	0.645	5.12	343	349	*(1.7%)*	340	*(-0.8%)*	348	*(1.4%)*
			0.3	0.644	5.17	371	377	*(1.5%)*	371	*(0.0%)*	376	*(1.4%)*
			0.5	0.643	5.25	410	416	*(1.5%)*	409	*(-0.2%)*	416	*(1.4%)*
			1	0.64	5.36	470	476	*(1.3%)*	466	*(-0.7%)*	476	*(1.4%)*
			10	0.613	5.91	749	752	*(0.5%)*	753	*(0.5%)*	756	*(1.0%)*
	HMD	0	0.1	0.646	5.03	292	300	*(2.7%)*	296	*(1.3%)*	298	*(1.8%)*
			0.2	0.645	5.12	332	341	*(2.9%)*	340	*(2.4%)*	329	*(-0.7%)*
			0.3	0.644	5.17	362	368	*(1.7%)*	369	*(2.0%)*	367	*(1.5%)*
			0.5	0.643	5.25	396	406	*(2.3%)*	408	*(2.9%)*	400	*(1.0%)*
			1	0.64	5.36	457	464	*(1.4%)*	472	*(3.2%)*	464	*(1.5%)*
			10	0.613	5.91	730	731	*(0.2%)*	749	*(2.5%)*	742	*(1.6%)*
	RM	0.5	0.1	0.646	5.21	266	272	*(2.5%)*	267	*(0.7%)*	273	*(2.7%)*
			0.2	0.645	5.28	315	322	*(2.2%)*	316	*(0.2%)*	321	*(1.8%)*
			0.3	0.644	5.33	346	353	*(2.0%)*	348	*(0.7%)*	352	*(1.8%)*
			0.5	0.642	5.4	387	394	*(1.8%)*	390	*(0.8%)*	394	*(1.8%)*
			1	0.639	5.5	451	458	*(1.6%)*	456	*(1.1%)*	458	*(1.6%)*
			10	0.611	5.98	747	752	*(0.6%)*	757	*(1.4%)*	756	*(1.2%)*
		1	0.1	0.643	5.28	237	244	*(3.0%)*	241	*(1.6%)*	242	*(2.0%)*
			0.2	0.641	5.34	294	302	*(2.6%)*	299	*(1.7%)*	300	*(2.0%)*
			0.3	0.64	5.38	330	338	*(2.2%)*	334	*(1.2%)*	336	*(1.9%)*
			0.5	0.638	5.44	376	383	*(1.8%)*	377	*(0.3%)*	382	*(1.7%)*
			1	0.635	5.54	442	447	*(1.2%)*	442	*(-0.1%)*	442	*(0.0%)*
			10	0.607	6.01	735	739	*(0.6%)*	748	*(1.8%)*	743	*(1.1%)*

Table 5.8. DEM results on *P*-wave velocity ($V_{P,dL/dt}$), low-pass frequency ($f_{low\text{-}pass}$), and low-pass wavelength ($\lambda_{low\text{-}pass}$) in Section 5.5. Theoretical values of $V_{P,dL/dt}$ (Eq. 5.5.6) and $f_{low\text{-}pass}$ (Eq. 5.5.7) for FCC samples are presented in brackets.

Test case	Packing	σ' MPa	μ_{prep} (μ_{wave})	e	$\overline{C_N}$	$V_{P,dL/dt}$ m/s	$f_{low\text{-}pass}$ kHz	$\lambda_{low\text{-}pass}/D$
P-1	FCC	0.01	0 (0.1)	0.353	12.0	523 (529)	94.14 (93.8)	1.4
P-2		0.1		0.353	12.0	767 (777)	138.1 (137.7)	1.4
P-3		1		0.351	12.0	1125 (1140)	202.8 (202.1)	1.4
P-4		10		0.341	12.0	1645 (1673)	294.5 (296.4)	1.4
P-5	R0	0.01	0 (0.1)	0.545	5.96	360	14.5	8.9
P-6		0.1		0.544	6.08	535	21.9	8.9
P-7		1		0.539	6.36	801	36.9	8.0
P-8		10		0.516	6.93	1229	65.2	7.0
P-9	R002	0.01	0.02 (0.12)	0.581	5.68	355	13.8	8.0
P-10		0.1		0.580	5.79	527	19.9	9.2
P-11		1		0.574	6.04	793	31.7	8.5
P-12		10		0.549	6.57	1216	56.0	7.3
P-13	R005	0.01	0.05 (0.15)	0.607	5.45	345	11.8	9.7
P-14		0.1		0.606	5.57	512	18.0	10.4
P-15		1		0.600	5.83	771	29.0	9.2
P-16		10		0.574	6.35	1186	49.5	8.9
P-17	R01	0.01	0.1 (0.2)	0.629	5.11	327	9.5	11.0
P-18		0.1		0.628	5.26	492	15.7	10.0
P-19		1		0.621	5.56	741	26.0	9.9
P-20		10		0.595	6.11	1150	45.4	8.7
P-21	R015	0.01	0.15 (0.25)	0.648	4.83	312	8.3	13.6
P-22		0.1		0.646	5.03	474	14.1	10.6
P-23		1		0.640	5.34	717	23.3	10.4
P-24		10		0.613	5.89	1119	44.1	7.3
P-25	R025	0.01	0.25 (0.35)	0.674	4.45	290	6.3	17.2
P-26		0.1		0.672	4.68	444	11.3	12.9
P-27		1		0.665	5.07	680	19.4	12.6
P-28		10		0.638	5.65	1070	37.4	10.1
P-29	R04	0.01	0.4 (0.5)	0.688	4.09	273	5.0	17.6
P-30		0.1		0.687	4.40	418	8.7	16.8
P-31		1		0.680	4.85	648	16.4	13.6
P-32		10		0.652	5.47	1040	33.7	9.8

Table 5.9. Resonant frequency (f_r) and corresponding wavenumber (κ_r) of samples at $\sigma' = 100$ kPa obtained from eigenmode analysis (Section 5.5).

Test case	e			Resonance mode									
				1	2	3	4	5	6	7	8	9	10
P-2 (FCC)	0.353	f_r	kHz	1.06	2.13	3.19	4.25	5.32	6.38	7.44	8.51	9.57	10.63
		κ_r	rad/m	8.73	17.5	26.2	34.9	43.6	52.4	61.1	69.8	78.6	87.3
P-6 (R0)	0.544	f_r	kHz	0.76	1.52	2.28	3.04	3.80	4.55	5.30	6.05	6.80	7.55
		κ_r	rad/m	8.73	17.5	26.2	34.9	43.6	52.4	61.1	69.8	78.5	87.3
P-10 (R002)	0.580	f_r	kHz	0.73	1.47	2.20	2.93	3.66	4.39	5.11	5.84	6.54	7.29
		κ_r	rad/m	8.70	17.4	26.1	34.8	43.5	52.2	60.9	69.6	78.3	87.0
P-14 (R005)	2.353	f_r	kHz	0.70	1.42	2.12	2.83	3.55	4.24	4.92	5.61	6.33	7.01
		κ_r	rad/m	8.64	17.3	25.9	34.6	43.2	51.9	60.5	69.1	77.8	86.4
P-18 (R01)	0.606	f_r	kHz	0.68	1.36	2.00	2.69	3.34	3.99	4.66	5.31	5.96	6.61
		κ_r	rad/m	8.60	17.2	25.8	34.4	43.0	51.6	60.2	68.8	77.4	86.0
P-22 (R015)	0.628	f_r	kHz	0.60	1.31	1.90	2.54	3.20	3.81	4.45	5.06	5.69	6.28
		κ_r	rad/m	8.57	17.1	25.7	34.3	42.8	51.4	60.0	68.5	77.1	85.7
P-26 (R025)	0.646	f_r	kHz	0.58	1.20	1.78	2.36	2.95	3.53	4.12	4.67	5.32	5.80
		κ_r	rad/m	8.51	17.0	25.5	34.0	42.5	51.1	59.6	68.1	76.6	85.1
P-30 (R04)	0.687	f_r	kHz	0.55	1.13	1.66	2.24	2.81	3.35	3.88	4.33	4.93	5.39
		κ_r	rad/m	8.48	17.0	25.4	33.9	42.4	50.9	59.4	67.8	76.3	84.8

5.8 Figures

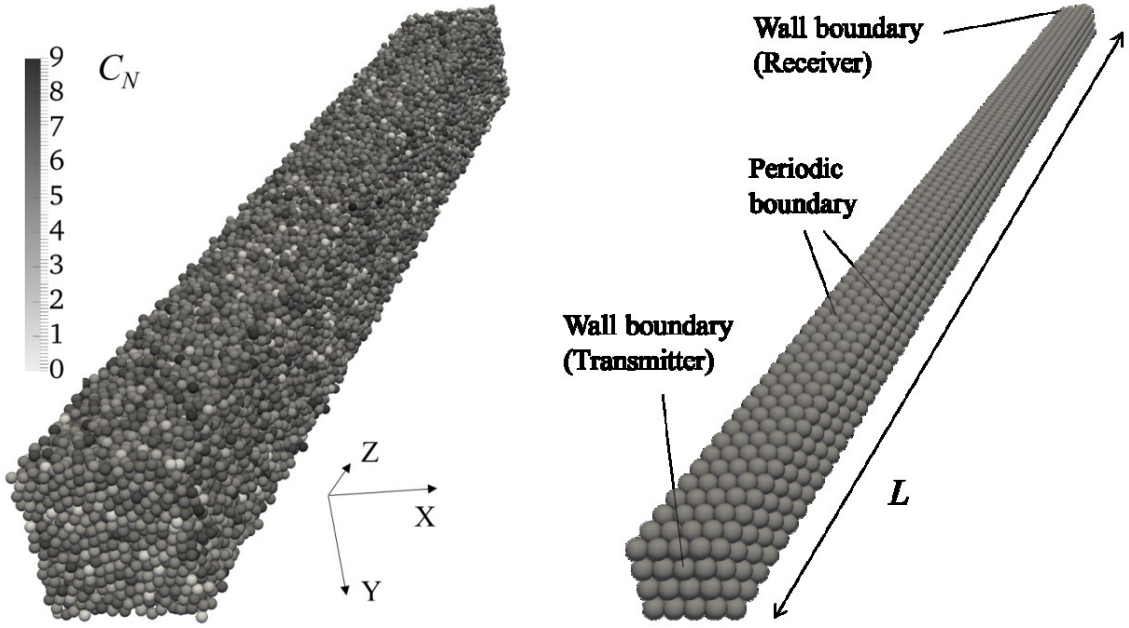

(a) (b)

Figure 5.1. Sample configurations. (a) Random configuration packing at σ' = 1kPa with μ_{prep} = 0.15. Grey-scale corresponds to coordination number per particle (C_N). (b) FCC packing with 200 layers.

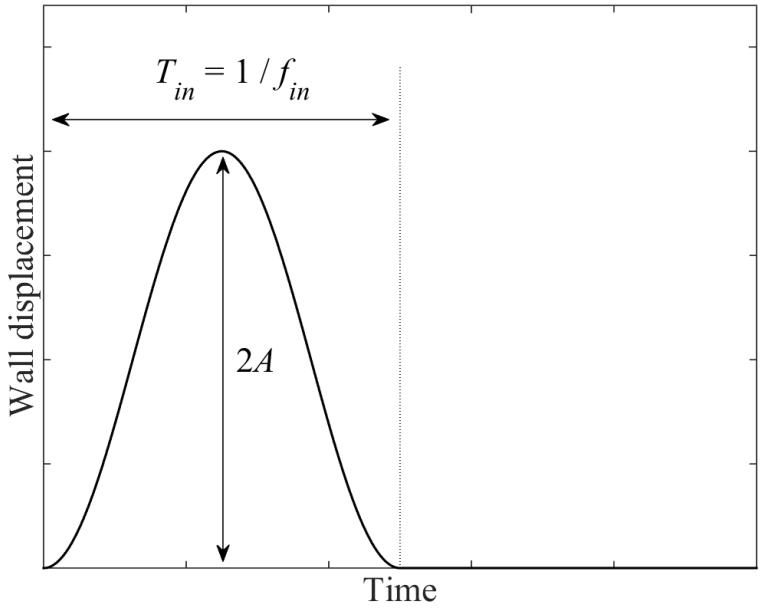

Figure 5.2. Displacement of transmitter wall to insert stress wave into sample. Range of double amplitude (2A), and frequency (f_{in}) of inserted wave considered in simulations are between 5 to 20 nm, and between 20 kHz and 200 kHz, respectively.

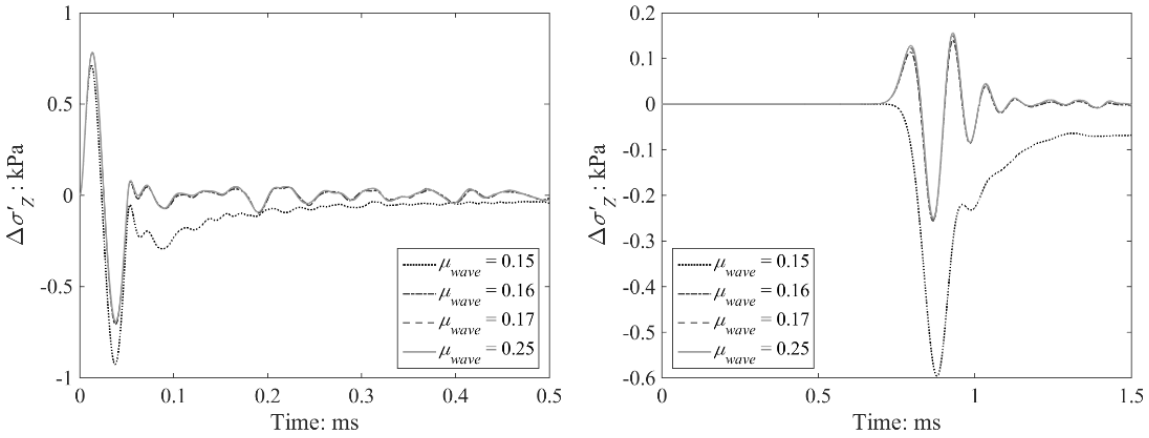

(a) (b)

Figure 5.3. Influence of inter-particle friction (μ_{wave}) on observed boundary response for wave propagation simulations with $\mu_{wave} \geq \mu_{prep}$ for μ_{prep} = 0.15 (random packing) at σ' = 100 kPa. (a) Stress response of transmitter wall. (b) Stress response of receiver wall.

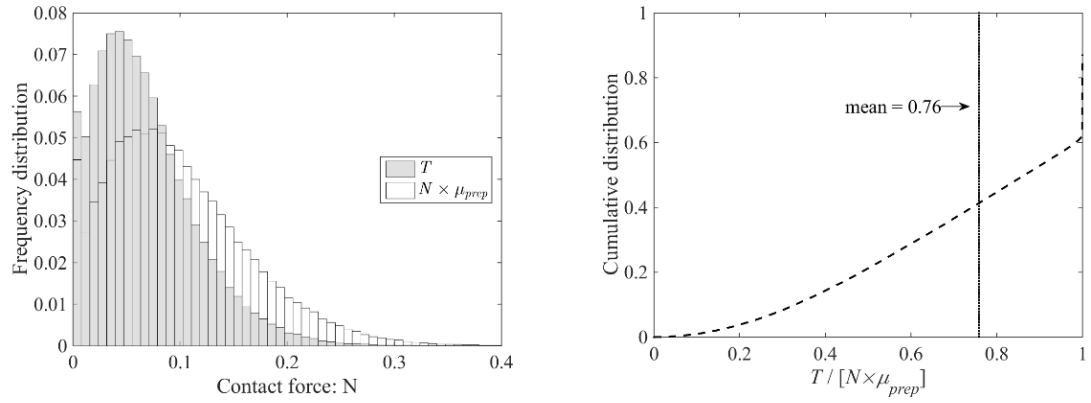

(a) (b)

Figure 5.4. Contact force distribution after isotropic compression (random sample with μ_{prep} = 0.15 at σ' = 100 kPa). (a) Frequency distribution of slip limit ($N \times \mu_{prep}$) and tangential contact force (T). (b) Cumulative distribution of ratio of tangential contact force to slip limit.

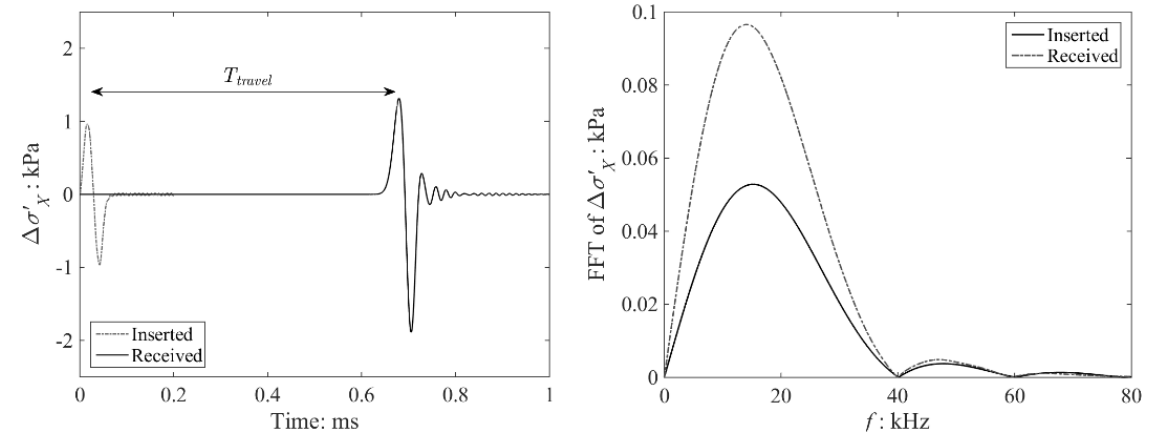

(a) (b)

Figure 5.5. Representative result of variation in wall stress with time using FCC sample with μ_{wave} = 0.2 at σ' = 100 kPa. (a) Travel time estimation using peak-to-peak method. (b) FFT amplitude of wall stress with frequency.

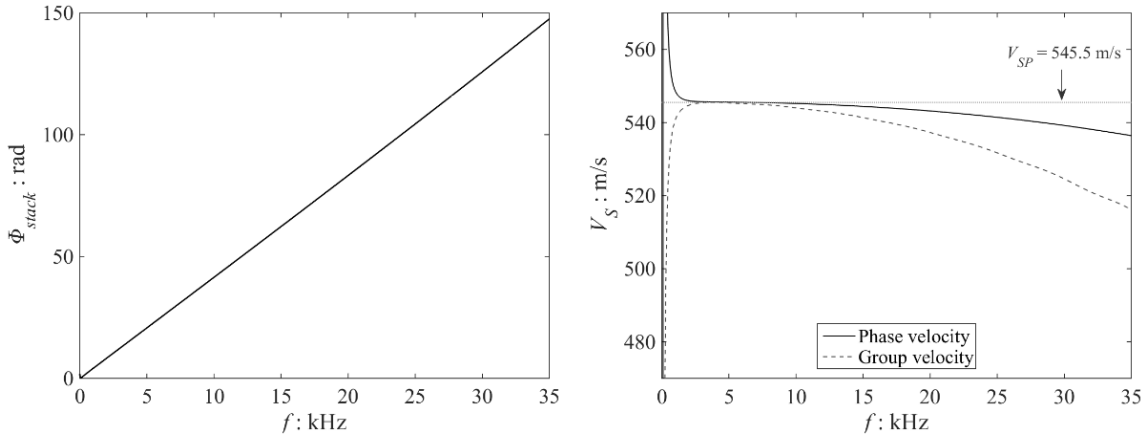

(a) (b)

Figure 5.6. Wave velocity estimation using stacked phase method using FCC sample with μ_{wave} = 0.2 at σ' = 100 kPa. (a) Relationship between stacked phase (Φ_{stack}) and frequency (f). (b) Variation in phase and group velocities with estimated wave velocity ($V_S = V_{SP}$).

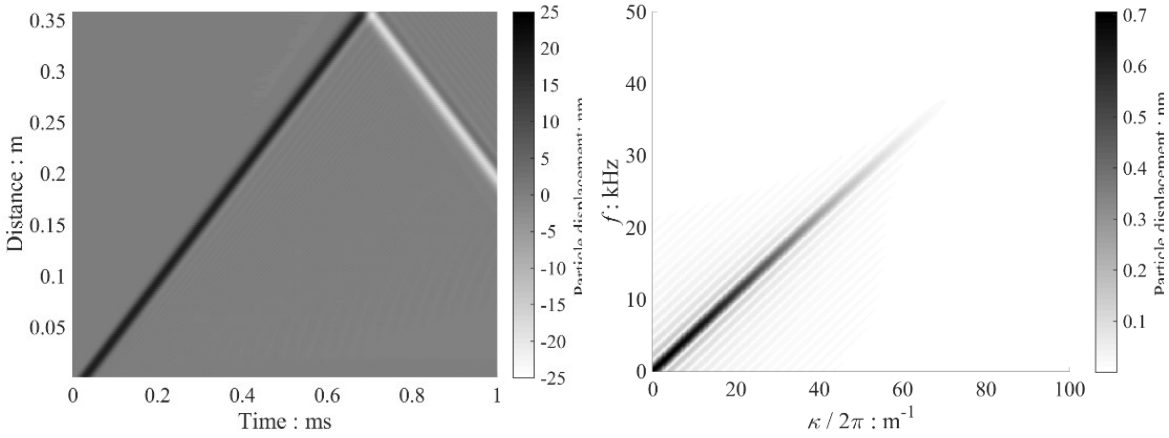

(a) (b)

Figure 5.7. Peak displacement method and dispersion method to deduce wave velocities using FCC sample with μ_{wave} = 0.2 at σ' = 100 kPa. (a) Variation of particle displacement with time and distance from transmitter wall. (b) Dispersion relation of *S*-wave.

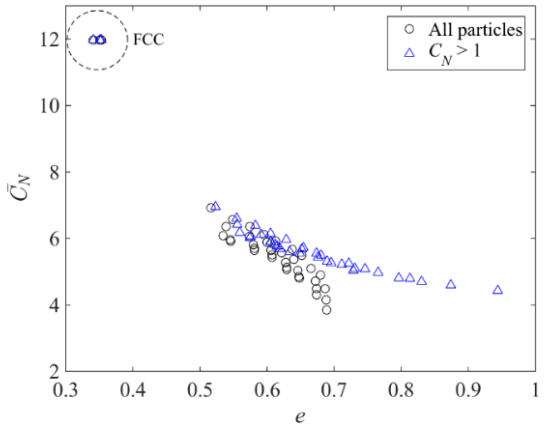

Figure 5.8. Relationship between mean coordination number and void ratio at isotropic confining stresses of 1 kPa, 10 kPa, 100 kPa, 1 MPa, and 10 MPa. The relationship for mechanical mean coordination number and corresponding void ratio is also plotted.

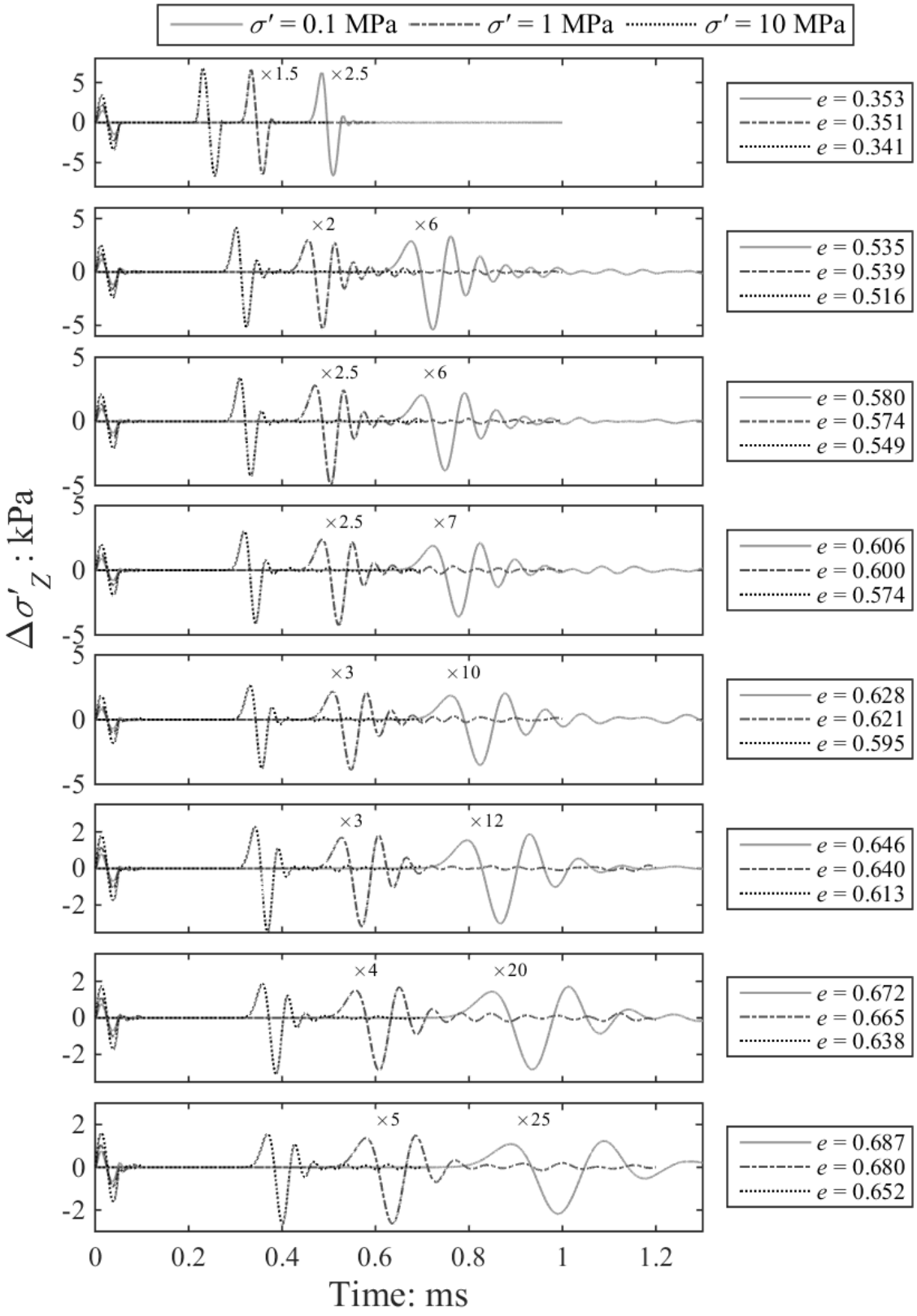

Figure 5.9. Time histories of stress response of transmitter and receiver walls during *P*-wave propagation at stresses of 0.1, 1 and 10 MPa. Sample types are FCC, R0, R002, R005, R01, R015, R025 and R04 (Table 5.3) from top to bottom. Void ratios were affected by stress level. Amplitude of received waves are magnified (scaled) using the scale factors indicated.

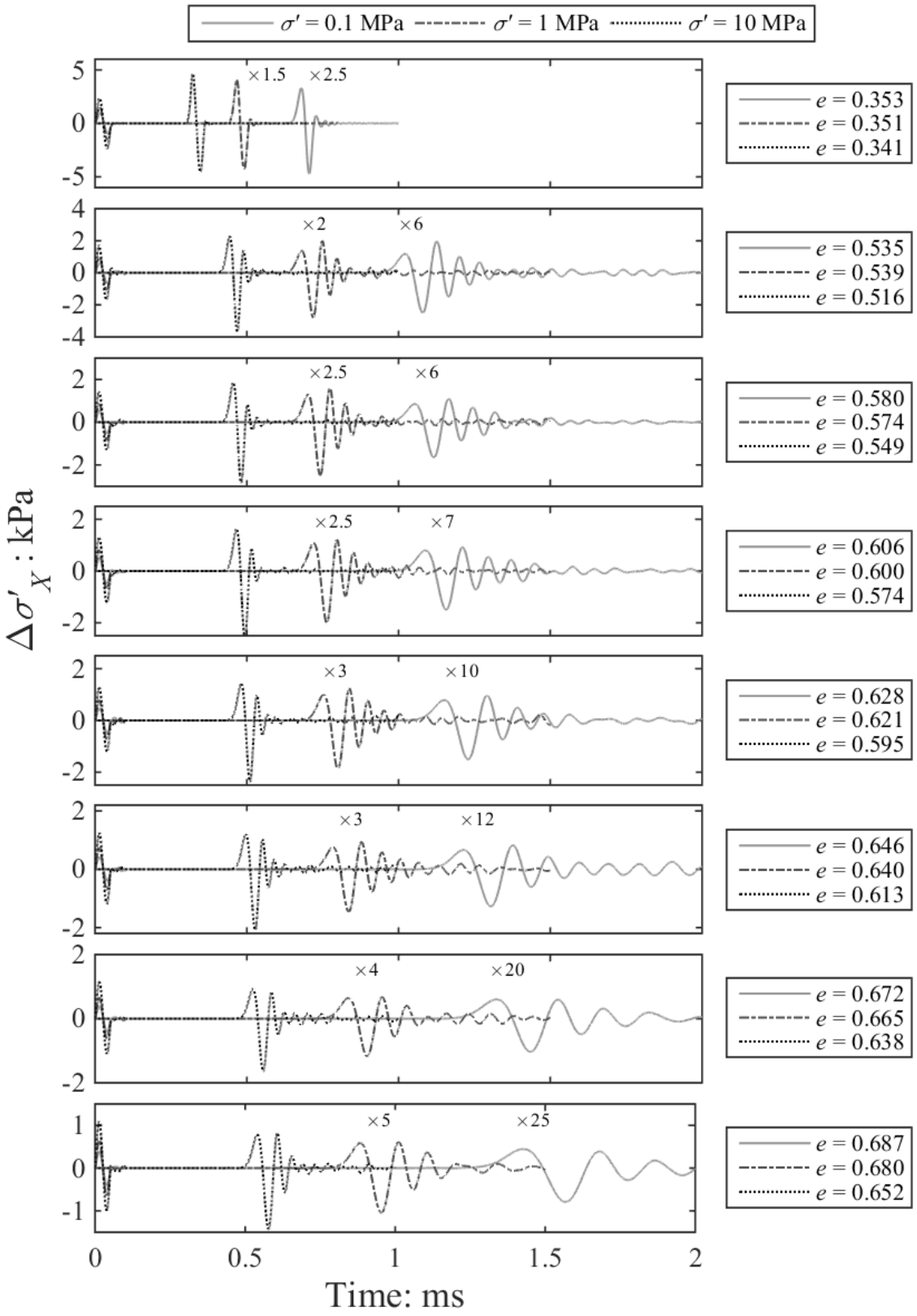

Figure 5.10. Time histories of stress response of transmitter and receiver walls during *S*-wave propagation at stresses of 0.1, 1 and 10 MPa. Sample types are FCC, R0, R002, R005, R01, R015, R025 and R04 (Table 5.3) from top to bottom. Void ratios were affected by stress level. Amplitude of received waves are magnified (scaled) using the scale factors indicated.

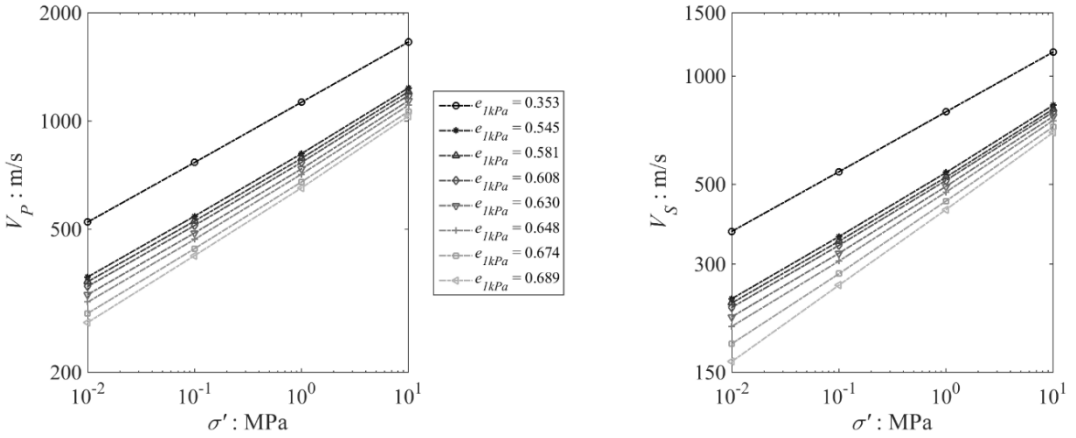

(a) (b)

Figure 5.11. Variation in wave velocities with isotropic stress (σ') for all the FCC and random samples listed in Table 5.3. (a) *P*-wave velocity. (b) *S*-wave velocity.

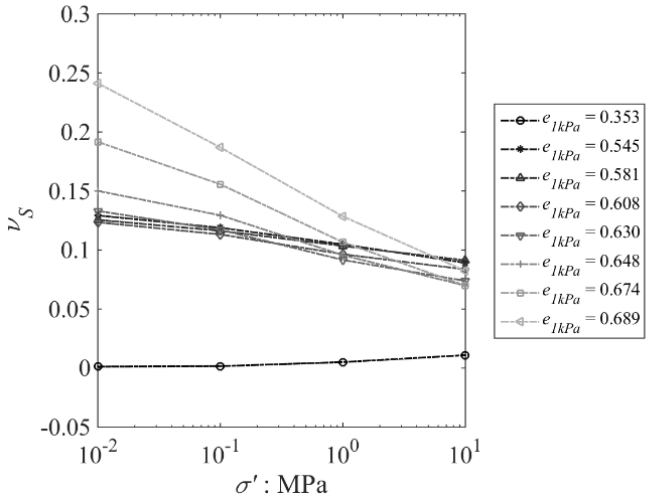

Figure 5.12. Variation in sample Poisson's ratio with isotropic stress (σ') for all the FCC and random samples listed in Table 5.3.

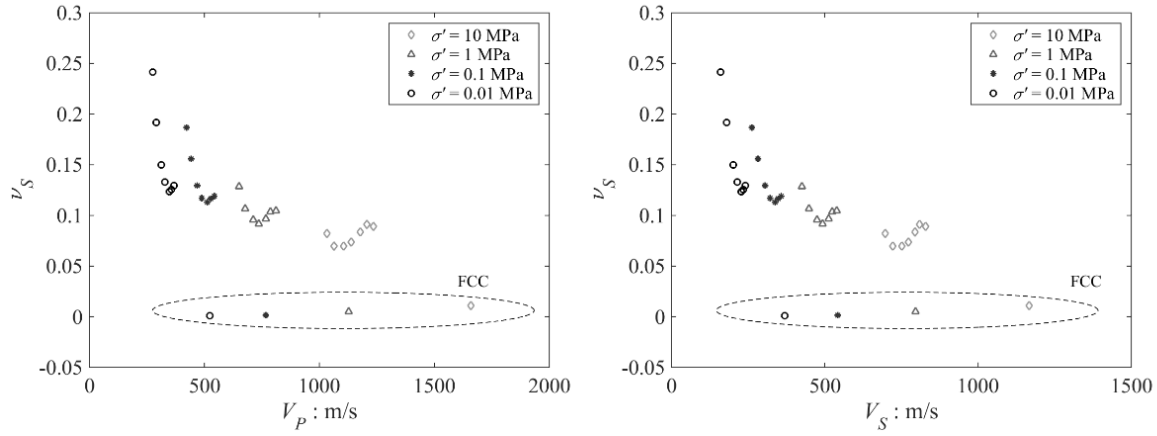

(a) (b)

Figure 5.13. Relationship between (a) *P*-wave velocity and sample Poisson's ratio, and (b) *S*-wave velocity and sample Poisson's ratio for all the FCC and random samples listed in Table 5.3.

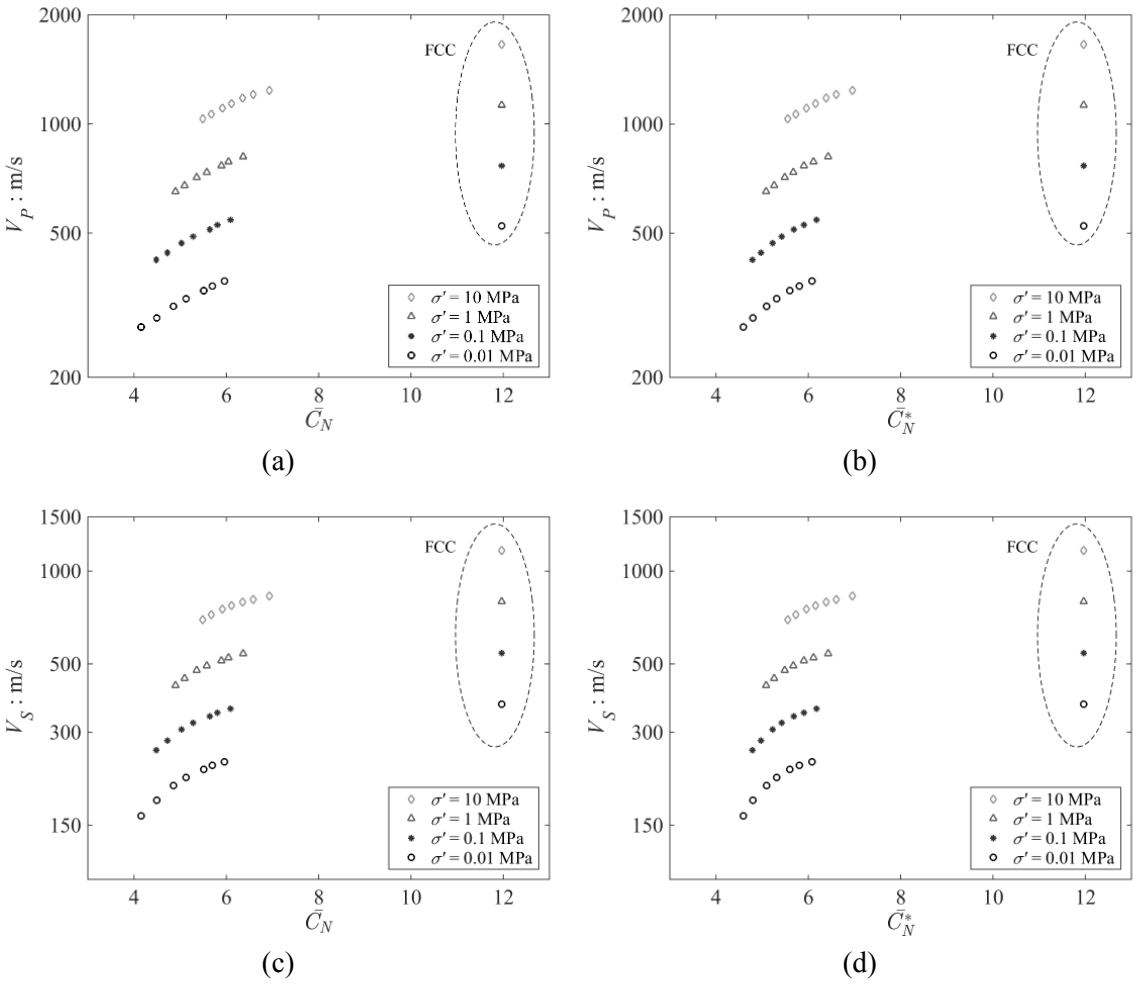

Figure 5.14. Variation in *P*- and *S*-wave velocities (V_P and V_S) with mean coordination number ($\overline{C_N}$) or mechanical mean coordination number ($\overline{C_N^*}$) for all the FCC and random samples listed in Table 5.3. (a) Relationship between V_P and $\overline{C_N}$. (b) Relationship between V_P and $\overline{C_N^*}$. (c) Relationship between V_S and $\overline{C_N}$. (d) Relationship between V_S and $\overline{C_N^*}$.

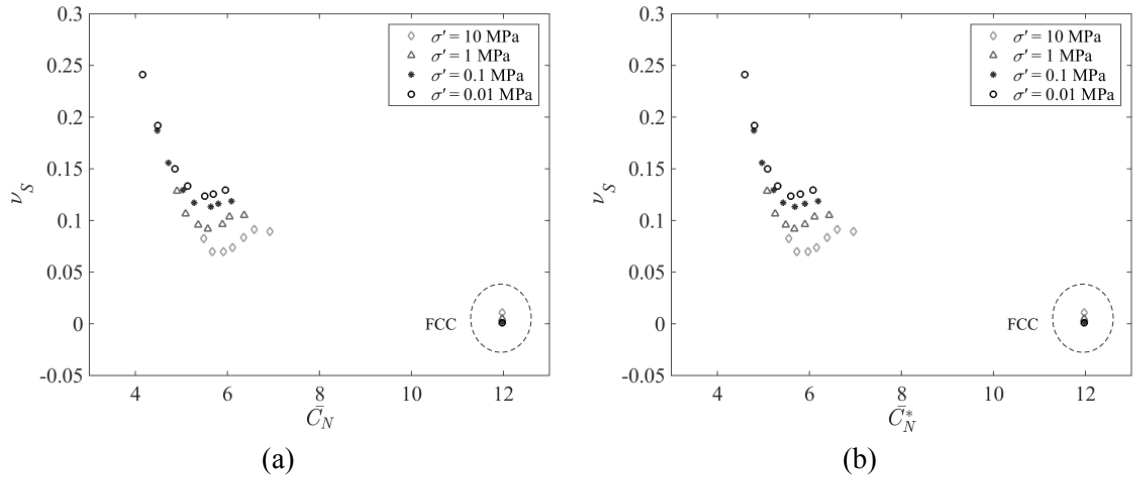

Figure 5.15. Variation in sample Poisson's ratio (ν_S) with (a) mean coordination number ($\overline{C_N}$), and (b) mechanical mean coordination number ($\overline{C_N^*}$) for all the FCC and random samples listed in Table 5.3.

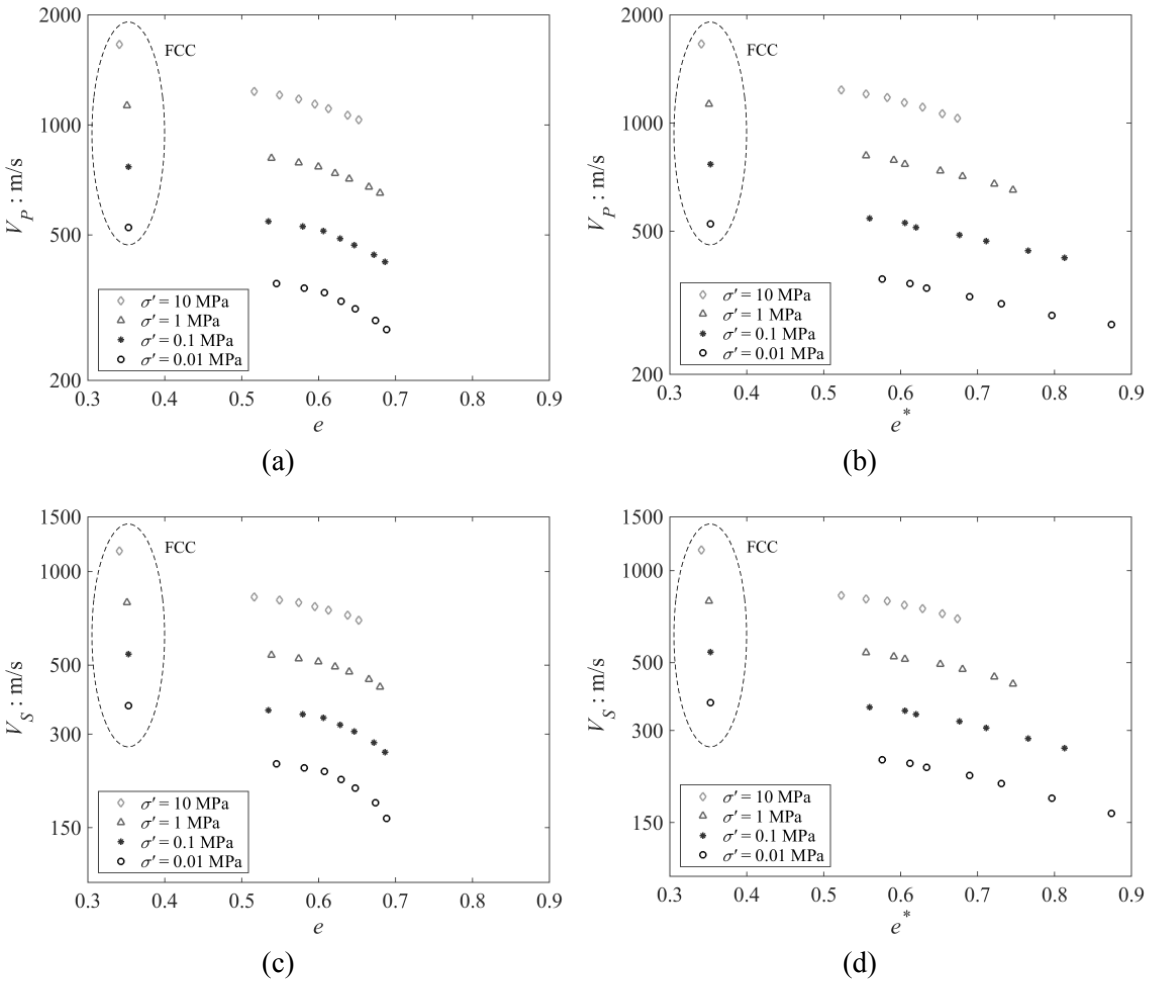

Figure 5.16. Variation in *P*- and *S*-wave velocities (V_P and V_S) with void ratio (e) or mechanical void ratio (e^*). (a) Relationship between V_P and e for all the FCC and random samples listed in Table 5.3. (b) Relationship between V_P and e^*. (c) Relationship between V_S and e. (d) Relationship between V_S and e^*.

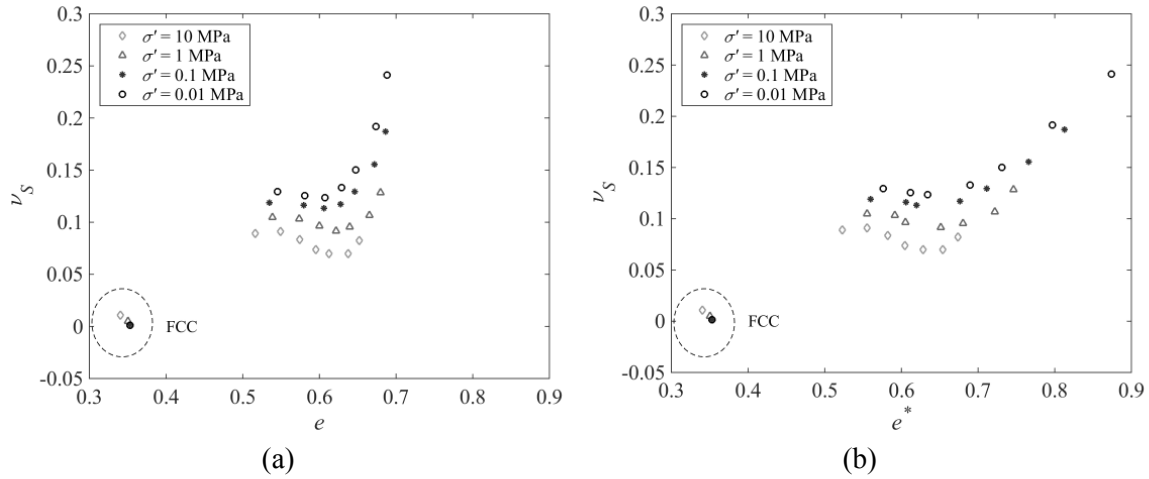

Figure 5.17. Variation in sample Poisson's ratio (ν_S) with (a) void ratio e, and (b) mechanical void ratio e^* for all the FCC and random samples listed in Table 5.3.

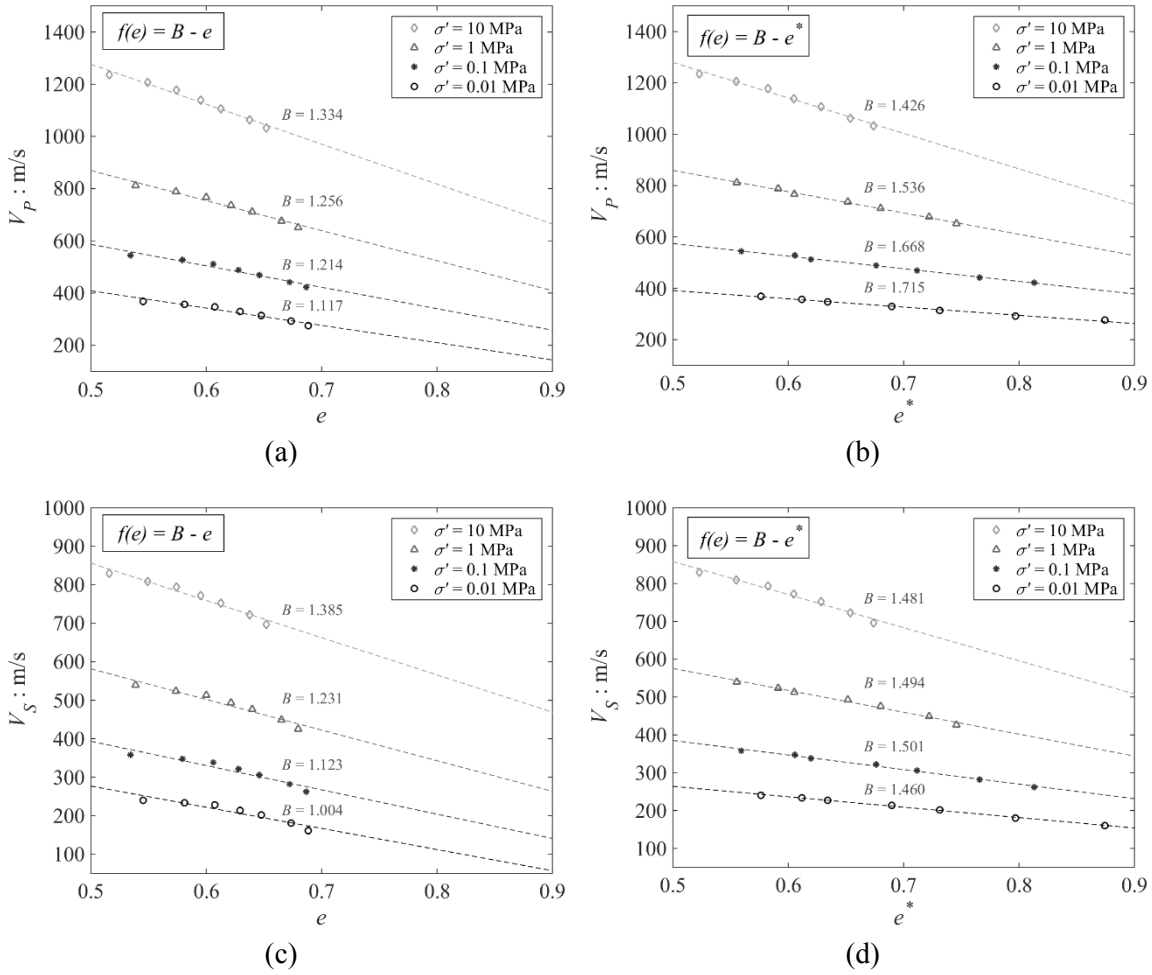

Figure 5.18. Linear curve fitting to variation in *P*- and *S*-wave velocities (V_P and V_S) with void ratio (e) or mechanical void ratio (e^*) for random samples. (a) Relationship between V_P and e. (b) Relationship between V_P and e^*. (c) Relationship between V_S and e. (d) Relationship between V_S and e^*.

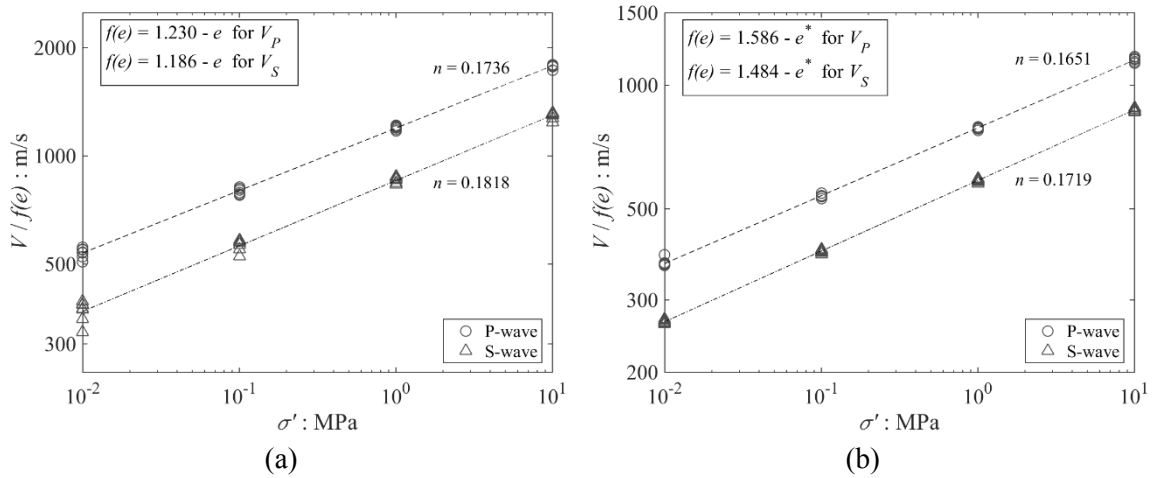

Figure 5.19. Variation in wave velocities normalised by void ratio function (*f(e)*) with isotropic stress for random samples. (a) *f(e)* is obtained based on bulk void ratio (e). (b) *f(e)* is obtained based on mechanical void ratio (e^*).

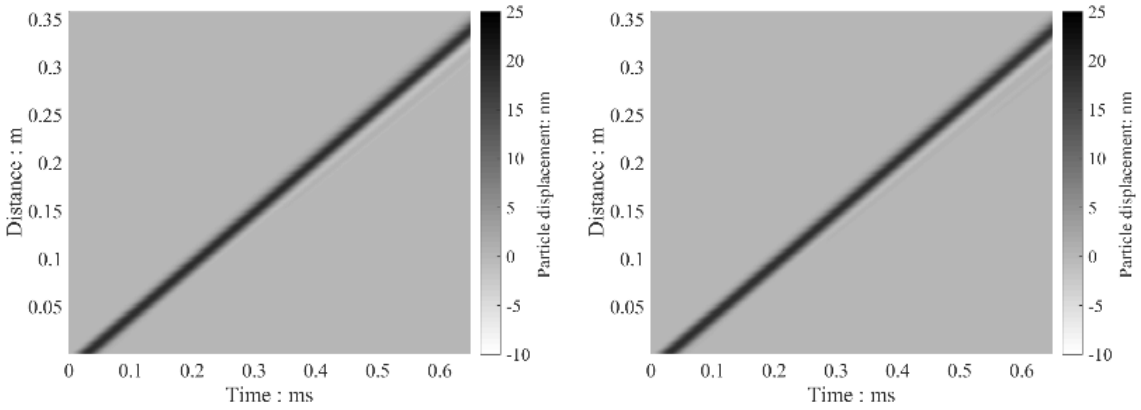

(a) FCC, HM (b) FCC, HMD

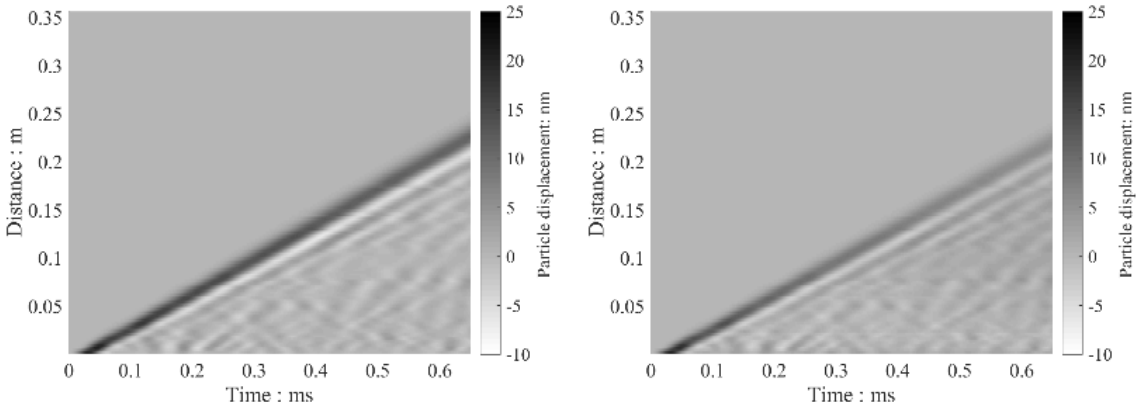

(c) RDP, HM (d) RDP, HMD

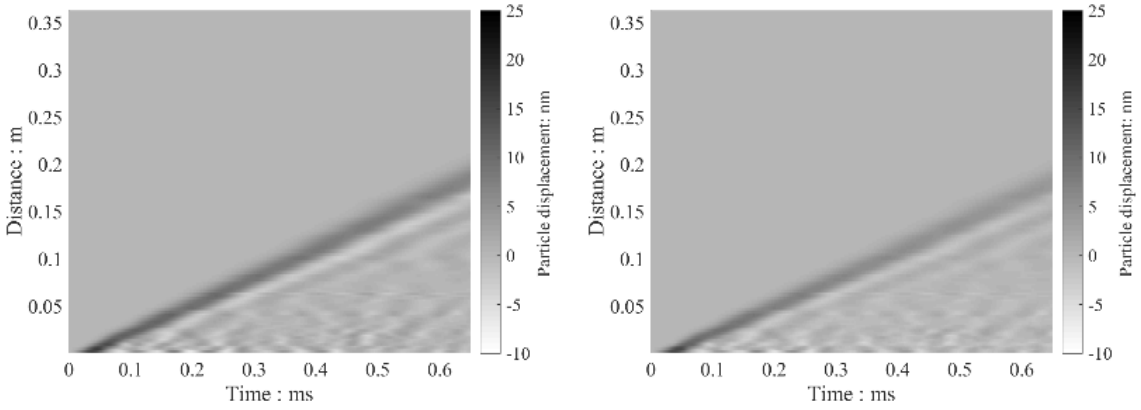

(e) RLP, HM (f) RLP, HMD

Figure 5.20. Variation of particle displacements in shear (X-) direction with time and distance from the transmitter wall at σ' = 100 kPa. (a) FCC sample with HM model, (b) FCC sample with HMD model, (c) RDP sample with HM model, (d) RDP sample with HMD model, (e) RLP with HM model, and (f) RLP sample with HMD model.

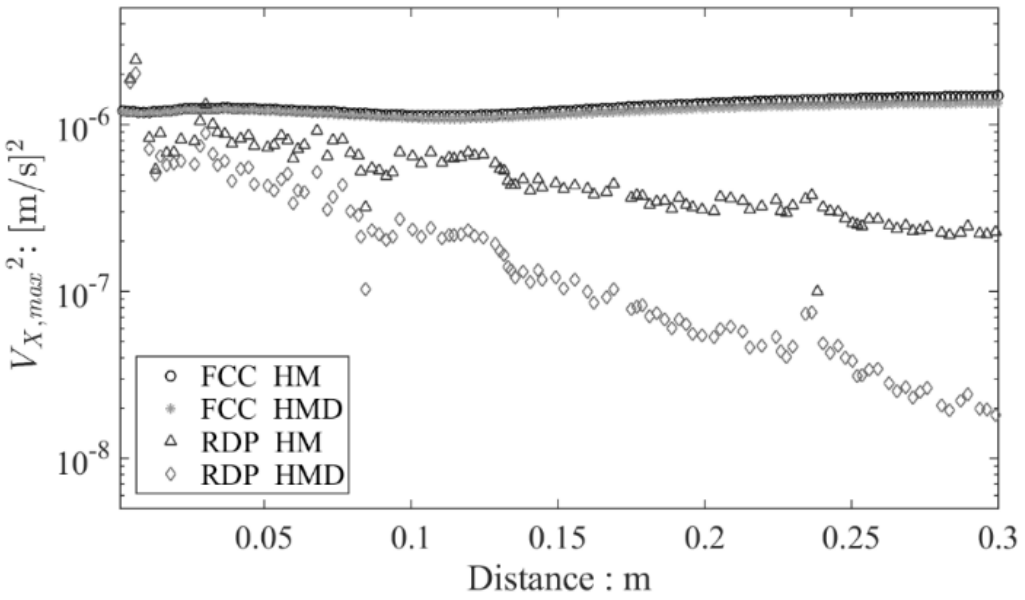

Figure 5.21. Variation in square of maximum particle velocity ($V_{X,max}$) in excitation direction with position along a line from transmitter to receiver walls at σ' = 100 kPa.

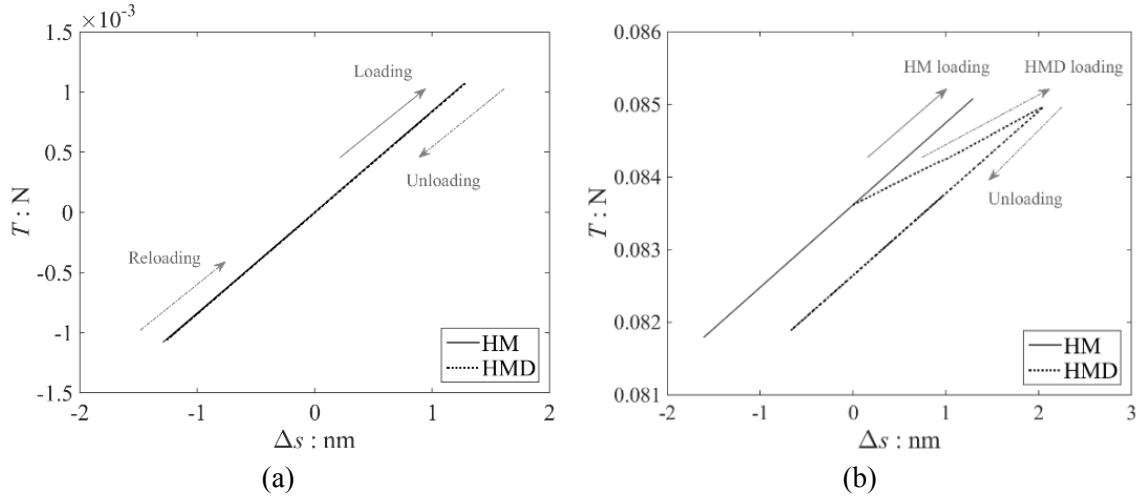

Figure 5.22. Representative examples of tangential contact interaction of samples at σ' = 100 kPa with μ_{wave} = 0.2 during wave propagation simulation. (a) FCC samples with N = 0.228 N, and. (b) RDP samples with N = 0.557N.

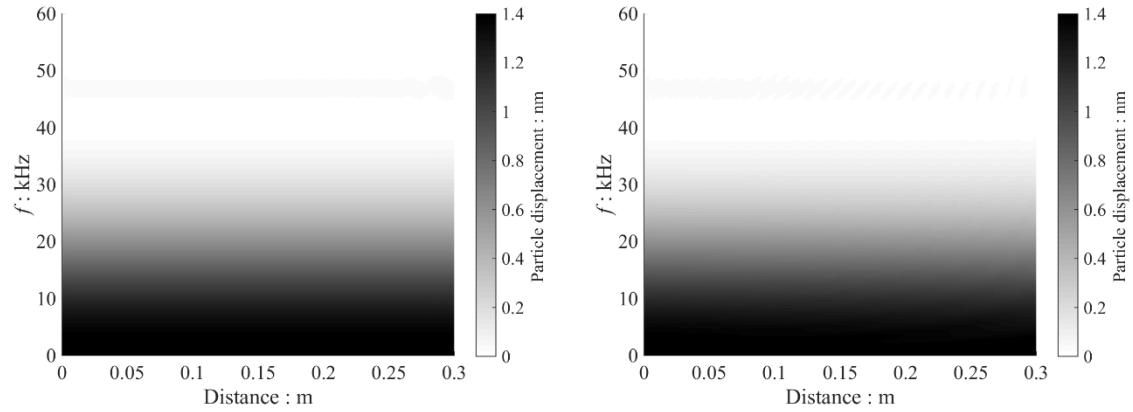

(a) FCC, HM

(b) FCC, HMD

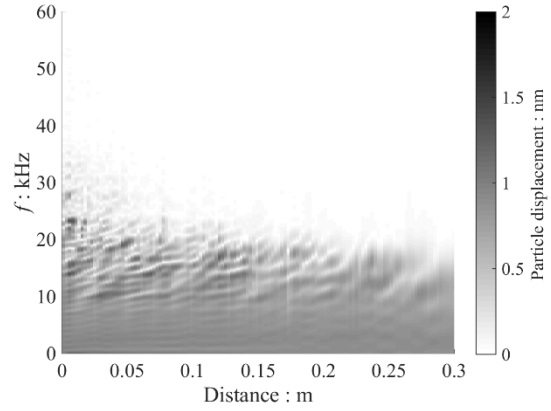

(c) RDP, HM

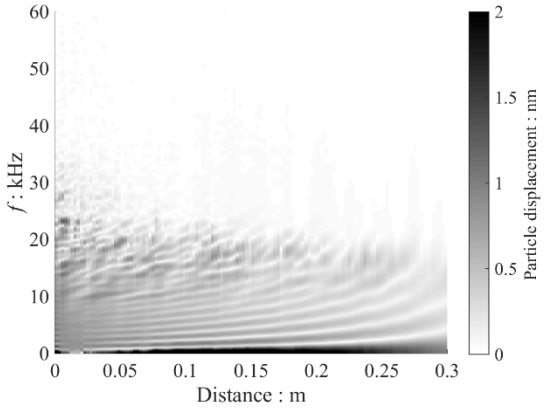

(d) RDP, HMD

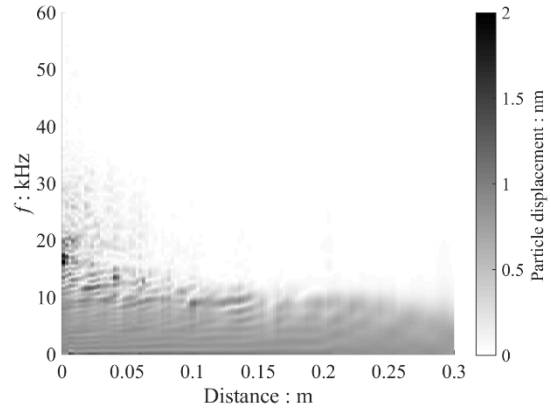

(e) RLP, HM

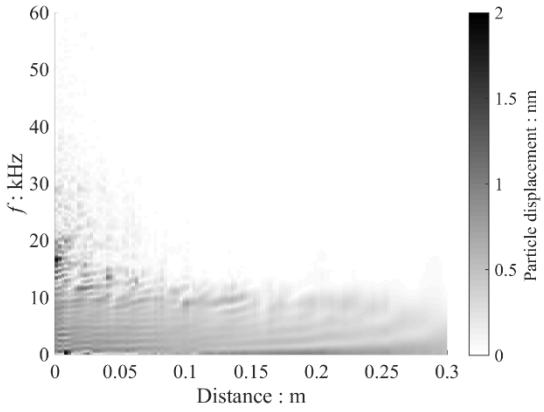

(f) RLP, HMD

Figure 5.23. Frequency domain response of particle displacement in shear direction at varying distances from transmitter wall at σ' = 100 kPa. (a) FCC sample with HM model, (b) FCC sample with HMD model, (c) RDP sample with HM model, (d) RDP sample with HMD model, (e) RLP with HM model, and (f) RLP sample with HMD model.

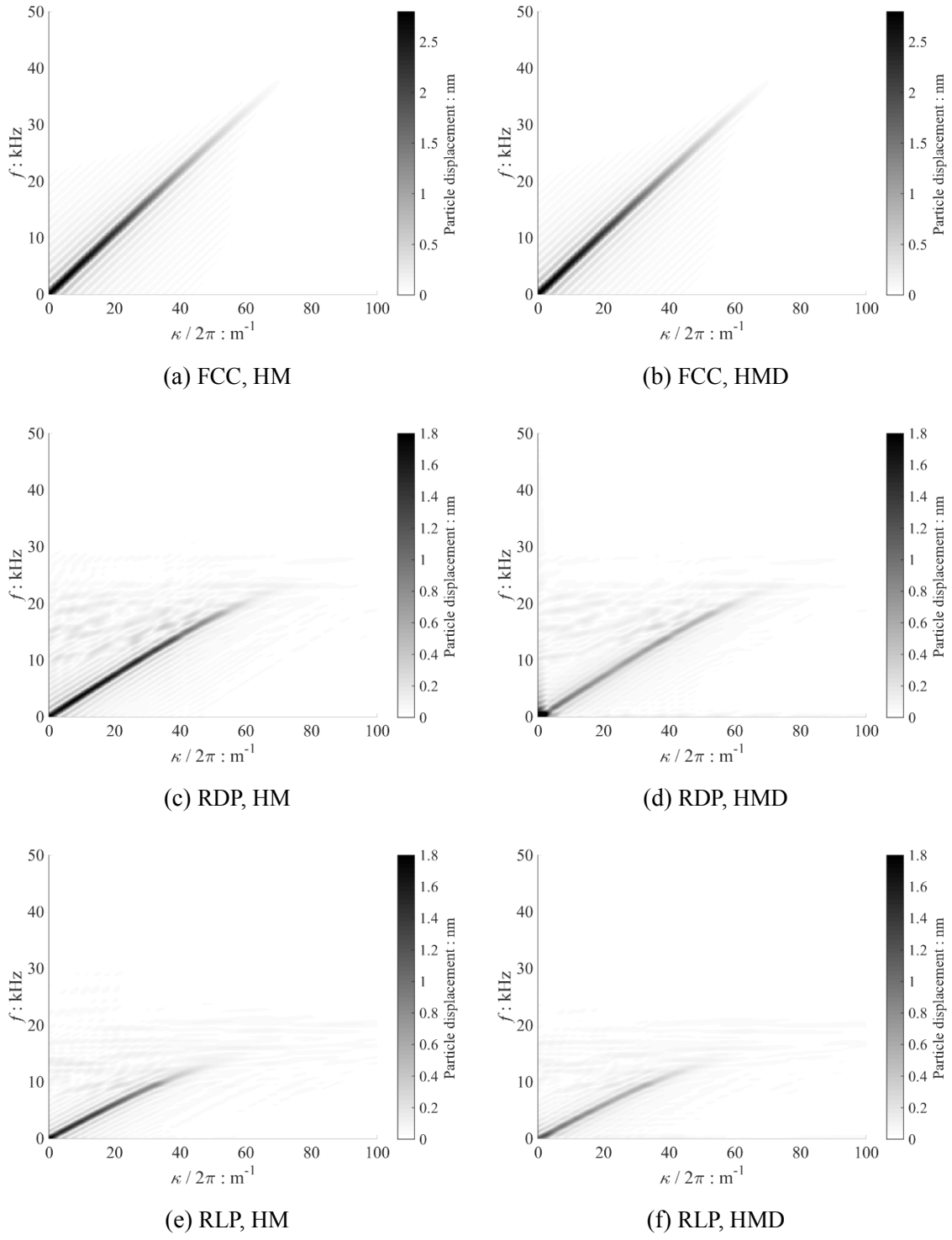

(a) FCC, HM (b) FCC, HMD

(c) RDP, HM (d) RDP, HMD

(e) RLP, HM (f) RLP, HMD

Figure 5.24. Dispersion relation of *S*-wave based on particle displacement in shear direction at $\sigma' =$ 100 kPa. (a) FCC sample with HM model, (b) FCC sample with HMD model, (c) RDP sample with HM model, (d) RDP sample with HMD model, (e) RLP with HM model, and (f) RLP sample with HMD model.

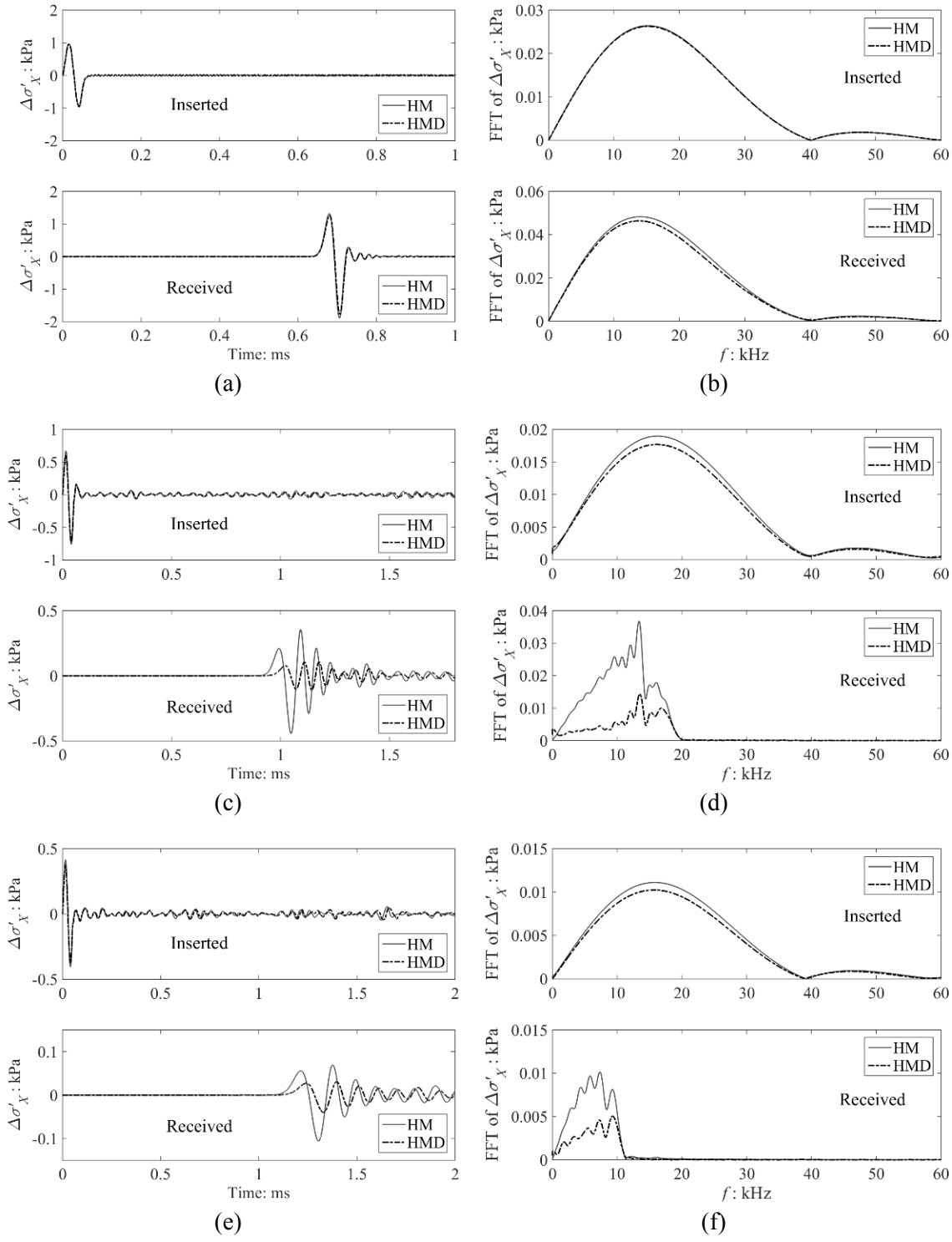

Figure 5.25. Stress response on wall boundaries using HM and HMD contact models. Time and frequency domain responses of incremental shear stress in excitation (X-) direction on transmitter and receiver walls at $\sigma' = 100$ kPa. (a&b) FCC, (c&d) RDP, and (e&f) RLP samples.

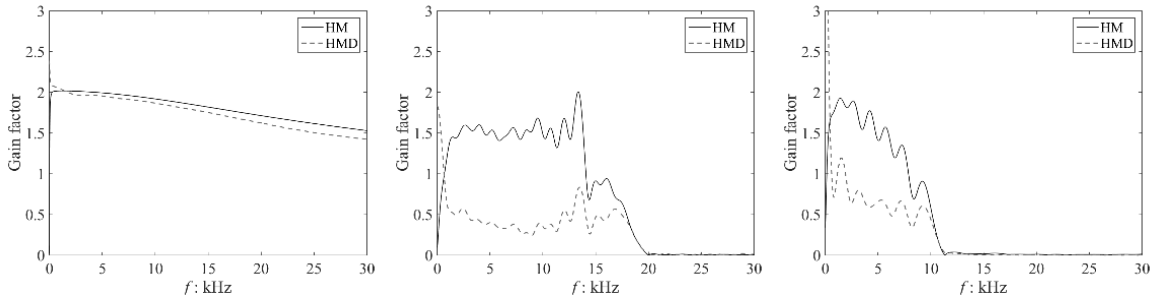

(a) (b) (c)

Figure 5.26. Gain factor of frequency domain responses obtained by comparing inserted and received stress responses at $\sigma' = 100$ kPa. (a) FCC, (b) RDP, and (c) RLP samples.

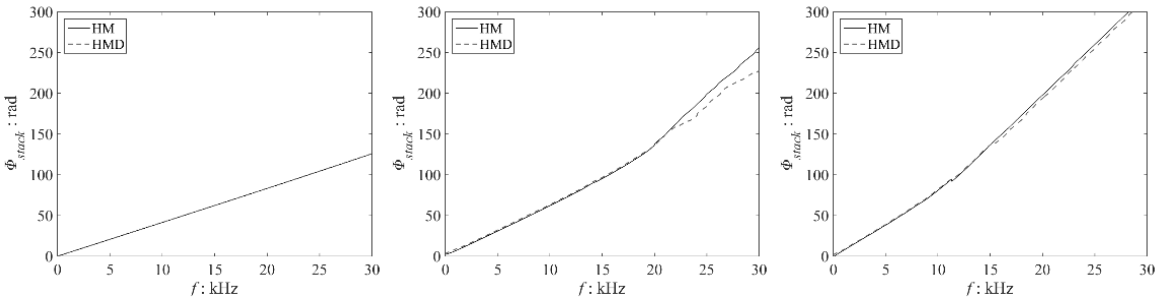

(d) (e) (f)

Figure 5.27. Stacked phase of frequency domain response obtained by comparing inserted and received stress responses at $\sigma' = 100$ kPa. (a) FCC, (b) RDP, and (c) RLP samples.

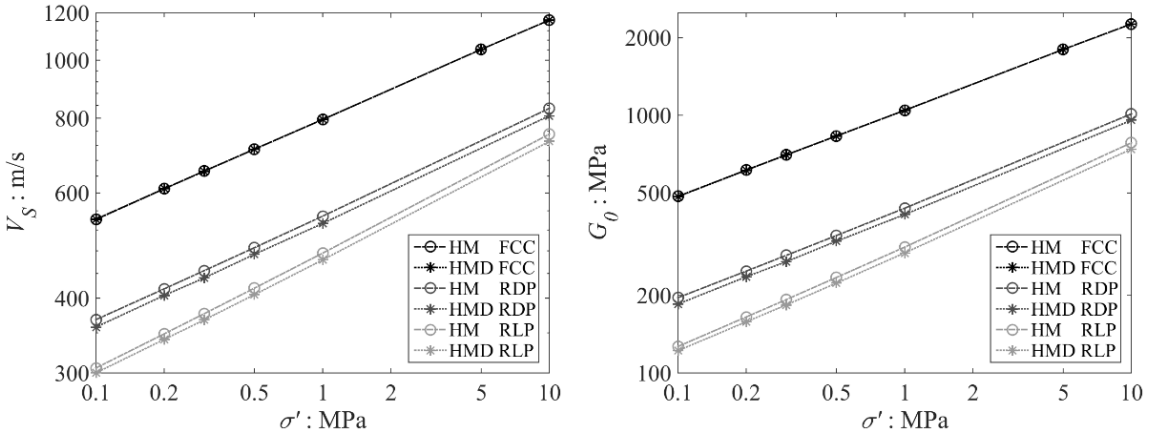

(a) (b)

Figure 5.28. Influence of partial-slip on (a) *S*-wave velocity (V_S) and (b) small-strain shear modulus (G_0) with varying isotropic confining stress.

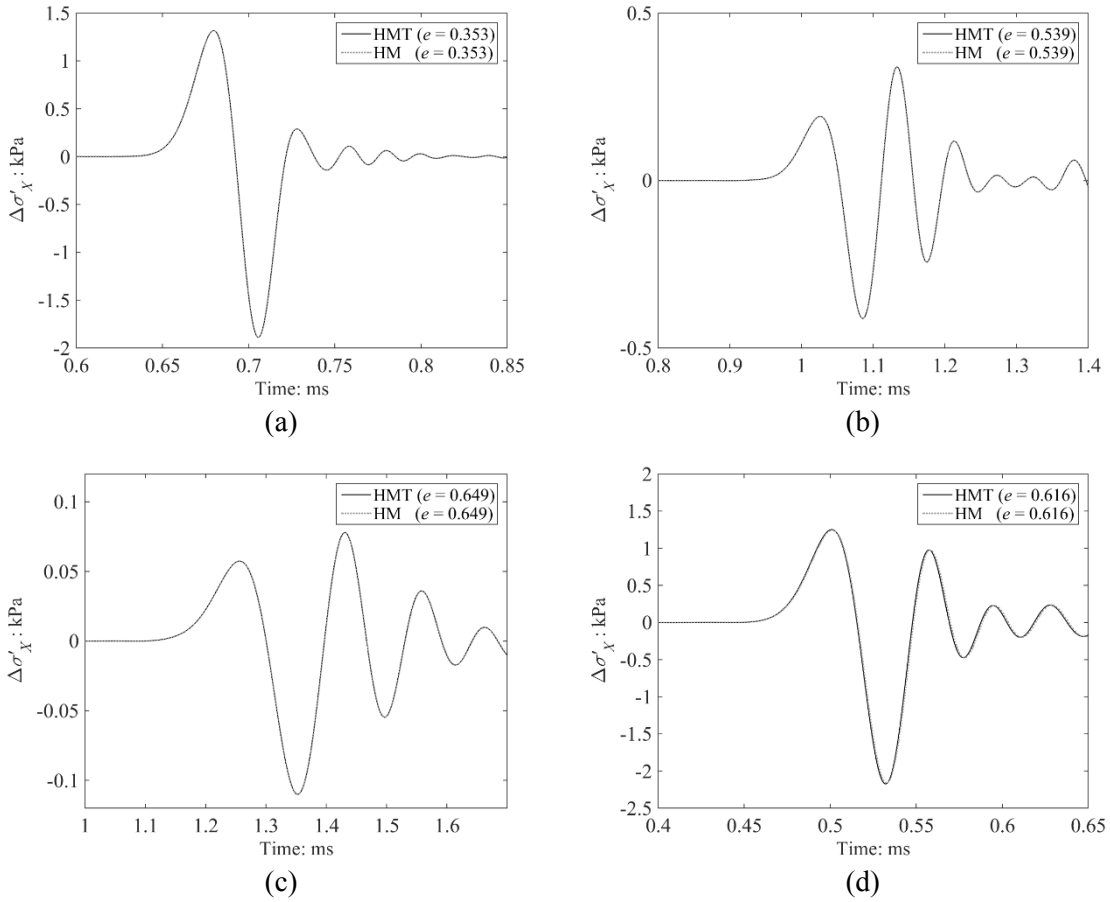

Figure 5.29. Influence of including spin resistance on received signals of *S*-wave propagation. (a) FCC sample at σ' = 100 kPa. (b) RDP sample at σ' = 100 kPa, (c) RLP sample at σ' = 100 kPa, and (d) RLP sample at σ' = 10 MPa.

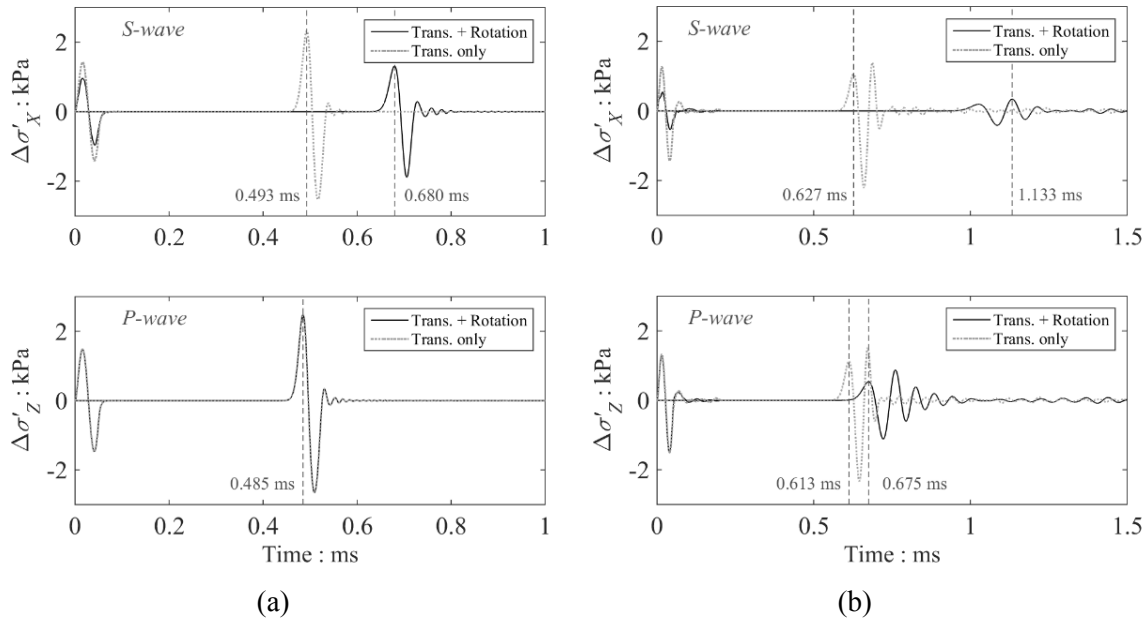

(a) (b)

Figure 5.30. Influence of excluding particle rotation on wave velocities for *P*-wave and *S*-wave at σ' = 100 kPa. (a) FCC sample and (b) RDP sample.

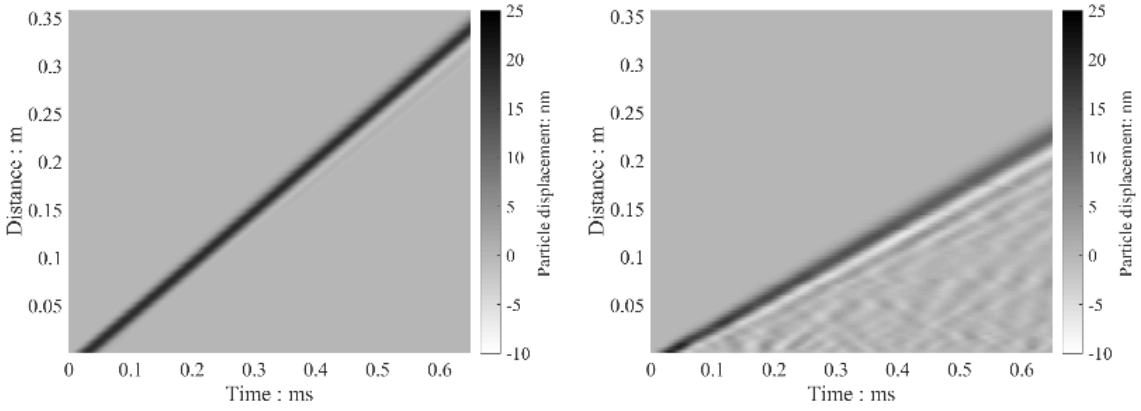

(a) FCC, S_q = 0 μm

(b) RDP, S_q = 0 μm

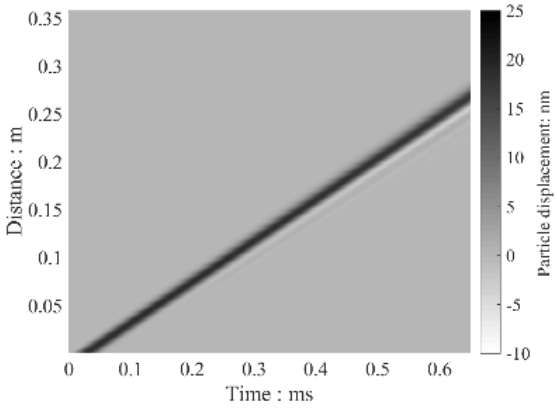

(c) FCC, S_q = 0.5 μm

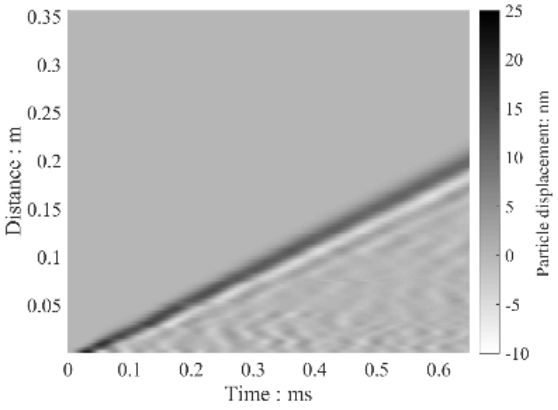

(d) RDP, S_q = 0.5 μm

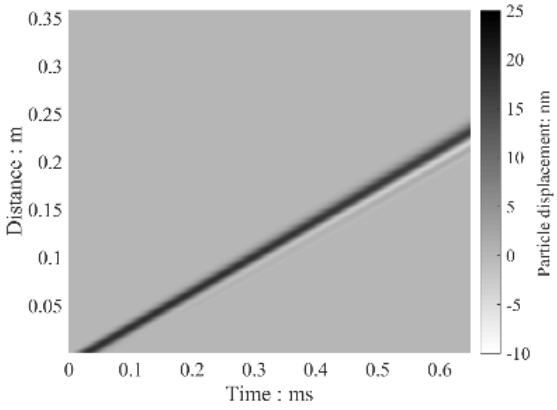

(e) FCC, S_q = 1 μm

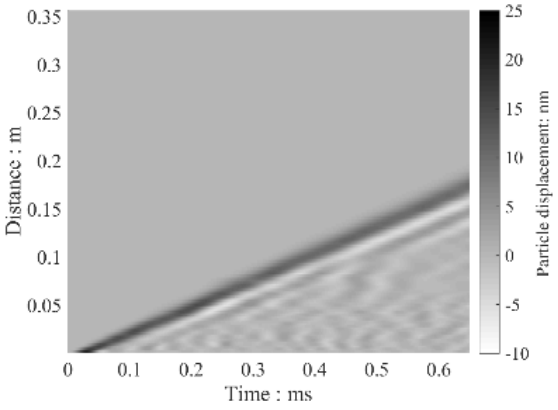

(f) RDP, S_q = 1 μm

Figure 5.31. Variation of particle displacements in shear (X-) direction with time and distance from the transmitter wall at σ' = 100 kPa. (a) FCC sample with S_q = 0 μm, (b) RDP sample with S_q = 0 μm, (c) FCC sample with S_q = 0.5 μm, (d) RDP sample with S_q = 0.5 μm, (e) FCC sample with S_q = 1 μm, and (f) RDP sample with S_q = 1 μm.

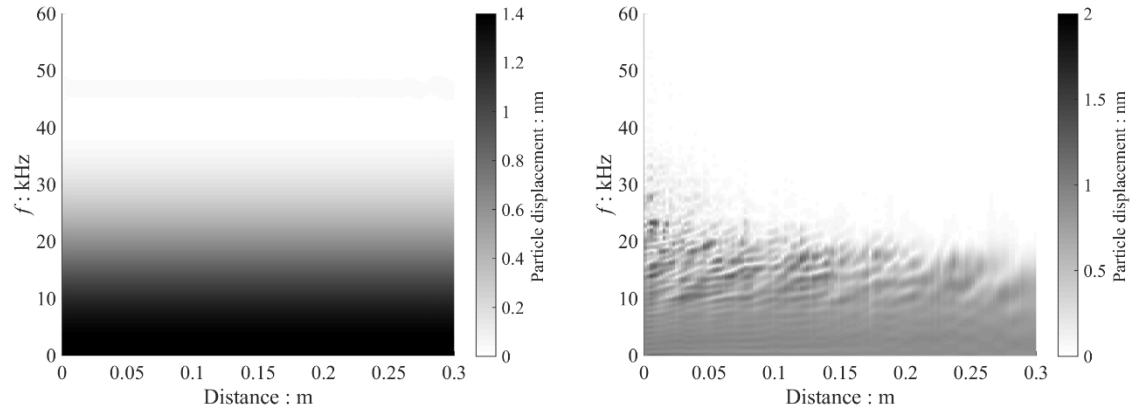

(a) FCC, S_q = 0 μm

(b) RDP, S_q = 0 μm

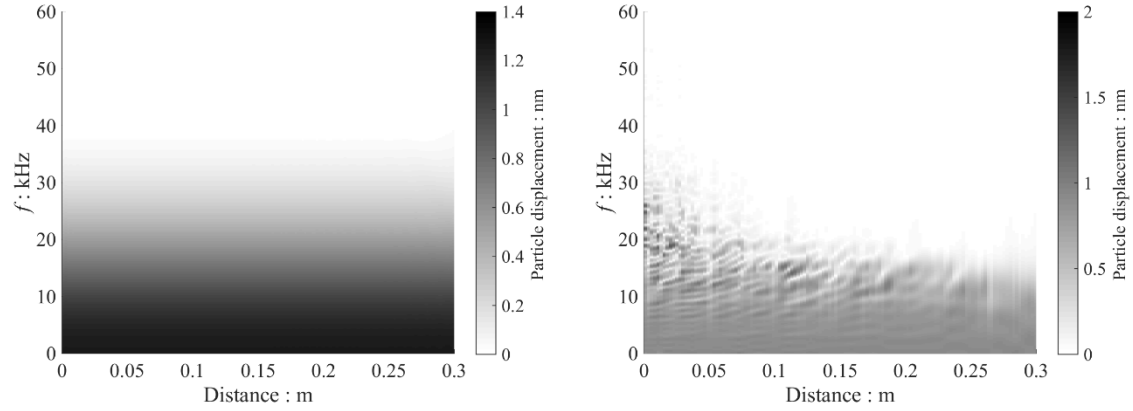

(c) FCC, S_q = 0.5 μm

(d) RDP, S_q = 0.5 μm

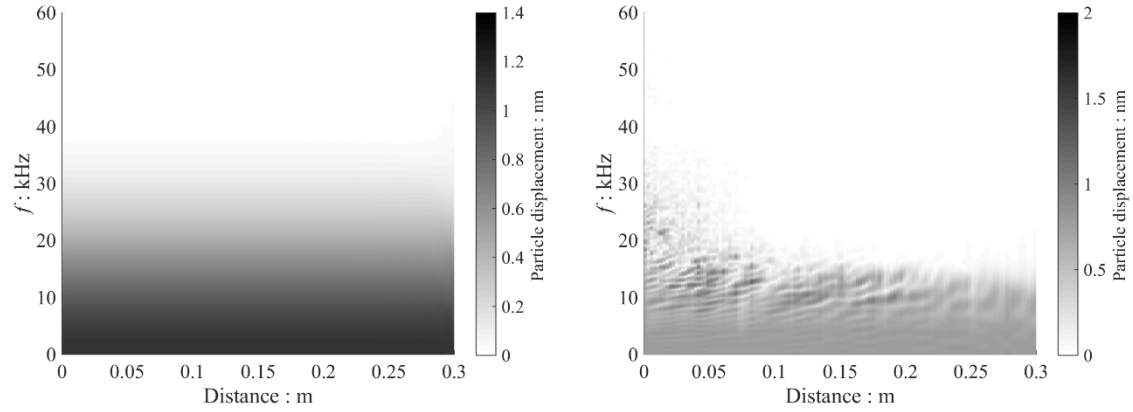

(e) FCC, S_q = 1 μm

(f) RDP, S_q = 1 μm

Figure 5.32. Frequency domain response of particle displacement in shear direction at varying distances from transmitter wall at σ' = 100 kPa. (a) FCC sample with S_q = 0 μm, (b) RDP sample with S_q = 0 μm, (c) FCC sample with S_q = 0.5 μm, (d) RDP sample with S_q = 0.5 μm, (e) FCC sample with S_q = 1 μm, and (f) RDP sample with S_q = 1 μm.

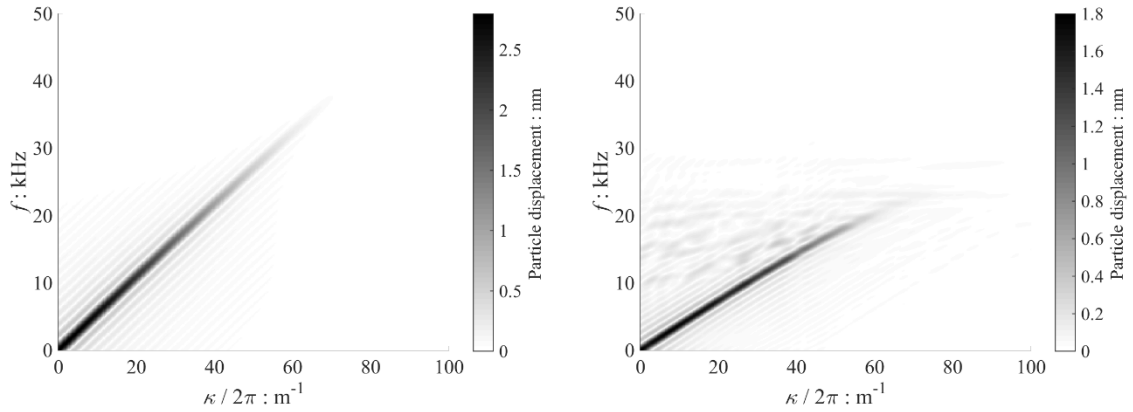

(a) FCC, S_q = 0 μm (b) RDP, S_q = 0 μm

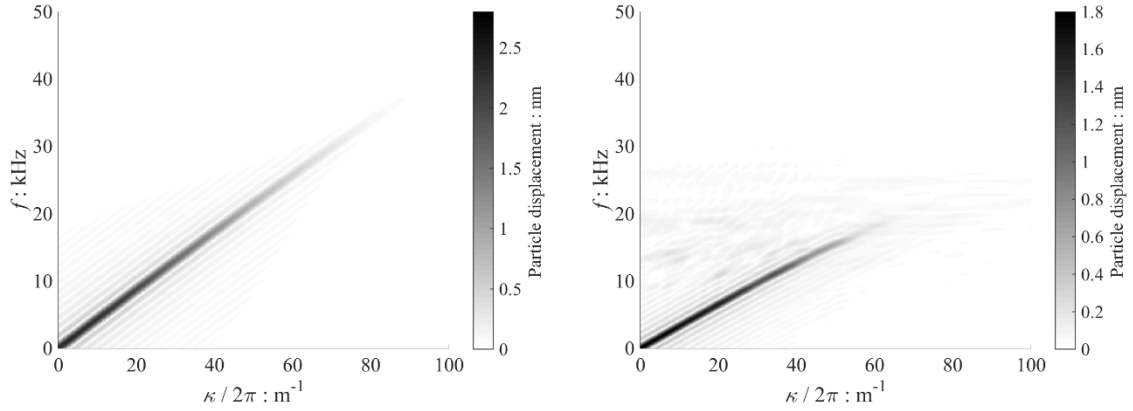

(c) FCC, S_q = 0.5 μm (d) RDP, S_q = 0.5 μm

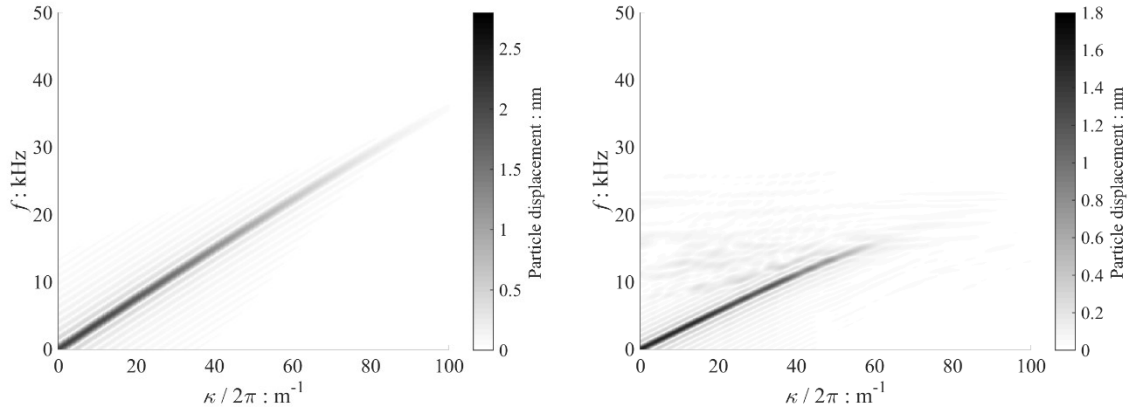

(e) FCC, S_q = 1 μm (f) RDP, S_q = 1 μm

Figure 5.33. Dispersion relation of *S*-wave based on particle displacement in shear direction at σ' = 100 kPa. (a) FCC sample with S_q = 0 μm, (b) RDP sample with S_q = 0 μm, (c) FCC sample with S_q = 0.5 μm, (d) RDP sample with S_q = 0.5 μm, (e) FCC sample with S_q = 1 μm, and (f) RDP sample with S_q = 1 μm.

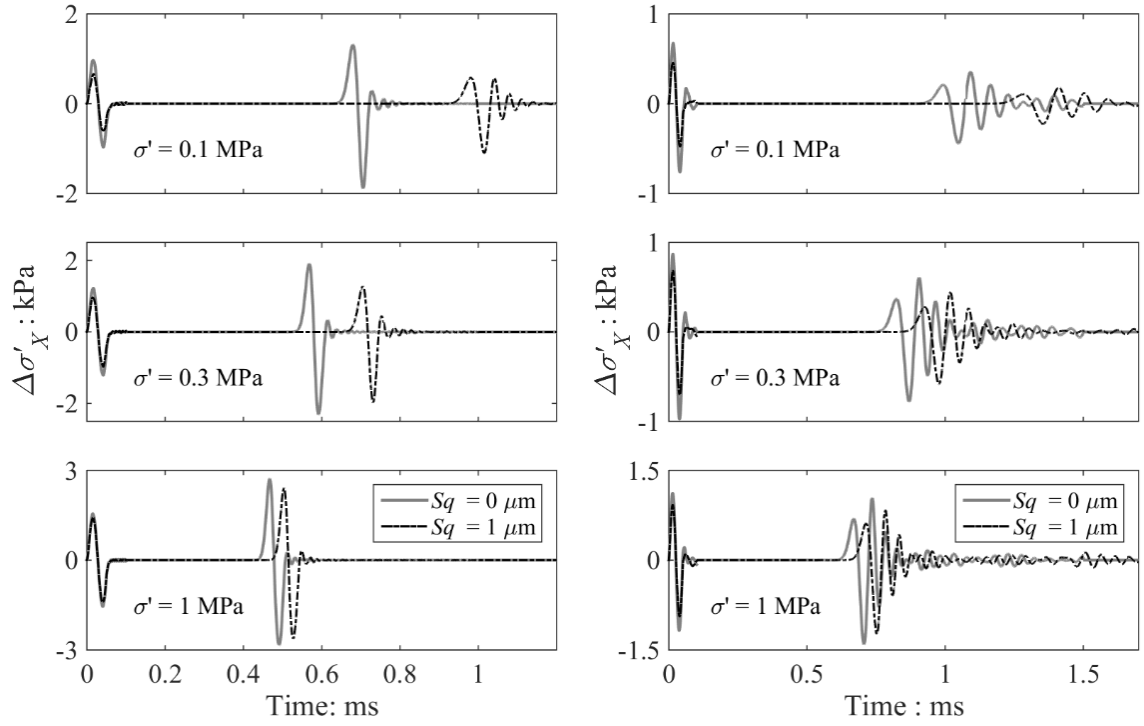

(a) (b)

Figure 5.34. Time history of incremental shear stress in shear (X) direction on transmitter and receiver walls for S_q = 0 μm (smooth), and S_q = 1 μm. (a) FCC samples at σ' = 0.1, 0.3, and 1 MPa, and (b) RDP samples at σ' = 0.1, 0.3, and 1 MPa.

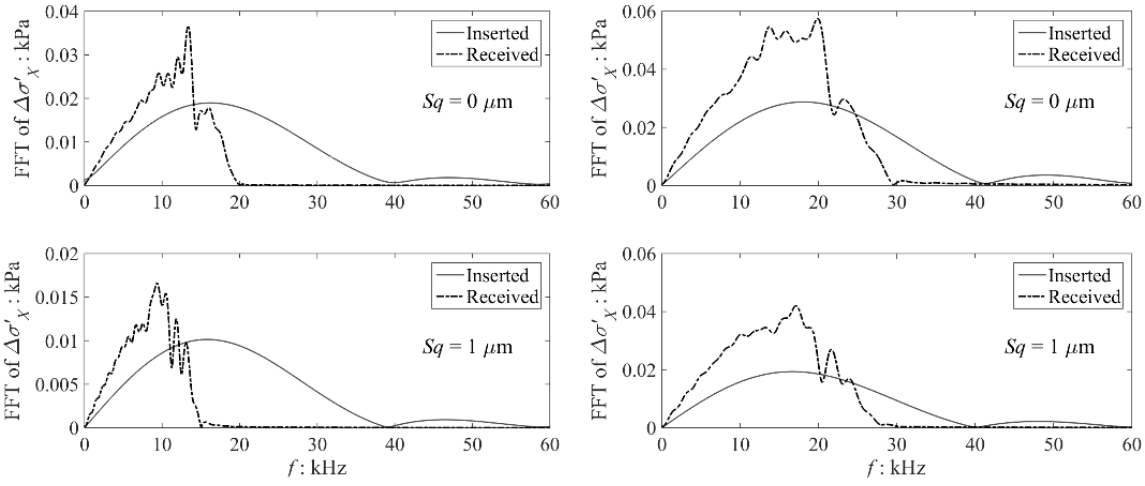

(a) (b)

Figure 5.35. Frequency domain responses of incremental shear stress in excitation (X) direction on transmitter and receiver walls for RDP samples with S_q = 0 (smooth) and S_q = 1μm at: (a) σ' = 0.1 MPa, and (b) σ' = 1 MPa.

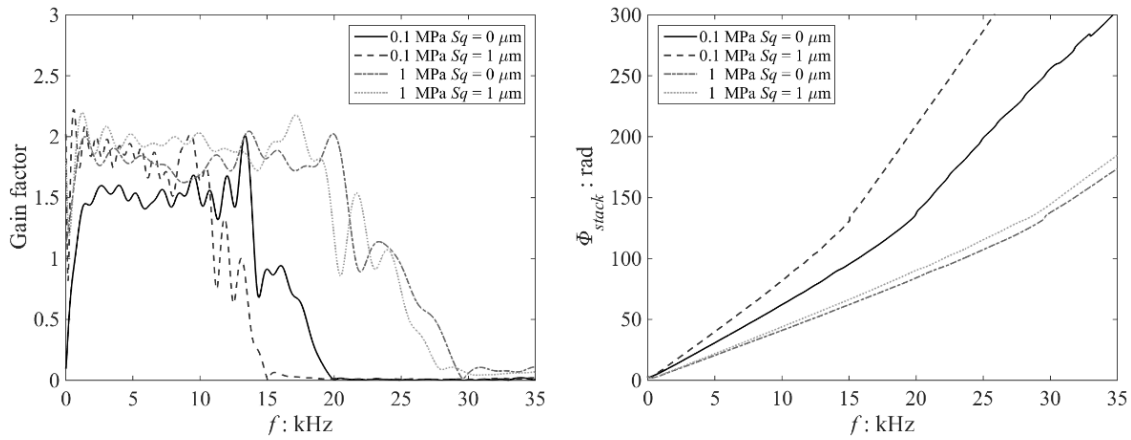

(a) (b)

Figure 5.36. Frequency domain responses of incremental shear stress in excitation (X-) direction for S_q = 0 (smooth) and S_q = 1 μm at σ' = 0.1 MPa and σ' = 1 MPa. (a) Variation of gain factor with frequency, and (b) Variation of stacked phase with frequency.

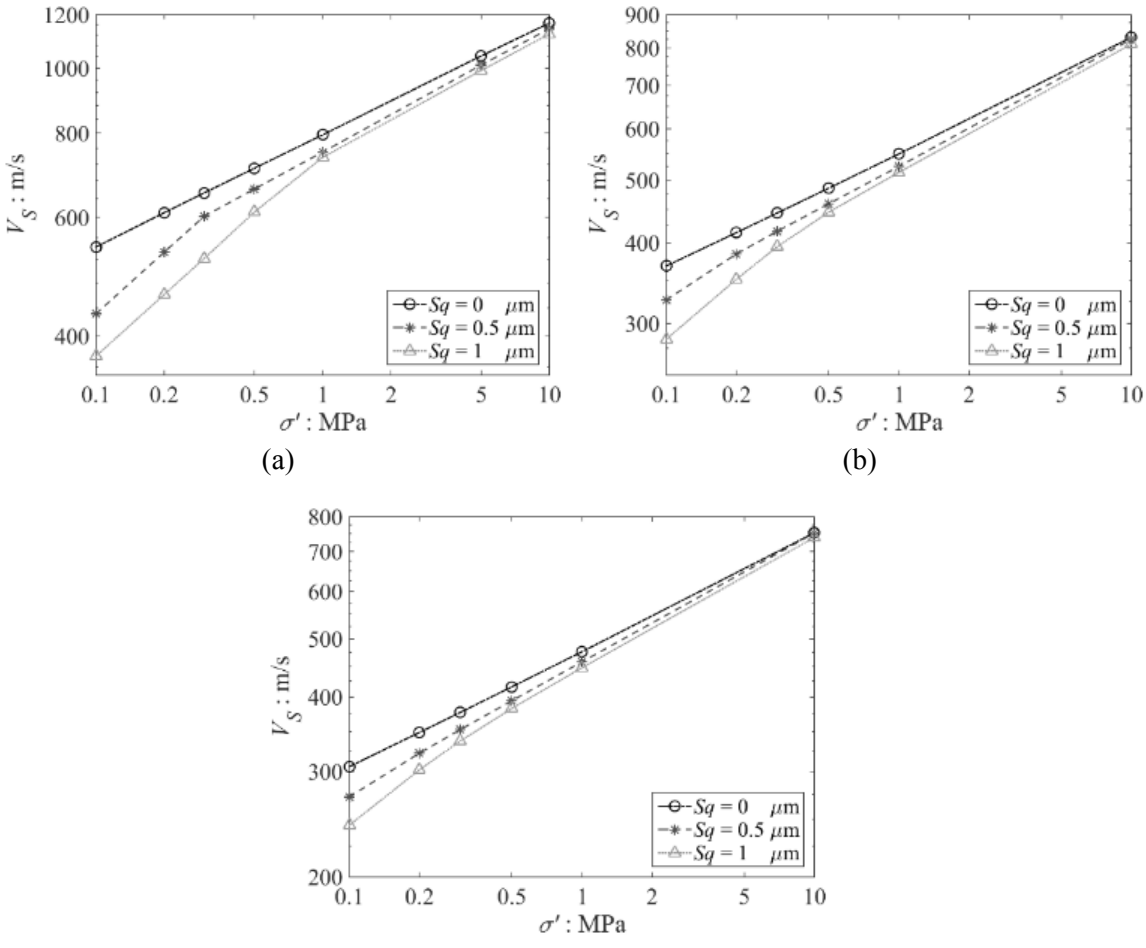

(a) (b)

(c)

Figure 5.37. Variation of shear wave velocity (V_S) with isotropic stress and surface roughness (S_q = 0, 0.5 and 1 μm) on (a) FCC, (b) RDP, and (c) RLP samples.

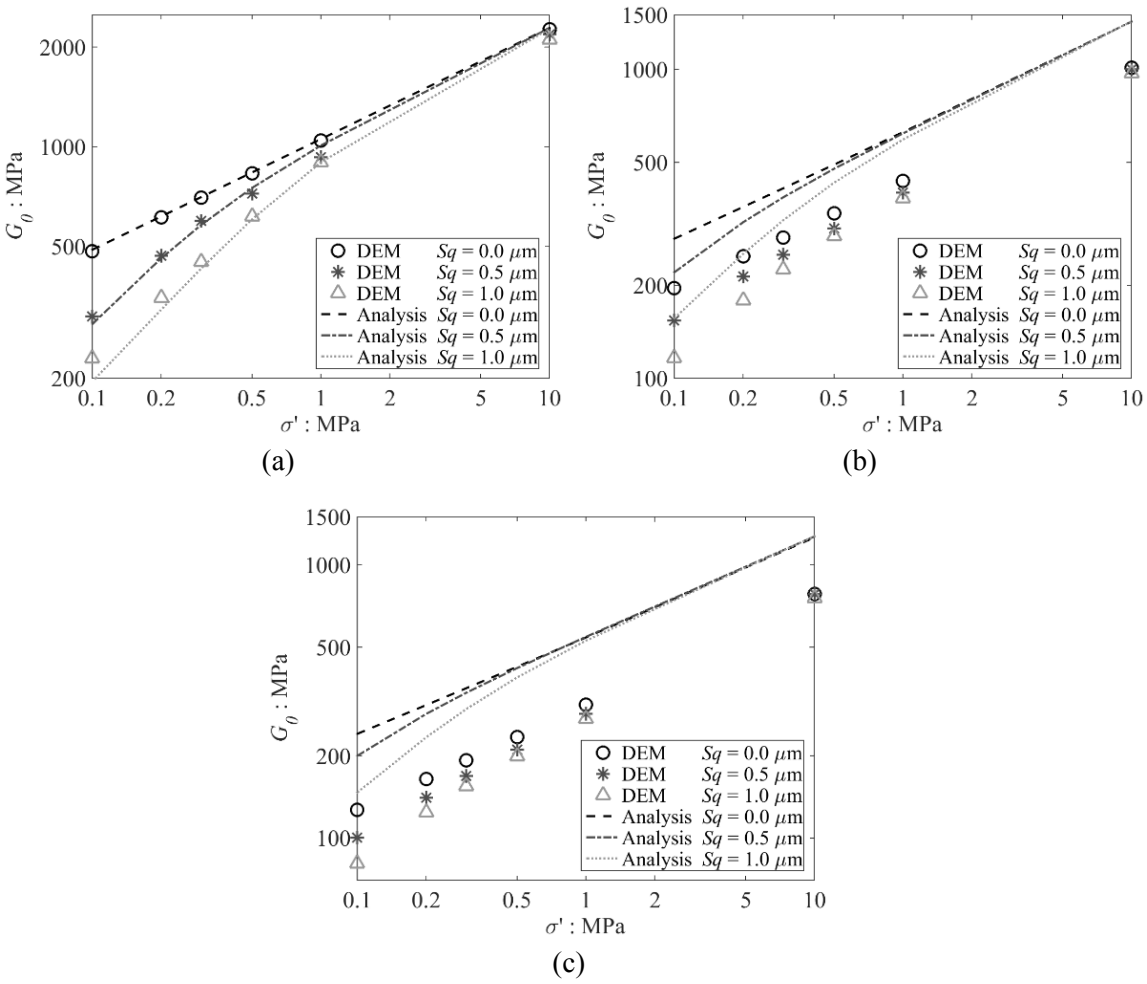

Figure 5.38. Variation of small-strain shear modulus (G_0) obtained using DEM simulations and micromechanical analysis with isotropic stress and surface roughness (S_q = 0, 0.5 and 1 μm) on (a) FCC, (b) RDP, and (c) RLP samples.

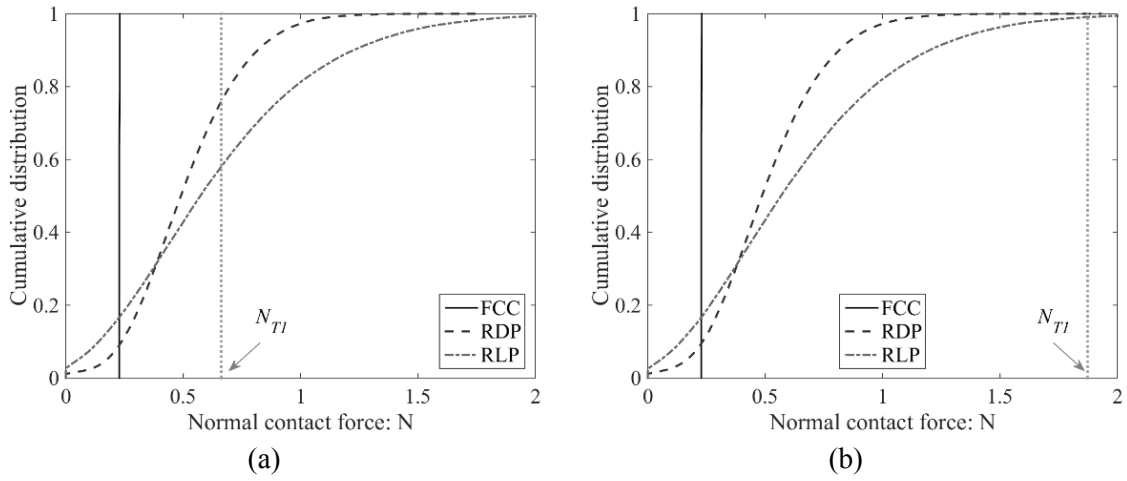

Figure 5.39. Cumulative distributions of normal contact forces for different packings at σ' = 100 kPa: (a) S_q = 0.5 μm, and (b) S_q = 1 μm.

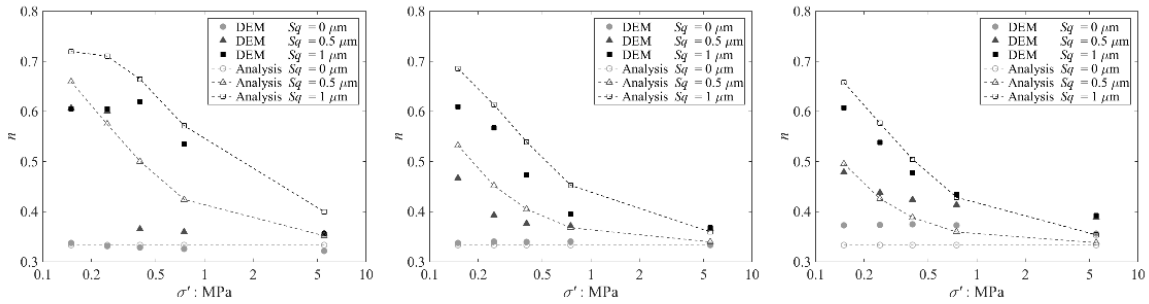

(a) (b) (c)

Figure 5.40. Evolution of power coefficient (n) in G_0 - σ' relationship obtained using DEM simulations and micromechanical analysis with varying isotropic stress and surface roughness (S_q = 0, 0.5 and 1 μm) on (a) FCC, (b) RDP, and (c) RLP samples.

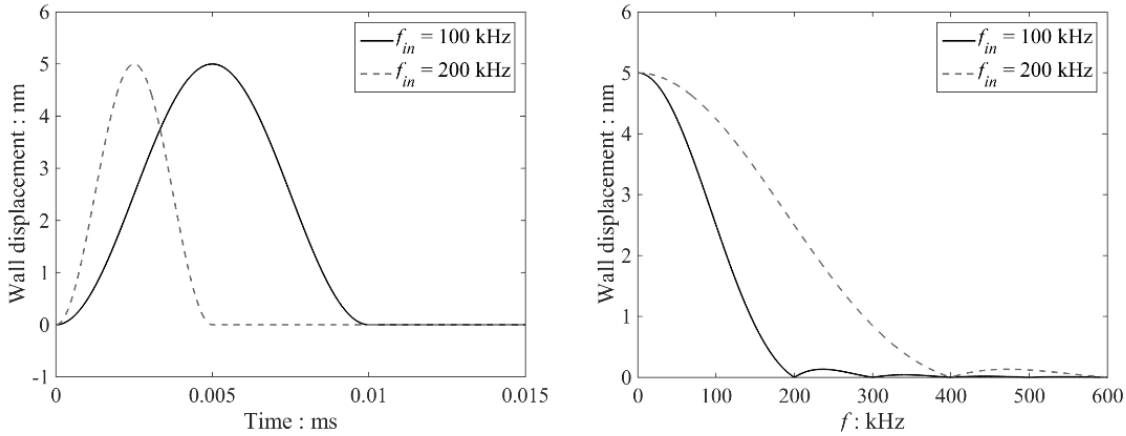

(a) (b)

Figure 5.41. (a) Displacement and (b) spectral amplitude of the transmitter wall for input nominal frequencies (f_{in}) of 100 kHz and 200 kHz.

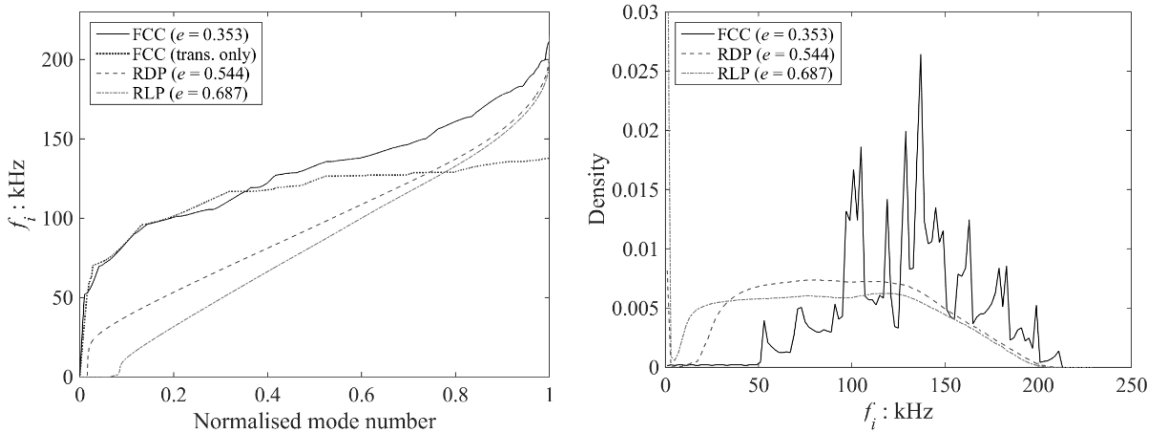

(a) (b)

Figure 5.42. Eigenfrequencies (f_i) for FCC sample (test case P-2), RDP sample (test case P-6) and RLP sample (test case P-30) at σ' = 100 kPa. (a) Relationship between f_i and normalised mode number, and (b) Density distribution of f_i values.

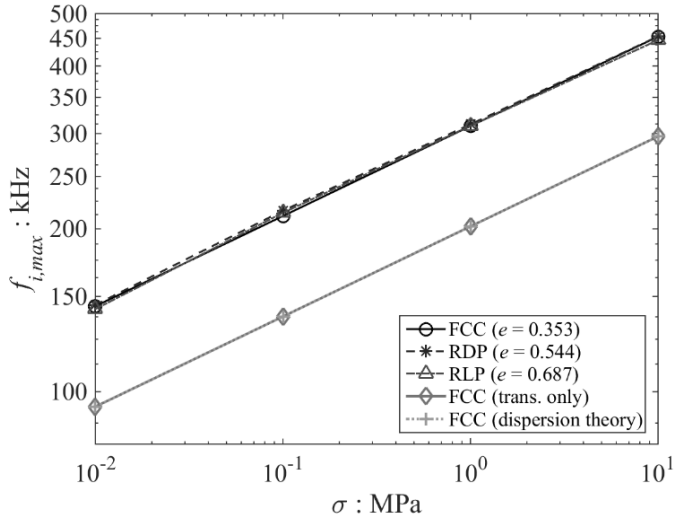

Figure 5.43. Stress-dependency of maximum eigenfrequency using FCC sample, RDP sample (R0), RLP sample (R04), FCC sample excluding rotational degrees of freedom, and theory of dispersion relation for *P*-wave propagation (Eq. 5.5.7).

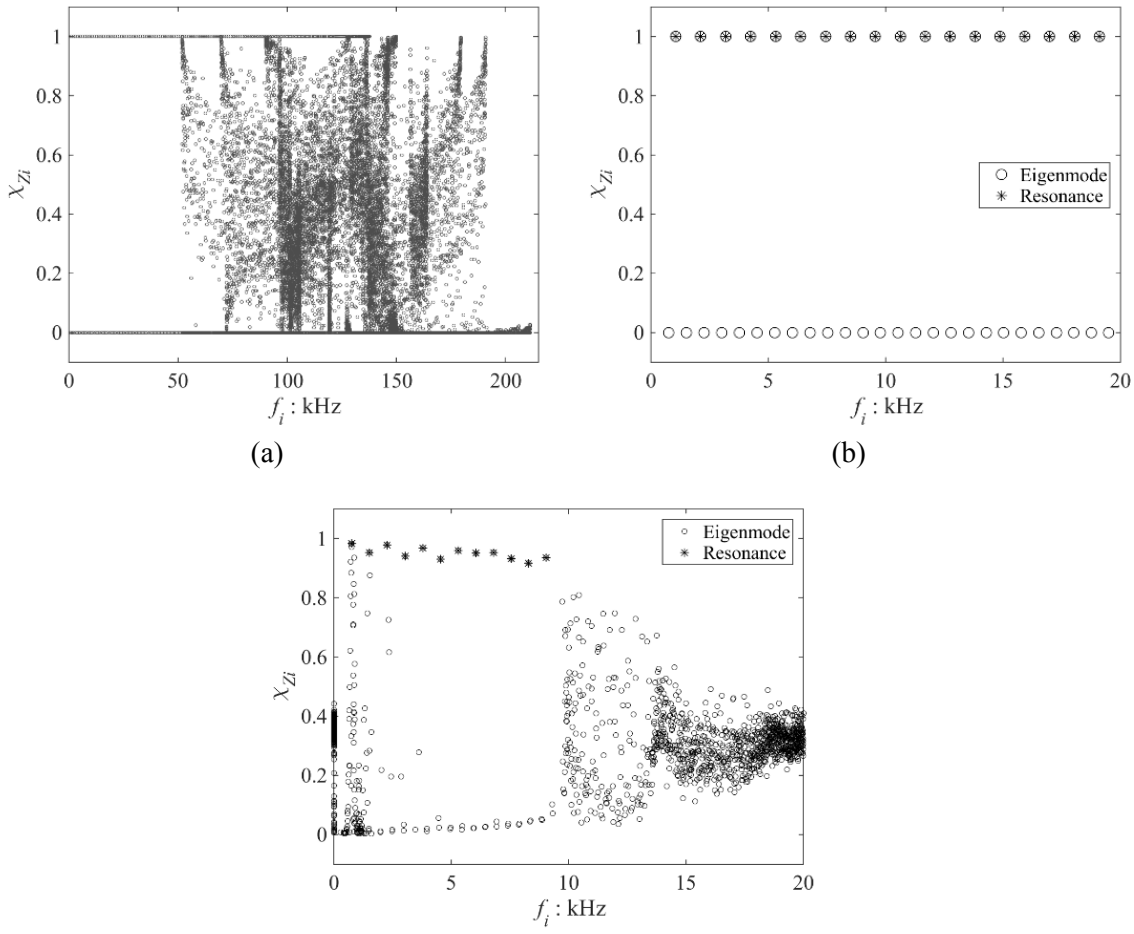

Figure 5.44. Correlation indices (χ_{zi}) against eigenfrequencies (f_i) for (a) FCC sample (test case P-2), (b) FCC sample for f_i = 0 - 20 kHz and (c) RDP sample (test case P-6) at σ' = 100 kPa.

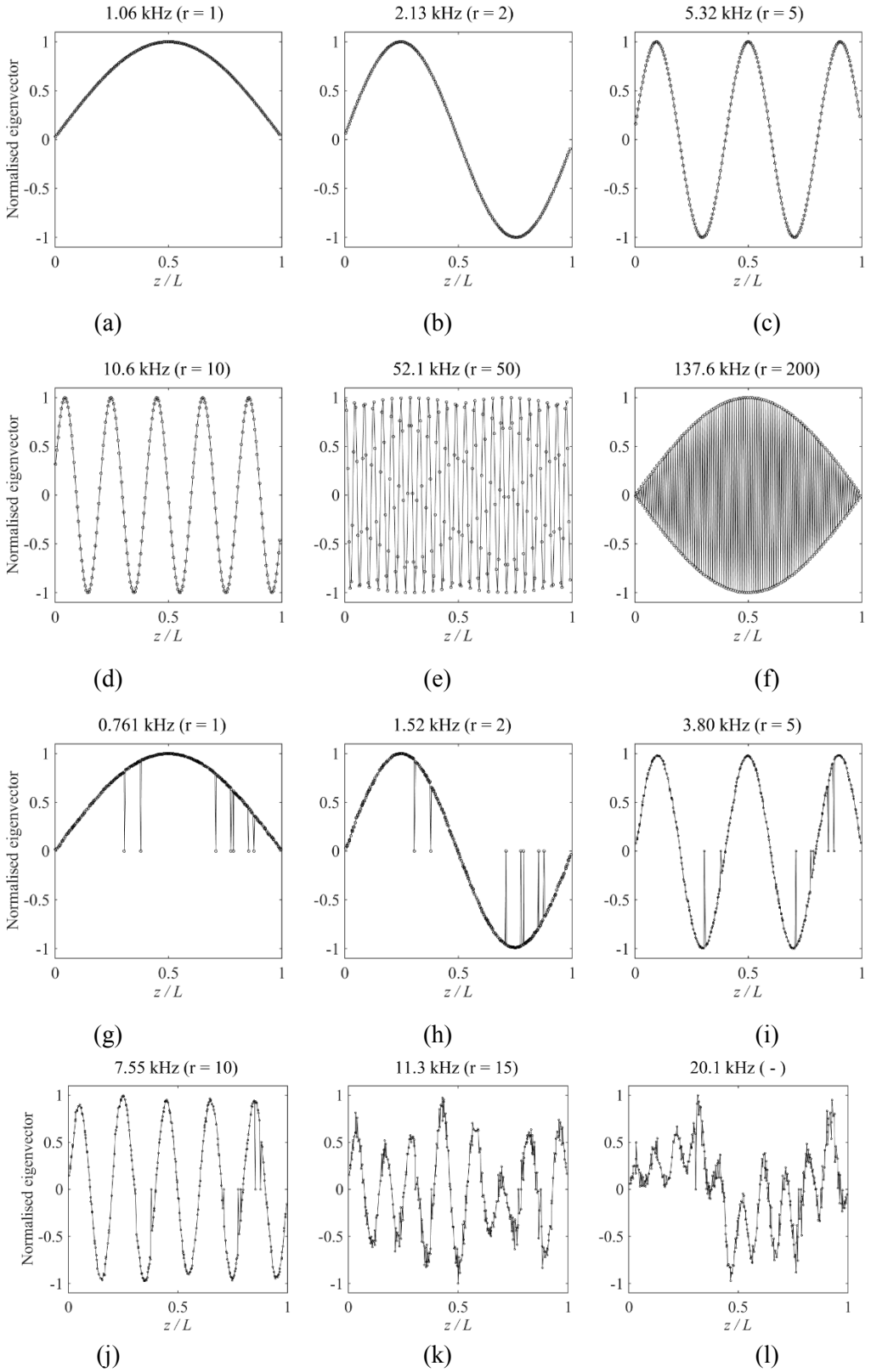

Figure 5.45. Normalised eigenvectors of fundamental resonant modes in the propagating (Z-) direction at σ' = 100 kPa. (a-f) correspond to r = 1, 2, 5, 10, 50 and 200 th mode of resonance for FCC sample (test case P-2), and (g-l) correspond to r = 1, 2, 5, 10, 15 and 20 th mode of resonance for RDP sample (test case P-6). The corresponding resonant frequencies (f_r) are indicated.

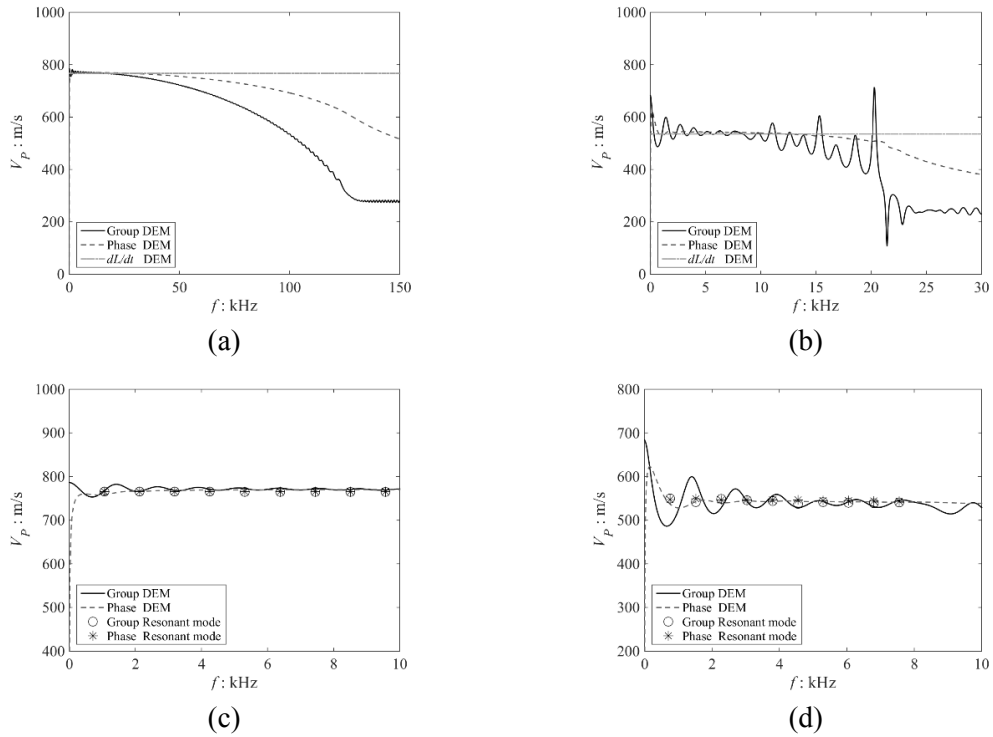

Figure 5.46. Group velocity and phase velocity at $\sigma' = 100$ kPa compared with $V_{P,dL/dt}$. (a) FCC sample (test case P-2), (b) RDP sample (test case P-6), (c) FCC sample compared with eigenmode analysis, (d) RDP sample compared with eigenmode analysis.

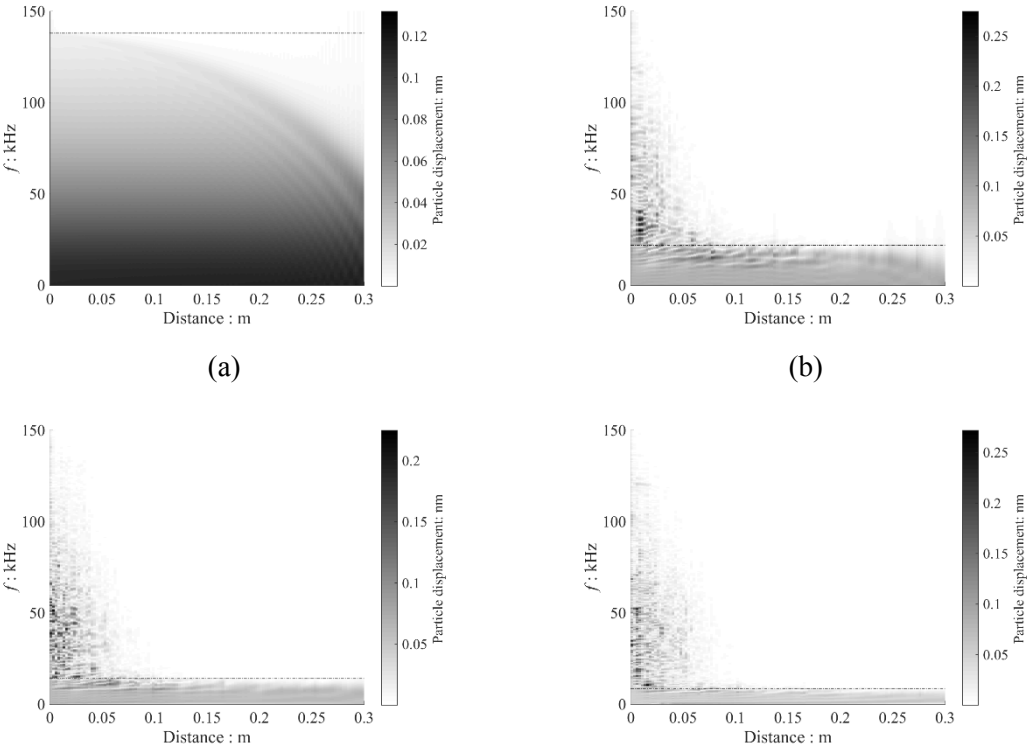

Figure 5.47. Frequency spectra at varying distances from the transmitter wall at $\sigma' = 100$ kPa. (a) $e = 0.353$ for FCC sample (test case P-2), (b) $e = 0.544$ (test case P-6), (c) $e = 0.646$ (test case P-22), and (d) $e = 0.687$ (test case P-30).

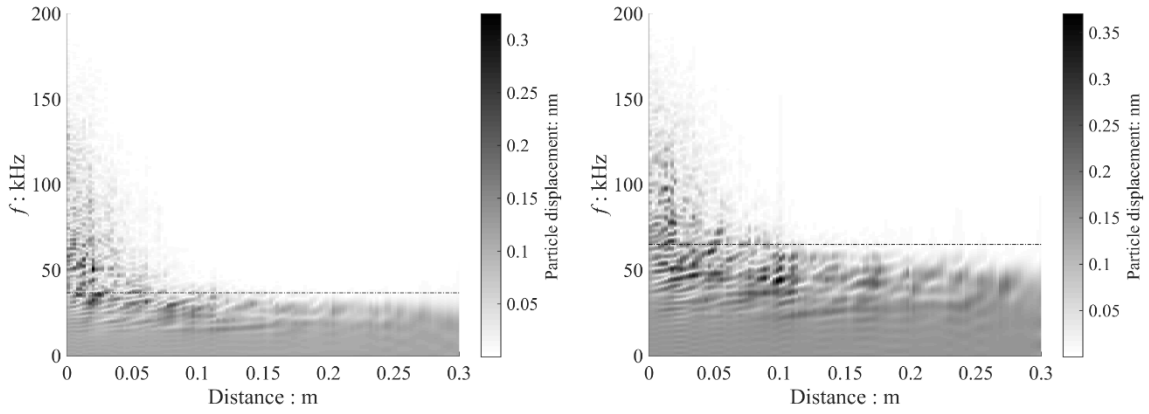

Figure 5.48. Frequency spectra at varying distances from the transmitter wall. (a) e = 0.539 at σ' = 1 MPa (test case P-7), and (b) e = 0.516 at σ' = 10 MPa (test case P-8).

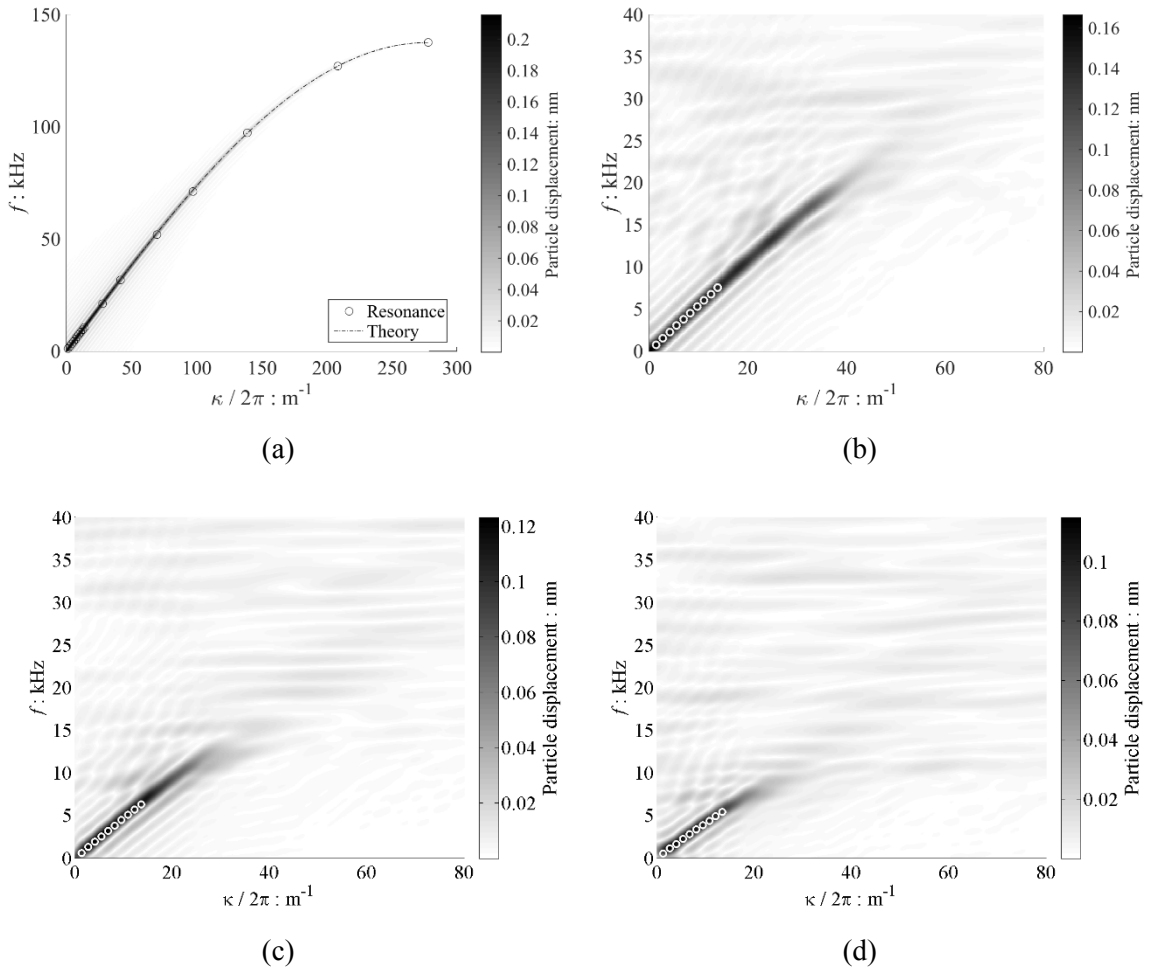

Figure 5.49. Dispersion relation of particle displacement for *P*-wave propagation at σ' = 100 kPa. (a) e = 0.353 for FCC sample (test case P-2), (b) e = 0.544 (test case P-6), (c) e = 0.646 (test case P-22), and (d) e = 0.687 (test case P-30).

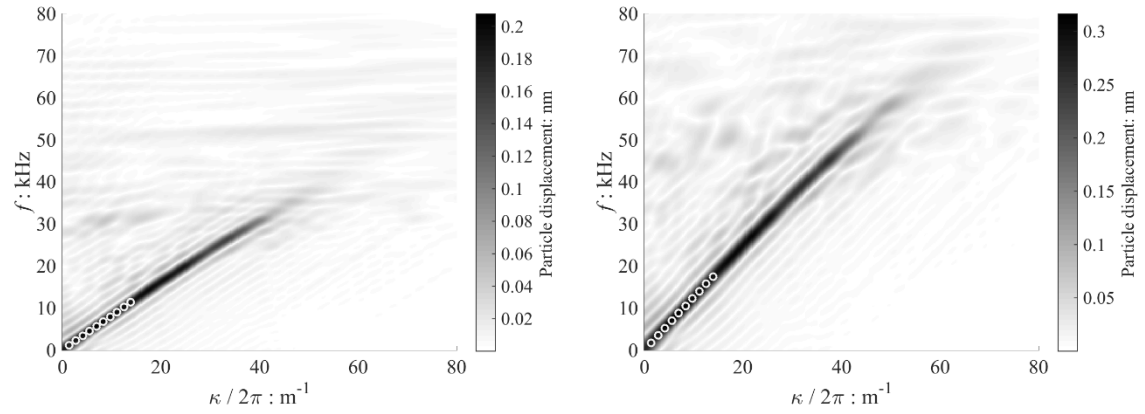

Figure 5.50. Dispersion relation of particle displacement for *P*-wave propagation. (a) $e = 0.539$ at $\sigma' = 1$ MPa (test case P-7), and (b) $e = 0.516$ at $\sigma' = 10$ MPa (test case P-8).

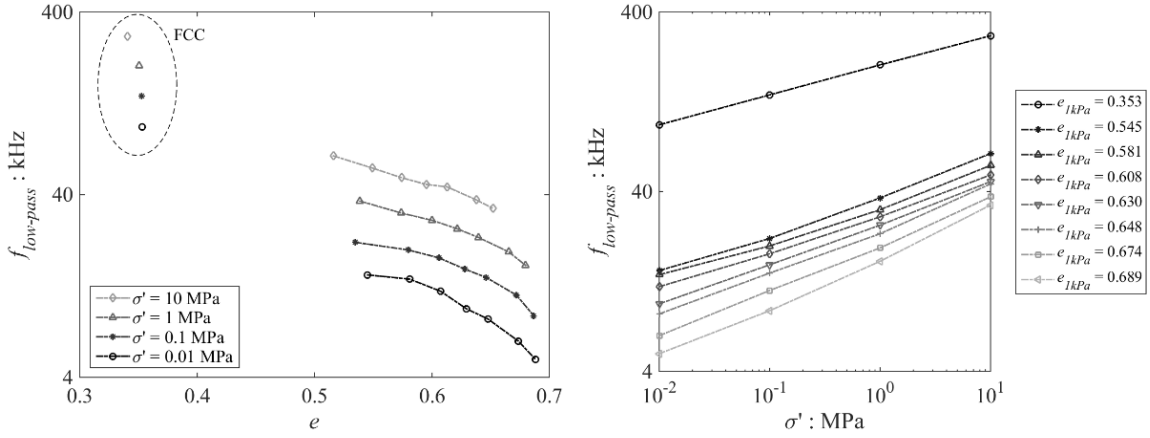

Figure 5.51. Variation of low-pass frequency ($f_{low\text{-}pass}$) with (a) void ratio and (b) isotropic stress.

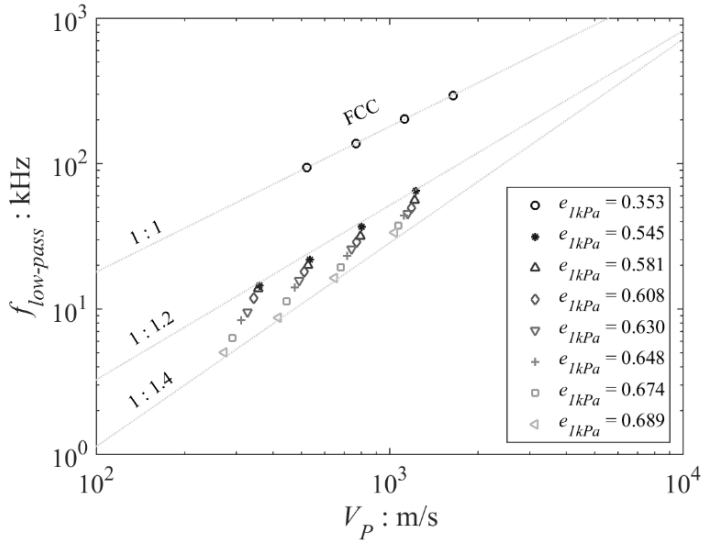

Figure 5.52. Relationship between *P*-wave velocity (V_P) and low-pass frequency ($f_{low\text{-}pass}$).

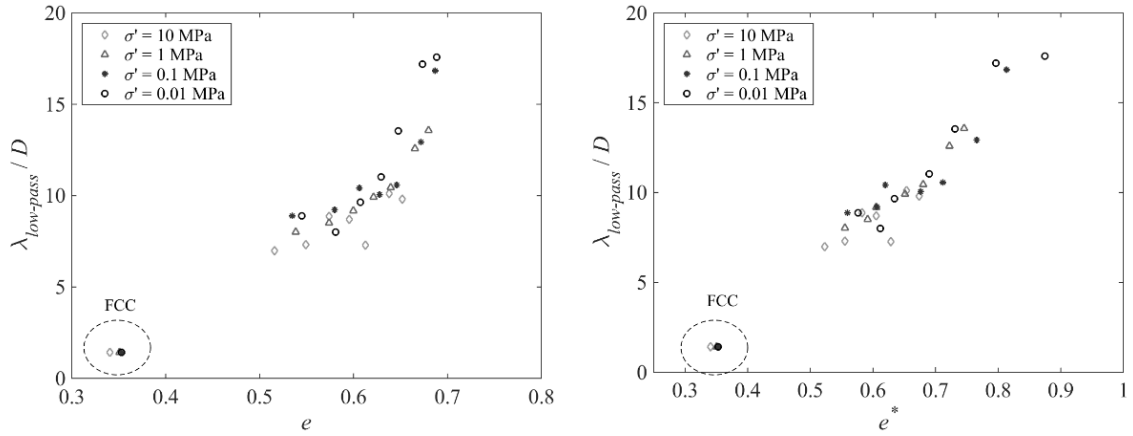

Figure 5.53. Relationship between low-pass wavelength ($\lambda_{low\text{-}pass}$) normalised by diameter and (a) void ratio (e), and (b) mechanical void ratio (e^*).

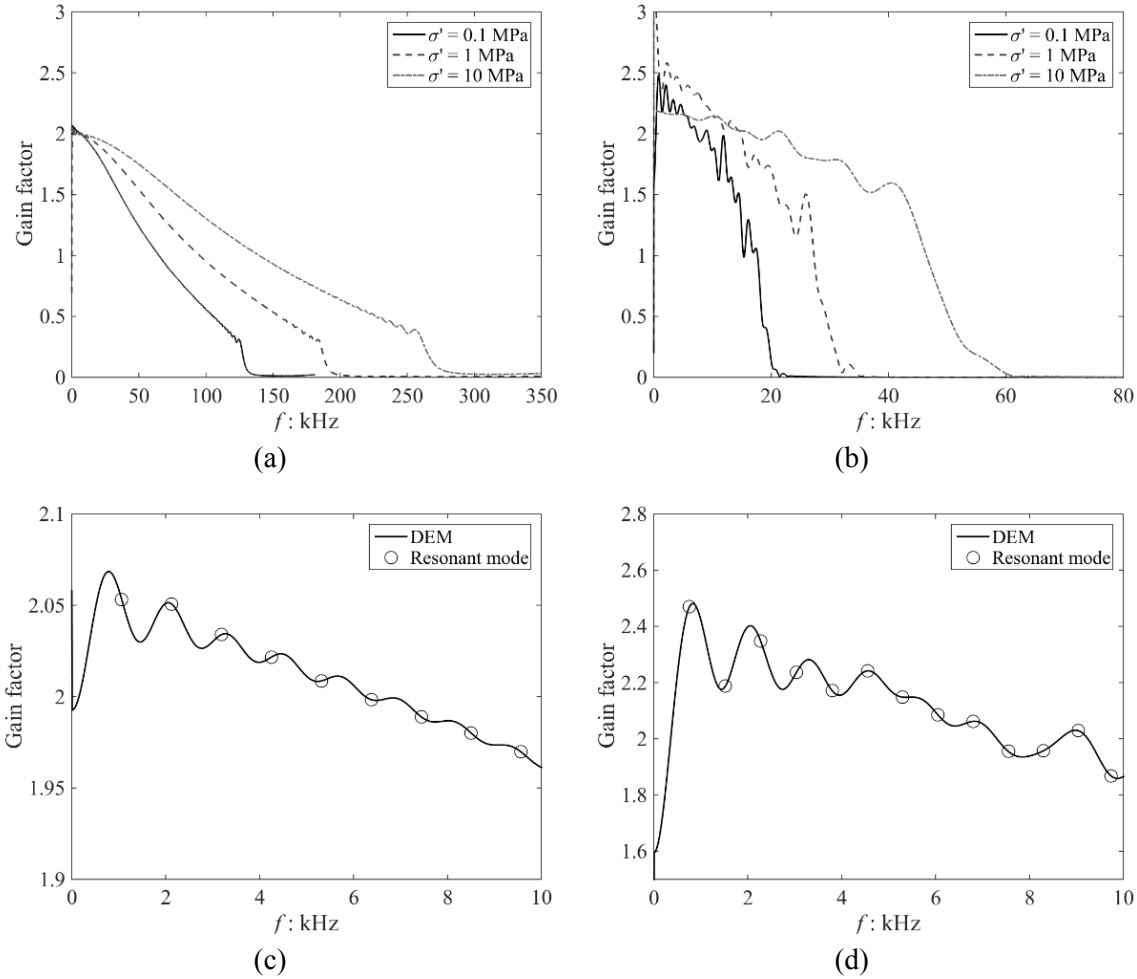

Figure 5.54. Variation of gain factor with frequency. (a) FCC sample at σ' = 0.1, 1, 10 MPa (test cases P-2-4), (b) RDP sample at σ' = 0.1, 1, 10 MPa (test cases P-6-8), (c) FCC sample at σ' = 0.1 MPa plotted with resonant frequencies, and (d) RDP sample at σ' = 0.1 MPa plotted with resonant frequencies.

CHAPTER 6

Experimental assessment of the effect of surface roughness on shear modulus

6.1 Introduction

This chapter documents experimental studies of the effects of particle surface roughness on sample small-strain shear modulus (G_0). As reviewed in Section 2.6.2, experimental assessments of this issue have rarely been reported most likely due to limitations associated with accurately measuring surface roughness. Although they did not quantify surface roughness values, Santamarina & Cascante (1998) and Sharifipour & Dano (2006) reported that increasing surface roughness reduces the shear wave velocity (V_S) and G_0 at a given stress level (σ') and that the power coefficient n in the G_0 - σ' relationship increases with the surface roughness. The current study relates surface roughness to G_0 using the glass ballotini with RMS surface roughness values (S_q) quantified as summarised in Chapter 3. Two series of experiments were carried out; the first used a cubical cell apparatus with conventional bender elements and the second used a triaxial apparatus with shear plates (Brignoli et al. 1996; Ismail & Rammah 2005; Suwal & Kuwano 2013). For the latter series of experiments where a wider range of stress was considered, supplemental DEM simulations were carried out to give additional insight into the system response using the contact models considered in Chapters 4 and 5.

The data generated in the experiments enables a fundamental assessment of the use of laboratory geophysics tests to determine elastic stiffness. Specifically the proposal to use shear plates (Brignoli et al. 1996) as an alternative to bender elements (Shirley & Hampton, 1978) is critically appraised.

In this chapter, Section 6.2 discusses surface roughness effects on G_0 experimentally using a cubical cell apparatus. Section 6.3 considers both shear plate tests using a triaxial apparatus and DEM simulations. Section 6.4 explores the influence of excitation and received area for dynamic tests and investigate actual sample response near transmitter using a novel design of shear plates, and Section 6.5 summarises findings from this chapter.

6.2 Bender element tests using a CCA apparatus

This section presents the results of bender element tests that were carried out to investigate the surface roughness effects on sample shear modulus G_0 using the cubical cell apparatus (CCA) at the University of Bristol (Fig. 6.1). The results of this series of experiments were partially reported in Otsubo et al. (2015).

6.2.1 Test procedure

The CCA apparatus was originally designed by Ko & Scott (1967), and details of the CCA at the University of Bristol are given in Sadek (2006) and Hamlin (2014). Five tests were conducted using the WLS, WLR, WSS and WSR ballotini (Table 6.1) used in Chapter 3 where test case UB-05 was carried out using WSR ballotini washed carefully with de-ionized water after testing for test case UB-04. Representative images and surface topographies of the ballotini used are illustrated in Fig. 6.2. The RMS surface roughness (S_q) data for WSR ballotini shown in Table 3.2 are for the washed ballotini, while S_q data for the other types of ballotini were measured for unwashed ballotini; however the S_q data for the WLR ballotini were not affected considerably by washing. Note that the rough ballotini samples tested using the triaxial apparatus (IC-02 and IC-03) were washed with distilled water before roughness measurements and shear plate tests as documented in Section 6.3 below.

The test procedure used with the CCA follows Hamlin (2014) and a general overview is given here. To conduct tests with the CCA, a cubical specimen was needed. To fabricate a cubical specimen, a two-part cubical membrane was used (Fig. 6.3(a)). Referring to Fig. 6.3(a), slots for inserting bender elements were created on each face of both parts of the cubical membrane. The 5 sided bottom part was placed inside a metal mold and a vacuum pressure was applied between the membrane and the mold (Fig. 6.3(b)). The samples were prepared by air pluviation. The pluviator used maintains a constant drop-height throughout the pluviation process by moving the bottom surface upwards (Fig. 6.3(d)). Use of this pluviator enables repeated preparation of similar samples. The packing characteristics induced via this process were analysed using DEM in earlier research by Camenen et al. (2013). After the ballotini were pluviated into the bottom part of the cubical membrane, the sample surface was levelled off and the lid of the membrane was carefully placed on the top of the sample (Fig. 6.3(c)). The two-part membrane was glued and sealed using latex glue with application of a vacuum pressure to the sample. The vacuum pressure was applied using a tube surrounded by a filter paper inserted into a corner of the sample (Fig. 6.3(c)). After the latex glue dried (and its colour changed from white to transparent), the dimensions of the sample were measured to obtain the initial void ratio (e_0) at σ' = 50 kPa of vacuum pressure. The dimensions of a cubical sample were approximately

100×100×100 mm. As can be seen in Fig. 6.3(c), all slots for inserting bender elements were temporally closed by a parchment paper with pieces of tape during the fabrication process.

The cubical sample was carefully placed inside the CCA apparatus (Figs. 6.4(a) and (b)) with only the bottom platen and flexible cushion in place to hold the sample. Grommets were attached and sealed onto the centre of the horizontal faces of the sample (Fig. 6.4(b)) to minimise pressure loss when the bender elements were installed into the sample. The flexible cushions that contact with the specimen were positioned and the gaps between the grommets and the cushions were sealed with latex glue (Fig. 6.4(c)). T-shaped bender elements were inserted into the grommets and penetrated into the sample by breaking the parchment paper (Fig. 6.4(d)). As a vacuum pressure was applied, the sample maintained its shape despite gaps between the bender elements and grommets, and the latex glue was applied immediately to avoid pressure loss. To record the change in sample dimensions, eighteen LVDT rods (three on each face) that were fixed to the steel platens were used (Fig. 6.4(e)). The edges of LVDT rods were designed to attach to the magnet buttons on flexible cushions. The steel platens were placed onto the cushions by applying silicone grease to minimise the pressure loss. After the horizontal platens were tightened by bolts, the CCA was rotated by 90 degrees to repeat the same procedure for the top and bottom faces. Six tubes were connected to apply air pressures into each cushion (six faces), which enabled independent control of the three orthogonal pressures (Fig. 6.4(f)). Completing the entire procedure described here required significant training. Further details of the procedure are explained in Hamlin (2014).

6.2.2 Test results and discussions

The samples were compressed by nominal isotropic confining pressures to discrete pressure of σ' = 50, 100, 200, 300, 400 and 500 kPa, followed by unloading to the same discrete pressure levels. Once each new pressure level was achieved, a pause was allowed for creep of the sample before conducting bender element tests. Hamlin (2014) analysed the time-dependency of wave velocity for WLS and WSS ballotini tested here and found that approximately 1 hour was needed to reach an equilibrium state. The relationships between e and σ' for all samples tested were compared in Fig. 6.5 where the e values were obtained after allowing for creep. For the small smooth (WSS) sample, an isotropic pressure of 400 kPa was lost during the creep period and an erroneous deviator stress was applied to sample inadvertently, and the test was discarded at this point. The data point at σ' = 400 kPa for the small smooth sample in Fig. 6.5(b) was obtained before the error. Similar e - σ' relationships were observed for all the materials; however, hysteresis effects observed during unloading were more noticeable for the rough surface ballotini. Note that the initial void ratio e_0 for the rough ballotini samples was larger than e_0 for the smooth samples as the same sample preparation method was used (Fig. 6.3(d)),

i.e. constant energy was applied. Recalling the data in Table 3.4, there is a significant difference in attainable e_{min} and e_{max} values between WLS and WLR ballotini. Consequently the e_0 values differed amongst the tested samples.

Referring to Fig. 6.6(a), the T-shaped bender elements used in this study enabled *S*-wave transmission in two directions and *P*-wave transmission, and these novel elements were proposed by Lings & Greening (2001). Interpretation of test results using this type of bender element is described in the literature (Lee & Santamarina, 2005; Leong et al., 2009). Considering three orthogonal directions in the cubical sample, nine elastic velocity values were obtained (i.e. $V_{P,X}$, $V_{P,Y}$, $V_{P,Z}$, $V_{S,XY}$, $V_{S,XZ}$, $V_{S,YX}$, $V_{S,YZ}$, $V_{S,ZX}$, and $V_{S,ZY}$). The subscript *P*- refers to compression wave and *S*- refers to shear wave. The additional subscripts give the propagation and oscillation directions. This section considers only two *S*-waves in the *XY* and *YX* directions, i.e. propagation in the *X* direction with oscillation in the *Y* direction, and vice versa, where *X* and *Y* are horizontal directions (Fig. 6.6(b)). A sinusoidal pulse with a phase delay of 270 degrees, amplitude of ±10V and a nominal frequency f_{in} = 15 kHz was used for all measurements as shown in Fig. 6.7. The voltage signals received at each stress level are illustrated in Fig. 6.8 for *XY* directions. The overall observations were similar for the *YX* direction. For all cases, as the confining stress increases, the first *S*-wave peak arrives earlier, indicating a progressive increase in V_S. When the large ballotini samples are compared, it is obvious that waves propagate faster in the smooth ballotini sample. Note that these plots include effects of *e* and travel distance, and the earlier arrival in the smooth ballotini samples is partially due to the lower *e* values. During unloading the wave velocities decreased with reducing stress level, and the unloading velocities appeared lower than the loading velocities at each stress.

This study used the peak-to-peak method to determine V_S. Note that similar results were obtained using the cross-correlation method in a check for quality assurance (data not presented here). The shear modulus (G_0) data were deduced by:

$$G_0 = \frac{\rho_p}{1+e} V_S^2 \tag{6.2.1}$$

where ρ_p = material density of ballotini (= 2230 kg/m^3). The parameters for the V_S - σ' relationship and the G_0 - σ' relationship were found for the following expressions:

$$V_S = a(1.33-e)\sigma'^{b} \tag{6.2.2}$$

$$G_0 = A\frac{(1.33-e)^2}{1+e}\sigma'^{n} \tag{6.2.3}$$

where the parameter B = 1.33 in this expression was derived from the experimental data using shear plates as discussed below in Section 6.3. The fitting parameters a, b, A and n obtained by regression analysis along with the associated R^2 values are summarised in Table 6.2. Note that the following relationships are valid from Eq. 6.2.1 as the same form of void ratio correction function is considered to be applicable to V_S and G_0.

$$A = \rho_p \, a^2$$
$$n = 2b \tag{6.2.4}$$

The variations in G_0 and $G_0/F(e)$ with σ' are illustrated in Fig. 6.9. In the earlier analysis documented in Otsubo et al. (2015), a different $F(e)$ expression was used so that:

$$G_0 = A \frac{(2.9 - e)^2}{1 + e} \sigma'^n \tag{6.2.5}$$

The value B = 2.9 in this expression was obtained by considering the results of a best-fitting process using V_S/σ'^b - e relationship where b was directly obtained using the V_S - σ' relationship without considering $f(e)$. The value B = 2.9 used by Otsubo et al. (2015) was determined based only on data from two samples on which tests in multiple directions were performed. Fig. 6.10 shows the variations in $G_0/F(e)$ with confining stress using B = 2.9. Comparing the data in Fig. 6.9(b) with B = 1.33 (Eq. 6.2.3) and the data in Fig. 6.10 with B = 2.9 (Eq. 6.2.5), the overall observations are similar despite the difference in the values of $G_0/F(e)$. Thus the conclusions drawn in Otsubo et al. (2015) are unaffected.

Referring to Figs. 6.9(a) and (b) for the large ballotini samples, the smooth case exhibits remarkably larger G_0 and $G_0/F(e)$ values at low stresses in comparison with the rough cases, where $G_0/F(e)$ for the smooth case is approximately twice that of $G_0/F(e)$ for the rough case. Discrepancies between $G_{0,XY}$ and $G_{0,YX}$ were noticed for the rough case, which probably resulted from the more heterogeneous packing of the looser sample for the rough case. As the stress increased, the rough sample data tended to converge to the fitting curve for the smooth case and this convergence is clearer when the void ratio correction is applied (Fig. 6.9(b)). In contrast, the small ballotini data showed similar variations in $G_0/F(e)$ with σ' for both the smooth and the rough cases (Figs. 6.9(c) and (d)). For the highest stress σ' = 400 kPa for the smooth sample, G_0 data were obtained using an input signal that was a normal sinusoidal pulse without a phase delay as it could be applied before the problem described above occurred. The S_q values for the smooth ballotini (WSS, S_q = 193 nm) were not as low as the S_q values for the WLS (S_q = 36 nm) or GSSw (S_q = 58 nm) ballotini (Table 3.2), and the change in S_q values induced by the milling process was not significant; the WSR ballotini had S_q = 222 nm. Referring to Fig. 6.9(d), the washed rough ballotini sample show larger $G_0/F(e)$ values than non-washed ballotini sample, while the smooth ballotini sample exhibits slightly larger $G_0/F(e)$; however, the variations

amongst the three samples are not significant compared with the large ballotini cases. To compare surface roughness effects between the large and small ballotini samples, it seems reasonable to normalise S_q values by the mean particle radius R_{mean}, i.e. S_q/R_{mean}. Fig. 6.11 compares the relationships between $G_0/F(e)$ and σ' classifying the data by S_q/R_{mean}. There is a clear trend that a larger S_q/R_{mean} results in a greater reduction in $G_0/F(e)$ at low stresses in comparison with the smooth test case.

To assess the reduction in $G_0/F(e)$ due to the surface roughness, the $G_0/F(e)$ data were normalised by the $G_0/F(e)$ data for the large smooth ballotini sample (S_q = 36 nm). Referring to Fig. 6.12, variations in the stiffness reduction associated with S_q/R_{mean} in both the *XY* and *YX* directions are compared at σ' = 50, 200 and 500 kPa. For the lowest stress level at 50 kPa, $G_0/F(e)$ decreased with increasing S_q/R_{mean} with a maximum reduction of $G_0/F(e)$ by approximately 60%; however, the limited range of S_q/R_{mean} data available inhibited identification of a clear relationship. As the stress level increased the reduction in $G_0/F(e)$ became insignificant. At the highest stress level considered (σ' = 500 kPa) the roughness induced reduced $G_0/F(e)$ by less than 20%.

The variation in the power coefficient n with σ' for each interval (increment) of σ' considered is illustrated in Fig. 6.13 with a best-fit exponential curve for each sample. The fitting parameters are summarised in Table 6.3. There is considerable scatter in the data points; however, the trend lines indicate that n increases with increasing S_q, whereas n decreases with increasing σ'. The highest n value observed here was approximately 0.9 at the lowest stress level. The best-fit curves for the n - σ' relationships for the four material types are compared in Fig. 6.14 by using an index of S_q/R_{mean}, and an increasing trend of n with increasing S_q/R_{mean} values is confirmed. As the stress increases n decreases so that the n values converge. These findings agree with the analysis of the DEM data in Section 5.4.

6.3 Shear plate tests and DEM simulations

A second series of experiments was carried out using a triaxial apparatus at Imperial College London. The objective of these tests was to extend the consideration of surface roughness effects to a larger stress level than can be applied in the CCA apparatus in the University of Bristol ($\sigma' \leq$ 500 kPa). When the logistics of carrying out bender element tests on the coarse ballotini samples at high stress levels were considered, there was a concern of that bender elements might be damaged; this concern was voiced by Mr. Steven Ackerley, a geotechnics laboratory research officer at Imperial College London. Results presented in the PhD thesis by O'Donovan (2013) were also considered; his DEM data suggest that the bender element signals are affected by the local packing around the element.

To overcome these potential problems, shear plates that can be embedded in the base pedestal and top cap were considered as alternative to bender elements. Previous researchers who used shear plates include Brignoli et al. (1996), Ismail & Rammah (2005) and Suwal & Kuwano (2013). In their discussions these earlier researchers emphasised that sample preparation becomes easier than using bender elements. In comparison with bender elements, experience of using shear plates in soil mechanics tests is limited. Therefore, supplemental DEM analyses were performed to better understand the system response when shear plates are used. To compare the experimental and DEM data, the system responses at the transmitter and receiver boundaries were considered. In the DEM simulations the shear plates were modelled using wall boundaries as described below.

Section 6.3.1 introduces the design and prototyping of shear plate configurations considered in this study. Section 6.3.2 describes laboratory sample preparation method and equivalent DEM simulation method, and the experimental and DEM data obtained are discussed in Section 6.3.3.

6.3.1 Design and prototyping of shear plate configurations

A shear plate is a planar piezo-electric element that converts applied forces to electric signals, and vice versa, and it operates in shearing mode (Fig. 6.15). Referring to Fig. 6.16, this study used two types of rectangle shear plate elements (PZT505) manufactured by Morgan Advanced Materials: the first small elements have dimensions of 15×15×1 mm (S-type) (Fig. 6.16(a)), and the large elements have dimensions of 30×15×1 mm (L-type) (Fig. 6.16(b)). The plate elements comprise lead zirconate titanate (PZT) with a density of 7800 kg/m^3 and a Poisson's ratio of 0.3. Two configurations of shear plates were used: for the 2L configuration two large plates were used (Fig. 6.16(a)) while for the 5S configuration five small plates were used (Fig. 6.16(b)). The same configurations were used on the base pedestal and top cap in each case. These shear plate elements were embedded into recessions in the pedestal and top cap with tiny gaps at the sides to allow the shear deformation of the elements, and pieces of tape were used to fix the position of the plates. For the 2L-case the plates covered 45.8% of the surface area of the base pedestal and top cap, whereas for the 5S-case the plates covered 57.3% of the surface area; this was reduced to 11.5% when the only centre element was excited. The polarization of all the elements was identical, and the movement of each element could be controlled individually using a function generator. When the wires of all the plates were connected in parallel, the movement of these elements was synchronised.

The test procedure when the shear plates were used to determine V_S is illustrated in Fig. 6.17, and this is almost identical to a conventional bender element test. To control the movement of a shear plate element, specified electric (voltage) signals can be inserted using a function

generator (Fig. 6.18(a)). This study used a TG1304 (Thurlby Thandar Instruments) function generator that can generate a sinusoidal shaped pulse. Two oscilloscopes each having two channels were used to receive three signals at the same time; the fourth channel was used for monitoring the inserted signal (Fig. 6.18(b)). The resolution of the digital data obtained depends on the capacity of the oscilloscope and software used to process the signals. The oscilloscope used here (TBS1042 Tektronix) can convert the analogue data shown in the display to a digital data output. When the received signals included background noise, a built-in function that averaged the data over 4 to 128 signals was used. Three custom-made amplifiers (Fig. 6.18(c)) were used to amplify received signals by a factor of 100, and the data generated by the three amplifiers were within 1%. Referring to Fig. 6.17, these electric devices were connected to the shear plates inside the triaxial cell.

6.3.2 Sample preparation and DEM models

A representative cylindrical specimen set up in the triaxial apparatus is shown in Fig. 6.19. The ballotini considered in the shear plate tests in this section were smooth (GSSw), medium rough (GSRw-5h), and rough ballotini (GSRw-25h) (Fig. 6.20 & Table 3.1). The measurable difference amongst the three materials was surface roughness, and the mean values of the RMS surface roughness (S_q) for the smooth, medium rough and rough ballotini were 58, 267, and 612 nm, respectively (Table 3.2). Referring to Table 3.4 considering the maximum and minimum void ratios (e_{max} and e_{min}), there is a narrow range of e between e_{min}=0.577 and e_{max}=0.626 which can be attained for the three materials. Three tests (IC-01, IC-02 and IC-03) were conducted using the three material types at similar e_0 values (0.606, 0.599, and 0.595) as listed in Table 6.1. The sample preparation method considered here was different from that considered in the CCA tests; an automatic pluviator was not used. Recall that samples with similar e values and different surface roughness could not be obtained using the pluviator system used in the CCA tests. For triaxial tests on the smooth ballotini, a relatively loose packing was required to achieve the target void ratio (e_{target}) and they were pluviated slowly into a metal mold using a funnel where the tip of the funnel was always just above rising sample surface. In contrast, to achieve e_{target} densification was required in the case of the rougher ballotini samples. For the rougher ballotini, the samples were prepared by dividing the volume into 10 layers, and the side wall of the mold was tapped by a metal bar for each layer until the e_{target} was obtained. The number of blows was set to be equal for each layer so that all the layers were densified equally. After placing a topcap on the sample, a vacuum (negative) pressure of 30 kPa was applied before dismantling the mold. The e data measured at σ' = 30 kPa of vacuum pressure are noted as initial void ratio (e_0) in Table 6.1.

The dimensions of the cylindrical samples prepared were approximately 110 mm in height and 50 mm in diameter. To measure the variation in the sample dimensions during isotropic compression, two axial displacement sensors (LVDT, linear variable differential transducers) were placed vertically at the opposite sides of the sample, and a radial displacement sensor was placed at the middle height of the sample (Fig. 6.19(a)). The axial LVDTs measured the displacement in the middle part of the specimen to reduce the effect of bedding errors at the bottom and top of the sample. These transducers were attached to the membrane using a glue. This study considers isotropic compression only, and the topcap of the sample was not fixed; the mass of the topcap added a vertical pressure of 1.5 kPa to the sample.

The topcap and pedestal with the L2-shear plate configurations (Fig. 6.16(a)) were used for the tests discussed in this section and no porous stone was placed so that the sample contacted the shear plates directly. The two shear plate elements on the topcap were excited together, and the signals received at two shear plate elements on the pedestal were summed. A plastic plate was placed beneath the base pedestal to reduce the effect from background noise. All the three tests were conducted under dry conditions and the cell pressure was supplied with air to keep the sample dry. The pressure levels used for wave propagation tests were typically σ' = 50, 100, 200, 400, 750 and 1500 kPa; additional finer increments were considered for the rougher ballotini samples. As the limit of the air pressure supplied in the laboratory was about 800 kPa, an air pressure amplifier was used to increase the air pressure up to σ' = 1500 kPa. Representative voltage signals with amplitude of ±10V and nominal frequencies f_{in} = 10 and 20 kHz applied to the shear plates are illustrated in Fig. 6.21. Referring to Fig. 6.21(b), these inserted sinusoidal pulses with f_{in} = 10 and 20 kHz contain a range of frequencies mainly up to 20 and 40 kHz, respectively. To examine frequency effects the values of f_{in} differed in some cases as discussed below.

The DEM simulation approach detailed in Chapter 5 was adopted for the DEM data presented in this chapter. Referring to Fig. 6.22(a) the dimensions of the rectangular samples considered were approximately 100 mm in height and 50 mm in width, and the samples were composed of 155,165 randomly placed spheres with diameters between D = 1.0 and 1.4 mm. The particle size distribution and material properties used were identical to those of the GSSw ballotini (Table 3.1). As described in Chapter 5, lateral periodic boundaries and longitudinal wall boundaries were applied (Fig. 6.22(a)). Referring to Fig. 5.2, for the DEM simulations, the entire bottom wall (transmitter wall) was moved in a transverse direction (X-direction) to generate *S*-waves in the longitudinal direction (Z-direction). The wall movement was a sinusoidal pulse with a phase delay of 270 degrees, double amplitude $2A$ = 5 nm and f_{in} = 20 kHz. To examine frequency effects the values of f_{in} differed in some cases as discussed below. Note that the DEM

simulations considered the stress responses at the transmitter and receiver walls, and the shape of the stress response was a sinusoidal pulse without a phase delay (Fig. 5.5); however, the wall displacement applied at the transmitter wall was a sinusoidal pulse with a phase delay (Fig. 5.2). The contact models used in this section were the HM (Hertz-Mindlin) contact model and the rough surface (RM) contact model (see Table 4.1), and four surface roughness values were considered: S_q = 0, 70, 280 and 600 nm.

6.3.3 Test results and discussions

Void ratio correction function

As discussed in Section 5.3, the void ratio correction function for wave velocity (*f(e)*) can be found from the V_S – e relationship at each stress level. Following Section 5.3 a linear function (Eq. 5.3.4) was used in this section where a B value (for $f(e) = B - e$) specific to the material considered here was required. Ideally, several stress levels should be considered to obtain *f(e)* with confidence; however, repeating tests where e is systematically changed takes time. Note that at higher stress levels the particle surface may be damaged precluding reuse of materials. Thus this study considered only the case where σ' = 50 kPa was applied using vacuum pressure so that the volume of a dry sample was measured accurately without using axial or radial displacement sensors. The materials used here were GSSw (S_q = 58 nm) and GSRw-25h (S_q = 612 nm). The same batch of materials were used repeatedly for this test series and so care was taken not to increase σ' larger than the tested pressure (σ' = 50 kPa) to avoid the effect of material yielding which might modify the contact behaviour. The test results showed no measurable effects of using the same materials repeatedly. A creep time was allowed for each sample to reach an equilibrium until no increase in V_S with time was measured. The creep time was typically about 1 hour for the smooth ballotini sample and 2 hours for the rough ballotini sample.

Figure 6.23 illustrates the time domain response of the smooth ballotini samples (GSSw, S_q = 58 nm) tested at e = 0.534, 0.567, and 0.615 with nominal inserted frequencies f_{in} = 5, 7, 10, and 15 kHz at σ' = 50kPa of vacuum pressure. The sample lengths (i.e. travel distances d_{travel}) were between 112.2 mm and 111.2 mm (< 1% tolerance), and so the time domain responses can be compared directly, i.e. an earlier S-wave arrival indicates larger V_S. The received signals were amplified by a factor of 100 using amplifiers for all tests, and it is the scaled signals that are shown in Fig. 6.23, while all the inserted signals with amplitude of $\pm$10V are scaled down to the maximum value for each subplot. The start time of the plots are adjusted to the first peak of the inserted signals. For all the frequencies considered, a larger e resulted in a later S-wave arrival with more attenuation in the received signals; however the overall shapes of the received signals were similar. Note that the amplitude may be slightly affected by the polarization of the

transmitter and receiver shear plates (see Fig. 6.16(a)) if they are not aligned perfectly in the same direction. The fact that overall wave forms were not affected by e indicates that the shapes of the received signals are controlled by the entire system used in the tests rather than the local configuration of particles. In contrast, the received signals were measurably affected by f_{in}. When a higher f_{in} was inserted, the observed signals included higher frequency components. Referring to Fig. 6.23(d) for the densest sample (e = 0.534) with f_{in} = 15 kHz, the first peak of the received signal was affected by the presence of near-field effects, whereas the subsequent response qualitatively agrees with the other looser samples. Near-field effects are discussed below in Section 6.4.

Equivalent results for the rough ballotini samples (GSRw-25h, S_q = 612 nm) are illustrated in Fig. 6.24 at e = 0.581, 0.624, and 0.684 (Table 6.1). The d_{travel} values varied between 112.4 mm and 111.6 mm (< 1% tolerance). Similar to the smooth samples, the waves travelled faster in the denser samples with less attenuation. The attenuation of signals were considerable for higher f_{in}, and the responses for f_{in} = 15 kHz included background noise. As the L2-shear plate configuration was used here, the voltages of the received signals were approximately 8 times those which would be obtained using a small shear plate element only. Use of a wider size of transmitter and receiver shear plates enables accurate measurements of wave signals even at low pressure levels. Compared with the smooth ballotini samples, the *S*-waves propagated more slowly in the rough ballotini samples, indicating that V_S was reduced due to the surface roughness. Referring to Fig. 6.24(d) for f_{in} = 15 kHz, higher frequency components do not appear in the received signals, which differs from the smooth equivalents (Fig. 6.23(d)). This indicates the presence and activation of the low-pass frequency limits, and that they are affected by the surface roughness. This observation agrees with the DEM simulations considering surface roughness in Section 5.4.

Frequency domain analysis was applied to the received signals for both the smooth and rough ballotini samples. The FFT amplitude of the received signals depends on f_{in} as given in Figs. 6.23 and 6.24, whereas the gain factors, that is the ratios of the received FFT amplitudes to the inserted FFT amplitudes as a function of frequency, describe direct relationships between the inserted and received signals and they are not affected by f_{in} (Alvarado & Coop, 2012). Fig. 6.25 compares the gain factors for both the smooth and rough ballotini samples. Referring to Fig. 6.25(a), the smooth samples exhibit a range of frequencies up to approximately 30 kHz, and denser packing shows larger maximum frequencies. There are two distinct peaks observed in the gain factors and the responses up to 10 kHz are similar for the three samples. Discussions on the two distinct peaks are given in Section 6.4. Referring to Fig. 6.25(b), the rough samples show a narrower range of frequencies in comparison with the smooth samples with a maximum

frequency limit of 13 kHz. The effect of surface roughness on the gain factor is more significant than that of e at σ' = 50kPa.

The interpretation of the shear plate data to determine V_S used the peak-to-peak method as was the case for the bender element tests. Variations in V_S with e for both material types tested are illustrated in Fig. 6.26. The V_S values are slightly affected by f_{in}; the fitting parameters for the best-fit lines in the V_S - e relationships for each f_{in} value are summarised in Table 6.4. For the smooth samples (Fig. 6.26(a)), when all the data points are considered together to obtain a best-fit line, all the data points align within a 3% tolerance with a coefficient of determination (R^2) of 0.936 (Table 6.4). For the rough samples (Fig. 6.26(b)), a consistent increase in V_S with increasing f_{in} is clear, and each f_{in} value indicates a good linear correlation between V_S and e with $R^2 > 0.995$ (Table 6.4). A linear variation in V_S with e for all the data points for the rough samples also holds with a 3% tolerance (Fig. 6.26(b)) with R^2 = 0.939. When the smooth and rough cases are compared, the V_S values for the smooth samples are larger than the V_S values for the rough samples by approximately 25% (Fig. 6.27). Referring to Table 3.4, the range of e tested here covers the attainable range of e values. At a given e and σ', a reduction in V_S can be attributed to the surface characteristics only. The B values in the void ratio correction function obtained for the smooth and rough samples were 1.374 and 1.288, respectively (Fig. 6.27 and Table 6.4), and it seemed reasonable to use their mean value B = 1.33 in this study. Referring to Table 5.4 which gives the B values obtained from the DEM analysis with uniformly sized spheres, B = 1.186 for S-wave, whereas consideration of mechanical void ratio (Eq. 3.5.2), which excludes the volume of non-contacting (i.e. C_N = 0) and one-contact (i.e. C_N = 1) particles, gave B = 1.484; this is reasonably close to the experimental data. The higher B values reported in sands (e.g. B = 2.714 (Hardin & Richart, 1963)) can be explained by the differences in particle shapes, particle size distributions, and the range of attainable e.

Stress-dependency

Referring to Table 6.1, the e_0 values were slightly different amongst the three samples tested (smooth, medium, and rough), and the evolution of the relationships between e and σ' are illustrated in Fig. 6.28(a). Before conducting a wave propagation test, creep time was allowed at each stress level, and Fig. 6.28(a) exhibits e data after the creep. The shape of e - σ' relationship was similar for the three samples although e_0 values were slightly higher for the smoother samples. During unloading from σ' = 1500 kPa to 50 kPa, a similar offset in e was observed for the three sample types. Fig. 6.28(b) illustrates the e - σ' response for the equivalent DEM samples considering only loading. The DEM samples for S_q = 0, 70, 280 and 600 nm had larger e values than the laboratory samples; the relevant data are summarised in Table 6.5. The overall trends observed in experiments and the DEM simulations are similar.

Figure 6.29 presents the experimental data giving the time domain responses for the case of isotropic loading from σ' = 50 kPa to 1500 kPa with f_{in} = 10 and 20 kHz. In Fig. 6.29, the voltage signals were normalised by the maximum amplitude over the entire recording time for the stress level of interest. The d_{travel} values differ slightly amongst the smooth, medium rough and rough samples (see the initial d_{travel} values in Table 6.1); however, the qualitative differences in the received signals can be evaluated. The arrival times of the stress waves appeared earlier as the confining stress increased for all the cases, and the difference (stress-sensitivity) was more marked for the medium and rough cases; the differences were most evident at σ' = 50 kPa. At the highest stress σ' = 1500 kPa, the three cases exhibited similar wave shapes with similar arrival times. For the rougher ballotini samples with f_{in} = 20 kHz, higher frequencies were not observed at lower σ' values, whereas the smooth ballotini samples could pass higher frequencies to receiver as discussed above.

When the data in Fig. 6.29 are compared with the equivalent bender element test data in Fig. 6.8, the bender element signals continue to vibrate for a longer period, e.g. after 1 ms, even at high stresses, which contrasts with the shear plate signals (Fig. 6.28) or the DEM simulations. A similar observation was reported in Brignoli et al. (1996) who compared bender element signals and shear plate signals for the same sample. This indicates that bender element signals may include waves reflected at side boundaries which travel longer distances prior to arriving at the receiver due to the nature of the point-source excitation. The size effect of transmitter and receivers are discussed in Section 6.4.

To check the effects of f_{in} on the wave arrival times, frequencies from 10 to 100 kHz were inserted to the smooth ballotini sample at σ' = 1500 kPa and e = 0.596. Fig. 6.30(a) compares the normalised received signals in the time domain for f_{in} = 10, 20, 40, and 80 kHz where the arrival time is noted by a dashed line in each subplot. For the lowest f_{in} (= 10 kHz) in Fig. 6.30(a), the first *S*-wave peak was affected by the interference of the *P*-wave components as also noted in relation to Fig. 6.23(d). As f_{in} increased, the shape of the received signals became similar and approached a sinusoidal shape. Considering the similar shape observed between f_{in} = 40 kHz and 80 kHz, it seems that frequency components higher than 40 kHz did not arrive at the receiver shear plates. This indicates the presence of a low-pass frequency limit between 40 and 80 kHz as discussed in Section 5.5. The V_S values for the range of f_{in} considered agreed within 1.5% (Fig. 6.30(b)).

Equivalent DEM simulations were carried out to further explore the influence of f_{in} on V_S and the system response. A DEM sample (Test case Dem-F in Table 6.6) composed of spheres that had the same material properties and particle size distribution as used in the physical tests was considered using the HM contact model. The DEM simulations were performed at σ' = 1600

kPa and e = 0.599. The normalised shear stress responses for f_{in} = 10, 20, 40, and 80 kHz were compared in Fig. 6.31(a). As the d_{travel} value was shorter in the DEM sample by approximately 15%, *S*-waves arrived at the receiver earlier than the experimental results. The shape of the received signals differs from the experimental data at lower f_{in} values, whereas at higher f_{in} values the observed responses are similar to the experimental data. Just as was the case in the experimental data, there were no very high frequency components in the received signals. Referring to Fig. 6.31(b), over the range of f_{in} values considered the V_S values differed by less than 1.5%, and the nature of the variation in V_S with f_{in} was similar considering both experimental and DEM results. The mean V_S value was slightly higher in DEM simulations due to the larger σ' value (= 1600 kPa) and the contact model for the smooth contact (S_q = 0).

The frequency domain responses for the experimental and DEM data are compared in Fig. 6.32 for f_{in} = 60 kHz to check the low-pass filter limits. Referring to Fig. 6.32, a sinusoidal pulse with a nominal frequency f_{in} = 60 kHz has measurable amplitudes at frequencies between 0 and 120 kHz; however, the received signals had a limited range of frequencies up to 65 kHz. Although the shape of the FFT data were not identical, a similar maximum frequency was observed for the DEM data. This agrees with the observation in the time domain data for f_{in} = 40 and 80 kHz in Figs. 6.30(a) and 6.31(a).

Variation in V_S and G_0 with σ'

The V_S data deduced using the peak-to-peak method and the corresponding shear modulus (G_0) data are illustrated in Fig. 6.33 considering three input frequencies of f_{in} = 10, 15 and 20 kHz for each sample. The G_0 data were calculated using Eq. 6.2.1 where ρ_p = 2600 kg/m^3. The fitting parameters for the V_S - σ' and the G_0 - σ' relationships were found using Eqs. 6.2.2 and 6.2.3, respectively, and they are tabulated in Table 6.5. The fitting parameters were obtained for the entire range of stresses examined (i.e. 50 to 1500kPa); however, for the rougher ballotini samples, the power coefficients (b and n) depend on the stress level as also discussed in Section 5.4.3. Referring to Table 6.5, the fitting parameters for each sample are not very sensitive to the f_{in} considered, while there is a trend for the medium and rough cases that a larger f_{in} gives a larger a and A but lower b and n although the resultant variations are small. Referring to Fig. 6.29 for f_{in} = 20 kHz, the travel times of *S*-waves were still longer than twice the nominal wave period (T_{in} = 1/f_{in}), and the dominant wave length in the received signals seems to be shorter than d_{travel}/2 so that near-field effects can be reduced (Sanchez-Salinero et al., 1986).

The V_S and $V_S/f(e)$ data for the three experimental samples are compared in Fig. 6.34, and the G_0 and $G_0/F(e)$ data are compared in Fig. 6.35 for f_{in} = 20 kHz. As the overall trend was similar for the V_S and G_0 data, the following discussions refer only to the G_0 data. As the e values were similar amongst the three samples, the effect of applying $F(e)$ was not significant. For the lower

stress levels, the smooth samples showed considerably larger velocities than the medium rough or rough samples where $G_{0,smooth} > G_{0,medium} > G_{0,rough}$ as expected, and the difference gradually decreased with increasing σ'. At the highest stress tested σ' = 1500 kPa, the three sample types had similar G_0 values. The difference in the variations in G_0 between the medium rough and rough samples were not obvious and $G_{0,rough} > G_{0,medium}$ was also observed at high stress levels. Based on an understanding of the system behaviour in Section 5.4 it was expected that $G_{0,smooth} > G_{0,medium} > G_{0,rough}$ for all the stress levels; however, this was not the case. The discrepancy is discussed in more detail together with the DEM results below in this section.

The DEM samples composed of spherical particles with random configurations were prepared at various stress levels as given in Table 6.7. The S_q values considered in the simulations were S_q = 0, 70, 280, and 600 nm. The variations in V_S and G_0 with σ' are illustrated in Figs. 6.36(a) and 6.37(a). Referring to Table 6.7, for the DEM samples, the initial e values were almost identical at a given stress level despite the difference in S_q values; thus consideration of $f(e)$ or $F(e)$ was not needed to discuss the DEM data in isolation. However, when they are compared with experimental results $f(e)$ or $F(e)$ should be applied to correct for the difference in e. Considering the difference in e between experimental and DEM data, e.g. e = 0.595 for lab and e = 0.635 for DEM, applying B = 1.33 gives $f(e)$ = 0.735 and 0.695 for lab and DEM, respectively, i.e. there is a 5.4% difference. When B = 1.186 is considered based on discussions in Section 5.3 (Eq. 5.3.5 and Table 5.4), $f(e)$ = 0.551 for lab and 0.591 for DEM; there is a 6.8% difference. There is a discrepancy in the $V_S/f(e)$ calculation by 1.4% (6.8% - 5.4%) due to the difference in B values; this is not significant. Thus this study used B = 1.33 for both the experimental and DEM data. To confirm this approach was appropriate, a denser DEM sample at e = 0.607 (σ' = 100 kPa) with S_q = 0 was prepared (Table 6.6, Test case Dem-A), and the V_S data (= 324.7 m/s) exceeded the V_S data for the looser sample (e = 0.635, V_S = 308 m/s) by 5.3%; this agrees with the 5.4% difference when B = 1.33 was used to correct the V_S value. The resultant $V_S/f(e)$ - σ' and the $G_0/F(e)$ relationships for the DEM data are presented in Figs. 6.36(b) and 6.37(b). The overall results are similar with those discussed in Section 5.4.

The variation in $V_S/f(e)$ with stress level for the experimental data for smooth samples (S_q = 58 nm) and for DEM models considering S_q = 0 and 70 nm are compared in Fig. 6.38(a). There is close agreement between the experimental and DEM data; all the DEM data points are within 5% of the experimental data points, indicating that the physical tests are well captured by the DEM analysis. A similar trend can be seen in Fig. 6.38(b) for the $G_0/F(e)$ - σ' relationship. Note that discrepancies in the G_0 values are approximately twice those for V_S. Fig. 6.39 compares the experimental data with S_q = 267 nm and DEM data with S_q = 280 nm; the experimental data give lower estimations of $V_S/f(e)$ and $G_0/F(e)$ compared to the DEM data and the lowest and

highest stresses show the best agreement. However, the mean discrepancy was not large, being approximately 5% and 10% for V_S and G_0, respectively. For the rough sample with S_q = 621 nm for experiment and S_q = 600 nm for DEM analysis (Fig. 6.40), the experimental results give larger $V_S/f(e)$ values by approximately 10% at the lowest stress level; however both data agree well at σ' > 400kPa. The discrepancy in $G_0/F(e)$ for the rough case was less than 20%. In summary it was observed that $G_0^{LAB} \approx G_0^{DEM}$ for the smooth sample, $G_0^{LAB} < G_0^{DEM}$ for the medium rough sample, and $G_0^{LAB} > G_0^{DEM}$ for the rough ballotini sample.

Following Fig. 6.12 for the CCA test data, the variations in stiffness reduction with normalised surface roughness surface roughness (S_q/R) are illustrated in Fig. 6.41. Referring to Fig. 6.41, the experimental and DEM data are compared at a given stress level in each plot. For the lowest stress level at 50 kPa (Fig. 6.41(a)), $G_0/F(e)$ decreases with increasing S_q/R; however the $G_0/F(e)$ - S_q/R relationship is not linear and the rate of reduction decreases with increasing S_q. For example, when compared with the smooth case, the medium rough cases show a reduction by approximately 40% in $G_0/F(e)$ while the rough cases give a reduction of 50%. As the stress level increases the stiffness reduction becomes less significant. At the highest stress level, the reduction was at most 20% from the smooth case. As discussed above, in the experimental results, the medium rough and rough ballotini samples gave similar results, and this may be because the surface roughness effects on G_0 reach a plateau at a certain roughness value. From a micromechanical perspective, there is a lack of experimental data of particle compression tests at a very low contact force in the literature as it has been difficult to measure reliable force-deformation curves for rough surface contacts (Greenwood et al., 1984). Greenwood & Tripp (1967) noted presence of the practical lower limit of the reduction in the normal contact stiffness. The rough surface model used in this study follows an assumption made by Yimsiri & Soga (2000), and there is no limit of surface roughness effects considered in the contact model. An additional point to consider is that the DEM simulations assume all the particles initially have the same S_q. In the experiments there is a distribution of S_q values. The stiffer contacts will attract load and these are the contacts with a lower S_q value, consequently it may not be valid to relate the response to the mean S_q value without also considering the distribution. Future numerical simulations should consider this issue.

In addition to the uncertainly in the rough contact behaviour at very low stress levels, the accuracy of surface roughness measurements should also be considered here. Referring to Fig. 6.20 for the surface elevation plots of the tested materials, when S_q values were measured using an optical interferometer, the scatter in surface elevation increased with increasing S_q value; however no filtering was applied in this study. Despite the difference in the surface roughness values between the medium rough ballotini (S_q = 267 nm) and the rough ballotini (S_q = 612 nm),

the e_{min} and e_{max} values were similar (Table 3.4): 0.574 and 0.691 for the medium rough, and 0.577 and 0.704 for the rough ballotini, respectively. Their similar values may be related to the similar G_0 values observed in Fig. 6.34.

The frequency domain responses were considered, and the gain factors of the system at the lowest and highest stress levels for both the experimental and DEM data are compared in Fig. 6.42. At the lowest stress $\sigma' = 50$ kPa (Fig. 6.42(a)) the experimental data for $S_q = 58$ nm exhibit two distinct peaks as also observed in Fig. 6.25(a), while the rougher cases showed a narrower range of frequencies with gain factors that are lower in magnitude especially for the rough case. In contrast, the DEM data show less variations in gain factor with frequency (Fig. 6.42(b)), this is in line which was also observed in Section 5.4. The maximum frequency propagated, defined here as $f_{low\text{-}pass}$, for the smooth case is in good agreement when the experimental data (≈27 kHz) and the DEM data (≈25 kHz) are compared, whereas the DEM data give higher $f_{low\text{-}pass}$ values (≈19 kHz) than the experimental data (≈14 kHz) for the rougher cases. As the stress increases $f_{low\text{-}pass}$ increases as given in Figs. 6.42(c) and (d) where magnitude of the gain factor also increases for the experimental results. Note that the e values were larger in the DEM samples, and this would result in smaller $f_{low\text{-}pass}$ all other system characteristics being similar. Considering the difference in e, the $f_{low\text{-}pass}$ values for the smooth case are in good agreement for the experimental data (≈60 kHz) and the DEM data (≈56 kHz). Referring to Figs. 6.42(c) and (d), the experimental data for the medium and rough ballotini samples showed a similar $f_{low\text{-}pass}$ value (≈50 kHz); this is smaller than $f_{low\text{-}pass}$ (≈54 kHz) for the DEM data. It is clear that the increase in $f_{low\text{-}pass}$ associated with the increase in stress is greater in the rougher samples than the smooth sample for both experimental and DEM data.

Using Eq.6.2.3, the power coefficients n for each section of the $G_0/F(e)$ - σ' relationship are presented in Fig. 6.43 where σ' indicates the mean of each stress interval. Referring to Fig. 6.43(a) for the DEM data, the rougher sample exhibits higher n values and n decreases with increasing σ', and the trends are similar to the findings for uniformly sized spheres in Section 5.4 (Fig. 5.40). Considering the smooth case, Fig. 6.43(b) shows good agreement between the experimental and DEM data; the experimental data ($S_q = 58$ mm) are located below 0.4 and n values are insensitive to σ'. The best-fit exponential curves added for the experimental data are summarised in Table 6.3. For the medium rough sample (Fig. 6.43(c)), there is considerable fluctuation in n between 0.415 and 0.580 for the experimental data; however, the overall trend is still captured by the DEM data. The rough sample had larger n values at low stresses than those for the medium and smooth samples (Fig. 6.43(d)); it is clear that n decreases with increasing σ'. When all the samples are compared the rougher ballotini samples result in the higher n values at low stresses, i.e. $n_{rough} > n_{medium} > n_{smooth}$, and the n values tend to approach the values for the

smooth case as σ' increases. Despite the observation that $G_{0,medium} \approx G_{0,rough}$ noted above, surface roughness clearly affected the n values. The highest n values observed here were approximately 0.7 in comparison with $n \approx 0.9$ for the equivalent data using CCA apparatus (Fig. 6.13) although similar roughness values were considered. As listed in Table 3.1, the ballotini used in the CCA apparatus and those used in the triaxial apparatus were different in the particle shear modulus due to difference in chemical composition. This indicates that the surface roughness effects may depend on the material properties in addition to stress levels.

Comparison between bender element tests and shear plate tests

The bender element test data obtained using the CCA apparatus as discussed in Section 6.2 and the shear plate test data discussed above were compared in term of the normalised small-strain shear modulus $G_0/F(e)$. For the smooth ballotini samples, it is possible to compare $G_0/F(e)$ values between different material types, e.g. the GSSw (S_q = 58 nm) ballotini sample used in the triaxial apparatus and the WLS (S_q = 36 nm) ballotini samples used in the CCA apparatus. Recall that the GSSw sample was prepared using a funnel (pluviation) and the WLS sample was prepared using an automated pluviator (Fig. 6.3). The $G_0/F(e)$ data for the GSSw sample (Fig. 6.35(b)) and the WLS sample (Fig. 6.9(b)) are compared in Fig. 6.44. Referring to Fig. 6.44, the GSSw sample exhibits larger $G_0/F(e)$ values than the WLS sample by approximately 10%; however, similar exponential slopes are observed. From a micromechanical perspective, using effective medium theory (EMT) gives the following relationship at a given stress, the particle Poisson's ratio and the mean coordination number (see Section 2.7.1 for details):

$$G_{0,HM}^{EMT} / F_{(e)} \propto G_p^{2/3} \tag{6.3.1}$$

where G_p is the material shear modulus, and Eq. 6.3.1 is valid for the Hertzian contact model. As compared above, the smooth ballotini can be modelled using the HM contact model. The G_p values for the GSSw and WLS ballotini are 29.2 GPa and 25 GPa, respectively (Table 3.1). This gives a shear modulus ratio ($G_{0,GSSw}/G_{0,WSL}$) to be $(29.2/25)^{2/3}$ = 1.11; this agrees with the observation in Fig. 6.44.

The surface roughness effects observed in both test types (CCA and triaxial apparatus) were compared considering the relationship between the reduction in $G_0/F(e)$ from the smooth ballotini data and the normalised surface roughness S_q/R (Fig. 6.45). As discussed above the two types of the smooth ballotini (GSSw and WLS) had different $G_0/F(e)$ values; the reduction was calculated for each material type as considered in Figs. 6.12 and 6.41. For the shear plate tests, the equivalent DEM data are also included in Fig. 6.45. At σ' = 50 kPa, the CCA data gave a greater reduction than the triaxial apparatus test (TX) data at approximately $S_q/R = 0.4\times10^{-3}$ (Fig. 6.45(a)). Good agreement for both the CCA and TX data was observed at σ' = 100 kPa

(Fig. 6.45(b)) and the data agreed with the observation in Fig. 6.41. As stress increased the reduction became less significant for the CCA data compared with the TX data. The difference may be related to the difference in the material properties as noted above.

Wave velocity for overconsolidated samples

The discussions above considered V_S data during the initial loading. In general, soils exhibit $G_0^{unload} > G_0^{load}$ for a given stress level, and this results partially from the fact e decreases due to overconsolidation. Referring to Fig. 6.46(a) for the experimental data for the smooth ballotini sample (f_{in} = 15 kHz), unloading from the highest stress level (σ' = 1500 kPa) gives a delayed arrival time for each stress, i.e. $V_S^{unload} < V_S^{load}$, although e and d_{travel} are lower in the unloading case for each stress (Fig. 6.28(a)). All the laboratory tests performed in this study including the bender element tests in the CCA apparatus (Fig. 6.8) showed the same trend. Santamarina & Cascante (1998) also reported lower V_S values with a higher power coefficient b value for an unloading case using rough metal spheres. This contrasts to the findings for soils in general. To check this point, a DEM simulation was carried out in which a DEM sample for smooth surface (HM contact model, S_q = 0) prepared by unloading from σ' = 1600 kPa (Test case Dem-6) to σ' = 100 kPa (Test case Dem-2U, Table 6.8). The resultant e = 0.634 is similar to an equivalent sample (e = 0.635) for an initial loading case (Test case Dem-2) at σ' = 100 kPa. The time domain responses for both samples are compared in Fig. 6.46(b), and the unloading case give a later arrival time with more attenuated stress responses compared to the loading case, which captures the experimental result. The V_S values were 308 m/s for the loading case and 298 m/s for the unloading case, and the resultant G_0 values were approximately 6% larger in the loading case. Referring to Table 6.8, this can be explained by the fact that the mean coordination number $\bar{C}_N$ (= 5.25) for the loading case is higher compared with $\bar{C}_N$ = 5.17 for the unloading case although e is slightly higher for the loading case, i.e. the higher $\bar{C}_N$ value resulted in the larger values of V_S and G_0; this indicates a stronger correlation between V_S and $\bar{C}_N$ rather than the V_S - e relationship. Magnanimo et al. (2008) prepared DEM samples with different methods to change $\bar{C}_N$ value while keeping e constant, and they reported that a higher $\bar{C}_N$ gave a larger G_0.

Considering the experimental data for the initial loading and unloading cases at σ' = 50 kPa, the influence of overconsolidation on the frequency domain responses was considered. The FFT amplitude of received signals and gain factors of these samples are compared in Fig. 6.47. Referring to Fig. 6.47(a) the normalised inserted signal for f_{in} = 20 kHz contains main frequencies up to 40 kHz; however, the received signals contain a narrower range of frequencies. It is clear that the unloading case give a lower $f_{low\text{-}pass}$ value with lower amplitude of gain factors at the higher frequencies. Recall that higher e gave a lower $f_{low\text{-}pass}$ for the loading

case as given in Fig. 6.25, whereas Fig. 6.47 exhibited an opposite trend where the loading sample had higher e (= 0.605) compared with the unloading sample (e = 0.603). This indicates that $f_{low\text{-}pass}$ is affected by change in contact fabric due to overconsolidation. Considering the change in both the V_S and $f_{low\text{-}pass}$, there may be a good correlation between V_S and $f_{low\text{-}pass}$.

6.4 Influence of shear plate size on system response

The data available from this study were explored to assess whether systems using shear plates give improved signal quality in comparison with bender element systems. Bender elements are a point-source transmitter and receiver, and the bender transmitter generates shear (*S*-) waves in the vicinity of its tip, and compression (*P*-) waves normal to the element (Lee & Santamarina 2005). Consequently while the received signals are dominantly *S*-waves they are distorted by the *P*-waves, this phenomenon is called the near-field effect (Sanchez-Salinero et al. 1986; Arroyo et al. 2003). O'Donovan (2013) observed significant diffusion of *S*-waves and the near-field effects using DEM simulations. Using shear plates should generate more planar *S*-waves with reduced near-fields effects.

This section explores the influence of shear plate size on the wave signals considering both experimental and numerical results. Referring to Table 6.8, two samples composed of the smooth ballotini (GSSw) were prepared using the 2L- and 5S-shear plate configurations at confining stress $\sigma' \approx$ 100 kPa. For both cases, f_{in} = 10 and 20 kHz were considered. Using DEM an equivalent random sample (Fig. 6.22(b)) and a FCC sample (Fig. 6.22(b)) were prepared with the HM contact model. For the random sample, e and σ' were adjusted to be close to the experimental conditions; however the sample lengths, i.e. travel distance d_{travel}, of the laboratory specimens were longer than DEM data by approximately 15%. The dimensions of the rectangular samples considered were approximately 100 mm in height and 50 mm in width both for FCC and random samples (Fig. 6.22). The FCC sample consisted of 191,634 spheres (41×41×114 layers) with a diameter of D = 1.2 mm, and the random sample composed of 155,165 spheres with diameters between D = 1 and 1.4 mm, with a particle size distribution identical to that of the GSSw ballotini (Table 3.1).

6.4.1 2L-shear plate configuration

Referring to Fig. 6.48, the two large elements (denoted here as T1 and T2) embedded in the topcap were used as transmitter shear plates, and the R1 and R2 elements used as receiver shear plates were attached to the pedestal. Three scenarios of wave generation were used: T1 only, T2 only, and both T1 and T2 at the same time. For each scenario, the R1 and R2 wave signals were

received individually, thus there are six combinations of wave paths as shown in Fig. 6.48. The following notations were used to distinguish each wave.

- u_{11} (or u_{12}): Received signals at R1 (or R2) with excitation from T1 only.
- u_{21} (or u_{22}): Received signals at R1 (or R2) with excitation from T2 only.
- u_{D1} (or u_{D2}): Received signals at R1 (or R2) with excitation from T1 and T2 together.

For a frequency of f_{in} = 10 kHz, when u_{11} and u_{22} are compared, almost identical responses were observed, and the responses u_{12} and u_{21} are also similar (Fig. 6.49(a)). Referring to Fig. 6.50, the difference between u_{11} and u_{21} can be explained by the difference in the travel distance between T1-R1 (L_{11}) and T1-R (L_{12}), and the direction from T1 to R2 deviates from the direction of stress wave propagation by an angle of θ. When both T1 and T2 are excited together, u_{D1} and u_{D2} are almost identical and the summation of u_{11} and u_{21} (or u_{22} and u_{12}) agrees well with u_{D1} (or u_{D2}). Thus the summation of u_{11}, u_{12}, u_{21} and u_{22} also agrees with the summation of u_{D1} and u_{D2} (Fig. 6.49(d)). These data confirm the sample response is elastic, and increasing the size of shear plates doesn't affect the dynamic response of the sample; however, the received signals became clearer and a larger amplitude is attained by using two transmitter plates simultaneously. The frequency domain responses for these plots are illustrated in Figs. 6.49(c) and (d), and the amplitude of the received spectra exhibits almost identical shapes considering u_{11} and u_{22} and also for u_{12} and u_{21}; however, u_{11} and u_{12} (or u_{22} and u_{12}) have the peaks of spectra at 10 and 7.5 kHz, respectively. The summation of u_{11}, u_{12}, u_{21} and u_{22} agrees with the summation of u_{D1} and u_{D2}, and there are local peaks observed at 10 and 7.5 kHz.

The influence of the inserted frequency on signal response was investigated by repeating the study using f_{in} = 20 kHz (Fig. 6.51). The overall conclusion is similar; however, the agreement is not as good as the case for f_{in} = 10 kHz. For example, u_{11} obviously differs from u_{22}, and the amplitude of $u_{D1} + u_{D2}$ is larger than the summation of the individual component, i.e. $u_{11} + u_{21} + u_{12} + u_{22}$. This trend was also confirmed using f_{in} = 15 kHz. The frequency spectra of these plots are illustrated in Figs. 6.51(c) and (d), and it is clear that the low frequencies below 10 kHz are almost identical, while the high frequencies above 20 kHz are not. This explains why the received signals showed disagreement when f_{in} = 20 kHz was used. Based on understanding from Section 5.5, lower frequencies excite fundamental vibration modes that are insensitive to the local configurations of particles but behave like a continuum (long-wave limit). In contrast, higher frequencies excite more localised vibration modes, and they are more sensitive to the path of wave propagation.

DEM simulations were performed using the random sample illustrated in Fig. 6.22(a) to examine the observations in more detail. Referring to Fig. 6.52, the DEM wall boundaries were

halved to model the T1 and T2 elements along the transmitter wall, and the R1 and R2 elements along the receiver wall. Six transmitter-receiver combinations were considered as was the case for experiments. Considering f_{in} = 20 kHz, the received shear stress responses are compared in Fig. 6.53. The findings from the physical experiments were confirmed in the DEM data, i.e. the sample response is linear-elastic. Referring to Chapter 5, source near-field effects (Arroyo et al. 2003) were not observed when planar waves are excited into a DEM sample, and this agrees with the results here. However, when a half of the transmitter wall is excited, a stress response prior to the *S*-wave arrival is observed (Fig. 6.53(a)). Considering the *P*-wave arrival time obtained in a simulation of planar *P*-wave propagation, it is indicated on Fig. 6.53(a) and is obvious that the initial fluctuation is caused by the *P*-wave arrival, i.e. near-field effects. It is interesting to note that the near-field effects disappear when the responses at the R1 and R2 receivers are summed, and the summation of u_{11}^{DEM}, u_{12}^{DEM}, u_{21}^{DEM} and u_{22}^{DEM} is identical to the planar wave response (Fig. 6.53(b)). Referring to Fig. 6.53(c) for the frequency domain responses, u_{11}^{DEM} and u_{22}^{DEM} disagree at higher frequencies as was the case for the experiments. Considering different frequencies associated with the local maxima for u_{11}^{DEM} and u_{12}^{DEM}, these peaks appear in the planar wave response as a summation (Fig. 6.53(d)).

For the rectangular-shaped transmitter wall, there are two directions of shearing, i.e. the X-direction as discussed above, and the Y-direction as illustrated in Fig. 6.54. The stress responses of u_{11}^{DEM} and u_{12}^{DEM} are compared in both shearing (X- or Y-) and normal (Z-) components for each scenario. As also illustrated in Fig. 6.53(a), the near-field effects were observed followed by the *P*-wave arrival for the excitation in the X-direction, whereas the near-field effects were not observed for the excitation in the Y-direction (Fig. 6.54(b)) although the *P*-wave components were detected at the receiver walls for the *S*-wave excitation as indicated by a measurable change in $\Delta\sigma'_Z$. The first negative peak in the $\Delta\sigma'_Z$ data agreed with the *P*-wave arrival time for the case of planar wave propagation. Note that the normal stress responses in the Z-direction are always present even for planar wave propagation due to the nature of random packing.

6.4.2 5S-shear plate configuration

Referring to Fig. 6.55, amongst the many possible combinations of wave generation using the five shear plate elements, the following four combinations were considered: (a) T5 (referred to here as $u_{5\rightarrow}$), (b) T1, T3 and T5 ($u_{135\rightarrow}$), (c) T2, T4 and T5 ($u_{245\rightarrow}$), and (d) all five elements ($u_{all\rightarrow}$). These combinations engaged different proportions of the surface area of the pedestal and topcap: (a) $u_{5\rightarrow}$: 11.5%, (b) $u_{135\rightarrow}$: 34.4%, and (c) $u_{245\rightarrow}$: 34.4%, (d) $u_{all\rightarrow}$: 57.3%. For a given receiver size, the influence of transmitter size is considered in Figs. 6.56(a) and (b) where the received voltages are normalised by the amplitude of the first *S*-wave peak as the voltage

amplitude is effectively proportional to the summation of the transmitter and receiver areas. Referring to Fig. 6.56(a), the main shear wave for $u_{5\rightarrow5}$ arrives at the R5 element earlier than $u_{all\rightarrow5}$, and the wave velocity is $V_S,u_{5\rightarrow5} > V_S,u_{245\rightarrow5} > V_S,u_{135\rightarrow5} \approx V_S,u_{all\rightarrow5}$. The earlier arrival of the wave contribution $u_{245\rightarrow5}$ compared with $u_{135\rightarrow5}$ can be explained by the DEM simulation results illustrated in Fig. 6.54 which showed that near-field effects are more significant when the direction of shearing aligns with the shorter side of the rectangle. For the 5S-shear plate configuration, exciting T2, T4, and T5 (Fig. 6.55(c)) may induce more near-field effects than exciting T1, T3 and T5. When all the receiver elements are summed, similar responses amongst the four signals in Fig. 6.56(b) are noticed, and the order of the wave arrival was the same as above, i.e. $V_S,u_{5\rightarrow all} > V_S,u_{245\rightarrow all} > V_S,u_{135\rightarrow all} \approx V_S,u_{all\rightarrow all}$. When all the transmitter elements were excited, the response of each receiver is compared in Fig. 6.56(c) where the order of wave velocity is $V_S,u_{all\rightarrow5} \approx V_S,u_{all\rightarrow2} \approx V_S,u_{all\rightarrow4} > V_S,u_{all\rightarrow3} \approx V_S,u_{all\rightarrow1}$. When the size of the transmitter and receivers were kept equal, the wave contribution $u_{5\rightarrow5}$ had an earlier arrival time than $u_{all\rightarrow all}$ (Fig. 6.56(d)) where the amplitude of $u_{all\rightarrow all}$ is approximately 10 times larger than $u_{5\rightarrow5}$. To summarise the observation, it is clear that using smaller size of shear plates tends to give a larger wave velocity. Discussions above were based on f_{in} = 10 kHz, and experimental results for f_{in} = 20 kHz are illustrated in Fig. 6.57, and this supports the observations using f_{in} = 10 kHz.

To understand the frequency components of the received signals, gain factors for the individual wave paths, $u_{1\rightarrow1}$, $u_{2\rightarrow2}$, $u_{3\rightarrow3}$, $u_{4\rightarrow4}$ and $u_{5\rightarrow5}$ are compared with $u_{all\rightarrow all}$ in Fig. 6.58. The variations in gain factor with frequency depend on each wave path where $u_{2\rightarrow2}$ and $u_{4\rightarrow4}$ exhibit higher gain factors at lower frequencies, while $u_{1\rightarrow1}$ and $u_{3\rightarrow3}$ show more uniform distributions of gain factors. The $u_{5\rightarrow5}$ signal gives higher gain factors at higher frequencies compared with the other cases. These discrepancies can be related to boundary effects; the outer plates are influenced by the membrane boundary transmitting a constant stress, giving lower frequencies compared with the centre plate. When all the plates are excited, the gain factor for $u_{all\rightarrow all}$ is similar to the summation of the each components. As noted in Section 6.3, the two distinct peaks in gain factors are observed. The reason may be linked with the presence of the membrane boundaries considering the discussion above. The results presented here highlight that the gain factor is not unique for a given sample; it is also affected by the source of excitation and presence of the nature of the sample boundary.

To assess the influence of the shear plate size, equivalent DEM simulations were carried out using the random sample considered for the 2L-shear plate configuration (Test case Dem-A in Table 6.6). Instead of modelling 5 shear plate elements, a circular area from the centre of each wall was considered as the transmitter and receivers (Fig. 6.59). Three distinct areas were

considered here: 2%, 20% and 100% of the walls, and the following notation was used; e.g. $u_{20\rightarrow100}$ stands for waves generated at the 20% area of the transmitter wall and received at the entire receiver wall (100%). Influence of size of receiver and transmitters are compared in Figs. 6.60(a) and (b), respectively. When the entire wall was excited to generate *S*-waves, the observed signals showed almost identical shapes, and the amplitude of stress response was proportional to the receiver area (Fig. 6.60(a)). When a smaller area was excited, the generated waves were too small to output the data with sufficient resolution (for double precision), thus the amplitude of wall displacement was multiplied by the reciprocal of the relative area, i.e. the displacement of the 20% transmitter wall was amplified by 5. The resultant signals are almost identical amongst the three receiver areas (Fig. 6.60(b)). Thus it is clear that received signals are not affected by transmitter or receiver size if either a full-size transmitter or a full-size receiver is considered. When the areas of the transmitter and receivers are reduced equally, the stress responses clearly include near-field effects (Fig. 6.60(c)). For $u_{20\rightarrow20}$, the first *S*-wave peak is remarkably affected by the *P*-wave components, whereas $u_{2\rightarrow2}$ leads completely different signals from $u_{100\rightarrow100}$ (plane wave), which gives a larger V_S. O'Donovan et al. (2016) reported near-field effects in their bender element simulations using DEM in which single particle was excited as transmitter (point-source excitation). When bender elements are considered, the source of excitation can be regarded as an area < 2% depending on sample dimensions and particle size (see Fig. 6.6(a) for a typical design).

To better understand the system response during *S*-wave propagation, the particle kinetic energy in the oscillation direction K_X (= 0.5×mass×$V_{p,X}^2$) and the propagation direction K_Z (= 0.5×mass×$V_{p,Z}^2$) are plotted in Figs. 6.61 and 6.62 for planar wave excitation ($u_{100\rightarrow}$) and a 2% area excitation ($u_{2\rightarrow}$), respectively. Snapshots taken at t = 0.025 ms (= 0.5T_{in}), 0.1, 0.2, and 0.3 ms along the middle slice of the XZ plane are considered. Referring to Fig. 6.61 for the case of plane wave propagation, a coherent wave front is seen in the X-direction, while more random oscillation can be seen in the Z-direction. It is observed that the K_X and K_Z components propagated with a similar speed and arrived at the top receiver wall at t around = 0.3 ms. In contrast, excitation of a 2% area of the transmitter wall shows a non-planar wave front in the X-direction (Fig. 6.62), which agrees with O'Donovan et al. (2012). As a periodic boundary is used in the lateral directions in this study, some complex interactions near the side boundaries can be seen. The propagation speed of K_X is similar with the planar *S*-wave, whereas the K_Z component travels faster with the same speed with the *P*-wave and arrived at the receiver wall by t = 0.2 ms. Referring to Fig. 6.60(c) for the $u_{2\rightarrow2}$ case, the results presented here capture the effects of the *P*-wave components on the *S*-wave received signals.

To investigate the relationship between V_S and the area ratio (i.e. area of shear plates to the entire area), additional simulations were performed, and Fig. 6.63 presents the variation in V_S with the area ratio. When only 10% of the excitation area was considered, the V_S value was overestimated by 10%. To reduce the error to be within 5%, it is advisable to use an area exceeding 20%. To check this effect for *P*-wave propagation, similar simulations were conducted by generating *P*-waves using various size of transmitter and receivers. Referring to Fig. 6.60(d), there is little effect of the size of excitation on the *P*-wave arrival times although the overall shapes deviate from the case for the planar wave response. Using the time domain responses shown in Figs. 6.60(c) and (d) the frequency domain responses of both *S*-waves and *P*-waves are illustrated in Fig. 6.64. Although the lateral boundary conditions differ in the experiments and the DEM simulations, the DEM data also exhibit complex variations in the frequency spectra as the size of the transmitter and receivers decreases. This confirms that frequency responses of the sample are affected by the excitation method.

The presence of near-field effects using a FCC sample was reported by O'Donovan et al. (2015) in their bender element simulations using DEM. It is difficult to prepare a perfect lattice packing in laboratory; however, DEM enables assessment of the near-field effects in a FCC sample. Considering the same approach above, $u_{2\rightarrow2}$, $u_{20\rightarrow20}$, and $u_{100\rightarrow100}$ were compared for both *S*-wave and *P*-wave tests using a FCC sample at $\sigma' = 100$ kPa (Fig. 6.22(b)). Referring to Fig. 6.65(a), using a smaller area of excitation results in an overestimation of V_S compared with the case for planar wave propagation ($u_{100\rightarrow100}$), which agrees with the observation above for the random sample. When a *P*-wave is considered, the FCC sample exhibits variation in V_P with the size of excitation area by splitting the first coherent wave into two parts (Fig. 6.65(b)). However, it is noted that the time for the first non-zero stress response was not affected by this, i.e. the start-to-start approach to estimate V_P gives more reliable measurements of V_P. Recalling Fig. 6.60(d) for the equivalent data for the random sample, both the start-to-start and peak-to-peak approaches give almost similar results. Applying the start-to-start method for *P*-wave interpretation can be valid assuming that it is the *P*-wave that propagates fastest amongst seismic body waves.

Actual sample response near the transmitter

When bender element tests are analysed, the input voltage signals are believed to be properly inserted and to represent the disturbance felt by the soil. This is questionable as there is a significant loss of energy when converted from voltage to force via shear plates or bender elements, and actual inserted signals cannot be checked using transmitter elements. For example, received voltage signals are typically smaller by a factor of 1000, and use of an amplifier for received signals is necessary to distinguish propagated signals from background noises. It has also been difficult to quantify the energy lost at the interface between electric signals and stress response.

Taking advantage of using multiple shear plates on each platen, the centre transmitter element (T5) of the 5S-shear plate configuration was used as a receiver element. Referring to Fig. 6.66(a), the 4 outer elements (T1 to T4) were excited, and the received signals at T5 on the same side and R5 on the opposite side are compared in Fig. 6.67 for f_{in} = 7 and 20 kHz. For f_{in} = 7 kHz, the response at T5 exhibited a sinusoidal-shaped pulse with a clear phase delay, and the amplitude is significantly smaller than the input voltage (±10) although the response was amplified by a factor of 100. The actual attenuation of the propagating wave from T5 to R5 was not significant, and even the waves reflected back to T5 (after traveling twice distance of the sample length) exhibited only small attenuation. When a higher frequency f_{in} = 20 kHz was inserted, the attenuation became more noticeable. Referring to Fig. 6. 67(b) for f_{in} = 20 kHz, the response at T5 exhibits a long period of residual fluctuation even after the period of the inserted signal, and this agrees with DEM data (e.g. Fig. 5.26) where this trend increases with increasing f_{in}. This may explain partially why the attenuation of wave increases with increasing f_{in}, i.e. some energy could not propagate into the sample.

To analyse the frequency responses at the T5 and R5 receivers, normalised frequency spectra for f_{in} = 20 kHz are compared in Fig. 6.68(a). The maximum frequency $f_{low\text{-}pass}$ arrived at R5 is about 25 kHz, while the response observed at T5 includes a wider frequency range. As indicated in Fig. 6.67(b), the first period of the response at T5 is denoted *F* and the remainder of the signal is denoted *S*, and the frequency contents for these sections are compared in Fig. 6.68(b). The *F* duration of the signal shows a similar response to the input response, and the *S* duration of the signal contains a wide range of frequencies. The maximum frequency observed in the *S* duration of the signal is close to 40 kHz, and this is larger than the $f_{low\text{-}pass} \approx$ 25 kHz for the R5 response. It can be concluded that the frequencies higher than $f_{low\text{-}pass}$ cannot penetrate into the sample from the vicinity of the transmitter and the particles keep vibrating around the transmitter wall. As discussed in Section 5.5, the $f_{low\text{-}pass}$ value is linked to grain size, stress, void ratio and surface characteristics.

Equivalent DEM simulations were performed as illustrated in Fig. 6.66(b) where the outside of centre 10% of the transmitter wall was excited while fixing the position of the centre part. Two types of wall displacements were considered: a sinusoidal pulse with a phase delay of 270 degrees (Fig. 6.7) and a normal sinusoidal pulse (Fig. 6.21). The resultant inserted stress responses differed, and the latter case exhibited a more complex response. The response of the centre part of the transmitter wall (denoted here as Receiver T) showed a completely different response compared with the inserted response, and the phases appeared to be reversed to the inserted signal. This can be explained by the fact that the shearing direction is opposite between the outside and inside the region of excitation. The differences between experiments and simulations include the parameter monitored quantity to record, i.e. energy (voltage) for the experiments and stress for the DEM analysis, and the boundary condition, i.e. a semi-fixed boundary for the experiments and a fixed wall boundary for the DEM analysis. These may affect the phase delay as the strain energy is a product of stress and deformation. However, the overall observation is still comparable between experiments and DEM simulations. Note that the DEM simulations did not include local or viscous damping, and the attenuation of waves was negligible when compared with the experiments. The frequency domain responses for the receivers R and T are illustrated in Fig. 6.70(a), and the frequency contents during the F and S durations of the signal at the receiver T (Fig. 6.69(a)) are compared in Fig. 6.70(b). Similar to the experimental data, the S duration of the signal at the receiver T contains a wider frequencies compared with $f_{low\text{-}pass}$ observed at receiver R.

6.5 Summary

The first part of this chapter investigated the influence of the surface roughness on the system response and the small-strain shear modulus (G_0) using experimental and DEM approaches. Based on bender element and shear plate tests the following conclusions can be drawn:

- The G_0 increases with increasing the stress level for both smooth and rough samples.
- Increasing surface roughness reduces G_0 especially at low stress levels.
- Increasing surface roughness increases the power coefficient n in the G_0 - σ' relationship.
- As the stress increases both G_0 and n for rough samples approach the smooth equivalent.
- The low-pass frequency $f_{low\text{-}pass}$ increases with increasing the stress level for both smooth and rough samples.
- The $f_{low\text{-}pass}$ is reduced with increasing surface roughness particularly at low stresses.

The results of equivalent DEM simulations considering the shear plate tests supported the experimental findings above. For smooth ballotini samples, close agreement of V_S was observed between the experiments and DEM simulations. The $f_{low\text{-}pass}$ values observed for the smooth samples in the experiments were also captured by DEM, indicating that dynamic responses of an assembly of smooth surface ballotini can be analysed using the HM contact model. The $G_0 - S_q$ relationship highlighted that there might be a limit of surface roughness effects on the sample stiffness, and this point should be studied in more detail to better understand surface roughness effects.

New shear plates were developed in this study to conduct dynamic tests at high stress levels using coarse ballotini. Compared with shear plate tests documented in the literature, larger shear plates were used in this study. Using the 2L- and 5S-shear plate configurations the size effects of shear plates on the system response were discussed, and the following findings were observed:

- For a given source voltage, using larger (wider) shear plates increased the excitation energy at the same strain level and enabled experiments even at low stress levels.
- The gain factors of the system response were affected by both shear plate size and lateral boundary conditions.
- The frequency response observed using larger shear plates was almost identical to the summation of that at each element, indicating that the system response is linear-elastic.
- The first *S*-wave peak appeared earlier when smaller shear plates were used.
- When higher frequencies were inserted into a sample, frequencies higher than $f_{low\text{-}pass}$ did not propagate from the vicinity of the transmitter shear plates.

The findings above were captured by the supplemental DEM analyses. Additional particle-scale study showed that the near-field effects are induced by generating *S*-waves using small transmitters. The DEM data clearly showed that V_S increases with reducing the size of transmitter and receivers due to near-field effects. When planar waves were generated the near-field effects were negligible in DEM analysis; however, real experimental data are affected by the near-field effects irrespective of the size of shear plate. This may be caused by presence of side boundaries as shown by O'Donovan (2013) using DEM.

6.6 Tables

Table 6.1. Test cases for laboratory experiments.

Test case	Ballotini	D_{mean} mm	$S_{q,\,mean}$ nm	S_q/R	e_0	ρ_d kg/m^3	$d_{travel,0}$ mm
UB-01	WLS	2.55	36	2.8×10^{-5}	0.632	1366	-
UB-02	WLR	2.55	661	5.2×10^{-4}	0.679	1328	-
UB-03	WSS	1	193	3.9×10^{-4}	0.647	1339	-
UB-04	WSR	1	222	4.4×10^{-4}	0.666	1339	-
UB-05	WSR	1	222	4.4×10^{-4}	0.656	1347	-
IC-01	GSSw	1.2	58	9.7×10^{-5}	0.606	1619	111.4
IC-02	GSRw-5h	1.2	267	4.5×10^{-4}	0.599	1626	112.5
IC-03	GSRw-25h	1.2	612	1.0×10^{-3}	0.595	1630	111.8

Table 6.2. Fitting parameters for V_S - σ' and G_0 - σ' relationships for bender element tests.

Material	Direction	$V_S = a\,(1.33 - e)\,\sigma'^{\,b}$ [m/s]			$G_0 = A\,(1.33 - e)^2/(1+e)\,\sigma'^{\,n}$ [MPa]		
		a	b	R^2	A	n	R^2
WLS	XY	189.9	0.187	0.998	80.42	0.374	0.998
	YX	209.2	0.168	0.992	94.73	0.344	0.997
WLR	XY	73.2	0.341	0.977	11.96	0.682	0.968
	YX	88.6	0.308	0.976	17.51	0.616	0.971
WSS	XY	86.3	0.321	0.999	18.77	0.614	0.990
	YX	91.9	0.315	0.999	18.84	0.629	0.999
WSR	XY	84.9	0.310	0.990	16.07	0.621	0.983
	YX	82.8	0.315	0.989	15.29	0.629	0.983
WSR washed	XY	99.7	0.290	0.998	22.16	0.580	0.997
	YX	96.8	0.296	0.993	20.88	0.592	0.991

Table 6.3. Fitting parameters for n - σ' relationship.

Test case	Ballotini	R_{mean} mm	$S_{q,\,mean}$ nm	S_q/R	$n = c\,\sigma'^{\,d}$		Validity kPa
					c	d	
UB-01	WLS	1.275	36	2.8×10^{-5}	0.716	-0.1349	
UB-02	WLR	1.275	661	5.2×10^{-4}	3.764	-0.3587	
UB-03	WSS	0.5	193	3.9×10^{-4}	2.114	-0.2577	50 -500
UB-04 UB-05	WSR	0.5	222	4.4×10^{-4}	2.951	-0.3222	
IC-01	GSSw	0.6	58	9.7×10^{-5}	0.382	-0.0014	
IC-02	GSRw-5h	0.6	267	4.5×10^{-4}	0.562	-0.0311	50 - 1500
IC-03	GSRw-25h	0.6	612	1.0×10^{-3}	0.934	-0.1070	

Table 6.4. Experimental results of linear fitting to V_S - e relationship at σ' = 50kPa.

Material	f_{in}	$V_S = C_1 + C_2\, e$			B
	kHz	C_1	C_2	R^2	$(-C_1/C_2)$
Smooth (GSSw)	5	489.7	-383.9	0.939	1.276
	7	468.1	-345.6	0.964	1.355
	10	463.2	-335.9	0.955	1.379
	15	461.8	-332.3	0.927	1.390
	20	436.8	-290.4	0.952	1.504
	all	463.9	-337.6	0.936	1.374
Rough (GSRw-25h)	5	356.6	-274.2	0.995	1.301
	7	359.2	-275.3	0.996	1.305
	10	371.3	-291.6	0.998	1.273
	15	376.0	-295.1	0.997	1.274
	20	379.2	-298.4	0.997	1.271
	all	368.5	-286.9	0.939	1.284

Table 6.5. Fitting parameters for V_S - σ' and G_0 - σ' relationships for shear plate tests.

Material	f_{in}	$V_S = a\,(1.33 - e)\,\sigma'^{\,b}$ [m/s]			$G_0 = A\,(1.33 - e)^2/(1+e)\,\sigma'^{\,n}$ [MPa]		
	kHz	a	b	R^2	A	n	R^2
Smooth (GSSw)	10	183.8	0.189	1.000	84.54	0.386	1.000
	15	180.3	0.192	1.000	84.30	0.385	1.000
	20	183.8	0.189	1.000	87.61	0.377	1.000
	mean	182.7	0.190	1.000	85.5	0.383	1.000
Medium (GSRw-5h)	10	113.7	0.247	0.998	33.51	0.493	0.997
	15	116.3	0.243	0.999	35.08	0.486	0.998
	20	118.0	0.241	0.998	36.11	0.481	0.997
	mean	116.0	0.243	0.998	34.9	0.487	0.998
Rough (GSRw-25h)	10	102.9	0.263	0.999	27.44	0.527	0.998
	15	107.8	0.257	0.998	30.14	0.513	0.997
	20	109.5	0.255	0.997	31.10	0.510	0.995
	mean	106.7	0.258	0.998	29.6	0.517	0.997

Table 6.6. DEM sample data for Dem-A (Section 6.4) and Dem-F (Section 6.3).

Test case	Contact model	D_{mean}	S_q	μ_{prep} (μ_{wave})	σ'	e	$\bar{C}_N$	d_{travel}	V_P^*	V_S^*
		mm	nm		kPa			mm	m/s	m/s
Dem-A	HM	1.2	0	0.05	100	0.607	5.55	96.77	493.8	324.7
Dem-F				(0.2)	1600	0.599	5.88	96.51	815.8	540.1

*V_P and V_S are obtained using f_{in} = 20 kHz.

Table 6.7. Test cases for DEM simulations to investigate surface roughness effects.

Test case	Contact model	S_q nm	S_q/R	μ_{prep} (μ_{wave})	σ' kPa	e	$\bar{C}_N$	V_S (P-P) m/s	G_0 MPa
Dem-1	HM	0	0	0.1 (0.2)	50	0.636	5.19	273	118
Dem-2					100	0.635	5.25	308	151
Dem-3					200	0.634	5.32	350	194
Dem-4					400	0.633	5.40	398	252
Dem-5					800	0.630	5.49	453	328
Dem-6					1600	0.627	5.60	519	431
Dem-7	RM	70	1.2×10^{-4}	0.1 (0.2)	50	0.635	5.30	253	102
Dem-8					100	0.634	5.35	292	136
Dem-9					200	0.633	5.41	335	179
Dem-10					400	0.632	5.49	386	237
Dem-11					800	0.629	5.58	445	316
Dem-12					1600	0.626	5.68	514	423
Dem-13	RM	280	4.7×10^{-4}	0.1 (0.2)	50	0.634	5.36	213	72.0
Dem-14					100	0.633	5.40	262	109
Dem-15					200	0.632	5.46	315	158
Dem-16					400	0.630	5.53	369	217
Dem-17					800	0.628	5.62	429	294
Dem-18					1600	0.624	5.72	497	396
Dem-19	RM	600	1.0×10^{-3}	0.1 (0.2)	50	0.633	5.42	183	53.5
Dem-20					100	0.632	5.47	228	82.6
Dem-21					200	0.630	5.53	282	127
Dem-22					400	0.628	5.59	347	192
Dem-23					800	0.626	5.66	414	274
Dem-24					1600	0.622	5.76	485	377

Table 6.8. DEM simulations to investigate unloading effects.

Test case	Contact model	S_q nm	S_q/R	μ_{prep} (μ_{wave})	σ' kPa	e	$\bar{C}_N$	V_S (P-P) m/s	G_0 MPa
Dem-2	HM	0	0	0.1 (0.2)	100	0.635	5.25	308	151
Dem-2U						0.634	5.17	298	142

Table 6.9. Experimental cases using 2L- and 5S-shear plate configurations in Section 6.4.

Test case	Ballotini	D_{mean} mm	$S_{q,\,mean}$ nm	σ' kPa	e	ρ_d kg/m^3	d_{travel} mm
IC-2L	GSSw	1.2	58	99.7	0.604	1621	111.4
IC-5S	GSSw	1.2	58	99.2	0.602	1623	112.0

6.7 Figures

Figure 6.1. Cubical cell apparatus at the University of Bristol.

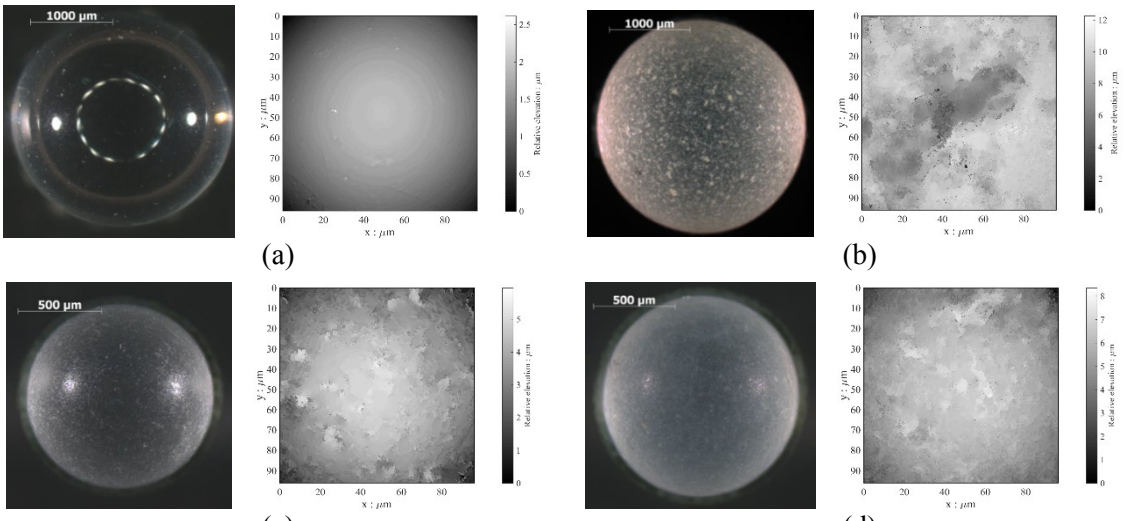

Figure 6.2. Representative images and surface elevations of glass ballotini used in the CCA tests. (a) WLS with S_q = 36 nm, (b) WLR with S_q = 661 nm, (c) WSS with S_q = 193 nm, and (d) WSR with S_q = 222 nm.

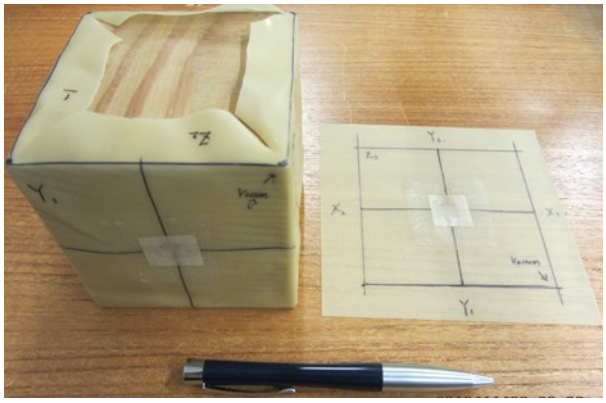

(a)

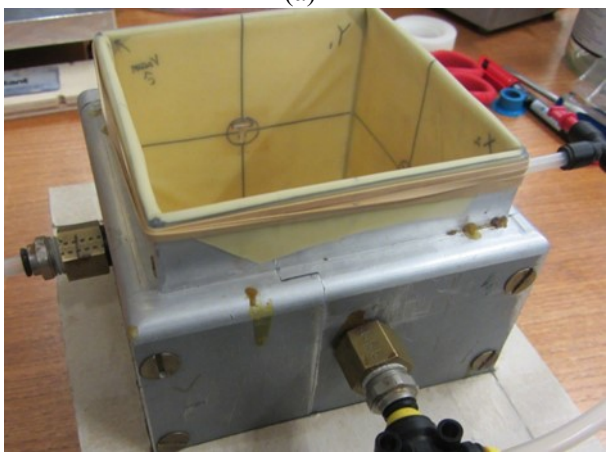

(b)

(c)

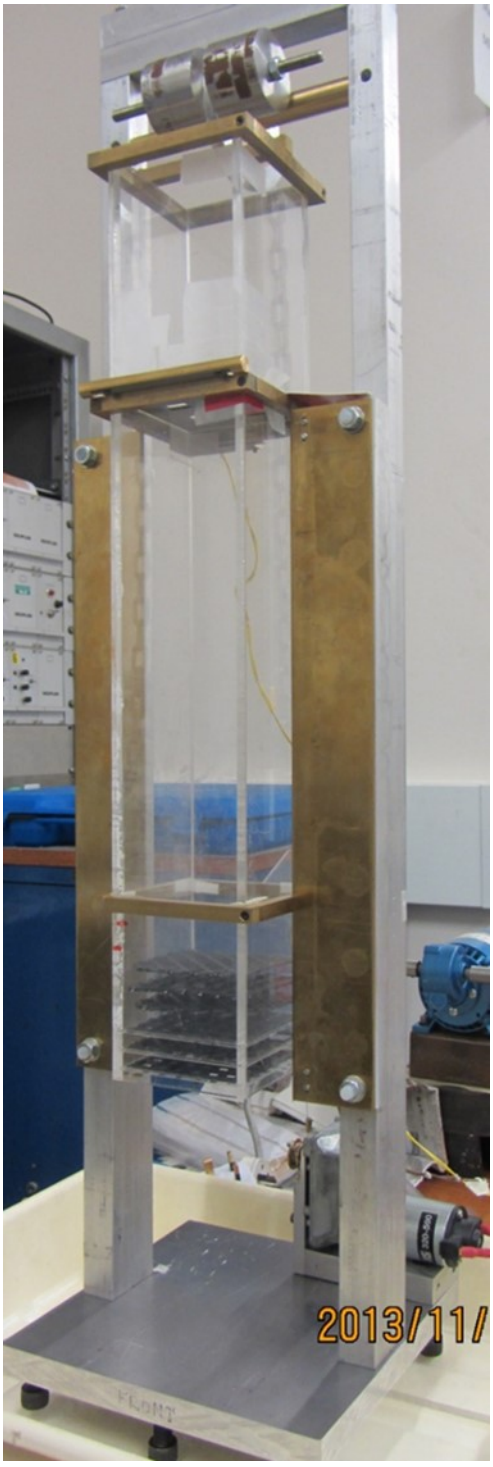

(d)

Figure 6.3. Preparation of cubical sample using modified pluviator (Camenen et al., 2013).

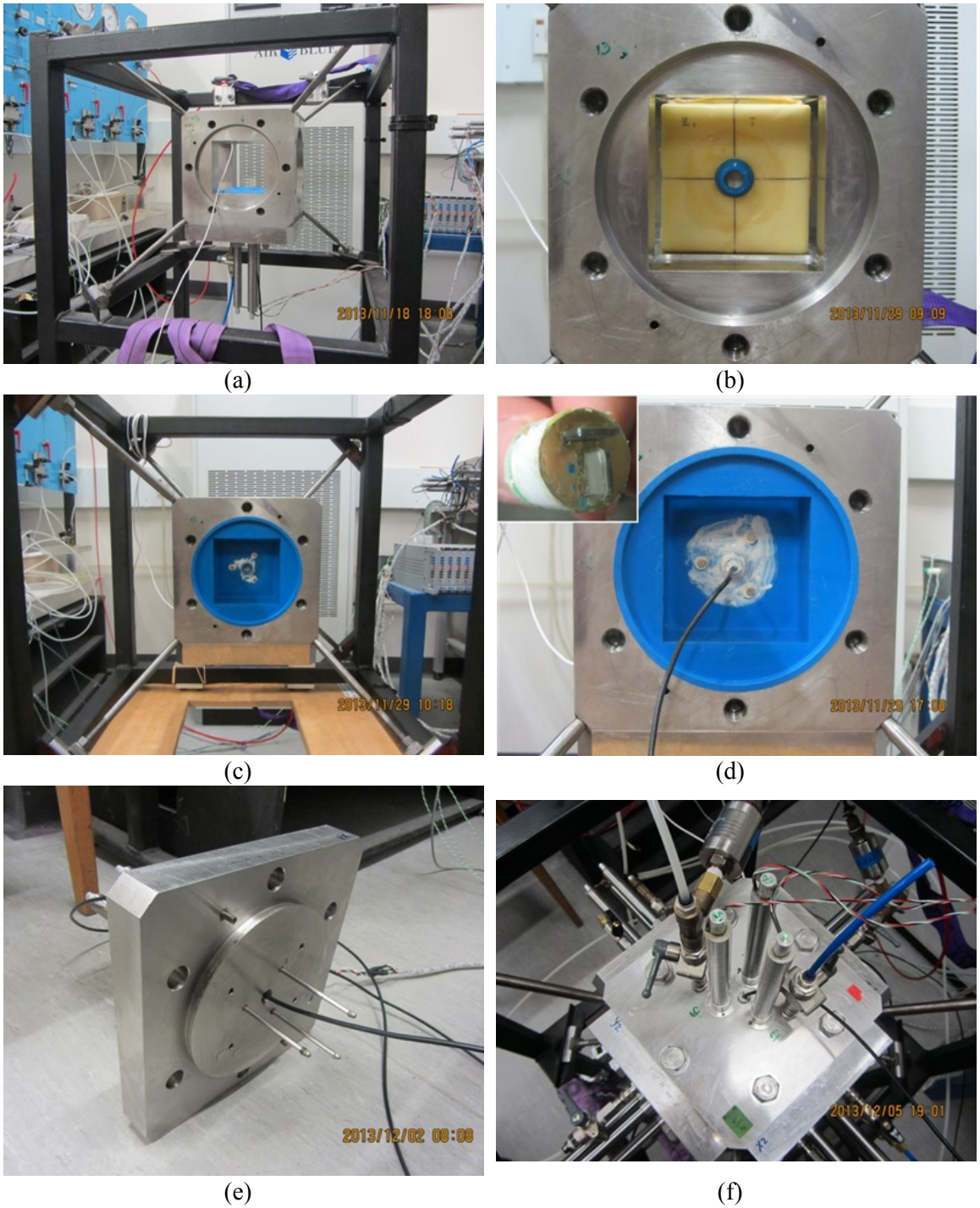

(a) (b)

(c) (d)

(e) (f)

Figure 6.4. Test procedure using the cubical cell apparatus.

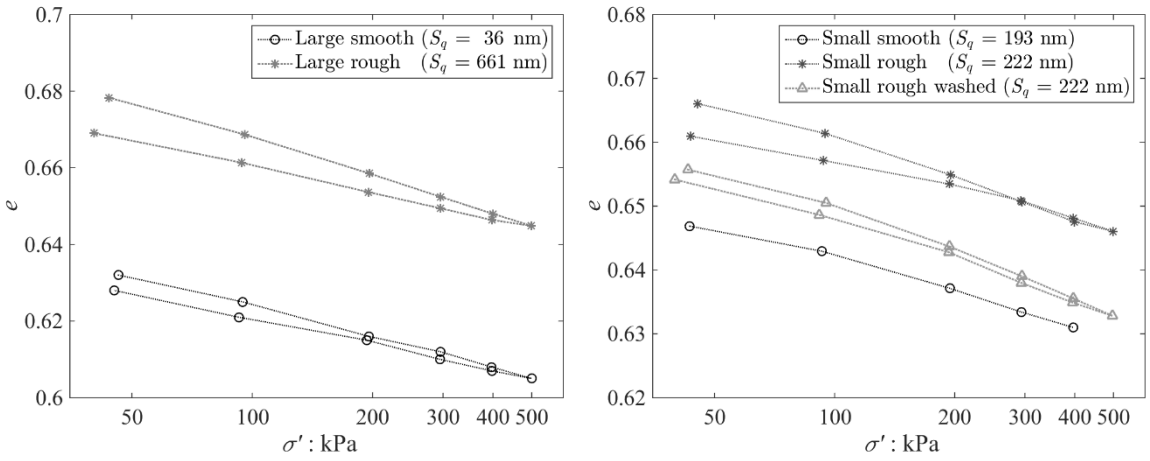

(a) (b)

Figure 6.5. CCA data giving relationship between void ratio and isotropic confining stress. (a) Large smooth (WLS) and rough ballotini (WLR), and (b) Small smooth (WSS) and rough (WSR) ballotini.

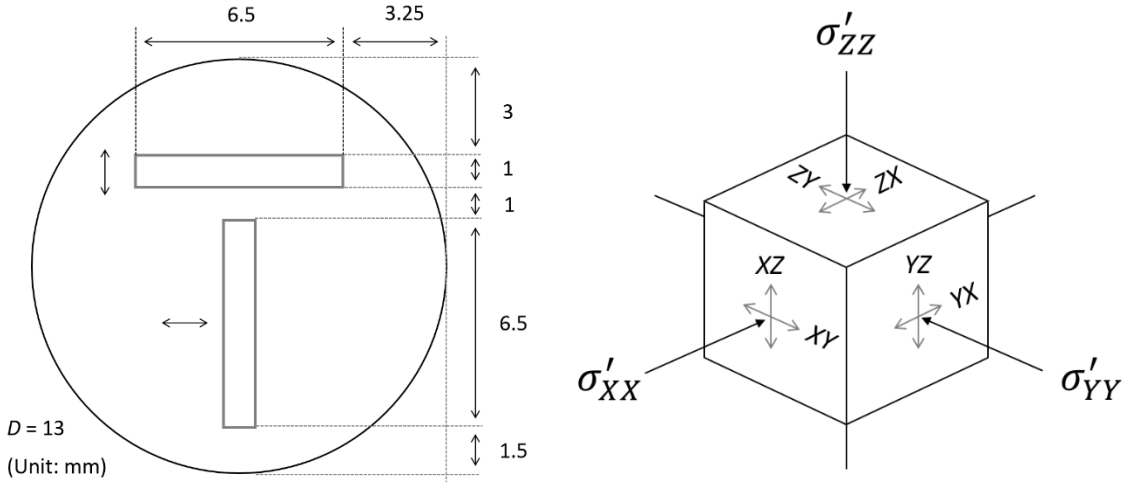

(a) (b)

Figure 6.6. (a) Design of T-shaped bender elements and (b) directions of shear wave propagation and oscillation.

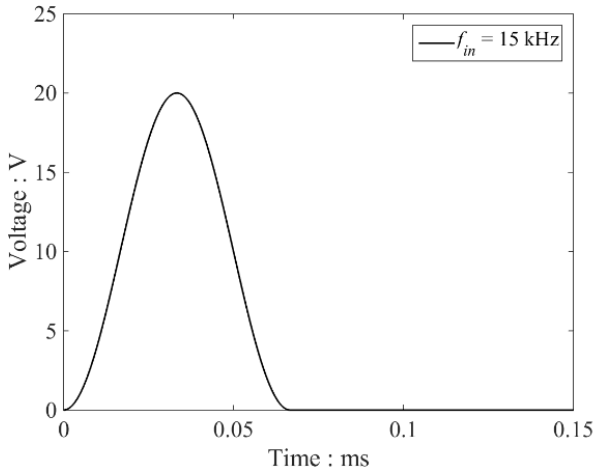

Figure 6.7. Inserted voltage signal for bender element tests in CCA apparatus.

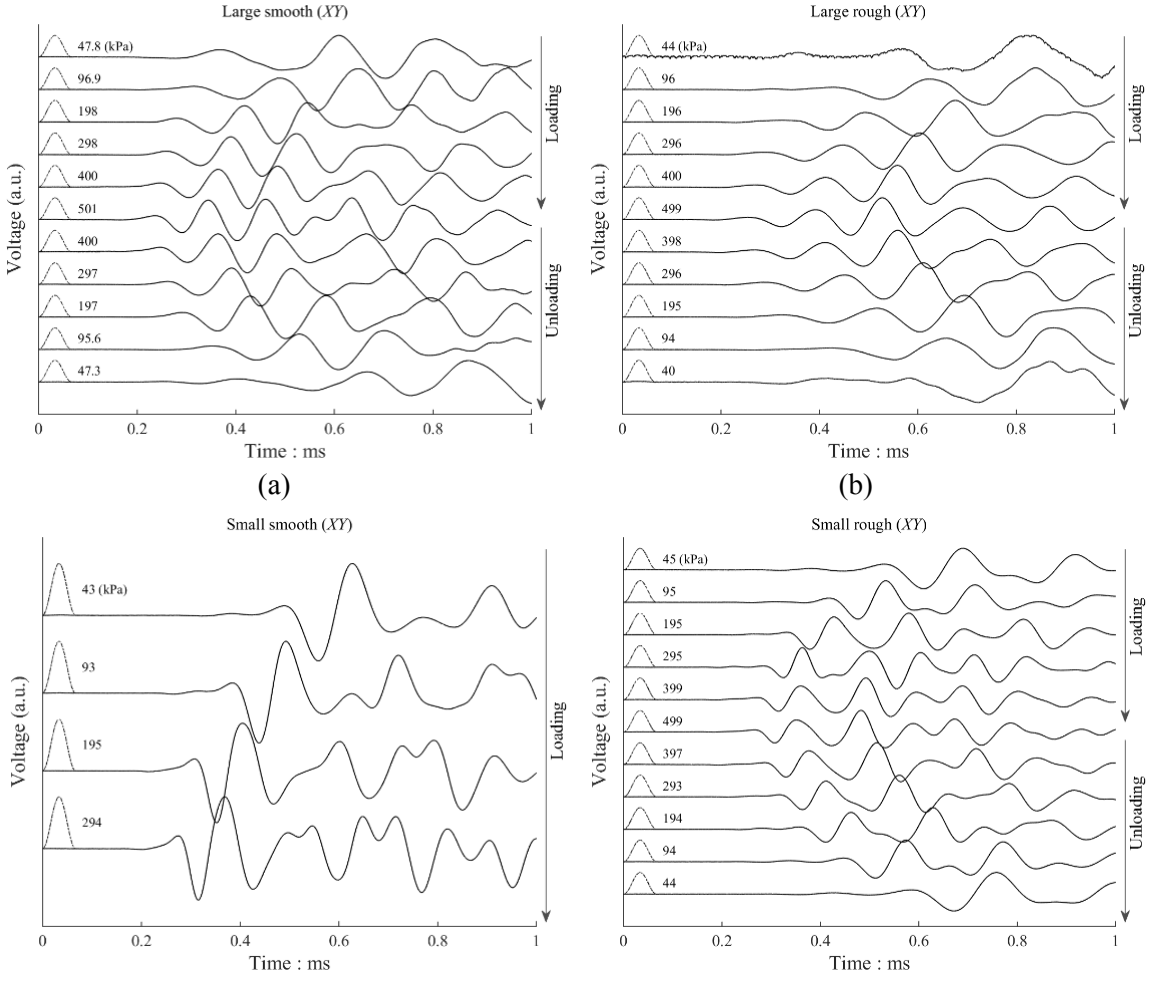

Figure 6.8. Time domain response of received signals in *XY* direction at various confining stress during initial loading and unloading with f_{in} = 15 kHz in CCA apparatus. (a) Large smooth ballotini (S_q = 36 nm) (b) Large rough ballotini (S_q = 661 nm), (c) Small smooth ballotini (S_q = 193 nm), and (d) Small rough ballotini (S_q = 222 nm).

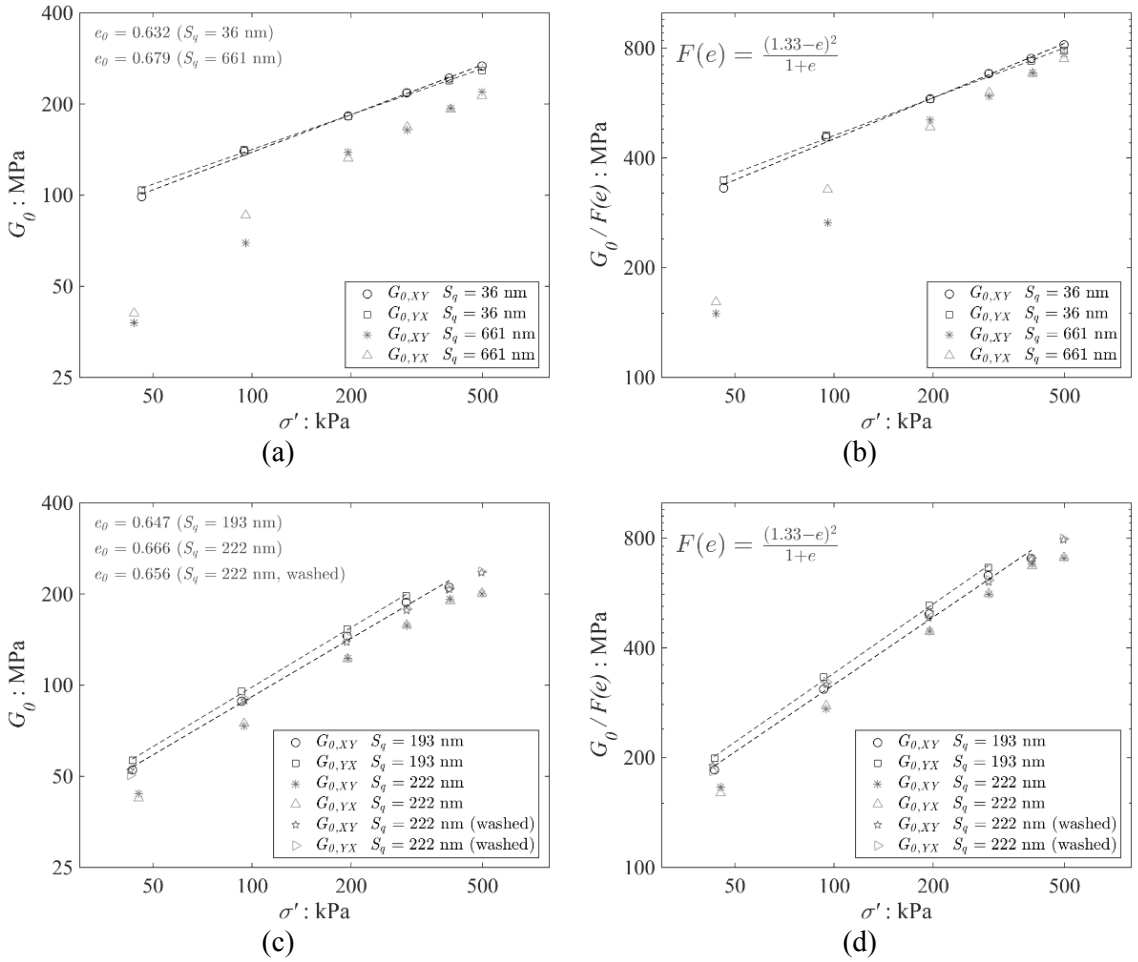

Figure 6.9. Variation in G_0 and $G_0/F(e)$ in XY and YX directions with confining stress in CCA apparatus. (a&b) Large ballotini (WLS and WLR), and (c&d) Small ballotini (WSS and WSR).

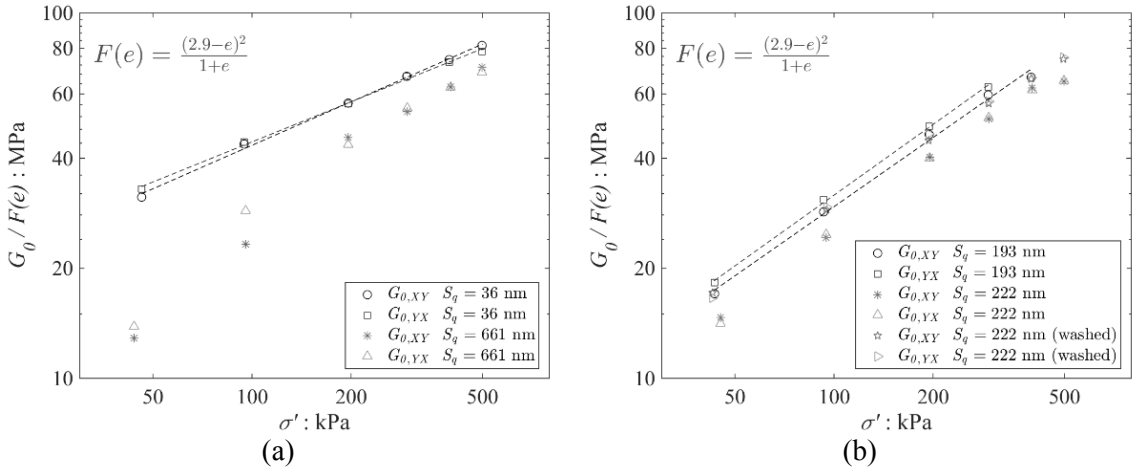

Figure 6.10. Variation in $G_0/F(e)$ (B = 2.9) with confining stress for (a) WLS and WLR samples and (b) WSS and WSR samples in XY and YX directions in CCA apparatus.

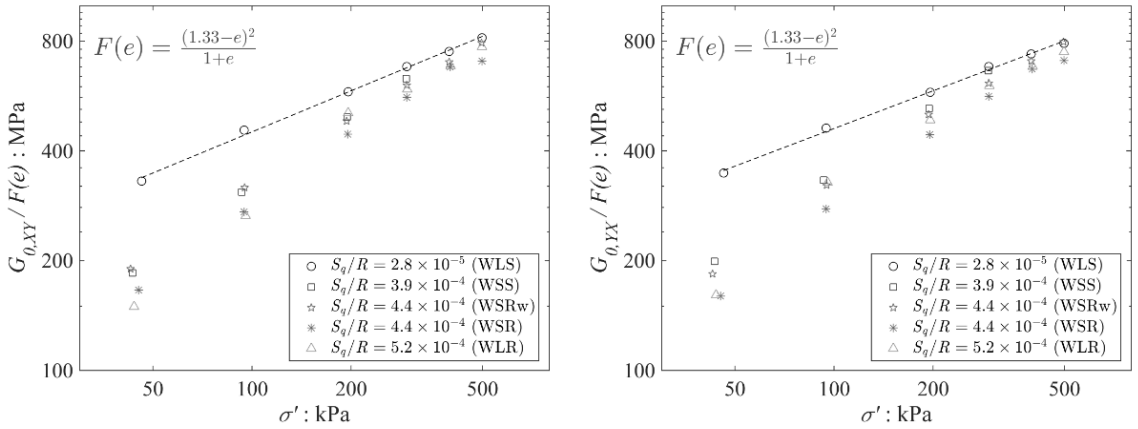

Figure 6.11. Variation in $G_0/F(e)$ with confining stress. (a) *XY* and (b) *YX* directions with confining stress for all the tested samples in CCA apparatus.

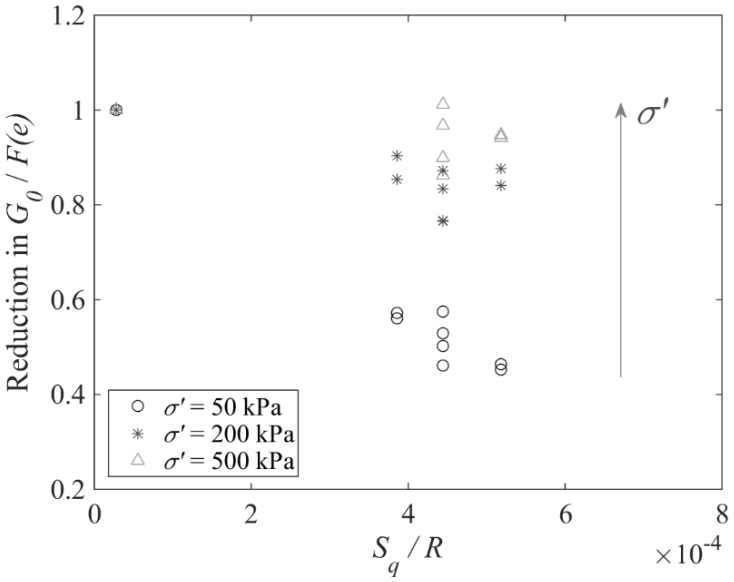

Figure 6.12. Variation in stiffness reduction with normalised surface roughness for both *XY* and *YX* directions at σ' = 50, 200 and 500 kPa in CCA apparatus.

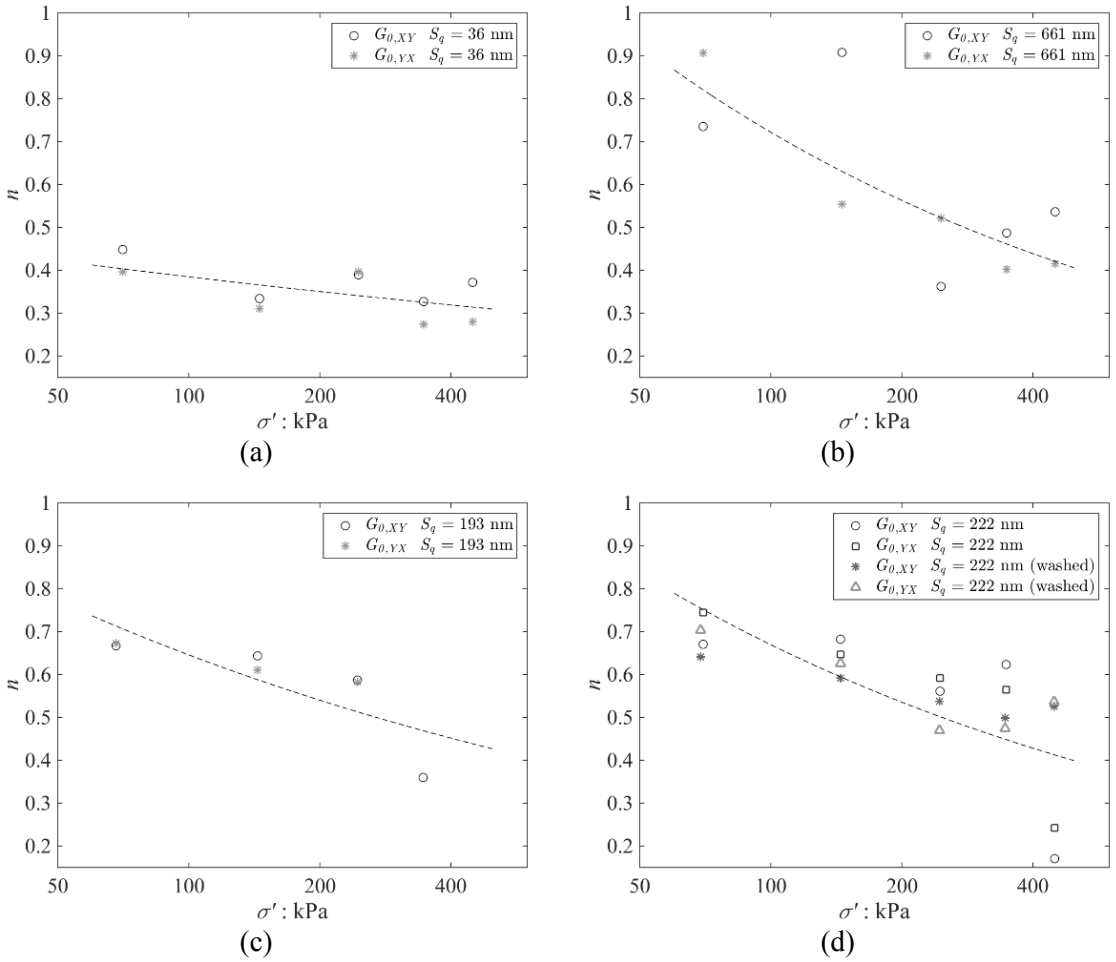

Figure 6.13. Relationship between power coefficient n and confining stress for CCA data. (a) Large smooth ballotini (WLS, S_q = 36 nm) (b) Large rough ballotini (WLR, S_q = 661 nm), (c) Small smooth ballotini (WSS, S_q = 193 nm), and (d) Small rough ballotini (WSR, S_q = 222 nm).

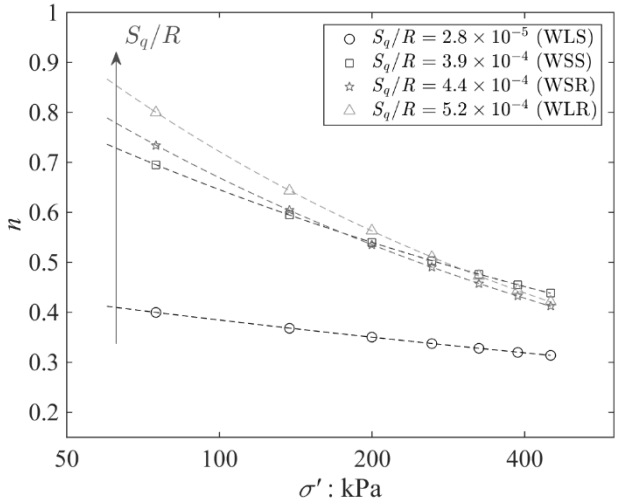

Figure 6.14. Comparison of n-σ' relationships for all the samples tested in CCA apparatus.

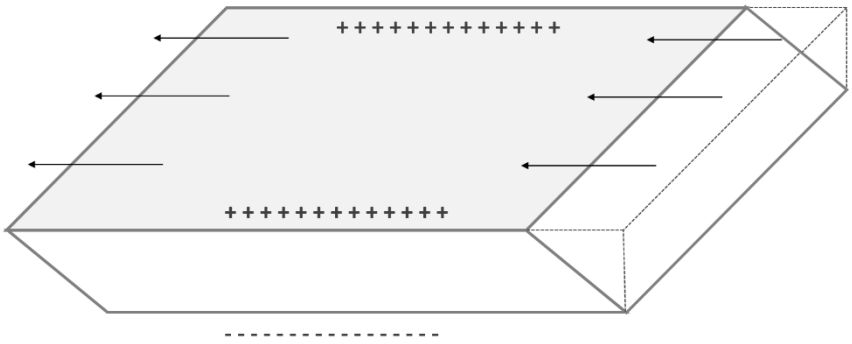

Figure 6.15. Schematic illustration of deformation of shear plate element.

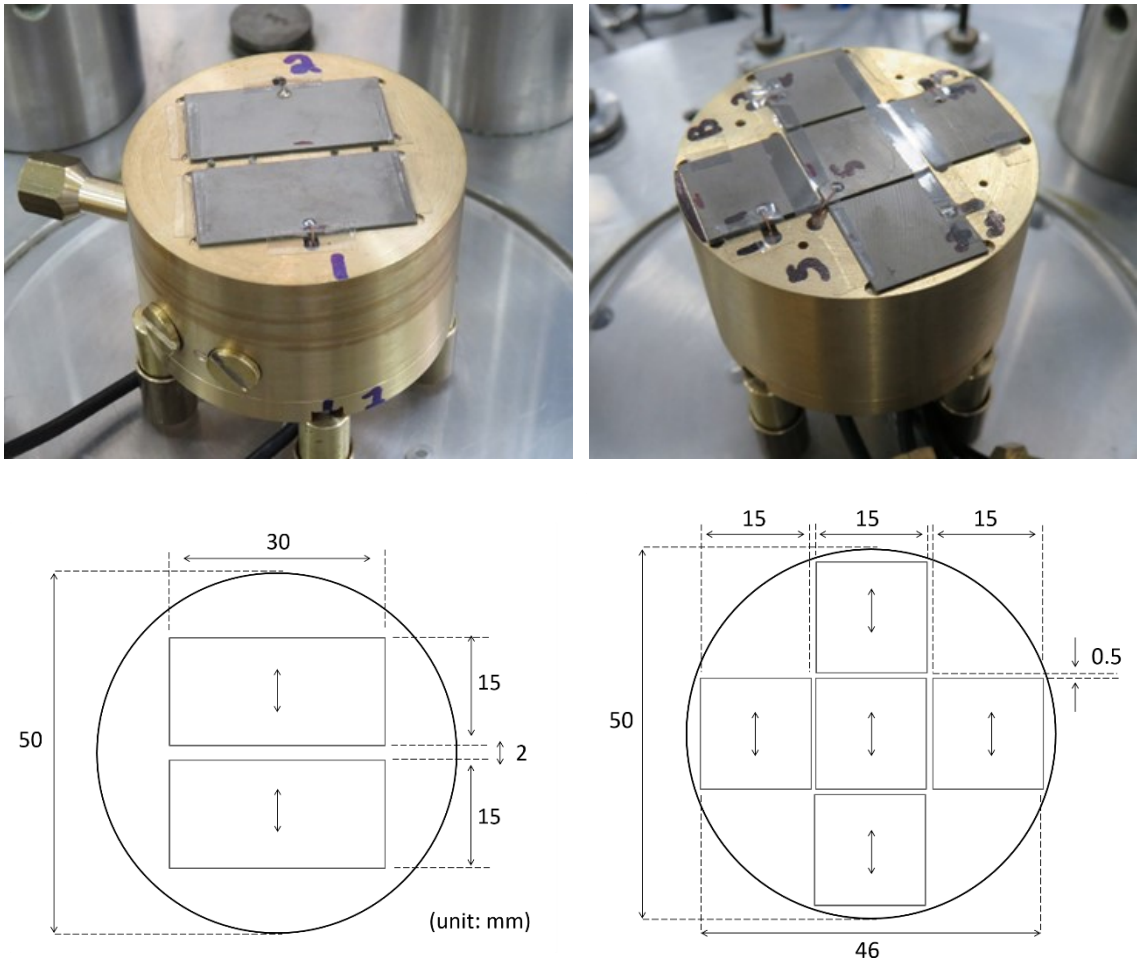

(a) (b)

Figure 6.16. Images and detailed design of shear plates embedded in base pedestal. (a) 2L-configuration, and (b) 5S-cofiguration.

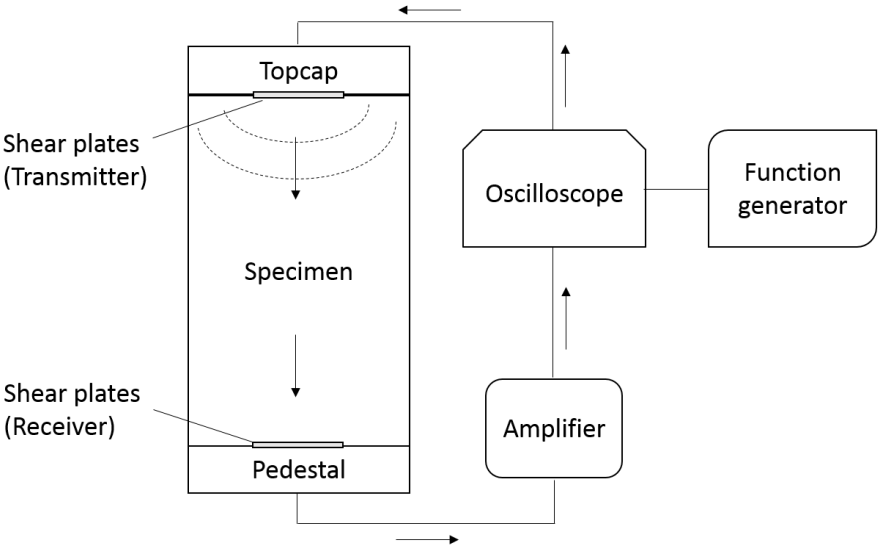

Figure 6.17. Schematic illustration of experimental setup for shear plate tests.

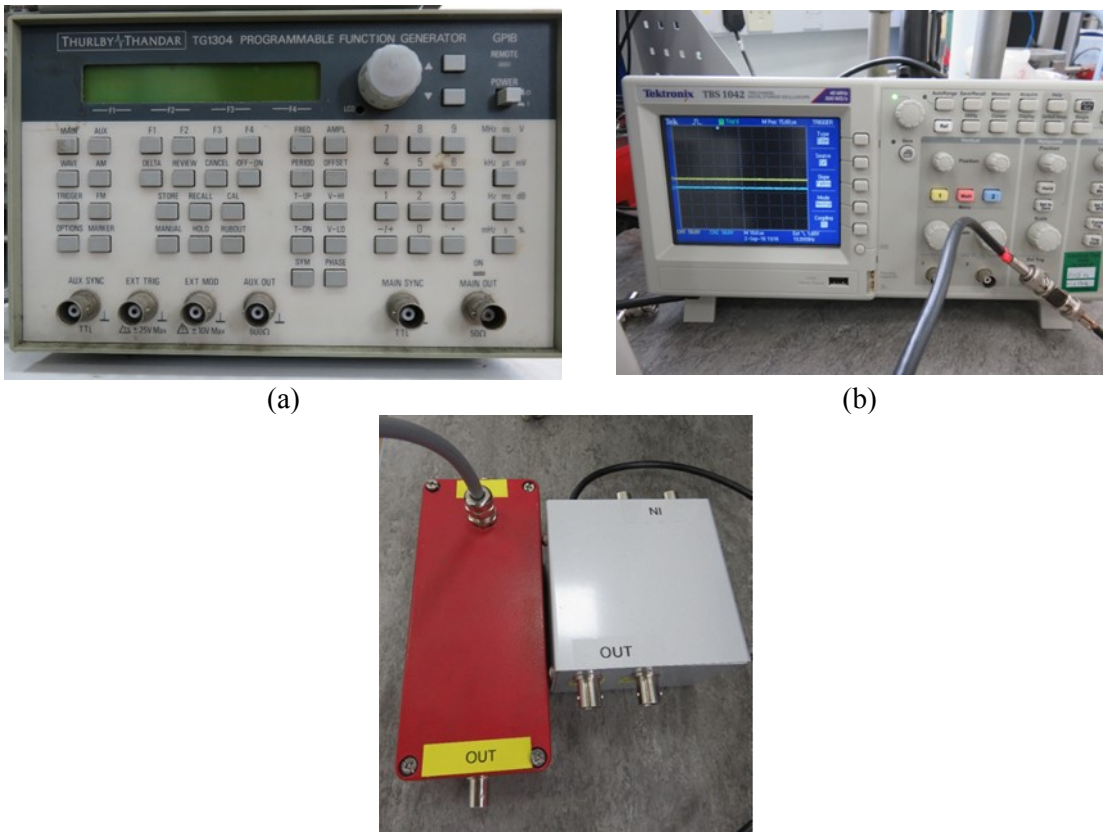

(a) (b)

(c)

Figure 6.18. Measurement devices for shear plate tests. (a) Function generator (TG1304), (b) Oscilloscope (TBS1042), and (c) Signal amplifiers.

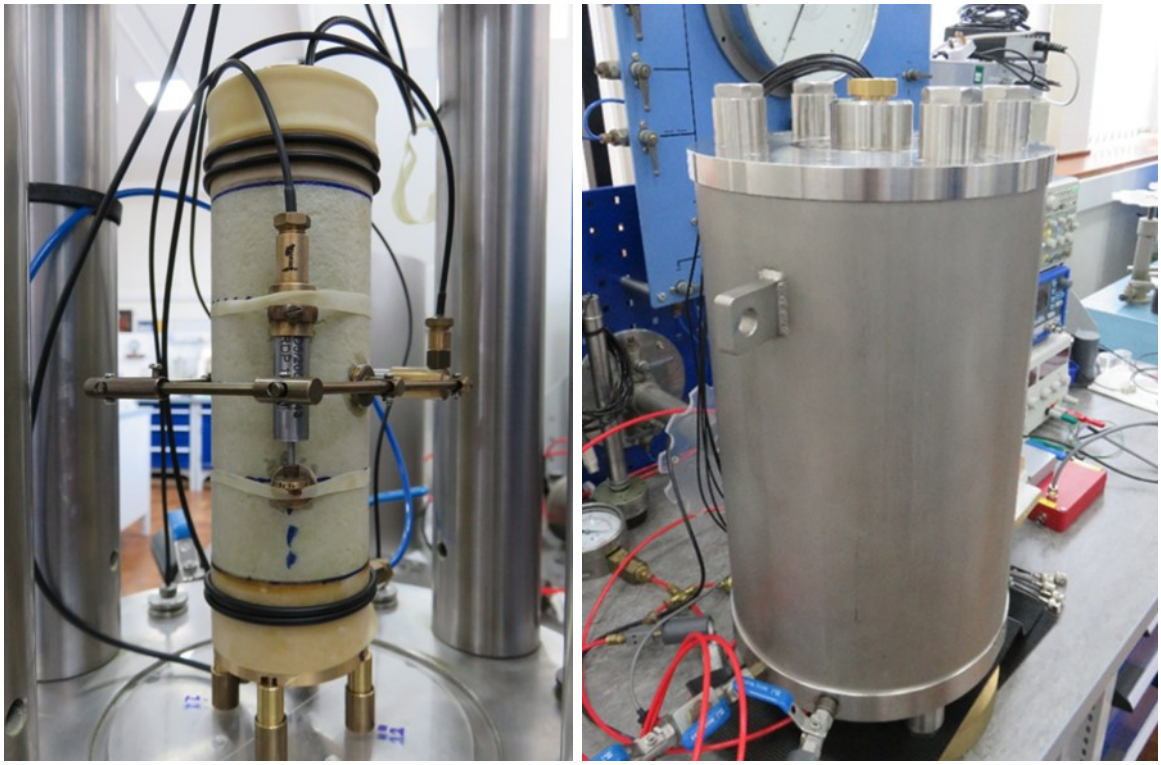

(a) (b)

Figure 6.19. (a) Representative cylinder specimen used in triaxial apparatus. (b) Metal cell of triaxial apparatus.

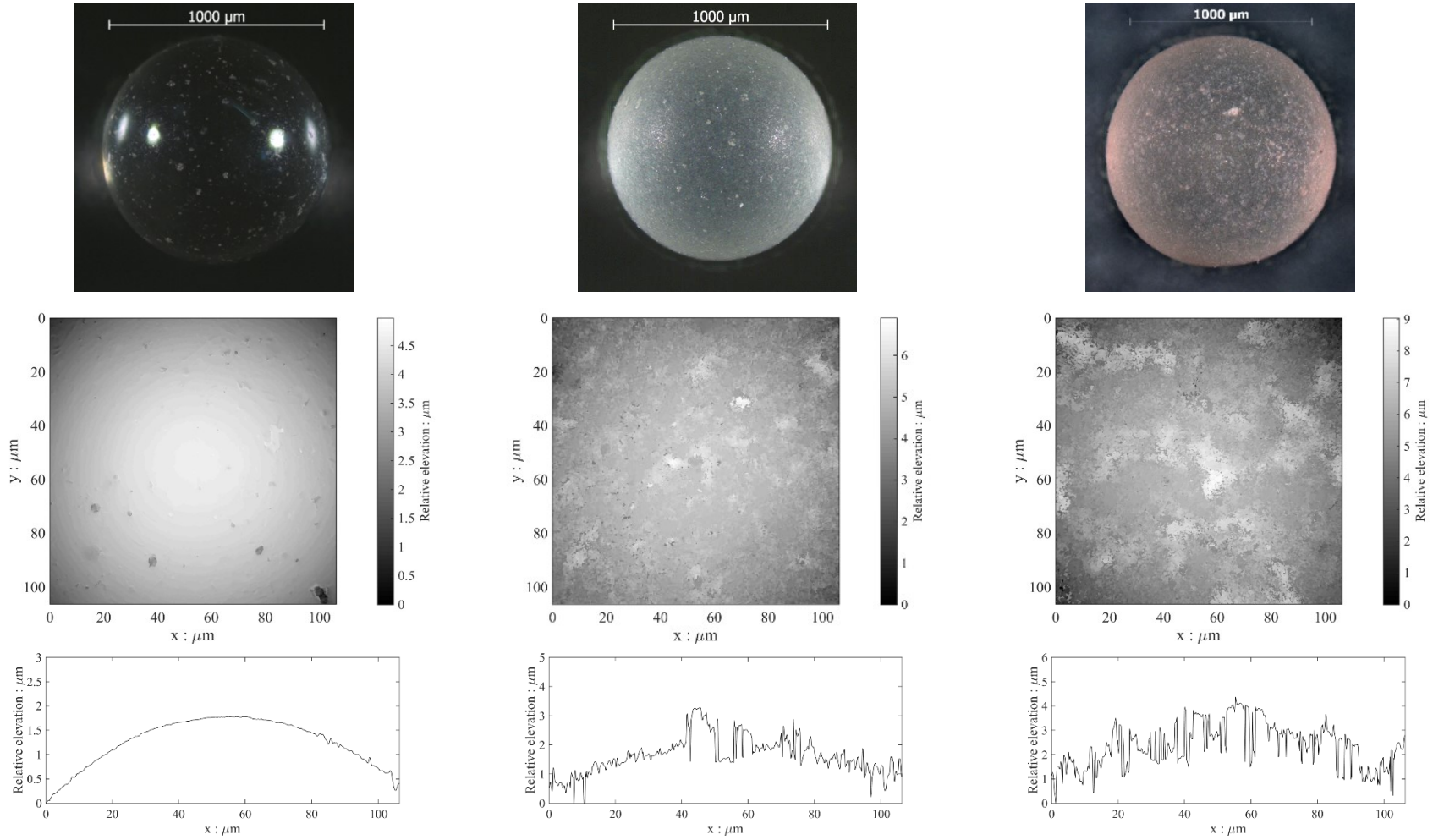

Figure 6.20. Representative image (top), relative elevation on the XY plane (middle) and cross section along the X-axis (centre line of Y) (bottom) of glass ballotini used for shear plate tests in triaxial apparatus. (a) GSSw ballotini with S_q = 58 nm, (b) GSRw-5h ballotini with S_q = 267 nm and (c) GSRw-25h ballotini with S_q = 612 nm.

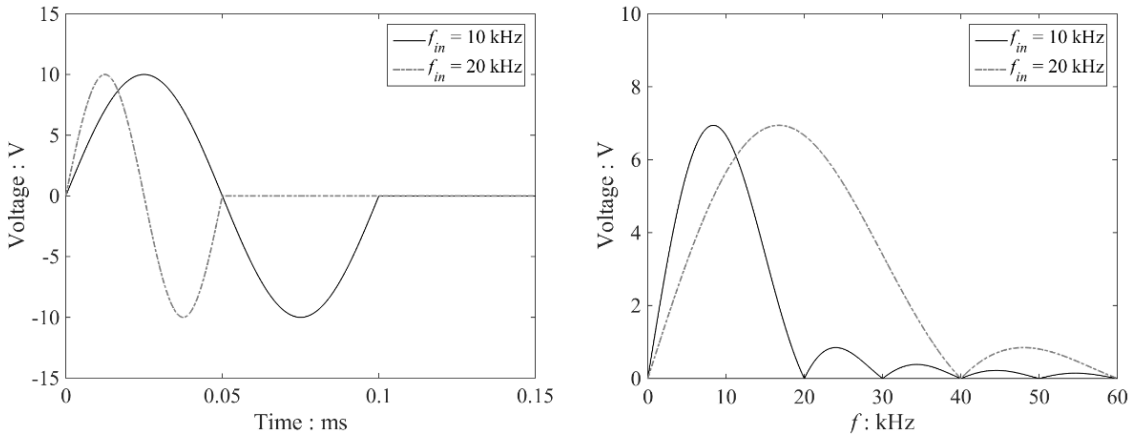

(a) (b)

Figure 6.21. Inserted voltage signal to transmitter shear plates in triaxial apparatus for nominal frequencies of f_{in} = 10 and 20 kHz. (a) Time domain data and (b) Frequency domain data.

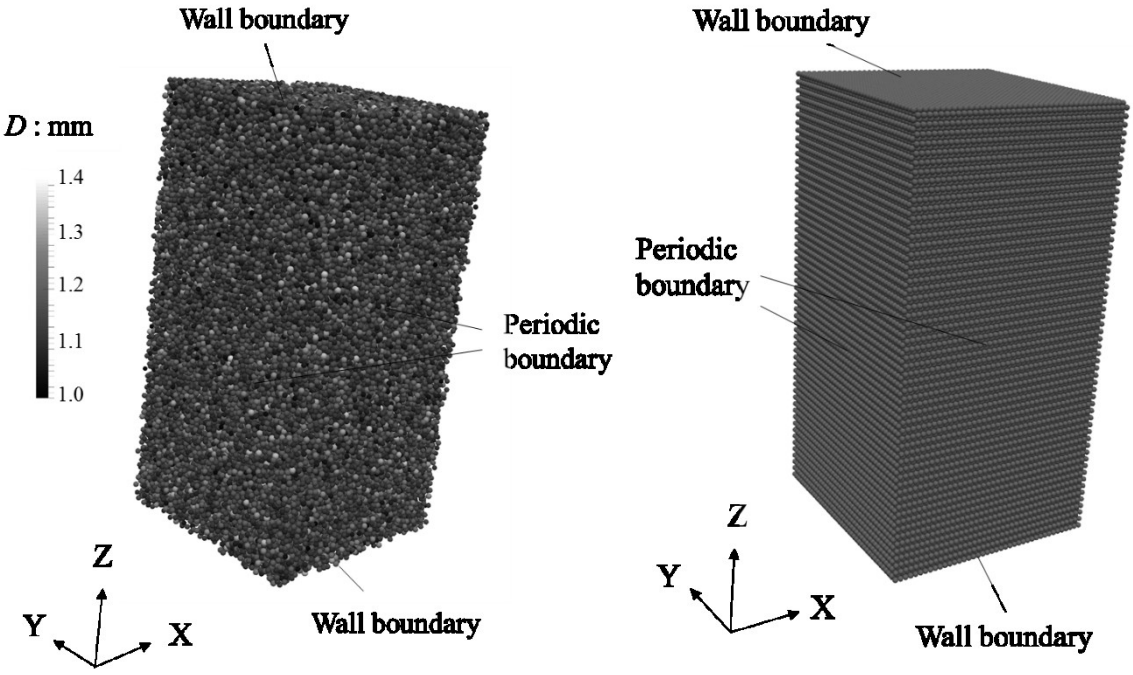

(a) (b)

Figure 6.22. Representative DEM samples used in Chapter 6. (a) Random sample composed of 155,165 particles. (b) FCC sample composed of 191,634 particles (41×41×114 layers).

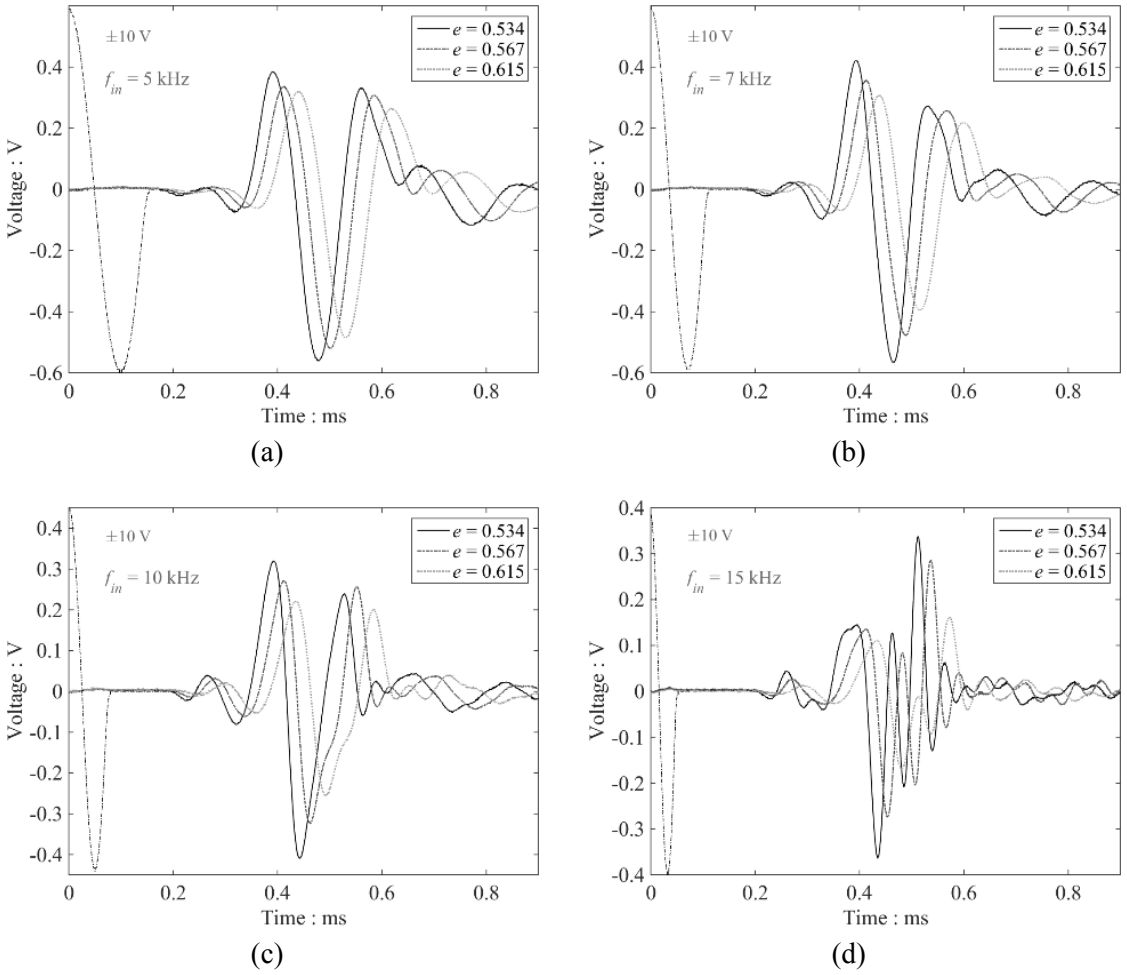

Figure 6.23. Influence of void ratio on time domain response of smooth ballotini samples (GSSw, S_q = 58 nm) tested in laboratory triaxial apparatus. (a) f_{in} = 5 kHz, (b) f_{in} = 7 kHz, (c) f_{in} = 10 kHz, and (d) f_{in} = 15 kHz.

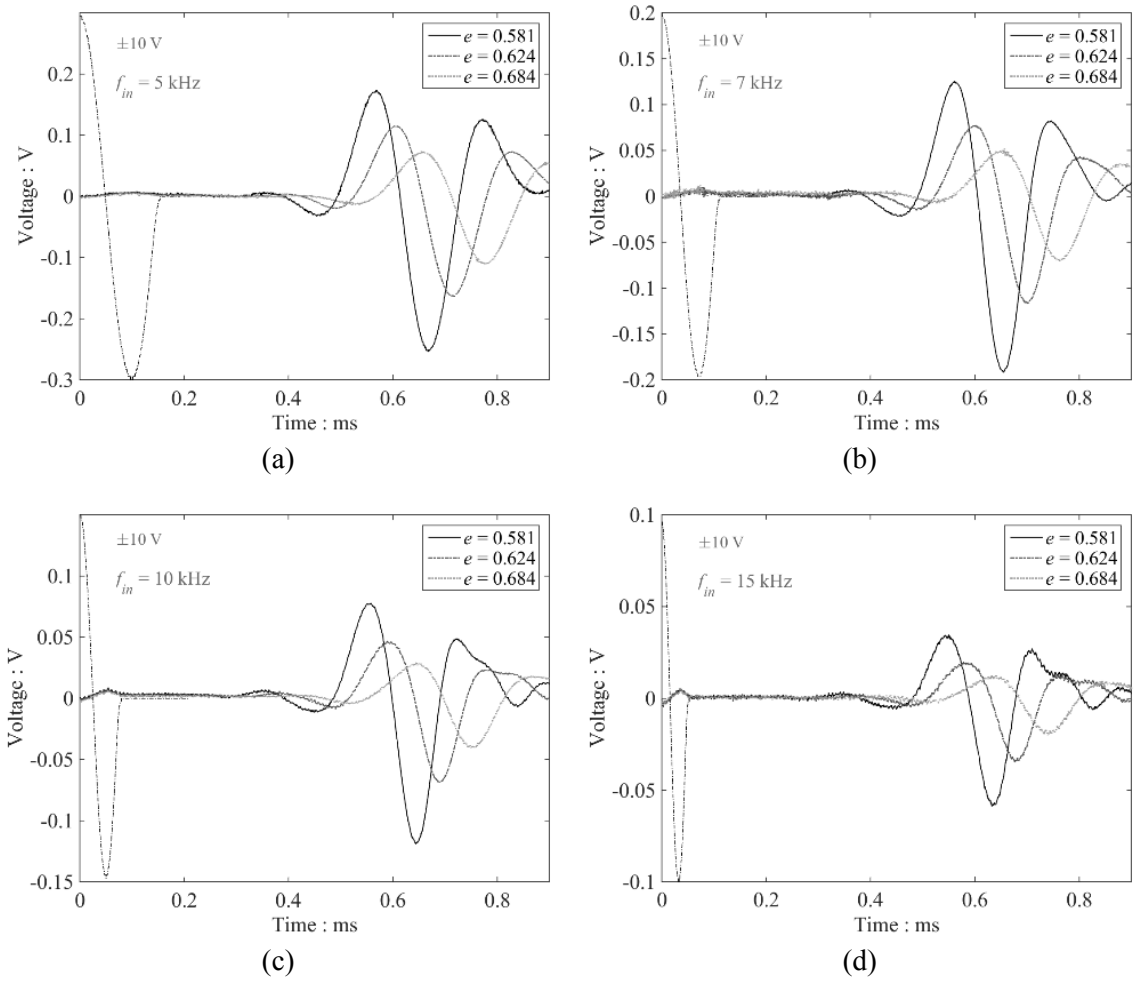

Figure 6.24. Influence of void ratio on time domain response of rough ballotini samples (GSRw-25h, S_q = 612 nm) tested in laboratory triaxial apparatus. (a) f_{in} = 5 kHz, (b) f_{in} = 7 kHz, (c) f_{in} = 10 kHz, and (d) f_{in} = 15 kHz.

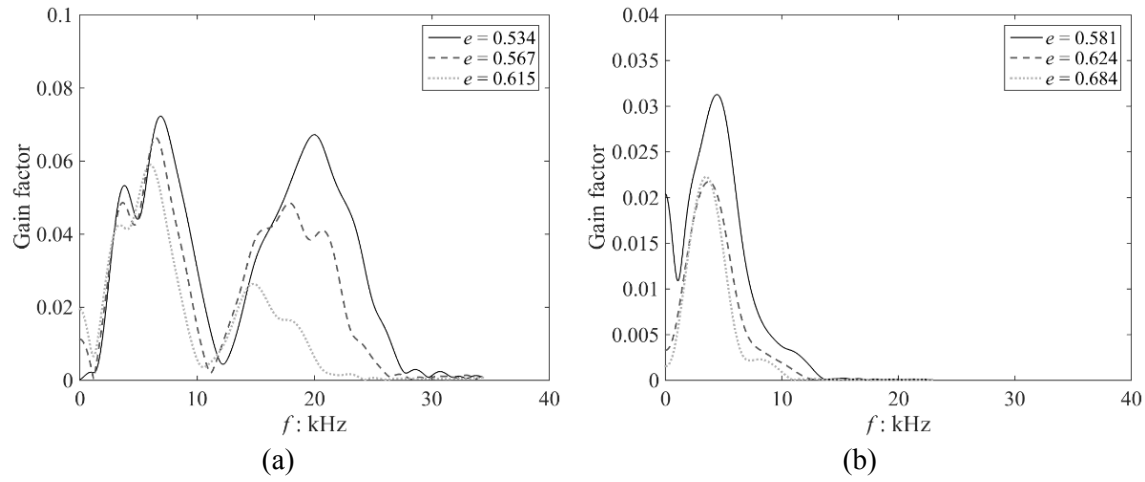

Figure 6.25. Influence of void ratio on frequency domain responses in laboratory triaxial apparatus. (a) Smooth ballotini samples (GSSw, S_q = 58 nm) and (b) rough ballotini samples (GSRw-25h, S_q = 612 nm).

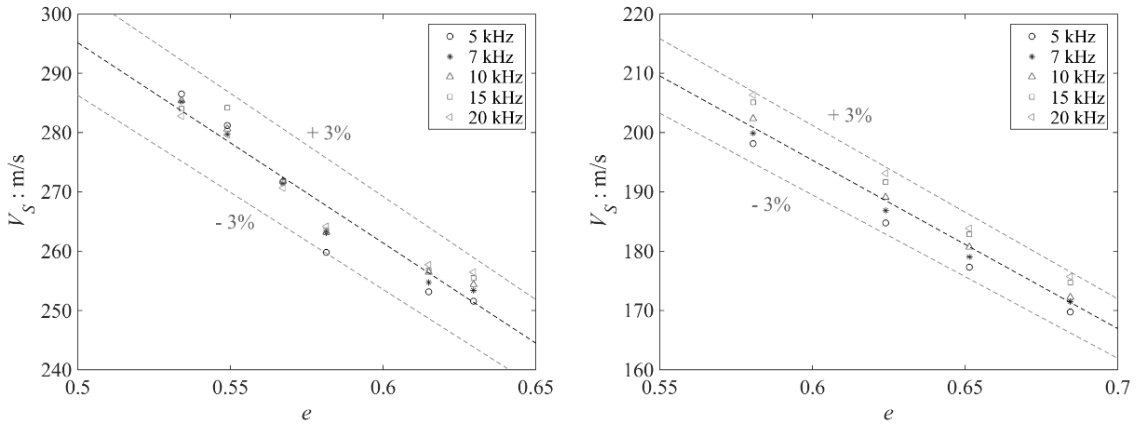

(a) (b)

Figure 6.26. Variation in V_S with e considering various f_{in} with best-fit curves for (a) smooth ballotini (GSSw, S_q = 58 nm), and (b) rough ballotini (GSRw-25h, S_q =612 nm) in laboratory triaxial apparatus.

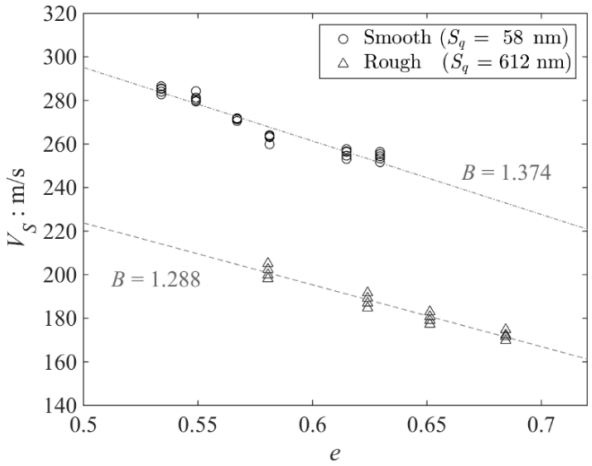

Figure 6.27. Relationship between V_S and e for smooth and rough ballotini samples in laboratory triaxial apparatus.

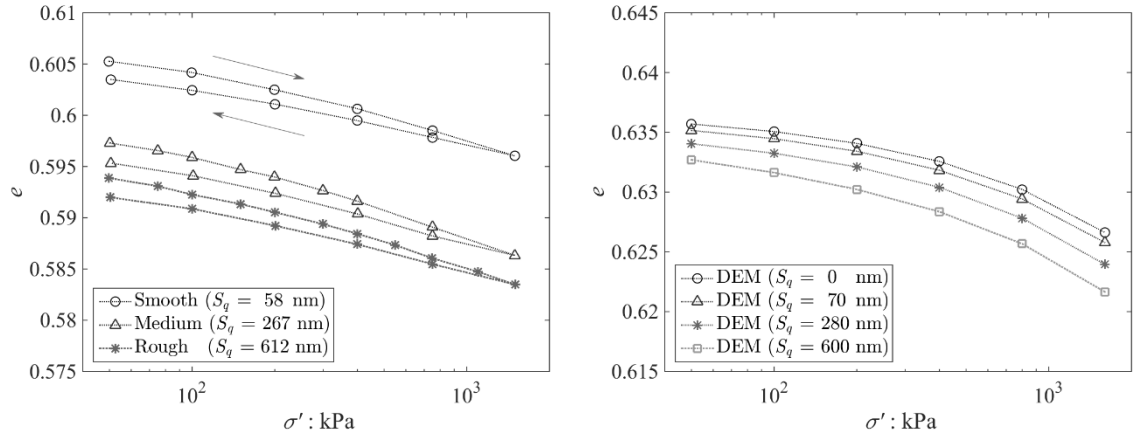

(a) (b)

Figure 6.28. Relationship between void ratio and isotropic confining stress. (a) Loading and unloading for triaxial experiments, and (b) Loading for DEM analysis.

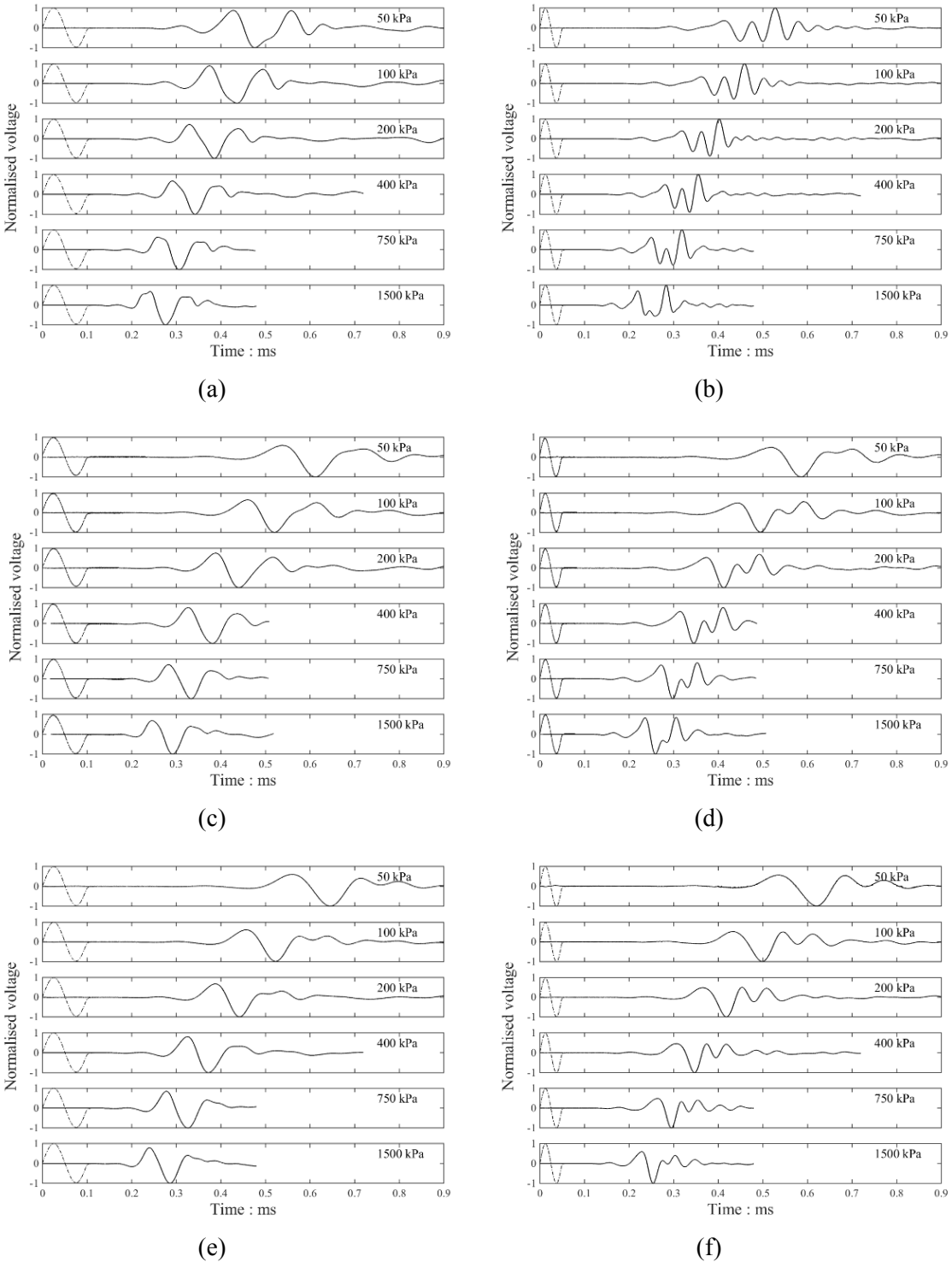

Figure 6.29. Experimental data giving the time domain response where the data are normalised by the maximum amplitude at the specified confining stress during initial isotropic loading. (a,c&e) f_{in} = 10 kHz and (b,d&f) 20 kHz. (a&b) Smooth (GSSw, S_q = 58 nm), (c&d) Medium (GSRw-5h, S_q = 267 nm), and (e&f) Rough samples (GSRw-25h, S_q = 612 nm).

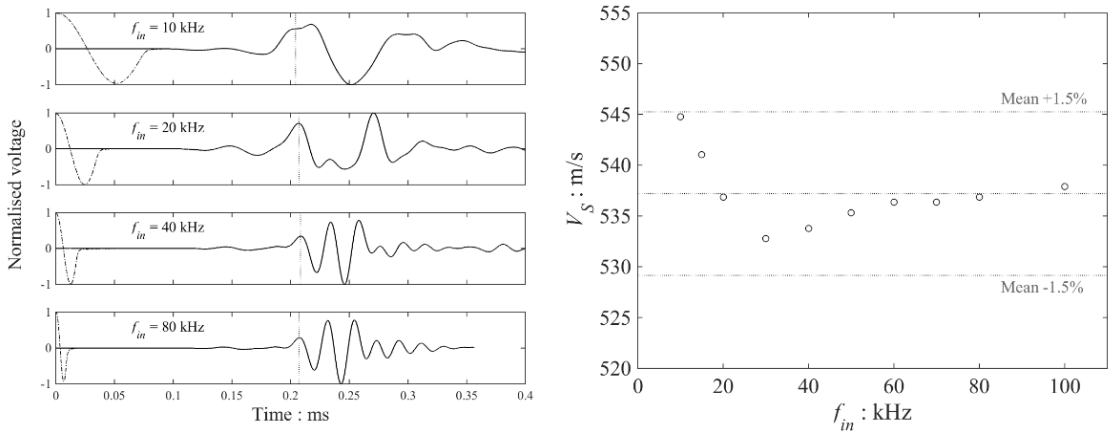

(a) (b)

Figure 6.30. Sensitivity of f_{in} on system response at σ' = 1500 kPa and e = 0.596 (Smooth, S_q = 58nm). (a) Time domain response of received signals. (b) Relationship between V_S and f_{in}.

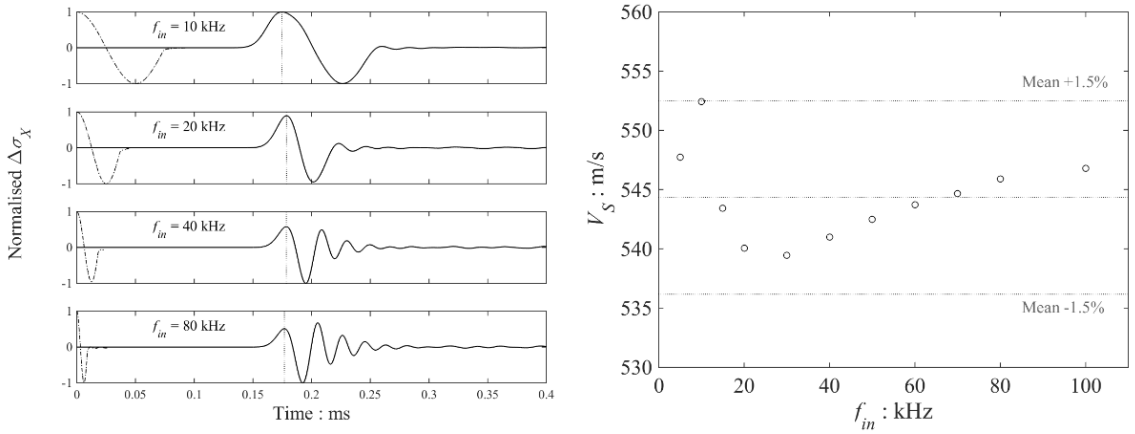

(a) (b)

Figure 6.31. DEM simulations of f_{in} effects on system response at σ' = 1600 kPa and e = 0.599 (S_q = 0). (a) Time domain response of received signals. (b) Relationship between V_S and f_{in}.

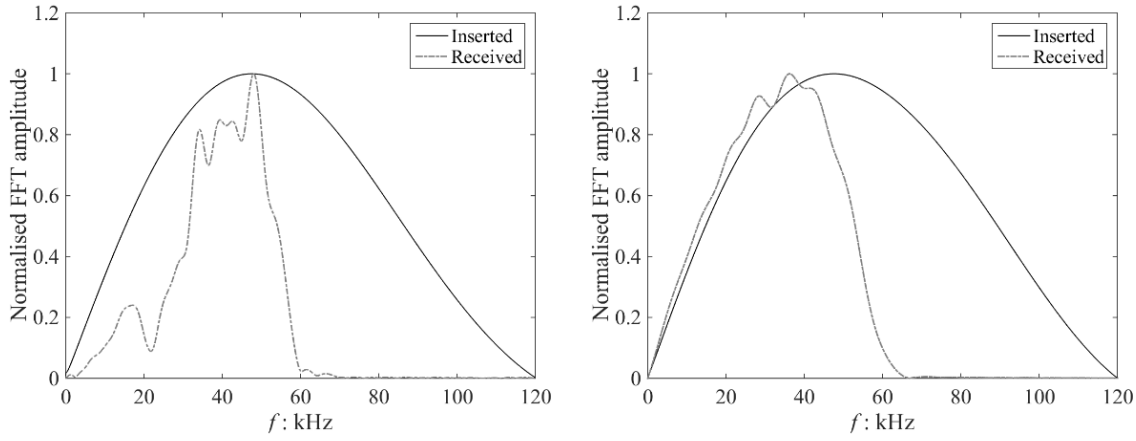

(a) (b)

Figure 6.32. Comparison on FFT spectra between (a) experimental and (b) DEM data using f_{in} = 60 kHz.

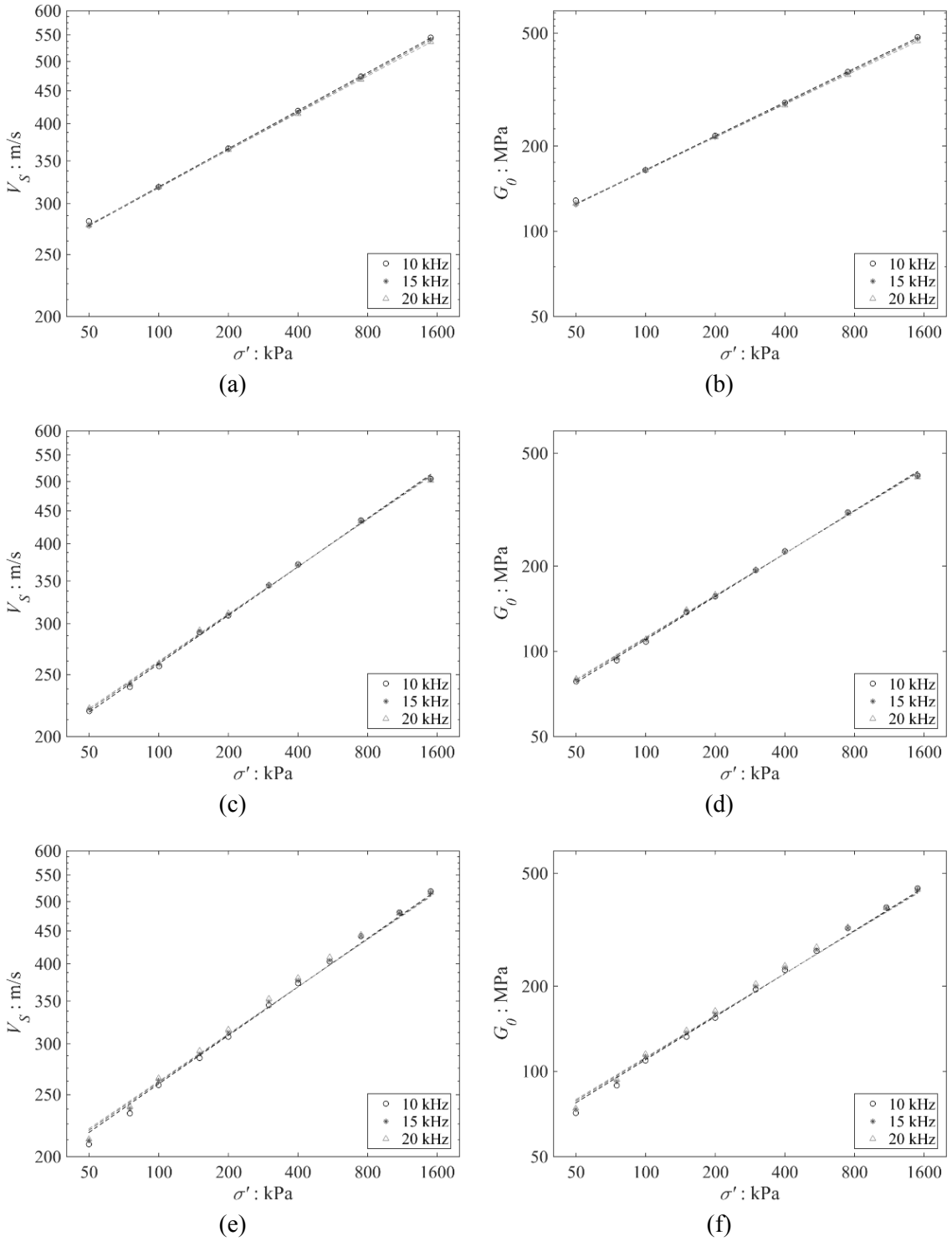

Figure 6.33. Experimental results of variation in (a,c&e) *S*-wave velocity and (b,d&f) shear modulus with isotropic stress for various inserted frequencies. (a&b) Smooth (S_q = 58 nm), (c&d) medium rough (S_q = 267 nm), and (e&f) Rough (S_q = 612 nm) samples.

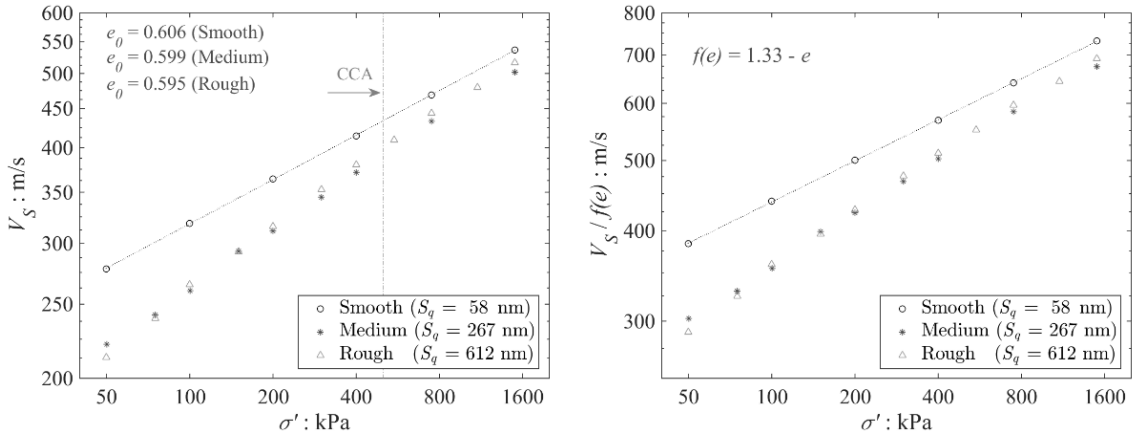

Figure 6.34. Experimental data for surface roughness effects on relationship between *S*-wave velocity (V_S) and isotropic stress. (a) V_S at similar void ratios, and (b) V_S normalised by void ratio function *f(e)*.

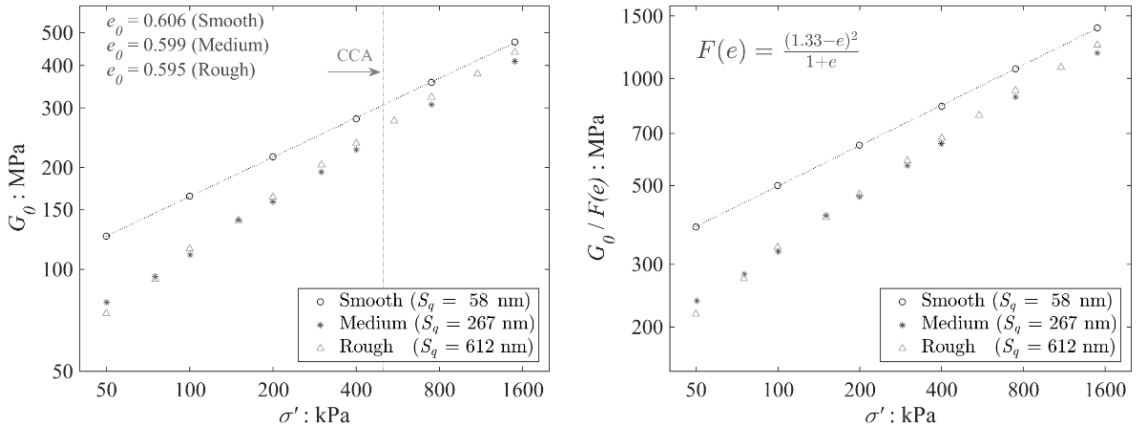

Figure 6.35. Experimental data for surface roughness effects on relationship between shear modulus (G_0) and isotropic stress. (a) G_0 at similar void ratios, and (b) G_0 normalised by void ratio function *F(e)*.

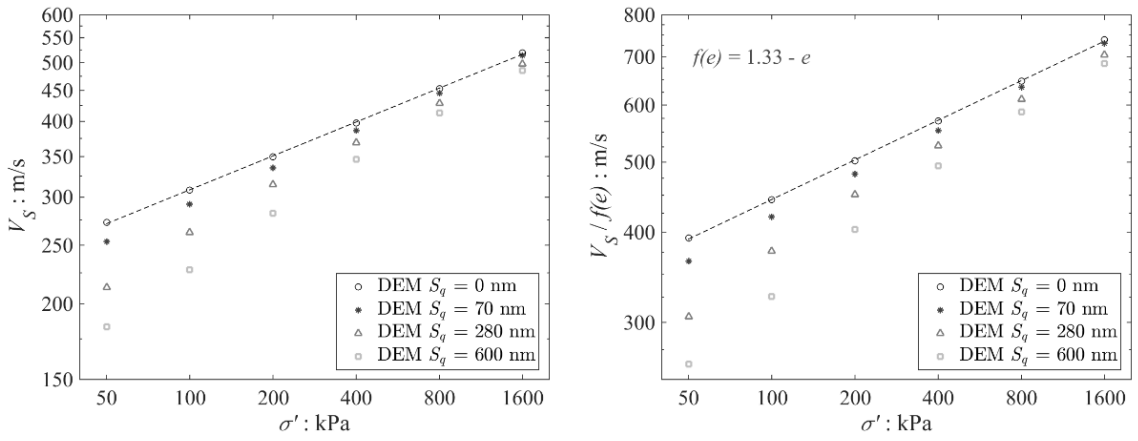

Figure 6.36. DEM results of *S*-wave velocity (V_S) with isotropic stress for various surface roughnesses. (a) V_S at similar void ratios, and (b) V_S normalised by void ratio function *f(e)*.

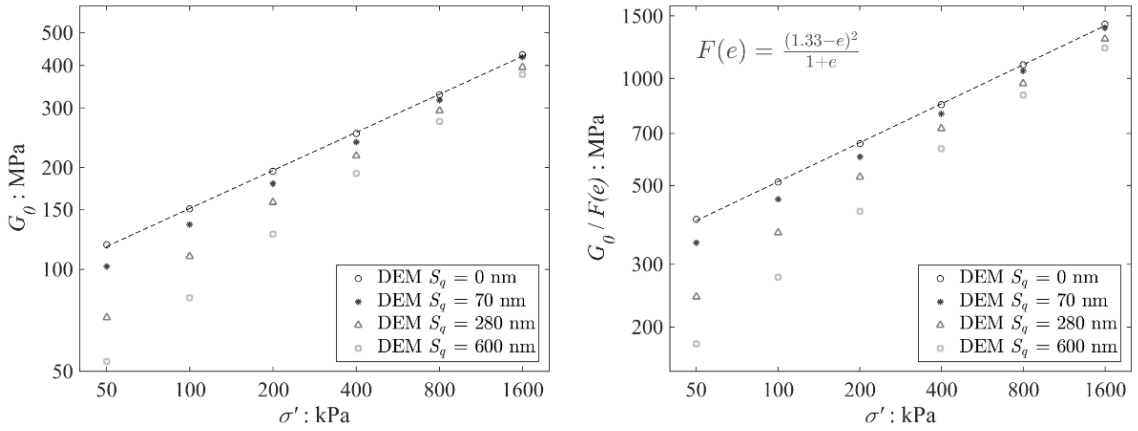

(a) (b)

Figure 6.37. DEM results of shear modulus (G_0) with isotropic stress for various surface roughness. (a) G_0 at similar void ratios, and (b) G_0 normalised by void ratio function $F(e)$.

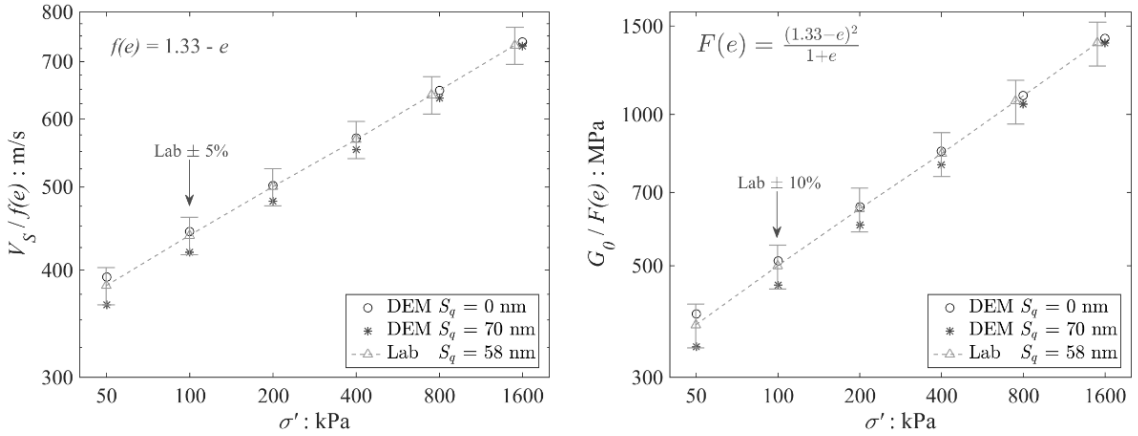

(a) (b)

Figure 6.38. DEM versus experimental results on (a) *S*-wave velocity and (b) shear modulus for smooth ballotini samples.

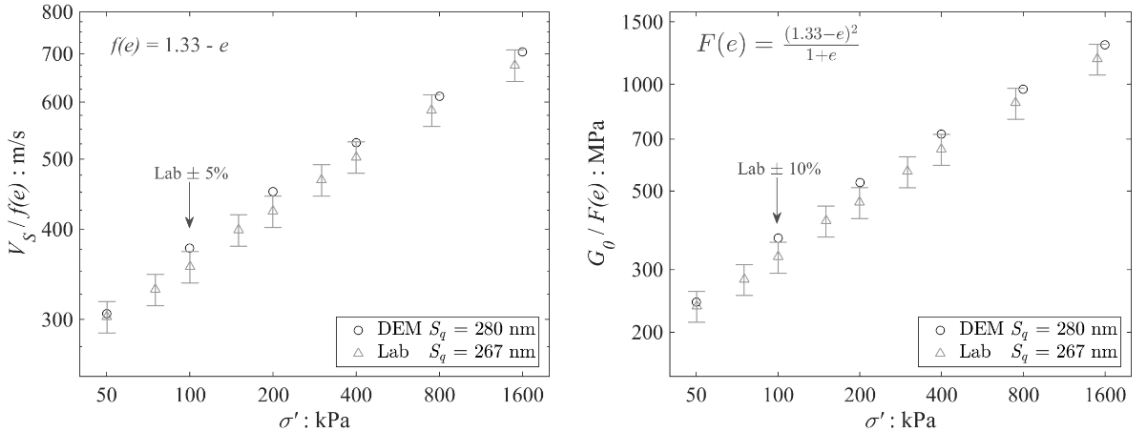

(a) (b)

Figure 6.39. DEM versus experimental results on (a) shear wave and (b) shear modulus for medium rough ballotini samples.

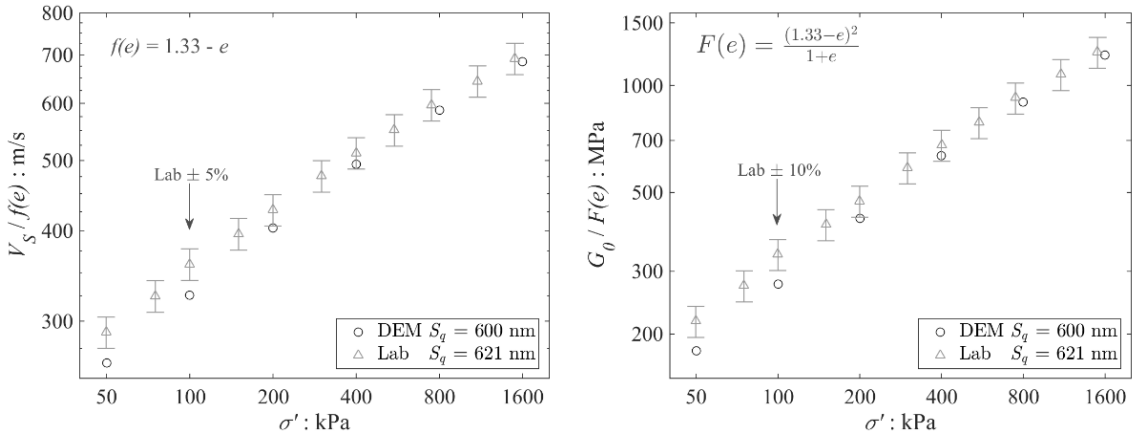

(a) (b)

Figure 6.40. DEM versus experimental results on (a) shear wave and (b) shear modulus for rough ballotini samples.

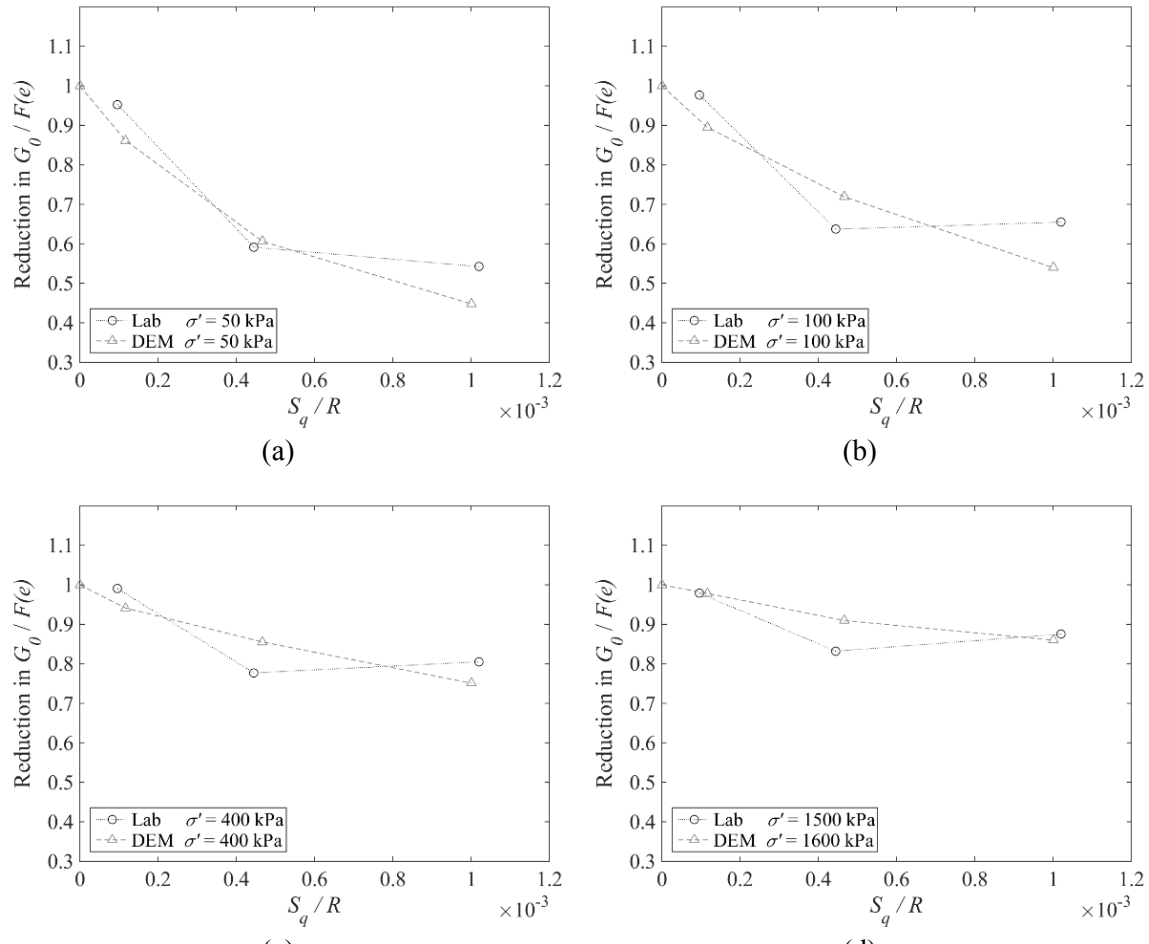

(a) (b)

(c) (d)

Figure 6.41. Variation in stiffness reduction with surface roughness for both experimental and DEM results. (a) σ' = 50 kPa, (b) σ' = 100 kPa, (c) σ' = 400 kPa, and (d) σ' = 1500 to 1600 kPa.

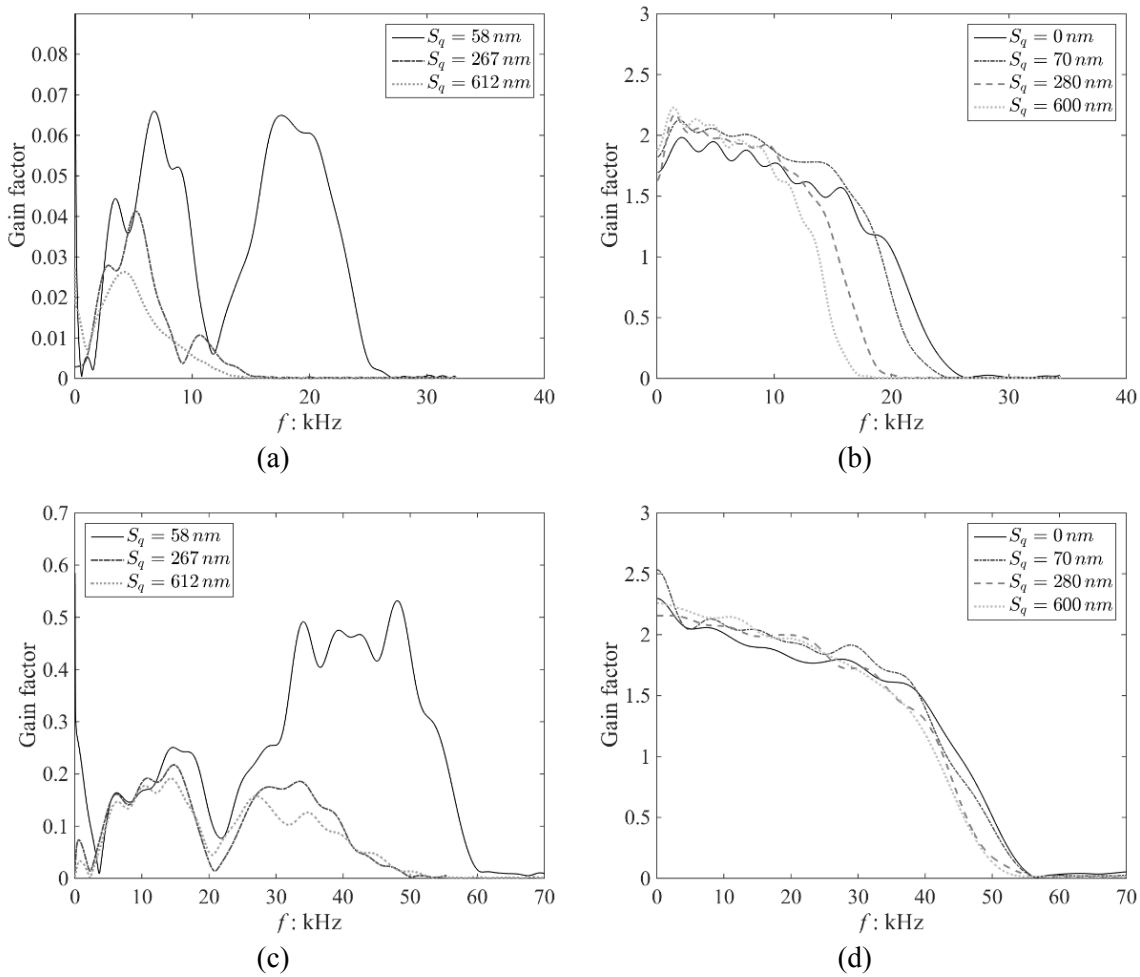

Figure 6.42. Comparison of gain factors for (a&c) experimental and (b&d) DEM data. (a&b) σ' = 50 kPa using f_{in} = 20 kHz. (c) σ' = 1500 kPa using f_{in} = 40 kHz (f_{in} = 30 kHz for medium rough sample, S_q = 267 μm). (d) σ' = 1600 kPa using f_{in} = 40 kHz.

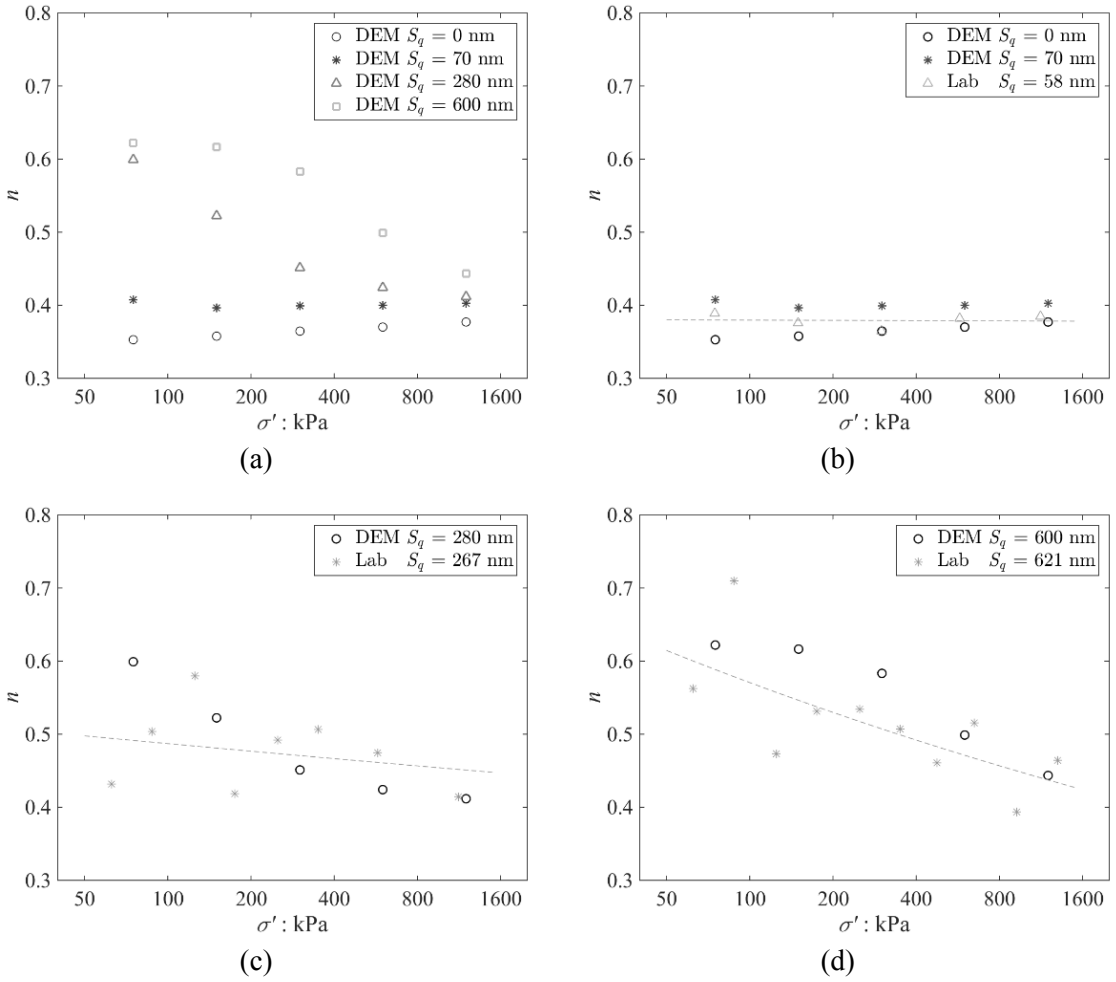

Figure 6.43. Variation in power coefficient n in the G_0 - σ' relationship. (a) DEM analysis for various surface roughness values, (b) Smooth samples, (c) Mild rough samples, and (d) Rough samples for both experimental and DEM data.

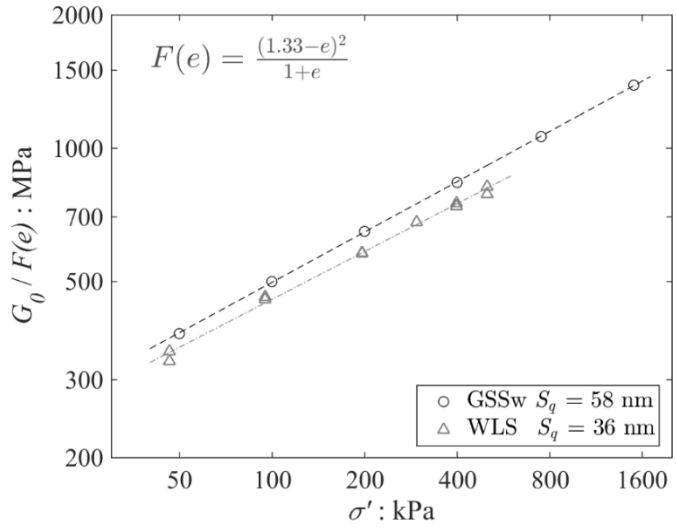

Figure 6.44. Comparison of G_0 normalised by void ratio function $F(e)$ between GSSw smooth sample used for triaxial test and WLS smooth sample used for CCA tests.

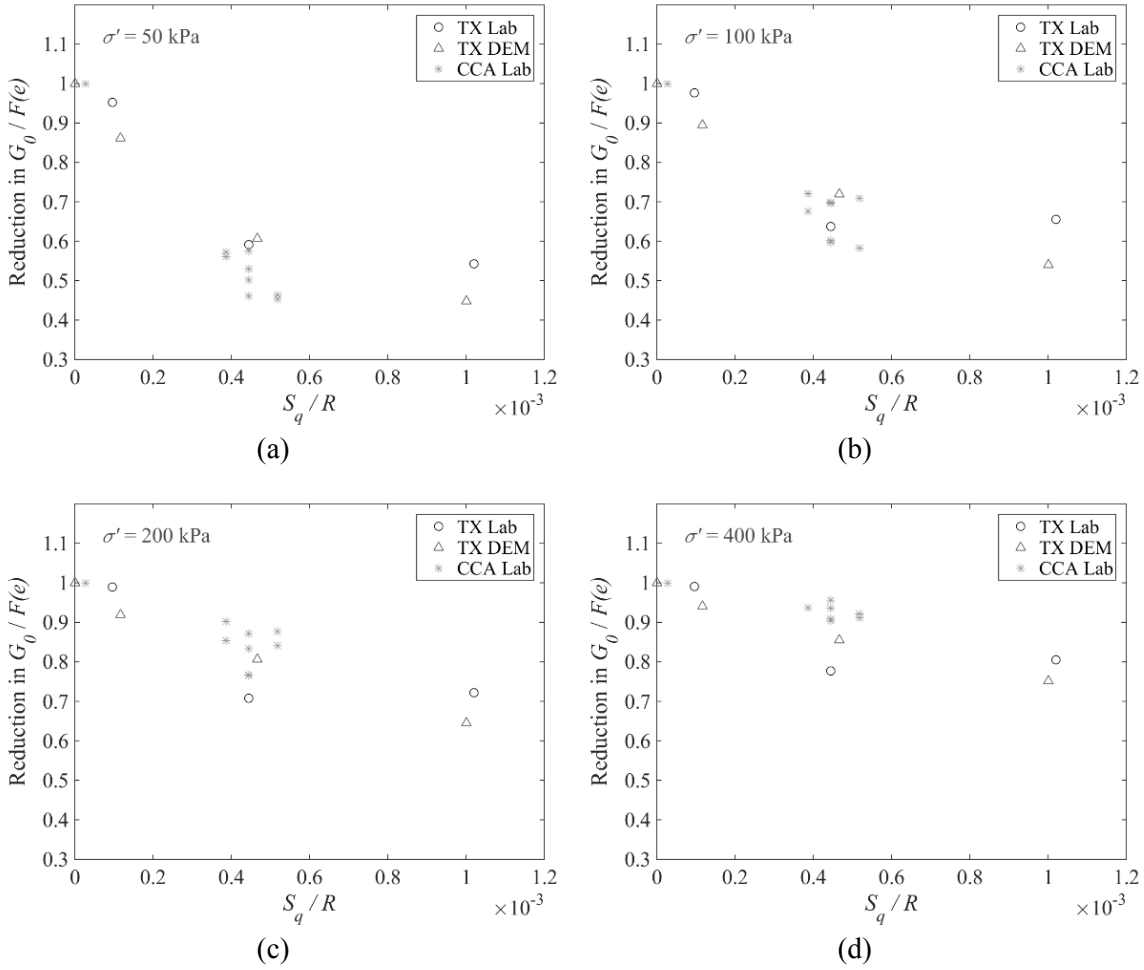

Figure 6.45. Comparison of variation in stiffness reduction with normalised surface roughness for both material types tested in CCA apparatus and triaxial apparatus (TX) including experimental and DEM data. (a) $\sigma' = 50$ kPa, (b) $\sigma' = 100$ kPa, (c) $\sigma' = 200$ kPa, and (d) $\sigma' = 400$ kPa.

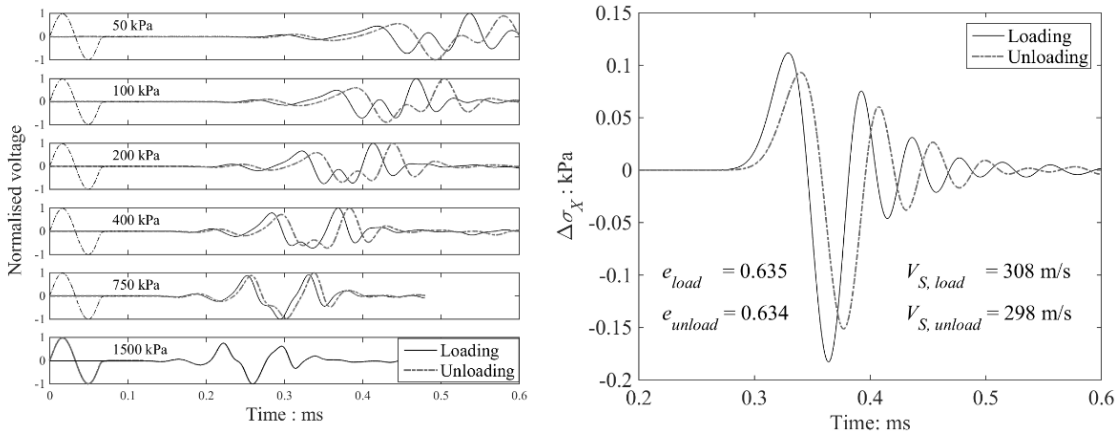

(a) (b)

Figure 6.46. Comparison of wave velocities between loading and unloading cases. (a) Experimental data for smooth sample (S_q = 58 nm) for f_{in} = 15 kHz. (b) DEM data at σ' = 100 kPa (unloaded from σ' = 1600 kPa).

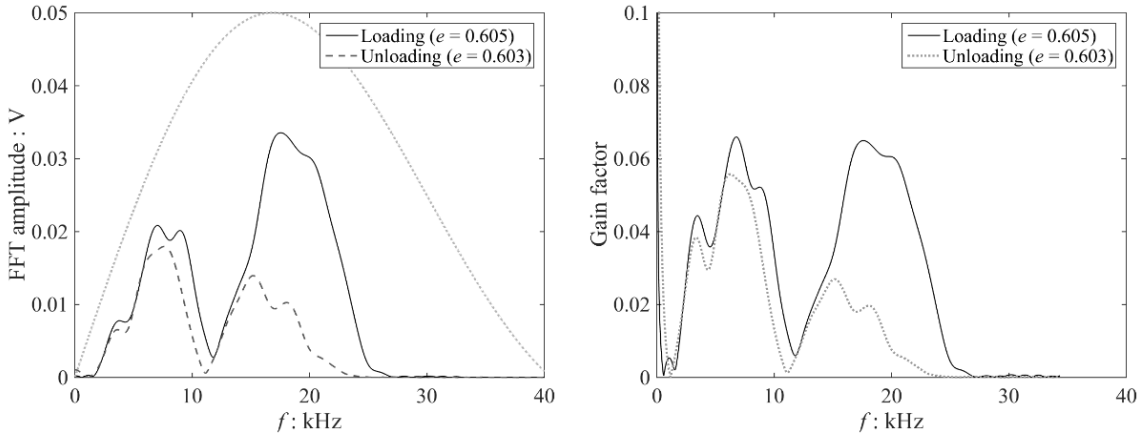

(a) (b)

Figure 6.47. Influence of overconsolidation on frequency domain response at σ' = 50 kPa for f_{in} = 20 kHz (experimental data using GSSw ballotini samples, S_q = 58 nm). (a) Received signals and normalised inserted signal, and (b) gain factor.

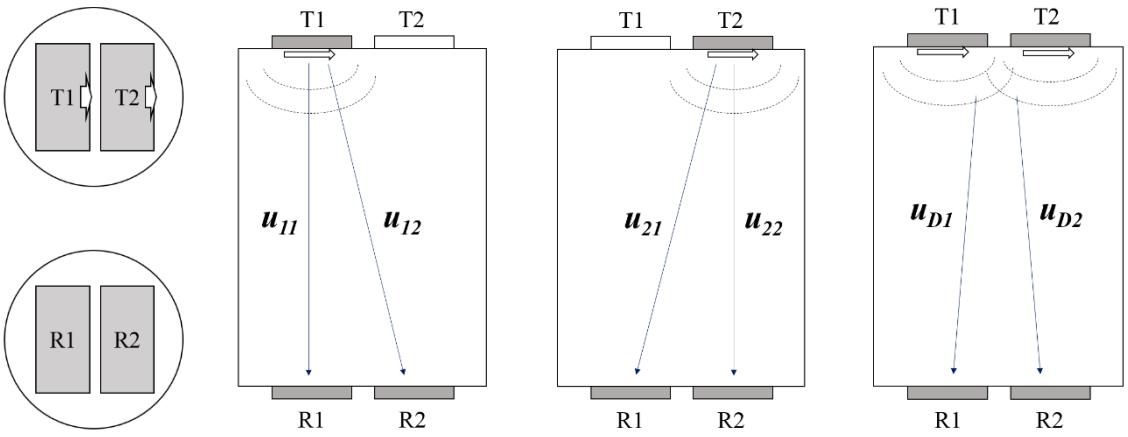

Figure 6.48. Schematic illustration of traveling waves using 2L-shear plate configuration. (a) Transmitters and receivers, (b) Waves generated at T1, (c) Waves generated at T2, and (d) Waves generated at both T1 and T2.

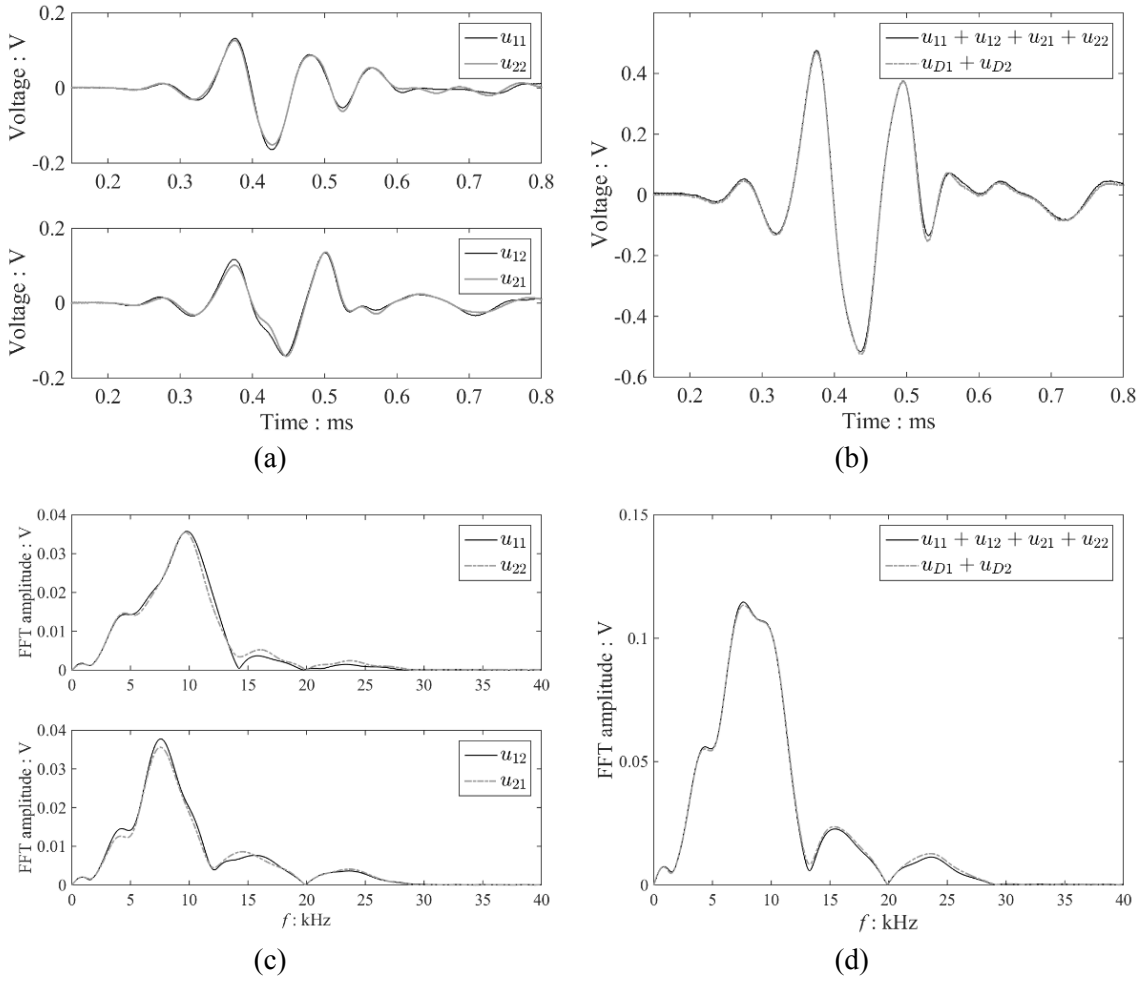

Figure 6.49. (a&b) Time domain and (c&d) frequency domain responses of received signals using 2L-shear plate configuration for inserted frequency f_{in} = 10 kHz. (a&c) Individual wave, and (b&d) Waves generated at T1 and T2.

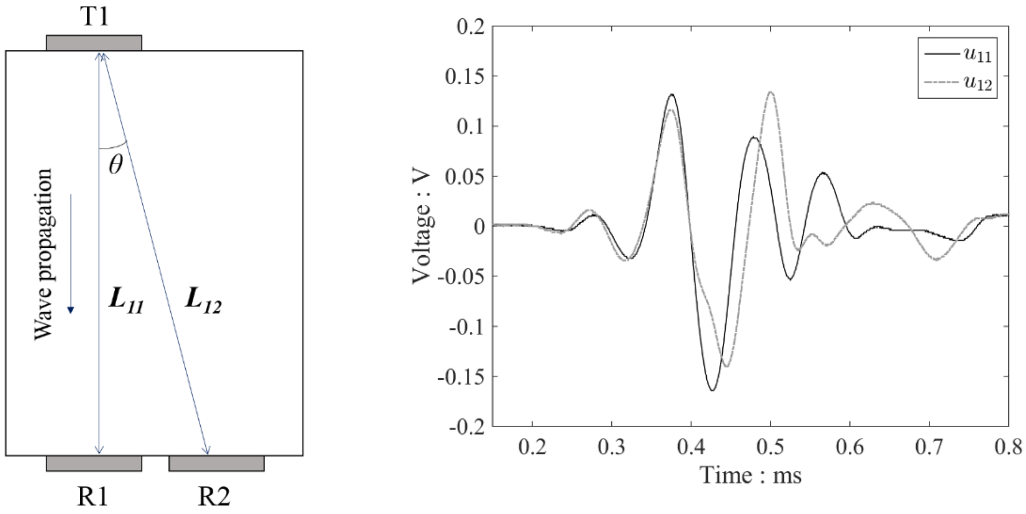

Figure 6.50. Comparison of waves received at R1 (u_{11}) and R2 (u_{12}) generated at T1 for f_{in} = 10 kHz.

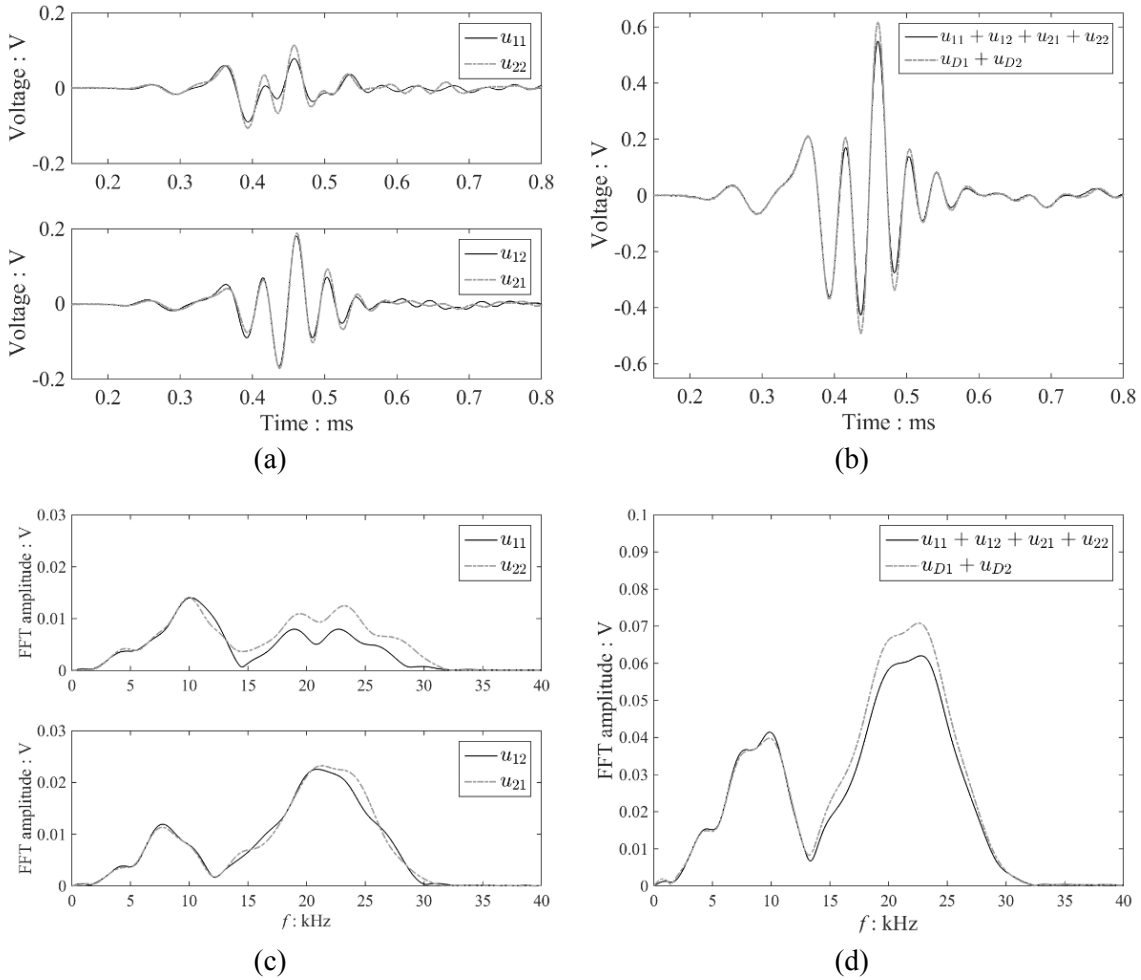

Figure 6.51. (a&b) Time domain and (c&d) frequency domain responses of received signals using 2L-shear plate configuration for inserted frequency f_{in} = 20 kHz. (a&c) Individual waves, and (b&d) Waves generated at T1 and T2.

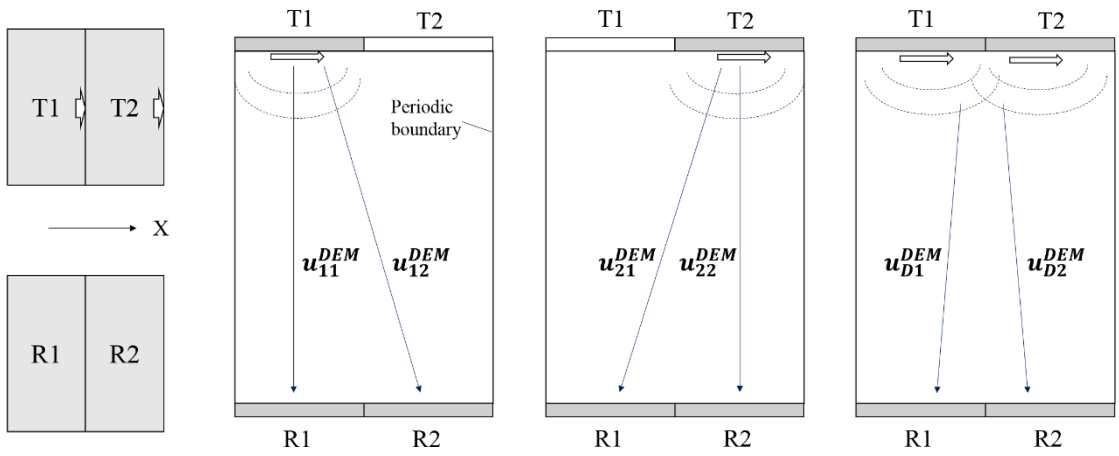

Figure 6.52. Schematic illustration of DEM simulations resembling 2L-shear plate configuration. (a) Transmitters and receivers, (b) Waves generated at T1, (c) Waves generated at T2, and (d) Waves generated at both T1 and T2.

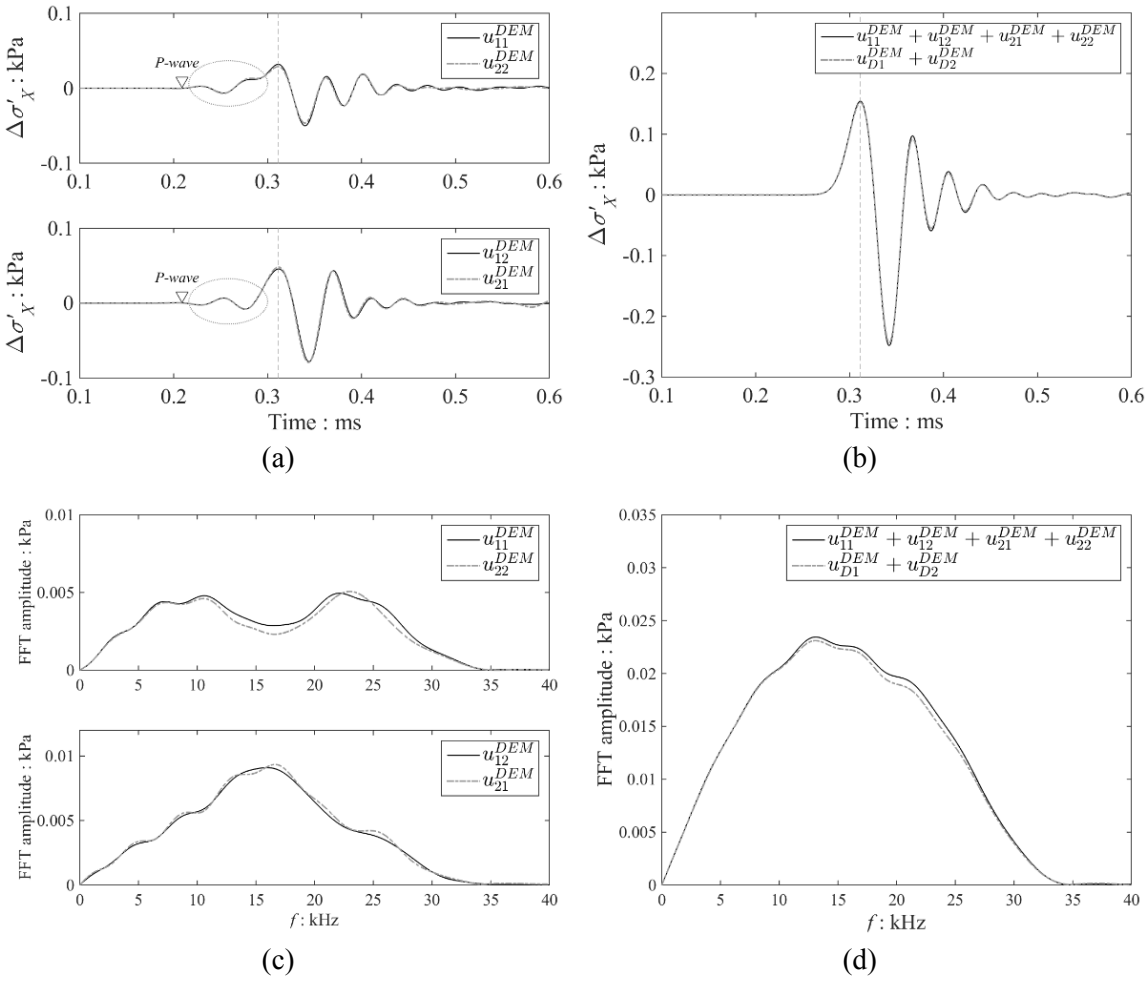

Figure 6.53. DEM data for (a&b) time domain and (c&d) frequency domain responses of received stresses using 2L-shear plate configuration for inserted frequency f_{in} = 20 kHz. (a&c) Individual wave, and (b&d) Waves generated at T1 and T2.

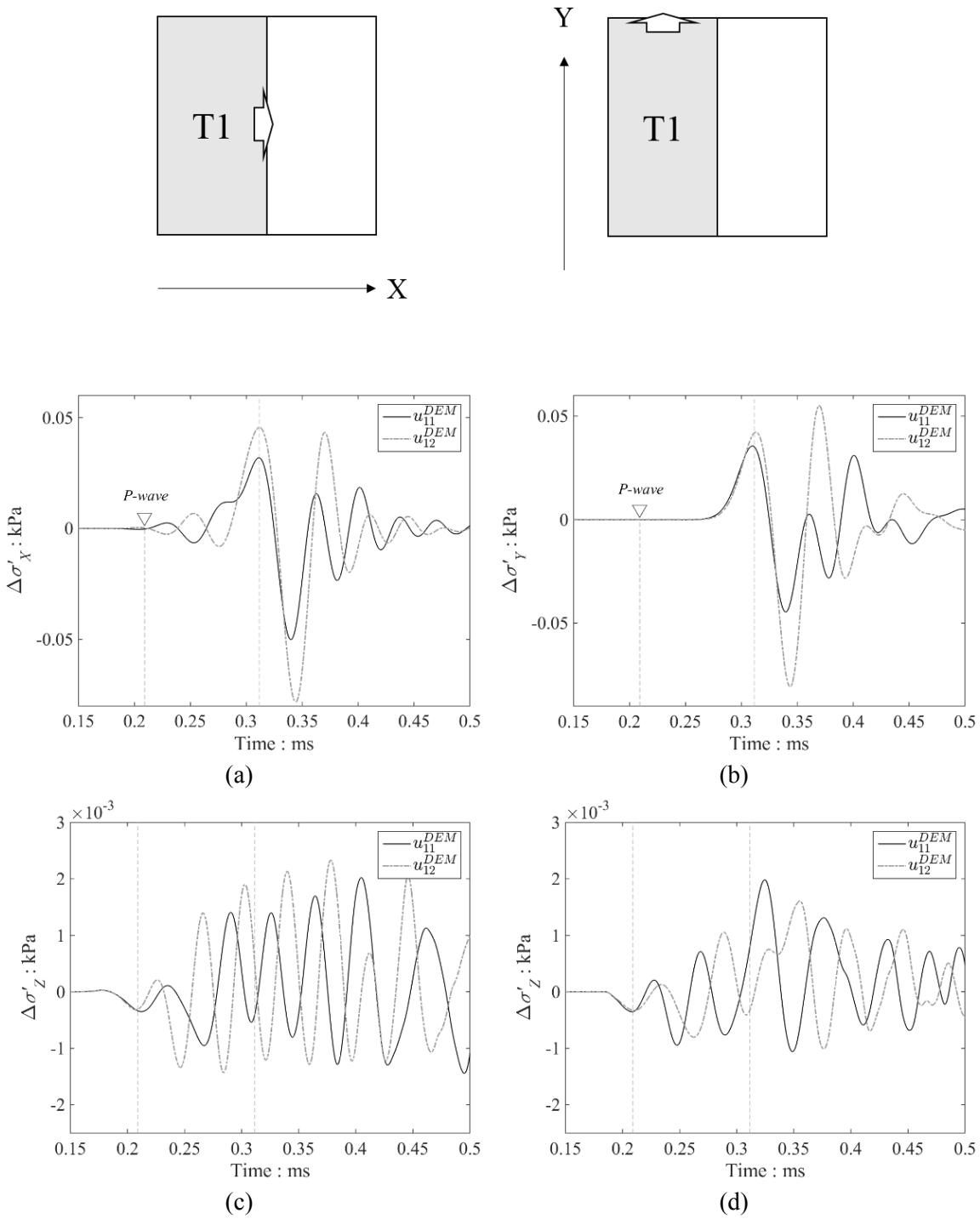

Figure 6.54. Influence of shearing direction on stress response using 2L-shear plate configuration. Rectangle wall excited in the direction of (a&c) shorter side, and (b&d) longer side. (a&b) Shear stress responses, and (c&d) Normal stress responses.

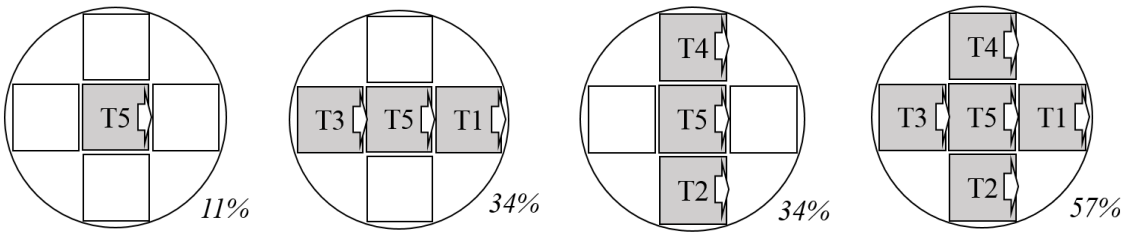

(a) (b) (c) (d)

Figure 6.55. Combinations of transmitter elements for 5S-shear plate configuration in triaxial apparatus.

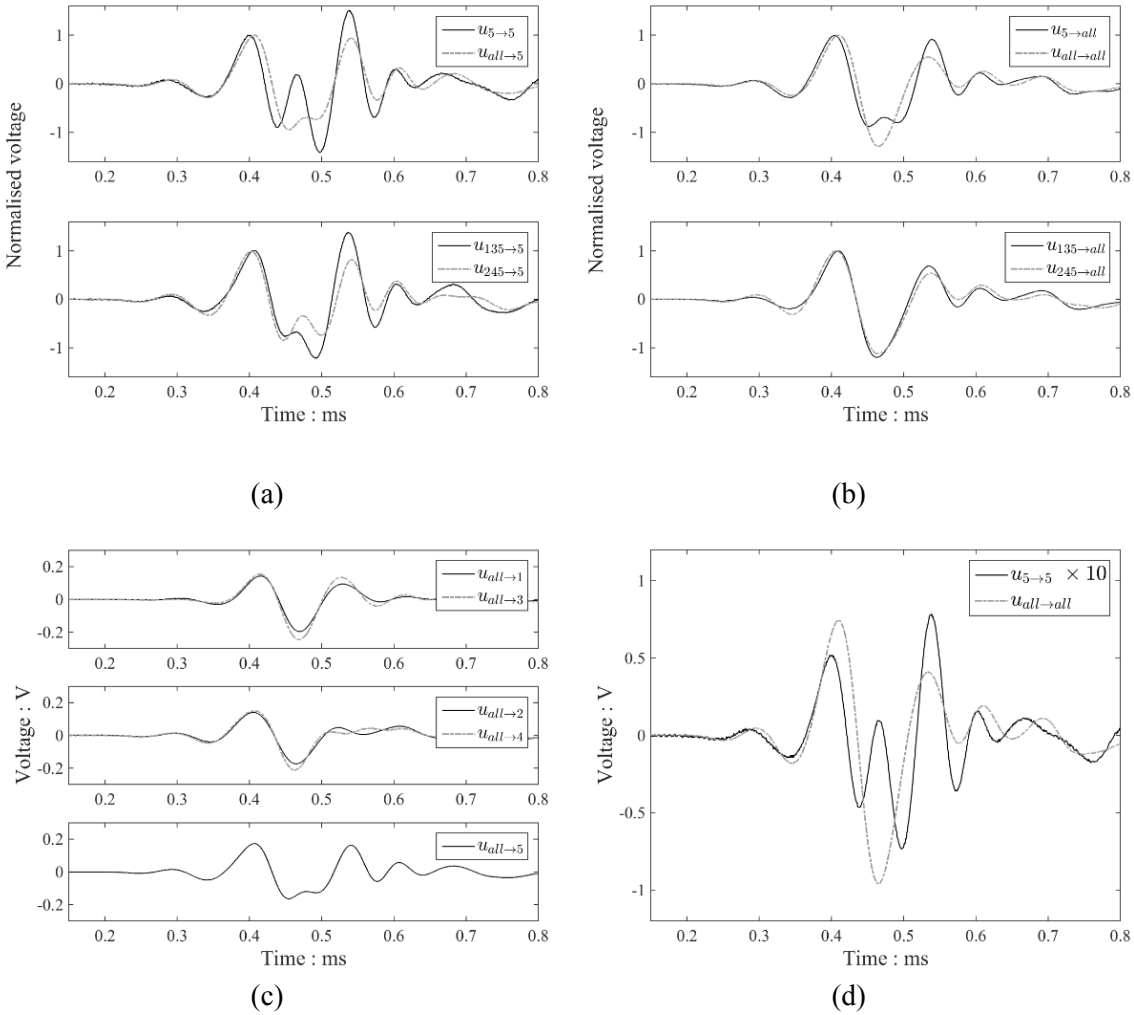

(a) (b)

(c) (d)

Figure 6.56. Experimental data obtained using 5S-shear plate configuration for f_{in} = 10 kHz. (a) Influence of transmitter size with a narrow receiver, (b) Influence of transmitter size with a wide receiver, (c) Each receiver response, and (d) Influence of size of both transmitter and receivers.

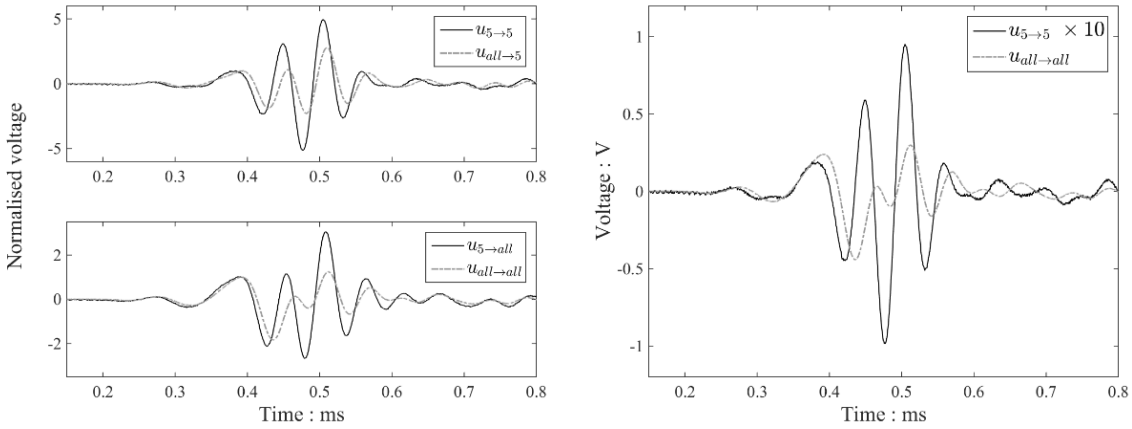

(a) (b)

Figure 6.57. Experimental data obtained using 5S-shear plate configuration for f_{in} = 20 kHz. (a) Influence of transmitter size with a narrow receiver or a wide receiver, and (b) Influence of size of both transmitter and receivers.

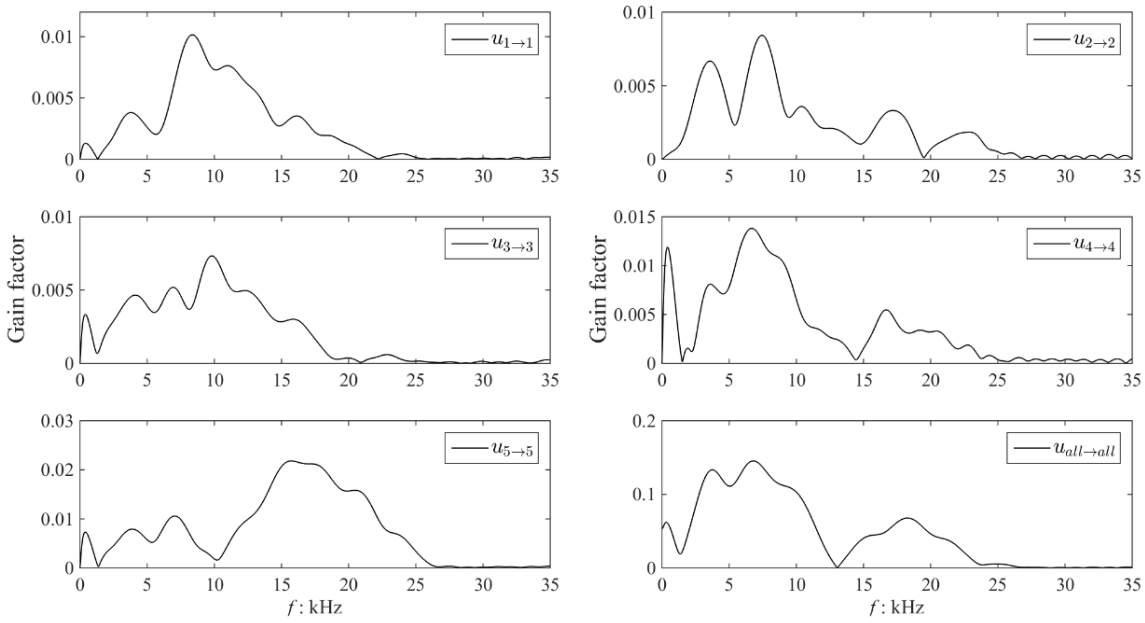

Figure 6.58. Analysis of experimental data to give variation in gain factors with frequencies obtained using 5S-shear plate configuration. Responses of individual shear plate compared with excitation at all the five plates together.

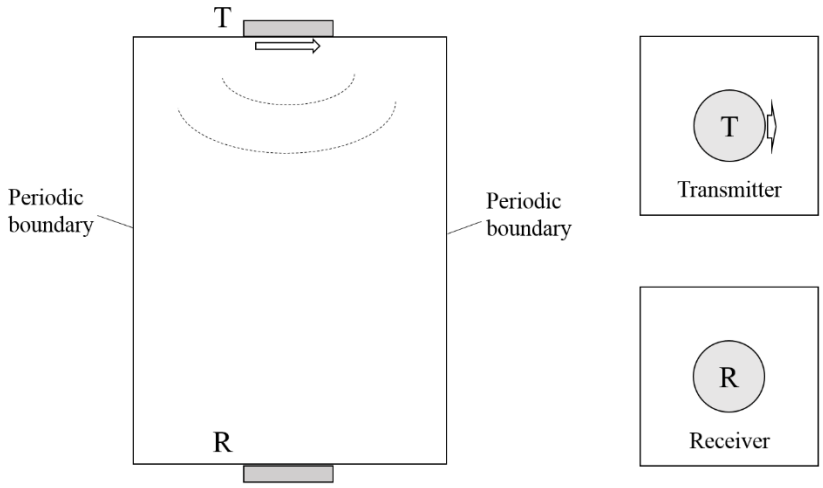

Figure 6.59. Schematic illustration of DEM simulations to investigate the size effects of transmitter and receiver.

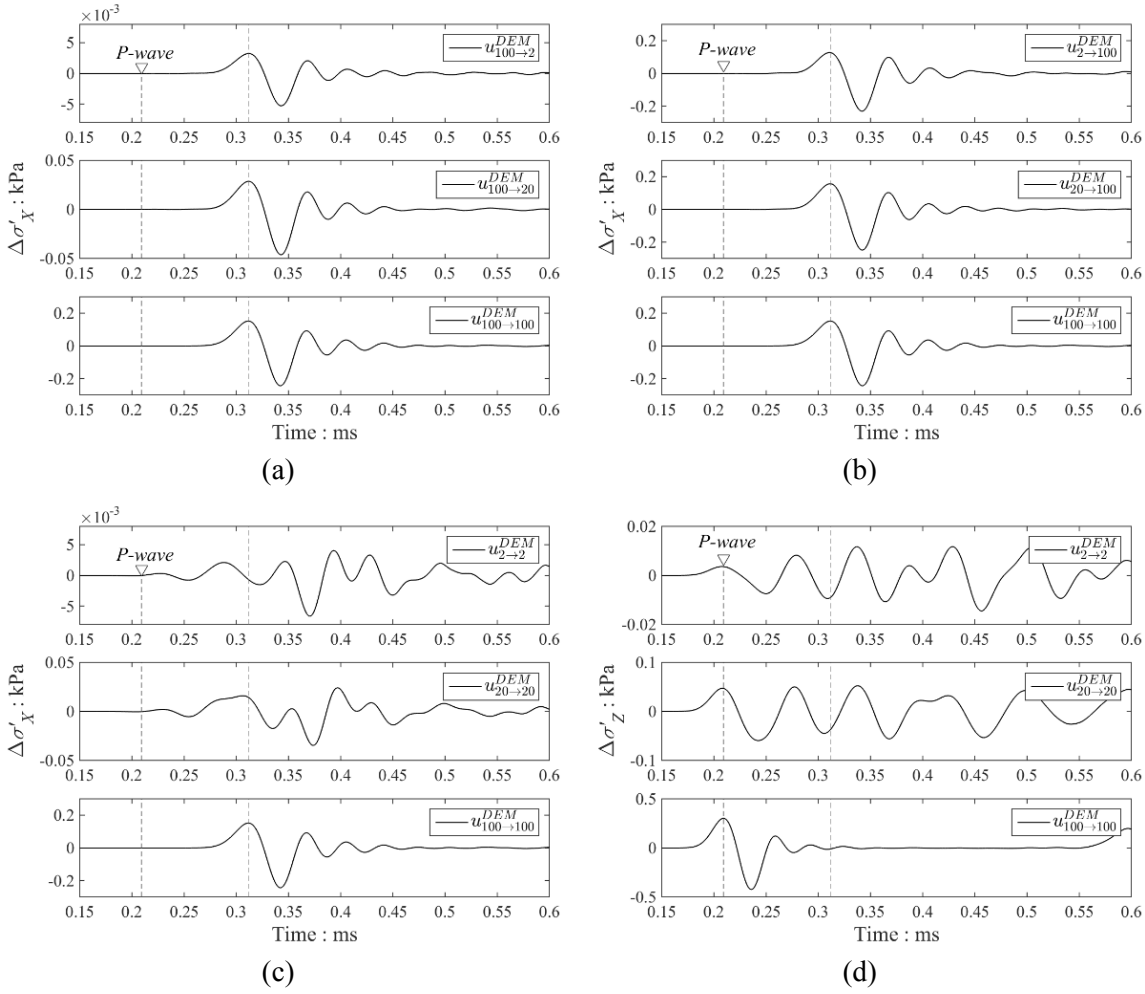

Figure 6.60. DEM data giving sensitivity of *S*-wave propagation to size of transmitter and receiver for f_{in} = 20 kHz. (a) Influence of receiver size, (b) Influence of transmitter size, (c) Influence of both transmitter and receivers, and (d) *P*-wave propagation with varying transmitter and receiver.

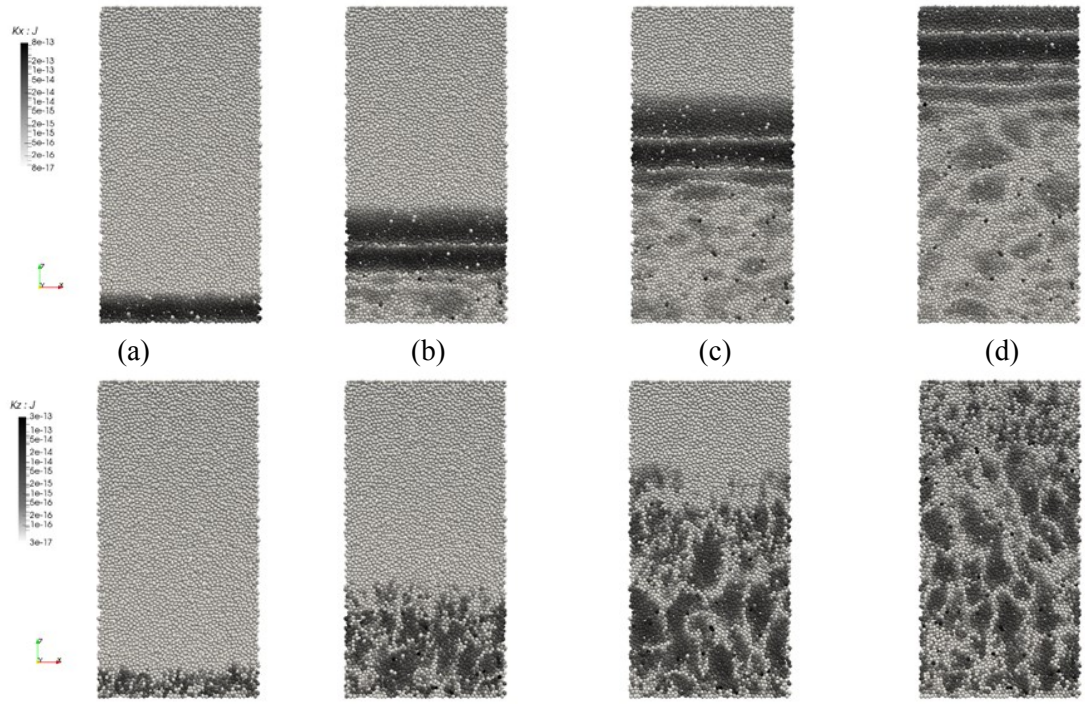

Figure 6.61. Propagation of particle kinetic energy in (a-d) X- and (e-h) Z-direction for planar *S*-wave. (a&e) t = 0.025 ms (= $0.5T_{in}$), (b&f) t = 0.1 ms, (c&g) t = 0.2 ms, and (d&h) t = 0.3 ms.

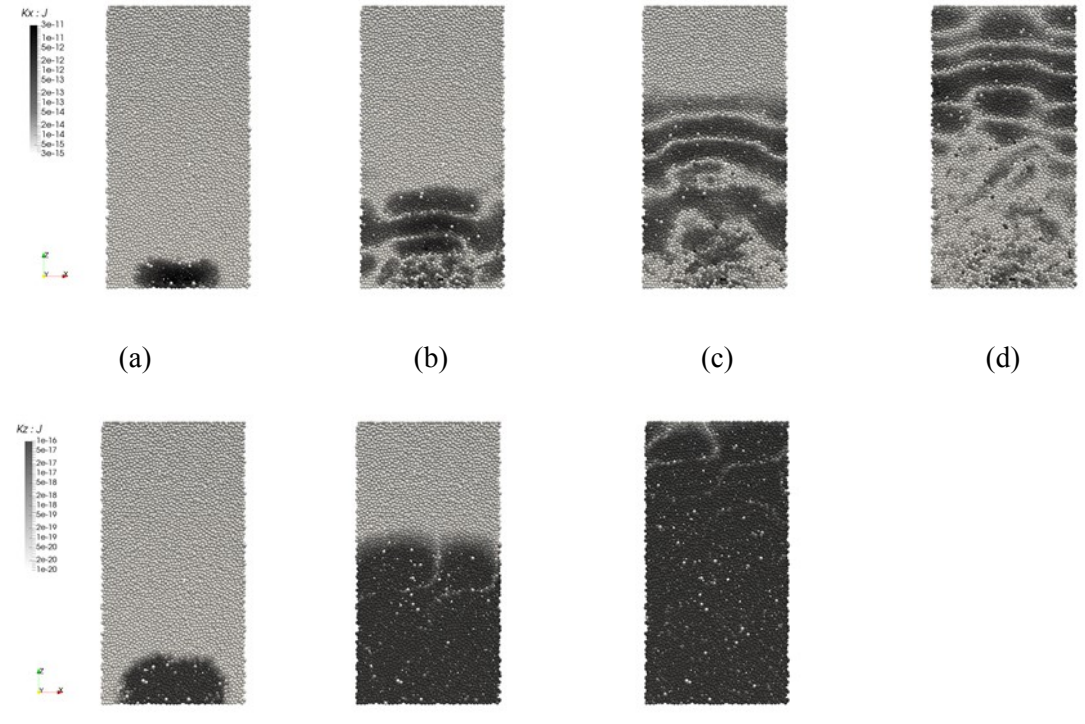

Figure 6.62. Propagation of particle kinetic energy in (a-d) X-and (e-g) Z-direction for *S*-waves excited at 2% area of transmitter wall. (a&e) t = 0.025 ms (= $0.5T_{in}$), (b&f) t = 0.1 ms, (c&g) t = 0.2 ms, and (d) t = 0.3 ms.

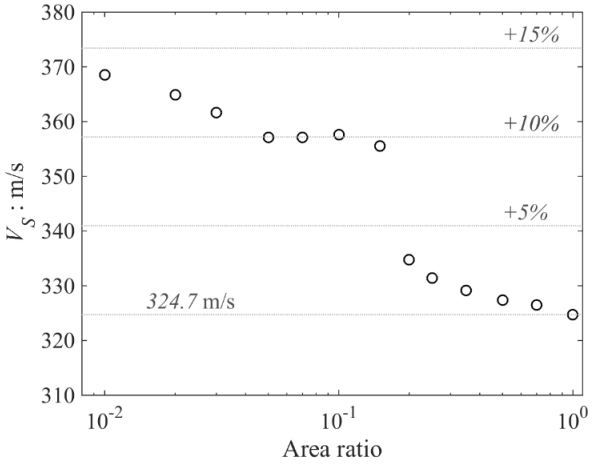

Figure 6.63. DEM data illustrating effect of size of transmitter and receiver on V_S where area of transmitters and receivers are kept equal.

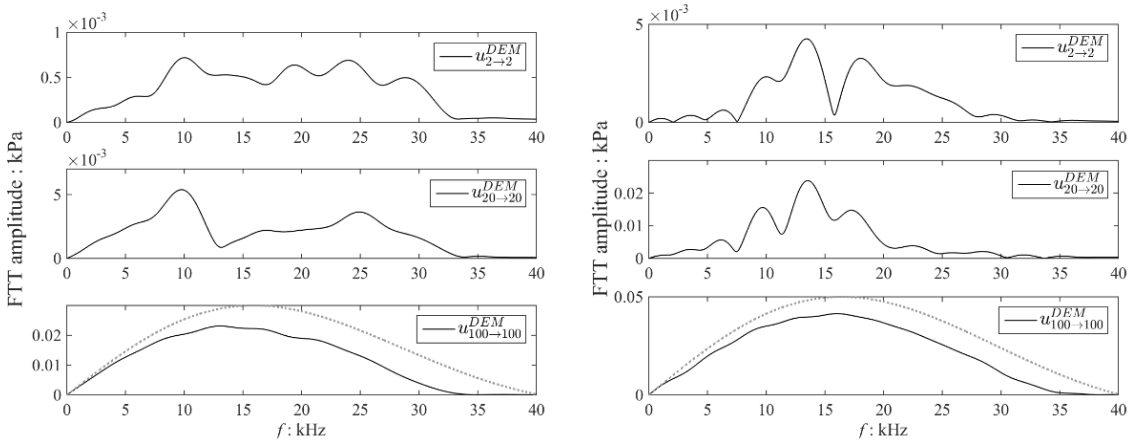

(a) (b)

Figure 6.64. DEM generated data giving frequency domain response for (a) *S*-wave and (b) *P*-wave propagation using f_{in} = 20 kHz.

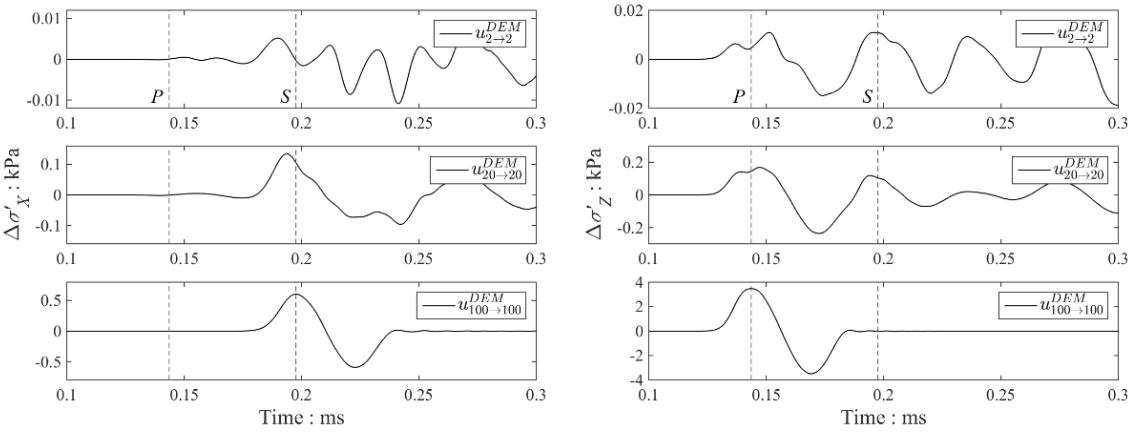

(a) (b)

Figure 6.65. DEM results for FCC sample with varying size of transmitter and receiver for f_{in} = 20 kHz. Influence of both transmitter and receivers on (a) *S*-wave, and (b) *P*-wave responses.

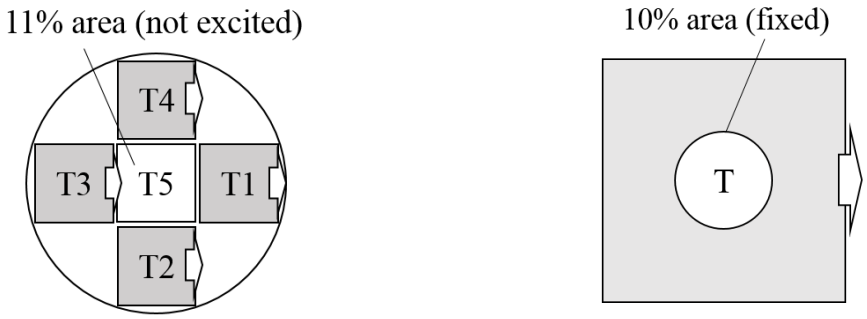

(a) (b)

Figure 6.66. Schematic illustration of excitation of outer elements only where the centre element is used as receiver element. (a) Experiments, and (b) DEM simulations where the size of the centre element is fixed to be 10% of the entire wall.

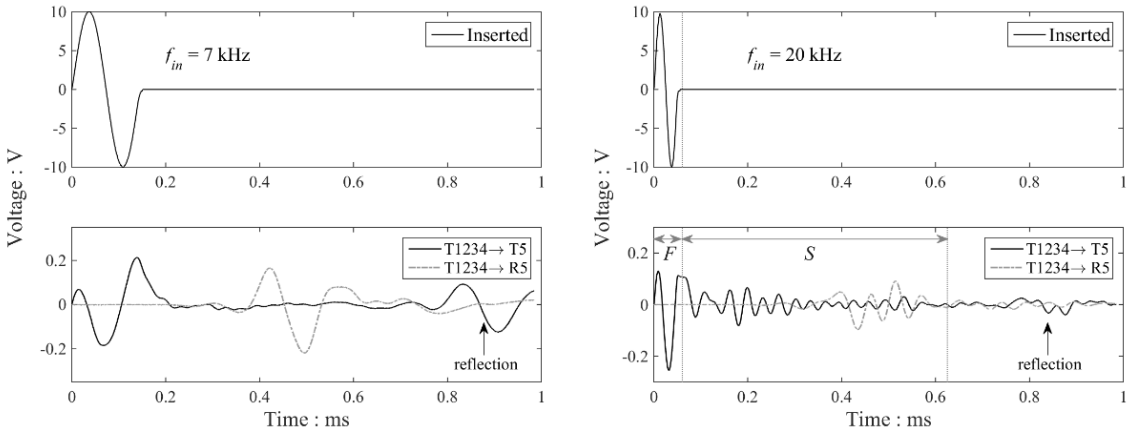

(a) (b)

Figure 6.67. Experimental analysis of local response using 5S-shear plate configuration. (a) f_{in} = 7 kHz, and (b) f_{in} = 20 kHz.

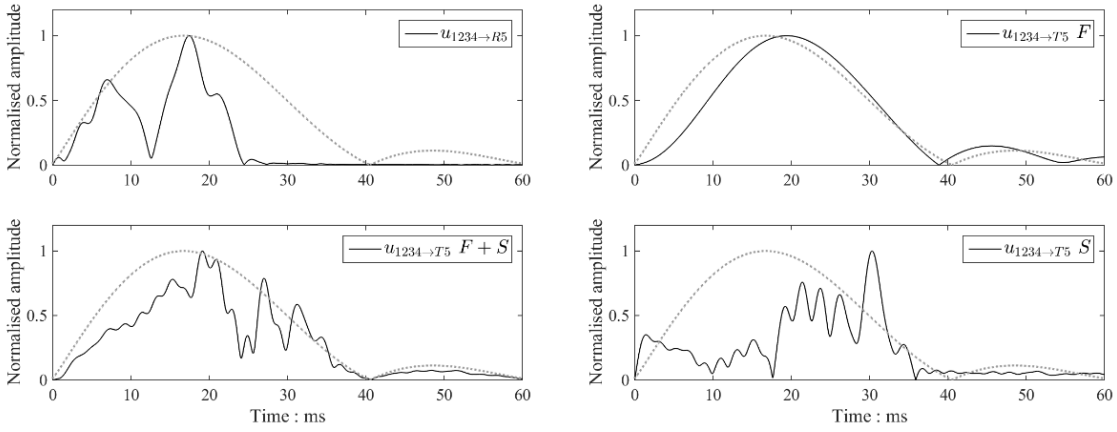

(a) (b)

Figure 6.68. Frequency domain analysis of experimental data of local response using 5S-shear plate configuration for f_{in} = 20 kHz. (a) Responses at T5 and R5 receivers, and (b) Details of response at T5 receiver.

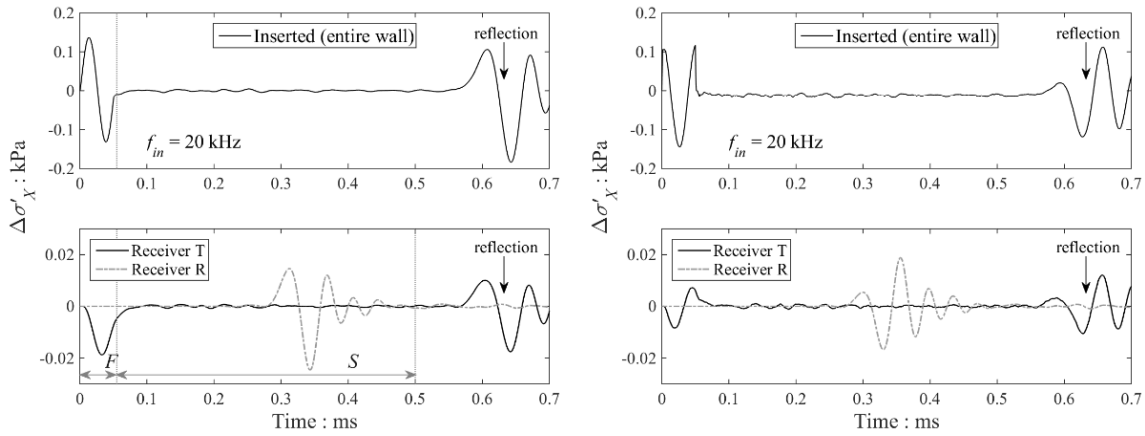

Figure 6.69. DEM analysis of local response for f_{in} = 20 kHz. The wall displacement follows (a) a sinusoidal pulse with a phase delay of 270 degrees, and (b) normal sinusoidal pulse.

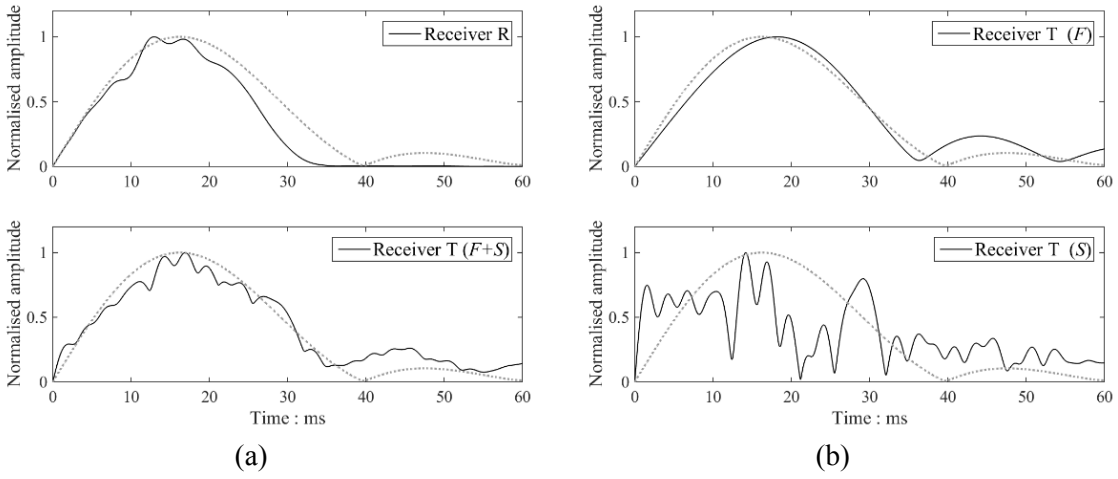

Figure 6.70. Frequency domain analysis of DEM data of local response for f_{in} = 20 kHz. (a) Responses at T and R receivers, and (b) Details of response at T receiver.

CHAPTER 7
Conclusions

7.1 Summary

The overall aim of the research was to understand the nature of the small-strain stiffness and system response of granular materials in laboratory small strain dynamic tests by adopting theoretical, numerical and experimental approaches.

Chapter 2 reviewed prior research to understand the contents of the thesis. To develop understanding of the nature of the soil stiffness, literature describing the particle interactions, packing and wave propagation was investigated.

In Chapter 3 the surface roughness values of the ballotini considered in later chapters were quantified using optical interferometry. The maximum void ratio (e_{max}) and minimum void ratio (e_{min}) of smooth and rough ballotini samples were measured, and the rough ballotini samples showed higher void ratios (e) than the smooth samples. The most plausible explanation for the effect of roughness on packing is a link between roughness and friction.

Chapter 3 also investigated the relationship between the mean coordination number ($\overline{C_N}$) and e of an assembly of spherical particles with diameters (D) from 1 to 1.18 mm using laboratory tests and the DEM analysis. Considering the mechanical mean coordination number and void ratio, the DEM results were in good agreement with a theoretical study by Suzuki et al. (1981), while the laboratory test showed better agreement with the earlier work of Nakagaki & Sunada (1968). Laboratory test results gave higher $\overline{C_N}$ values than those obtained from the DEM analyses; however, the discrepancy was within the tolerance established by considering the accuracy of laboratory tests. It was found, through the DEM analysis, that the $\overline{C_N} - e$ relationship is essentially independent of stress level and loading type (for the isotropic and K_0 compression loadings applied here), i.e. all the factors are empirically included in the $\overline{C_N} - e$ relationship.

Chapter 4 summarised mathematical expressions of contact models and they were implemented into a modified version of the LAMMPS molecular dynamic (DEM) code (Pinson et al., 1998). The full derivation of the rough surface (normal) contact model proposed in this study was

provided. The new model captures the soft responses induced by interacting surface asperities at lower normal contact forces, and gradually approaches a Hertzian contact response with increasing normal force. Partial slip effects in tangential and twisting contact interactions were also implemented. Both the tangential and torsional contact stiffnesses decrease with partial slip, and approach full slip gradually.

Chapter 4 also documented single contact simulations carried out to validate and explore the influence of the implemented contact models. To validate the Hertz-Mindlin-Deresiewicz (HMD) contact model, which considers partial slip effects in sliding, shearing under gravity and oblique impacts were considered to compare with prior research (Thornton & Yin, 1991; O'Donovan, 2013), and good agreement was observed. The surface roughness effects were explored and the soft responses due to surface asperities caused larger contact displacement at given input kinetic energy. The torsion-spin relationship including partial slip effects were examined, and it was found that the twisting contact stiffness is sensitive to the variation in normal contact force. The angular velocity was affected considerably when a softer material was considered. A newly implemented servo-control using wall boundaries was introduced to enable stress controlled simulations using LAMMPS in Chapters 5 and 6. Drained triaxial loading simulations were carried out to check the peak stress ratio of a FCC sample using the implemented contact models and new boundary conditions. Good agreement with Itasca (2007) and theory were observed when the peak stress ratio of the assembly was considered. The influence of twisting contact model on the peak stress ratio was negligible.

Chapter 5 described a series of DEM simulations of plane wave propagation in both FCC and random samples. In all the cases the particles were uniformly sized spheres to isolate inertia effects on the observed response. Various methods to determine the wave velocity were compared considering both the time domain (TD) and frequency domain (FD) methods applied to analyse the responses of the particles and the boundary walls. Taking the wave velocity measured using particle displacement data as the base or reference case, the maximal discrepancy observed amongst the other methods considered was 5.6%, for the stacked phase method using the boundary wall data. The other methods showed better agreement (typically within 3%) for various contact models, e and stress levels (σ'). These data indicate that provided the signal quality is adequate the simple peak-to-peak approach can be used to interpret S-wave signals. The agreement was more consistent than that observed in a similar comparison by O'Donovan (2013) who simulated bender element tests.

The DEM data presented in Chapter 5 showed that the sample shear modulus (G_0) at small strain levels increases with increasing σ' and reducing e. Increasing the surface roughness (S_q) reduced G_0; the reduction in G_0 was substantial at a low σ', whereas it gradually disappeared as

σ' increased. The power coefficient (n) in the G_0 - σ' relationship increased with increasing S_q; however as σ' increased, n decreased and approached the value for S_q = 0 (Hertzian contact model). This finding qualitatively agrees with the prior analytical model proposed by Yimsiri & Soga (2000); the quantitative differences from the micromechanical model can largely be attributed to a number of simplifying assumptions in the analytical model. The effect of partial slip on G_0 was also explored. For the FCC lattice packing, partial slip did not influence the response. The random packings were more sensitive to partial slip; accounting for partial slip gave a maximum reduction in G_0 by 6.4%. Adding spin resistance to the HM contact model did not show measurable effects for either the FCC sample or the random sample.

The natural frequencies of the DEM samples were obtained using an eigenvalue decomposition approach. The resonant frequencies and corresponding wavelengths associated with *P*-wave modes agreed with the dispersion relation obtained using the DEM data; this also agreed with the dispersion theory for the FCC samples. The agreement verifies the use of the simple analysis of the received signals to infer elastic parameters from laboratory geophysics experiments. The low-pass frequency ($f_{low\text{-}pass}$) and wavelength ($\lambda_{low\text{-}pass}$) were studied using the FD analysis of the received signals. For *P*-wave propagation, $f_{low\text{-}pass} < f_{i,max}$ (maximum eigenfrequency) for all the samples. Increasing either σ' or density resulted in a larger wave velocity and higher $f_{low\text{-}pass}$. The $\lambda_{low\text{-}pass}$ was not sensitive to σ' but was affected considerably by e. For the FCC samples $\lambda_{low\text{-}pass}/D \approx \sqrt{2}$, i.e. $\lambda_{low\text{-}pass}$ is identical to twice the layer spacing. The ratio $\lambda_{low\text{-}pass}/D$ observed for the random samples varied between 7 and 18 depending on e. These data highlight that for non-crystalline materials it is difficult to quantitatively relate $\lambda_{low\text{-}pass}$ to a characteristic of the sample. The gain factor of the received waves was analysed to examine an earlier hypothesis that the peaks in the gain factor represent resonant frequencies (Alvarado & Coop, 2012). While the resonant frequencies were found close to the local maxima in the gain factor, the data presented here do not support the hypothesis exactly.

Chapter 6 investigated the influence of the surface roughness on G_0 using the experimental and DEM approaches. The DEM samples considered here have similar dimensions to those of the laboratory specimens and they were prepared using the same material properties. Based on bender element and shear plate tests the overall observations in the DEM analyses were supported by the experiments; G_0 decreases with increasing surface roughness (S_q) especially at low σ', while G_0 approaches the smooth equivalent at high σ'. The $f_{low\text{-}pass}$ value decreased with increasing S_q particularly at low σ', which also agrees with the DEM results. A non-linear relationship between G_0 and S_q was highlighted and this point is recommended to be studied in more detail to better understand the surface roughness effects. For the smooth limit, close agreement between the experimental and DEM data was observed.

New shear plate configurations were described in Chapter 6 for laboratory dynamic tests at high σ' using coarse ballotini. In general good signals were observed using shear plates. When compared with shear plate tests documented in the literature, larger shear plates were used in this study. For a given source voltage, using larger (wider) shear plates increased the excitation energy at the same strain level and enabled experiments even at low σ'. The gain factor of the system response was affected by both shear plate size and lateral boundary conditions. The frequency responses observed using larger shear plates were almost identical to the summation of that at each small element, indicating that the system response is linear-elastic. The first *S*-wave peak appeared earlier when smaller shear plates were used due to near-field effects (Arroyo et al., 2003); this agrees with the DEM data.

Chapter 6 also showed that frequencies higher than $f_{low\text{-}pass}$ do not propagate into the sample from the vicinity of the transmitter shear plates. This finding was captured by the supplemental DEM analyses. An additional particle scale study revealed that near-field effects are induced by generating *S*-waves using a small transmitter size. The DEM data clearly showed that V_S increases with reducing the size of transmitter and receivers. When plane waves were generated the near-field effects were negligible in the DEM analysis; however, physical experimental data were always affected by near-field effects. This may be caused by the presence of side boundaries as shown by O'Donovan (2013) using DEM.

7.2 Key observations

The following key observations were made in this study.

<u>Shear modulus and surface roughness</u>

- DEM simulations showed that increasing $\overline{C_N}$ or reducing e gives larger wave velocity and lower sample Poisson's ratio.
- Both the experimental and DEM data agreed that surface roughness reduces G_0 particularly at low σ', and G_0 approaches that for smooth equivalent as σ' increases. The exponent n in the G_0 - σ' relationship increased with surface roughness.
- G_0 was not sensitive to partial slip in tangential contact or additional spin resistance considered in this DEM study.
- The G_0 values estimated using micromechanical effective medium theory (EMT) was in good agreement with the DEM data for the FCC samples; however, EMT overestimated G_0 for the random samples.

Dynamic response

- DEM data highlighted both the time domain (TD) and frequency domain (FD) approaches give similar wave velocities considering the wall boundary response or the particle scale response available in DEM.
- Eigenvalue analyses were performed using DEM data. The natural vibration frequencies and the wavenumbers associated with *P*-wave modes were extracted; they were well captured by dispersion relations observed using the DEM data.
- The local maxima of gain factor of the system observed using DEM appeared at close to resonant frequencies of the system; however it was not exact match.
- Experimental data showed that frequencies higher than $f_{low\text{-}pass}$ do not penetrate far into the sample from the transmitter, which agreed with the DEM analyses.
- Both experimental and DEM data agreed that $f_{low\text{-}pass}$ is sensitive to both e and σ', and the DEM data indicated that the contact model also affects $f_{low\text{-}pass}$. The DEM data also showed that $\lambda_{low\text{-}pass}$ is a function of e for a given particle size.

Shear plates

- Sample preparation using shear plates was less complicated than that using bender elements.
- Larger (or wider) shear plates showed more clear signals than small shear plates, which led better interpretation of the received signals.
- The near-field effects were not removed and the influence of membrane boundary on the frequency domain response was observed.
- Use of shear plates allowed reasonable comparison with equivalent DEM data.

Packing

- Ballotini with larger surface roughness showed higher e_{max} and e_{min} as well as wider range of the two extremes (i.e. e_{max} - e_{min}).
- Experimental data (ink test and μCT test) gave slightly higher $\overline{C_N}$ values than DEM data at a given e; however, the upper and lower bounds were in good agreement with prior studies of Nakagaki & Sunada (1968) and Suzuki et al. (1981), respectively, for almost mono-sized spherical particles.

7.3 Recommendations for further research

This study aimed to develop understanding of the nature of the small-strain stiffness of soils using theoretical, numerical and experimental approaches. The following aspects are recommended for future research to extend the micromechanical study to engineering applications.

Numerical study

The DEM simulations provided useful particle scale data during the wave propagation. All the simulations performed in this study used lateral periodic boundaries rather than membrane boundaries as was used in O'Donovan (2013). This study revealed that the source near-field effects are negligible during the planar *S*-wave propagation through a sample surrounded by lateral periodic boundaries, whereas the effects became significant with reducing the size of transmitter and receivers. Considering the experimental observations in this study, using wider shear plates enabled enhanced analyses of the TD and FD responses of the system; however, the near-field effects were always observed. O'Donovan (2013) observed non-negligible near-field effects despite using the planar *S*-wave in their simulations, and it is most probably caused by the lateral membrane boundary during the *S*-wave propagation. To fully understand the source of the near-field effects and improve laboratory test quality, additional DEM analyses would be helpful to explore this boundary issue more carefully.

To achieve more realistic simulation of soil response, the effect of particle size distribution (PSD) and particle shape on the small-strain stiffness needs to be understood. The PSD-dependency can be examined straightforward as the same simulation approach used in this study can be adopted. The heterogeneity observed in the random packing of equal spheres would be more significant when a wide PSD or gap graded sizes is considered. Comparison with spherical particles, underlying micromechanical theories to validate DEM models using non-spherical particles might not be sufficient, and the computational costs would be more expensive. It seems to be a challenging topic but it will help develop DEM study towards engineering applications.

Experimental study

The procedure for measuring surface roughness for soil mechanics research should be standardised. Recent developments of interferometry techniques have enabled accurate measurement of surface roughness. A challenge is how to remove the surface curvature, and a method should be established to do this. This study used a built-in function of a motif analysis to separate the surface roughness from the base surface. When a surface is measured using

different interferometers and software, the discrepancy should be small enough. To achieve this, it is necessary to develop a guideline which describes a standardised methodology to remove the effect of curvature and documents a database of reference values for typical soil grains.

It was not possible to conduct ink tests successfully using rough surface ballotini as the tracer ink was not printed well on the rough surface. This might be improved by applying a pressure to ink and circulating the tracer ink until good prints on contacts are achieved. This enables better understanding of the relationship between the $\overline{C_N} - e$ relationship for rough surface ballotini.

Shear plate tests showed clear signals that were comparable with the supplemental DEM data especially for smooth surface ballotini. The effect of surface roughness was obvious at low pressure levels; however, $G_{0,medium} \approx G_{0,rough}$ was observed. Additional experiments using slightly roughened ballotini will add more insight into the surface roughness effects on the G_0 - S_q relationship. A goal for this research might be to develop an empirical correlation between G_0 and σ' by introducing a simple parameter that accounts for the pressure-dependent roughness effects.

Using the 5S-shear plate configuration, it was found that the frequency response differs for the centre part and the outer part of the sample; a wave through the centre path contained higher frequencies. The difference may be caused by the lateral membrane boundary. This has not been reported in prior literature of bender elements. To isolate the lateral boundary effect it is recommend to use a full-size shear plate which covers the entire surface of the pedestal and topcap. Due to technical limitations, such large plates could not be deployed in the current study. Alternatively it is recommended to place a thin surface plate that contacts with two shear plate elements with polarization in X, two shear elements with polarization in Y and one compression element with polarization in Z (Figure 7.1). Using this design would allow researchers to excite planar *S*-waves in two directions and *P*-wave (or unconstrained wave). This has capacity of a triaxial loading as usual for a triaxial apparatus. This design would also be comparable with the resonant column test method that excites a torsional wave using a full-size interface.

Analytical study

Effective medium theory (EMT) captured the small-strain stiffness of a FCC sample obtained using DEM accurately, while it showed disagreement for random samples especially for looser packing. A reason for the discrepancy can be related to the fact that the EMT has been developed for porous rocks and assumes a homogeneous materials, i.e. the affine assumption (Digby, 1981) is inherent as pointed by Makse et al. (1999). The presence of non-affinity is related to the nature of random packing, and use of some type of index that can quantify the

degree of randomness should help estimate the small-strain stiffness for random samples more accurately. The DEM data gave $\lambda_{low\text{-}pass} = \sqrt{2}D$ for the FCC samples (D = particle diameter), while $7D < \lambda_{low\text{-}pass} < 18D$ for the random samples. This discrepancy also results from the heterogeneity of the random samples, and again a means to measure the degree of the heterogeneity would help improve the accuracy of this type of model.

Strain-dependent surface roughness effects

This study investigated the surface roughness effects on the small-strain stiffness of granular materials, and found that spherical particles with rougher surfaces have a lowered sample stiffness when compared with equivalent smooth particles. In contrast, surface roughness may increase the peak and residual strength of the sample at larger strains. Santamarina & Cascante (1998) and Lee et al. (2013) compared the evolution of the deviatoric stress developed during the triaxial compression using specimens composed of smooth or rough surface spherical particles, and observed greater deviatoric stress for rough case at axial strains from approximately 0.5% to 25%. Lee et al. (2013) showed that the friction angle at axial strains between 15% and 25% is larger for rough case by approxiamtely 10% although they did not quantify the surface roughness of tested galss ballotini. This result can be understood by the fact that the inter-particle friction would increase with increasing surface roughness as observed in the inter-particle shearing tests by Cavarretta (2009).

The strain-dependent effects of surface roughness has not been discussed deeply in the literature and should be understood correctly to apply this consideration to practice. The attainable range of void ratios is affected by surface roughness as discussed in Chapter 3, indicating that the critical state lines for smooth and roughened particles may differ. To interpret the impact of surface roughness on the sample stiffness from small to large strains, future research should be carried out recognising the state parameter framework.

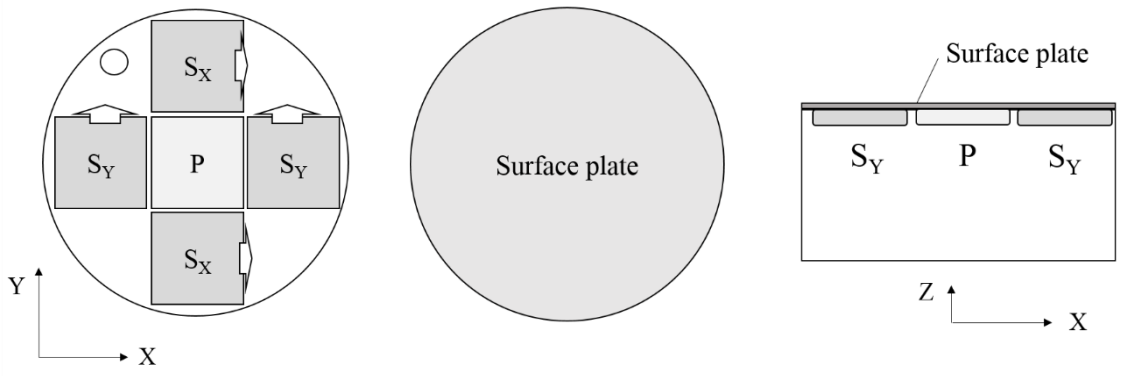

(a) (b) (c)

Figure 7.1. Schematic illustration of proposed shear plate design.

References

12085, B.E.I., 1997. Geometrical product specification (GPS). Surface texture. Profile method. Motif parameters,. *Ergonomics of human-computer interaction - Part 910: Framework for tactile and haptic*.

Ai, J., Chen, J.F., Rotter, J.M. & Ooi, J.Y., 2011. Assessment of rolling resistance models in discrete element simulations. *Powder Technology*, 206(3), pp.269–282.

Al-Raoush, R., 2007. Microstructure characterization of granular materials. *Physica A: Statistical Mechanics and its Applications*, 377(2), pp.545–558.

Alshibli, K. & Alsaleh, M., 2004. Characterizing surface roughness and shape of sands using digital microscopy. *Journal of computing in civil engineering*, 18(1), pp.36–45.

Altuhafi, F.N. & Coop, M.R., 2011. Changes to particle characteristics associated with the compression of sands. *Géotechnique*, 61(6), pp.459–471.

Alvarado, G. & Coop, M.R., 2012. On the performance of bender elements in triaxial tests. *Géotechnique*, 62(1), pp.1–17.

Antwerpen, W. Van, Toit, C.G. & Rousseau, P.G., 2010. A review of correlations to model the packing structure and effective thermal conductivity in packed beds of mono-sized spherical particles. *Nuclear Engineering and Design*, 240(7), pp.1803–1818.

Arakawa, M. & Nishino, M., 1973. Contact number and porosity in randomly packed sphere mixtures of various sizes (in Japanese). *Zairyo*, 22(238), pp.658–662.

Arroyo, M., Butlanska, J., Gens, A., Calvetti, F. & Jamiolkowski, M., 2011. Cone penetration tests in a virtual calibration chamber. *Géotechnique*, 61(6), pp.525–531.

Arroyo, M., Muir Wood, D. & Greening, P.D., 2003. Source near-field effects and pulse tests in soil samples. *Géotechnique*, 53(3), pp.337–345.

Atkinson, J., 2000. Non-linear soil stiffness in routine design. *Géotechnique*, 50(5), pp.487–508.

Baltazar, A., Rokhlin, S. & Pecorari, C., 2002. On the relationship between ultrasonic and micromechanical properties of contacting rough surfaces. *Journal of the Mechanics and Physics of Solids*, 50(7), pp.1397–1416.

Barreto, D., 2009. *Numeriacal and experimental investigation into the behaviour of granular materials under generalised stress states*. PhD thesis, Imperial College London.

Barreto, D. & O'Sullivan, C., 2012. The influence of inter-particle friction and the intermediate stress ratio on soil response under generalised stress conditions. *Granular Matter*, 14(4), pp.505–521.

Belytschko, T., Liu, W.K. & Moran, B., 2000. *Nonlinear finite elements for continua and structures*, Wiley.

Bernal, J.D. & Mason, J., 1960. Packing of spheres: co-ordination of randomly packed spheres. *Nature*, 188(4754), pp.910–911.

Bernhardt, M.L., Biscontin, G. & O'Sullivan, C., 2016. Experimental validation study of 3D direct simple shear DEM simulations. *Soils and Foundations*, 56(3), pp.336–347.

Bernhardt, M.L., O'Sullivan, C. & Biscontin, G., 2014. Effects of sample preparation methods in DEM. In *Proceedings of the TC105 ISSMGE iInternational Symposium on Geomechanics from Micro to Macro, IS-Cambridge 2014*. pp. 97–102.

Biwa, S., Hiraiwa, S. & Matsumoto, E., 2009. Pressure-dependent stiffnesses and nonlinear ultrasonic response of contacting surfaces. *Journal of Solid Mechanics and Materials Engineering*, 3(1), pp.10–21.

Boore, D.M., 2006. Determining subsurface shear-wave velocities : A review. In *Third International Symposium on the Effects of Surface Geology on Seismic Motion*. Grenoble, France, Paper No. 103.

Brignoli, E.G.M., Gotti, M. & Stokoe II, K.H., 1996. Measurement of shear waves in laboratory specimens by means of piezoelectric transducers. *Geotechnical Testing Journal*, 19(4), pp.384–397.

Brillouin, L., 1946. *Wave propagation in periodic structures*, McGraw-Hill Book Co.

Butlanska, J., Arroyo, Marcos., Gens, Antonio & O'Sullivan, C., 2014. Multi-scale analysis of cone penetration test (CPT) in a virtual calibration chamber. *Canadian Geotechnical Journal*, 51(1), pp.51–66.

Calvetti, F., 2008. Discrete modelling of granular materials and geotechnical problems. *European Journal of Environmental and Civil Engineering*, 12(7-8), pp.951–965.

Camacho-Tauta, J.F., Cascante, G., Da Fonseca, A.V. & Santos, J.A., 2015. Time and frequency domain evaluation of bender element systems. *Géotechnique*, 65(7), pp.548–562.

Camacho-tauta, J.F., David, J. & Álvarez, J., 2013. Comparison between resonant-column and bender element tests on three types of soils. *Dyna*, *year 80*, 182, pp.163–172.

Camenen, J.F., Hamlin, S., Cavarretta, I. & Ibraim, E., 2013. Experimental and numerical assessment of a cubical sample produced by pluviation. *Géotechnique Letters*, 3(2), pp.44–51.

Campañá, C., Persson, B.N.J. & Müser, M.H., 2011. Transverse and normal interfacial stiffness of solids with randomly rough surfaces. *Journal of Physics. Condensed Matter*, 23(8), p.085001.

Cavarretta, I., O'Sullivan, C., Ibraim, E., Lings, M., Hamlin, S. & Muir Wood, D., 2012. Characterization of artificial spherical particles for DEM validation studies. *Particuology*, 10(2), pp.209–220.

Cavarretta, I., 2009. *The influence of particle characteristics on the engineering behaviour of granular materials*. PhD thesis, Imperial College London.

Cavarretta, I., Coop, M. & O'Sullivan, C., 2010. The influence of particle characteristics on the behaviour of coarse grained soils. *Géotechnique*, 60(6), pp.413–423.

Cha, M., Cho, G. & Santamarina, J.C., 2009. Long-wavelength P-wave and S-wave propagation in jointed rock masses. *Geophysics*, 74(5), pp.E205–E214.

Chang, C.S. & Liao, C.L., 1994. Estimates of elastic modulus for media of randomly packed granules. *Applied Mechanics Reviews*, 47(1 Part 2), pp.S197–S206.

Chang, C.S., Misra, A. & Sundaram, S.S., 1991. Properties of granular packings under low amplitude cyclic loading. *Soil Dynamics and Earthquake Engineering*, 10(4), pp.201–211.

Cho, G.-C., Dodds, J. & Santamarina, J.C., 2006. Particle shape effects on packing density, stiffness, and strength: natural and crushed sands. *Journal of Geotechnical and Geoenvironmental Engineering*, 132(5), pp.591–602.

Chopra, A.K., 2011. *Dynamics of structures*, Prentice Hall.

Clayton, C.R.I., 2011. Stiffness at small strain: research and practice. *Géotechnique*, 61(1), pp.5–37.

Clayton, C.R.I., Priest, J.A., Bui, M., Zervos, A. & Kim, S.G., 2009. The Stokoe resonant column apparatus: effects of stiffness, mass and specimen fixity. *Géotechnique*, 59(5), pp.429–437.

Cui, L. & O'Sullivan, C., 2006. Exploring the macro- and micro-scale response of an idealised granular material in the direct shear apparatus. *Géotechnique*, 56(7), pp.455–468.

Cundall, P.A. & Strack, O.D.L., 1979. A discrete numerical model for granular assemblies. *Géotechnique*, 29(1), pp.47–65.

Deresiewicz, H., 1954. Contact of elastic spheres under an oscillating torsional couple. *Journal of Applied Mechanics*, 21(1), pp.52–56.

Digby, P.J., 1981. The effective elastic moduli of porous granular rocks. *Journal of Applied Mechanics*, 48(4), pp.803–808.

Drnevich, V.P., 1978. Resonant-column testing-problems and solutions. *Dynamic geotechnical testing*, (ASTM STP 654), pp.384–398.

Duffaut, K., Landrø, M. & Sollie, R., 2010. Using Mindlin theory to model friction-dependent shear modulus in granular media. *Geophysics*, 75(3), pp.E143–E152.

Duffy, J. & Mindlin, R.D., 1957. Stress-Strain Relations and Vibrations of a granular medium. *Journal of Applied Mechanics*, 24, pp.585–593.

Edwards, S.F., 1998. The equations of stress in a granular material. *Physica A: Statistical Mechanics and its Applications*, 249(1-4), pp.226–231.

Fogale, 2005. Fogale nanotech user manual version 1.5. Nimes, France: Fogale.

da Fonseca, A.V., Ferreira, C. & Fahey, M., 2009. A framework interpreting bender element tests, combining time-domain and frequency-domain methods. *Geotechnical Testing Journal*, 32(2), pp.91–107.

Fonseca, J., Sim, W., Shire, T. & O'Sullivan, C., 2014. Microstructural analysis of sands with varying degrees of internal stability. *Géotechnique*, 64(5), pp.405–411.

Fonseca, J., O'Sullivan, C., Coop, M.R. & Lee, P.D., 2013. Quantifying the evolution of soil fabric during shearing using directional parameters. *Géotechnique*, 63(10), pp.818–829.

German, R.M., 2014. Coordination number changes during powder densification. *Powder*

Technology, 253, pp.368–376.

Goddard, J.D., 1990. Nonlinear elasticity and pressure-dependent wave speeds in granular media. *Proceedings of the Royal Society A: Mathematical, Physical and Engineering Sciences*, 430(1878), pp.105–131.

Gonzalez-Valadez, M., Baltazar, A. & Dwyer-Joyce, R.S., 2010. Study of interfacial stiffness ratio of a rough surface in contact using a spring model. *Wear*, 268(3-4), pp.373–379.

Gotoh, K., 1978. Liquids and powders - a random packing structure of equal sphere (in Japanese). *Journal of the Society of Powder Technology*, 15(4), pp.220–226.

Graton, L.C. & Fraser, H.J., 1935. Systematic Packing of Spheres: With Particular Relation to Porosity and Permeability. *The Journal of Geology*, 43(8), pp.785–909.

Greening, P.D. & Nash, D.F.T., 2004. Frequency domain determination of G0 using bender elements. *Geotechnical Testing Journal*, 72(3), pp.1–7.

Greenwood, J., Johnson, K. & Matsubara, E., 1984. A surface roughness parameter in hertz contact. *Wear*, 100(1-3), pp.47–57.

Greenwood, J.A., 1967. The area of contact between rough surfaces and flats. *Journal of Lubrication Technology*, 89(1), p.81.

Greenwood, J.A. & Tripp, J.H., 1970. The contact of two nominally flat rough surfaces. In *Proceedings of the institution of mechanical enginners*. 185(1), pp. 625–633.

Greenwood, J.A. & Tripp, J.H., 1967. The elastic contact of rough spheres. *Journal of Applied Mechanics*, 34(1), pp.153–159.

Group, F.V.S., 2015. Avizo 9.0.0 user guide.

Hamlin, S.M., 2014. *Body wave propagation in an analogue granular material in a cubical cell apparatus*. PhD thesis, The University of Bristol.

Hanaor, D.A.H., Gan, Y. & Einav, I., 2013. Effects of surface structure deformation on static friction at fractal interfaces. *Géotechnique Letters*, 3(2), pp.52–58.

Hanley, K. & O'Sullivan, C., 2016. Analytical study of the accuracy of discrete element simulations. *International Journal for Numerical Methods in Engineering*, 10.1002/nm.

Hardin, B.O., 1965. Dynamic and static shear modulus for dry sand. *Materials Research & Standards*, 5(5), pp.232–235.

Hardin, B.O. & Richart, Jr., F.E., 1963. Elastic wave velocities in granular soils. *Journal of the Soil Mechanics and Foundations Division*, 89(1), pp.33–66.

Hasan, A. & Alshibli, K.A., 2010. Experimental assessment of 3D particle-to-particle interaction within sheared sand using synchrotron microtomography. *Géotechnique*, 60(5), pp.369–379.

Hasan, M.A., Cho, S., Remick, K., Vakakis, A.F., McFarland, D.M. & Kriven, W.M., 2014. Experimental study of nonlinear acoustic bands and propagating breathers in ordered granular media embedded in matrix. *Granular Matter*, 17(1), pp.49–72.

Hazzard, J.F., Maxwell, S.C. & Young, R.P., 1998. Micromechanical modelling of acoustic

emissions. In *Eurock 98*. Trondheim, Norway: Society of Petroleum Engineers, pp. 519–526.

Hertz, H.R., 1882. Über die Beruhrüng fester elastischer Körper. *Journal fur die reine und angewandte Mathematik*, 92, pp.156–171.

Huang, X., Hanley, K., O'Sullivan, C. & Kwok, C.Y., 2016. Implementation of rotational resistance models: a critical appraisal. *Particuology*, In press.

Ismail, M.A. & Rammah, K.I., 2005. Shear-plate transducers as a possible alternative to bender elements for measuring Gmax. *Géotechnique*, 55(5), pp.403–407.

Itasca Consulting Group, 2007. PFC3D version 4.0 user manual.

Iwasaki, T. & Tatsuoka, F., 1977. Effects of grain size and grading on dynamic shear moduli of sands. *Soils and foundations*, 17(3), pp.19–35.

Iwashita, K. & Oda, M., 1998. Rolling resistance at contacts in simulation of shear band development by DEM. *Journal of Engineering Mechanics*, 124(3), pp.285–292.

Jia, X., 2004. Codalike multiple scattering of elastic waves in dense granular media. *Physical Review Letters*, 93(15), p.154303.

Jia, X., Caroli, C. & Velický, B., 1999. Ultrasound propagation in externally stressed granular media. *Physical Review Letters*, 82(9), pp.1863–1866.

Jiang, M., Shen, Z. & Wang, J., 2015. A novel three-dimensional contact model for granulates incorporating rolling and twisting resistances. *Computers and Geotechnics*, 65, pp.147–163.

Johnson, K.L., 1985. *Contact mechanics*, Cambridge, UK: Cambridge University Press.

Kartal, M.E., Mulvihill, D.M., Nowell, D. & Hills, D., 2011. Determination of the frictional properties of titanium and nickel alloys using the digital image correlation method. *Experimental Mechanics*, 51(3), pp.359–371.

Kartal, M.E., Mulvihill, D.M., Nowell, D. & Hills, D.A., 2011. Measurements of pressure and area dependent tangential contact stiffness between rough surfaces using digital image correlation. *Tribology International*, 44(10), pp.1188–1198.

Ke, T. & Bray, J., 1995. Modeling of particulate media using discontinuous deformation analysis. *Journal of Engineering Mechanics*, 121(11), pp.1234–1243.

Kittel, C., 2004. *Introduction to solid state physics*, Wiley.

Ko, H. & Scott, R., 1967. A new soil testing apparatus. *Géotechnique*, 17(1), pp.40–57.

Krolikowski, J. & Szczepek, J., 1993. Assessment of tangential and normal stiffness of contact between rough surfaces using ultrasonic method. *Wear*, 160(2), pp.253–258.

Lawney, B.P. & Luding, S., 2014. Frequency filtering in disordered granular chains. *Acta Mechanica*, 225(8), pp.2385–2407.

Lawrence, F.V., 1965. Ultrasonic shear wave velocity in sand and clay. *Research report R65-05, Soil Publication No. 175. Massachusetts Institute of Technology, Cambridge, MA.*

Lee, J., Yun, T.S., Lee, D. Lee, J., 2013. Assessment of K_0 correlation to strength for granular materials. *Soils and Foundations*, 53(4), pp.584–595.

Lee, J. & Santamarina, J., 2005. Bender elements: performance and signal interpretation. *Journal of Geotechnical and Geoenvironmental Engineering*, 131(9), pp.1063–1070.

Leong, E.C., Cahyadi, J. & Rahardjo, H., 2009. Measuring shear and compression wave velocities of soil using bender–extender elements. *Canadian Geotechnical Journal*, 46(7), pp.792–812.

Lim, C.T. & Stronge, W.J., 1994. Frictional torque and compliance in collinear elastic collisions. *International Journal of Mechanical Sciences*, 36(10), pp.911–930.

Lings, M. & Greening, P., 2001. A novel bender/extender element for soil testing. *Géotechnique*, 51(8), pp.713–717.

Lubkin, J.L., 1951. The torsion of elastic spheres in contact. *Journal of Applied Mechanics*, 73, pp.183–187.

Madhusudhan, B.N. & Kumar, J., 2010. Effect of relative density and confining pressure on Poisson ratio from bender and extender elements tests. *Géotechnique*, 60(7), pp.561–567.

Magnanimo, V., Ragione, L. LA, Jenkins, J. T., Wang, P. & Makse, H. A., 2008. Characterizing the shear and bulk moduli of an idealized granular material. *Europhysics Letters*, 81(3), p.34006.

Makse, H.A., Gland, N., Johnson, D.L. & Schwartz, L.M., 1999. Why effective medium theory fails in granular materials. *Physical Review Letters*, 83(24), pp.5070-5073.

Makse, H. A., Gland, N., Johnson, D. L. & Schwartz, L., 2004. Granular packings: Nonlinear elasticity, sound propagation, and collective relaxation dynamics. *Physical Review E*, 70(6), pp.061302.

Makse, H.A., Johnson, D.L. & Schwartz, L.M., 2000. Packing of Compressible Granular Materials. *Phys. Rev. Lett.*, 84(18), pp.4160–4163.

Marketos, G. & O'Sullivan, C., 2013. A micromechanics-based analytical method for wave propagation through a granular material. *Soil Dynamics and Earthquake Engineering*, 45, pp.25–34.

MathWorks, 2015. MATLAB user guide.

McDowell, G. & Bolton, M., 2001. Micro mechanics of elastic soil. *Soils and foundations*, 41(6), pp.147–152.

McNamara, S.C., 2015. Acoustics and frictional sliding in granular materials. *Granular Matter*, 17(3), pp.311–324.

Medina, S., Nowell, D. & Dini, D., 2013. Analytical and numerical models for tangential stiffness of rough elastic contacts. *Tribology Letters*, 49(1), pp.103–115.

Medina, S., Olver, A. V. & Dini, D., 2012. The influence of surface topography on energy dissipation and compliance in tangentially loaded elastic contacts. *Journal of Tribology*, 134(1), p.011401.

Mindlin, R.D., 1949. Compliance of elastic bodies in contact. *Journal of Applied Mechanics*, 16, pp.259–268.

Mindlin, R.D. & Deresiewicz, H., 1953. Elastic spheres in contact under varying oblique forces. *American Society of Mechanical Engineers - Transactions - Journal of Applied Mechanics*, 20(3), pp.327–344.

Mitchell, J.K. & Soga, K., 2005. *Fundamentals of soil behavior* 3rd ed., Hoboken, New Jersey: John Wiley and Sons Ltd.

Mouraille, O., 2009. *Sound propagation in dry granular materials : discrete element simulations, theory, and experiments*. PhD thesis, University of Twente.

Mouraille, O. & Luding, S., 2008. Sound wave propagation in weakly polydisperse granular materials. *Ultrasonics*, 48(6-7), pp.498–505.

Mouraille, O., Mulder, W.A. & Luding, S., 2006. Sound wave acceleration in granular materials. *Journal of Statistical Mechanics: Theory and Experiment*, 07(23), pp.1–15.

Mulvihill, D.M., Brunskill, H., Kartal, M.E., Dwyer-Joyce, R.S. & Nowell, D., 2013. A comparison of contact stiffness measurements obtained by the digital image correlation and ultrasound techniques. *Experimental Mechanics*, 53(7), pp.1245–1263.

Nakagaki, M. & Sunada, H., 1963. Theoretical calculation of sedimentation volume. III. The case of spherical particles without drawing interaction. *Yakugaku Zassi*, 83(1), pp.73–78.

Nakagaki, M. & Sunada, H., 1968. Theoretical studies on structures of the sedimentation bed of spherical particles. *Yakugaku Zassi*, 88(6), pp.651–655.

Nayak, P.R., 1973. Some aspects of surface roughness measurement. *Wear*, 26(2), pp.165–174.

NikonMetrology, 2013. CT Pro 3D user manual.

O'Connor, J.J. & Johnson, K.L., 1963. The role of surface asperities in transmitting tangential forces between metals. *Wear*, 6(2), pp.118–139.

O'Donovan, J., O'Sullivan, C., Marketos, G. & Muir Wood, D., 2015a. Analysis of bender element test interpretation using the discrete element method. *Granular Matter*, 17(2), pp.197–216.

O'Donovan, J., O'Sullivan, C., Marketos, G. & Muir Wood, D., 2015b. Anisotropic stress and shear wave velocity: DEM studies of a crystalline granular material. *Géotechnique Letters*, 5(3), pp.224–230.

O'Donovan, J., Ibraim, E., O'Sullivan, C., Hamlin, S., Muir Wood, D. & Marketos, G., 2016. Micromechanics of seismic wave propagation in granular materials. *Granular Matter,* 18, 56.

O'Donovan, J., 2013. *Micromechanics of Wave Propagation through Granular Material*. PhD thesis, Imperial College London.

O'Donovan, J., O'Sullivan, C. & Marketos, G., 2012. Two-dimensional discrete element modelling of bender element tests on an idealised granular material. *Granular Matter*, 14(6), pp.733–747.

O'Sullivan, C., 2014. Advancing geomechanics using DEM. In K. Soga et al., eds. *Proceedings of the TC105 ISSMGE iInternational Symposium on Geomechanics from Micro to Macro, IS-Cambridge 2014*. Cambridge, UK: CRC Press, pp. 21–32.

O'Sullivan, C. & Bray, J.D., 2004. Selecting a suitable time step for discrete element simulations that use the central difference time integration scheme. *Engineering Computations*, 21(2/3/4), pp.278 – 303.

Oda, M., 1977. Co-ordination number and its relation to shear strength of granular material. *Soils and foundations*, 17(2), pp.29–42.

Okuyama, K., Fujiwara, M., Ochi, H. & Inoue, M., 1999. Expansion of maximum particle size limitation value in test for maximum and minimum densities of sands (in Japanese). *Journal of Japan Society of Civil Engineers*, 638(Ⅲ-49), pp.11–27.

Otsubo, M., O'Sullivan, C., Sim, W. & Ibraim, 2015. Quantitative assessment of the influence of surface roughness on soil stiffness. *Géotechnique*, 65(8), pp.694–700.

Otsubo, M., O'Sullivan, C., Hanley, K. & Sim, W., 2016. The influence of particle surface roughness on elastic stiffness and dynamic response. *Géotechnique,* DOI: 10.1680/jgeot.16.P.050 (In press).

Otsubo, M., O'Sullivan, C. & Shire, T., 2017. Empirical assessment of the critical time increment in explicit particulate discrete element method simulations. *Computers and Geotechnics*, 86, pp.67–79.

Otsubo, M., O'Sullivan, C. & Sim, W., 2014. A methodology for accurate roughness measurements of soils using optical interferometry. In K. Soga et al., eds. *Proceedings of the TC105 ISSMGE iInternational Symposium on Geomechanics from Micro to Macro, IS-Cambridge 2014*. Cambridge, UK: CRC Press, pp. 1117–1122.

Otsubo, M., Sim, W. & O'Sullivan, C., 2015. Experimental assessment of the influence of load-induced deformation on interparticle contacts. In *Int. Symp. on Deformation Characteristics of Geomaterials, Buenos Aires*. pp. 535–542.

Ouchiyama, N. & Tanaka, T., 1980. Estimation of the average number of contacts between randomly mixed solid particles. *Industrial & Engineering Chemistry Fundamentals*, 19(4), pp.338–340.

Paggi, M., Pohrt, R. & Popov, V.L., 2014. Partial-slip frictional response of rough surfaces. *Scientific Reports*, 4, p.5178.

Pinson, D., Zou, R.P., Yu, A.B., Zulli, P. & McCarthy, M., 1998. Coordination number of binary mixtures of spheres. *Journal of Physics D: Applied Physics*, 31(4), pp.457–462.

Plimpton, S., 1995. Fast parallel algorithms for short-range molecular dynamics. *Journal of Computational Physics*, 117(1), pp.1–19.

Potts, D., 2003. Numerical analysis-a virtual dream or practical reality. *Geotechnique*, 53(6), pp.535–573.

Pouliquen, O., Nicolas, M. & Weidman, P.D., 1997. Crystallization of non-Brownian spheres under horizontal shaking. *Physical Review Letters*, 79(19), pp.3640–3643.

Radin, C., 2008. Random close packing of granular matter. *Journal of Statistical Physics*, 131(4), pp.567–573.

Ridgway, K. & Tarbuck, K.J., 1967. The random packing of spheres. *British Chemical Engineering*, 12, pp.384–388.

Rothenburg, L. & Bathurst, R.J., 1989. Analytical study of induced anisotropy in idealized granular materials. *Géotechnique*, 39(4), pp.601–614.

Sadek, T., 2006. *The multiaxial behaviour and elastic stiffness of hostun sand*. PhD thesis, The University of Bristol.

Sanchez-Salinero, I., Roesset, J.M. & Stokoe, K., 1986. *Analytical studies of body wave propagation and attenuation*, Report GR 86-15, Civil Engineering Department, University of Texas at Austin.

Santamarina, J.C. & Cascante, G., 1998. Effect of surface roughness on wave propagation parameters. *Géotechnique*, 48(1), pp.129–136.

Santamarina, J.C. & Aloufi, M., 1999. Small strain stiffness : A micromechanical experimental study. In M. Jamiolkowski, R. Lancellotta, & D. Lo Presti, eds. *Proceedings of pre-failure deformation charactertics of geomaterials*. Torino, Italy: A.A. Balkema, Rotterdam, pp. 451–458.

Santamarina, J.C. & Cascante, G., 1996. Stress anisotropy and wave propagation: a micromechanical view. *Canadian Geotechnical Journal*, 33(5), pp.770–782.

Santamarina, J.C., Klein, K.A. & Fam, M.A., 2001. *Soils and waves*, Hoboken, New Jersey: John Wiley and Sons Ltd.

Scott, G.D., Charlesworth, A.M. & Mak, M.K., 1964. On the Random Packing of Spheres. *The Journal of Chemical Physics*, 40(2), pp.611–612.

Scott, G.D. & Kilgour, D.M., 1969. The density of random close packing of spheres. *British Journal of Applied Physics*, 2(6), pp.863–866.

Senetakis, K., Coop, M.R. & Todisco, M.C., 2013(a). The inter-particle coefficient of friction at the contacts of Leighton Buzzard sand quartz minerals. *Soils and Foundations*, 53(5), pp.746–755.

Senetakis, K., Todisco, M.C. & Coop, M.R., 2013(b). Tangential load–deflection behaviour at the contacts of soil particles. *Géotechnique Letters*, 3(2), pp.59–66.

Sharifipour, M. & Dano, C., 2006. Effect of grains roughness on waves velocities in granular packings. In Proceedings of the 1st EuroMediterranean symposium on advances on geomaterials and structure, Hammamet, Tunisia (ed. F. Darve). pp. 123–128. Tunis, Tunisia: LGC-ENIT (Laboratoire de Génie Civil, LGC ENIT).

Sherif, H.A. & Kossa, S.S., 1991. Relationship between normal and tangential stiffness of nominally flat surfaces. *Wear*, 151(1), pp.49–62.

Shire, T. & O'Sullivan, C., 2013. Micromechanical assessment of an internal stability criterion. *Acta Geotechnica*, 8(1), pp.81–90.

Shirley, D., 1978. An improved shear wave transducer. *The Journal of the Acoustical Society of America*, 63(5), pp.1643–1645.

Shirley, D.J. & Hampton, L.D., 1978. Shear-wave measurements in laboratory sediments. *The Journal of the Acoustical Society of America*, 63(2), pp.607–613.

Smith, W.O., Foote, P.D. & Busang, P.F., 1929. Packing of homogeneous spheres. *Physical Review*, 34(9), pp.1271–1274.

Somfai, E., Roux, J.N., Snoeijer, J.H., van Hecke, M. & van Saarloos, 2005. Elastic wave propagation in confined granular systems. *Physical Review E*, 72(2), pp.021301.

Suwal, L.P.L. & Kuwano, R., 2013. Disk shaped piezo-ceramic transducer for P and S wave measurement in a laboratory soil specimen. *Soils and Foundations*, 53(4), pp.510–524.

Suzuki, M., Makino, K., Yamada, M. & Iinoya K., 1981. A study on the coordination number in a system of randomly packed, uniform-sized spherical particles. *International Chemical Engineering*, 21(3), pp.482–488.

Taylor, H., 2016. *Assessing the potential for suffusion in sands using x-ray micro-CT images*. PhD thesis, Imperial College London.

The Japanese Geotechnical Society, 2009. Test method for minimum and maximum densities of sands, JGS 0161:2009 (JIS A 1224:2009).

Thomas, C.N., Papargyri-beskou, S. & Mylonakis, G., 2009. Wave dispersion in dry granular materials by the distinct element method. *Soil Dynamics and Earthquake EngineeringDynamics*, 29(5), pp.888–897.

Thomas, T.R., 1982. *Rough surfaces*, London: Imperial College Press.

Thornton, C., 2000. Numerical simulations of deviatoric shear deformation of granular media. *Géotechnique*, 50(1), pp.43–53.

Thornton, C., 1979. The conditions for failure of a face-centered cubic array of uniform rigid spheres. *Géotechnique*, 29(4), pp.441–459.

Thornton, C., Cummins, S.J. & Cleary, P.W., 2011. An investigation of the comparative behaviour of alternative contact force models during elastic collisions. *Powder Technology*, 210(3), pp.189–197.

Thornton, C. & Yin, K., 1991. Impact of elastic spheres with and without adhesion. *Powder technology*, 65, pp.153–166.

Ting, John M., Corkum, Brent T., Kauffman, Claudia R. & Greco, Carlo, 1989. Discrete numerical model for soil mechanics. *Journal of Geotechnical Engineering*, 115(3), pp.379–398.

Tory, E. M., Church, B. H., Tam, M. K. & Ratner, M., 1973. Simulated random packing of equal spheres. *The Canadian Journal of Chemical Engineering*, 51(4), pp.484–493.

Viggiani, G. & Atkinson, J.H., 1995. Interpretation of bender element tests. *Géotechnique*, 45(1), pp.149–154.

Walton, K., 1987. The effective elastic moduli of a random packing of spheres. *Journal of the*

Mechanics and Physics of Solids, 35(2), pp.213–226.

Wan-Manshol, W., 2015. *Experimental study of the influence of loads and packing density on coordination number*. MSc thesis, Imperial College London.

Xu, X., Cheng, Y. & Ling, D., 2013. The influence of void ratio on small strain shear modulus of granular materials: A micromechanical perspective. In *AIP Conference Proceedings*. pp. 201–204.

Xu, X.M., Ling, D.S., Cheng, Y.P. & Chen, Y.M., 2015. Correlation between liquefaction resistance and shear wave velocity of granular soils: a micromechanical perspective. *Géotechnique*, 65(5), pp.337–348.

Yamashita, S., Kawaguchi, T., Nakata, Y., Mikami, T., Fujiwara, T. & Shibuya, S., 2009. Interpretation of international parallel test on the measurement of Gmax using bender elements. *Soils and Foundations,*, 49(4), pp.631–650.

Yang, H., Baudet, B.A. & Yao, T., 2016. Characterization of the surface roughness of sand particles using an advanced fractal approach. *Proceedings of the Royal Society A: Mathematical, Physical and Engineering Sciences*, 472(2194), pp.1–20.

Yang, J., Silvestro, C., Khatri, D., De Nardo, L. & Daraio, C., 2011. Interaction of highly nonlinear solitary waves with linear elastic media. *Physical Review E - Statistical, Nonlinear, and Soft Matter Physics*, 83(4), pp.046606.

Yimsiri, S. & Soga, K., 2000. Micromechanics-based stress–strain behaviour of soils at small strains. *Géotechnique*, 50(5), pp.559–571.

Yoshioka, N. & Scholz, C., 1989. Elastic properties of contacting surfaces under normal and shear loads: 1. Theory. *Journal of Geophysical Research*, 94(B12), pp.17,681–17,690.

Yoshioka, N. & Scholz, C., 1989. Elastic properties of contacting surfaces under normal and shear loads: 2. Comparison of theory with experiment. *Journal of Geophysical Research*, 94(B12), pp.17,691–17,700.

Zhang, L. & Thornton, C., 2005. Characteristics of granular media at the “critical state.” In R. García-Rojo, H. J. Herrmann, & S. McNamara, eds. *Powders and Grains 2005*. Stuttgart, Germany: CRC Press, pp. 267–270.

Zhang, Z.P., Liu, L.F., Yuan, Y.D. & Yu, A.B., 2001. A simulation study of the effects of dynamic variables on the packing of spheres. *Powder technology*, 116(1), pp.23–32.

Zienkiewicz, O.C. & Taylor, R.L., 2000. *The finite element method*, Butterworth Heinemann.

Appendix A

Referring to Section 5.5.2 this appendix derives the layer stiffness (C^{FCC}) for a face-centred cubic (FCC) packing associated with a *P*-wave mode. Fig. A(a) shows a representative image for a FCC packing composed of 8 spheres. In accordance with Chapter 5, the three orthogonal axes shown are X, Y and Z. The FCC array has a transverse isotropy and the view of the XZ and YZ planes are identical (Fig. A(b)). In addition to the three axes, an axis J is defined here to be X = Y in the XY plane (Fig. A(c)). This study considers a *P*-wave mode propagating along the Z-axis only.

The X, Y and Z coordinates of the particles in the bottom layer (1, 2, 3, 4) are given by:

1: $(0,0,0)$ 2: $(2R,0,0)$ 3: $(0,2R,0)$ 4: $(2R,2R,0)$

where R = particle radius, and the coordinates of the particles in the upper layer (5, 6, 7, 8) are:

5: $\left(R,R,\sqrt{2}R\right)$ 6: $\left(3R,R,\sqrt{2}R\right)$ 7: $\left(R,3R,\sqrt{2}R\right)$ 8: $\left(3R,3R,\sqrt{2}R\right)$

Considering (a) the transverse isotopy in the XY plane, (b) an assumption of uniform strain fields (kinematic assumption), and (c) *P*-wave motion in the Z-axis, there is no interaction between the neighbouring particles in the XY plane, e.g. 1 & 2 or 7 & 8. Thus the stiffness in the same XY plane can be ignored. Note that if the particle deforms due to an applied force, this assumption is not strictly valid.

As there is no interaction in the horizontal plane the inter-particle responses between particle 5 and the particles in the bottom layer can be considered. From the assumptions above it is deduced that the inter-particle response is identical for sets of particles 1 & 5, 2 & 5, 3 & 5, and 4 & 5. Thus it is sufficient to consider the contact response between particles 1 and 5. The unit vector from the centre of particle 1 to the centre of particle 5 (the branch vector) is given by:

$$\overrightarrow{n_{15}^{XYZ}} = \frac{1}{2}\left(1,1,\sqrt{2}\right) \tag{A.1}$$

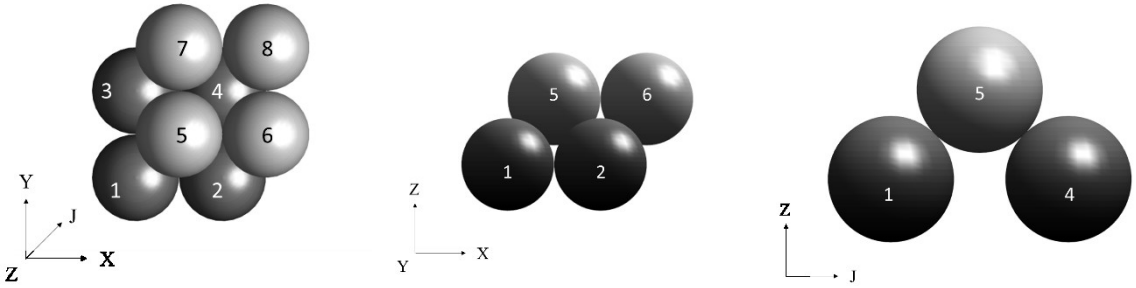

(a) (b) (c)

Figure A. Images of FCC packing. (a) XY plane, (b) XZ plane and (c) JZ plane.

To reduce the three-dimensional problem to two dimensions the contact response in the JZ plane can be considered (Fig. A(c)). In this case, the branch vector becomes:

$$\overrightarrow{n_{15}^{JZ}} = \frac{1}{\sqrt{2}}(1,1) \tag{A.2}$$

The displacement of particle 1 in the Z direction (Δu_z) can be decomposed into the incremental contact overlap ($\Delta\delta$) and the incremental tangential displacement (Δs) as illustrated in Fig. B(a). As the angle between $\overrightarrow{n_{15}}$ and the Z axis is $\pi/4$ in the JZ plane, $\Delta\delta$ and Δs can be expressed as:

$$\begin{aligned} \Delta\delta &= \cos\left(\frac{\pi}{4}\right)\Delta u_Z = \frac{1}{\sqrt{2}}\Delta u_Z \\ \Delta s &= \sin\left(\frac{\pi}{4}\right)\Delta u_Z = \frac{1}{\sqrt{2}}\Delta u_Z \end{aligned} \tag{A.3}$$

The resultant normal contact force (ΔN) and tangential contact force (ΔT) can be expressed using the incremental normal contact stiffness (k_N^{FCC}) and tangential contact stiffness (k_T^{FCC}) as:

$$\begin{aligned} \Delta N &= k_N^{FCC}\Delta\delta = \frac{1}{\sqrt{2}}k_N^{FCC}\Delta u_Z \\ \Delta T &= k_T^{FCC}\Delta s = \frac{1}{\sqrt{2}}k_T^{FCC}\Delta u_Z \end{aligned} \tag{A.4}$$

The virtual work done in the system can be determined. The internal work ($W_{internal}$) done inside the sample is the summation of the incremental contact strain energy in the normal and tangential directions as:

$$W_{\text{int}ernal}^{15} = \Delta N\,\Delta\delta + \Delta T\,\Delta s = \frac{1}{2}\left(k_N^{FCC} + k_T^{FCC}\right)\Delta u_Z^2 \tag{A.5}$$

There are four identical contact configurations involving particle 5, i.e. 1 & 5, 2 & 5, 3 & 5 and 4 & 5; so the internal work is multiplied by 4, giving:

$$W_{\text{int}ernal} = 2\left(k_N^{FCC} + k_T^{FCC}\right)\Delta u_Z^2 \tag{A.6}$$

The external work ($W_{external}$) is done by the displacement of particle 1 (Δu_z) multiplied by the reaction force that can be expressed using the layer stiffness C^{FCC} as:

$$W_{external} = \left(C^{FCC}\Delta u_Z\right)\Delta u_Z = C^{FCC}\Delta u_Z^2 \tag{A.7}$$

As $W_{external} = W_{internal}$,

$$C^{FCC} = 2\left(k_N^{FCC} + k_T^{FCC}\right) \tag{A.8}$$

This is identical to Eq. 5.5.5 in Section 5.5.2.

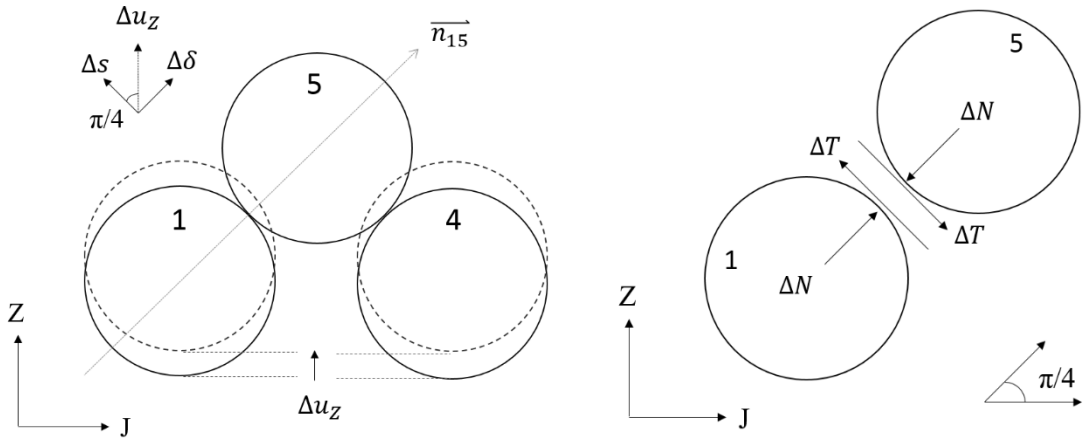

(a) (b)

Figure B. Schematic illustration of contact response between particle 1 and particle 5.